Politecnico di Torino

ScuDo
Scuola di Dottorato ~ Doctoral School
WHAT YOU ARE, TAKES YOU FAR

Doctoral Dissertation
Doctoral Program in Mathematics (36^{th}cycle)

Epigenetic and geometrical characterisation of cancer cell populations

A personalised-medicine oriented mathematical study of tumour evolutionary dynamics and therapies

By

Giulia Chiari

******

Supervisor(s):
Prof. Marcello Edoardo Delitala, Supervisor
Prof. Federico Frascoli, Co-Supervisor

Doctoral Examination Committee:
Prof. Haralampos Hatzikirou, Referee, Full Professor, Khalifa University, Abu Dhabi, UAE/ TU Dresden, Germany
Prof. Thomas Stiehl, Referee, Professor, RWTH Aachen University, Germany

Politecnico di Torino
2024

Declaration

I hereby declare that, the contents and organization of this dissertation constitute my own original work and does not compromise in any way the rights of third parties, including those relating to the security of personal data.

Giulia Chiari
2024

* This dissertation is presented in partial fulfillment of the requirements for **Ph.D. degree** in the Graduate School of Politecnico di Torino (ScuDo).

Durante le sedute di EMDR ti chiedono di mettere a fuoco
delle immagini precise alle quali tornare.
Dei porti sicuri.

Queste pagine, ma forse più questi anni,
sono dedicati ai posti in cui tornerei sempre a rifugiarmi,
fatti di pelle e scogli, di alberi e respiro.

A quei luoghi e quelle persone che mi hanno accolto nelle mie mancanze,
che mi hanno mostrato ciò che non so vedere,
che mi hanno infuso la forza di affrontare
ciò che mi fa sentire troppo piccola
e di azzardare quando ho paura di credere.

Alla mia Stellina, l'abbraccio più caldo della mia esistenza.
Riparo e strapiombo, maestro di cura e avventatezza,
esempio infinito di amore.
E a chiunque trovi un posto tra queste parole.

Grazie.

Abstract

Cancer can be considered a complex system consisting of a heterogeneous cell population interacting with its environment. Cancer cellular behaviour is guided by intrinsic rules and regulatory dynamics in the interplay with abiotic factors and other cell populations. This influences not only the evolutionary history of the tumour mass in the organism but also its reaction to applied therapies. Moreover, the therapies themselves and the selective pressure exerted by the environment in turn influence the composition of the tumour mass and its evolution in time.

The complexity and the overlap of all these processes make it difficult to find a biologically coherent explanation or observe the underlying dynamics of numerous emerging phenomena. The idea behind the use of mathematical modelling in the biological field, specifically oncology here, is to provide a tool that, built on the scientific knowledge we possess, can fill the gap with the observed phenomena.

In this thesis, with the aim of investigating the phenomena of resistance and relapse in cancer treatment, we focus on characteristics of the tumour mass that are relevant both for their impact on the outcome of therapies and for the benefit of the use of the mathematical tool: geometry and heterogeneity.

In detail, with geometry, we refer to the growth, movement, shape, and spatial location of the mass. Addressing heterogeneity, we consider the different genetic and epigenetic signatures that characterize cell subpopulations, altering, together with environmental conditions, their phenotype.

In order to catch these features, in the various models of the thesis, spatial PDEs are adopted and structured or multiple cell populations are employed, with a predominance of non-local continuous modelling strategies with multi-scale derivation. In all our models, the description of the tumour population is characterized by proliferative, mortality, and motile dynamics and the (epi)genetic signature determines the performance potential of each. Furthermore, when considered in the models,

external factors are directly entered into the framework. In particular, we consider the interaction with abiotic factors and other populations.

In this thesis, great importance among the environmental factors is given to the oxygenation state of the tissues. Many of the models we present include hypoxia, considering its influence on proliferativity as its regulator, on mortality as a selective pressure, and on cell movement as a trigger of chemotactic drift.

Particular attention is given to anti-tumour processes, which include the defence reaction of the immune system and therapies, such as radiotherapy and oncolytic virotherapy. Even when studying treatments, the influence of oxygenation is taken into account.

Both the works already carried out and the future perspectives move in the direction of therapeutic optimization from a personalised medicine perspective. In this sense, mathematical modelling represents an adjuvant tool alongside clinical analysis in the diagnosis and treatment. The final aim is to propose an alternative to the systematic use of standard protocols and against the paradigm of aiming at eradication as the only therapeutic strategy, in the attempt to avoid the emergence of relapses and extend patient's life, keeping its quality as uncompromised as possible.

Contents

Introduction

Almost every paper on mathematical modelling for oncology begins with citations of global cancer mortality statistics. I think it is not necessary. The evidence of the criticality of the presence of this disease occurs daily in everyone's life through direct experience or contact.
The motivation for this thesis is among the most banal in research: when faced with something scary and painful, try to use what you have to do something. Readers will forgive me for the lack of scientific language (which will even get boring in the following pages), but the point is that cancer is ugly, but above all, difficult to observe and understand.
When it comes to cancer, the biggest problem is not understanding. Not understanding the cause-effect relationships and the activation pathways that govern its behaviour and not understanding the dynamics by which treatments that work on paper result in outcomes that are often only temporarily successful and then end in resistance, recurrences and mortality.
The mathematical tool tries to fill the gap between the scientific knowledge acquired and the medical observations, in the attempt to bring to light underlying unobservable dynamics motivating unexplained phenomena.

This thesis focuses on the study of tumour masses in their evolutionary dynamics, considering the changes in shape and cellular composition and analysing the contribution of the interaction with the environment on the history of the cancer cell population.
Specifically, we consider oxygen concentration a predominant factor in delineating evolutionary processes, and we investigate dynamics such as movement, proliferation, and survival. These emerging traits of the tumour mass are analysed as a

characterisation of its features and as factors in the reaction to the immune system, as well as clinical treatments, e.g. radiotherapy and oncolytic virotherapy.
The general perspective of the entire thesis is that of personalised medicine, with the aim of making the mathematical tool a continuous map between the patient, the evolutionary history of the tumour and the outcomes of the various therapies, being able to optimize the treatment based on specific, individual characteristics.

We now present a brief map of the contents. The thesis is structured in three parts. **Part I** introduces the biological and mathematical framework for the works. It provides all the basic knowledge needed to understand the mathematical models introduced in the various chapters and the biological processes described. A general state of the art is included. **Part II** collects all the research results obtained so far, including the contents of already published or submitted papers. **Part III** presents ongoing works and future perspectives and finally summarizes the current point of arrival and future steps.

Let us firstly consider **Part I**.

In **Chapter 1**, we introduce the needed biological background to understand the tumour dynamics involved in our mathematical models. All specific biological terms used in this section, which may not be immediately clear to the reader and cannot be introduced in detail for the sake of conciseness, are exhaustively explained in this chapter. We begin by introducing some basic knowledge on the biology of normal cells and then pass on to enlighten the differences between cancer cells and the different levels of heterogeneity expressed in cancer cell populations. After presenting cancer cells and their characteristics, we introduce essential information on their interaction with the microenvironment. We exploit dynamics such as angiogenesis and invasion to underline the fundamental role of signalling and epigenetic mutation. Moreover, we describe the interaction between tumour cells and the immune system, concentrating on immunoevasion dynamics. We then move to therapies, giving an overview of clinical strategies and focusing on two treatments we model later in the thesis: radiotherapy and oncolytic virotherapy. Finally, we explain the meaning of analysing cancer as an evolutionary process, enlightening its multi-scale nature, describing it in its temporal phases, and considering the trade-offs that its cells face. At the end of the chapter, we explicitly state each notion's relevance in the models we present in the subsequent chapters.

In **Chapter 2** we present an overview on the adoptable mathematical strategies in order to catch the biological dynamics introduced in the previous chapter. We explain the role and interest of mathematical modelling in oncology, providing a characterisation of the main strategies (continuous/discrete/hybrid, deterministic/stochastic) and describing the pros and cons of different approaches. Given the wide range of themes, we present a common review of mathematical models for the general subject and then introduce a specific state of the art for each single theme in the relative section of each chapter. We then specify which strategies are adopted in the models we introduce in the following chapters.

We then move to overview **Part II**, in which each chapter presents a different model, each built for the investigation of a specific dynamic (every chapter refers to an already published or submitted paper). With a generic map, Chapter 3 and 4 are linked by common dynamics of proliferation and survival with respect to the oxygenation of the environment, considering the cancer mass evolution (Chapter 3) or also radiotherapy (Chapter 4). Chapter 5 and 6 are related due to the presence of migratory dynamics, with a specific interest in environmental-driven invasive and metastatic dynamics (Chapter 5) and epigenetic characterisation of EMT dynamics (Chapter 6).

Let us analyse the content of the various chapters a little more in detail.

Chapter 3 concentrates on cancer evolution, particularly in the critical tumour-environment interaction. We focus on the central role of oxygen concentration in determining the phenotypic heterogeneity of cancer cell populations, whose qualitative and geometric characteristics are predominant factors in determining the outcome of the cancer mass history. Contents of this chapter are published in Ref. [112]. We propose a mathematical model able to describe the eco-evolutionary spatial dynamics of tumour cells in their adaptation to hypoxic microenvironments. As a main novelty with respect to the existing literature, we combine an epigenetic indicator reflecting the experimentally observed metabolic trade-off between the hypoxia-resistance ability and the proliferative potential with a 2d geometric domain without the constraint of radial symmetry. The model is settled in the mathematical framework of epigenetically structured population dynamics, and it is formulated in terms of systems of coupled nonlinear integro-differential equations. The computational outcomes demonstrate that hypoxia-induced selection results in a geometric characterisation of phenotypic-defined tumour niches that impact tumour

aggressiveness and invasive ability. Furthermore, results show how the knowledge of environmental characteristics provides a predictive advantage on tumour mass development in terms of size, shape, and composition.

In **Chapter 4**, we stick to the context of the previous chapter but insert radiotherapy as a treatment. We consider the pivotal role of eco-evolutionary dynamics in the study of therapeutic strategies for cancer treatment. Contents of this chapter are published in Ref. [111]. Keeping our interest on the geometric and epigenetic characterisation of the tumour, we analyse the impact of the characteristics of the tumour population, the interaction with the environment, and the effects of the treatment. These different triggers have direct consequences on the efficacy of the therapy and possible relapses. In particular, considering radiotherapy, we investigate the central role played by oxygen concentration both in determining the effectiveness of the treatment and the selective pressure due to hypoxia. In the chapter, we propose a mathematical model, settled in the framework of epigenetically structured population dynamics and formulated in terms of systems of coupled nonlinear integro-differential equations, that aims to catch these phenomena and provide a predictive tool for the tumour mass evolution and therapeutic effects. The outcomes of the simulations show how the model is able to explain the impact of environmental selection and therapies on the evolution of the mass, motivating observed dynamics such as relapses and therapeutic failures. Furthermore, it offers a first hint for developing therapies that can be adapted to overcome resistance and relapse problems.

In **Chapter 5**, we focus on epithelial-mesenchymal transition in cancer cells and introduce novel hybrid modelling for it. Contents of this chapter are published in Ref. [110]. In order to take into account the typical heterogeneous and time-evolving composition of cell populations in biological systems, and in particular in cancer masses, we propose a modelling framework in which a discrete structuring variable distinguishes cells according to their genotype while a specific mathematical representation (i.e., individual/pointwise vs. collective/density-based) is assigned to each individual based on its phenotypic hallmarks. We provide a mathematical expression of phenotypic plasticity, accounting for the role played by stochasticity and environmental conditions. The modelling environment is then enriched with migratory dynamics, duplication/apoptotic processes, and chemical kinetics. We apply the resulting model to the scenario of a heterogeneous tumour aggregate cultured in vitro.

In **Chapter 6**, we pay particular attention to the critical phenomenon of tumour cell migration within their microenvironment in the intricate landscape of cancer progression. Again, we put specific interest on hypoxia as a potent factor influencing tumour behaviour in this context. We analyse how insufficient oxygen levels act as a stressor on cells, prompting them to exhibit biased migration and undergo phenotypic changes. Concerning this, in this chapter, we concentrate on the role of Snail transcription factors, which play a central role in how cells respond to hypoxic conditions since they influence various cellular processes such as epithelial-mesenchymal transition, migration, proliferation, and invasiveness. We propose an innovative multi-scale mathematical model to address the intricate interplay of cellular and molecular dynamics underlying tumour migration. This model seamlessly integrates single-cell behaviour driven by Snail expression with macroscopic tumour migration dynamics. Initially, we formulate kinetic transport equations that delineate the evolution of cell distribution based on detailed microscopic dynamics. Subsequently, utilizing appropriate scaling principles, we derive equations describing the statistical properties of the cell distribution. These equations capture migratory dynamics influenced by dispersion, oxygen-mediated drift, and the evolving average Snail expression within the tumour cell population. We conduct numerical simulations across diverse biologically relevant scenarios, providing insights into the role of chemotactic-driven motion, anti-crowding effects, and the impact of Snail expression on cell proliferation. Qualitative validation against experimental data demonstrates the model's capacity to reproduce hypoxia-induced migration patterns and gradients of Snail expression observed in tumour tissues. Moreover, quantitative comparison with experimental data validates the model's efficacy in assessing the impact of Snail transcription on cell migratory potential. These findings underscore the potential of our mathematical framework as a promising approach to integrate molecular signalling pathways with cell dynamics, offering novel interpretations of experimental data and advancing our understanding of the biological mechanisms driving tumour progression. This investigation is presented in a preprint [109]), submitted in April 2024 to *Communications in Nonlinear Science and Numerical Simulation* journal.

Finally, we present **Part III**, in which we keep a similar chapter organisation as in the previous part (with the only difference that works inserted here are still under investigation) and finally present an overview of the current state of research, underlining what has already been "concluded" and which are the future perspectives. Chapter 7 keeps a link with Chapter 5 and Chapter 6 concerning migration dynamics

focusing on go or/and grow dynamics. Chapter 8 introduces an independent analysis of oncolytic virotherapy to open the path to a possible combination of radiotherapy in further works. Chapter 9 introduces the immune system with a future perspective on immunotherapy.

In particular, in **Chapter 7**, we present six models grouped under two modelling strategies for cell movement: Fisher-like and anti-crowding. For every strategy, we propose three different models differentiated for the epigenetic structure choice adopted for the cell population: no epigenetic structure, a structure based on the proliferative epigenetic trait or a double structure based on both proliferative and motility epigenetic traits. The idea behind the work is the investigation of the stratification of tumour spheroids that present an inner quiescent core and an outer proliferative near the edge, beyond which fingers of motile cell populations infiltrate healthy tissue. In this model, we neglect the investigation of the environmental impact to focus on how the dynamics of proliferation and migration, influenced by the heterogeneity and epigenetic evolution of the cell population, can alone confer to the tumour mass: (i) growth speed and shape characterisation (ii) specific geometric features to the epigenetic and phenotypic traits. The results obtained so far are part of a joint project with the Mathematical Oncology Laboratory (MOLAB) in Ciudad Real.

In **Chapter 8**, we focus again on environmental factors and therapies, introducing a novel mathematical approach to oncolytic virotherapy, accounting for the effect of hypoxia. Results are related to the modelling approach adopted in Chapter 3 and Chapter 4, we build our model in order to catch the evolutionary dynamics of a tumour population that we differentiated in uninfected cells, epigenetically structured, and infected cells, all grouped despite their characteristic trait. The epigenetic variable confers a trade-off between the proliferative rate on one side and the resistance both to the killing action of the virus and hypoxia on the other side. Other agents included in the model are the virus and the oxygen. The main idea of the work is to determine the impact of the epigenetic evolution of the mass, both in terms of composition and geometry, on the effectiveness of the treatment, evaluated in terms of eradication or growth control of the tumour mass. In the first moment, the investigation treats a simple scenario with homogeneous oxygen distribution in a stationary state. Then, we move to spatially heterogeneous abiotic conditions. Finally, the study aims to consider scenarios in which both the presence of the tumour itself and the tissue characterisation cause a time evolution of the environmental state

in terms of oxygenation. This chapter contains partial results of a joint work with Prof. Federico Frascoli (Swinburne University of Technology) and David Morselli (Politecnico di Torino, Università di Torino, Swinburne University of Technology) (currently under submission).

In **Chapter 9**, we present the early results of an initiated project in collaboration with Professor José A. Carrillo (Oxford University). We start from an already presented model built to describe the behaviour of two cell populations, characterised by adhesive properties, which cohabit in a shared space, and we propose an adaptation of the same to catch interaction dynamics between the cancer population and the immune system. In particular, we start to characterize the cancer population in terms of proliferative rate, detectability by the immune system and death factor due to the immune action. We propose a trade-off between the first trait and the second two, supposing that highly proliferative cells are more visible and less resistant to immune action. We are first interested in the effect of these rates on (i) the possibility of eradication and (ii) the outcome in terms of hot/cold tumours. Moreover, we pass to consider a heterogeneous cancer population, admitting (at the first moment) two subpopulations with opposite features (one highly proliferative, one highly resistant). We aim to investigate the effect of the proportion of the two subpopulations and their spatial location in the tumour mass on the outcomes (considered as above). This initial setting opens the path to a structured population model.

In the **Conclusions**, we summarize the results obtained and the future perspectives specifically related to each work and already presented in every chapter. We deduce a *fil rouge*, which we show as a proposed path for the next steps in this research direction.

Part I

Framework and basic knowledge

Chapter 1

Biological framework

According to the US National Cancer Institute, a tumour is defined as an abnormal mass of tissue that forms when cells grow and divide more than they should or do not die when they should. Cancer is a group of diseases caused by the uncontrolled growth and spread of abnormal cells. Tumours can be cancerous, but not all tumours are. Despite this, in this discussion, we consider cancerous tumours, and for this reason, we refer indiscriminately to cancer or tumour cells.

If seen from a physical point of view, a tumour can be considered a mass; from a population point of view, it is a set of cells (precisely a population) governed by dynamics involving displacement and metabolic activity. Moreover, it is a population composed of different subpopulations, each of which is characterised by a distinctive signature.

Cancer cells, coming from but distinct from normal cells, are distinguished by well-known characteristics such as proliferating uncontrollably, resisting death and manipulating their surroundings for survival, breaking the usual cellular order. Emerging from the normal somatic cell features, they evolve selfish traits, prioritising individual fitness over the multicellular group [193]. Interactions among cancer cells and with normal cells create complex tumours with organised systems. Diversifying to occupy ecological niches, cancer cell communities exhibit cooperation within and between subpopulations (also called *clones*) [87]. However, the drivers of these interactions and the transition from exploiting cooperation with normal cells to engaging in cooperative behaviours with other cancer cells remain unclear.

In order to simplify the view, we could think of the tumour mass as an emerging cell formation that breaks the equilibrium of the healthy host, entering a competition for the same resources needed by healthy cells. In the context of this discussion, oversimplifying the complex biology that would deserve an exhaustive discussion of oncological dynamics, we can say that the life of the tumour mass is determined by four predominant and overlapping dynamics:

- competition with healthy cells of the host tissue,
- the interaction with the abiotic factors of the environment that contains it,
- interaction with the body's immune system,
- the effect of the applied therapies.

The intra-tumoural heterogeneity, both considered in terms of the presence of different subpopulations and of their spatial collocation in the tumour mass, plays a central role in all these four dynamics. On the one hand, the presence of this heterogeneity, initially caused by intrinsic cancer characteristics determined at a cellular level, influences the outcome of all the interactions. On the other hand, these outcomes induce the survival or not of a subpopulation, having a determinant effect on the evolution of the intra-tumoural heterogeneity.

For this reason, concerning the healthy-cancer cell interaction (Section 1.1), in this chapter, we begin with a brief overview that aims to explain the functioning of a generic healthy cell of the human body as a single agent and as part of a multicellular organism (Section 1.1.1). We then move to characterise generic cancer cell biology, underlining the difference between healthy cells and the effect of these on the competitive dynamics (Section 1.1.2). Moreover, we seek an explanation at the microscopic level of the intrinsic intra-tumoural heterogeneity, then subsequently analyse how this level intersects with dynamics of selection or expansion of heterogeneity at the population level (Section 1.1.3).
Following, we consider the interaction between the tumour and its microenvironment (Section 1.2), concentrating on resulting dynamics such as angiogenesis (Section 1.2.1) and metastasis (Section 1.2.2).
Moreover, regarding the interaction of the tumour mass with the immune system (Section 1.3), we first explain its normal functioning (Section 1.3.1) and then highlight how cancer cell-specific features could affect the dynamics observed (Sections 1.3.2 and 1.3.3).
We then give an overview of the biology behind therapies and their effectiveness

(Section 1.4), focusing, later, on radiotherapy (Section 1.4.1) and oncolytic virotherapy (Section 1.4.2).
Finally, we give a evolutionary point of view of cancer (Section 1.5), considering it in its multiscale nature (Section 1.5.1), analysing its phases (Section 1.5.2). Lastly we present an interpretation of the cancer mass history coherent with an ecological, evolutionary developmental biology perspective (Section 1.5) and we analyse the trade-offs that cancer cells must face (Section 1.5.4). Note that the role of abiotic factors is strictly interconnected with all these interactions, and instead of dedicating a different section, we treat it in all these contexts.

1.1 Cancer cell and host tissue

Cellular biology, and in particular that of tumour cells, is vast, still little understood, although much investigated, and includes a series of mechanisms too broad to be exhaustively treated in their individuality, even more difficult in their interaction. Without going into the role of the cells present in the various organs and tissues of the human body, and therefore the actions carried out by each to ensure the overall functioning of the organism, let us start from a simple but central fact: living organisms need functional and organised cells to exist, and this condition is met by processes that include reproduction, maintenance and cell death. Cancer originates from healthy cells. Many theories, the most accredited of which are presented subsequently, have been exposed to the dynamics with which this happens. To delve into the exploration of what leads to the formation of a tumour mass and what characterises it, we first provide a brief overview of the mechanisms of generic healthy cells in the dynamics of life, reproduction and death and then try to enlight which dysregulations within themselves cause and "regulate" the tumour mass.

1.1.1 Cell biology

The focus of this first section will be on essential dynamics common to most cells: the cell cycle, the production of energy necessary for the various phases of the same, and the mechanisms regulating the life and death of cells.

Cell cycle

The cell-division cycle is the sequence of events that leads to the formation of two daughter cells through a process of preparation and division of a cell called the mother cell. All eukaryotic cells can be in three different states: resting, interphase or division. The cell cycle determines the passage between these states. Cell division states include mitosis and cytokinesis, two consequent subprocesses of the M phase. Between two division states, cells face an interphase state, in which the cell prepares itself for the new reproduction process. Interphase state includes G1 (gap one), S (synthesis), and G2 (gap two) phases. When a cell abandons the cycle, it goes into a resting state that matches with the G0 (gap zero) phase. Proper progression through each phase is essential (see Fig. 1.1).

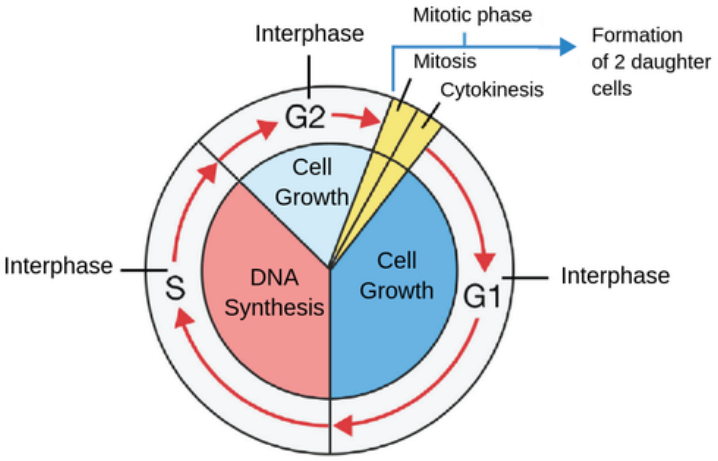

Fig. 1.1 Cell cycle representation. Figure taken from [350].

- G0 phase
  The resting phase is characterised by the absence of division. Cells usually exit the cell cycle in phase G1 and can enter the G0 phase reversibly (this is called *quiescence*) or permanently (as it happens in senescence).

- G1 phase
  This phase is recognised as the growth phase, as the cell increases the number of organelles and grows in size. These developments are made possible by the resuming of biosynthetic activities at a high rate (after a slowdown during phase M), which causes an increase in the supply of proteins. At the end of the G1 phase, there is regulated by G1/S cyclins, which cause a transition from

the G1 to the S phase or stop the cells if they are not ready for the division process (they can be sent either backwards in the progression of the cycle or out of it entering the G0 phase).

- S phase
  The subsequent S phase initiates with the onset of DNA synthesis, culminating in the replication of all chromosomes, resulting in two sister chromatids for each chromosome. Consequently, the cell's DNA content doubles while ploidy and chromosome number remain constant. This phase is characterised by very low rates of RNA transcription and protein synthesis, with the exception of histone production, which is predominantly active during the S phase.

- G2 phase
  After DNA replication, in phase G2, the cell synthesises proteins and grows in size rapidly. This phase includes microtubule reorganisation to form a spindle (preprophase). Before entering the mitotic phase, cells undergo a G2 checkpoint to check for any DNA damage. The G2 checkpoint is primarily regulated by the tumour protein p53, which, if the DNA is damaged, can either facilitate DNA repair or initiate apoptosis. In this phase, the presence of mutated p53 may be the cause of cancer cell formation, allowing cells with damaged DNA to progress through the cell cycle.

- M phase

  – Mitosis: M phase takes little time in comparison with the cell cycle but is a complex one, made of different subphases. In this process, mitosis occurs, i.e. the chromosomes in the nucleus divide into two identical sets in two nuclei. This happens because the pairs of chromosomes attach to microtubules, and the sister chromatids are pulled to the opposite side of the cell.

  – Cytokinesis: After mitosis, the DNA material of the cell has been completely duplicated. In cytokinesis, the cell undergoes division of the nuclei, cytoplasm, organelles, and cell membrane, resulting in the formation of two cells with approximately equal shares of these cellular components.

Energy production

Cells operate a series of metabolic reactions and processes to convert chemical energy from nutrients into adenosine triphosphate (ATP), which contains the energy necessary to fuel cell activities. This process is referred to as cellular respiration. In order to happen, cellular respiration needs the presence of an inorganic electron acceptor. Cell respiration strategies are differentiated into two categories, aerobic and anaerobic, whether this acceptor is oxygen or not.

Both aerobic and anaerobic respiration starts in the cytosol with *glycolisis*, which is considerable as a "sugar-splitting" phase. This process takes as reagents one molecule of glucose, NAD+ and ADP, transforming them into two molecules of pyruvate (pyruvic acid), four molecules of ATP (two of which are consumed as part of the preparatory phase) and two NADH molecules. This is where aerobic and anaerobic respiration split their paths.

Aerobic respiration

The first step of aerobic respiration is the oxidation of pyruvate to acetyl-CoA by the pyruvate dehydrogenase complex (PDC), in a process called *oxidative decarboxylation* (Ox. D.) that occurs in mitochondria and also produces one molecule of NADH and one molecule of CO2. When oxygen is present, the acetyl-CoA molecules enter what is called *Krebs cycle*. Krebs cycle includes the action of eight enzymes that oxidise acetyl-CoA into two molecules of CO2 and H_2O each. For every acetyl-Coa molecule that enters, the several oxidative steps included in the cycle produce the following transformations:

- Three equivalents of NAD+ are turned into three equivalents of NADH.
- One equivalent of flavin adenine dinucleotide (FAD) is transformed into one equivalent of $FADH_2$.
- One equivalent of guanosine diphosphate (GDP) and inorganic phosphate (Pi) are turned into one equivalent of guanosine triphosphate (GTP).

GTP molecules are directly converted in ATP, but the main ATP production of aerobic respiration is due to *oxidative phosphorylation* (Ox. P.), in which electrons derived from NADH and FADH2 combine with O_2, and the energy released from

these oxidation/reduction reactions is used to drive the synthesis of ATP from ADP. In particular, the net production rate of ATP is 2.5 from NADH and 1.5 from $FADH_2$. The complete process is represented in Fig. 1.2.

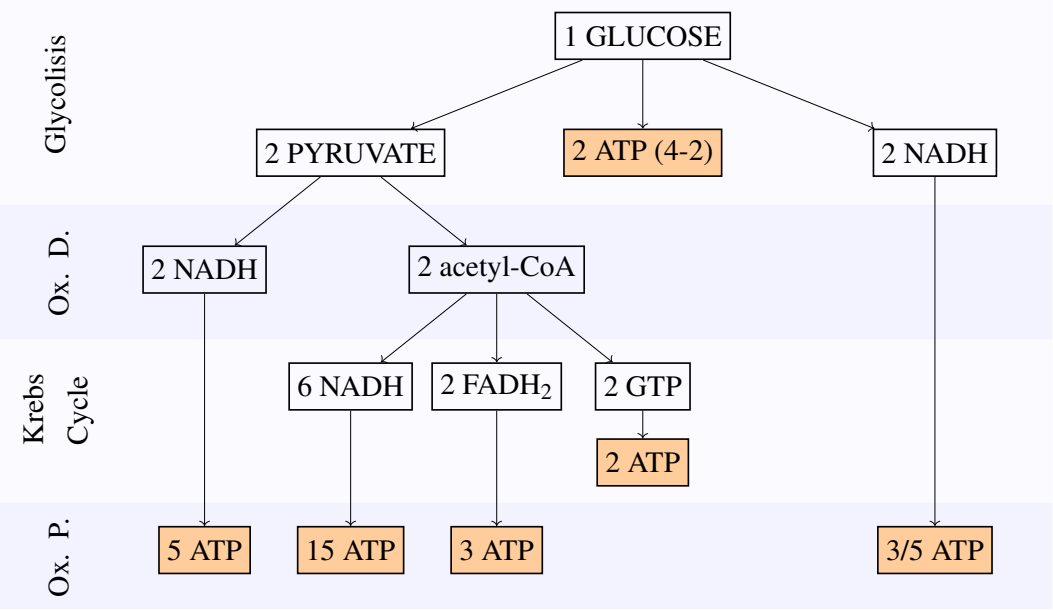

Fig. 1.2 Schematic representation of aerobic respiration.

Thus, considering the whole aerobic respiration, starting from one molecule of glucose, we have:

- 2 net ATP molecules directly produced during glycolysis (4 released, 2 used);
- 2 ATP molecules directly produced from GTP during Krebs cycle;
- respectively 2 and 6 NADH molecules released during glycolysis producing $2*1.5/2.5 = 3/5$ ATP molecules in the oxidative phosphorylation (here the uncertainty stands in the possibility of a drop in the conversion rate due to the necessity of NADH produced in the cytosol to pass through the mitochondria membrane);
- respectively 2 and 6 NADH molecules released respectively during oxidative decarboxylation and Krebs cycle, producing $(2+6)*2.5 = 20$ ATP molecules in the oxidative phosphorylation;
- 2 $FADH_2$ molecules released in Krebs cycle producing $2*1.5 = 3$ ATP molecules in the oxidative phosphorylation;

for a total of a net ATP production of 30/32 molecules per glucose molecule. The final side products of the whole process are CO_2 and H_2O.

Anaerobic respiration

We stated that aerobic and anaerobic respirations split their path after glycolysis, but the reason is not that oxygen is strictly necessary to pyruvate oxidation. The problem is that, in the lack of oxygen, the electron transport chain is not functional. Thus, since the NADH made in glycolysis is not useful in producing additional ATP in oxidative phosphorylation, the only purpose for which it can be used is to drop its electrons off to turn back into the NAD+ required to fuel glycolysis. The process used to do that is called *fermentation* and can occur on different molecules.

- Alcohol fermentation
  In the pyruvate oxidation occurs in the absence of oxygen, the process stops a step above, resulting in the production of acetaldehyde, whose molecule is similar to acetyl-CoA but does not allow the entrance into the Krebs cycle. In this case, NADH ceases its electrons to acetaldehyde, regenerating NAD+ and forming ethanol as a side product.

- Lactic acid fermentation
  In the case pyruvate oxidation does not occur, NADH releases its electrons directly to pyruvate, again with the effect of regenerating NAD+, but forming lactic acid as a side product.

Thus, the net ATP production of anaerobic respiration lies in the only two molecules produced during glycolysis.

A comparison

It is evident that the net production rate of ATP, with respect to the same amount of glucose involved, is $15 - 16$ times higher for aerobic respiration. Moreover, side products of aerobic respiration are easier for the organism to handle since lactate and ethanol are acids and tend to create a hostile environment for healthy cells. On the other side, anaerobic respiration needs fewer conditions to be possible and takes less time (it can be 100 times faster). Thus, considering the regulatory pathways that control an organism (the next session makes this clearer), we can say that in

healthy conditions, aerobic respiration is the preferred one when possible, while anaerobic is used when strictly needed. Later in the discussion, we highlight how this choice is not always implemented. In particular, we will discuss how this not-obvious preference is not only a characteristic feature of tumour cells but also has a great impact on the evolutionary dynamics of cancer in intra-tumoural and tumour-environment competition.

Cell regulation: homeostasis and its maintenance

Homeostasis is a concept that could be defined as a state of a functional, stable equilibrium. The pursuit of maintaining homeostasis underlies the regulatory dynamics of an organism at different scales. Cellular homeostasis ensures that cells maintain stable conditions necessary for optimal cell function, metabolism, growth, and survival. This process relies on complex signalling pathways that detect and respond to environmental changes, preventing fluctuations that may jeopardise cellular integrity. Cells adeptly modulate their metabolism in response to the availability of nutrients, energy, and growth factors. The flexibility of these cellular systems is precisely controlled by intricate signalling networks that integrate intracellular and extracellular information [202].

On a broader scale, maintaining tissue homeostasis involves the fundamental components that make up a tissue, a feedback loop within the tissue, and how cells within the loop respond to environmental pressures such as space availability, growth factors, cytokines, oxygen, and tension. The equilibrium in tissue homeostasis relies on precise control of tissue renewal throughout life, balancing cellular proliferation and differentiation. Essential to this balance is transcriptional regulation at both the genetic and epigenetic levels [12]. In general, we can say that single-celled entities, typically considered individualistic, have undergone cooperative interactions during the evolution of multicellularity. This cooperative behaviour, enhancing the fitness of the multicellular organism, was initially driven by the emergence of new cooperation genes or the co-option of existing genes with individual-level functions. Among all cell processes, the more involved in regulatory dynamics are reproduction, death and differentiation.

We can provide a very general overview of homeostatic maintenance, saying that in multicellular individuals, cells are part of signalling pathways thanks to which the organism is informed about the number of cells which are present and can start

cell division if more cells are needed or death if too many are present. The cell division process has already been introduced and explained in the cell cycle. We can further introduce a specification about cell division that takes into account not only the chance to proliferate but also the product of this division. In fact, cells (even in the same tissue) are not all the same, and every tissue has a differentiation cascade, which is a sequence of cell degrees of specialisation. Among dividing cells, there are multiple levels of cell potency, which is the cell's ability to differentiate into other cell types. A greater potency indicates a larger number of cell types that can be derived. We define a cell [408]:

- *totipotent*, if can differentiate into all cell types;
- *pluripotent*, if it can differentiate into all cell types of the adult organism;
- *oligopotent*, if it has a more restricted reproductive potential than multipotent but can still differentiate into a few closely related cell types;
- *unipotent*, if it is only capable of self-renewal (production of daughter cell in the same compartment);
- *terminal differentiated*, if it has permanently exited the cell cycle, disassembled the cell cycle machinery, and activated the genes indicative of its ultimate function.

Less specialised cells are less capable of specific functional activities and have the task of maintaining the cell population in the right number. More specialised cells, on the other hand, are the ones that, with their specific activities, contribute to the actual function of the tissue/organ. When they proliferate, less differentiated cells are hinted by the environmental signalling in producing daughter cells, which are the same as the mother or differentiated in the next specialisation step, according to what is needed. We do not go into the details of this complex signalling system, which includes chemical, genetic and epigenetic factors. We will only consider, in the next session, the processes that differentiate cancer cell functioning from healthy cells or the formation of cancer cells itself.

Considering the death program, there are two main mechanisms that cells adopt. One is senescence, which is a stable cell cycle arrest triggered by diverse stimuli that stops its proliferative potential. Senescent cells undergo continuous evolution,

exhibiting distinct phenotypic alterations and a complex secretory phenotype. Unresponsive to mitogenic signals, these cells impact tissue repair and ageing and possess both beneficial and detrimental effects on health. Senescence serves as an antitumour mechanism, hindering cancer cell proliferation. Removal of senescent cells extends healthspan, showcasing its dual nature as a program of evolutionary antagonistic pleiotropy [274]. The other mechanism is apoptosis, which is known as a "programmed" cell death, which involves the genetically determined elimination of cells. It is identified by specific morphological features and energy-dependent biochemical processes, and it plays a crucial role in diverse processes such as regular cell turnover, immune system development and function, and cell death induced by chemicals [168].

1.1.2 Cancer cells

In order to operate the needed process, all cancers acquire and apply common abilities and strategies, which are known as *cancer hallmarks* [213, 214, 211]. Acquired capabilities and enabling characteristics accepted to be cancer hallmarks are self-sufficiency in growth signal, evading apoptosis, insensitivity to antigrowth signal, limitless replicative potential, sustained angiogenesis, tissue invasion and metastasis, genome instability, reprogramming cellular metabolism, avoiding immune destruction, tumour-promoting inflammation. Moreover, additional proposals for elements to be introduced in the list of hallmarks are: unlocking phenotypic plasticity, non-mutational epigenetic reprogramming, polymorphic microbiomes, and senescent cells (see Fig. 1.3).

In later sections, we insert a brief explanation of these characteristics and the dynamics in which they are involved, grouping them as belonging to the same general strategies:

- oncogenesis
- alternative self-regulation
- promoting tumour heterogeneity.

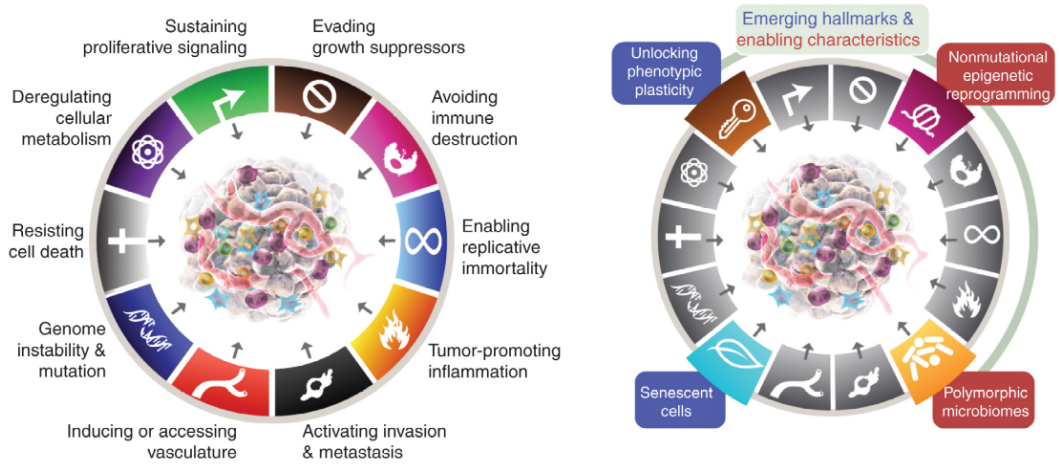

Fig. 1.3 Comparison between the cancer hallmarks introduced and recognized in Ref. [213] and [214] and the suggested expansion proposed in Ref. [211]. Figure taken from [211].

Oncogenesis

Oncogenesis, also called carcinogenesis or tumourigenesis, is the formation of a cancer. The two main theories regarding the dynamics that activate carcinogenesis are the Somatic Mutation Theory (SMT), more conventional and rooted in oncology research, and the tissue organisation field theory (TOFT), which has recently emerged as an alternative to the first [40] (see Fig. 1.4 for a representation of both the theories). What the two theories have in common is the occurrence of an event that alters the *homeostasis* of the organism, that is, an alteration in the regulation of the processes of cell proliferation and programmed death (apoptosis) in order to maintain the optimal number of cells to preserve the functionality of the organism. What distinguishes the theories are the supposed causes that lead to this alteration [411].

The Somatic Mutation Theory posits that the initiation of cancer is caused by a mutational event endowing cells with a proliferative advantage, thereby instigating clonal expansion and subsequent iterations of mutations, followed by additional clonal expansions. The foundational tenets of SMT are expressed through the following postulates:

1. cancer derives from a solitary somatic cell that has accrued multiple DNA mutations;

2. the inherent state of cell proliferation defaults to quiescence;

3. cancer manifests as a disorder of cellular proliferation induced by mutations in genes governing both proliferation and the cell cycle.

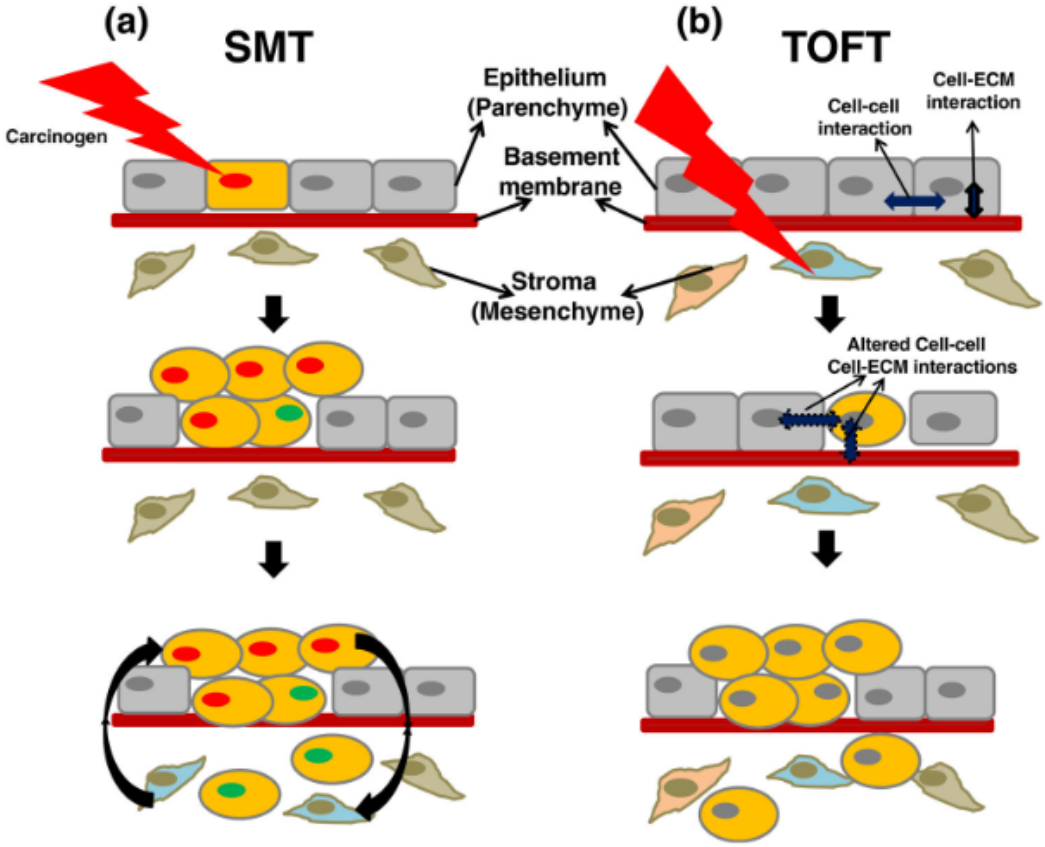

Fig. 1.4 Illustration of SMT and TOFT models: (a) The SMT posits that carcinogens lead to mutations in the cellular DNA of epithelial cells, leading to the propagation of cells carrying advantageous mutations. Paracrine factors secreted by the growing tumour alter the tumour stroma. The altered or 'activated' stroma, in turn, contributes to cancer progression, enabling a conducive environment for tumour cell invasion and metastasis. (b) The TOFT model predicts that carcinogens affect the stroma, leading to altered cell–ECM and cell-cell interactions in the epithelium, which then results in tumour formation in the epithelium Figure and caption taken from [40].

The role of adjacent tissues, which in TOFT (as explained later) is central as a trigger, is present here as support, as they influence the evolutionary dynamics, changing adaptive fitness of clonal expansion or augmenting the neoplastic phenotype through the recruitment of surrounding stromal cells. Considering the postulates of SMT, we can state that in this theory, mutations are considered a necessary prerequisite

for the onset of cancer, protracted in time as they are infrequent events and persist when they lead to carcinogenesis. This implies that for a tissue to develop a tumour, it must be exposed to carcinogens.

Tissue Organization Field Theory [412] says that cancer arises from the disruption of interactions with adjacent tissue, which can be mediated by intercellular chemical signals, mechanical forces, and bioelectric changes. TOFT is summarised by the "development gone awry" expression, as these interactions are thought to play a role in embryonic development. Differently from what is stated in the second postulate of SMT, proliferation is considered the default state of all cells. The premise of TOFT is that carcinogenesis represents a problem of tissue organisation comparable to organogenesis and can, therefore, occur in tissue which has not been exposed to a carcinogen. Symmetrically to the supporting role of interactions between adjacent tissues in SMT, in TOFT, mutations are not necessary but still have a role as genetic instability is considered a byproduct of carcinogenesis.

In Ref. [40], it is suggested that, in light of current knowledge and observations, neither of the two theories is able to motivate all the dynamics shown in the medical literature, both in tumour induction experiments and in clinical practice. In fact, observations such as recurrent mutations (mutation with a higher frequency in the tumour than expected by chance), tumour clonality, hereditary cancer, transgenic experiments (in which mutated genes inserted into animals lead to cancer), and remission of tumours following the inhibition of enzymes activated by mutated genes (observed, as an example, in some chronic myelogenous leukaemia cases) would seem to support SMT theory. On the other hand, SMT is not capable of explaining other experiments that appear more coherent with TOFT. Among them, there are cases of induction of cancer mass formation through the insertion of foreign-body (in which the cause of carcinogenesis is identified in the shape and position of the body and not in the carcinogenic nature of the material), and of nongenotoxic carcinogens (chemicals that induce cancer without DNA alterations). Consequently, the article suggests that in order to obtain a comprehensive explanation, further investigations should be made into a possible joint theory.

Uncontrolled proliferation and death of cancer cells

Insensitivity to anti-growth signal

Antigrowth signals can block normal cell proliferation either by reversible or irreversible mechanisms (forcing quiescent (G0) state or inducing postmitotic differentiation-associated states). These mechanisms are part of checkpoint dynamics during the G1 phase when cells monitor their external environment and decide whether to proliferate, be quiescent, or enter into a postmitotic state. This decision is made on the basis of sensed signals, many antiproliferative of which are funnelled through the retinoblastoma protein (pRb). Since the pRb pathway strictly depends on TGF-β (which is a soluble signalling molecule that prevents the phosphorylation that inactivates pRb), cancer cells can use a loss of TGF-β responsiveness (obtained through downregulation of their TGF-β receptors) to avoid sensitivity to antigrowth signals. Another strategy to avoid quiescence relies on turning off the expression of cell adhesion molecules that send antigrowth signals (with a pathway that impinges on the pRb circuit as well) in favour of pro-growth molecules.
Among strategies to avoid differentiation, we found overexpression of the c-myc oncogene, whose growth-stimulating action is usually balanced by alternative complexes that elicit differentiation-inducing signals.

Limitless replicative potential

Numerous scientific investigations have highlighted that in order to ensure the expansion of a clone of cells to a size that constitutes a tumour mass, acquired uncorrelation of the cellular growth program from the environment is not sufficient. For this to be possible, tumour cells must also deprive themselves of senescence and crisis, two consequent processes independent of cell-to-cell signalling pathways, which provide a finite replicative potential. The most credible hypothesis is that unlimited replicative potential is an essential phenotype acquired in vivo during tumour progression [220]. Healthy cells show in vivo potential of 60-70 doublings in their lifespan, the full use of which is, however, limited by homeostatic regulations. The absence of this regulation in tumour cells, together with the neutralisation of senescence, would lead to a higher cell number than that observed, necessitating the hypothesis of chronic apoptosis in malignant masses, which is thought to undergo significant cell attrition concurrently with the accumulation of cells [454].
The cause of the replicative limitation of healthy cells due to crisis state has been

recognised as the shortening of telomeres (the final part of the chromosome) with each reproductive cycle of the cell, a process that gradually leads to end-to-end chromosome fusions, producing the karyotypic disorder associated with crisis and resulting, almost inevitably, in the death of the affected cell [132]. Whether by upregulation of telomerase enzyme, which supplies additional hexanucleotide at the end of DNA chromosomes, or activation of ALT mechanism, responsible for telomeres maintenance, malignant cells are able to evade this crisis state induction.

However, there is less certainty about the causes of the induction of senescence, which are hypothesised to be similar to those of the crisis state but also possibly identified in conflicting growth signals that force aberrant cells irreversibly into a G0-like state. Thus, it is less clear if the two telomeres maintenance mechanisms are sufficient to evade both senescence and crisis or if other anti-signalling strategies are necessary to evade the first one.

Self-sufficiency in growth signal

Normal cellular proliferation necessitates mitogenic growth signals to transit from a quiescent to an actively proliferative state. In contrast, tumour cells exhibit a significantly reduced dependence on exogenous growth stimulation, suggesting that they generate many of their own growth signals. This feature makes them less reliable in the microenvironment and more independent in their ability to proliferate. Cancer cell strategies include receptor overexpression that allows them to become hyper-responsive to ambient growth factors and favour the expression of extracellular matrix receptors (integrins) that transmit pro-growth signals. Integrins link cells to the extracellular matrix (ECM), influencing cell behaviour from quiescence to motility, apoptosis resistance, and entry into the cell cycle.

Nevertheless, acquisition of growth signalling autonomy by cancer cells can explain the deregulated growth of tumour only when paired with the contribution of the ancillary cells present in a tumour. Intercellular growth signalling is expected to function in most human tumours. A hypothesis suggests that successful tumour cells may excel in co-opting their normal neighbours, inducing them to release substantial amounts of growth-stimulating signals [407]. Additionally, inflammatory cells attracted to neoplastic sites may paradoxically promote, rather than eliminate, cancer cells [130, 133, 228], directly inducing their uncontrolled growth potential or

modifying the environment in such a way that favour tumour overcome of a healthy cell.

Evading apoptosis

As we stated before, apoptosis is a programmed death strategy triggered by a variety of physiologic signals that allow the organism to maintain homeostasis. Apoptosis is a process that lasts between thirty minutes and a couple of hours, after which the leftovers of the dead cell are engulfed by the other cells of the tissue and disappear within a day [454]. In order to make it possible, a sequence of processes is needed, including disruption of cellular membranes, breach of cytoplasmic and nuclear skeletons, extrusion of the cytosol, degradation of the chromosomes, and fragmentation of the nucleus [405]. The apoptotic machinery is operated by two different components. Sensors monitor extracellular conditions (such as adjacency of other cells) and lack of intracellular non-functional abnormalities (such as DNA defects or hypoxia). When needed, they give the signal to effectors, which operate apoptotic death. One of the principal players of this cellular mechanism is the oncosuppressor p53. Resistance to apoptosis can be acquired by cancer cells through a variety of strategies, but the mostly known include mutation of this gene, leading to the inactivation of its product protein and thus resulting in the removal of a key component of the DNA damage sensor that can induce the apoptotic effector cascade.

Cancer cell metabolism

Both SMT and TOFT agree on recognising that uncontrolled cell proliferation represents the essence of neoplastic disease. This behaviour makes it necessary for tumour cells to dispose of the necessary amount of energy to support their proliferative activity. In general, both healthy and cancer cell depend on adenosine triphosphate (ATP) as a fuel for their processes and are able to produce this nucleotide processing available nutrients provided by the environment.

In the previous section, we highlighted that normal cells under aerobic conditions prefer aerobic respiration to produce energy, as according to homeostatic regulation it is more efficient and has favourable side products. Cancer cells are also capable of both aerobic and anaerobic respiration. The difference stands in the need for hypoxic conditions to pass to anaerobic respiration. Either due to lack of necessary nutrients,

or due to abnormal behaviour conferred on tumour cells by genetic and epigenetic mutations or interaction with the environment, cancer cells are able to adopt different energy production strategies without favouring aerobic respiration.

Otto Warburg first observed an anomalous characteristic of cancer cell energy metabolism [348, 432]: even in the presence of oxygen, cancer cells can reprogram their glucose metabolism, and thus their energy production, by limiting their energy metabolism largely to glycolysis, leading to a state that has been termed "aerobic glycolysis." This "choice" that would seem disadvantageous if adopted by a cell that is part of homeostatic-focused regulation seems comprehensible if adopted by cancer cells, which are not programmed to be part of an assembly line (at least not with the aim of host tissue functionality). "Selfish" typical cancer cell behaviour could be in line with this time-optimising strategy. Moreover, the side products of anaerobic respiration, which are a source of acidification of the environment harmful to healthy cells, represent an evolutionary advantage for tumour cells, which are not only resistant to this hostile environment but are triggered by that in dynamics of metastasis and mutation.

1.1.3 Tumour heterogeneity

Genotype, phenotype and epigenetic of cancer

Genomic changes contributing to the generation of cancer cells can occur at different levels. We talk about *genetic mutations* when there is an alteration in the nucleotide sequence of genomic DNA. Otherwise, if it is not the sequence of genes that varies, but their expression, we speak of *epigenetic mutations*. Other possible variations affect the number of chromosomes through errors in mitosis (*aneuploidy*) or abnormal fusion of adjacent ones.

The genotype of an organism is its complete set of genetic material. Genotype contributes to phenotype, defined the observable traits and characteristics in an individual or organism, which are a results also of environmental and epigenetic factors. Primary cancers frequently exhibit significant phenotypic and genetic intratumour heterogeneity (ITH). Heightened levels of ITH have been associated with increased tumour aggressiveness, resistance to therapies, and an overall unfavourable prognosis [87].

Genome instability

The prevailing evidence indicates that most cancer-related mutations are acquired, either directly or indirectly, through alterations in the genomes of cancer cells. The mutation of specific genes is an inefficient process due to the constant and meticulous maintenance of genomic integrity by a complex array of DNA monitoring and repair enzymes. Consequently, mutations are rare events, and the presence of multiple mutations in tumour cell genomes is highly unlikely to occur within a human lifespan. Thus, oncogenesis and tumour mass evolution seem compatible only with increased mutability caused by dysfunctions in specific components of genomic "caretaker" systems. Notably, the functionality of the p53 is lost in most human cancers. The p53 tumour suppressor protein is a key member that responds to DNA damage by inducing either cell cycle arrest for repair or apoptosis if the damage is excessive. Additionally, various genes involved in sensing and repairing DNA damage or ensuring accurate chromosomal segregation during mitosis are found to be lost in different cancers, designating them as tumour suppressors.

Phenotypic plasticity

In healthy cells, terminal differentiation marks the point at which progenitor cells cease their growth following the completion of these developmental processes. The antiproliferative state resulting as the outcome of cellular differentiation establishes a significant barrier to the non-regulated proliferation required for neoplastic transformation. The abnormal activation of phenotypic plasticity (which is a limited capability in a healthy state), enabling evasion or escape from the constraints of terminal differentiation, stands as a critical determinant in the pathogenesis of cancer [460].

Phenotypic plasticity mechanisms include:

- *Dedifferentiation*: a transient process by which cells become less specialised and return to an earlier cell state (as in colon carcinogenesis);
- *Blocked differentiation*: the results of regulatory changes that stop the differentiation cascade of progenitor cells (for example, in acute promyelocytic leukaemia (APL) cells are the results of myeloid progenitor cells made unable

to differentiate into granulocytes, resulting in cells trapped in a proliferative stage [146].

- Transdifferentiation: a marked change of morphology through which cells of a particular differentiated phenotype become clearly recognisable as another type of cell. This mechanism, historically observed in the form of tissue metaplasia, recently proved to be typical also of cancer. A clear example of transdifferentiation role in tumourigenesis is pancreatic ductal adenocarcinoma (PDAC), wherein the pancreatic acinar cell (which is one of the responsible for cancer origin) can become transdifferentiated into a ductal cell phenotype.

Nonmutational epigenetic reprogramming

Some physical and chemical abnormalities of the tumour microenvironment can induce mechanisms of epigenetic reprogramming. These alterations, conducive to the phenotypic selection of hallmark capabilities, culminate in the clonal outgrowth of cancer cells endowed with augmented fitness for proliferative expansion. One prevalent feature characterising tumours is insufficient vascularisation. This leads, on the one hand, to *hypoxia*, a condition of oxygen supply deprivation. This state can affect the whole tumour or just a region of it. Hypoxia is able to cause hypermethylation through the inhibition of TET demethylases [432]. On the other hand, the lack of sufficient vascularisation likely imposes constraints on the bioavailability of essential nutrients. For instance, nutrient deprivation has been demonstrated to induce changes in translational control, thereby augmenting the malignant phenotype of breast cancer cells [189].

Alongside these microenvironmental mechanisms of epigenetic reprogramming, epigenetic regulatory heterogeneity also plays a role in these non-mutational dynamics. Intra-tumoural heterogeneity plays a pivotal role in the generation of phenotypic diversity. This diversity provides a milieu in which the fittest cells undergo proliferative expansion and invasion, ultimately driving malignant progression. Genomic instability, either chronic or episodic, and the resultant genetic heterogeneity within the tumour cell population represent one facet of this phenotypic heterogeneity. Moreover, emerging evidence underscores the presence of non-mutationally based epigenetic heterogeneity. A notable example of this epigenetic heterogeneity is observed in the dynamic expression and repression of the linker histone H1.0 within

subpopulations of cancer cells across various tumour types. This dynamic regulation results in subpopulations of cancer cells in which the suppressed H1.0 expression leads to stem-like characteristics and heightened tumour-initiating capability [424].

Moreover, the epigenetic reprogramming of cells also involves tumour microenvironment cells that actively contribute to the acquisition of hallmark capabilities, which, on the contrary, are generally postulated not to undergo genetic instability and mutational reprogramming to augment their tumour-promoting functionalities. For example, it is postulated that cancer-associated fibroblasts, innate immune cells, as well as endothelial cells and pericytes of the tumour vasculature, undergo epigenetic reprogramming orchestrated by soluble and physical factors that delineate the distinctive characteristics of the solid tumour microenvironment [214, 212].

1.2 Cancer cell and its microenvironment

1.2.1 Sustained angiogenesis

Tumour angiogenesis is the growth of blood vessels, induced by cancer cell signalling, which causes infiltration of the tumour mass [208]. In fact, while normal diffusion of nutrients can support the growth of the tumour mass up to a radius of about 2-3 mm, direct delivery of nutrients and removal of waste become necessary above this size. The presence of vessels inside the mass is also necessary to permit metastasis in hostile environments (as we show in the next section).

In mechanical terms, angiogenesis involves different sequential phases. First step is proteases, by which basement membrane is degraded. Subsequently, endothelial cells (ECs) migrate into the interstitial space and proliferate. This way the proper vessel is formed: the lumen (a cavity within a tubular structure) is formed, pericytes are recruited and wrap around the ECs forming a new basement membrane, anastomoses are created and finally the blood can flow. Tumour cells release factors influencing endothelial cell functions through various intracellular signalling pathways. This process begins with tumour cells releasing molecules that signal surrounding normal tissue to activate specific genes, leading to protein production and the promotion of new blood vessel growth. This ability of tumour cells, also referred to as *angiogenic phenotype*, is not innate but acquired via a phenotype switch. Tumour cells may

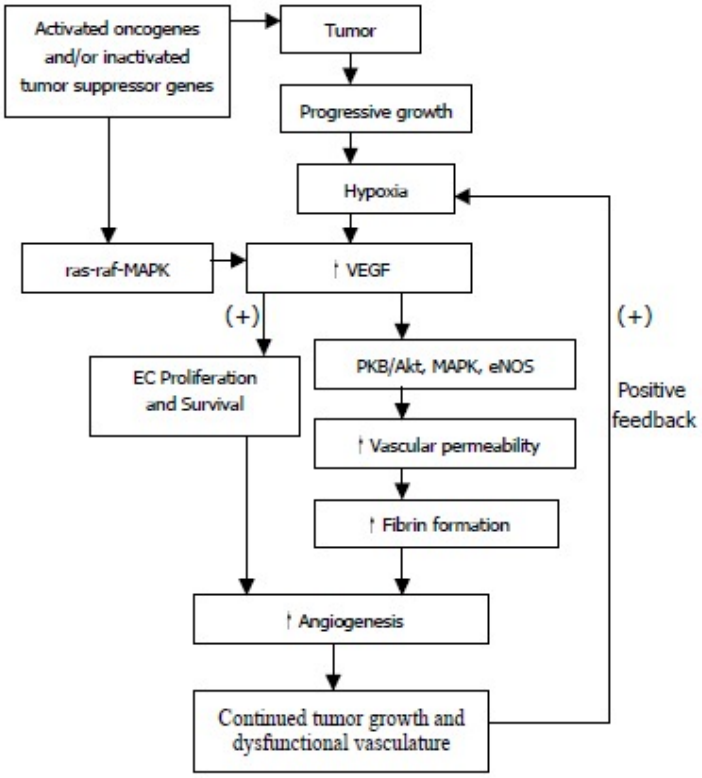

Fig. 1.5 Scheme of angiogenesis activation pathways. Figure taken from [208].

induce angiogenesis by overexpressing positive regulators, mobilising angiogenic proteins, or recruiting host cells. Tumour-secreted growth factors like VEGF and bFGF interact with EC receptors, triggering angiogenesis. Up-regulation alone isn't sufficient; down-regulating negative regulators is often necessary. The balance between angiogenic and angiostatic factors in the local environment determines vessel growth or regression, with angiostatic factors inducing apoptosis or cell cycle arrest in ECs. The switch to the angiogenic phenotype is governed by this balance. In particular, known to be involved in cancer advancement due to direct activation of glycolysis, EMT and apoptosis suppression and undirect interaction with c-Myc and p53 pathway, hypoxia-inducible factor (HIF) activation also stimulates angiogenesis, glycolysis, EMT, and suppressing apoptosis [306].

1.2.2 Tissue invasion and metastasis

Usually driven by the lack of nutrients or by specific signals, both caused by a certain advance in the growth of the tumour mass, cancers tend to spawn pioneer cells that move out, invade adjacent tissues, and thence travel to distant sites where they may succeed in founding new colonies. If this happens, the initial mass is called the primary tumour, and the distant settlements of tumour cells are called *metastases*. Metastases are considered the cause of 90% of human cancer deaths [414] and enable cancer cells to escape the primary tumour, colonising new areas with initially abundant nutrients and space. Metastases form from a blend of cancer and host tissue cells. The genetic and biochemical determinants of invasion and metastasis processes are not fully understood. Mechanistically, both processes involve changes in cell coupling to the microenvironment and activation of extracellular proteases.

Proteins essential for cell tethering to tissue undergo changes in cells with invasive or metastatic capabilities. These proteins, including cell-cell adhesion molecules (CAMs) and integrins connecting cells to extracellular matrix substrates, participate in regulatory signalling through "adherence" interactions [32]. A prevalent alteration in cancer's cell-to-environment interactions is the modification of E-cadherin, a homotypic cell-to-cell interaction molecule expressed ubiquitously on epithelial cells. E-cadherin coupling between adjacent cells transmits antigrowth signals through cytoplasmic contacts.

It appears clear how invasive and metastatic phenotypes link to the concept of epithelial-mesenchymal transition (EMT). EMT is a biological process that allows a polarised epithelial cell, which normally interacts with the basement membrane via its basal surface, to undergo multiple biochemical changes that enable it to assume a mesenchymal cell phenotype, which includes enhanced migratory capacity, invasiveness, elevated resistance to apoptosis, and greatly increased production of ECM components [251]. This process (shown in Fig. 1.6 di [252]), which is important and useful during implantation, embryogenesis, and organ development and is also associated with tissue regeneration and organ, provides cancer with a more aggressive feature. According to that, EMT activation has been associated with the generation of cancer stem cells (CSCs) [379], which are cells within the cancer cell population associated with tumourigenic potential, but also treatment-resistant phenotypes due to their quiescence and plasticity tendency [103].

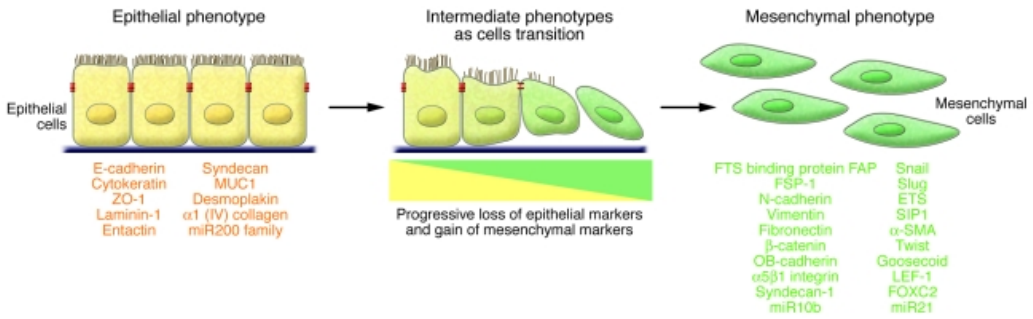

Fig. 1.6 Schematic representation of epithelial-mesenchymal transition. Figure taken from [364].

1.3 Cancer cells and immune system

1.3.1 An overview on the immune system

The immune system comprises two primary defence mechanisms: innate immunity and adaptive immunity. Innate immunity acts as the initial response to combat invading pathogens, initiating a rapid generic immune reaction. In contrast, adaptive immunity is antigen-specific and dependent, featuring the ability to form a memory. This memory capability enables the host to generate a quicker and more effective immune response if exposed to the antigen again [311].

Innate immunity to pathogens relies on pattern recognition receptors (PRRs) that recognise pathogen-associated molecular patterns (PAMPs), which are shared by a wide range of pathogens. Innate immunity plays a vital role in mobilising immune cells to infection and inflammation sites. This occurs through the production of cytokines and chemokines, which are small proteins facilitating cell communication and recruitment. Common strategies to fight the pathogen are the increase of the temperature, acidification, and inflammation. When innate immunity is ineffective in eliminating the pathogen, adaptive immunity is activated. The main steps of adaptive immunity are:

1. recognition of "non-self" antigen;
2. generation of pathogen-specific immunologic effector pathways;
3. development of an immunologic memory.

In the specific case of cancer, innate immunity is essential to the onset and maintenance of adaptive immunity, which is the main agent in the "fight". The cells of the adaptive immune system include APCs, antigen-specific T cells and B cells.

APCs stands for antigen-presenting cells and are a set of cells (usually dendritic cells, but also macrophages, B cells, fibroblasts and epithelial cells) able to recognise a specific antigen. The surfaces of APCs express a group of proteins known as the major histocompatibility complex (MHC). The MHC protein displays fragments of antigens (peptides) when a cell is infected with an intracellular pathogen. The scope of APCs is activating T cells.

T cells derive from hematopoietic stem cells in the bone marrow and, following migration, mature in the thymus. The membrane of every T cell is covered with specific receptors (TCR, a single type per T-cell) able to bind to specific foreign peptides. When the T-cell meet an APC displaying the matching peptide, it gains the capacity to rapidly proliferate and differentiate. The chance for this to happen is increased by the circulation of T cells throughout the body (via the lymphatic system and bloodstream) and their accumulation (together with APCs) in lymph nodes. T cells can differentiate into either:

- CD8+ cells, which are cytotoxic T cells directly involved in the killing of tumour cells with the corresponding antigen;
- CD4+ cells, which are T-helper cells that act, releasing cytokines that influence the activity of many cell types. Some of them are regulatory cells that limit the immune response.

Both T cell types die upon resolution of their role: the majority of them are cleared by phagocytes, while a few of them are retained as memory cells.

Finally, B cells are antibody producers. They originate from bone marrow hematopoietic stem cells and express unique antigen-binding receptors after maturation (thus, they do not need APCs). When activated by specific antigens, B cells proliferate and mainly become antibody-secreting plasma cells, which have a short life but provide effective protection. Some B cells differentiate in memory B cells, which are long-lived survivors of past infections able to quickly respond upon re-exposure.

Thus, we can summarise that in order to effectively eliminate cancer cells from a clinically detectable tumours through an anti-cancer immune response, a series of steps known as the cancer-immune cycle must be repeated:

- step 1) Neoantigens released during tumour formation are acquired by dendritic cells (DCs) and move to the draining lymph node (DLN).
- step 2) DCs present the antigen to T cells via MHC.
- step 3) Activated effector T cells recognise the antigen.
- step 4) T cells with antigen recognition migrate to the tumour.
- step 5) T cells infiltrate the tumour.
- step 6) T cells recognise the MHC–antigen complex on cancer cells through the T cell receptor (TCR).
- step 7) Cancer cells are killed through processes involving CD8+ T cells.

This cycle repeats as cancer cells die, releasing new neoantigens and sustaining the immune reaction.

1.3.2 Hot and cold tumours

tumours can be classified in different terms. Considering the relation with the immune system, tumours are called *hot* or *cold* [441]. Tumour "hotness" or "coldness" depends on cancer cell information, immune features, microenvironment, and signalling mechanisms, influencing clinical efficacy. The switch between these states, along with their characteristics and treatment strategies, is crucial in tumour treatment. Effectively distinguishing and understanding causes, microenvironments, and characteristics are vital for optimising tumour response and treatment efficacy.

Predictive indicators for immunotherapy fall into two groups: tumour immune microenvironments (TME) and molecular characteristics of tumour cells (e.g., TILs). "Hot tumours" have TME rich in TILs (Tumour-infiltrating lymphocytes), PD-L1 overexpression (ligand for protein PD-1 that is a suppressor of the inflammatory activity promoted by T-cells), genomic instability, and antitumour responses. "Cold tumours" exhibit opposite traits.

Immunotherapy, as a promising cancer treatment, reactivates the antitumour immune cycle, aiming to regulate and eliminate tumours. This therapeutic approach, primarily employing immune checkpoint inhibitors (ICIs), restores the body's innate antitumour immune response. ICIs are more effective against "hot tumours," requiring combinations for "cold" or "variable" tumours. Converting them to "hot" tumours holds promise in treating malignancies, presenting a crucial area for research.

1.3.3 Immunoevasion

Avoiding immune destruction is considered one of the hallmarks of cancer. Whether we are considering hot or cold tumours, the strategies adopted by cancer cell to evade the immune-system are different. When considering hot tumours, we are referring to an infiltrated tumour that has successfully performed the initial five stages of the immune response; thus, evading mechanisms usually exploit reactivity to immune checkpoint inhibitors and include:

- Inhibition of recognition by immune cells (cycle step 6): cancer cells remove, reduce, or transform MHC on the surface of cancer cells as a mechanism to evade recognition by T cells.
- Immune checkpoint molecule expression (cycle step 7): T-cells response to chronic antigen stimulation with a mechanism known as *exhaustion*, resulting in poor effector function, sustained expression of inhibitory receptors and a dysfunctional transcriptional state [63].
- Immunosuppressive cells in the TME (cycle step 7): cancer cells secrete substances that stimulate the action of immunosuppressive cells.

In contrast, cold tumours are characterised by immune non-infiltration; thus, immunoevasive mechanisms need to be found earlier in tumour history. Among them, we find:

- Decrease in tumour immunogenicity (evasion of step 1): cancer clones which have formed the tumour mass are the ones that evaded immunosurveillance at early stages and, thus, have fewer immunogenic antigens.

- Inhibition of dendritic cell maturation (evasion of step 2): tumour-derived factor, together with immunosuppressive cells in the TME, suppress DC maturation, reducing the production of inflammatory cytokines and inhibiting T-cell proliferation.
- Suppression of T cell activity (evasion of step 3): cancer cells reduce the expression of co-stimulatory factors, which are needed, together with antigen recognition, for a full T-cell activation.
- Inhibition of T cell migration and infiltration (evasion of steps 4-5): cancer cells reduce the expression of chemokines that attract T cells. Modify blood vessel layout, making the tumour less reachable, and secern substances that alter T-cell mobility.

1.4 Cancer cells and therapies

Several therapies against cancer exist. Usually, biomarker testing, together with the analysis of the state of progression of the tumour and its phenotypic characteristics, is the tool used to decide which treatment or combination of treatments to apply to the patient. Generally, treatment can be used alone as main therapy, combined with other treatments, to reduce the tumour before the main therapy (*neoadjuvant*) and/or to destroy surviving cancer cells after the main treatment (*adjuvant*). Moreover, according to the chance to eradicate the tumour, treatments can be given with curative, control or palliative aims.

One of the typical treatments of cancer is chemotherapy, a term that denotes the non-specific usage of intracellular poisons to inhibit mitosis (cell division) or induce DNA damage [375]. Chemotherapy is usually used as systemic therapy, meaning that, once introduced into the bloodstream, it is able to address cancer at any location in the patient's body. Despite its high potential for killing tumour cells, chemotherapy has the limitation of acting on cells in their mitotic phase (and therefore running into the risk of resistance caused by cellular quiescence) and of having a very high damaging effect also on healthy cells, causing many side effects. For this reason, in clinical practice, they try, when possible, to combine chemotherapy with complementary treatments in terms of effectiveness and less impact on the patient's health. Radiation therapy is another typical treatment, often used synergistically with chemotherapy.

Radiotherapy acts in the same way as chemotherapy, but in order to induce the same effect on cells, it uses ionising radiation, generally delivered by a linear particle accelerator, instead of chemical reactions. Being a local treatment, it reduces the chance to address the body, gaining in reduced and more localised side effects [67].

Another category of treatment is targeted therapies, which are based on the concept of identifying genetic mutations and abnormal proteins that drive the growth of specific cancers and using them as a target. Targeted therapy drugs specifically target these abnormal proteins and not all the fast-dividing cells, preserving healthy tissue. These therapies are effective only if the cancer exhibits the specific target and faces the problem of resistance to these agents developing over time. They work by acting on molecular targets such as cell surface antigens, growth factors, receptors, or signal transduction pathways that influence cell cycle progression, cell death, metastasis, and angiogenesis. These therapies can be monoclonal antibodies, small-molecule drugs, hormone therapies, signal transduction inhibitors, gene expression modulators, apoptosis inducers, angiogenesis inhibitors, immunotherapies, or toxin delivery molecules. By blocking signals that promote cancer cell growth, interfering with cell cycle regulation, or inducing cell death, targeted therapies aim to effectively kill cancer cells. Immunotherapy can be considered as part of targeted therapies. Among them, also oncolytic virotherapy is an emerging treatment modality that uses replication-competent viruses to destroy cancers.

Given the interest in solid tumours in this thesis, and in particular, in their geometrical characterisation, we take into account radiotherapy that, for its nature, can be delivered with spatial precision. Moreover, considering the lack of this treatment, it is easy to observe that targeted therapy could be considered as a complementary choice since the pros of one seem to match the cons of the other. Thus, coherently with the content of this thesis and the models developed in the same, we now concentrate on two treatments: radiotherapy and oncolytic viruses.

1.4.1 Radiotherapy

Radiotherapy remains consistently effective in cancer treatment, with approximately half of all patients undergoing it at some point in their management [46]. Ionising radiation (IR), primarily consisting of photons, is widely used in radiotherapy. The principal damaging effects result from the ability of IR to ionise molecules within

cells, particularly DNA. Historical experimental evidence strongly supports DNA as the primary target for radiation-induced cell killing [248].

The DNA damage response (DDR) is a complex system that coordinates cellular reactions to radiation-induced DNA damage. Specialised sensing proteins detect DNA lesions, signalling to the cell and initiating the DDR. This response focuses the cell's attention on the damage, halting processes like transcription and cell-cycle progression while initiating DNA repair.

Cell sensitivity to radiation varies, with actively reproducing cells being more susceptible due to their need for accurate DNA information. This highlights the necessity for considering phenotype heterogeneity when analysing not only therapy effectiveness but also selection processes induced by the therapy itself. Successful radiation treatment primarily involves causing the death of individual tumour cells through direct or indirect mechanisms. Direct death can be induced through apoptosis, autophagy, or other means, while indirect death involves inducing senescence or occurring late after attempted mitosis.

The surviving fraction (SF), representing the number of colonies relative to individual cells' plating efficiencies after treatment, is a crucial measure. A cell survival curve, used in radiobiology, illustrates the relationship between the fraction of cells retaining reproductive integrity and the absorbed dose of radiation.

In order to model and quantify the killing potential of radiation, we can think of some specific regions of the DNA as the only ones responsible for maintaining the reproductive ability of cells. The survival of a cell after radiation exposure could be interpreted, from a probabilistic point of view, as the chance of not being hit in these sensitive regions. The simplest idea is to think that one hit by radiation on a single sensitive target would lead to the death of the cell. This is called single- target single-hit inactivation. Under the assumption that a large number of hits takes place on different cells, but the is a very small probability (p) that, considered a given cell, a next hit could occur, Poisson statistics can be used to derive an equation for the related survival curve. Thus, we have:

$$p(\text{survival}) = p(0\text{ hits}) = e^{-\frac{D}{D_0}}$$

where D_0 is defined as the dose that gives an average of one hit per target.

A more general version of target theory called *multi-target single-hit inactivation* can be used to better fit the experimentally observed survival curve. In this idea, the cell is supposed to have n sensitive targets, and, in order to die, it needs to be hit at least once per target. Repeating the same argument as before, we obtain:

$$p(survival) = 1 - p(1hitoneverytarget) = 1 - \left(1 - e^{-\frac{D}{D_0}}\right)^n.$$

Trying to consider a simplified mechanistic interpretation of irradiated cell dynamics, one could synthesise as follows:

1. DNA double-strand break (DSB) number is proportional to radiation dose (D).
2. Considering an average repair half time T_R, these DSBs can be repaired, with first-order rate constant $\lambda = \frac{ln2}{T_R}$.
3. Binary misrepair of pairs of DSBs produced from different radiation tracks can produce lethal lesions with a yield proportional to the square of the dose. The occurrence of the two independent radiation tracks may be separated in time within the overall regimen. This temporal gap enables the repair of the first double-strand break (DSB) before it can engage in pairwise misrepair with the second.
4. Single radiation tracks can produce lethal lesions with a yield that is proportional to the dose.

Using this mechanistic view (and also supported by the empirical observation that a cell survival can simply be fitted by a second-order polynomial), the following formulation, which is termed the *linear-quadratic (LQ) model*, is determined:

$$p(survival) = e^{-(\alpha D + \beta D^2)}.$$

The main parameters of this model, α and β, represent the intrinsic radiosensitivity of the irradiated cells: the higher their values, the higher the tumour sensitivity to radiation. The α component includes the effect of nonrepairable (lethal) lesions in the DNA from a single radiation event. In contrast, the β component represents lethal damage arising from the interaction of repairable (sublethal) lesions, each produced by independent radiation events [116]. Several protocols could be adopted, meaning that one could choose different amounts of radiation to be provided, but

the radiation amount could also be fractionated using a different amount of single doses and varying the timing. The ratio of the two parameters, α/β, is a measure of the fractionation sensitivity of the cells: cells with a α/β, are less sensitive to the sparing effect of fractionation [430].

Different protocols, also with the same total amount of radiation, could lead to very different scenarios. For example, prolonged irradiation could be partially useless if in a first moment all sensitive cells have been killed. Moreover the environment itself is can be modified by the therapy directly or via the killing effect on the tumour, whose cells are responsible for secreting abiotic factors and consuming nutrients. This is the specific case of oxygen.

The response of cells to ionising radiation is strongly dependent upon oxygen [204]. On the one hand, oxygen presence avoids hypoxia-inducible factor (HIF) that is responsible, among different effects, for proliferation inhibition, thus ensuring a greater number of cell divisions, which, as mentioned before, increases cellular radiosensitivity. On the other hand, broken DNA strands binding with oxygen molecules fix the damage and avoid the chance of DNA repair. From a modelling point of view, this is caught by the insertion of oxygen enhance ratio (OER) in the probability of survival formula (as a modifier of α and β parameters). OER is evaluated as the ratio of the needed radiation dose in hypoxia on The need for radiation dose in the air allows for the same level of biological effect.

The LQ approach leads to various formulae for calculating isoeffect relationships for radiotherapy in order to compare the effectiveness of protocols. The simplest method to do this is converting each schedule into an isoeffective schedule in 2 Gy fractions. We use:

$$EQD2 = D\frac{d+\alpha/\beta}{2+\alpha/\beta}$$

where EQD2 is the total dose in 2 Gy fractions that is biologically equivalent to a total dose D given with a fraction size of d Gy, assuming a relationship between D and d which is defined by α/β.

1.4.2 Oncolytic viruses

As noted in Section 1.3 various mechanisms of tumour cells can cause an impoverishment of the defence capacity of the immune system, with consequent negative

outcomes both on the natural response of the human body and on the outcome of any immunotherapy treatments. Moreover, both (epi)genetic and environmental factors can impact the effectiveness of therapies. In reference to this, we have already addressed the impact of hypoxia on treatments such as radiotherapy.

This made it necessary to design therapies that would be able to fill these gaps. Target therapies were thought with this aim. In particular, here we stick to a class of target therapies that are interesting in particular for their overlapping with both the immune system and the hypoxia problems: the oncolytic viruses.

With oncolytic viruses (OVs), we refer to some organisms capable of recognising (naturally or by genetic manipulation [388]) and destroying various cells within the tumour milieu, with the goal of stabilising and reducing tumour growth [390]. Different viruses are used for OVs, such as adenovirus, herpes virus, vaccinia virus, and vesicular stomatitis virus, among others.

The mechanism that viruses use to kill tumour cells is lysis, which consists of the breaking down of cells membrane, compromising their integrity and functionalities [329]. When the infected cancer cell is destroyed, it releases virions (which are infectious virus particles) that are able to spread and infect other tumour cells [173].

With respect to the immune system, there is an ambivalent correlation. On the one hand, the immune system tends to impede the spread of viral infection [142]. On the other hand, oncolytic virus therapy seems to trigger the immuno-action on tumour cells and enhance its effectiveness. In fact, when considering T-cell role, some tumours have the ability to prevent their activation [384] and, in the case of target ICIs, to lose targeted antigen [186]. In Ref. [384], they affirm that oncolytic viruses have the ability to create an immunostimulatory signal that increases immune cell trafficking toward the tumour [429] to reverse the immunosuppressive status of the microenvironment [387], but even more significantly to stimulate the development of a new, specifically tailored immune response against certain markers (epitopes) present on the tumour cells that have been lysed [450].

Moving to hypoxia, the heterogeneity of OVs, including different therapies according to the kind of virus chosen, makes it impossible to state a common behaviour in hypoxic conditions [207]. For example, with respect to replication, viruses that seem to be affected by hypoxia are adenovirus (whose replication is hindered) and herpes simplex virus (whose is boosted [6, 172]). Considering the cytotoxicity, the vaccinia virus demonstrates an increase in certain hypoxic cancer cells despite no im-

pact on viral protein synthesis or transgene expression. The vesicular stomatitis virus, which is not affected by its replication properties, exhibits effectiveness in killing hypoxic cancer cells. However, in renal cancer, it is vulnerable to elevated levels of hypoxia-inducible factor-1α, which drastically enhances resistance to cytotoxicity. Various hypoxia-selective and tumour-type-specific oncolytic adenoviruses, created by incorporating hypoxia-responsive elements into synthetic promoters to regulate crucial genes for viral replication or therapeutic genes, have proven to be both safe and effective. Note also that hypoxic tumour-homing macrophages can efficiently act as carrier cells, delivering an oncolytic adenovirus to the hypoxic/necrotic regions of the tumour.

An example of exploitation of the knowledge of tissue oxygenation in order to optimise therapies can be the breast cancer case [117]. In breast cancer, hypoxia has the double effect of conferring resistance to both radio- and chemotherapy and of desensitising estrogen-receptor-positive tumours to hormonal therapy. One improvement could be trying a combined therapy, with standard therapy acting on normally oxygenated tumour cells and genetically engineered herpes virus (with induced reduced virulence to limit infection of normal tissues) acting on hypoxic ones. Another possibility could be given by exploiting the lack of oxygen in breast cancer and the augmented replication rate of herpes viruses. The main idea is to operate genetic mutation of the virus to target cancer cells through deletion of UL39, which is the gene that encodes the large subunit of ribonucleotide reductase (RR). Hypoxia, in fact, stimulates RR production, significantly enhancing the cytotoxicity of the multimutated virus in hypoxic breast cancer cells [358].

1.5 Cancer as an evolutionary process

1.5.1 Cancer: a multi-scale system

When we talk about cancer, we can think about a mass or its components. Different dynamics occur in the tumour and at different levels. We distinguish three different scales, and we refer to them as *microscopic*, *mesoscopic* and *macroscopic*.

- The microscopic scale is the lowest level that includes all the dynamics occurring at the subcellular level. This involves membrane receptor activity,

cell internal processes, and all the dynamics which are results of intracellular pathways, intrinsic or triggered by the communication with the outside through the receptors.

- The mesoscopic scale refers to all the processes happening at the cell level. It is an intermediate scale since it still considers the cell as a single entity and as an agent that interacts with other cells (healthy, tumour cells of the same population or another) or with the extracellular environment. This means that we consider the effect of these in terms of behaviour (death, proliferation, displacement, phenotypic switches) but without considering the microscopic processes that regulate these changes (focus moves from the intracellular processes to the intercellular ones).

- The macroscopic scale is the largest one. At this level, we lose the focus on the agents' dynamics to directly describe the processes occurring in the population of cells, which is considered an identity in its totality. Tumour dynamics is coupled with the evolution of other tissues or cell populations (blood vessel network evolution, competition for space and resources, ECM remodelling, etc.).

Not only different scales refer to different "zooms" on the system. Dynamics involved in different scales occur in completely different time ranges, meaning that processes included in a scale can be considered important if taken into account at the time scale of the upper level.

1.5.2 Cancer phases and characteristics

Every cancer has its history, but its evolution is divided into different phases. Cancer is typically labelled in stages from I to IV, when a mass is present. The classification is based on tumour mass characteristics and the impact on the rest of the host body.

At stage 0, the tumour mass has not yet formed. This is the phase of abnormal cell formation, with the potential to become cancer. This is also called *carcinoma in situ*.
At stage I, cancer cells have formed a proper tumour mass, but they are still reduced in size and limited to one area. At this phase, the nutrients provided by the host are sufficient for cancer cell division so that there is an (almost) competition-free

proliferative dynamics. This is also called *early-stage cancer*.
During stages II and III, tumour mass grows in size and extends to surrounding tissues or lymph nodes. In this stage, the tumour induces angiogenesis, i.e., the formation of new blood vessels, in order to increase the transport of nutrients (carried by the blood) inside the tumour mass. Moreover, a hypoxic condition due to increased oxygen consumption induces epigenetic changes that promote invasive potential (migratory skills) in cancer cells.
Finally, when reaching stage IV, the cancer has spread to non-adjacent parts of the host body (metastasis). This is also called metastatic cancer.

It is then important to know:

1. the mechanisms that, from a healthy state, allow for the entry in stage 0;
2. the mechanisms that make the cancer mass evolve in the different stages.

1.5.3 Eco-evo-devo in cancer evolution

Neoplasms are composed of an ecosystem of evolving clones, competing and co-operating with each other and other cells in their microenvironment, and this has important implications for both neoplastic progression and therapy. But if the transformations themselves can be considered as results of cellular evolution influenced by genetic and epigenetic modifications, the effective advantage in terms of survival and predominance that they confer is not intrinsic and immutable in time but is determined by the microenvironmental ecology.

For example, in the first phase of tumour growth, when there is full availability of nutrients, clones characterised by high proliferation rates (but needing more resources to fuel the division process) would have an advantage. Growing up, the tumour will sensitively decrease the amount of available nutrients, changing the fittest trait from highly proliferative cells to more resistant cells or more motile cells. Also, bigger tumours usually induce a higher immune response, giving an advantage to cells which are able to evade T cell activity. Moreover, if the tumour is detected, therapy is usually applied. A lot of treatments, such as radiotherapy, act on dividing cells, giving an advantage to cells able to enter a quiescent state during the treatment and then go back to proliferative dynamics once the other populations have been reduced by the therapy and the nutrient availability increases. Under an

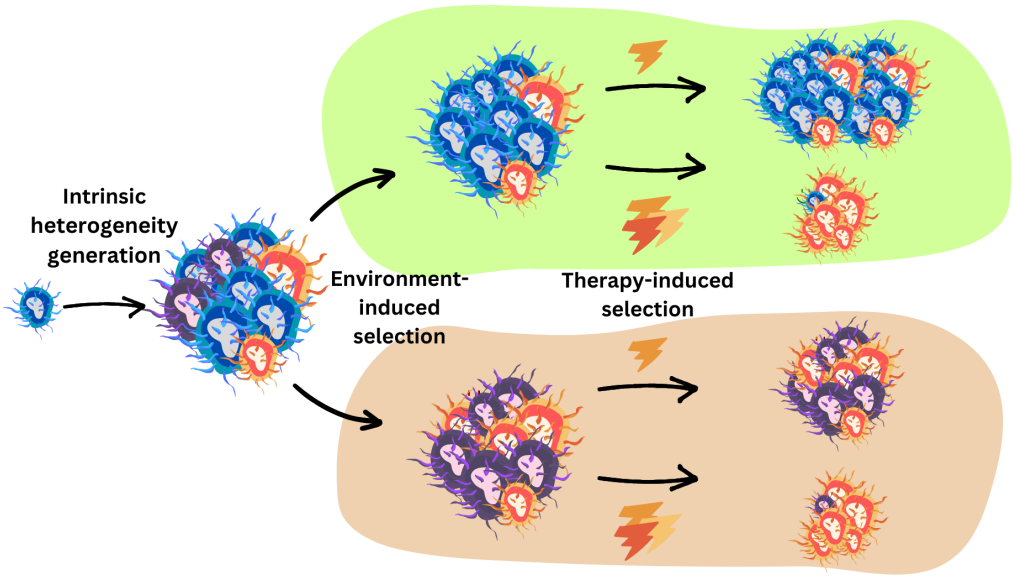

Fig. 1.7 Graphic representation of the evolutionary process of a tumour mass. Starting from an initially small number of tumour cells (born following tumourigenesis), the cell population undergoes heterogenisation or homogenisation due to intrinsic mutation or selection factors or triggered by the environment and therapies. Original figure.

ecological, evolutionary developmental biology point of view (eco-evo-devo), the key idea is to study cancer history in order to uncover the rules that underlie the interactions between its environment, its genetic (and associated), and development and to incorporate these rules into evolutionary theory [2]. In Ref. [308], a possible simple classification of ecological and evolutionary factors is provided.

As it can be seen in Fig. 1.8, the proposed ecological index (eco-index) is composed of two factors: hazards (H) and resources (R) available to the neoplastic cells. The evolutionary index (Evo-index) is also composed of two factors: heterogeneity over space (D) and over time (Δ). Heterogeneity is considered in terms of genetic, epigenetic and phenotypic alterations, quantified in absolute values and frequencies. All these indexes have a low value (1) or high value (2). tumour mass can end up showing different index values coming from different developmental histories due to selective pressures. For example, an ecological index of H1-R1 would select highly resistant cells with a tendency to move to locate more resources. H2-R2 tumours would probably undergo massive cell turnover as highly proliferative cells would rapidly replace cells that have been killed by the hazards but would then be exposed to the same death potential. For the evolutionary counterpart, an initial D1

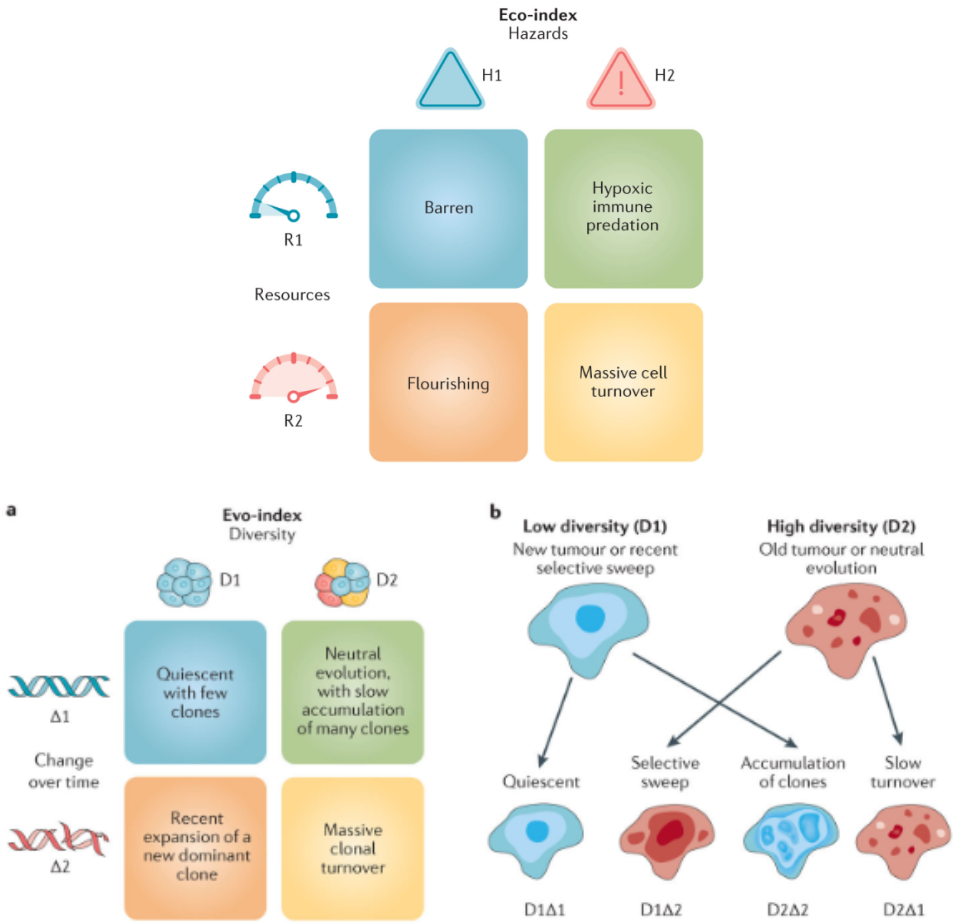

Fig. 1.8 Graphic representation of ecological (top) and evolutionary (bottom left) indexes proposed in Ref. [308]. Map of possible index evolution in time (bottom right). Figures taken from [308].

tumour could preserve its low heterogeneity by quiescence or accumulate mutation, becoming D2 in a second moment; in the same way, environmental pressure could amplify the internal heterogeneity of an initial D2 tumour or homogenise it via selective sweep. In Ref. [308], these features and the relative proposed classification are connected with possible therapy design strategies. As shown in Fig. 1.9, aware of tumour and environment-specific characteristics, it could be possible to apply and combine different therapies, trying not only to maximise the killing potential of the treatment but also to control the evolutionary history of the cancer cell population in order to move toward directions that keep a possible therapeutical strategy open.

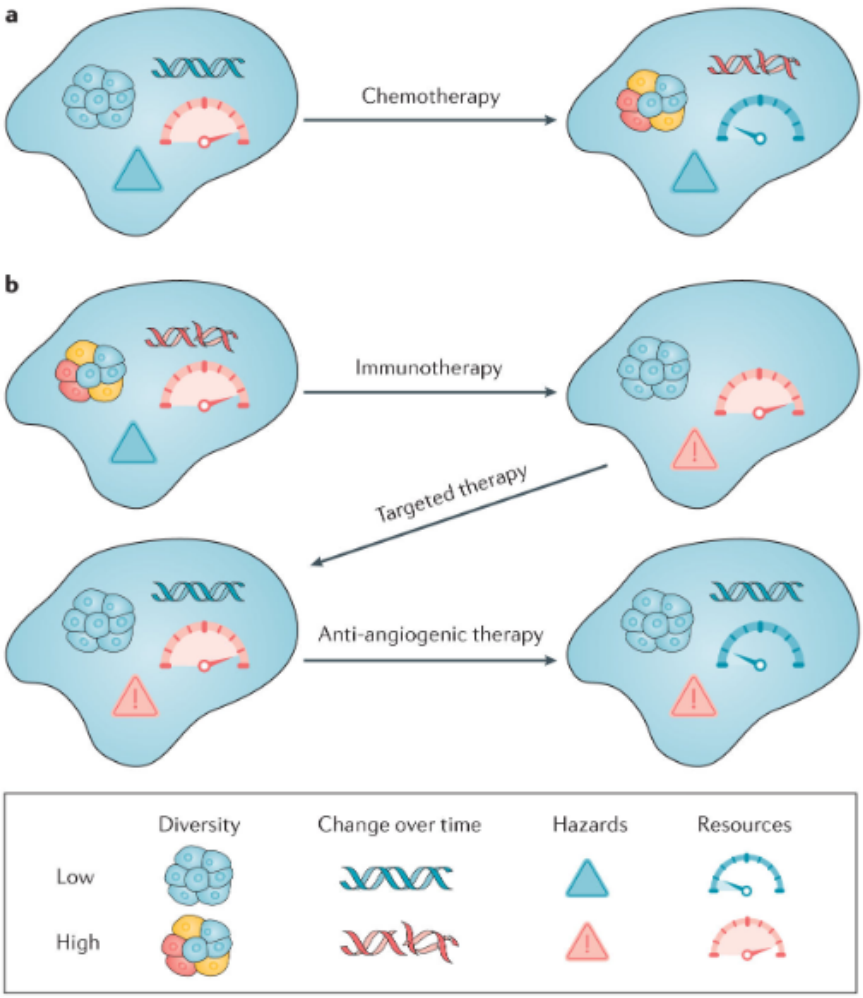

Fig. 1.9 Graphic representation of possible time evolution of eco-evo indexes due to delivery of different therapies. Figure taken from [308].

1.5.4 Trade-off

The concept of trade-off is central in evolutionary dynamics [236, 219, 65]. At a cellular level, this means that a cell has a finite amount of resources to be allocated, and using them for a function results in depriving another possible functionality of the fuel needed to be performed. Cancer trade-offs happen both at phenotypic and genetic levels.

One of the most famous trade-off mechanisms is the one between proliferation and motility, referred to as "go or grow" ([215]). Cancer cells are able to switch

between migratory and proliferative phenotypes [60], as we previously considered when introducing epithelial-mesenchymal transition. According to theoretical studies, motility in cells (and also in cancer cells) is usually triggered by a disadvantage in staying, usually caused by harsh conditions or lack of nutrients [280]. Based on this assumption, in Ref. [215] they propose as a cause for EMT this microscopic 'Go or Grow' mechanism (migration/proliferation trade-off) triggered by the nutrient shortage (in this case hypoxia).

Due to the same limited resource conditions, another well-known trade-off in malignant cell dynamics is between proliferation and survival. In rich environments, cells prioritise rapid proliferation but are vulnerable to apoptosis. In adverse conditions, cells exhibit slower proliferation but enhanced survival. Cancer cells adapt to their environment, displaying either proliferation or survival phenotypes. Selection for strategies may change over time due to tumourigenesis and therapies, favouring extreme phenotypes in later stages, such as highly proliferative cells with compromised survival or seemingly dormant cells with enhanced survival abilities ([15, 65]).

Finally, to close the triangle, a direct trade-off between migration and survival also exists. The cost of migration due to environmental adversity and resource fluctuations in the resource may include increased risk of predation and hazards associated with exposure to the new environment [157], leading to the preference of allocating resources to improve phenotypic plasticity in the direction of gaining survival chance in harsh conditions. In this light, trade-off dynamics underlie the importance of a deep knowledge of activation pathway in response to environmental factor in order to quantify phenotypic composition of the tumour mass according to observed conditions and to be able to predict cancer behaviour.

1.6 Relevance for this thesis

This chapter aims to provide the basic biological knowledge to understand the modelling choices of the works presented later, both in terms of processes selected to be captured by models and with respect to the mathematical form adopted.

As will become clear in chapters relating to the models, the biological treatment surpasses the mathematical formulation in precision of detail (in most cases).

However, we consider it important to give a "complete" vision of the biological framework for two main reasons. On the one hand, the mathematical model does not contain all the degrees of detail of biological knowledge due to the need for modelling simplification: the objective is to minimize the number of parameters and components of the model equations without affecting the ability to replicate the observed phenomenon with a biologically consistent formulation. This does not make it any less important to be aware of the biological knowledge that lies upstream of this reduction process. On the other hand, mesoscopic and macroscopic mathematical models often include terms that seem to lack in connection with the microscopic dynamics. On the contrary, in a well-built model this connection is "hidden" but does exist and it is important to have full awareness of the process of derivation from the microscopic scale (accompanied with the biological precision exposed here). In fact, without it, parameter estimation would be excessively dependent on data and hard to evaluate in its biological reliability. This manuscript contains many models investigated from a theoretical point of view and verified in qualitative terms. The subsequent steps, aimed at creating a link with the available medical data, involve a parametric quantification which requires awareness of the "hidden" biological processes in the mathematical model.

Section 1.1 gives a general overview of cell functioning. In particular, cell cycle, metabolism, and homeostasis explain some common assumptions made in the various models. In our models, cells are characterised by proliferation activity, which, according to the biological information provided, appears to be a central point in the cell cycle, respiration and regulation. Some of the processes that cells undergo (such as nutrient consumption or therapy effectiveness) in our models are related to their proliferative dynamics. Proliferative switching according to cell selection and oxygen availability is included, capturing the metabolic consideration observed. Additional information provided stands as a hint for further work. An idea is to include more specific models based on cell phase in the cell cycle. Another possible direction is the formulation of a mathematical model for the Warburg effect, considering the switch in the respiration strategy of the cell, its correlation with its survival chance in harsh environment and with its impact on oxygen consumption. The characterisation of cell functionality with respect to their specialisation degree is a central theme going in the direction of developing models addressing stemness and also considering liquid tumours.

The dissertation on oncogenesis highlights discrepancies in the knowledge of the actual trigger for the generation of tumour cells but also coherence regarding the recognition of an internal heterogeneity of the tumour population supported by mutation processes. This explains our common choice in the models not to directly insert tumourigenesis, starting from a small set of tumour cells already formed, but admitting heterogeneity within the same and evolutionary dynamics (of mutation and selection) in favour of it (as presented in Section 1.1.3).

Furthermore, for reasons of simplification of the models, we do not include healthy cells among the populations described. Despite this, when healthy cell behaviour has effects on the individual components included in the models, we directly insert them (for example, when we consider tissue nutrients, we allow a decay term that takes into account the consumption by healthy cells).

Cancer hallmarks presented in Section 1.1.2 are included in the models, both in the dynamics themselves and in the parameter estimations. Cancer cells in our model proliferate faster than healthy ones and slow down in the proliferative dynamics, which are connected with environmental stressor-inducing quiescence. In our model, in fact, quiescent cells do not create a separate population but are determined by their phenotypic state. Together with the insertion of a carrying capacity, which is only determined by space availability, this reflects self-sufficiency in growth signal, apoptosis evasion and cancer metabolism information. Moreover, phenotypic plasticity and epigenetic alterations jointly with the concepts about the evolutionary processes presented in Section 1.5, are central in all the models presented in the thesis, with epigenetic expression being linked to phenotypic behaviour in terms of proliferation (all models), survival (models in Chapter 3, 4), motility (models in Chapter 5, 6, 7), therapy effectiveness (models in Chapter 5, 8), and immunoevasion (models in Chapter 9). In particular, proliferative dynamics are typically seen as a trade-off with the others, with the only exception of Chapter 7 where motility and proliferation are considered as two independent traits, whose eventual trade-off dynamics emerge as a consequence of evolutionary dynamics.

Cancer cell's interactions with the environment, described in Section 1.2 have a strong impact on the thesis's modelling choices, with models presented in Chapter 3, 4, 5, 6 directly including oxygen as an environmental factor influencing cancer cell dynamics. In particular, oxygen is responsible for selective dynamics (Chapter 3, 4) and modulating proliferative and/or motile dynamics (all chapters cited above).

Tissue invasion described in Section 1.2.2 is a central topic in Chapter 5 and 7, with Chapter 5 directly addressing metastatic dynamics. Sustained angiogenesis (Section 1.2.1) is a future work perspective for the work presented in Chapter 5.

Cancer cell's interaction with the immune system, presented in Section 1.3, is central in the ongoing work presented in Chapter 9 and provides a hint for future perspective in relation to oncolytic viruses considering a model in Chapter 8. In particular, in Chapter 9, cells are characterised by a trade-off between proliferation and immunoevasion (see Section 1.3.3), with highly proliferating cells being more visible and killed more easily by the immune system.

Two models presented in the thesis describe therapies. In Chapter 4, according to what was introduced in Section 1.4.1 from a biological point of view, the effectiveness of radiotherapy is correlated with the oxygenation of the environment and the effective proliferative state of the cells, with cells being more hit when diving in normoxic conditions and resistance when quiescent and hypoxic. Moreover, oncolytic virus therapies are modelled in Chapter 8, where interaction with oxygenation of the tissue is investigated (as depicted in Section 1.4.2, that also put the bases for an overlap of works presented in Chapter 8 and 9).

Finally, evolutionary processes of Section 1.5, with dynamics underlying the tumour mass and actions operated by the environment and the medical practice influencing the history of the tumour, are present in all the works presented in the thesis. Specifically, the multi-scale nature of the oncological disease, described in Section 1.5.1 has a direct mathematical counterpart in the model presented in Chapter 6, where we start from a model describing the microscopic dynamics of tumour cells, and we adopt mathematical procedures to obtain a macroscale model.

Chapter 2

Mathematical framework

2.1 The need for mathematical modelling

Resistance, metastasis and treatment failure are rather common events in clinical practice. The complexity of cancer, considered as a system, and the dynamics that occur at the cellular and mass level are two of the main complications that currently make it impossible to fully understand the pathways and mechanisms underlying. Therefore, we lack complete knowledge that explains the reasons behind the failures of treatments which are supposed to be tailored to cancer cell properties.

However, although it is clear that there are many aspects of the biology of the tumour mass that we do not know, we cannot reduce the problem to a lack of knowledge. In fact, even dynamics of which, taken individually, we have a profound understanding, inserted in the context of a system, connected and interacting with other pathways, are not fully controllable and predictable. This is the paradigm of *system biology*, which is a biology-based interdisciplinary field involving computational and mathematical sciences that has the aim of analysing and modelling complex biological systems. In system biology, this is done consistently with the concept of *holism* [396], according to which a whole system is expected to reveal properties (referred to as *emergent*) beyond its part, in contrast with the *reductionist* theory which thinks of a system as completely understandable as the result of simpler, separable processes.

This is a key point in which mathematical modelling has the potential for improvement. Mathematical models describe, in mathematical terms, the state variations and

behaviours of a component of a system (be it a cell, a cell population, a tissue, etc.) in relation to its action potential, its condition and interaction with other components or with the environment. This gives the possibility, starting from biological knowledge on individual pathways, of superimposing the cause-effect chains and seeing the effect of the interactions between them. Furthermore, the equations that govern the behaviour of agents in the biological system have the advantage of being analytically and/or numerically solvable. These solutions not only give the possibility of trying to reproduce the available data but also, through a process of estimating the parameters present in the model, making the mathematical approximation as faithful as possible to the observed phenomenon (with the intent of fulfilling reproducibility). Moreover, they additionally provide a forecast intent, as once validated, models can be used with a predicting aim.

In the oncological context, this predictive potential has the utility of being able to bypass the lack of accessibility to data typical of cancer masses, whether it is a physical problem (such as the non-reachability of the tumour location) or a temporal problem (such as the inaccessibility of future information or data that precede the diagnosis). On the one hand, medical practice has a limit to observability. Some easier-to-access information, such as the shape and global development of the mass, could be provided by non-invasive imaging (i.e. MRI), which, however, lacks accuracy on the (epi)genetic characterisation of the tumour. This type of information is poorly accessible because it requires complicated surgeries, which can even negatively affect the patient's outcome (see the example of biopsies and related risks [234]). Furthermore, even by obtaining analysed samples of the tumour, in vitro observation excludes all the variables that are influenced by the interaction with the environment, and therefore, the reliability of the information obtained is partial.

A mathematical approach could prove, via biological coherent formulation of a model and numerical approximation of the same, prove or explain theoretical cell hypotheses such as the selective pressure of therapies [308, 214] and chronic hypoxia [462, 320] or the co-optation of normal physiologic processes due to tumour cell biochemical and biomechanics communication with stromal cells [372, 250]. Another aspect is that the analysis of the solutions and the sensitivity with respect to the parameters used can provide a suggestion on the possible evolution of the mass before it occurs and an indication of the statistical validity of this prediction. In this sense, being able to provide a realistic model not only for the evolution of the

tumour mass but also for the therapies themselves allows the numerical simulation of the same to be used as an *in silico* patient. This term refers to the practice of using mathematical models as virtual laboratories in which real patients are "substituted" by computational approximations to investigate emergent clinical behaviours and therapeutical protocols. The main aim would be to provide a suggestion that supports the doctor in the delineation of the optimal treatment modality, dose and timing.

Consequently, once the effective contribution of the mathematics-medicine synergy has been proven [461], the question arises spontaneously as to which is the best modelling technique to use. The honest answer is there is no answer. On the one hand, the concept of the model's optimality is affected by the importance of various factors in its qualitative evaluation. If, on the one hand, precision and replicative effectiveness are important, on the other, the simplicity of the model guarantees greater ease in analytical resolution and, therefore, greater control of data dependence and greater predictive capacity; from a further point of view, more complex models, which aim more at coherence with reality, require complex numerical techniques for their simulation. Another factor to take into consideration is that of optimising the necessary computational resources. Furthermore, even if the optimality evaluation criterion of the model had been decided, the complexity of the cancer system and the heterogeneity of the processes, which includes different aspects such as nature (chemical, mechanical, etc.), scale (cell, tissue, etc.) and times, makes it impossible to find a single model that is optimal for each of these processes.

In this sense, we evade the question by saying that different modelling strategies have been proposed over time, and their analysis has led to a conscious knowledge of what the strengths and weaknesses of each are and what genres of processes are better represented by each of them. In the following sections, we present the modelling strategies that are included in the thesis, focusing on the reasons that led to adopting them in the analysis of specific oncological dynamics.

2.2 Continuous modelling

Continuous models abandon the single agent detail to gain the possibility of describing a set of them as a population or mass whose modelled quantity is density or numerousness (see [53]). This limits the use of these models to meso-macro scales (in the sense that continuous modelling of microscale processes is possible

only considering one cell per time), and to describe (portions of) tissues and cell aggregate, reaching intercellular dynamics as the highest degree of precision. Here, a difference arises. From a biological point of view, a tumour is a set of cancer cells that can be considered as follows:

- a phenomenological system: a population regulated as a whole by laws which are the results of cell properties, interactions and dynamics;
- a mechanical system: a mass governed by physical laws which are influenced by its aggregate of cell nature.

The choice between these two ways of visualising the tumour is not an aut-aut since its behaviour is likely to be determined, in reality, by dynamics both arising from mechanical and phenomenological processes. For example, in both views, the tumour population can include growth and movement. But if, from a biological point of view, the two aspects can be easily considered overlapped, from a mathematical point of view, the choice of which to make prevalent is needed as it leads to the selection of a specific modelling approach.

Referring to the two examples before, mechanical models include proliferation effects, but the phenomenological aspect is not considered, as it is only described as its results on the mass size and shape change in time (the daughter cells exert a "pressure," displacing nearby cells and causing a growth in tumour size). On the other hand, phenomenological models include movement but make the assumption of ignoring mechanical effects, i.e. the only allowed movements are the ones explainable as a combination of diffusion and *taxis* (attractive or repulsive response to an external stimulus) such as *chemotaxis* (directional movement in response to certain diffusible chemicals in the environment) or *haptotaxis* (directional movement up a gradient of cellular adhesion).

Mechanical models are characterised by the use of force-balance or momentum-balance interactions to determine how the cell, matrix and fluid components move in response to the physical forces involved [53]. In mechanistic models, cellular and tissue deformation are tracked, taking into account stresses and strains. In order to do that, a choice in the description of tumour tissue, matrix and interstitial fluid is necessary (if treated as elastic fluids or porous medium, for example). Some well-known works describing tumours based on the so-called *mixture theory* are, for example, [22, 81, 79]. In these cases, the tumour is described as a multiphase

material of cells, ECM and extracellular fluid. The underlined assumption is that at every point in the space, there is a fraction of each constituent type. Although this concept is of great relevance for the morphological and physical description that it can provide of the tumour, during this thesis, we will mainly adopt a point of view more similar to the first, in which the tumour is seen as a cellular population. While on the one hand, the interest in the geometry of the tumour could lead to the deduction of the optimality of mechanical treatment of the tumour, in our case, the interest in the volumetric and spatial characteristics of the tumour mass is closely linked to the connection with the evolutionary and selective dynamics which are best represented in population models. We will refer to the mechanical aspect when considering closure techniques for scale connection in multi-scale modelling (see Section 2.4) in Chapter 7. Later, when considering phenomenological modelling, we will use the term mass, but not strictly related to physical properties, rather as a physical quantity resulting from the juxtaposition of the cells belonging to the population, but whose properties we do not mathematically model in terms of the continuous mechanics of liquids/solids.

Coupled ordinary differential equations can be employed to simulate extensive cell population systems. In this framework, each dependent variable represents a specific, well-defined biological property common to all cells within a given population. These models are constructed by averaging across both the spatial variable and the biological functions associated with each population. Consequently, the system's state is only characterised by the number density of cells within each population. The formulation of these models involves technical adaptations of Lokta–Volterra type equations. Perthame's book [354] offers an overview of population models in biology, drawing upon an extensive bibliography documented in various books. In this context, it is clear that tumours that are not distinguished by a particular spatial characterisation are the best candidates for this modelling technique. Among all, liquid tumours are the most striking example. Liquid tumours, such as leukaemia, are characterised by a strong differentiation cascade (similar to the one of the hematopoietic system, starting from stem cells and moving to fully differentiated cells across a variety of intermediate stages). This usually leads to the modelistic choice of adopting different ODEs to describe different *compartments* (differentiation stages). [310, 462, 286, 416, 417]. ODEs also have the advantage of being easily attributable to treatment medical studies since the efficacy of therapies is usually quantified in term of "number of death of cells". Moreover, ODEs leave more space for analytical

studies that benefit from a simple mathematical formulation, such as optimal control [334].

ODE models are also adopted in order to quantify tumour spheroid growth when only considering reaction terms such as proliferation and death without characterising them in spatial terms [378, 371, 345, 114].

If there is no interest in average information, it is possible to catch the spatial and biological heterogeneity of the population using systems of partial differential equations. In this case, the variable is usually expressed in terms of cell density, and the multidimensional domain includes independent variables related both to the physical and biological space. Physical space is usually referred to as a time evolution and a spatial characterisation. Models that dedicate more dimensions to geometrical space allow us to avoid radial symmetry constraints. The biological internal variables (usually a scalar one) could be an indicator of any cell characteristics that impact specific cell functions and the related biological events under consideration. For example, it could indicate the age of cells or quantify the expression of a gene responsible for the determination of a particular behaviour, such as apoptosis or proliferation. This category of models takes the name of *structured population models* (a complete introduction and state of art in this field can be found in Ref. [354, 230, 138, 422, 423, 355]).

In particular coupling partial differential equations allow to represent all the players: cell populations, matrices, abiotic factors. Considering tumour spheroid modelling, previously introduced by ODE techniques, when considering spatial characterisation, the typical growth-limited behaviour of Lotka-Volterra modelling is usually conserved in Fisher-like models, and different approaches are mainly based on resource distribution, factors of growth inhibition and diffusive motion (to cite some early works, we find [404, 100, 4, 5, 319, 318, 98]). These works are characterised by the presence of non-uniform resource consumption (such as oxygen in Ref. [319]) and the insertion of apoptosis as a volume loss mechanism [318]. These biologically coherent introductions enable the model to reproduce clinically observed growth patterns. In particular, the model is able to characterise some conditions under which non-viable states can be distinguished among necrosis and dormancy. Mathematically, competition is also studied between populations evolving in fluctuating environments, using different modelling approaches, including deterministic predator-prey models and stochastic models. In Ref. [35], the evolu-

tionary dynamics of competing phenotype-structured populations are studied in a periodically fluctuating environment, and in Ref. [137], authors study Lotka-Volterra equations for two competing species under the assumption of coefficients being periodic functions. Also, [176] considers a phenotypically structured population inserted in a fluctuating environment. Here, the dynamics of mutations and selection are again described by a parabolic Lotka-Volterra type equation, this time under the assumption of non-local competition and time-periodic growth rate. One could also consider a spatially-variable environment as done in Ref. [108] where a general model of competitive and apparent competitive interactions is analysed to compare findings on coexistence in a temporally variable environment.

Considering, in particular, the fitting dynamics of phenotype with respect to the environment, in Ref. [357] authors use evolutionary bet-hedging, which consists of a trade-off between the mean and variance of fitness due to which phenotypes with reduced mean may be at a selective advantage under certain conditions. In general, integro-differential equations and PDEs (usually non-local parabolic ones) are used to exploit mathematical modelling in order to achieve a more in-depth understanding of phenotypic adaptation mechanisms in different biological contexts. In Ref. [148] authors model dynamics occurring due to mutualistic interactions between specialist and generalist species, where the specialist population is structured by a continuous phenotypical trait (here, quantifying the ability of individuals to consume specific resources).

This approach has also been used when considering therapies, for example in Ref. [368] where authors couple two integro-differential equations, modelling cancer and healthy cells, both exposed to therapy (here chemotherapy). The phenotypic structure, which is here related to the treatment resistance capability, is applied to both populations.

Following the tumour mass phases described in Section 1.5.2, after the formation of the primary mass and its growth up to a certain size, angiogenesis mechanisms are necessary to provide the necessary nutrients to go on with the mass development. This makes the tumour enter the vascular phase, which is characterised by two main dynamics: tumour-signalling-driven vessel formation and invasive phenotype switch of cancer cells. Considering the first one, even if the strong predominance of stochasticity makes it easier to model angiogenesis using discrete modelling, some successful attempts of adopting continuous modelling can be found, for example, in

Ref. [26], where the continuous approach is used to directly describe TAF (tumour angiogenesis factor) and the vessel building process is considered as a result of the interaction between endothelial cells and ECM. On the other hand, considering the invasive trend engaged by cancer cells in this phase, in Ref. [98, 97], authors study the coincidence of the critical tumour size that triggers the transition with the one that separates avascular and the start of angiogenesis. Moreover, going on again in the steps described in Section 1.5.2, the presence of intratumoral vascularisation is considered the mean by which cancer can metastasise. In Ref. [160] a theoretical description of cell population dynamics coupled with molecular binding to cell membranes is provided.

This spatio-temporal structure is used to illustrate dynamics arising from cancer invasion. Some works also use double structure, such as [338] where the population is structured both in terms of phenotypical trait and age. For instance, in Ref. [27, 28, 30], authors describe tumour invasion considering the interactions between tumour cells, ECM, matrix-degradative enzymes (MDE) and (later also) oxygen, while a local model based on haptotaxis is presented in Ref. [196]. In the same work, a non-local model for cancer cell invasion based on cell adhesion is discussed.

Local models assume that the dynamics of a dependent variable at a point in the domain are determined only by the value of independent and dependent variables at that point in the domain. On the contrary, if the dependency basin is not punctual, we talk about non-local models. For some biological settings, non-local models seem more coherent [76]. This is the case, for example, of particles that, with their presence, modify some sensing field. Moreover, if we consider agents secreting substances which act as chemo-attractors for some other agents, one could decide not to directly insert the abiotic factor in the models but consider an attraction kernel of the second population toward the first, dependent on their distance (based on an assumption of instant diffusion). As an example, Ref. [89] introduces a modelling set in which cells interact with each other by repulsion (if the distance between cells decreases excessively with respect to volume size constraints around the nuclei) or attraction (at medium distances through chemo-sensitivity or mechanically via formation of protrusions). Moreover, the forces exerted by each cell type on the others are included as non-local terms. Here again, a limit to the continuous counterpart is operated as presented in Section 2.4.

Based on the non-local setting of [196], in [159], the model is extended to catch dynamics resulting from cell-cell and cell-ECM adhesion properties of cancer cells for considering heterogeneous cell populations. Moreover, in Ref. [61], non-local modelling is adopted to describe cancer cell invasion and movement, considering the impact of integrin on adhesion properties. Also, in Ref. [307] authors study tumour growth in the absence of necrotic core formation, considering the heterogeneity in cancer cell population and the interaction with the TME in order to discover their results in terms of tumour progression and morphology.

In Chapter 1, we underlined the cross-correlation of heterogeneity that characterises both microenvironment and tumour cells. The mathematical framework of structured populations allows individuals to be differentiated with respect to their characteristics, whether they are phenotypical or genotypical. Keeping a generic perspective on structured population, not necessarily directly connected with the cancer field, in Ref. [70] authors start from a simple reaction-diffusion equation structured in spacial and motility capabilities term (resulting in a two-dimensional domain) and study front acceleration and selection of the most motile individual dynamics. Moving to a more complicated non-local parabolic Lotka-Volterra type equation, structured by a two-dimensional space variable and a one-dimensional phenotypical trait, in Ref. [71] authors keep into account spatial diffusion, mutations (as diffusion on the phenotypical trait) and space-local competition between the individuals. Even if not explicitly in the cancer context, in Ref. [69], authors propose an interesting use of structured population in the context of the study of the invasion of cane toads in Australia, introducing a structuring variable quantifying motility ability and investigating spatial propagation in a using a non-local reaction-diffusion–mutation model. Moreover, in the generic context of structured population, they demonstrate the presence of significant stable conditions in reaction-diffusion equations featuring a continuous parameter relevant to models of selection, mutation, competition, and migration within structured populations characterised by spatial and continuous trait variations. Keeping a more theoretical point of view, in Ref. [14], authors consider a non-local reaction-diffusion equation as a model structured as the previous, and they investigate the existence of travelling wave solutions, identifying a minimal speed above/under which waves exist/do not exist. Later, in a model based on this, environmental factors are added [13]. In Ref. [84], authors explore super-linear spreading within a reaction-diffusion model akin to the Fisher-KPP equation but

with the introduction of both a structuring variable linked to the dispersal ability of individuals and a non-local saturation factor with respect to one variable.

Moving to the oncological context, a theoretical investigation motivated by a basic model of tumour growth in order to explain the emergence of resistance to therapy is presented in Ref. [323]. Here, the equations of the model capture the competition for resources among individuals, which are phenotypically and spatially structured, regardless of their traits. The solutions demonstrate a concentration effect, favouring the fittest individuals. Authors establish the convergence of the solution towards a Dirac mass in the physiological trait, which varies over time and spatial location, exhibiting Lipschitz continuity. In [105] tumour growth dynamics are analysed via a system in which two hyperbolic equations govern cell densities in proliferating and quiescent states, while two elliptic equations model nutrient concentration and pressure. In a free boundary framework, authors establish the solution's existence, uniqueness, and regularity over short time intervals. Sticking to the hyperbolic part, in Ref. [104], the linear asymptotic stability of the stationary solution is proved. A multi-scale tumour model incorporating gene mutations' effects on tumour cell population density is introduced in Ref. [183], where oxygen and chemokine concentrations are considered. Analytical results include the solution's existence, uniqueness, and certain properties of the free boundary. Another approach in Ref. [456] considers a time delay in proliferation compared to apoptosis due to mitosis time and demonstrates that tumour volume self-limits, either disappearing or evolving to a dormant state, under the hypothesis of a small enough diffusion/doubling time ratio. In Ref. [457], angiogenesis is considered, investigating the existence and stability of steady-state solutions for a tumour under the hypothesis of a constant rate of tumour-induced blood vessel attraction. In Ref. [160], authors establish a general spatio-temporal-structural framework to enable the description of molecular binding to cell membranes coupled with the cell population dynamics in order to analyse the interplay between collective movement and the various molecules present in the biological system. Ref. [235] includes an examination of the impact of numerous small mutations on a model of population dynamics structured by phenological traits and spatially heterogeneous. In this model, various sub-populations compete for the same nutrient diffusing through the spatial environment. In Ref. [300, 436], the role of abiotic factor variation in mediating intra-tumour phenotypic heterogeneity is studied via a phenotypic structure based on the resistance to hypoxia and involving a trade-off with proliferation speed. The connection between the tissue scale changes

in tumour morphology and the cell-scale dynamics of proteolytic enzymes in the neighbourhood of the tumour interface is explored in Ref. [426] via a mathematical analysis based on a structured population model. In Ref. [301], the same type of model, this time structured by the expression level of a phenotype of resistance to cytotoxic drugs, is used to investigate the effects of cytotoxic and cytostatic drugs.

Moreover, continuous models are also suitable for testing different therapeutic protocols that simulate treatment strategies like surgery, vessel renormalisation, antiangiogenic therapy, chemotherapy, radiotherapy, immunotherapy, or oncolytic viruses. In Ref. [419], authors address perfusion challenges in tumours via vascular normalisation and decompression methods. Despite the promise, optimal strategy guidelines are absent. The so-developed mathematical model integrates vascular, transvascular, and interstitial fluid dynamics alongside tumour vessel properties to optimise a therapeutic intervention for enhanced perfusion. In Ref. [327] mathematical modelling is used to demonstrate the potential of metronomic chemotherapy as an alternative to maximum tolerated doses in normalising tumour blood vessels, enhancing perfusion, improving drug delivery, alleviating hypoxia, and boosting the immune response against cancer, including resistant cells. In a study presented in Ref. [439], authors examined vessel co-option dynamics in gliomas and brain metastases, particularly in response to antiangiogenic treatment. The mathematical model revealed how coopted vessels lead to hypoxia and secondary angiogenesis. In Ref. [57], authors extend a computer model that enables quantitative comparison of different metastasis formation models with clinical and experimental data in order to incorporate chemotherapy, radiation, and therapies. In the paper, they utilise discrete event simulation and piecewise growth functions to model tumour behaviour. Considering the investigation of radiotherapy effectiveness, in Ref. [95, 94], tumour diversity in oxygenated tissue is explored considering stemness levels influence on cell behaviour and response to treatment. Phenotypic evolution is linked to oxygen levels, revealing multiple steady states. The importance of oxygen levels in treatment efficacy is also emphasised with respect to radiotherapy responses. A rich review examination of vascularised tumour growth models can be found in Ref. [209], focusing on continuum-based approaches with the potential for clinical translation. Topics include tumour perfusion, drug delivery mechanisms, and personalised medicine challenges and opportunities.

2.3 Discrete and hybrid modelling

We hereby present a brief overview of discrete modelling (see reviews [325, 163, 162, 28, 134]). In discrete modelling, formulae that describe the dynamics of the observed agents are fit to discrete data, which are not infinitely divisible. In discrete models, each agent is provided with a set of rules that govern its behaviour according to its state and the interaction with other agents and with the environment. In contrast to continuous modelling, discrete modelling captures individual details.

As we stated in Section 2.1, various modelling approaches have been employed to simulate multicellular systems, each corresponding to distinct levels of approximation of biological reality, and each approach requires specific mathematical structures. In this case, we can easily see that the advantage of single agent precision can lie both in the ability to analyse dynamics at a subcellular scale (microscale) and in the possibility of describing single cells (mesoscale) or agglomerations (macroscale) characterised by a precise shape, state and spatial position.

The range of characteristics attributable to the agent, behaviours that can be adopted and influences perceivable by other agents and the environment are limited by the capacity of the chosen method, i.e. by how agents and environments are mathematically described. Discrete models can be divided into two main categories.

The first one is *lattice-based models*, which confine cells to a regular two-dimensional or three-dimensional lattice, with each computational mesh point updated over time based on deterministic or stochastic rules derived from physical conservation laws and biological constraints. Adopting a sufficient resolution degree allows subcellular details to be captured. A specific case within this framework is *cellular automata* (CA) models that represent each cell with a single computational mesh point. Other possible modelling choices include *lattice gas cellular automata* (LGCA) models where the same mesh point can host multiple cells and *cellular Potts models* (CP) that allows the usage of more lattice site to represent each single cell. In addition to the precision that can be achieved with sufficient mesh fineness, lattice-based models have the advantage of the simplicity of the spatial arrangement, which makes them accessible even without advanced computational expertise. Moreover, it reduces the need for complex interaction testing between discrete cells and facilitates direct coupling with the microenvironment by assigning continuum variables to each mesh point.

However, these two features also translate into some limitations. High-resolution mesh requires computational resources. To overcome this problem, one can limit the application to small systems of cells, incurring a limitation of applicability to real-life problems, or move to low-resolution lattices, with the risk of introducing artificial constraints on cell arrangement, orientation, and interaction. This, together with the chance of oversimplification of the spatial arrangement, could result in a struggle to capture specific patterns observed in normal tissues and cancers. Thus, if these limitations are impactful for the specific biological system considered, *lattice-free models* could be used instead. Lattice-free models, the second macro set of discrete approaches often known as agent-based (AB) models, allow agents to move without the constraints of discrete *voxels* so that distance and direction only depend on the physical characterisation of the dynamics. It is clear that, on the one hand, this strategy leads to a gain in degrees of freedom; on the other hand, the loss of discretisation of the spatial domain makes a mechanical characterisation of particle collisions necessary. AB models treat cells as distinct objects or agents capable of individual movement and metabolic activity, such as division or death, based on biophysically informed rules. Every agent can be characterised by the chosen level of detail. Cells can be described as pointwise elements or be characterised by size and shape. Also, signalling networks, genotypic and phenotypic traits, different gene expressions and epigenetic characterisation can be linked to single agents.

Agent-based models are particularly well-suited for scenarios involving freely moving and nonuniformly arranged cells. This is the case for immune system interactions with tumour cells and metastasis.

This complexity of individual cells, together with the freedom of movement in space, on the one hand, offers a better level of precision and overcomes the problems of layout constraints of lattice-based models. On the other hand, this can lead to high computational expenses, limiting their application to small cell systems. Here, the high cost not only comes with a large number of agents but is additionally increased by cell-cell interaction and heavy testing due to the lack of a regular cell arrangement.

In general, whether lattice-based or lattice-free, we can summarise the advantages of discrete modelling in simplicity and single agent precision, as well as its lack of analytical solution and high computational costs.

As called by its name, hybrid modelling pairs continuous and discrete modelling. Based on the observations that we highlighted in the previous sections, it is intuitive

to think that such a choice can be made in heterogeneous situations in which the elements to be modelled have such great differences that they cannot be adequately described by a single type of mathematical formulation, instead requiring a specification capable of capturing their characteristics. Such heterogeneity can match, for example, biological systems in which the essential dynamics occur at different times or spatial scales, i.e., "microscopic vs. macroscopic". In these cases, classical approaches typically rely on the idea that the optimal choice is using a density-based description for systems composed of high amounts of particles with negligible mass (such as molecules), while the discrete counterpart better fit a population made of agents that need to be considered as individuals (such as cells whose behaviour is influenced by the state in which it is). These mathematical frameworks are typically based on coarse-graining procedures [161], mean-field limits [90], or heuristic laws of large numbers [86]. Macroscopic formulations have also been derived by selected lattice-gas cellular automata (LGCA) in Ref. [82]. One typical setting, for example, when considering cell population evolution in a determined space and time, is to use agent-based modelling for cells, continuous chemical kinetic equations for microscopic processes happening inside the single cell and macroscopic continuous modelling (usually PDEs) for nutrients diffusion in the space. In this case, different modelling settings (discrete vs continuous) are used not to describe different players but to describe the elements of the same type having different behaviours, where the modelling strategies are chosen to better catch the specific dynamics. For example, one could have a cell population made of proliferative and moving cells, and in this case, the increase in cell density due to division could be easily caught by continuous modelling, while lattice-free discrete modelling would better fit a precise determination of the movement (as done in [122, 392]).

When going into biological details characterising cancer dynamics, one can easily understand how discrete and hybrid modelling can be exploited to represent them [321]. It is important to underline that, due to the great importance attributed to the tumour-microenvironment interaction, and given the preference of adopting a continuous description for abiotic factors (usually undergoing diffusive dynamics), discrete modelling has strongly moved towards a hybrid modelling approach. Nevertheless, recently, a variety of works have also adopted a pure discrete modelling approach to catch specific cell dynamics. One of the first advantages of using discrete modelling is that it allows for a detailed determination of phenotypical specific characteristics. One of the first works in which phenotypic heterogeneity of the tumour mass is

formally included is [253], where a three-dimensional CA model for brain tumour includes differences in proliferation capabilities and necrotic dynamics. In such a way, the model is able to reproduce experimentally observed phenotypic stratification of cancer spheroids. Phenotypically layered tumour structures, where proliferating, necrotic, quiescent and motile cells settle at different positions with respect to the tumour "centre", were also investigated using analogous discrete modelling techniques [164, 421]. Further works in the direction of [253] include treatments and clone evolutionary dynamics, mechanical interactions between tumour cells and stroma, the degradation of ECM by outer layer cells, and the nutrient gradient-driven cell motion [391, 174, 410, 245, 244]. In the same direction, a series of works starting from [152] and followed by [217, 115, 216, 218] analyse the role of the environment in term of re-orientation of migrating cells. Considering the characterisation of cancer stem cells, discrete modelling has been adopted in Ref. [180, 361, 192].

Hybrid modelling, more in general, appears to fit the interest in analysing cell populations characterised by different behaviours. Addressing one of the major trade-offs presented in the previous chapter, the proliferation-migration dichotomy, we see that, in particular when studying gliomas, agent-based models have been used to investigate the glucose- and mechanics-drive selection of migration versus proliferation for glioma cells [266], the quantification of parameters of a tumour's invasive dynamics [83], the oxygen role in influencing cell division, re-orientation, migration, or apoptosis [215]. When considering the switch between epithelial and mesenchymal states, in Ref. [267], authors investigate the interaction of tumour cells and signal-secreting cells (discrete) and the ECM (continuous). Correlation between hypoxia and tumour growth is studied with a hybrid approach in Ref. [25]. In Ref. [409], a hybrid cellular automation approach is developed to investigate the mediation of somatic evolution of cancer cells due to cell-microenvironmental interactions. Moreover, cell-based models are adopted to investigate the correlation between hypoxia and tumour growth, both in correlation with phenotypic plasticity and migration capabilities, in several works [29, 194].

Also, CP models [201] are adopted with the same modelling aim. Being able to use more mesh points to describe a single cell, this category of models allows for the mechanical characterisation of cells, which are modelled as deformable objects with a certain volume, able to adhere to each other and to the medium in which they live. After their generic application to cell sorting when introduced [203], this class of model has been applied to study tumour growth. In particular,

growth factors, nutrients and abiotic factors are inserted in the model [243, 403, 420]. Also, interaction with extracellular materials is considered in Ref. [428] using the same approach. The capability of mechanically characterising single agents in discrete modelling exploits its potential in models such as the one presented in Ref. [288, 287] where the emergence of invasive phenotypes is studied as a result of cell interactions, in particular considering how different proliferation, motility and apoptosis rates tailor the evolutionary dynamics. In Ref. [164], each cell is considered a physical agent characterised by elasticity, compressivity, deformability and adhesiveness properties. An even deeper mechanical cell characterisation is adopted in Ref. [393, 395, 394], where cell internal structure is described by a differentiation of the nucleus and the cytosolic region.

Another cancer aspect in which hybrid modelling is widely used is angiogenesis and the possible resulting metastasis dynamics. For example, in Ref. [27, 317, 316], authors use the discrete model in order to describe the formation of capillaries via chemical-stimuli-induced endothelial cell migratory and proliferative dynamics. They also examine fluid flow through these network structures and explore therapeutic delivery from tumour-associated vasculatures.

In Ref. [362], a lattice-based agent-based model is implemented in order to study cancer stem cell role in tumour growth, exploiting discrete modelling using in vitro assay to inform and calibrate behavioural rules and fitting in vitro and in vivo experiments to validate emerging population-level dynamics. In Ref. [340], authors develop an in silico agent-based model of triple-negative breast cancer that considers surface receptor CCR5-high and CCR5-low cells and breast cancer stem cells to predict the tumour growth rate and spatio-temporal distribution of cells in primary tumours. Again, considering the same cancer class, in order to allow for a detailed determination of phenotypical specific characteristics of cancer stem cells, discrete modelling has been also adopted in Ref. [339]. In this study, authors focus on the contributions of macrophages, fibroblasts, and endothelial cells on tumour evolution. Model introduced in Ref. [59] study cancer stem cells in which cancer cell agents are distinguished based on the differentiation stage associated with the malignancy. The investigation is driven by a treatment optimisation aim. Furthermore, keeping into account therapeutic perspectives, in Ref. [284], an off-lattice model is adopted to study cell heterogeneity in treatment responses.

The immune system is another context in which individual agent modelling is widely used since the motion and action dynamics of agents (such as T cells) benefit from individual characterisation. For example, in Ref. [17], tumour cells and T cells are modelled as individual agents, while abiotic factors driving the chemotactic movement of the immune system players towards the tumour are modelled as a continuum.

2.4 Multi-scale derivation of models

The biological interconnection between different scales needs to be found in correspondence with the mathematical counterpart. It is essential that macroscopic models are formally derived from underlying cellular models. One way to do this is considering dynamics at a cellular scale and then using the so-called *asymptotic methods*, which are based on the procedure of using a limit of intercellular distances toward those at the tissue level.

We can group these techniques into two main strategies:

- *parabolic limit* (low field) emphasises diffusion processes in the solutions, leading to drift-diffusion or reaction-diffusion systems;
- *iperbolic limit* (high field) emphasises convective or interaction terms, leaving diffusion at a lower order of magnitude.

See that multicellular models include a characterisation of active particles based on position and velocity (as in classical physics), but also on microscopic state coherent with their biological functioning, that influence macroscopic phenomena [92, 68, 353]. Another possible derivation strategy, based on a similar limit procedure of the previous, is starting from the tentative of representing multicellular systems using stochastic individual-based models [101]. In this mathematical formulation, a single-cell dynamic is captured by stochastic rules that can be tailored to enhance descriptive precision. Here, the advantage stands in being able to consider stochastic fluctuations in single-cell biophysical properties even in situations in which cellular densities are too low to be captured by the continuum model (with the same advantage of agent-based modelling highlighted when considering hybrid strategies for multi-scale phenomena). The limit procedure is to reproduce the emergence of population-

level phenomena that are induced by these low-level processes (see Ref. [16] for a full explanation of the theoretical aspects of the derivation). This kind of discrete-continuous derivation can be exploited in order to catch either transport dynamics (like chemotaxis) from velocity-jump process [222] or linear and nonlinear diffusion from discrete modelling of random walks [352] or systems of discrete equations [332]. One of the main advantages of these derivation strategies is not only the deduction of the "shape" of the equations defining the continuous model, but also the direct estimation of global parameters showed at the macroscopic level from the individual ones present in the discrete modelling (which are more easily observable).

2.5 Relevance for the thesis

Given the mathematical nature of the work, the thesis focuses mainly on continuous models, which as anticipated have the advantage of greater predictability and theoretical analysability. Furthermore, the numerical tools in our possession guarantee us effective simulations of the same, without exceeding computational costs (for every model we show the chosen numerical approach).

Given the interest in tumour spatial configuration, all continuous models are based on PDE systems. In particular, with the sole exception of the model presented in Chapter 7, which presents radial symmetry, our models are set on two-dimensional spatial domains free from symmetry constraints.

All the models presented can be said to be multi-scale since they take into consideration dynamics belonging to different temporal and spatial scales. However, a rigorous multi-scale derivation in mathematical terms characterises the model presented in Chapter 6. Also, the model introduced in Chapter 7 presents a formal derivation starting from a stochastic discrete model (characterised by single-cell dynamics) and leading to a continuous model at a macroscopic scale.

The interest in the epigenetic characterisation of cancer cell populations leads to the choice of the structured population in models introduced in Chapters 3, 4, 7, and 8 (moreover in Chapter 6 when considering micro- and meso-scale and in Chapter 9 as a future perspective) or multiple populations differentiated by epigenetic traits in Chapters 5 and 9.

Part II

Research results

Chapter 3

Continuous modelling for geometric characterisation of hypoxia-resistance and proliferation heterogeneity in tumours

In this chapter, we focus on a key aspect of tumour growth and evolution: the tumour-environment interaction. In Chapter 1 we observed that, in particular, the several pathways involves oxygenation of the tissues, inducing relevant co-implications with tumour dynamics (see Chapter 1). We deepen the investigation on the role of oxygen concentration in the determination of the epigenetic-phenotypic heterogeneity of cancer cell populations (part of the analyses and results included in this chapter were also previously published in Ref. [112]). The investigation of the evolution of the tumour mass, in terms of shape, size, and geometrical and epigenetic characterisation, does not only have an exploratory interest; when considering therapy, such features are predominant factors in the occurrence of relapses after treatment or failures in the eradication of the mass. While we keep the explicit therapeutical analysis for the next chapters, inspired by the interest in these specific features of the tumour, we hereby propose a mathematical model able to describe the eco-evolutionary spatial dynamics of tumour cells in their adaptation to hypoxic microenvironments [111]. The main novelty with respect to the existing literature is the combination of an epigenetic indicator used to structure the population with a 2d geometric domain that allows for the abandonment of radial symmetry. The epigenetic independent variable

included in the model is a descriptor for the experimentally observed metabolic trade-off between the proliferative potential and the ability to resist under hypoxic conditions. The model is settled in the mathematical framework of epigenetically structured population dynamics. We formulate it in terms of systems of coupled non-linear integro-differential equations, where dependent variables include cancer cells, necrotic cells, and oxygen.
Computational simulations show the strong effect of hypoxia-induced selection on the geometric characterisation of epigenetic- and phenotypic-defined tumour niches. This population composition, together with its spatial features, impacts tumour invasive ability and aggressiveness. Furthermore, we show the importance of the knowledge of environmental characteristics with the aim of providing a predictive advantage on tumour mass development.
Detailing chapter organisation, we present the biological framework and the modelling state of the art in Section 3.1. Section 3.2 introduces the model and foundational assumptions guiding our research. Section 3.3 details the numerical implementation, starting with parameter estimation and metrics for measuring tumour progression as outlined in Subsection 3.2.1. We proceed to examine tumour growth in a designated standard scenario, referred to as the reference case, in Subsection 3.3.1. Subsequent sections, 3.3.2 and 3.3.3, explore potential deviations from this reference scenario, specifically focusing on tumour invasion capabilities. Through selected examples, we underscore the significance of tumour-environment interactions in tumour development. In Subsection 3.3.2, we investigate how the spatially variable distribution of intra-tumoural blood vessels contributes to niche formation driven by blood vessel dispersion. Subsection 3.3.3 examines the effects of oxygen-related selective pressures on tumour cells, especially in light of adjustments in the proliferation-survival trade-off, and its influence on developing hypoxic resistance within tumours. The document concludes with Section 3.4, where we summarize key findings, discuss our approach's limitations, and suggest future research directions.

3.1 Introduction

The dynamic evolution of cancer, fuelled by its genetic and epigenetic instability, is a critical factor in the failure of cancer treatments [31]. The variability in the genotypic and phenotypic characteristics of cancer cells, which can fluctuate across different

locations and over time, coupled with the significant influence of environmental factors, leads to considerable variations in tumour progression among patients with the same histological types. Such variability, both within individuals and across different tumours, lays the groundwork for developing intra- and inter-tumour heterogeneity, posing significant challenges to the eradication of cancer [178].

Niche construction theory provides a robust framework for understanding the robustness of cancer; it positions cancer cells as exemplary invasive species that have thrived across thousands of generations, creating niches that enhance their proliferation and ability to invade new territories [231].

Oxygen levels play a pivotal role in this scenario. Clinical observations reveal that oxygen distribution within solid tumours is highly uneven, ranging from standard to mildly hypoxic, severely hypoxic, and even anoxic conditions [335]. The lack of oxygen acts as an environmental stressor, triggering a series of genetic and especially epigenetic mutations that significantly influence the eco-evolutionary dynamics of tumours. Cancer cells adapt by modulating their cellular physiology and metabolism, upregulating genes such as p53, HIF-α, GLUT-1, or IAP-2, which enables them to thrive in hypoxic environments and evade cell death [386].

This behaviour highlights a crucial consideration: despite their extensive capacity for adaptation, cancer cells must navigate trade-offs in allocating energy to essential functions such as growth, maintenance, reproduction, and movement. As a result, while they possess significant evolutionary potential, they cannot achieve optimality across all traits [144, 167]. Specifically, cancer cells may face a *trade-off* between enhancing cell survival under adverse conditions, such as oxygen deprivation and maximizing cell proliferation. This is evident in *hypoxia-resistant* cells, which show a reduced proliferation rate, with doubling times twice as long as those of normal cells [312].

The impact of hypoxia on the eco-evolutionary dynamics of tumour cells also has critical implications for therapy. The emergence and extinction of dominant clones, whether occurring in bursts or more steadily, necessitate tailored clinical approaches. Variability in tumour responses may be linked to the spatially heterogeneous distribution of blood vessels within tumours; this dispersion creates ecological niches that select for cells with differing resistance capabilities. Furthermore, variations in the blood vessel network can lead to heterogeneity in the tumour microenvironment among patients, affecting tumour responses [119, 19, 283].

Mathematical models serve as valuable tools in this domain, acting as *in-silico laboratories* for testing various environmental conditions, tumour compositions, and therapeutic strategies. These models can streamline experimental trials, enhancing the efficiency of experimental protocols and clinical interventions while reducing the need for animal testing.

The phenotypic plasticity of cancer cells and their role in tumour development has been extensively studied through a broad array of modelling techniques, particularly within the framework of structured populations. This approach has shed light on various growth-related factors, including resource distribution, environmental heterogeneity, and cancer cell diversity [70, 160, 235, 296].

In the specialized field of hypoxia research, the use of integro-differential equations and partial integro-differential equations has been a critical methodological approach for exploring how oxygen distribution influences the development of phenotypic heterogeneity within tumours. This analytical strategy has been effectively applied in several studies, as evidenced by the work documented in Ref. [36, 418, 437, 300, 301, 436, 175]. These studies collectively underscore the ecological significance of oxygen levels in shaping the diverse phenotypic landscape of tumour cells, highlighting the complex interplay between genetic factors and environmental conditions in cancer progression.

Adopting a different mathematical approach, the examination of hypoxia's effect on the proliferative and invasive capabilities of cancer has been conducted through the lens of hybrid cellular automaton models. This approach is well-represented in the literature, particularly in the pioneering work of Ref. [194], which has opened new avenues for understanding the dynamic responses of cancer cells to hypoxic stress. Further advancing this field, a novel methodological perspective was introduced in Ref. [110] (see Chapter 5), which delves into the role of hypoxia as a catalyst for phenotypic instability. This instability encourages tumour cells to adopt more aggressive characteristics, employing a hybrid model that distinguishes cells based on both their genetic and phenotypic attributes. Additionally, the development of a mechanical model that simulates tumour growth by depicting cellular switches between aerobic and anaerobic metabolisms under hypoxic conditions has made significant contributions to our understanding of cancer cell survival strategies [38].

Building on the foundations laid by these diverse modelling efforts [175, 437, 36], our current study is designed to further investigate the interplay between tumour mass

and the availability of essential resources, mainly focusing on oxygen distribution. We aim to explore: *(i)* how this interaction can lead to a geometric delineation of tumour niches, characterized by their spatial extent and the delineation between active and necrotic zones; *(ii)* the implications of such geometric characterisation on the phenotypic makeup of the tumour, specifically regarding cell survival and invasion capabilities; and *(iii)* how these elements, in conjunction, influence overall tumour growth. Moreover, this research direction sets the stage for examining the impact of a tumour's pre-therapeutic exposure to varying oxygen levels on the likelihood of treatment failures. The emergence of hypoxic cells resistant to treatment, stemming from these dynamics, poses a challenge for controlling tumour growth and preventing the spread of cancer to regional and distant sites. This scenario underscores a critical therapeutic challenge that demands extensive exploration to develop more effective treatment strategies and, potentially, to mitigate the risk of cancer relapse.

3.2 The mathematical model

We construct our model using a system of interconnected nonlinear integro-differential equations. Through numerical simulations, we investigate various eco-evolutionary scenarios by adjusting both cancer cells' biophysical/biochemical traits and environmental parameters. Specifically, our model addresses a spatially explicit, epigenetically structured population reliant on environmental resources, which are supplied through a spatially heterogeneous distribution and diffuse across the environment. The behaviour of our virtual tumour cells is shaped by individual phenotypic traits, environmental conditions, and their interplay, facilitated by spatially explicit phenotypic relationships. Our focus is solely on the role of oxygen, which is considered the sole metabolic resource available in this context. We consider a spatial bi-dimensional domain $\Omega_s \subset \mathbb{R}^2$ where the tumour mass can expand. This represents a tissue slice in which the tumour mass grows. Considering the population of malignant cells, we designate *viable* cells as those that are *metabolically active* (i.e., their counterparts are *necrotic* individuals). This viable group is structured based on the epigenetic trait $u \in \Omega_p = [0,1]$, which characterizes their resistance level, namely their ability to survive in harsh environmental conditions such as hypoxic tumour areas. Specifically, the phenotypic state $u = 0$ (referred to as the *proliferation promoting phenotype*) denotes the cell clone with the highest mitotic potential but the lowest

level of hypoxia-resistance, while $u = 1$ (termed the *survival promoting phenotype*) confers the highest survival ability but the lowest duplication capacity. Between these extreme values lies a continuum spectrum of possible states, encompassing cell variants with intermediate levels of both survival and proliferation. In ecological terms, this implies a population composed of two *specialists*—proliferating and resistant cells—and a range of *hybrid* ones, known as *generalists*, capable of allocating their energies partly to proliferation and partly to survival.

This choice to represent the phenotype of a cell via a continuous variable could reflect existing biological evidence. For example, it allows us to tightly represent how the over-expression of some genes could result in a spectrum of distinct abilities, as shown by the histological data presented in Ref. [139], where different levels of expression of GLUT-1 arise in a heterogeneous distribution of cells in terms of hypoxia resistance. In the same veins, it could be particularly suitable to describe the phenotype of a cell as the result of the interaction among several genes that could combine, conferring maxima, minima but also hybrid characteristics, as shown in the epithelial-mesenchymal transition, [58].

In accordance with these assumptions, the function $a(t,\mathbf{x},u) : T \times \Omega_s \times \Omega_p \mapsto \mathbb{R}_0^+$ henceforth delineates the local arrangement of active tumour cells across the trait space. Put differently, $a(t,\mathbf{x},u)$ mirrors the phenotypic constitution of the tumour mass at the specified time t and domain point $\mathbf{x}$. Consequently, the local density of viable individuals can be calculated as follows:

$$\rho(t,\mathbf{x}) = \int_{\Omega_p} a(t,\mathbf{x},u), du, \tag{3.2.1}$$

to encompass all individuals within the mass, irrespective of their phenotype (i.e., integration over the phenotypic domain Ω_p).

Conversely, the necrotic subpopulation is assumed to lack differentiation, its density determined by the function $n(t,\mathbf{x}) : T \times \Omega_s \mapsto \mathbb{R}_0^+$. The concentration of oxygen is denoted by $O(t,\mathbf{x}) : T \times \Omega_s \mapsto \mathbb{R}_0^+$.

Cellular scale: tumour cells undergo proliferation, engage in resource competition, infiltrate surrounding tissue, and experience natural selection that optimizes their nutrient uptake for proliferation and enhances their survival in challenging environments, such as hypoxic regions. However, there exists a trade-off that prevents

the simultaneous maximisation of these traits. Additionally, cancer cells can alter their biochemical and biophysical properties, potentially leading to necrosis. Their behaviour is influenced by the surrounding tumour microenvironment, which, in a feedback/feedforward manner, is affected by the presence of cancer cells. Metabolically active cells are expected to (*i*) undergo random phenotypic transitions, (*ii*) move randomly, and (*iii*) either proliferate under selective environmental pressures or irreversibly transition to a necrotic state. The evolution of their distribution can be described by the following trait-structured integro-differential equation (IDE):

$$\frac{\partial a(t,\mathbf{x},u)}{\partial t} = \underbrace{\beta_p \frac{\partial^2 a(t,\mathbf{x},u)}{\partial u^2}}_{\text{epigenetic variations}} + \underbrace{\beta_s \Delta_{\mathbf{x}} a(t,\mathbf{x},u)}_{\text{movement}} + \underbrace{R(u,O(t,\mathbf{x}),\rho(t,\mathbf{x}),n(t,\mathbf{x}))a(t,\mathbf{x},u)}_{\text{proliferation/selection/necrosis}}. \tag{3.2.2}$$

The diffusion operator on the right-hand side concerning the variable u in Equation (3.2.2), with a constant coefficient $\beta_p > 0$, represents the minute epigenetic fluctuations within the tumour mass stemming from random mutation events due to the non-genetic instability present in malignant cells. This modelling approach, highlighted in Ref. [113] and its bibliography, underscores the interplay between a cell's genetic heritage and its environmental context in shaping its phenotype. Incorporating a diffusive term allows for two key considerations: firstly, variations in gene expression leading to minor phenotype differences are the most common, occurring with high probability based on biological evidence. Secondly, although rare, there are instances where changes in the expression of a few genes can significantly impact the observed phenotype, giving rise to individuals with markedly different characteristics. The diffusion operator regarding the $\mathbf{x}$ variable on the right-hand side encapsulates the random movement exhibited by cells, described by isotropic Fick's law of diffusion with a diffusivity coefficient $\beta_s > 0$.

The reaction term in Equation (3.2.2) resumes local variations in the mass of viable cells due to proliferation, natural selection and necrosis phenomena:

$$R(u,O(t,\mathbf{x}),\rho(t,\mathbf{x}),n(t,\mathbf{x})) = \underbrace{P(u,O(t,\mathbf{x}),\rho(t,\mathbf{x}),n(t,\mathbf{x}))}_{\text{proliferation}} - \underbrace{S(u,O(t,\mathbf{x}))}_{\text{selection}} - \underbrace{N(O(t,\mathbf{x}))}_{\text{necrosis}}. \tag{3.2.3}$$

In particular, the proliferation rate P is assumed to depend on (*i*) the individual actual epigenetic trait, (*ii*) the oxygen availability and (*iii*) the physical limitations of space availability. In this respect, we factorize P in three terms catching these

aspects, as follows:

$$P(u,O(t,\mathbf{x}),\rho(t,\mathbf{x}),n(t,\mathbf{x})) = p_1(u)\,p_2(O(t,\mathbf{x}))\,p_3(\rho(t,\mathbf{x}),n(t,\mathbf{x})). \tag{3.2.4}$$

The duplication law p_1 accounts for the fact that the epigenetic state $u = 0$ corresponds to the trade-off level at which cells have the highest proliferation rate, $\gamma_{\max}$, whereas a trait value $u = 1$ lead to the lowest rate $\gamma_{\min}$ characterizing the cell clones whose high resistant feature pays in poor chances to undergoes mitotic events. In order to quantify the proliferation-resistance trade-off, we adopt a linear trend, defining p_1 as:

$$p_1(u) = (\gamma_{\min} - \gamma_{\max})u + \gamma_{\max}. \tag{3.2.5}$$

Aware of the possibility of shaping this trade-off with other curves, we focus on the linear function considered as an average condition between a concave choice, characterized by an initially weak and cheap trade-off, and a convex choice, in which the trade-off is initially strong and costly [65].

Considering the already mentioned decrease of proliferative activity due to HIFs in case of lack of oxygen, we assume that active cells proliferate proportionally to the quantity of oxygen. In particular, we consider a basal concentration O_n, corresponding to the amount of molecular substance needed to remain viable and avoid necrotic transition. Under this level, proliferation is considered blocked; above that, there is a positive proportionality to the exceeding amount of oxygen. We stick to a classical formulation for the relation between cell duplication rate and available chemicals, given by the Michaelis-Menten law:

$$p_2(O(t,\mathbf{x})) = \frac{O(t,\mathbf{x}) - O_n}{\alpha_O + (O(t,\mathbf{x}) - O_n)} H(O(t,\mathbf{x}) - O_n), \tag{3.2.6}$$

being $H(O(t,\mathbf{x}) - O_n) = \{1\,,\text{ if } O(t,\mathbf{x}) \geq O_n; 0\,,\text{ if } O(t,\mathbf{x}) < O_n\}$ the Heaviside function. Equation (3.2.6) therefore implies that mitotic events are prohibited in the case of insufficient presence of oxygen. The factor p_3 in Equation (5.5.8) is finally inserted in the models to catch the typical compression-driven disruption of the mitotic cycle. In order to replicate this aspect from a mathematical point of view, we consider a local carrying capacity $k > 0$, which represents the maximum allowed density according to space availability in the tissue, and we set the following logistic-like

law:

$$p_3(\rho(t,\mathbf{x}),n(t,\mathbf{x})) = 1 - \frac{\rho(t,\mathbf{x}) + n(t,\mathbf{x})}{k}. \tag{3.2.7}$$

In Equation (3.2.7), both viable and necrotic cells contribute to occupying space.

The function $S(u,O(t,\mathbf{x}))$ in Equation (5.5.9) can be considered as a death rate representing the oxygen-driven natural selection according to the resistance trait expressed by the cells. We refer to theoretical results and experimental data (in particular, see Ref. [272] and Ref. [434]) to depict a scenario based on the following biological assumptions:

Assumption 1. There exist two oxygen concentration levels $O_M > O_m > 0$ that can be considered as the threshold for three possible oxygenation scenarios for cells: hypoxic if $O \leq O_m$; moderately oxygenated if $O_m < O < O_M$; normoxic (i.e. well oxygenated) if $O \geq O_M$.

Assumption 2. Given a fixed concentration of oxygen, a hypoxia-resistant epigenetic trait exists, which is the fittest. Considering this as the fittest expression of genes that correlates with hypoxia-resistance, cells showing a lower expression have a higher death rate when exposed to a lack of oxygen because of the inability to survive. On the other side, the decrease in cell proliferation associated with the acquisition of resistance to hypoxia (according to the already presented trade-off) results in a correlation of a higher level of gene expression with a higher fitness cost and then an increased death factor due to competition with more proliferative traits. Thus, the closer the gene expression level to the fittest one, the higher the chance of survival. Hence, cells with a gene expression far from the fittest one are more likely to die due to oxygen-driven selection.

Assumption 3. As considered in the previous assumption, the fittest level of expression of the hypoxia-resistant gene depends on the oxygen concentration. In particular, the minimal level of gene expression (i.e. $u = 0$) is the fittest in the case of normoxic environments (i.e. when $O \geq O_M$), the maximal level of gene expression (i.e. $u = 1$) is the fittest in the case of hypoxic environments (i.e. when $O \geq O_M$); when considering moderately-oxygenated environments (i.e. intermediate cases $O_m < O < O_M$), the fittest level of gene expression is a function of the oxygen concentration, continuous and with decreasing monotonicity (i.e. as the oxygen concentration increases, it decreases continuously from $u = 1$ to $u = 0$).

Under Assumptions 1, 2 and 3, the oxygen-driven selection term $S(u,O(t,\mathbf{x}))$ is defined as:

$$S(u,O(t,\mathbf{x})) = \eta_O \left(u - \varphi_O(O(t,\mathbf{x}))\right)^2. \tag{3.2.8}$$

Here, the parameter $\eta_O > 0$ is a quantifier for the intensity of oxygen-driven selection. Function $\varphi_O(O(t,\mathbf{x}))$ can be chosen as wanted in order to provide a mathematical formulation for Assumption 3. The oxygen concentration $O(t,\mathbf{x})$ is the expression for the environmental conditions and, for our model, we choose a linear expression for $\varphi_O(O(t,\mathbf{x}))$ as it is the simplest function respecting the continuity and decreasing monotonicity condition. Its explicit formulation is given by:

$$\varphi_O(O(t,\mathbf{x})) = \begin{cases} 0, & O(t,\mathbf{x}) \geq O_M, \\ \dfrac{O_M - O(t,\mathbf{x})}{O_M - O_m}, & O_m < O(t,\mathbf{x}) < O_M, \\ 1 & O(t,\mathbf{x}) \leq O_m. \end{cases} \tag{3.2.9}$$

Finally, in order to catch the irreversible necrotic fate acquired by viable cells in case available oxygen concentration drops below the level O_n, the term N in Equation (3.2.3) reads as follows:

$$N(O(t,\mathbf{x})) = \eta H(O_n - O(t,\mathbf{x})). \tag{3.2.10}$$

Here, η represents a transition rate, and H is again the Heaviside function. We are indeed assuming a deterministic necrosis in the case of a hypoxic condition, reflecting the disruption of intracellular metabolic activity in the environments characterized by a lack of resources, which is common among all viable cell variants.

Necrotic cells dynamics

Viable cells undergoing the just shown metabolic inactivation are incorporated in the necrotic population so that the same rate $N(O(t,\mathbf{x}))$ establishes the growth term in the relative equation, i.e.,

$$\frac{\partial n(t,\mathbf{x})}{\partial t} = N(O(t,\mathbf{x}))\rho(t,\mathbf{x}). \tag{3.2.11}$$

Here, $\rho(t,\mathbf{x})$ is the number density of viable individuals since the irreversibility of necrosis and the lack of metabolic activity in this population allow the collection of cells regardless of their epigenetic characterisation. Equation (3.2.11) implies that necrotic cells have no movement; thus, they remain frozen in space.

Molecular scale

The equation governing the local concentration of oxygen includes a source term $V(\mathbf{x})$, which is spatially heterogeneous and aims to capture intra-tumoural vessels bringing oxygen into the tissue where the tumour settled. Once provided by vessels, the oxygen movement is determined by a purely diffusive dynamic. Then oxygen naturally decays (here, the term also includes the consumption by healthy cells) and is consumed by metabolically active cancer cells. The mathematical formulation of oxygen concentration kinetics results in the following parabolic PDE:

$$\frac{\partial O(t,\mathbf{x})}{\partial t} = \underbrace{\beta_{\mathrm{O}}\Delta_{\mathbf{x}}O(t,\mathbf{x})}_{\text{diffusion}} - \underbrace{\lambda_{\mathrm{O}}O(t,\mathbf{x})}_{\text{natural decay}} - \underbrace{\zeta_{\mathrm{O}}\int_{\Omega_p} p(O(t,\mathbf{x}))a(t,\mathbf{x},u)\,\mathrm{d}u}_{\substack{\text{consumption by}\\ \text{active tumour cells}}} + \underbrace{V(\mathbf{x})}_{\substack{\text{inflow from}\\ \text{the blood vessels}}} . \tag{3.2.12}$$

Here λ_{O}, β_{O} and ξ_{O} are constant coefficients.

As a notation, we use $\Upsilon = \{(\mathbf{v}_i, I_i) \in \Omega_s \times \mathbb{R}^+\}_{i=1}^{N_V}$ to refer to the set of blood sources present in the tissue, where a couple defines the i-th element: the first element $\mathbf{v}_i$ provides its geometrical position and the second element I_i gives the rate of oxygen inflow in the tissue *via* it. Thus, mathematical formulation of the inflow $V(\mathbf{x})$ in (3.2.12) can be of the form of a geometric source given by:

$$V(\mathbf{x}) = \sum_{i=1}^{N_V} I_i\, e^{-\frac{(\mathbf{x}-\mathbf{v}_i)^2}{\sigma_V^2}} . \tag{3.2.13}$$

Coherently with the model introduced in Ref. [436], the variance is taken such that $\sigma_V << 1$ to simulate a quasi-pointwise source. In this modelling arrangement, source characteristics and numbers are time-independent. This leaves space for different generalisations in future. For example, one could consider variations in time of the number of vessels $N_V = N_V(t)$ to take into account blood vessel destruction or

formation or intensities dependent on time $I_i = I_i(t)$ to be able to reproduce the effect on the inflow capabilities caused by external factors, such as therapies. Moreover, we specify that we do not take into account any physical characterisation of vessels so that there are no mechanical interactions between tumour cells and blood sources and no tumour cell extravasation is allowed (this model does not consider tumour metastatic dynamics).

3.2.1 Simulation details

The spatial domain Ω_s represents a 2-dimensional section of a tissue. In particular, we take into account a square with a side of 4 cm, i.e. $\Omega_s = [-2,2]^2$ cm. We denote by t_F the final observation, letting it vary in each experiment according to the dynamics to be captured (being $t_\mathrm{F} = 1000$ days the longest time-window adopted for a simulation).

Initial and boundary conditions

Considering Equation (3.2.2) and Equation (3.2.11) (describing cell dynamics), we impose the following initial conditions:

$$a(0,\mathbf{x},u) = A\ \exp\left(-\frac{(\mathbf{x}-\mathbf{x}_C)^2}{2\sigma_\mathbf{x}^2} - \frac{(u-u_0)^2}{2\sigma_u^2}\right), \quad \text{for } \mathbf{x}, u \in \Omega_s \times \Omega_p; \quad (3.2.14)$$

$$n(0,\mathbf{x}) = 0, \quad \text{for } \mathbf{x} \in \Omega_s, \quad (3.2.15)$$

with $A > 0$ s.t. $\rho(0,\mathbf{x}) = \int_{\Omega_p} a(0,\mathbf{x},u)du < k$. Note that $\mathbf{x}_C$ is the barycentre of cancer cell population at the initial time and it is explicitly expressed in every different simulation setting.

According to the already stated decision to not catch oncogenesis dynamics and not explicitly insert healthy cells in the model, we assume that, at the beginning of all experiments, the tissue already contains a set of malignant viable cells with the following characteristics: (i) Each cell phenotype exhibits a complete Gaussian distribution along the spatial dimension, centred at the initial point $\mathbf{x}_C$, with a variance of $\sigma^2\mathbf{x} = 8 \cdot 10^{-3}$ cm^2. (ii) The cell mass follows a half-normal distribution in the

trait space, peaking at $u_0 = 0$ and with a variance of $\sigma_u^2 = 8 \cdot 10^{-2}$. This distribution choice is justified by the initial phase of tumourigenesis in simulations, characterized by a low cell count and a propensity for proliferation to establish within the tissue. Initially, the cell configuration reaches a maximum density of $A = 89.20$ cells/cm^2. At $t = 0$, the overall density ρ of active individuals is symmetrically distributed with respect to $\mathbf{x}_C$, primarily consisting of proliferative-promoting cell variants with only a tiny fraction of survival-promoting agents. The initial growth phase of malignancy lacks a necrotic core, as depicted schematically in Figure 3.1 for the case where $\mathbf{x}_C = (0,0)$.

The Equation (3.2.2) adheres to zero-flux conditions at the boundary of the epigenetic domain, denoted as $\partial_u a(\cdot,\cdot,0) = \partial_u a(\cdot,\cdot,1) = 0$. This condition aligns with the inherent limitation that malignant cells cannot possess a trait value less than 0 or greater than 1. This principle extends to the domain Ω_s, particularly when considering mass growth within a tissue slice.

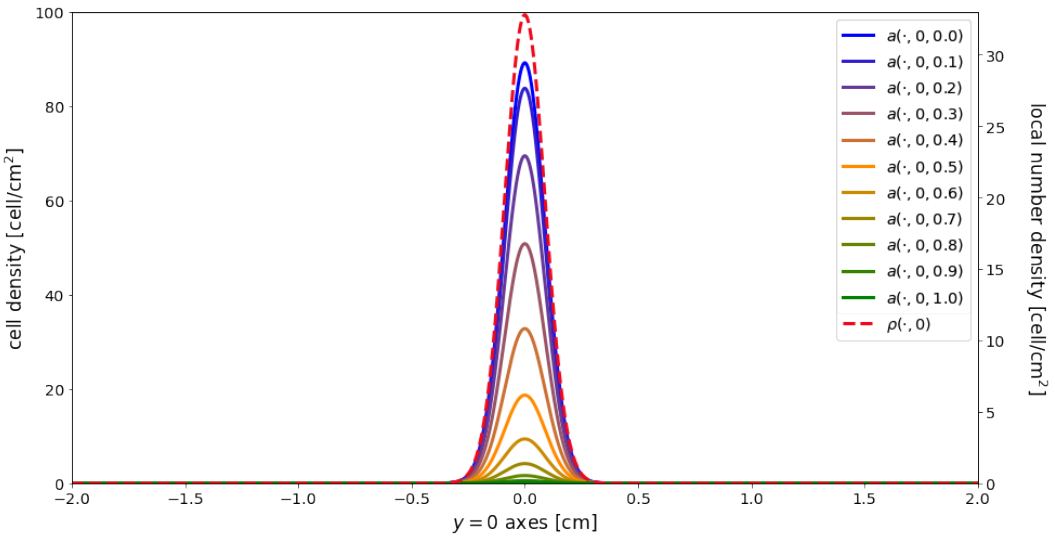

Fig. 3.1 Initial condition for the tumour mass. For example, the node of malignant viable cells is centred at $\mathbf{x}_C = (0,0)$. Cell density $a(0,\mathbf{x},u_i)$ is projected on the segment $\overline{(-2,0),(2,0)}$ that crosses diametrically the mass. u_i for $i = 1...10$ correspond to the nodes of the discretisation of the epigenetic domain that is considered. Each line refers to one of the discretized phenotypes.

Here, physical barriers such as bones, boundaries of breast ducts, or the absence of extracellular matrix prevent the mass from expanding beyond them.

In the context of chemical kinetics, the equation (3.2.12) is supplemented with an initial condition:

$$O(0,\mathbf{x}) = O^0(\mathbf{x}), \tag{3.2.16}$$

where $O^0(\mathbf{x})$ denotes the steady-state oxygen distribution in the tissue in the absence of tumour cells, considering a distribution of blood vessels. We enforce zero-Dirichlet conditions at the boundary of the spatial domain Ω_s, assuming a sufficiently large tissue with anoxic regions at the boundaries.

Two different geometrical layouts for blood vessels are considered. The first, simpler layout consists of a single vessel placed at the centre of the domain $(0,0)$, termed the SV-layout (Single Vessel layout). The second layout involves three vessels positioned at coordinates $(-1,1)$, $(1.2,-0.8)$, and $(0.8,-1.2)$, referred to as the 3V-layout (Three Vessels layout). Various simulations will explore the effects of different vessel intensities. Specifically, we denote the standard intensities for the SV-layout and the 3V-layout as I_{SV} and I_{3V}, respectively. We will consider different combinations of their full values (I^F_{SV} and I^F_{3V}, respectively) and half values (I^H_{SV} and I^H_{3V}, respectively). This enables us to describe all potential configurations of the oxygen source distribution as follows:

$$\Upsilon^W_{SV} = \left\{\left((0,0), I^W_{SV}\right)\right\} \tag{3.2.17}$$

and

$$\Upsilon^{WXY}_{3V} = \left\{\left((-1,1), I^W_{3V}\right), \quad \left((1.2,-0.8), I^X_{3V}\right), \quad \left((0.8,-1.2), I^Y_{3V}\right)\right\}, \tag{3.2.18}$$

with all possible half and full intensity choices $W,X,Y = H,F$, see Figure 3.2 for the disposition of the vessels, as well as the respective oxygen initial condition map, for layouts Υ^F_{SV} and Υ^{FFF}_{3V}.

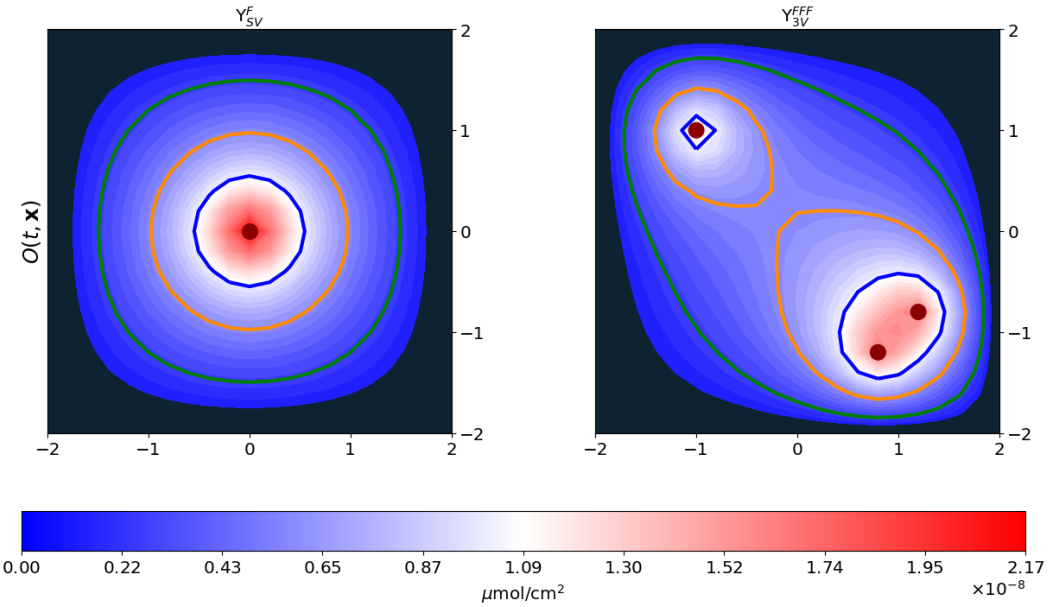

Fig. 3.2 Initial condition for the oxygen map in the two geometrical blood vessel layouts adopted (SV- and 3V-layout, left and right panel, respectively). For example, all vessels are set with full intensity (i.e. Υ^{F}_{SV} and Υ^{FFF}_{3V}). The regions outlined by the blue, orange and green lines highlight the optimal areas for low, medium and high epigenetic bands, respectively. A Definition of these quantities is provided in 3.2.2. Caption and Figure from Ref. [112].

Parameter Estimation

Most model coefficients possess explicit and biologically meaningful interpretations, allowing for accurate estimations derived from the empirical literature. Given the generic tumour scenario under consideration, we have drawn upon a diverse array of experimental studies encompassing various diseases.

The diffusion coefficient governing random epigenetic variations, denoted as β_p, has been calibrated to $8.64 \cdot 10^{-9}$ day^{-1}, exceeding the rate of somatic DNA mutations by one or two orders of magnitude, as documented in Ref. [158] within the context of vascularized tumours. Similarly, the tissue diffusion coefficient, β_s, is determined as $\beta_s = 3.11 \cdot 10^{-5}$ cm^2/day, consistent with findings reported in Ref. [312].

The coefficients γ_{min} and γ_{max} quantify the minimal and maximal cellular proliferation abilities relative to their epigenetic state u, considering oxygen availability and space constraints. Selected values, $\gamma_{\text{min}} = 3.46 \cdot 10^{-1}$ day^{-1} and $\gamma_{\text{max}} = 6.94 \cdot 10^{-1}$

	Parameter	Description	Value [Units]	Reference(s)
cell dynamics	β_p	epigenetic variation rate	$8.64 \cdot 10^{-9}$ [day^{-1}]	[158]
	β_s	spatial diffusion rate	$3.11 \cdot 10^{-5}$ [cm^2/day]	[312]
	$\gamma_{\min}$	minimal cell duplication rate	$3.46 \cdot 10^{-1}$ [day^{-1}]	[312]
	$\gamma_{\max}$	maximal cell duplication rate	$6.94 \cdot 10^{-1}$ [day^{-1}]	[312]
	k	tissue carrying capacity	10^6 [cell/cm^2]	[400]
	η_O	oxygen selection gradient	1 [day^{-1}]	model estimate
	η	rate of necrotic transition	1 [day^{-1}]	model estimate
	A	initial maximal cell density	89.20 [cell /cm^2]	[54]
	$\sigma^2_{\mathbf{x}}$	Variance in geometrical space	0.008 [cm^2]	model estimate
	σ^2_u	Variance in epigenetic space	0.08	model estimate
oxygen kinetics	β_{O}	oxygen diffusion coefficient	$8.64 \cdot 10^{-1}$ [cm^2/day]	[312]
	λ_{O}	oxygen natural decay rate	$8.64 \cdot 10^{-3}$ [day^{-1}]	[136]
	α_{O}	Michealis-Menten oxygen constant	$4.28 \cdot 10^{-9}$ [μmol/ cm^2]	[140]
	ζ_{O}	oxygen consumption rate	$8.64 \cdot 10^{-16}$ [μmol/cell]	model estimate
	O_n	oxygen necrotic threshold	$1.20 \cdot 10^{-9}$ [μmol/cm^2]	[74]
	O_m	oxygen hypoxic threshold	$2.57 \cdot 10^{-9}$ [μmol/cm^2]	[74]
	O_M	oxygen normoxic threshold	$1.37 \cdot 10^{-8}$ [μmol/cm^2]	[74]
	I^F_{SV}	full vessel inflow for SV-layout	1.58 [μmol/cm^2 ·day]	model estimate
	I^F_{3V}	full vessel inflow for 3V-layout	1.03 [μmol/cm^2 ·day]	model estimate

Table 3.1 Reference parameters setting. Table from Ref. [112].

day^{-1}, correspond to doubling times of 24 and 48 hours, respectively, in line with biological data [312]. Furthermore, they fall within the range of duplication rates observed for glioblastoma cell lines under both hypoxic and normoxic conditions [436].

The carrying capacity denoted as k, is set to 10^6 cells/cm^2, assuming a mean cell diameter of 10 μm as measured in Ref. [400].

Oxygen concentration thresholds are specified as follows: $O_n = 1.20 \cdot 10^{-9}$ μmol/cm^2 for necrosis, $O_m = 2.57 \cdot 10^{-9}$ μmol/cm^2 for cell viability and duplication, and $O_M = 1.37 \cdot 10^{-8}$ μmol/cm^2 for normoxia, consistent with observations in Ref. [74]. The characteristic constant α_{O} of the Michaelis-Menten proliferation law is determined as $4.28 \cdot 10^{-9}$ μmol/cm^2, consistent with existing findings [140].

The oxygen diffusion coefficient is specified as $\beta_{\mathrm{O}} = 8.64 \cdot 10^{-1}$ cm^2/day, as reported in Ref. [312]. The oxygen decay rate, $\lambda_{\mathrm{O}} = 8.64 \cdot 10^{-3}$ day^{-1}, is determined based on [136]. All other parameters are defined based on the specific dynamics of the model. Table 3.1 outlines the complete parameter setup.

Numerical method

The domain is discretized in the following manner:

- For the temporal and epigenetic domains, a uniform one-dimensional discretisation is employed.
- A triangular mesh with radial symmetry discretises the two-dimensional geometric domain.

To numerically solve the system of partial differential equations, a mixed solution scheme is employed:

- For the one-dimensional components of the domain (time and epigenetic trait), the explicit Euler method is used to approximate the derivatives.
- For the dynamics on the geometric domain, a Galerkin finite element method is applied, employing a weak formulation of the problem.

A Python code has been developed for the domain mesh and the implementation of the numerical resolution algorithm, utilizing the FEniCS and Dolfin packages [279].

3.2.2 Quantification of model results

As previously stated, our research aims to explore the impact of environmental conditions and biophysical factors on tumour growth. Specifically, we will examine the dynamics of variables pertaining to both the disease's overall (macroscopic) traits and its internal (microscopic) features, including heterogeneity.

In order to provide some qualitative indicators of tumour evolution and quantify the description of the phenotypes distribution inside the mass, we split the epigenetic domain Ω_p in three bands, referring to them by the term *epigenetic bands*, that we denote with L (low), M (medium) and H (high):

$$\Omega_p = \Omega_p^L \cup \Omega_p^M \cup \Omega_p^H$$

with

$$\Omega_p^L = [0, 0.3),\ \Omega_p^M = [0.3, 0.7],\ \text{and}\ \Omega_p^H = (0.7, 1].$$

To strengthen the connection between environmental conditions and the epigenetic characteristics of the individuals inhabiting them, we establish a link between the *epigenetic bands* and the tissue regions where they are most advantageous. This linkage is facilitated by the function $\varphi_o(O(t,\mathbf{x}))$, which identifies the most suitable trait based on the local oxygen concentration $O(t,\mathbf{x})$. To achieve this, we first identify the area where the oxygen level falls below the hypoxic threshold O_n, leading to necrosis. This region is denoted as

$$\Omega_s^N(t) = \{\mathbf{x} \in \Omega_s :, O(t,\mathbf{x}) \in [0, O_n]\}$$

and is referred to as the *necrotic area*. Subsequently, we partition the spatial domain according to the subsets of the epigenetic domain. Specifically, we delineate regions where the optimal epigenetic traits correspond to those in the low, medium, or high *epigenetic band*:

$$\Omega_s(t) = \Omega_s^L(t) \cup \Omega_s^M(t) \cup \Omega_s^H(t) \cup \Omega_s^N(t) \qquad \forall t \in T$$

with

$$\Omega_s^L(t) = \{\mathbf{x} \in \Omega_s \, s.t. \, O(t,\mathbf{x}) \in (\varphi_O^{-1}(0.3), \varphi_O^{-1}(0.0)]\},$$

$$\Omega_s^M(t) = \{\mathbf{x} \in \Omega_s \, s.t. \, O(t,\mathbf{x}) \in [\varphi_O^{-1}(0.7), \varphi_O^{-1}(0.3)]\}, \text{ and}$$

$$\Omega_s^L(t) = \{\mathbf{x} \in \Omega_s \, s.t. \, O(t,\mathbf{x}) \in [\varphi_O^{-1}(1.0), \varphi_O^{-1}(0.7))\} \setminus \Omega_s^N(t).$$

We will refer to $\Omega_s^L(t)$, $\Omega_s^M(t)$, and $\Omega_s^H(t)$ as the low, medium, and high *optimal areas* respectively.

Correspondingly, we introduce their local number densities. Again, we denoted with low (ρ_L), medium (ρ_M) and high (ρ_H) respectively, and we computed as:

$$\rho_I(t,\mathbf{x}) = \int_{\Omega_p^I} a(t,\mathbf{x},u)\, du \qquad \text{for } I \in \{L,M,H\}. \tag{3.2.19}$$

We refer to them as *band-specific local number densities*. Furthermore, considering a global counterpart of numerosity, we introduce the *total cell count* provided by the integration of the local number density on the spatial domain:

$$\Gamma(t) = \int_{\Omega_s} \rho(t,\mathbf{x})\, d\mathbf{x} \tag{3.2.20}$$

and the corresponding *band-specific cell counts*:

$$\Gamma_I(t) = \int_{\Omega_s^I} \rho_I(t,\mathbf{x})\, d\mathbf{x} \qquad \text{for } I \in \{L,M,H\}. \tag{3.2.21}$$

In order to better represent the epigenetic spectrum in the mass, we introduce:

- the *spatial average epigenetic map*:

$$f(t,\mathbf{x}) = \frac{1}{\rho(t,\mathbf{x})} \int_{\Omega_p} a(t,\mathbf{x},u) u\, du,$$

  which is an indicator of the spatial location of the epigenetic traits;

- the *epigenetic global density*:

$$g(t,u) = \int_{\Omega_s} a(t,\mathbf{x},u)\, d\mathbf{x}, \tag{3.2.22}$$

  that provides a quantification of the number of tumour cells in the entire mass characterized by a specific epigenetic firm;

- the *average epigenetic trait*:

$$F(t) = \frac{1}{\Gamma(t)} \int_{\Omega_p} u\, g(t,u)\, du, \tag{3.2.23}$$

  that corresponds to the average epigenetic trait characterizing the mass during the evolution.

Finally, we evaluate the spatial extension evolution during tumour development in the case of masses characterized by radial symmetry. We introduce the time-evolving quantity $r(t)$ that measures the radius of the mass as:

$$r(t) = \sup\left\{ \|\mathbf{x}-\mathbf{x}_c\| \; s.t. \; \mathbf{x} \in \Omega_s \text{ and } \rho(t,\mathbf{x}) > \sigma_r \right\} \tag{3.2.24}$$

with $\sigma_r = k/10$ in the meaning of a non-detectable tumour density.

3.3 Results

3.3.1 Reference simulation

As a prototype of a growing malignant mass, focusing on the metabolic transition between normoxic and hypoxic cells, we investigate the evolutionary dynamics during tumour expansion in a relatively straightforward scenario. Considering the previously mentioned possible geometrical layouts for blood vessels, we opt for the SV-layout, as illustrated in the left panel of Figure 3.2. At the onset of the numerical simulation, a single node of malignant viable cells is assumed to be already present at the centre of the domain $\mathbf{x}_C = (0,0)$, aligned with the blood vessel. These cells possess epigenetic characteristics outlined in Section 3.2.1. For a one-dimensional depiction of the cancer population at the initial condition, refer to Figure 3.1. The resulting modelling context aims to replicate the development of a *tumour cord*, representing a cylindrical mass composed of tumour cells encircling the blood vessel. For a schematic representation of tumour cord formation from both cross-sectional and side views, see Figure 3.3.

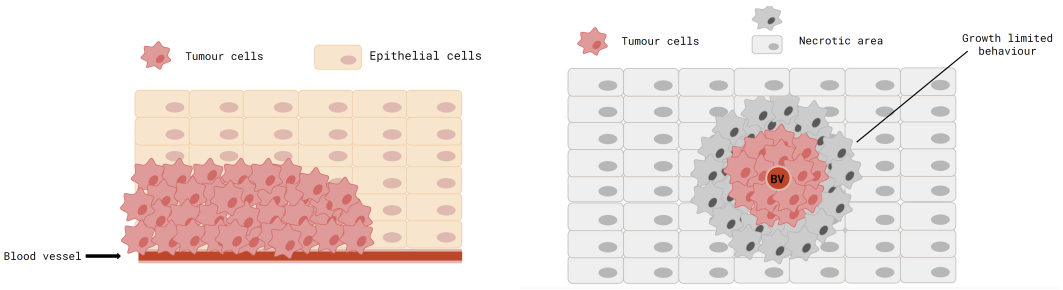

Fig. 3.3 Schematic representation of a tumour cord formation from a cross and a side point of view (left and right panel, respectively). Caption and Figure from Ref. [112].

Oxygen dynamics

As depicted in the left panel of Figure 3.2, the interplay of oxygen's reaction-diffusion dynamics, influenced by inflow through the blood vessel and consumption by tumour cells, results in its concentration reaching stable values. These values gradually decrease as one moves away from the oxygen source. Notably, the resulting profile

resembles a Gaussian distribution, with oxygen levels transitioning from normoxic to mild, severe, and even anoxic conditions as one moves away from the blood vessel.

Cell dynamics

From a morphological perspective, we can understand the overall behaviour of our simulated mass by observing its spatial extension through the measurement of its radius, denoted as $r(t)$ (top panel of Figure 3.4, depicted by the lilac line), and its volume, indicated by the total cell count $\Gamma(t)$ (top panel of Figure 3.4, represented by the red line). Upon analysing their temporal evolution, we notice an initial plateau phase followed by a subsequent increase, characterized by a gradually decreasing velocity, throughout the entire observation period.

Initially, the total count of active individuals $\Gamma(t)$ exhibits exponential-like growth during the earliest phases, which then transitions to a semi-linear trend. Ultimately, it converges toward a steady-state value (around $t \approx 365$ days) in a second phase relative to the time when the tumour cord achieves its maximum expansion (around $t \approx 270$ days), reflecting an invasion dynamic consistent with physical constraints. The initial rapid growth dynamics, observed in quantity and radial expansion, align with the mass development in regions abundant in resources primarily composed of "proliferation-promoting" cells.

Conversely, the subsequent slower dynamics emerge as the mass encounters increasingly inhospitable regions characterized by low nutrient concentrations, thereby promoting the expansion of more resistant phenotypes with a lower mitotic potential. Consequently, the radial expansion of the mass and the increase in quantity decelerate as cells require more time to establish and populate new regions.

The multi-phase growth pattern observed here evokes findings from various experimental studies. Notably, research dating back to the early 1970s, such as the investigation into the self-regulation of growth in three-dimensional spheroids [181], provides insights into similar growth dynamics. More recent works have also delved into the analysis of volume extensions in different cell lines cultured in vitro [346]. This growth behaviour aligns with Gompertz-like kinetics when extending the monitoring time window, as illustrated in the top panel of Figure 3.5. Specifically, the total cell count $\Gamma(t)$ exhibits a sigmoidal profile, ultimately converging asymptotically to a maximum threshold value. This threshold value

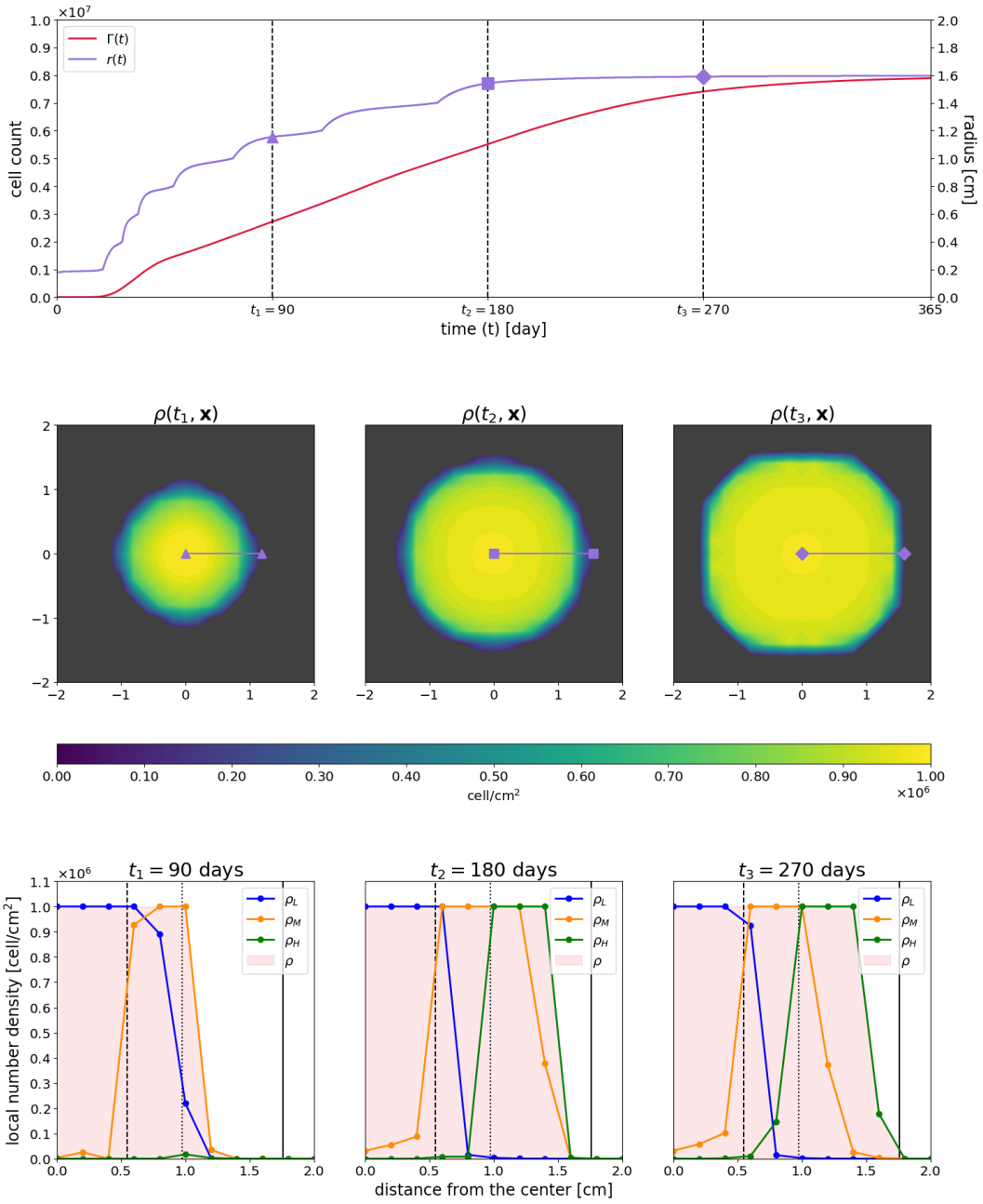

Fig. 3.4 Results of the reference simulation relative to cancer cell dynamics and tumour morphology. (a) The first row represents the evolution in time of the total cell count $\Gamma(t)$ and radius $r(t)$ of the tumour mass. Vertical lines detect the times chosen for instantaneous representation in the second and third rows. (b) The second row is a two-dimensional spatial representation of $\rho(t,\mathbf{x})$ for $t = 90, 180, 270$ days. The cancer mass radius, along with plots in the third row, is projected and highlighted with the lilac segment. (c) Third row provides a one-dimension representation of *band-specific* and *global number densities* $\rho_L(t,\mathbf{x})$, $\rho_M(t,\mathbf{x})$, $\rho_H(t,\mathbf{x})$, $\rho(t,\mathbf{x})$ along the segment $\overline{(0,0),(2,0)}$ for $t = 90, 180, 270$ days. Caption and Figure from Ref. [112].

corresponds to the maximum carrying capacity of the entire tissue, reflecting the tissue's limitations in accommodating further cell proliferation.

In the middle panel of Figure 3.4, we observe the evolution of the virtual mass through its cell number density $\rho(t,\mathbf{x})$ at three distinct time points (90, 180, and 270 days). Initially, cell clones begin to spread radially, moving away from the blood vessel and occupying all available space until nutrient concentrations are adequate for survival. However, upon encountering anoxic tissue regions, cells undergo a necrotic transition, halting the invasion dynamics. This growth-limiting behaviour aligns with the evolutionary dynamics observed in *in vivo* neoplasm development. Experimental evidence indicates that neoplasms reach a maximum average radius during the avascular phase and get surrounded by necrotic regions. This quasi-steady state arises due to the high oxygen consumption by proliferating cancer cells, coupled with oxygen diffusion limits, leading to a radial decline in essential nutrients and the formation of anoxic areas.

Examining the mass's evolution from a radial cross-sectional perspective, depicted in the bottom panel of Figure 3.4, we gain insight into the synergistic interaction between cell proliferation and movement, enabling tumour cell invasion into the surrounding tissue. The cell number density $\rho(t,\mathbf{x})$ along the segment $\overline{(0,0),(2,0)}$ behaves akin to an invading front, saturating growth at the local tissue's carrying capacity k. This saturation is illustrated by the pink-coloured regions summarizing its evolution at three different time points ($t = 90$, 180, and 270 days).

In this regard, our research highlights how tissue colonisation results from cooperative interactions among different specialised cell variants, underscoring the significance of phenotypic composition in tumour development. Analysis of the *band-specific number density* of various sub-groups ρ_I for $I = L,M,H$ (representing low, medium, and high hypoxia-resistant cells - depicted by blue, orange, and green curves, respectively) reveals dynamic changes in tumour composition that mutually shape with the tumour microenvironment. Spatial variations in oxygen concentration create environmental gradients, leading to the selection of cells with epigenetic traits that vary with distance from the blood vessel.

The emergence of specific phenotypic traits correlates with the region of the tumour mass under analysis. Notably, black vertical lines delineate oxygenation areas: the dashed line separates optimal areas for the low and medium bands, the dotted line demarcates optimal areas for the medium and high bands, and the continuous

line signifies the limit of the non-necrotic area. Observably, the prevailing clones in each region strike a balance between replicative ability and reduced proliferation rates due to heightened survival capabilities, ensuring their adaptation to prevailing environmental conditions.

Consistent with biological principles, this selection mechanism unfolds gradually, as evident from the comparison between the left and central panels in the bottom row of Figure 3.4. The temporal evolution of different cell fractions indicates that in the initial phase (left side of Figure 3.4, bottom panel), *proliferation-promoting* cells dominate (blue curve), colonizing even distant regions from the blood vessel. However, in subsequent phases (central and right sides of Figure 3.4, bottom panel), these cell variants progressively diminish in external regions of the mass, giving way to new clones characterized by an increasing overexpression of *survival-promoting* genes (orange and green curves). By the end of the simulation, a ring structure emerges, comprising a central group of proliferating cells surrounded by two concentric rims of medium and high-resistant cells, mirroring the evolutionary selection of more resistant cell clones under harsh tissue conditions (and vice versa), as documented in the existing literature. Thus, our findings not only capture this phenomenon but also provide insights into its mechanisms and timing.

Expanding the observation time window to better understand the evolutionary processes requiring a longer time scale to manifest, we observe a trend toward the development of hypoxia-resistant phenotypes characterizing tumour evolution, as depicted in Figure 3.5. Gradually, the entire disease exhibits a phenotypic shift towards greater resistance to hypoxia, evident from the time evolution of the *band-specific cell counts* $\Gamma_I(t)$ for $I \in L, M, H$ across the entire mass, illustrated in the top panel of Figure 3.5.

Initially, the mass predominantly comprises *proliferation-promoting* cells (blue curve). Still, over time, they are progressively supplanted by increasingly resistant phenotypes (medium and high resistant cells - depicted by orange and green lines, respectively). By the final observation time ($t = 1000$ days), approximately 70% of the mass consists of high-resistant cells, with medium-resistant cells constituting nearly 20%, while only a tiny fraction comprises low-resistant ones.

This trend aligns with the evolution of the *epigenetic global density* $g(t,u)$, shown in the middle panel of Figure 3.5, which initially concentrates around $u = 0$ before gradually shifting towards high resistance development. This evolution

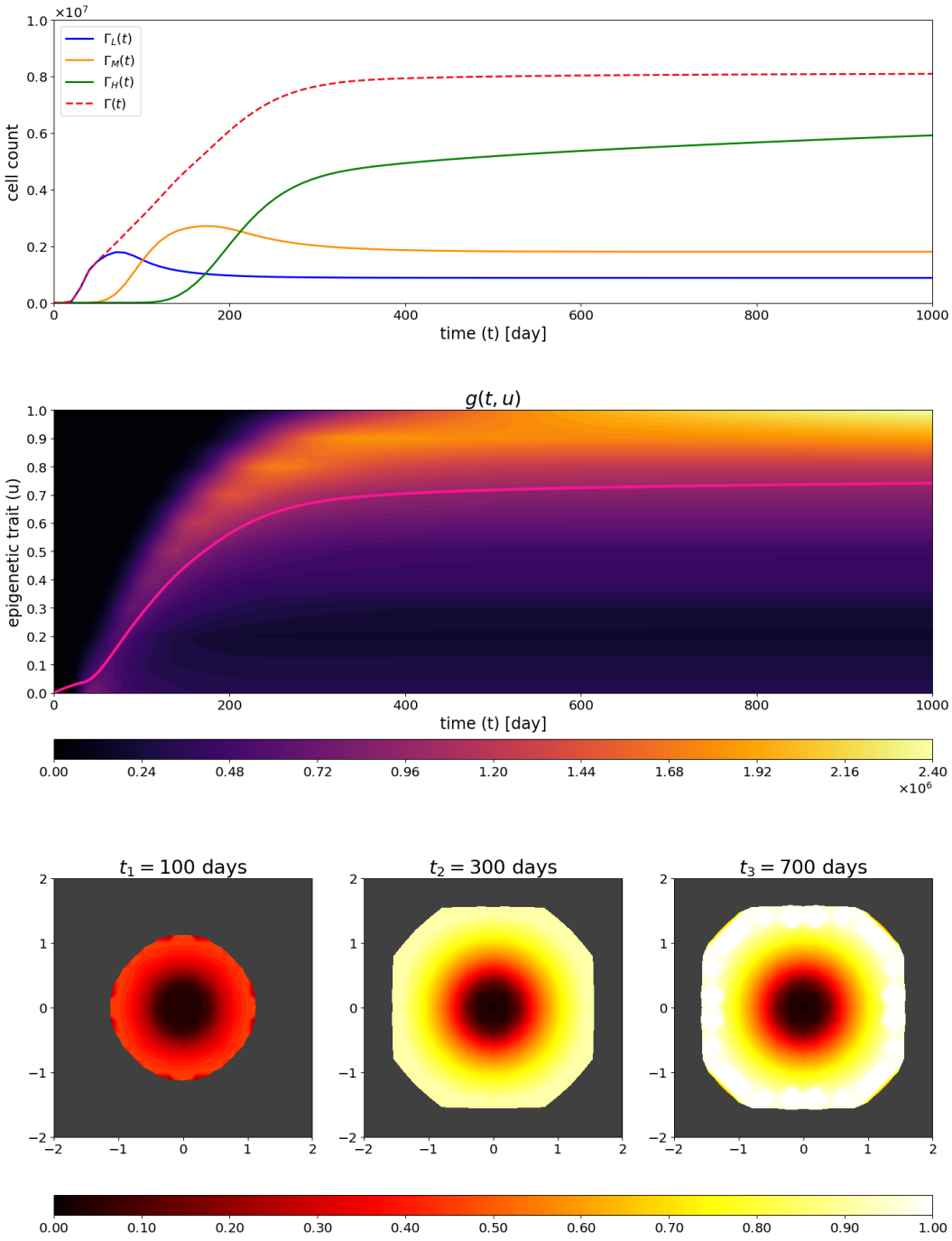

Fig. 3.5 Reference simulation results relative to numerical and geometrical epigenetic composition. (a) The first row represents the evolution in time of band-specific and global cell counts $\Gamma(t)$, $\Gamma_L(t)$, $\Gamma_M(t)$, $\Gamma_H(t)$. (b) The second row shows the epigenetic global density $g(t,u)$. The pink line represents the time evolution of the average epigenetic trait $F(t)$. (c) The third row provides the spatial two-dimension representation of the average epigenetic map $f(t,\mathbf{x})$ at times $t = t_1 = 100$ days, $t = t_2 = 300$ days, $t = t_3 = 700$ days. These quantities are defined in 3.2.2. Caption and Figure from Ref. [112].

of the epigenetic landscape provides insights into the emergence of intra-tumour heterogeneity during mass growth. The spectrum of phenotypes observed at the final simulation time ($t = 1000$ days) expands significantly compared to earlier phases, encompassing all phenotypes from low to high resistance, with a notable increase in intensity towards resistance development. This is consistent with the findings depicted in Figures 3.4 and 3.5, as well as the evolution of the *average epigenetic trait* $F(t)$ of the mass (pink line).

Further confirmation comes from analyzing the *spatial average epigenetic map* $f(t,\mathbf{x})$, shown in the bottom panel of Figure 3.5, at three different time steps ($t = 100, 300, 700$ days). This map reflects the dynamics of mass development described earlier in terms of epigenetic composition over an extended time window, consistent with the evolutionary time scale. Notably, the previously described ring structure is vividly discerned, indicating that, by the end of the mass expansion, the prevailing epigenetic profiles lie between $u = 0.7$ and $u = 1$, representing the more resistant phenotypes.

In summary, our findings indicate that during the initial stages of progression, tumour growth and expansion within the host are driven by collective cell dynamics. This process is facilitated by the emergence of intratumoral phenotypic heterogeneity, demonstrating how cells with diverse characteristics and functions cooperate to survive and effectively invade the host. This phenomenon will be further investigated in the subsequent sections.

3.3.2 Geometric characterisation of the environment and its impact on tumour niches

It is essential to study the vascular network responsible for tissue oxygenation to explore the interaction between a tumour and its surrounding environment, mainly focusing on the impact of hypoxia.

The diverse configurations of blood vessels, characterized by differences in inflow intensity and geometric organisation, can naturally result in varying spatially heterogeneous oxygen distributions. When combined with different primary tumour locations within the tissue, these variations have the potential to alter the mass's invasive capabilities significantly.

In this section, we focus on examining the influence of oxygen inflow intensity on tumour morphology, including growth rate, size, and epigenetic composition. Figure 3.6 illustrates the setup used for the study, with the only variation being the intensity of the vessel inflow. The experiment is conducted twice: the left column depicts a tumour cord developing around a vessel with the same intensity as the reference case (Υ_{SV}^{F}). In contrast, the right column represents a vessel with half the intensity (Υ_{SV}^{H}).

The initial oxygen distribution in both cases is shown in the first row. Indicative bands corresponding to oxygen concentration levels are depicted to elucidate the relationship between environmental characteristics and the epigenetic makeup of potentially colonizing individuals. Specifically, the *anoxic* area, where oxygen falls below the threshold O_n, leading to tumour cell necrosis, is highlighted in dark blue. The *hypoxic* area, characterized by oxygen levels between O_n and O_m, where maximal gene expression fitness occurs ($u = 1$), is represented in blue. The *moderately-oxygenated* area, ranging from O_m to O_M, is subdivided into three different bands: Ω_s^H, Ω_s^M, and Ω_s^L, corresponding to optimal survival areas of high (indigo), medium (light blue), and low (light pink) *epigenetic bands* (Ω_p^H, Ω_p^M, and Ω_p^L), respectively. Lastly, the *normoxic* area, characterized by oxygen levels higher than O_M, where minimal gene expression fitness occurs ($u = 0$), is represented in cherry.

Comparing the two oxygen maps reveals differences in proliferation speed, extension, and epigenetic distribution of the tumour mass. In the case of higher oxygen concentration (left column of Figure 3.6), the mass exhibits faster growth due to more efficient oxygenation of proliferation and the presence of a substantial node of *proliferation-promoting* individuals, as indicated by the formulation of the proliferation factor p_2 in Equation (3.2.6). Conversely, in a more hypoxic environment (right column of Figure 3.6), higher epigenetic traits are selected, resulting in slower tumour growth but increased hypoxia resistance.

The observed trend in hypoxia-resistance enhancement, evident in both scenarios, is mirrored in the temporal evolution of the *total* and *band-specific cell counts*, depicted in the second row of Figure 3.6. Vertical blue and yellow lines mark the times at which $\Gamma_L(t)$ and $\Gamma_M(t)$ reach their maximum values, respectively. Upon comparison of the two dynamics, it becomes apparent that in the case of lower oxygenation, the growth of the *global cell count* $\Gamma(t)$ (magenta dotted line - right

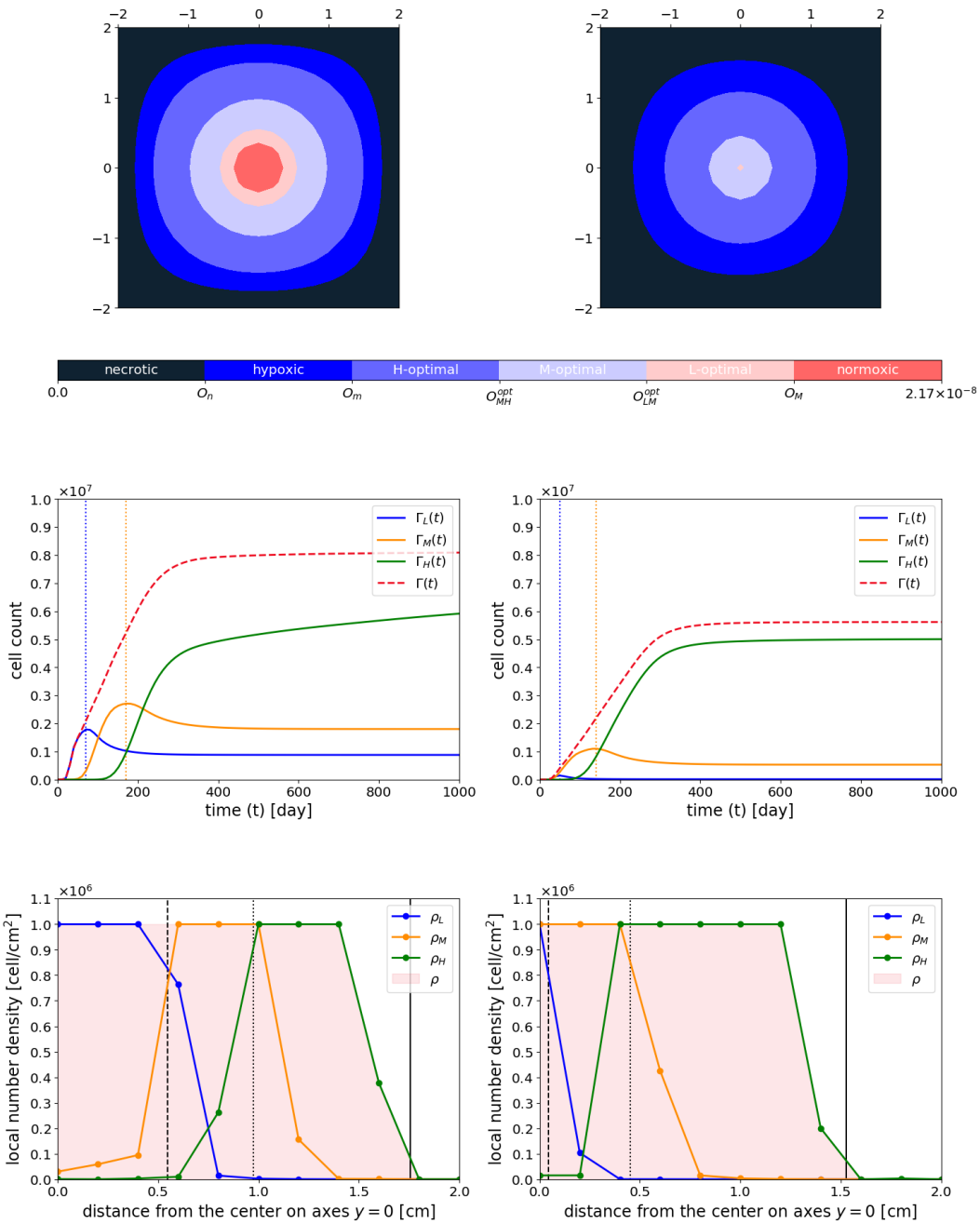

Fig. 3.6 This experiment compares results from the simulation in the reference setting (Υ^F_{SV}, left column) with results from a simulation with the same parameters and setting, with the exception of a half value for the vessel intensity (Υ^H_{SV}, right column). (a) The first row shows the initial oxygen map $O(t_0, \mathbf{x})$. (b) The second row provides evolution in time of *band-specific* and *global cell counts* $\Gamma(t)$, $\Gamma_L(t)$, $\Gamma_M(t)$, $\Gamma_H(t)$. (c) The third row represents the profiles of the densities ρ, $\rho_L(t,\mathbf{x})$, $\rho_M(t,\mathbf{x})$, $\rho_H(t,\mathbf{x})$, along the segment $\overline{(0,0),(2,0)}$ at the final observation time $t = t_F = 1000$ days. Vertical lines partition the spatial domain, from left to right, in $\Omega^L_s(t_\mathrm{F})$, $\Omega^M_s(t_\mathrm{F})$, $\Omega^H_s(t_\mathrm{F})$, and $\Omega^N_s(t_\mathrm{F})$ i.e. the final low, medium, and high optimal areas and the necrotic one. Caption and Figure from Ref. [112].

panel) proceeds at a slower pace than its counterpart in the higher oxygenation scenario (magenta dotted line - left panel), with a lower plateau value observed, consistent with the diminished nutrient availability.

Remarkably, in both experiments, the *band-specific cell counts* ($\Gamma_L(t)$, $\Gamma_M(t)$, $\Gamma_H(t)$, represented by blue, orange, and green curves respectively) underscore the evolutionary interplay between species and the competitive exclusion principle. This principle posits that two species with similar needs cannot coexist sympatrically; one will invariably out-compete the other, leading to either adaptation or exclusion through emigration or extinction. The higher proliferative rate initially confers an evolutionary advantage to *proliferation-promoting* phenotypes over other epigenetic traits, resulting in their dominance within the population. Subsequently, this dominance persists in regions of high oxygenation where the low epigenetic trait is optimal. Conversely, environmental selective pressures in areas with lower oxygenation lead to increased mortality rates among low epigenetic trait cells. Consequently, *proliferation-promoting* cells undergo apoptosis rapidly, creating space for the expansion of other cancer subpopulations. Despite their slower proliferation, these subpopulations exhibit greater resistance to environmental hostility, driving a competitive out-competition-like dynamic.

In the third row of Figure 3.6, the cross-sectional profiles of densities ρ, ρ_L, ρ_M, ρ_H along the segment $\overline{(0,0),(2,0)}$ at the final observation time $t_F = 1000$ days are depicted. The dynamics of phenotypic diversity observed in tissue area colonisation follows a pattern similar to that described in the corresponding panel of Figure 3.4, which pertains to the case of a more hypoxic environment.

As anticipated, both the optimal area for high resistant phenotypes Ω_s^H and the necrotic region Ω_N exhibit greater extension, consistent with a less efficient vasculature. This results in a less extensive mass, as evidenced by the radius measure, which is roughly about 20% smaller than that in the reference case ($r(t_F) \approx 1.5$ cm versus $r(t_F) \approx 1.8$ cm).

In summary, our findings suggest that the success of a tumour in terms of adaptation, survival, and expansion is closely linked to the niche characteristics that tumour cells encounter, in conjunction with the optimality of the epigenetic profile relative to these characteristics.

In this context, another aspect that naturally emerges and could be of particular interest in understanding the development of a malignant mass is the possibility of

observing completely different evolutionary trajectories, depending on the region of the tissue in which the primary tumour cells originate, as illustrated in Figure 3.7. Here, we consider a 3V-layout with Υ_{3V}^{FFF} configuration and vary the tissue region for the onset of the primary tumour cells.

The resulting oxygen map shows the highest concentration area in the bottom-right corner of the tissue slice due to the proximity of two of the three blood vessels considered. The second-highest oxygenation area is located near the single vessel in the top-left corner of the domain. Specifically, the simulation is repeated nine times, considering all combinations of $x_C = (x_1, x_2)$ with $x_1, x_2 \in -1, 0, 1$ as primary locations for tumour settlement (denoted with red stars in Figure 3.7).

Differences in tumour emergence are highlighted in terms of global descriptors such as the global cell count $\Gamma(t)$ and the morphological shape of the mass, detected at two different time instants $t_1 = 50$ and $t_2 = 100$ days as measures of intermediate and final growth stages. The tumour mass morphology is investigated via the analysis of tumour density ρ, plotted at the final time of observation t_2, with a pink contour representing the tumour mass profile detected at the intermediate time t_1. Detection is considered possible when the local tumour number density ρ reaches at least 10% of the local carrying capacity k. Under each plot, the cell count at time instants t_1 and t_2 is reported.

Our results reveal radical differences in the morphology of the tumour mass closely related to the local concentration of resources in the malignant primary nidus location. It is observed that in cases where tumours originate in one of the higher oxygenated areas, the mass develops faster in terms of both extension and cell count. This is due to two factors: firstly, a higher amount of oxygen ensures faster proliferation; secondly, the initial cancer population is characterized by an epigenetic distribution that is predominantly *proliferation-promoting*. Thus, in regions characterized by high oxygenation, the predominant epigenetic trait will already be optimal, resulting in fewer cells facing apoptosis due to environmental selection forces.

Phenotypic optimality plays a crucial role in this dynamic, particularly when tumours start developing in low-oxygenated areas. Their initial growth is slow and accelerates as they reach regions of the domain closer to the vessels, ensuring better oxygenation. Interestingly, our results show that the malignant mass is not even detected at the intermediate time in four cases. From a clinical perspective, this

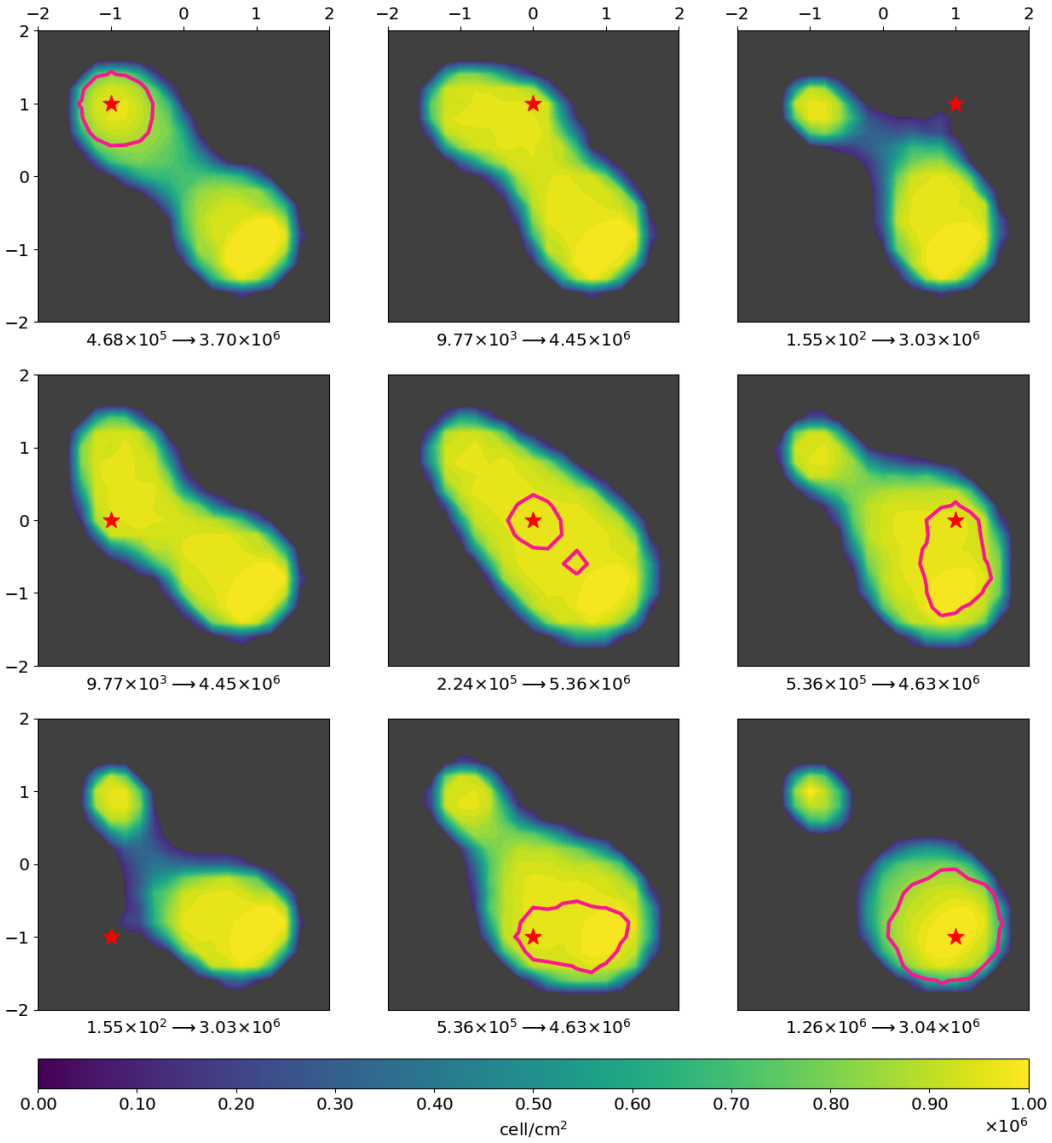

Fig. 3.7 This experiment compares the results from nine simulations in which we vary the primary settlement of the tumour. In particular, we consider a 3V-layout in which all vessels are set with full intensity (Υ_{3V}^{FFF}), and we keep unaltered the parameters of the reference simulation, with the exception of the geometrical starting points x_C for the cancer population. All combinations of $x_C = (x_1, x_2)$ with $x_1, x_2 \in \{-1, 0, 1\}$ are considered (depicted with red stars in the different panels). The pink lines identify the tumour edge at an intermediate time of $t_1 = 50$ days, while the contour plot represents the $\rho(t, \mathbf{x})$ at the final time $t = t_2 = 100$ days. The numerical values shown below the graphs are the cell counts: $\Gamma(t_1) \longrightarrow \Gamma(t_2)$. Caption and Figure from Ref. [112].

suggests that imaging analysis at an intermediate time may not reveal the presence of a tumour, even if it is slowly developing. Therapeutically, this implies that detecting the tumour from medical images at a given time may determine the area for therapy or resection. However, as the comparison between intermediate and final times reveals, the edges detected by the tumour images in the initial phase can differ significantly from the definitive ones.

As seen in plots related to final times, even if small in number and slowly proliferating, cells in areas with adverse environmental characteristics are present. When they reach the optimal epigenetic trait to survive, they minimize the death rate due to selection, and the tumour mass begins to expand even in areas not initially considered for surgery. In this context, medical images alone provide indispensable information but may not be sufficient to determine the outcome of the tumour. Therefore, awareness of the characteristics of the environment and the capability of modelling and simulating their impact on the evolutionary dynamics of the cancer population may provide predictive support. As mentioned earlier, our results suggest that favourable environmental conditions can accelerate tumour growth and expansion, making it detectable in a shorter time and exhibiting more predictable behaviour. Conversely, unfavourable environmental conditions may slow down tumour growth, leading to a less predictable course and the development of more resistant characteristics, potentially impacting therapy efficacy.

Motivated by these considerations, we now explore how variations in the morphology and epigenetic/phenotypic composition of the tumour mass occur across a wide range of oxygen maps. To achieve this, we fix the tumour's primary nidus at the centre of the domain and consider a three-vessel layout with variations in blood vessel intensity, encompassing all possible combinations of full-intensity and half-intensity inflows.

In Figure 3.8, we present results from three different settings: (i) all vessels with full intensity ($\Upsilon^{FFF}3V$ configuration, results shown in the first column), (ii) all vessels with half intensity ($\Upsilon^{HHH}3V$ configuration, results shown in the second column), and (iii) a mixed setting with two vessels characterized by half-intensity and one vessel by full intensity (Υ^{HFH} configuration, results shown in the third column).

The first row of Figure 3.8 displays oxygen maps with boundaries indicating corresponding optimal areas Ω_s^L, Ω_s^M, and Ω_s^H for low, medium, and high epigenetic

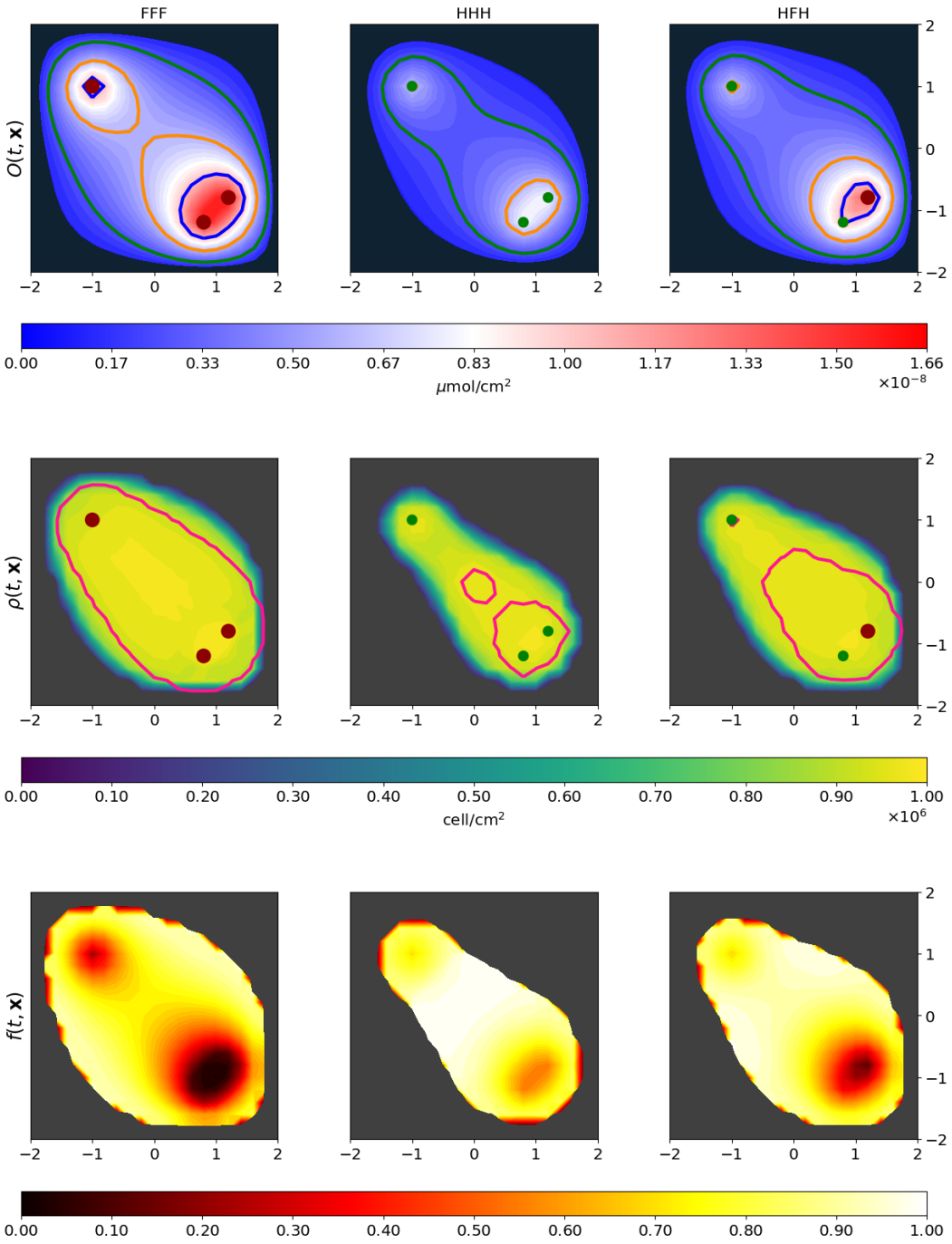

Fig. 3.8 This experiment compares the results from three different simulations in which we vary the blood vessel network in terms of potency. In particular, we adopt the 3V-layout, keeping unaltered parameters from the reference simulation, with the exception of the intensities of the vessels. All possible combinations between full (F) and half (H) intensities are considered. In this plot, we show the results of the configurations FFF (first column), HHH (second column), and HFH (third column). (a) The first row shows the initial oxygen maps. (b) In the second row, pink lines identify the tumour edge at an intermediate time $t_1 = 100$ days, while the contour plot represents the $\rho(t,\mathbf{x})$ at the final time $t = t_2 = 200$ days. (c) The third row shows $f(t,\mathbf{x})$ at the final time $t_2 = 200$ days. Caption and Figure from Ref. [112].

bands, respectively. The same colours used for the band-specific cell counts (blue, orange, and green contours) represent these optimal areas. In the first experiment, at least one optimal area is identified for each tumour cell sub-group, ensuring low-resistant cells' survival. The mixed configuration also allows for the colonisation of tissues by proliferation-promoting phenotypes, except for one region close to two vessels in the bottom-right corner. Conversely, in the second experiment, some areas are optimal only for medium and high-resistant phenotypes.

The second row of Figure 3.8 presents tumour local density profiles ρ at the final observation time $t_2 = 200$ days, with the boundary of the tumour mass at an intermediate time $t_1 = 100$ days projected in pink. We extend the observation time window compared to previous experiments due to the presence of less oxygenated areas, which slow down tumour growth and extend the time scale of environmental selection dynamics. Different blood source networks directly influence tumour growth speed and morphology in terms of both cell count and extension.

In environments with high oxygenation (left panel), the tumour mass edge at the intermediate time is similar to that at the final time. Conversely, in hypoxic environments, tumour mass development at the intermediate time appears limited to the highest oxygenated region. Still, with a more extended observation period, expansion occurs near the single vessel, ultimately connecting two cell islands. This aligns with our previous observations: well-oxygenated tumours tend to exhibit more aggressive growth and expansion, with shorter detection times and predictable behaviour. At the same time, unfavourable environmental conditions may slow growth but lead to less predictable outcomes.

The third column of Figure 3.8 represents a middle ground, where the tumour mass at the intermediate time already shows a trend towards unexplored regions around the single vessel. Finally, the third row of Figure 3.8 illustrates each case's different epigenetic distributions of tumour cells. Comparing these distributions to the oxygenation maps in the first row, we observe that the extent of the optimal area for the low-specific epigenetic band is reflected in the corresponding regions of the graph in the third row. Conversely, lighter colours dominate in the second and third columns, reflecting the prevalence of optimal areas for medium and high bands.

Significantly, our research indicates that a tumour mass developing in well-oxygenated areas tends to approach its steady state profile earlier than one growing in an adverse environment, as evidenced by the earlier convergence of the pink

boundaries projected in the second row. From a medical standpoint, these findings hold particular interest, especially in cases requiring surgical removal of a mass. They provide insights into scenarios where a larger region, compared to what is detected through imaging analysis at a specific point, might be safer to remove. Specifically, our results highlight that in harsh microenvironments, such as those depicted in the second column, there is a higher likelihood of silent regions in terms of density, yet characterized by strong invasive capabilities where the mass is already proliferating. These considerations are crucial for surgical planning and underscore the importance of accounting for environmental factors in treatment strategies.

3.3.3 The impact of environmental selection forces

When examining the interaction between tumour and abiotic factors on the eco-evolutionary trajectory of a mass, it is crucial to recognize that two tumours may exhibit similar clonal compositions at a given moment, but this does not necessarily imply shared evolutionary histories. Moreover, it does not preclude the possibility of significant future divergence, even under identical environmental conditions [308]. The resulting potential for multiple evolutionary pathways adds another layer of complexity, making it challenging to pinpoint the ecological and evolutionary mechanisms driving tumour phenotypic evolution.

One possible explanation for this variability lies in the varying strength of natural selection, i.e., the force with which environmental conditions influence cancer population dynamics and how individuals perceive their environment—a concept aligned with niche construction.

With this in mind, we investigate how variations in selective pressures due to oxygen deprivation affect the evolutionary trajectory of tumour cells and their impact on tumour morphology. Selection gradients can be viewed as indicators of how individuals interact with their environment, so changes in their values reflect variations in selective pressures.

To explore this, we maintain the same setup as the reference simulation (Υ^{F}_{SV}) and adjust the selection parameter η_O. Specifically, we conduct three experiments representing low (LS), medium (MS), and high (HS) selection rates, corresponding to $\eta_O = 0.1$, 1, and 10, respectively. The summarized results are presented in Figure 3.9. The first row of Figure 3.9 illustrates the evolution of the global cell count (Γ)

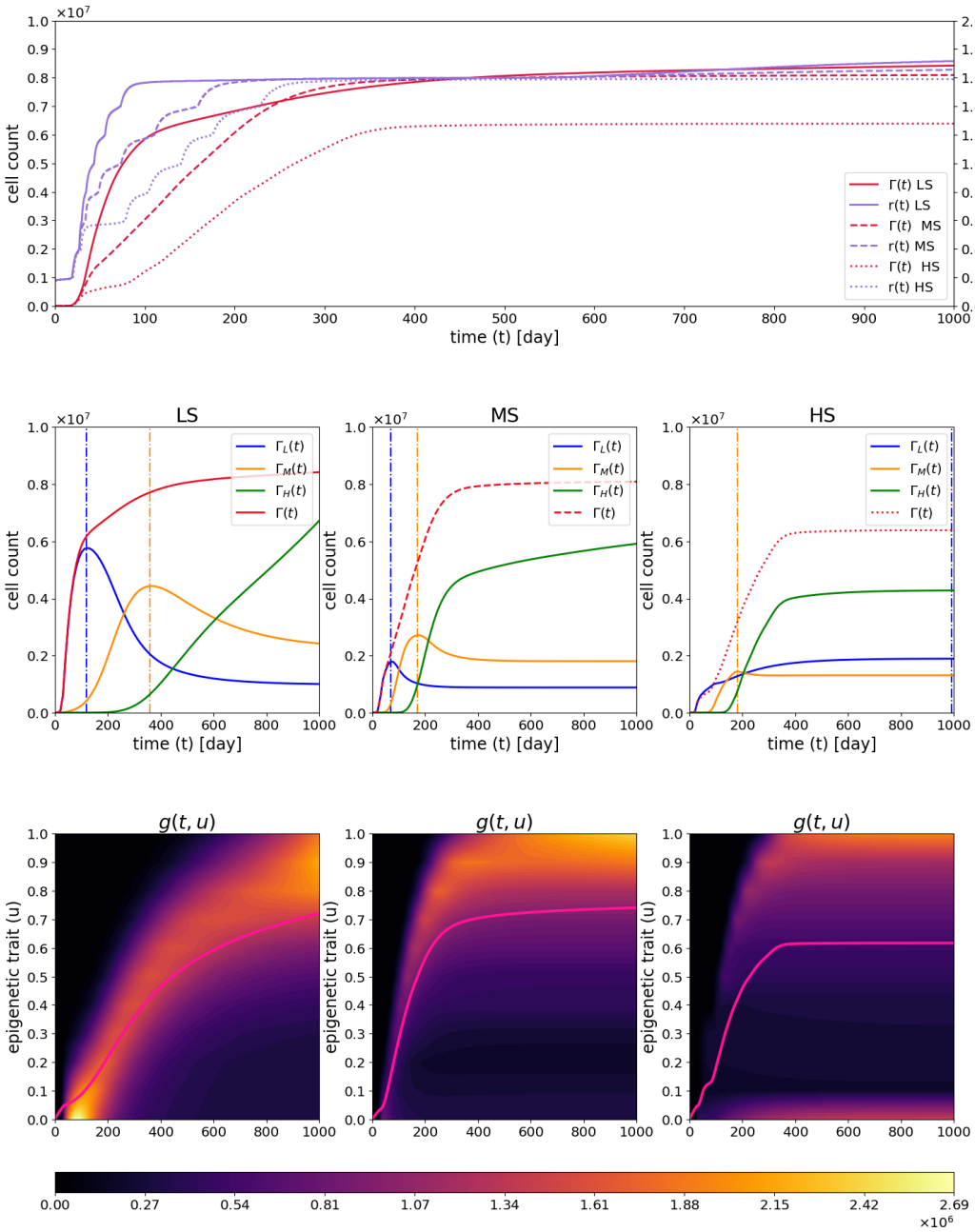

Fig. 3.9 This experiment compares the results from three different simulations in which we vary the intensity of natural selection. In particular, we keep unaltered parameters from the reference simulation, with the exception of the selection gradient. We focus on the analysis of a low (LS), medium (MS) and high (HS) selection rate impact that corresponds to $\eta_O = 0.1, 1, 10$ respectively. (a) In the first row, the time evolution of cell counts $\Gamma(t)$ and radius $r(t)$ are provided for the three different settings over a time span of 1000 days. The second and third rows are divided into columns according to LS (first), MS (second) and HS (third). (b) The second row shows the evolution in time of band-specific and global cell counts $\Gamma(t)$, $\Gamma_L(t)$, $\Gamma_M(t)$, $\Gamma_H(t)$ for $t \in [0, 1000]$ days. Vertical lines highlight the times at which cell counts show maximum peaks. (c) The third row provides evolution in time of the epigenetic global density $g(t,u)$) of the population (contour plot) and highlights the average epigenetic trait $F(t)$ evolution (pink line). Caption and Figure from Ref. [112].

and radius (r) across the three different settings over a span of 1000 days. Notably, all cell counts and radii converge towards the same steady states, with the selection rates influencing only the speed and intermediate dynamics of interaction between cancer cell subpopulations. While this trend holds for the high selection (HS) setup as well, it is less apparent due to the slower mass extension and the limited observation time.

Comparing the cases, both Γ and r profiles reveal that higher selection rates correspond to slower growth speeds, indicating that selective solid pressures impede the initial mass expansion. Regarding the evolution of r, the selection rate impacts both the rate at which the tumour advances spatially (higher selection rates correlate with slower advancement) and the invasion mechanism, significantly shaping its profile.

A distinct step-like behaviour is observed, particularly pronounced with higher selection rates, accompanied by more prolonged plateaus. Lower selection rates imply a more extended time required to select the fittest epigenetic trait at a given point in the domain, allowing cells to survive and proliferate even when suboptimal for a region. Consequently, lower epigenetic traits enjoy an evolutionary advantage, evading apoptosis and proliferating more rapidly, especially in less oxygenated regions. This is evidenced by the earlier saturation of the radius (r) in the case of lower selection, indicating faster maximum extension relative to resource availability. Here, proliferation dominates the selection mechanism, becoming more influential in later phases.

Conversely, higher selection rates expedite the selection of optimal epigenetic traits, leading to rapid apoptosis of proliferation-promoting cells in oxygen-deprived regions. Consequently, mass expansion is slower, with surviving cells exhibiting reduced proliferation rates, necessitating more time to conquer tissue regions. The mass takes at least three times longer to reach maximum extension under stronger selective pressures compared to lower selection.

In summary, the tumour rapidly spreads due to abundant proliferation-promoting individuals, optimizing survival in each area. Conversely, under high selection, selective pressures immediately counteract proliferation, allowing only optimal epigenetic traits to resist in specific domain points, penalizing proliferative cells outside their optimal zones and limiting significant spreads.

The step-like behaviour observed in the mass invasion reflects the profound influence of natural selection intensity on its invasion capacity. A high selection

rate implies that individuals in each mass area share the optimal or nearly optimal epigenetic trait. Consequently, as the tumour progresses, it attempts to conquer new areas where more efficient individuals may possess different characteristics from those already present in the mass. However, since the clonal expansion of new, better-adapted individuals in earlier growth phases was limited by the previous optimal ones, only a small portion of the population consists of these newly adapted individuals, resulting in an apparent cessation of mass invasion into new tissues.

Additionally, a variation in the selection gradient can be interpreted as a change in the shape of the Proliferation-Survival trade-off affecting cancer cells. A lower selection gradient allows cells to proliferate for longer periods even without the best epigenetic traits, indicating that survival is less costly under lower selection, as evidenced by the higher proliferation/death ratio observed in the dynamics.

This is prominently reflected in the dynamics of the global and band-specific cell counts, as depicted in the second row of Figure 3.9, comparing low and high selection cases. In the low selection scenario (first column of Figure 3.9), the high proliferation/death ratio enables cells with lower epigenetic traits to proliferate rapidly in the early phases, significantly increasing their fraction in the population. However, as the mass approaches tissue carrying capacity, selection becomes predominant, leading to a decrease in the population of non-optimal cells, characterized by an expansion-contraction dynamic, particularly evident in the low-specific cell count. Conversely, in the high selection scenario (last column of Figure 3.9), no such dynamics are observed, indicating immediate selection and preventing significant decreases in the number of low and medium sub-populations.

Expanding the observation time window reveals that the cell count of each band tends towards the same numerical value in all experiments, regardless of the selection rate. This is reflected in the results presented in the last row of Figure 3.9, which shows the evolution over time of the epigenetic global density on which the average epigenetic trait is projected in pink. In the low selection case (first column), peak dynamics are observed, indicating the expansion-contraction phenomenon affecting almost all epigenetic traits. Conversely, in the high selection case (third column), only a significant peak is observed for cells characterized by high hypoxia resistance. Notably, the strength of natural selection strongly influences tumour composition during mass expansion. Lower natural selection promotes longer coexistence phenomena, whereas higher selection rates promote quick out-competition, leading to

a predominant presence of high resistance cells in the mass, consistent with the hypoxia-driven development observed.

With respect to the evolution in time of the *average epigenetic trait* F, it is possible to formally demonstrate that its steady state is not influenced by the varying selection rates utilized in the three experiments. The pink line indeed converges towards the same profile in all three plots of the last row, although this dynamic is not fully discernible within the selected time range. Nonetheless, the results indicate that the dynamics in approaching the steady state differ significantly, consistent with previous observations. The first column exhibits a gradual growth characterized by a relatively constant rate; the second column displays a rapid initial growth phase followed by a transition to a linear trend with nearly zero slope; while the third column demonstrates a sudden spike in growth followed by a stable trend. These trends align with the notion that a lower selection rate promotes *coexistence*, whereas a higher one promotes *out-competition*.

Spatial-focused evidence of this dynamic is represented in Figure 3.10. The graphs refer to the two opposite LS and HS experiments shown in Figure 3.9. The top panels refer to the LS case, and the bottom ones refer to the HS case. The six contour plots (three for each case) represent the number density of viable individuals characterized by the epigenetic trait $u = 0.5$, with a variance of 0.05 at three different times instants ($t = 100, 500, 900$ days) that we denoted with:

$$\rho_{0.5}(t,\mathbf{x}) = \int_{0.45}^{0.55} a(t,\mathbf{x},u)\,du. \tag{3.3.1}$$

The red circles highlight the domain areas where, according to the oxygen map, the phenotype $u = 0.5$ is optimal, indicating that the tumour mass at the stationary stage should contain all cells characterized by the phenotype $u = 0.5$ within these rings. The other plots depict the *band-specific number densities* ρ_L, ρ_M, and ρ_H at $t = 1000$ days along the radius $\overline{(0,0),(2,0)}$.

Consistent with our earlier observations, in the LS case, weak selective pressures allow the tumour to expand uncontrollably outside the optimal area. As it nears the carrying capacity, the *proliferative potential* diminishes, and selective dynamics become predominant, resulting in progressive cell death in areas where hypoxia resistance is insufficient for survival. Consequently, the maximum radius at which

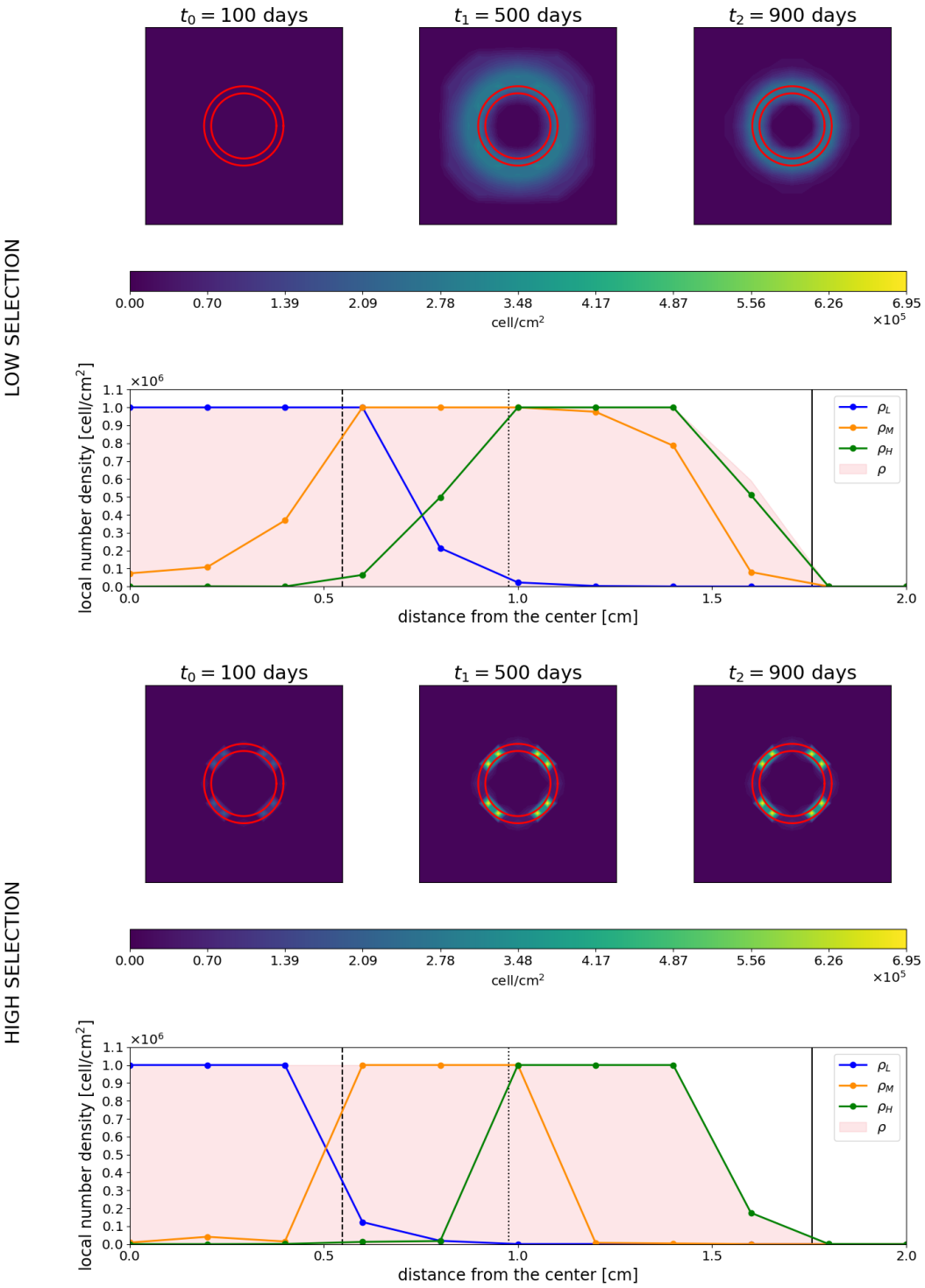

Fig. 3.10 A spatial focused evidence of the dynamic presented in Figure 3.9 is here shown. The top panels refer to the LS case, and the bottom ones refer to the HS case. The six contourf plots (three for each case) represent the number density $\rho_{0.5}(t,\mathbf{x})$ of viable individuals characterized by the epigenetic trait $u = 0.5$ with a variance of 0.05 at three different times instants ($t = t_1 = 100$ days, $t = t_2 = 500$ days, $t = t_3 = 900$ days). Second and fourth rows provide bands-specific number densities $\rho_L(t,\mathbf{x})$, $\rho_M(t,\mathbf{x})$, $\rho_H(t,\mathbf{x})$ at $t = t_F = 1000$ days along the segment $\overline{(0,0),(2,0)}$. Vertical lines detect, from left to right, $\Omega_s^L(t_F)$, $\Omega_s^M(t_F)$, $\Omega_s^H(t_F)$, and $\Omega_s^N(t_F)$ (low, medium, and high optimal areas and necrotic area). Caption and Figure from Ref. [112].

individuals with the specified epigenetic trait can be detected progressively decreases, although, within the observed timeframe, it has not yet reached the optimal area.

This dynamic is reflected in the *band-specific cell* plot, which indicates that the medium band ρ_M, housing the chosen phenotype $u = 0.5$, remains prevalent even in areas farther from the vessel, where the high epigenetic band is optimal. This aligns with our earlier observations that low selection promotes longer *coexistence* periods. In contrast, in the HS case, invasion dynamics are slower but more regulated. The cell density $\rho_{0.5}$ is concentrated more distinctly and immediately within the optimal area. Similarly, the *band-specific cell counts* plot demonstrates that, in the HS case, each epigenetic band is localized within the optimality area by the end of the simulation, consistent with the notion that high selection rates promote *out-competition*.

In summary, our results illustrate that the intensity of selective pressures exerted by oxygen, quantified by the selection gradient η_O, may influence the emergence of hypoxic resistance in tumours. Additionally, they suggest that the observed trade-off between *proliferation* and *survival* in cancer cells plays a crucial role in shaping future evolution. The nature of this trade-off can either promote or inhibit *coexistence* or *out-competition*, leading to significant changes in tumour composition during expansion, affecting both morphology and invasion capability.

3.4 Conclusion and future perspectives

The proposed mathematical modelling approach comprehensively simulates the eco-evolutionary spatial dynamics of tumour cells as they adapt to hypoxic microenvironments, shedding light on the impact of the experimentally observed trade-off between *maximizing cell survival* (by increasing tolerance to unfavourable conditions) and *maximizing cell growth* affecting cancer cells [8].

Our results affirm the substantial influence of the oxygen map on tumour mass development, delineating the areas where cancer progression occurs and elucidating differences in tumour growth speed and epigenetic composition of the population [386]. Notably, our findings align with experimental observations, indicating that favourable environmental conditions predominantly lead to tumours exhibiting heightened aggressiveness in terms of growth and expansion. These tumours are detectable in a shorter time, exhibit more predictable behaviour, and show less re-

sistance to treatments. Conversely, unfavourable environmental conditions tend to decelerate tumour growth, resulting in a less predictable course and more aggressive characteristics in terms of therapeutic resistance [139]. Furthermore, our model highlights potential mechanisms underlying these dynamics: slow growth favours a less invasive malignant mass, while gradual expansion allows for prolonged tumour undetectability, enabling the cancer population to gradually shift its epigenetic dominance toward resistance phenotypes to both hostile environments and treatments.

Our findings underscore the profound impact of tumour oxygenation heterogeneity on tumour mass evolution, leading to variations in the geometry of the growing malignant mass. Specifically, tumour cells characterized by lower expression levels of hypoxia-resistant genes (*proliferation-promoting* phenotypes) predominantly colonize well-oxygenated regions. Conversely, cells expressing more aggressive resistance phenotypes (*survival-promoting* phenotypes) populate more hypoxic areas. These theoretical insights align with histological data on tumour cords, reflecting the up-regulation of genes such as p53, HIF-1α, and GLUT-1, as apoptosis repressors increase from the centre to the external region of the tumour cord [386].

From an evolutionary standpoint, our modelling approach captures a crucial aspect of neoplasm eco-evolutionary narratives: two tumours may possess a similar clonal composition at a given time, yet this does not necessarily indicate similar evolutionary histories. Additionally, under the same environmental conditions, their future evolution may diverge significantly. Specifically, depending on the oxygen selection gradient η_o, multiple evolutionary pathways can lead to the development of hypoxia resistance.

Concerning the *Proliferation-Survival trade-off*, our findings suggest that its existence and intensity, linked to the strength of natural selection, play pivotal roles in determining the phenotypic composition of a cancer population. The trade-off's intensity significantly influences individuals' evolutionary trajectories and the diversity of trait values among them. In this regard, our results align with the classification of neoplasm evolutionary and ecological features, identifying the selection gradient η_o as a measure of hypoxia's impact on tumour cell eco-evolutionary dynamics. Notably, our results demonstrate that the strength of selective pressures exerted by oxygen on tumour cells fundamentally shapes the emergence of hypoxic resistance, altering the pathways through which such resistance develops.

These findings find justification in a niche construction evolutionary perspective. Selection gradients can be interpreted as measures of how individuals interact with their environment, suggesting that changes in individuals' perception of their environment can completely alter the population's evolutionary trajectory. This perspective expands upon the traditional view of evolution by Darwinian natural selection, considering both natural selection via environmental variables and the alterations of these conditions by the organism itself, resulting in additional evolutionary or ecological consequences.

As possible extensions of the model here presented, different aspects can be of particular interest from both the evolutionary and the physical point of view. In this respect, it would be interesting to consider additional components of the tumour environment and their effects on the characterisation of the geometric evolution of the tumour mass. This would include: (*i*) the mechanical aspects of the intracellular fluid, (*ii*) the interaction with extracellular matrix in the expansion dynamics, (*iii*) the competition for space and resources with the healthy cells of the host tissue, and (*iv*) the interplay between metabolically active, quiescent and necrotic cells.

With respect to the latter, the necrotic population is already present in the mathematical formulation of our model but not particularly investigated. This is because, in this work, we focus on tumour cords, in which the necrotic population develops at the edge of the mass and can, therefore, be reached by macrophages, which are responsible for its elimination. On the contrary, in the case of tumour spheroids, the necrotic core develops inside the mass due to hypoxic conditions induced by the consumption of oxygen by the tumour population itself. From this perspective, it would be interesting to apply the same model to tumour spheroids formation and consider the effects of the presence of a necrotic core on the morphology and invasion ability of the mass. Necrotic regions have indeed an active role in the evolutionary dynamics of malignant populations, being responsible for the secretion of cytokines which exert tumour-promoting activity triggering angiogenesis, proliferation, and invasion, [281]. Moreover, in spheroids development, necrotic core extension can be a relevant parameter to be considered since, in multiple experimental works, a substantial proportion of necrosis in histopathology samples has been indeed proposed as an indicator of tumour aggressiveness associated with poor clinical outcomes, identifying in necrosis extension a valid clinical index to define the tumour degree of advancement and the invasive potential of a growing mass, [365]. In fact, necrotic regions play an active role in the evolutionary dynamics of malignant populations,

secreting cytokines that promote tumour activity by triggering angiogenesis, proliferation, and invasion. Regarding the latter, while our mathematical formulation already includes the necrotic population, it has not been extensively explored in this work. This is due to our focus on tumour cords, where the necrotic population develops at the mass's edge and can be reached by macrophages responsible for its elimination. In contrast, in tumour spheroids, the necrotic core forms inside the mass due to hypoxic conditions induced by oxygen consumption. It would be fruitful to apply the same model to tumour spheroid formation and consider the effects of a necrotic core on mass morphology and invasion ability. The extension of the necrotic core could be a significant parameter to predict, as histopathology samples often propose a substantial proportion of necrosis as an indicator of tumour aggressiveness and poor clinical outcomes.

From the evolutionary point of view, it can be of interest to improve our modelling approach including in a more realistic way the trade-offs that affect tumour evolution. Biologically, the intensity of a trade-off can be defined as how much, in a population, the development of a determined characteristic is made at the expense of the improvement of another. As reported in literature, it is affected by ecological conditions since the availability of the resources and the hazards of the environment influence how the increase in fitness associated to a change in one trait correlates with a decrease in fitness due to a change in another one.

In this respect, it could be interesting to introduce an environment-driven dynamical evolution of the intensity of trade-offs to analyze the double influence of (*i*) the epigenetic predisposition and (*ii*) the ecological pressures on the actual behaviour assumed by the cell population. This approach would enable us to consider the whole spectrum of trade-off intensity involving both convex and concave profiles, thus improving our results. The model aims to give a mathematical coherent description of the so-called *phenotypic plasticity* i.e. the capability of cells to change their behaviour reversibly (i.e. their phenotypic characterisation) as a result of the interaction between (*i*) the constraints imposed by their genetic heritage (that is intrinsic in individuals) and (*ii*) the environmental conditions faced. Two phenomena that play a fundamental role in the development of tumour masses development can be achieved in this context: the so-called fingering formation that drives the invasion phenomena and the dispersal mechanisms of cells at the basis of metastasis formation, [380].

Finally, one of the most important and triggering extension for this model (only partially implemented in next chapter) is to include therapies. The kinetics investigated, as well as the choice of the abiotic factor considered, are indeed able to capture, as done in the simulations, some dynamics that directly impact on therapies efficacy in an early stage tumour, in particular in the case of radiotherapy. With respect to resection, as already anticipated in Section 3.3.2, our model indeed gives the possibility of considering spatial heterogeneity and different environmental layouts, showing its potential in predicting the location and shape of the tumour. From a therapeutic and surgical point of view, this could have a great impact and would deserve further investigations.

In this light, the model presented in this chapter laid the groundwork to develop a new mathematical model to investigate how the pre-therapeutic history of a tumour could affect the effectiveness of radiotherapy, how the treatment can be designed to be improved in terms of potency, and how a tumour could evolve in the case of non-eradication (*resistance ability acquisition*), taking into account the impact of environmental geometric characterisation and selection forces in the development. This aspect is particularly suitable to be investigated *via* our approach since, in an eco-evolutionary perspective, the emergence of a resistant population can be described in terms of tumour evolution and stems from its intrinsic heterogeneity. All the treatment procedures have indeed a strong impact on our body and act as an environmental stressor on tumour cells, [193]. This implies, coherently with the results presented in this chapter, that therapeutic agents, inducing modifications of tumour ecology and, consequently, of the fitness landscape of tumour cells, could allow substantial variations in tumour composition. Resistance to therapies reflects, in this sense, the temporal and spatial heterogeneity of the tumour microenvironment as well as the evolutionary potential of cancer phenotypes to adapt to therapeutic perturbations. The treatment-resistant hypoxic cells serve indeed as a nidus for subsequent tumour regrowth and repopulation, as well as for regional and distant dissemination, representing a therapeutic dilemma that needs to be deeply investigated to guarantee the most effective treatment protocol to possibly avoid relapses.

Furthermore, an extension in this direction of the model could take into account how the effects of radiotherapy doses differ according to the heterogeneity faced at the instant and the location at which the therapy is applied (from both a physical and a phenotypical point of view) investigating how this divergent response could be explicated via niche construction theory. In our eco-evolutionary setting, the

experimental evidence of patient-specific response can be indeed justified as a mirror of the inter-patient heterogeneity in the tumour microenvironment, tumour composition and the ways in which these two aspects mutually interact. Our work, under this light, could represent a first step towards the development of a model of radiotherapy which could adapt to patient-specific characteristics, in line with the innovative personalized medicine approach, [179]. As potential expansions of the model we have presented, various aspects emerge as particularly intriguing from both evolutionary and physical perspectives. One avenue of interest involves incorporating additional components of the tumour environment and exploring their effects on the geometric evolution of the tumour mass. This entails considering: (*i*) the mechanical properties of intracellular fluid, (*ii*) interactions with the extracellular matrix during expansion dynamics, (*iii*) competition for space and resources with healthy host tissue cells, and (*iv*) the interplay among metabolically active, quiescent, and necrotic cells.

From an evolutionary standpoint, enhancing our modelling approach to more realistically incorporate trade-offs that affect tumour evolution is of interest. Biologically, trade-off intensity reflects how much development of one characteristic occurs at the expense of another. Ecological conditions influence trade-off intensity, as resource availability and environmental hazards affect how changes in one trait correlate with changes in another. In this regard, it could be valuable to introduce an environment-driven dynamic evolution of trade-off intensity, analyzing how epigenetic predisposition and ecological pressures influence cell population behaviour. This approach would consider a full spectrum of trade-off intensities, including both convex and concave profiles, thereby refining our results.

The model aims to mathematically describe phenotypic plasticity, where cells reversibly change behaviour due to genetic heritage constraints and environmental conditions. Two critical phenomena in tumour development, fingering formation driving invasion and cell dispersal mechanisms underlying metastasis, can be understood within this context.

Lastly, a significant extension of the model, partially implemented in the next chapter, involves incorporating therapies. The kinetics studied, and the abiotic factor considered capture dynamics are impacting therapy efficacy in early-stage tumours, particularly in radiotherapy. Regarding resection, our model offers the possibility to assess spatial heterogeneity and various environmental layouts, showcasing potential

in predicting tumour location and shape. From a therapeutic and surgical standpoint, this could have substantial implications and warrants further investigation.

Our model lays the groundwork for developing a new mathematical model to explore how a tumour's pre-therapeutic history affects radiotherapy efficacy, how treatment can be optimized for potency, and how tumours evolve in the case of non-eradication (acquisition of resistance). This aspect is suitable for investigation via our approach, as the emergence of a resistant population can be described in terms of tumour evolution and arises from intrinsic heterogeneity. Therapeutic agents induce modifications in tumour ecology and the fitness landscape of tumour cells, leading to variations in tumour composition. Resistance to therapies reflects the temporal and spatial heterogeneity of the tumour microenvironment, as well as cancer phenotypes' evolutionary potential to adapt to therapeutic perturbations.

Furthermore, an extension of the model could explore how radiotherapy dose effects differ based on the heterogeneity encountered at the instant and location of therapy application. Investigating this divergent response through niche construction theory could provide insights into patient-specific responses, reflecting inter-patient heterogeneity in tumour microenvironment and composition. Our work may serve as a first step toward developing a model of radiotherapy that adapts to patient-specific characteristics, aligning with the personalized medicine approach.

Chapter 4

Continuous modelling for radiotherapy and geometric characterisation of resistant traits according to oxygenation

Basing on the study presented in Chapter 3, we now move to take into account therapies. The eco-evolutionary dynamics we included in the investigation in the previous chapter are of particular interest also in the study of therapeutic strategies for the treatment of cancer. In fact, the characteristics of the tumour population, the interaction with the environment, and the effects of the treatment influence the geometric and epigenetic characterisation of the tumour with direct consequences on the efficacy of the therapy and possible relapses. Considering different therapies move the attention on different environmental factors that influence the treatment effectiveness. Here, we concentrate on radiotherapy, in which oxygen concentration plays a central role both in determining the effectiveness of the treatment and the selective pressure due to hypoxia. In Chapter 3 we settled in the framework of epigenetically structured population dynamics and formulated a model for tumour mass evolution in terms of systems of coupled non-linear integro-differential equations. Here we extend the model, aiming to catch the previously intoduced clinical phenomena and to provide a predictive tool for the tumour mass evolution and therapeutic effects. The content of this chapter is published in Ref. [111].

4.1 Introduction

Because of its high cytotoxic potential, radiation therapy is a standard of care in many solid tumours [47]. Since its inception, the objective of cancer research has been to discover novel methods of quality treatment approaches to eradicate malignancies. Presently, due to its high diffusion, over 60% of all ongoing medical quality treatment trials worldwide are concentrating on them [1].

In this light, the main goal of radiotherapy is to deprive cancer cells of their multiplication potential, damaging their genetic material and thus blocking their ability to divide and proliferate further *via* high-energy radiation (we recall the content of Section 1.4.1). Tumour cells are, in general, not as efficient as normal cells in repairing the damage caused by radiation, resulting in differential cell killing. For this reason, radiotherapy is mainly delivered through fractionated schemes to maximise the radiation effects on abnormal cancer cells while minimising exposure to normal ones [48].

Prediction of tumour response after irradiation has been a challenge at the very beginning since it became rapidly clear that the biological effect of irradiation is a complex phenomenon not uniquely determined by the total dose but also by the characteristics of the treatment protocol (such as fraction dose and dose schedule) as well as by physiological conditions in which it is applied that can widely range between patients [151].

The success of radiotherapy depends indeed on multiple sub-cellular, cellular, and microenvironmental parameters, together referred to as the "*6Rs of radiation therapy*": *repair* of irradiation-induced DNA damages, *redistribution* of cells within the cell cycle, *repopulation* of mass after radiation, *reoxygenation* of the tumour microenvironment, intrinsic *radiosensitivity* of different cell subpopulations and *reactivation* of the anti-tumour immune response [376].

A crucial factor that impacts all these aspects is tumour heterogeneity in terms of both microenvironmental conditions and cancer cell populations. In particular, it has been observed that the local oxygen concentration can significantly influence radiation-induced cell death, with well-oxygenated regions being shown to exhibit up to threefold greater radiosensitivity than hypoxic tumour populations [225].

Hypoxia is a consequence of the high tumour cell proliferation rate and the abnormal structure of the tumour vasculature. Oxygenation level is generally reduced and heterogeneous within malignant masses, compared to the oxygenation found in associated healthy tissues; this lack of oxygen is a critical feature in tumours promoting their progression. It is indeed clinically observed that, in solid tumours, oxygen tissue deprivation acts as an environmental stressor, promoting a long series of genetic, but especially, epigenetic mutations that strongly impact the tumour eco-evolutionary dynamics. Cancer cells are indeed able to adjust their cellular physiology and metabolism via the up-regulation of different genes such as p53, HIF-α or GLUT-1 or IAP-2, acquiring the ability to grow in hypoxic microenvironments and to evade apoptosis [187].

The reason for which low oxygen tensions are associated with radiation resistance relies on the mechanism of cell killing by ionising radiation. It is indeed experimentally shown that oxygen plays a fundamental role in fixing the damage on cancer cells induced by radiotherapy that leads to their death [265]. In fact, it is observed that hypoxia can cause topographically defined cellular subpopulations protected at the time of radiation without being killed by severe oxygen starvation; the oxygen tension for hypoxic cells could be indeed high enough to allow for clonogenic survival but low enough to protect them from the effects of ionising radiation [381].

In this view, it is clear that hypoxia impacts all the *6Rs* mentioned before, becoming a fundamental factor to be considered in a successful treatment protocol. In particular, we are interested in investigating its effects on three of them: (*i*) *radiosensitivity*, (*ii*) *repopulation* and (*iii*) *reoxygenation*. *Radiosensitivity* defines the intrinsic sensitivity of tumour cells to the therapy; it is influenced by hypoxia at two levels: a *direct* one since, as underlined before, oxygen is responsible for the enhancement of the detrimental effect of ionising radiation implying that radiotherapy is less efficient in the areas in which a lack of oxygen is observed; an *inverse* one by the fact that hypoxia selects for cells equipped by high resistance to hostile environments and low proliferative rates. *Repopulation* defines instead the renewal and proliferation of surviving cancer cells following irradiation and is affected by hypoxia since it promotes treatment-resistant hypoxic cells that serve as a nidus for subsequent tumour regrowth and repopulation. Finally, *reoxygenation* defines the fact that, between radiotherapy fractions, well-oxygenated cell death leads to oxygen release, reduction of oxygen demand, and tumour bulk shrinkage, allowing

better oxygen diffusion, turning back initially refractory hypoxic areas to a more radiosensitive state [376].

The emergence of a resistant population can be described in terms of tumour evolution and stems from its intrinsic heterogeneity. In an eco-evolutionary perspective, a tumour can be indeed interpreted as a cell population characterised by an accumulation, via natural selection, of genetics and epigenetics alterations that appear both due to intrinsic cell variability and to their mutual interactions with the surrounding microenvironment. In this light, all the treatment procedures could act as an environmental stressor on tumour cells, inducing strong modifications of tumour ecology and, consequently, of the fitness landscape of tumour cells, promoting variations in tumour composition. The resulting strong selective bottleneck enriches for resistant phenotypes within cancer cells as a mirror of the evolutionary capacity of cancer phenotypes to adapt to therapeutic perturbations as well as of the modifications of the temporal and spatial heterogeneity of the tumour microenvironment [193, 78, 165]. In this view, ecologically informed therapeutic strategies can potentially define and use novel treatment approaches that could vary among patients whose landscapes could be completely different. Such an adaptive approach implies that each patient therapeutic protocol is strictly personalised on the basis of the tumour state and response rather than a one-size-fits-all fixed treatment regime [72, 131].

Mathematical models constitute a good investigative instrument in this sense since they can allow testing different environmental conditions, different tumour compositions, as well as different therapeutic protocols. They can be seen as *in silico* laboratories to evaluate the mutual interactions between the above-mentioned aspects and their consequences on tumour development. In this respect, the effect of tumour-host interaction, in particular considering tissue oxygenation and its role in shaping the phenotypic composition of tumour masses and their double impact on radiotherapy efficacy has been deeply investigated *via* a wide range of modelling techniques [36, 418, 437, 300, 301, 436, 175]. For example, in Ref. [94], the authors presented a mathematical model that describes how tumour heterogeneity in terms of stemness evolves in a tissue slice oxygenated by a single blood vessel, determining the proliferative capacity, the apoptosis propensity and the response to radiotherapy protocols. A similar dynamics is investigated in Ref. [210] via a hybrid cellular automaton in which the authors analysed the spatio-temporal dynamics and the evolution of the intratumoral heterogeneity of a mass under the action of radiotherapy, showing how the treatment results more effectively in well-oxygenated tumours than

in the poorly oxygenated ones. In the same veins but with particular attention to tumour cell repopulation, reoxygenation and redistribution of proliferative states, in Ref. [275], is proposed a spatially-distributed continuous mathematical model of solid tumour growth treated by fractionated RT. Other interesting results are collected in Ref. [285], in which numerical and analytical techniques are developed to investigate the radiation response of tumours with different intratumoral oxygen distribution profiles. Finally, without an explicit description of tumour oxygenation but in a more general framework of tumour-host interaction in terms of competition for space and resources and tumour heterogeneity, in Ref. [363], the authors proposed a prognostic factor for personalised radiotherapy, named Proliferation Saturation Index (PSI), to identify the best fractionation scheme.

Following this research line, a particularly promising treatment modality is Intensity-Modulated Radiotherapy (IMRT), which has the potential to be an effective method for delivering customised radiation therapy to small, specific regions of a tumour based on its oxygenation level [290, 49]. This approach is called *dose painting* and involves selectively boosting doses to regions of the tumour that are known to be particularly resistant to treatment [206]. To fully exploit this technique, however, additional information about the tumour composition, specifically in terms of its resistance to hypoxia, is necessary in order to define the most effective radiation dosimetry plan.

Motivated by the above considerations, in this work, we are interested in investigating how low oxygen levels and hypoxia-associated tumour cell adaptions affect radiotherapy efficiency in the specific case of solid tumours. We aim, in this sense, to develop a tool which could adapt to patient-specific characteristics, in line with the innovative personalised medicine approach [179].

In our previous work presented in Ref. [112], we deeply investigated how the mutual interactions between the tumour mass and oxygen distribution (i) can result in a geometric characterisation of tumour niches in terms of masses spatial extension, how this characterisation could affect the phenotypic composition in terms of survival and invasive abilities and finally how both these two aspects in synergy affect the mass growth. This approach naturally laid the groundwork to investigate how the pre-therapeutic history of a tumour dictated by oxygen distribution could determine therapeutic failures. This is due to the possibility of taking into account the differences in tumour conformation and invasive ability coupled with the emergence

of treatment-resistant hypoxic cells that result from this dynamics. It indeed perfectly matches with the necessity to take into account two crucial events: (*i*) hypoxia selects for cells equipped by high resistance to hostile environments and low proliferative rates; (*ii*) these cells are intrinsically less exposed to treatment action with respect to the normal cells since radiotherapy damages the DNA consequently blocking the replication process.

This setting clearly results in being particularly suitable to investigate *radiosensitivity* development dictated by hypoxia since we can naturally map cell mitotic potential with their intrinsic resistance ability. A *low proliferant* cell is indeed intrinsically *more resistant* to the action of radiotherapy in light of what we previously observed. Moreover, the eco-evolutionary approach that we there adopted allows us to investigate the effects on tumour growth and regrowth of therapeutic perturbations coupled with the spatial and temporal variations observed in the tumour microenvironment, leading to the investigation of the dynamics that govern the *repopulation* of a tumour mass after the treatment. Finally, considering the interaction between the tumour mass and the microenvironment in which it lives also allows us to focus on the dynamics of oxygen and to evaluate the impact of *reoxygenation* phenomena.

In this work, we present an extension of the previous model in Ref. [112] to describe how the effects of radiotherapy differ according to the heterogeneity faced at the instant and the location at which the therapy is applied (from both a physical and a phenotypical point of view) investigating how a divergent response could be observed within and among patients. In this perspective, we consider a specific formulation for the survival fraction of the already treated tumour cells, able to capture both parameters directly associated with clinical data and specific mortality rates with respect to different doses and treatment timings. This new modelling structure of radiotherapy gives the possibility to explore the tumour-therapy interaction in two mutual directions, i.e. (*i*) the impact of tumour developmental dynamics on the efficacy of therapy, (*ii*) the impact of therapy on the spatial and epigenetic characteristics of the tumour mass.

Moreover, the action of the environmental selection is taken into account to characterise the spatial heterogeneity of proliferative potential, identify the tumour regions composed of cells with low proliferative rates, and study how their evolution could largely influence treatment success. Since the terms phenotypic and epigenetic (both already introduced in this work) are often used in the literature with the same

meaning, we specify that in the sequel of this chapter, we refer to the epigenetic trait (and the relative mutation) when we intend to refer to the molecular imprint on the genotype which determines the degree of activation of the genes, keeping unaltered their sequence. Instead, we refer to the phenotype as the observable actualisation of interactions between its genome, epigenome, and local environment.

The rest of the chapter is organised as follows: in Section 4.2, we present the proposed model with the underlying assumptions (see Subsection 4.2.1); details on the parameters estimate and on its numerical implementation as well as on the indices that quantity tumour progression is given in Subsection 4.2.2 and Subsection 4.2.3, respectively. We then turn on describing the model results in Section 4.3. Specifically, we simulate the growth of the malignancy in two specific settings, referred to as Case 1 - highly efficient single vessel (see Subsection 4.3.1) and Case 2 - inefficient single vessel (see Subsection 4.3.2) that differ with respect to the oxygenation level of the tissue. We compare them applying the same radiotherapy protocol to highlight the differences that could be observed in tumour response due to tumour-host interaction. Subsection 4.3.3 is instead devoted to investigating possible variations of radiotherapy efficacy varying the total dose amount delivered in the two experimental settings to explore the potency of *dose painting*. Finally, in Subsection 4.3.4, we analyse the effect of spatially heterogeneous distributions of the intra-tumoural blood vessels to highlight their role in the creation of ecological niches due to the relative blood vessels dispersal that influence the treatment response. The discussion ends in Section 4.4 with a summary of the main results with hints for possible developments.

4.2 Materials and methods

4.2.1 Mathematical model

As mentioned in the introduction, building upon our previous work [112], we extend the model to include the effects of radiotherapy. To this aim, we set a spatial bi-dimensional domain $\Omega_s \subset \mathbb{R}^2$ in which the mass can expand, assuming to observe a tumour evolving in a tissue slice. In particular, in our setting: (*i*) oxygen is the main environmental factor that affects tumour evolution, and in the determination of the different areas of therapeutic efficacy; (*ii*) tumour cells' behaviour will be

influenced by the epigenetic characteristics of individuals in terms of their double *resistance* to hypoxia and radiotherapy, the environmental conditions faced and the mutual interaction between these two aspects.

In this respect, the virtual tumour mass is differentiated in *metabolically active* (*i.e.*, viable) and *necrotic* individuals. As in the previous model, the necrotic subpopulation is assumed to be undifferentiated, with number density given by the function $n(t,\mathbf{x}) : T \times \Omega_s \mapsto \mathbb{R}_0^+$. The viable tumour portion is structured with respect to the same epigenetic trait $u \in \Omega_p = [0,1]$, which in this model not only describes the *double* resistance level of malignant cells *i.e.* w.r.t. the ability to *survive in hypoxic tumour areas*, but is also associated with their *radiosensitivity* (we formalise this in mathematical term later). We recall that the epigenetic state $u = 0$ characterises the cells that show the highest mitotic potential and, relatively, the highest sensibility to both lack of oxygen and radiotherapy action (*proliferation promoting or sensible cells*); the epigenetic state $u = 1$, instead is linked to cells that show the potentially highest survival ability but the lowest duplication capacity (*survival promoting or resistant cells*).

The evolution of the tumour mass distribution, based on Equation (3.2.2), reads:

$$\frac{\partial a(t,\mathbf{x},u)}{\partial t} = \underbrace{\mu_p \frac{\partial^2 a(t,\mathbf{x},u)}{\partial u^2}}_{\text{epigenetic variations}} + \underbrace{\mu_s \Delta_{\mathbf{x}} a(t,\mathbf{x},u)}_{\text{movement}} + \underbrace{R(u,O(t,\mathbf{x}),\rho(t,\mathbf{x}),n(t,\mathbf{x}))a(t,\mathbf{x},u)}_{\text{proliferation/selection/necrosis}}. \tag{4.2.1}$$

in which $O(t,\mathbf{x}) : T \times \Omega_s \mapsto \mathbb{R}_0^+$ represents the oxygen concentration and $\rho(t,x)$ denotes the local number density of the non-necrotic tumour area, computed as in Equation (3.2.1). With respect to the previously introduced model, we keep unaltered the random epigenetic transitions and the diffusive spatial dynamics. Reaction term reads:

$$\begin{aligned} R(u,O(t,\mathbf{x}),\rho(t,\mathbf{x}),n(t,\mathbf{x})) = &\overbrace{P(u,O(t,\mathbf{x}),\rho(t,\mathbf{x}),n(t,\mathbf{x}))}^{\text{proliferation}} - \overbrace{S(u,O(t,\mathbf{x}))}^{\text{selection}} \\ &- \underbrace{N(O(t,\mathbf{x}))}_{\text{lack of oxygen}} - \underbrace{T(u,O(t,\mathbf{x}))}_{\text{radiotherapy}}. \end{aligned} \tag{4.2.2}$$

It includes a simplified proliferation expression P, unaltered selective pressures by environmental conditions S (see Equations (3.2.8) and (3.2.9)) and necrosis terms

which include the already presented N due to *lack of oxygen* (see Equation (3.2.10)) and add the new T due to *irradiation*.

In detail, the proliferation rate P is factorised as in Equation (3.2.4), p_1 and p_3 , respectively depending on the epigenetic trait and the cell densities, defined as in Equations (3.2.5) and (3.2.7). We simplify the oxygen-dependent term p_2 with the following classical Michaelis-Menten law:

$$p_2(O(t,\mathbf{x})) = \frac{O(t,\mathbf{x})}{\alpha_O + O(t,\mathbf{x})}, \tag{4.2.3}$$

With respect to the previous model, we allow cells proliferation even under the O_n oxygen threshold, enhancing the role of the necrotic term responsible for death of cells below this reference oxygen concentration. As a consequence, the variable appearing in the Michaelis-Menten term is the oxygen concentration itself, without considering a basal level O_n under which the presence of oxygen is not significant in the count of available nutrient.

Finally, the term $T(u,O(t,\mathbf{x}))$ represents the radiobiological response of cells under the action of the treatment. To define it, we rely on the standard linear-quadratic (LQ) model [249], which describes the surviving fraction SF of cells in response to a single radiation dose. In our setting, cell mortality is defined following an innovative approach in the light of what we mentioned before, i.e. in the function of both (i) oxygenation of the tissue and (ii) intrinsic radiosensitivity of cell clones with respect to their epigenetic firm. Generally, the main parameters of the LQ model α and β are tissue-specific coefficients, and we introduce variability in the action of radiotherapy according to the biological situations in which the therapy is applied [431]. Specifically, we consider that the effectiveness of radiotherapy is related to hypoxia, which affects therapeutic efficacy in two ways. A direct one is the fact that, as underlined before, oxygen is responsible for the enhancement of the detrimental effect of ionising radiation, which implies that radiotherapy is less efficient in the areas in which a lack of oxygen is observed. An inverse one by the fact that hypoxia selects for cells equipped with high resistance to hostile environments and low proliferative rates; this second characteristic makes cells, as already mentioned, intrinsically less exposed to radiotherapy action with respect the normal cells since the power of radiotherapy is to be able to damage the DNA consequently blocking the replication process. In this light, we assume that the coefficients α and β coefficients depend on introducing a variable z which takes

into account both the oxygen concentration (to simulate that the treatment is less effective in hypoxic areas) and the epigenetic characterisation of cells (to simulate that hypoxia-resistant cells are even less sensitive to radiotherapy). This concept is formalised describing z as a product of two weights: (i) the former, here named w_u, which depends on the epigenetic trait of the cell u and (ii) the second, here named w_O, from the oxygen concentration $O(t,s)$:

$$z(u,O(t,\mathbf{x})) = w_u(u)\cdot w_O(O(t,\mathbf{x})) \tag{4.2.4}$$

where

$$w_u(u) = \frac{p_1(u)}{\gamma_{\max}} \quad \text{and} \quad w_O(O(t,\mathbf{x})) = p_2(O(t,\mathbf{x})), \tag{4.2.5}$$

to highlight the relation that exists between *proliferation* and *survival* (*proliferation-survival trade-off*). In this light, inspired from the work presented in Ref. [95], we model the increasing dependence of α and β parameters on the eco-evolutionary variable z as:

$$\alpha(z) = \alpha_{min} + (\alpha_{max} - \alpha_{min})z, \tag{4.2.6}$$

and

$$\beta(z) = \beta_{min} + (\beta_{max} - \beta_{min})z, \tag{4.2.7}$$

where $\alpha_{min}, \alpha_{max}, \beta_{min}$ and β_{max} are non-negative constants with $\alpha_{min} < \alpha_{max}$ and $\beta_{min} < \beta_{max}$, which represent the maximum and minimum sensitivity to treatment (estimations of their values can be found in Ref. [248]). Finally, we characterise cell mortality under the action of radiotherapy as follows:

$$T(u,O(t,\mathbf{x})) = (\alpha(z)d + \beta(z)d^2)\cdot \delta_{\text{times}}(t) \tag{4.2.8}$$

where: (i) $\delta_{\text{times}}(t) = \sum_{T\in\text{times}} \delta_T(t)$, being δ the Dirac-delta, models the fact that the death factor due to therapy is only present during the administration time of the chosen protocol and (i) d is the administered dose. To complete the modelling of cancer cells, we include Equation (3.2.11) in the models.

Switching on the molecular scale, in the same setting presented in Ref. [112], the local concentration of oxygen is governed by a parabolic PDE where the spatially heterogeneous source term $V(\mathbf{x})$ captures the presence of intra-tumoural blood vessels which bring oxygen into the tumour tissue. Moreover, oxygen diffuses within the tissue, naturally decays, and is consumed by viable cells. The equation regulating

oxygen dynamics is directly derived from Equation (3.2.12) and reads

$$\frac{\partial O(t,\mathbf{x})}{\partial t} = \underbrace{\mu_{\mathrm{O}}\Delta_{\mathbf{x}}O(t,\mathbf{x})}_{\text{diffusion}} - \underbrace{\lambda_{\mathrm{O}}O(t,\mathbf{x})}_{\text{natural decay}} - \underbrace{\zeta_{\mathrm{O}}\rho(t,\mathbf{x})O(t,\mathbf{x})}_{\substack{\text{consumption by}\\ \text{active tumour cells}}} + \underbrace{V(\mathbf{x})}_{\substack{\text{inflow from}\\ \text{the blood vessels}}}, \quad (4.2.9)$$

Here, the sole modification is introduced in the consumption term, which appears simplified with respect to the one used in Equation (3.2.12). There, consumption formally depends on proliferative activity of the cells. In this new model, oxygen is consumed at a rate ζ_{O} by all viable tumour cells. We point out that this, while retaining the advantage of leaner modelling, does not lose the biologically coherent connection between proliferation and increased oxygen consumption. In fact, cells that proliferate more increase cell density more, consequently increasing consumption via the term introduced here. Concerning the inflow, we recall the source description provided by Equation (3.2.13).

4.2.2 Simulation details

The spatial domain Ω_s represents a bi-dimensional section of a four cm-large tissue, i.e. $\Omega_s = [-2,2]^2$ cm. The final observation time is denoted by t_{F} and varies among simulations in correspondence with the relapse, identified as the time at which the total cell count reaches the detection threshold ($4 \cdot 10^6$) again after the radiotherapy administration.

Initial and boundary conditions: Equation (4.2.1) that establishes cell dynamics, is equipped by the following initial condition:

$$a(0,\mathbf{x},u) = A\ \exp\left(-\frac{(\mathbf{x}-\mathbf{x}_C)^2}{2\sigma_{\mathbf{x}}^2} - \frac{(u-u_C)^2}{2\sigma_u^2}\right), \quad \text{for } \mathbf{x},u \in \Omega_s \times \Omega_p; \quad (4.2.10)$$

$$n(0,\mathbf{x}) = 0, \quad \text{for } \mathbf{x} \in \Omega_s, \quad (4.2.11)$$

with $A > 0$ s.t. $\rho(0,\mathbf{x}) = \int_{\Omega_p} a(0,\mathbf{x},u)du < k$. The geometric point around which the cancer cell population is located at the initial time is denoted by $\mathbf{x}_C$; without loss of generality, we consider the case in which it is fixed at the centre of the domain $\mathbf{x}_C = (0,0)$. Biologically, this setting reproduces, at the beginning of the numerical realisations, a node of malignant viable cells already present within the tissue, with

the following characteristics: (i) each cell epigenetic state has a full Gaussian profile along the spatial dimension, centred at the starting point $\mathbf{x}_C$ and with a variance of $\sigma_{\mathbf{x}}^2 = 0.008$ cm^2 and (ii) the cell mass has a half-normal distribution in the trait space, with peak at $u_C = \varphi_O(O(0,x_C))$ which is the optimal epigenetic trait with respect to the oxygen concentration given by the initial condition and with variance $\sigma_u^2 = 0.08$. The initial cell configuration has a maximum value of $A = 89.20$ cell/cm^2. In this respect, at $t = 0$, the overall density ρ of active individuals is symmetrically disposed w.r.t. $\mathbf{x}_C$ and, in normoxic condition, it is mainly composed of proliferative promoting cell variants with only a small fraction of survival-promoting agents.

Equation ((4.2.1)) has zero-flux conditions at the boundary of the epigenetic domain, i.e., $\partial_u a(\cdot,\cdot,0) = \partial_u a(\cdot,\cdot,1) = 0$. This is consistent with the fact that malignant cells can not be characterised by a trait smaller than 0 or higher than 1. The same holds on the domain Ω_s under the assumption of considering the growth of the mass in a tissue slice where physical barriers (for instance, bones) bounds of breast ducts or the lack of extra-cellular matrix prevent the expansion of the mass out of them.

Turing on chemical kinetics, Equation (4.2.9) is completed with initial condition $O(0,\mathbf{x})$ that represents the steady-state of oxygen distribution in the tissue in the absence of tumour cells with respect to different vessels intensity whose value is specified case by case. We couple Equation (4.2.9) with zero-Dirichlet conditions at the boundary of the spatial domain Ω_s under the assumption of considering a sufficiently large tissue in which anoxic areas at the boundaries of the domain. In this respect, two geometrical layouts for blood vessels are adopted in this work: (i) one with a single vessel at the centre of the domain, considering two inflow cases; we refer to them as $\Upsilon^{FV} = \{((0,0),\tilde{I})\}$ (full vessel layout) and $\Upsilon^{HV} = \{((0,0),0.5\tilde{I})\}$ (half vessel layout); (ii) the other is a three vessel layout, where all the vessel are around the antibisector in the configuration $\Upsilon^{3V} = \{((-1.3,1.3),0.5\tilde{I}),(1.4,-1.2),0.65\tilde{I}),(1.2,-1.4),0.65\tilde{I})\}$. In the sequel, we set the reference oxygen inflow $\tilde{I} = 1.57\mu mol/(cm^2 day)$.

Parameters estimate: The majority of model coefficients have a clear and direct biological meaning, and therefore, a proper estimate has been done by taking advantage of the empirical literature. In this respect, we have referred to experimental works dealing with a wide spectrum of diseases since we here account for a generic tumour. The full parameters set up is listed in Table 5.1.

	Parameter	Description	Value [Units]	Reference(s)
cell dynamics	μ_p	epigenetic variation rate	$8.64 \cdot 10^{-9}$ [day^{-1}]	[158]
	μ_s	spatial diffusion rate	$3.11 \cdot 10^{-5}$ [cm^2/day]	[312]
	$\gamma_{\min}$	minimal cell duplication rate	$3.46 \cdot 10^{-1}$ [day^{-1}]	[312]
	$\gamma_{\max}$	maximal cell duplication rate	$6.94 \cdot 10^{-1}$ [day^{-1}]	[312]
	k	tissue carrying capacity	10^6 [cell/cm^2]	[400]
	η_O	oxygen selection gradient	1 [day^{-1}]	model estimate
	η	rate of necrotic transition	1 [day^{-1}]	model estimate
	α_{min}	Minimum α value for radiotherapy	0.007 [Gy^{-1}]	[248]
	α_{max}	Maximum α value for radiotherapy	0.21 [Gy^{-1}]	[248]
	β_{min}	Minimum β value for radiotherapy	0.003 [Gy^{-2}]	[248]
	β_{max}	Maximum β value for radiotherapy	0.15 [Gy^{-2}]	[248]
oxygen kinetics	μ_O	oxygen diffusion coefficient	$8.64 \cdot 10^{-1}$ [cm^2/day]	[312]
	λ_O	oxygen natural decay rate	$8.64 \cdot 10^{-3}$ [day^{-1}]	[136]
	α_O	Michealis-Menten oxygen constant	$4.28 \cdot 10^{-9}$ [μmol/ cm^2]	[140]
	ζ_O	oxygen consumption rate	$8.64 \cdot 10^{-16}$ [μmol/cell]	model estimate
	O_n	oxygen necrotic threshold	$1.20 \cdot 10^{-9}$ [μmol/cm^2]	[74]
	O_m	oxygen hypoxic threshold	$2.57 \cdot 10^{-9}$ [μmol/cm^2]	[74]
	O_M	oxygen normoxic threshold	$1.37 \cdot 10^{-8}$ [μmol/cm^2]	[74]

Table 4.1 Reference parameters setting.

Numerical method: For the domain mesh and the implementation of the numerical resolution algorithm, a Python code is developed using FEniCS and Dolfin packages [279]. Specifically, we adopt a uniform discretisation for the temporal and epigenetic domains and a triangular mesh with radial symmetry for the two-dimensional geometric domain. The system of partial differential equations is solved via a mixed solution scheme. We couple an explicit Euler method for the one-dimensional components of the domain (time and epigenetic trait) and a Galerkin finite element method for the dynamics of the geometric domain.

4.2.3 Quantification of model results

Following our previous approach [112], to provide some qualitative indicators of tumour evolution and a more quantitative description of epigenetic trait distribution inside the mass, we divide the epigenetic domain Ω_p in three *epigenetic bands*, denoted with L (low), M (medium) and H (high): $\Omega_p = \Omega_p^L \cup \Omega_p^M \cup \Omega_p^H$ with $\Omega_p^L = [0, 0.3)$, $\Omega_p^M = [0.3, 0.7]$, $\Omega_p^H = (0.7, 1]$. We link the *epigenetic bands* to the tissue regions in which they are the "optimal" ones in terms of environmental selection *via* the function $\varphi_o(O(t, \mathbf{x}))$, Equation (3.2.9). We obtain a time-dependent partition of the spatial domain $\Omega_s(t) = \Omega_s^L(t) \cup \Omega_s^M(t) \cup \Omega_s^H(t) \cup \Omega_s^N(t)$, $\forall t \in T$ where L, M, H superscripts correspond to the areas of the domain where the fittest epigenetic

trait belongs to the correspondent epigenetic band and $\Omega_s^N(t)$ is the necrotic area (oxygen below O_n). To analyse the results of our simulations, we use local and global indicators.

In order to spatially characterise the tumour mass, we take into account the local number density $\rho(t,x)$ already presented in Section 4.2 and we introduce the *band-specific local number densities*:

$$\rho_j(t,\mathbf{x}) = \int_{\Omega_p^j} a(t,\mathbf{x},u)\,du \qquad \text{for } j \in \{L,M,H\} \tag{4.2.12}$$

To give some global indicators and analyse their evolution over time, we introduce the following:

- the *total cell count*, providing the size of the tumour population:

$$\Gamma(t) = \int_{\Omega_s} \rho(t,\mathbf{x})\,d\mathbf{x} \tag{4.2.13}$$

- the *average epigenetic trait*, providing a representation of the epigenetic spectrum present in the mass:

$$\bar{g}(t) = \frac{1}{\Gamma(t)} \int_{\Omega_p} u \left(\int_{\Omega_s} a(t,x,u)\,d\mathbf{x} \right) du, \tag{4.2.14}$$

- the *average radiosensitivity index*:

$$\bar{\alpha}(t) = \frac{1}{\Gamma(t)} \int_{\Omega_p} \int_{\Omega_s} \alpha(z(u,O(t,\mathbf{x})))\,a(t,x,u)\,d\mathbf{x}\,du, \tag{4.2.15}$$

With respect to the radiotherapy parameters, we here use α as a qualitative indicator since we are interested in the relative variation with respect to minimum and maximum values, and β has the same dependence on the z function, just rescaled in its range, Eqs. (4.2.6), (4.2.7).

Finally, we introduce a global index for the environment description, which is the *oxygen total amount*

$$O(t) = \int_{\Omega_s} O(t,\mathbf{x})\,d\mathbf{x}. \tag{4.2.16}$$

4.3 Results

The rationale of this work is to investigate how differences in the tumour radiotherapy response could be related to the spatially heterogeneous distribution of intratumoral blood vessels in tumour tissues. One of the factors that may lead to therapeutic failures is the development of intra- and inter-patient resistance. Different ecological niches, in terms of vessel potency and relative dispersal, lead to the selection of cells with different characteristics that may pave the way to the emergence of therapeutic resistance. In these veins, the resulting heterogeneous tumour microenvironment is of clinical interest to find the optimum *patient-specific* protocol.

To investigate this phenomenon, according to the approach settled in our previous work [112], we firstly focus on studying these evolutionary dynamics in a relatively simple setting choosing, as a prototype of a growing malignant mass, a *tumour cord* i.e. a cylindrical mass formed by tumour cells that wrap around a blood vessel. Specifically, we are interested in two different environmental conditions designed to represent a high- and low-efficient vascular network, respectively, and finally, we are comparing them in terms of therapy efficacy. In both cases, we assume that the treatment is applied only in the presence of a sufficient highly concentrated tumour mass to reflect that, to be treated, masses have to be visible via diagnostic imaging. Specifically, we set a detecting threshold in correspondence of masses constituted by $4 \cdot 10^6$ cells. With respect to the applied protocol, we focus on one of the most common in conventional clinical practice, according to which patients receive the same radiation dose in all the different subregions of the tumour volume, following a fractionation schedule that provides for a dose of approximately 2 Gy (Gray) delivered once a day, Monday to Friday, up to a total of 50-70 Gy. Specifically, in our case, the therapy ends up in 6 weeks for a total dose amount of 60 Gy. The mass evolution is described in terms of numerosity, morphology and epigenetic characterisation, investigating the relation between these different aspects in *repopulation* phenomena. Moreover, special emphasis is devoted to tumour-host interaction, looking to oxygen dynamics in relation to the *radiosensitivity* of the mass considered.

4.3.1 Case 1 - highly efficient single vessel

In the first simulation setting, Fig. 4.1, we observe the growth of a tumour mass in a sufficiently oxygenated environment provided by Υ^{FV} layout. Looking at the evolution of its total cell count $\Gamma(t)$, panel (A) of Fig. 4.1, the presence of a functional blood vessel guarantees an efficient nutrient supply, leading to a rapid evolution of the mass. The malignant cell number shows a Gompertz-like profile, coherently with the biological evidence, see for instance Ref. [346, 181]. Assuming that the tumour burden can be diagnosed as soon as the mass approaches the detection threshold, radiotherapy is applied, according to the above-mentioned protocol, leading to quasi-total tumour eradication. The shape of the curve, week by week, fits the decreasing strength of the treatment in time, showing a strong efficacy in the first phases that gradually reduces in correspondence of a smaller portion of cells that could be hit. As it can be observed, once the treatment protocol is completed, the failed eradication allows for a quick relapse of the mass that restarts to grow even faster than the settlement phase, a restored bulk of the same dimension as the one before the clinical intervention could be observed at the end of the simulation.

The three-phase *expansion-contraction-expansion* dynamics is even more highlighted by looking at the evolution of the local density $\rho(t,x)$, represented in panel (C) of Fig. 4.1. Specifically, we focus on observing its profile at four representative time points: *i)* the tumour detection (DG - diagnosis), *ii)* the end of the treatment (PT - post-treatment), *iii)* during the tumour regrowth (RP - repopulation) and *iv)* the final configuration (RL - relapse). As can be observed, the mass develops almost radially around the vessel, and no differences in terms of shape could be highlighted comparing the first and the last panel. This is coherent with the fact that the tumour invasion is the result of the proliferative and diffusive potential with respect to the environmental conditions faced. Interestingly, at the end of radiotherapy administration, the cell density of the mass is widely underneath the detection threshold, see panel (D)-PT of Fig. 4.1; however, looking at the corresponding DG and PT panels in panel (D) of Fig. 4.1, where the tumour densities of the three different *epigenetic bands* ρ_j for $j = L,M,H$, are locally summed in space, the radiotherapy reduction corresponds to approximately the 99% of both tumour bulk and edges, switching in number from 10^6 to 10^4 and 10^5 to 10^3 [cells/cm^2], respectively. The remaining small node of cells, constituted by the 1% of the original mass, is responsible for tumour relapse, in accordance with the *repopulation* phenomena. The rapid growth

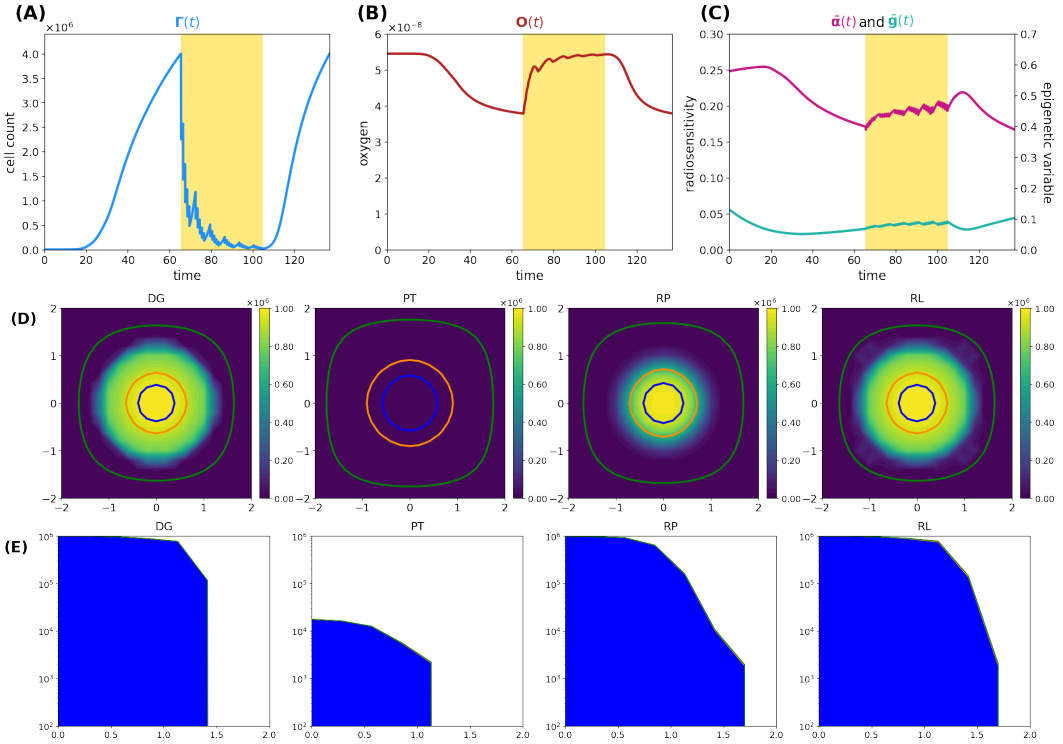

Fig. 4.1 Simulation of tumour mass, growing from the centre of the domain, with oxygen provided by the full vessel layout Υ^{FV}. (A) Global cell count evolution. (B) Total oxygen amount evolution. (C) Average radiosensitivity index and average epigenetic trait evolution. (D) $\rho(t,\mathbf{x})$ for t corresponds to diagnosis (DG), post-treatment (PT), repopulation (RP) and relapse (RL) times. Contour lines detect the optimal areas for high (green), medium (orange) and low (blue) epigenetic bands (necrotic area outside the green line). (E) Slice of $\rho(t,\mathbf{x})$ taken on the positive bisector in logarithmic scale. The edge represents the total amount $\rho(t,\mathbf{x})$ while coloured areas represent the epigenetic composition of the tumour (blue for low, orange for medium and green for the high epigenetic band). Caption and Figure from Ref. [111].

of the mass observed could be reasonably linked to tumour-host interaction and, in particular, to the *reoxygenation* after the radiotherapy. From a local point of view, this can be seen by analysing the contour lines at different time steps in panel (D) of Fig. 4.1, which detects the optimal areas for the three epigenetic bands (green for high, orange for medium and blue for low). The areas enclosed by the contour are wider after therapy (PT plot) due to the lowering of oxygen consumption as a consequence of the elimination of the tumour mass by the radiation administration.

From a global point of view, looking indeed to the evolution in time of total oxygen amount available in the tissue slice, panel (B) of Fig. 4.1, a rapid increase in

terms of its concentration occurs during the treatment administration. The rationale, as already anticipated in the Introduction chapter, is that the reduction in number of tumour cells during the treatment is reflected in a minor consumption of the available nutrients, leading to restored oxygen delivery in the tissue that was, in the early development phases, compromised due to the high metabolic requirement. As we can see, at the end of the radiotherapy protocol, the survived tumour cells could completely exploit the available oxygen, leveraging all their duplication potential and leading to quick mass regrowth.

In eco-evolutionary terms, it is interesting to investigate how the *cooperation* and/or *out-competition* phenomena could potentially influence these dynamics. In particular, as shown in our previous work [112], the selection dynamics occurring in the tumour-host interaction could carry out a crucial role in terms of tumour aggressiveness and treatments could act, in terms of environmental stressors, as bottlenecks that fuel these dynamics. Three aspects are of particular interest from our point of view: *i*) how the pre-treatment history of a tumour could impact the radiosensitivity of the mass at the beginning of treatment delivery; *ii*) the effect of radiotherapy as a bottleneck selecting for resistant epigenetic traits and finally *iii*) How could the consequences of the treatment action on the tumour microenvironment impact the future of tumour mass?

In this direction, we focus on investigating the evolution in time of the global average epigenetic expression of the mass $\bar{g}(t)$, Equation (4.2.15) and the corresponding one of the radiosensitivity index $\bar{\alpha}(t)$, Equation (4.2.14). Analysing the $\bar{g}$ profile in time, we can observe that the high oxygenated environment that characterises the early phases of tumour growth leads to an initial deflection of the average epigenetic expression. Indeed, in proximity to the blood vessel, proliferating cells have a strong evolutionary advantage with respect to all the other epigenetic traits present in the mass, out-competing them and becoming the predominant ones in the mass. As the mass expands, conquering less oxygenated regions, the action of natural selection slowly leads to the emergence of more resistant epigenetic traits, mildly shifting the tumour towards resistance to hypoxia development. However, a strong epigenetic switch in terms of the average composition of the mass during and after the treatment is not remarkably highlighted. Indeed, under these specific environmental conditions, the growth of the mass is only slightly affected by natural selection in the short time interval before detection, and thus, it is mainly composed of proliferating cells. *Reoxigenation* after the treatment gives a further advantage to

the proliferating cells. This is confirmed by looking at the epigenetic composition in terms of specific epigenetic band densities represented in panel (E) of Fig. 4.1. In this light, $\bar{g}(t)$, coherently, remains pretty constant with only small fluctuations. The jagged $\bar{g}(t)$ profile is due to the fact that: on the one hand, during the resting days of the treatment, in accordance with resources availability, proliferating cells quickly *repopulate* the tumour mass; on the other hand, during the effective treatment days, the higher effect of radiotherapy on proliferating cells leads to their decrease.

A more dynamic profile characterises the evolution in time of the *radiosensitivity* of our mass. As we can observe, in the early expansion phases, despite the promising tumour composition in terms of radiotherapy efficacy, the radiotherapy index rapidly decreases. This is due to the fact that the growing mass approaches less oxygenated regions due to both an increased oxygen consumption by the mass and the further distance from the vessel, and thus, the tumour results are less sensible to radiotherapy administration, independently by its epigenetic characterisation. In contrast, the *reoxygenation* phenomenon observed during the radiotherapy leads instead to increasing the responsiveness of mass to the treatment. The jagged profile of $\bar{\alpha}(t)$ is less regular with respect to the one observed for the average epigenetic index $\bar{g}(t)$, and, in this respect, our results suggest that the heterogeneity in terms of radiotherapy efficacy are mostly oxygen-driven with a minor role of epigenetic mass composition. The latter seems to become more crucial when *reoxygenation* phenomena completely restore the oxygen level (at time $t = 85day$ in the panels (B) and (C) of Fig. 4.1). In this case, oscillations due to the selection of more resistant epigenetic traits or the out-competition of proliferating epigenetic traits are indeed more evident. Unfortunately, coherently with the experimental evidences [224], the benefits of radiotherapy in terms of *reoxigenation* and thus, the increase of *radiosensitivity* of the mass has only a temporary effect: in a quick time window, the tumour mass re-acquires its scarce sensibility, being able to conquer and to survive in hypoxic regions where oxygen concentration is high enough to allow for clonogenic survival, but it is low enough to protect tumour cells from the effects of ionising radiation.

4.3.2 Case 2 - inefficient single vessel

In the second simulation setting, we observe the growth of a tumour mass in a harsher environment as a consequence of an inefficient tumour vasculature.

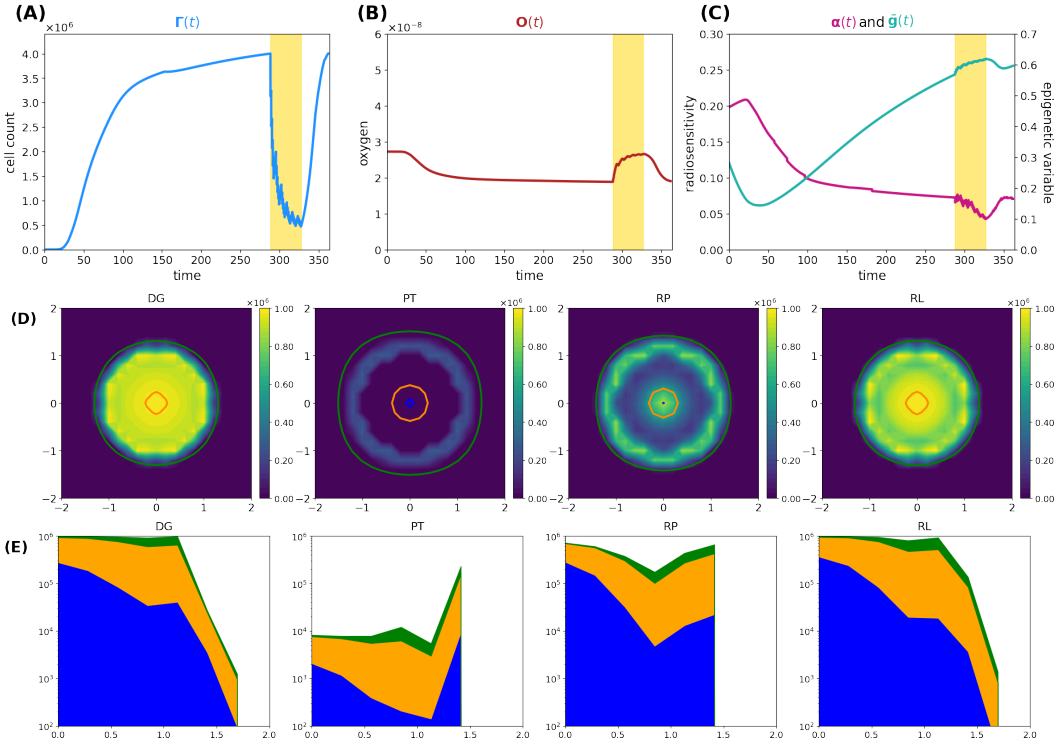

Fig. 4.2 Simulation of tumour mass, growing from the centre of the domain, with oxygen provided by the half vessel layout Υ^{HV}. Plot description as in caption of Fig. 4.1. Caption and Figure from Ref. [111].

From this perspective, we consider that the tissue is supplied by a blood vessel whose influx is halved, with respect to the previous case, and we analyse the same eco-evolutionary features. Looking at the results shown in Fig. 4.2, marked differences can be observed in tumour evolution with respect to the previous case.

First of all, the evolution of tumour cells total count $\Gamma(t)$ is significantly different (panel (A) of Fig. 4.2); the smaller amount of available resources slows down the tumour development, leading to a mass that needs approximately four times more to reach the detecting threshold (280 days *vs* 65 days). Its profile, moreover, reveals that the radiotherapy protocol is less effective with respect to the previous case; the mass reduces again, but, as evident in (panel (A) of Fig. 4.2), over the 10% of the cell population is not eradicated. Additionally, once the treatment protocol is completed, the failed eradication allows for a quick relapse of the mass; the restored bulk at the end of the simulation is indeed morphologically identical to the one before the clinical intervention, but it reaches the same volume, in a shorter time-window with respect the early stages of the mass growth (approximately 230 days *vs* 30 days).

The characteristic three-phase *expansion-contraction-expansion* dynamics is again observed. However, it is affected by completely different mechanisms with respect to the previous case, as it is shown by the rest of the eco-evolutionary dynamics.

The evolution in time of the tumour density ρ reveals, in contrast with the previous scenario, a moderately dense ring of resistant cells still present at the end of the treatment protocol. Its presence naturally affects the regrowth of the mass; and, as it could be observed in panel (D)-RP of Fig. 4.2, two simultaneous dynamics could be detected: *i*) a *repopulation* of the tumour region that starts from the centre of the mass in the proximity of the vessel, suggesting that, also in this case, a silent mass is not eradicated coupled with *ii*) an uninterrupted expansion of the rim of resistant cells.

This macroscopic difference between the two cases strongly depends on the different interactions between the tumour and the microenvironment that lead to completely different *radiosensitivity* and, consequently, different *repopulation* and *reoxygenation* dynamics in the mass. In particular, two are the aspects that have to be considered to identify the underpinning dynamics: *i*) a less oxygenated environment could lead to the emergence of intrinsically more resistant epigenetic traits; *ii*) An inefficient vasculature naturally suppresses the efficacy of radiotherapy.

Focusing on the first aspect, coherently with what we showed in our previous work [112], in the early stages of mass development, the tissue colonisation results from the cooperative relations between different specialised cell variants, enhancing the importance of epigenetic composition on tumour development. Analysing the local number densities of the different sub-groups ρ_j for $j = L, M, H$, it can be noticed that the tumour composition is affected by the spatial variability of oxygen concentration and environmental gradients leads to the selection for cells with epigenetic characteristics that vary with distance from the blood vessel. In particular, cells characterised by medium and high resistance start to colonise the mass in percentages that increase, moving far away from the nutrient source. This emerging dynamics suggests the development of the classical ring structure that characterises both tumour cords and spheroids; in this specific case, the mass is evolving, developing an inner core of proliferation promoting epigenetic traits surrounded by two concentric rims of medium and high resistant cells. A mixed composition of this type shapes the radiosensitivity of the mass and results in a heterogeneous response with respect to the cellular subtypes involved. In this sense, a double effect is particularly

visible. On the one hand, the presence of a greater number of resistant cells, environmentally favoured by the poor oxygenation, causes a lower general effectiveness of the treatment. On the other hand, the evident greater effectiveness on proliferative cells, initially hindered only by environmental selection, leaves more space and resources for resistant cells, which can thus consolidate and increase their presence in the tumour mass following treatment. We can in fact notice that proliferating cells strongly reduce in percentage, being out-competed by cells characterised by medium and high resistance with increasing intensity in lower oxygenated regions. These results highlight how, in tumour-host interaction, the selection dynamics could carry out a crucial role in terms of tumour aggressiveness and that treatments could act as environmental stressors and bottlenecks that fuel these dynamics. In particular, looking at panels DG and PT of (D) plots of Fig. 4.2, two aspects of particular interest naturally emerge: *i*) the impact of pre-treatment history of a tumour could impact on the radiosensitivity of the mass; *ii*) the role of radiotherapy as a bottleneck in selecting resistant epigenetic traits.

From this perspective, the residual ring that emerges at the end of the treatment is the result of the presence of pre-existing, more resistant epigenetic traits in the region of interest. This is perfectly in line with the biological hypothesis that the action of radiotherapy is affected by the tissue oxygenation level in a two-fold way: *i*) low oxygenation levels promote the emergence of radio-resistant cells, and we refer to it as *epigenetic-driven resistance*; *ii*) oxygen is fundamental to fix on the DNA of the cells the damage induced by radiation, and we refer to it as *purely oxygen-driven resistance*. Notably, also in this second case, *reoxygenation* could be observed as a consequence of tumour cells killing by radiotherapy, but its restoring dynamics is characterised by a slower slope with respect to the previous case. The underpinning reason relies on tumour mass composition: the presence of a heterogeneous mass with medium and high resistant cells implies that not all the viable cells are killed by the treatment and, thus, that the oxygen consumption does not stop during the treatment. Despite the slower dynamics, *reoxygentation* fuels more remarkably the tumour *repopulation*. The larger nidus of survived cells is indeed strongly advantaged by the presence of newly available resources, favouring their proliferation. It is interesting to notice how the *repopulation* of the mass is the result of *cooperation* phenomena in which more proliferating cells completely exploit their evolutionary advantage, colonising the inner region of the tumour tissue, as well as harsher regions are instead repopulated by increasing resistant epigenetic

traits. This phenomenon is highlighted in panel (D-RL) of Fig. 4.2 in which the ring structure, previously sketched, definitively emerges; an entire rim completely constituted by medium and high resistant epigenetic traits bounds indeed the tumour mass.

The eco-evolutionary indices that we are considering, the average epigenetic trait, Equation (4.2.14), and the radiosensitivity index, Equation (4.2.6), are able to reveal additional interesting information. Looking at the average epigenetic trait evolution, the interaction with a harsh environment strongly forces the hypoxia-resistance development trend. The epigenetic shift that is observed rapidly converges towards resistant epigenetic traits in the class of medium and high resistant cells, and thus, the mass is constituted in a higher percentage by these cellular subtypes. Its profile moreover highlights: *i*) the strength of the selective bottleneck induced by the action of the treatment that provides a further shift towards an increasing radio-resistance and *ii*) the effect of *reoxygenation* on *radiosensivity* of the mass as confirmed by the deflection in the immediate time window after the treatment. The last information could be exploited from the therapeutic point of view, being a mass sensible to proliferation targeting approaches. In the same vein, the evolution of the radiosensitivity index shows a decreasing profile during the entire time window of observation. This sharp trend is due to the harsh environment in terms of oxygenation: Hypoxia, already by itself, constitutes a valid element to decrease the radiosensitivity of the mass, which is affected by oxygen deprivation also in an indirect way via the selection of resistant epigenetic traits. Notably, the radiosensitivity index suggests that this specific protocol could not be the best therapeutic choice; indeed, in the current condition, it acts as a further bottleneck that forces the tumour to be more insensible to the treatment, as highlighted by the deflection that can be observed in the time-window of intervention. Moreover, the radiosensitivity index shows more irregular dynamics with respect to the previous case, coherently with the fact that, in this case, the radiotherapy response is guided by both the oxygenation levels and its epigenetic characterisation.

To summarise, a comparison of the dynamics is plotted in Fig. 4.3; bold and thin lines refer respectively to low and high-oxygenated microenvironments. Interestingly, our results suggest that nominal tumour size alone is insufficient to predict growth dynamics and that personalised indices are needed to define an efficient therapeutic plan. In fact, the time evolution of the total cell counts, panel (A) of Fig. 4.3, reveals how two patients with a similar tumour volume could have a distinct tumour–host

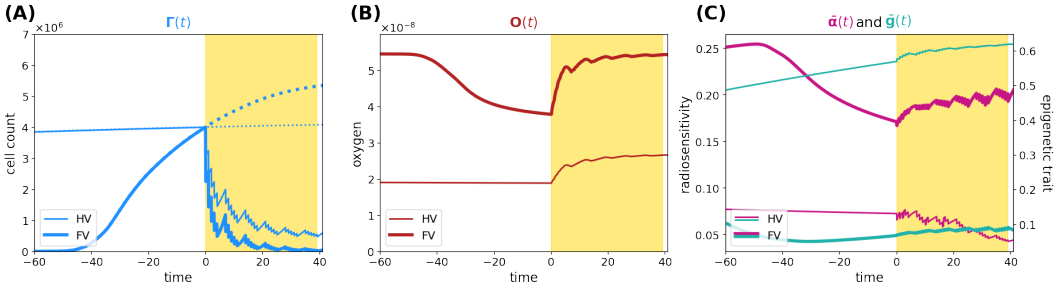

Fig. 4.3 Comparison between case 1 and case 2. The figure shows an overlap of (A), (B), and (C) plots presented in Fig. 4.1 and Fig. 4.2). The time axis has been rescaled so that time zero coincides with the beginning of the therapy for both experiments, and plots are zoomed around it. Caption and Figure from Ref. [111].

co-evolution history, which results in different responses to the same radiotherapy protocol, coherently with the clinically observed inter-patient variability in terms of therapy response. Furthermore, a particular behaviour is highlighted: tumour volumes close to their carrying capacity (the maximum tumour extension that can be reached with respect to the available resources) result in being less sensitive to radiation-induced damage (low oxygen case); on the other hand, tumours far from their carrying capacity are instead more sensitive to the radiation (high oxygen case). In this light, our results are interestingly in line with the ones presented in Ref. [363], in which a patient-specific index, named the Proliferation Saturation Index (PSI), estimated on patient data, is introduced as a predictive tool of the radiotherapy response. In their work, the authors hypothesise that tumours characterised by a high PSI, i.e. close to their carrying capacity, are composed of only a small proportion of proliferating cells highly sensitive to radiation-induced damage; thus, a less effective therapeutic impact could be expected. Our results confirm this hypothesis, further revealing the dynamics that determine the differences in tumour composition as a result of the heterogeneity from patient to patient in the tumour microenvironment. In this respect, see panel (B) of Fig. 4.3, our findings moreover suggest that even if the restoring oxygenation is, in percentage terms, the same in the two cases (close to the 25%), a completely different dynamics is observed. Indeed, in the first case (high oxygen level), looking at the in-time evolution of the radiosensitivity $\bar{\alpha}$ in panel (C) of Fig. 4.3, the radio-induced reoxygenation is sufficient to prompt the mass towards a higher sensibility to the treatment; at the contrary, in the case of low oxygenation, a degenerating dynamics towards a more resistant mass is observed, even in presence of higher quantity of available oxygen. In this view, our approach

enriches the number of information that can be harvested, providing a platform that targets both the microenvironment and the epigenetic characteristics of the mass. Therefore, it can potentially used to make predictions based on the state of the mass once discovered and to guide the protocol choice.

4.3.3 Dose painting

In conventional clinical practice, most patients treated with radiotherapy receive a similar dose and fractionation scheme. In particular, at present, the same radiation dose is delivered to all subregions of the tumour volume, regardless of their individual biology and radiosensitivity. As shown, oxygen concentration can greatly modify the patient response; in this light, new treatment modalities such as Intensity-Modulated Radiotherapy (IMRT) have emerged, aiming to modulate the delivered dose over small volumes that are distinguished with respect to the oxygenation level, see e.g. Ref. [290, 49]. This customisation of radiotherapy, based on spatial information drawn from hypoxia imaging, is generally known as *dose painting* and, in principle, it consists of the delivery of selective boosting dose to radio-resistant regions [206]. However, to fully exploit the strength of these new techniques, information on hypoxia levels needs to be coupled with knowledge of tumour composition in terms of therapy resistance that, as mentioned, strongly impacts treatment efficacy. Thus, detailed information about the internal structure of the tumour in terms of epigenetic traits and phenotypes is required to define the best radiation dosimetry plan.

In these veins, we handle our modelling approach to investigate the dose-efficacy relationship with dose escalation to suggest the optimal total dosage while reducing treatment-induced toxicity; specifically, our aim is to explore how a different prescription of radiation in regions characterised by higher hypoxia may or may not affect the success of treatment. To do this, we compare our previous results with two additional radiotherapy protocols that differ from the previous one in terms of the total radiation dose administered; in particular, we study the effect of a lower and a higher dosage compared to the previous case (46 total Gy and 74 total Gy vs. 60 Gy, respectively) while maintaining once-daily administration from Monday to Friday for 6 weeks. Fig. 4.4 shows a representative indication of the differences in efficacy for the three different scenarios in relation to tumour microenvironment oxygenation and epigenetic composition of the mass.

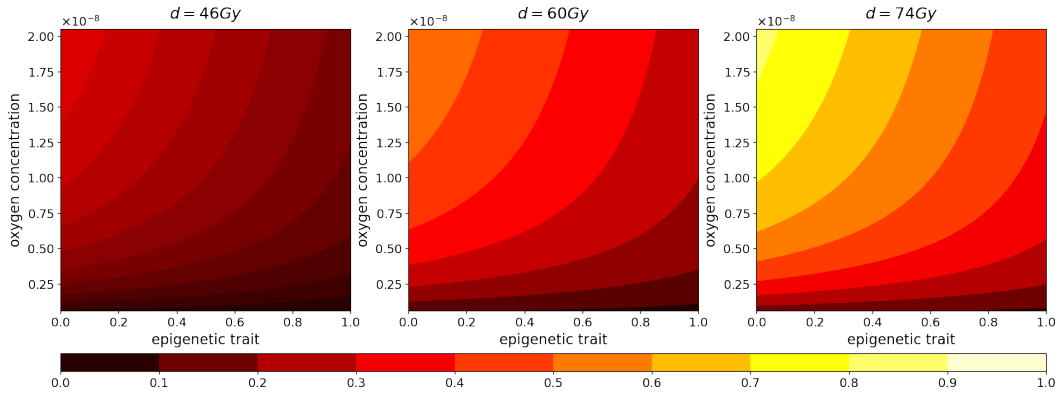

Fig. 4.4 Normalised radiotherapy effectiveness depending on the epigenetic trait (x-axis) and oxygen density (y-axis) in the cases of a total dose of 46, 60, 74 Gy. Caption and Figure from Ref. [111].

The results of the experiment in terms of *repopulation*, *reoxygenation*, and *radiosensitivity* are shown in Fig. 4.5: the first row (FV) refers to the case of high oxygenation, while the second row (HV) refers to the case of low oxygenation. The colour code indicates that lighter colours correspond to higher total doses. As we can see in both cases, the effectiveness of the treatment is strictly dependent on the dose administered. In fact, higher doses correspond to smaller portions of the tumour that can survive, although, as previously mentioned, it is observed that, at the same dosage, radiation therapy is less efficient in the case of low oxygenation compared to panels (A-FV) and (A-HV) of Fig. 4.5.

Regarding *reoxygenation* phenomenon, both panels (B-FV) and (B-HV) of Fig. 4.5 reveal that, in both low and high hypoxia case, the higher the dosage, the more effective is the tissue *reoxygenation*. In the case of high oxygenated tissues, the epigenetic composition that characterises a mass under this condition, shown in panel (D) of Fig. 4.1, is mainly composed by proliferating cells at the time of treatment administration; therefore, as expected, a lower dosage of radiotherapy implies a lower percentage of destruction of highly sensitive cells. Comparing the two cases with different oxygenation (FV) and (HV), the different speeds at which the tissue reoxygenates in all three tested dosages are consistent with the selection phenomenon mentioned above. We indeed expect that, as indicated by the radiosensitivity index and by the average epigenetic composition in the case of low oxygenation (shown in plots (C-FV) and (C-HV) of Fig. 4.5, there will be a

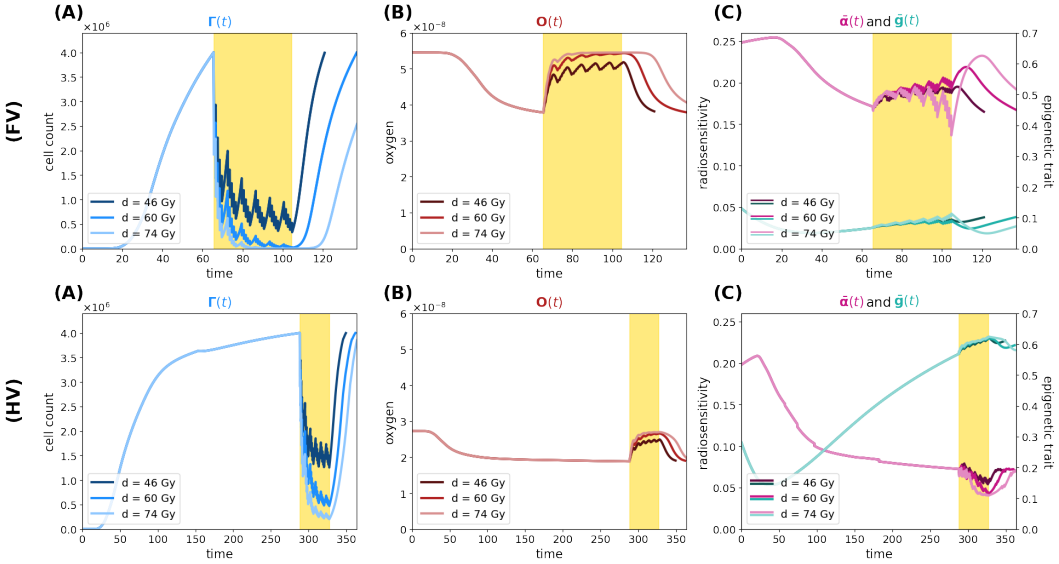

Fig. 4.5 Simulation of tumour mass, growing starting from the centre of the domain, with oxygen provided by the full vessel layout Υ^{FV} (first row) and half vessel layout Υ^{HV} (second row). In each row, plot descriptions follow Figure4.1 caption. Different colours depict experiments in which different total amounts of radiation are used (46, 60 and 74 Gy as indicated in legends). Caption and Figure from Ref. [111].

smaller portion of radiosensitive cells, therefore a smaller portion of cells killed and consequently a slower reoxygenation, due to higher oxygen consumption.

The dynamics revealed by the model in terms of *radiosensitivity* and epigenetic composition of the mass, as a function of the dose amount, are interesting from a therapeutic point of view. Indeed, looking at the results shown in panel (C) of Fig. 4.5, in the presence of high oxygenation, it is strongly visible how radiotherapy acts as an evolutionary bottleneck: the higher the selective pressure exerted by its administration (higher dosage corresponds to higher selective pressure), the more the mass is pushed to develop radio-resistance, even in the presence of complete *reoxygenation*. In fact, at the highest radiation dosage, a more marked epigenetic shift (light blue curve) and a more rapid decrease in the radiosensitivity of the mass (pink curve) are observed, panel (C) of Fig. 4.3. In particular, the latter profile reveals how, under oxygenation conditions that do not strongly affect the effectiveness of therapy, the heterogeneity of the mass plays a crucial role in the development of treatment resistance. It is indeed observed how the selection of progressively more resistant epigenetic traits leads to a drastic and increasingly evident decrease in radiosensitivity as the treatment is iteratively applied.

In the same veins, the dynamics observed in the case of low oxygenation are even more interesting in terms of *dose painting*. As we can indeed see, the selective pressure exerted by the treatment is less evident; in fact, variations of lower intensity with respect to the previous case are observed as the dosage increases in terms of both radiosensitivity and epigenetic firmness (pink and light blue curve, respectively of panels (C-FV) and (C-HV) of Fig. 4.3). This is particularly fascinating in terms of potentially heterogeneous radiation delivery; the predictions reveal, indeed, a greater reduction in mass for higher doses but, at the same time, not an equally large variation in terms of composition and radiosensitivity compared to those observed at lower doses. This supports the idea of targeting hypoxic areas with higher doses since no stronger selection with respect to treatment resistance is observed. In this view, we hypothesise that the sensibility of the model in describing these dynamics potentially lays the groundwork to investigate, via this modelling approach, different administration scenarios in the case of, for example, innovative techniques as Stereotactic Body Radiation Therapy (SBRT) in which a small number of high doses of radiation are delivered to a target volume using highly accurate equipment in order to maximise cancer control, while minimising side effects on healthy tissues, see, e.g. [292].

4.3.4 Heterogeneous vasculature

In this last experiment, we focus on a heterogeneous vasculature, considering three blood vessels in the υ^{3V} configuration. With such a blood vessels layout, the most oxygenated areas are concentrated at the ends of the domain antibisector, leaving a condition of low oxygenation between them and along the bisector (see plots (D) of Fig. 4.6 where the optimal oxygenation areas are outlined). Thus, keeping the starting point of the tumour unchanged at the centre of the domain, the optimal trait, determined by the initial condition of the oxygen, is in the high epigenetic band. Consequently, our tumour is initially characterised by a low reproductive rate and a high resistance; thus, at the beginning of the simulation, the average epigenetic trait is very high, see plot (C) of Fig. 4.6. Then, in the first phase, there is a slow decrease due to the fact that the tumour remains in areas where the low oxygenation selects high epigenetic traits and slows down cell reproduction. However, when the tumour reaches areas of high oxygenation, the selection of low epigenetic traits leads to a clear decrease in the medium epigenetic trait. This dynamic is confirmed (in

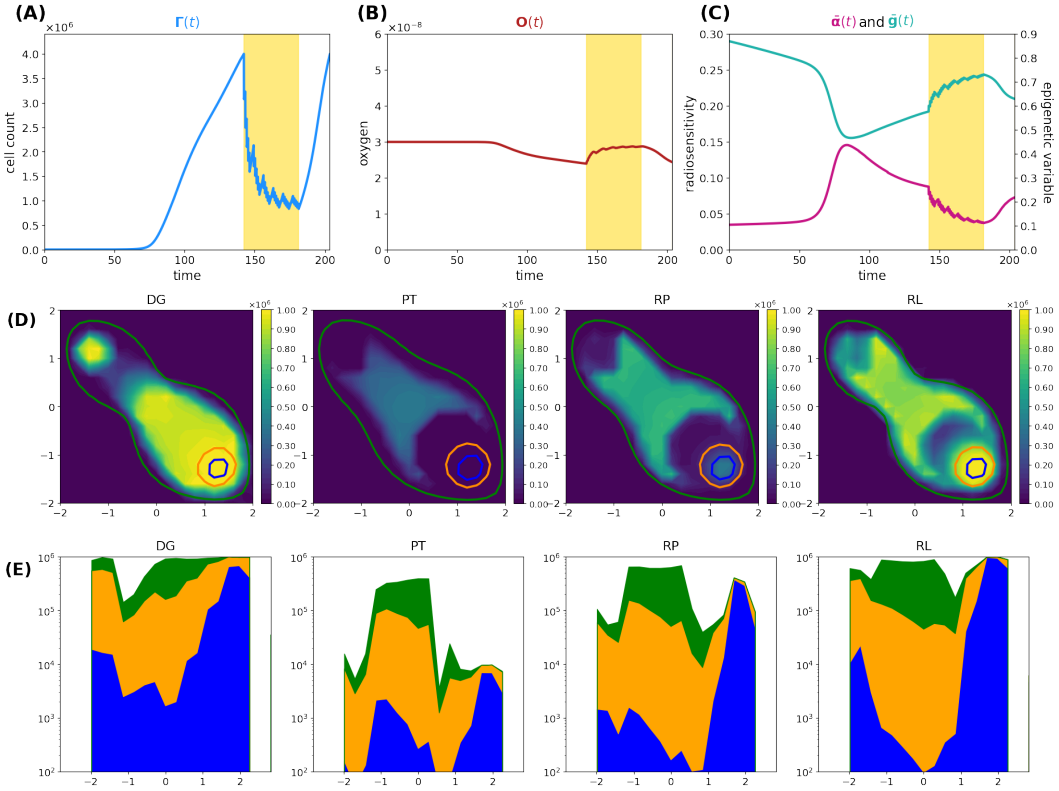

Fig. 4.6 Simulation of tumour mass, growing from the centre of the domain, with oxygen provided by the three vessel layout Υ^{3V}. Plot description as in caption of Fig. 4.1. Caption and Figure from Ref. [111].

the same plot) by the fact that this steep descent corresponds to a rapid increase in the mean radiosensitivity. The small decrease in tumour oxygenation due to consumption, plot (B) of Fig. 4.6, has little impact compared to the clear change in the average epigenetic trait due to the higher oxygenation of the local environmental conditions. Consistently, plot (A) of Fig. 4.6 shows a slow initial growth of the population size. Then, when therapy is applied, despite an initial high mortality rate due to radiotherapy, its effectiveness decreases significantly in the second phase of administration, see plot (A) of Fig. 4.6. On the one hand, in this experiment, the total oxygen level has no significant variations, and reoxygenation fails to substantially influence and enhance the outcome of the therapy. On the contrary, the low level of oxygenation in the central area of the domain maintains an important effect both of direct reduction of the therapeutic efficacy in this area and of selection of treatment-resistant epigenetic traits, plot (D)-PR of Fig. 4.6. Thus, therapy speeds up and assists the same dynamic that occurs due to environmental selection.

Analysing the temporal phases of each epigenetic band, plots (D) and (E) of Fig. 4.6, it is clear how the overlap of selective dynamics and therapy can modify the conformation of the tumour mass. In fact, comparing the first and last image, which refer to the moment of diagnosis (DG column) and to the moment of relapse (RP column), while The tumour is the same size in terms of numerosity, but it shows many differences from the point of view of the shape and of the composition. Indeed, in the first phase (until diagnosis time), the high epigenetic band has the selective fitness advantage (except the area in the lower right corner), but it suffers from the proliferative dominance of lower epigenetic signatures. During therapy, the overlap of therapeutic resistance and environmental selection gives the high epigenetic band an advantage, which is largely maintained in the *repopulation* phase, with the only exception of the lower right corner, where the fitness of the low epigenetic band promotes an accumulation of highly proliferative cells, plot (E)-RP of Fig. 4.6. When the relapse occurs, from an epigenetic composition point of view, Low epigenetic band cells maintained their unaltered ratio with respect to the total mass near the corner but were almost absent at the centre of the domain, which is different from the previous times.

The above results highlight how a heterogeneous vasculature may lead to profound differences between the epigenetic composition of the tumour and its geometric characterisation at the time of diagnosis and relapse. In conclusion, this experiment therefore shows the deep impact of therapy on the environment and on the characteristics of the tumour, and it highlights, even more than the previous experiments, the potential of the model as a basis for therapeutic optimisation strategies based on knowledge and predictive ability of the development of the mass.

4.4 Conclusions and future perspectives

In this work, we presented a mathematical approach to explore how low oxygen levels and hypoxia-associated tumour cell adaptions affect radiotherapy efficiency in the specific case of solid tumours. Specifically, we compared the effect of tumour microenvironment in the case of efficient or inefficient tumour vasculature, evaluating (*i*) how it can influence the heterogeneity in terms of proliferative potential of tumour cells and (*ii*) how its evolution could strongly influence the treatment success. The rationale of the work was (*i*) to identify the tumour regions composed of cells with

low proliferative rates that are intrinsically more resistant to radiotherapy action, (*ii*) to study the consequences of the treatment in influencing their geometrical characterisation and (*iii*) to investigate if and how they can be potentially separately treated to maximise the tumour response, in a *dose painting* perspective [206].

The results show how the proposed approach is, first of all, able to reproduce the biological effect of irradiation as the result of both the total dose delivered and the physiological conditions in which it is applied. Moreover, the findings support the ability of the model to show specific eco-evolutionary features of different tumour masses, making predictions based on conditions that can widely range between patients. Specifically, our tool suggests how three of the 6*R* that characterize tumour response after radiotherapy administration, *repopulation*, *reoxygenation* and *radiosensitivity*, could display different dynamics in dependence on tumour oxygenation and the consequent distinct tumour-host interaction [376]. In summary, the model keeps two relevant dynamics from a clinical point of view. Firstly, coherently with the clinically observed inter-patient variability in terms of therapy response, the nominal tumour size alone is insufficient to predict growth dynamics and personalised indices are needed to define an efficient therapeutic plan. In this respect, the model results suggest that two patients that present a similar tumour volume could have a distinct tumour–host co-evolution history, which results in different responses to the same radiotherapy protocol [363]. In this respect, in the two cases analysed, the in-time evolution of the radiosensitivity of the mass is significantly distinct, guided by both the different radio-induced reoxygenation and epigenetic composition. Our predictions show indeed that, in the case of high oxygenation, *reoxygenation* is sufficient to prompt the mass towards a higher sensibility to the treatment; on the contrary, in the case of low oxygenation, a degenerating dynamics towards a more resistant mass can be observed, even in the presence of a higher quantity of available oxygen, highlighting the central role of epigenetic heterogeneity in tumour therapy response. Secondly, to maximise the effect of the treatment in terms of a balance between the portion killed and the selective bottleneck induced, the choice of dose administration turns out to be necessary in relation to tumour oxygenation. The model results suggest indeed that, under oxygenation conditions that do not strongly affect the effectiveness of therapy, the heterogeneity of the mass plays a crucial role in the development of treatment resistance; at the highest radiation dosage, a marked epigenetic shift towards resistant epigenetic traits and a rapid decrease in the radiosensitivity of the mass are indeed observed. On the

contrary, in strongly hypoxic conditions, the predictions reveal a greater reduction in mass for higher doses but, at the same time, not an equally large variation in terms of composition and radiosensitivity compared to those observed at lower doses, supporting the idea of *dose painting*, which consists in delivery selective boosting dose to radio-resistant (in this specific case hypoxic) regions.

Supported by the results, we speculate that the sensibility of the model in catching these dynamics potentially paves the way to investigate, via this modelling approach, different administration scenarios in the case of, for example, innovative techniques such as Stereotactic Body Radiation Therapy (SBRT) in which a small number of high doses of radiation are delivered to a target volume using highly accurate equipment in order to maximise cancer control [206]. As natural evolution, future studies will focus on the model outcomes varying the total dosage, the target regions but additionally the fractionation scheme. There is indeed biological evidence that alternative radiation fractionation protocols sometimes improve the outcome while worsening in other cases; altered schemes, such as hyperfractionation, accelerated fractionation and hypofractionation, have been suggested as alternatives for certain indications [277, 427]. This, in addition to the results already shown, potentially allows us to exploit our tool to investigate possible therapeutic strategies to optimise the radiotherapy outcome in light of the epigenetic and geometric inhomogeneities, considering the inter-patient variability experimentally observed.

Chapter 5

Novel heterogeneity-based hybrid modelling approach for EMT in tumours

5.1 Introduction

Tumour masses are only an example of a vast set of biological systems composed of cells that are heterogeneous for genotype and phenotype. This heterogeneity is usually a time-evolving phenomenon which depends on the response to internal or external stimuli. As stated in Chapter 2, a variety of modelling strategies exists, and the need to represent a specific biological process make it necessary the choice and development of specific mathematical structures in order to optimise the quality of the description. The aim of this chapter is to introduce a modelling setting in which cells have a distinct mathematical description according to their genotype and phenotype so that their dynamics can be affected by both.

To do that, it is important to clarify the biological understanding of the concept of genotype and phenotype. Genotype can be considered as the determinant for cell potential, like a code that determines what a cell can do. Phenotype, on the other hand, can be seen as the actual behaviour of the cell in the range of its possibility according to its genotype. In this light, we can think of making the following assumption.

- Cells can have different behaviour, and every behaviour has an optimal mathematical representation.
- The behaviour is induced by external pressure.
- Within the same behaviour, the cell performance is regulated by its potential.

In order to take these aspects into account, we here propose a modelling framework in which a specific mathematical representation (i.e., individual/pointwise vs. collective/density-based) is assigned to each individual based on its phenotypic hallmarks, while a discrete structuring variable distinguishes cells according to their genotype. In order to reproduce phenotypic plasticity, switches between mathematical representations have to be made possible. The spatial distribution of the mass of a single cell is provided via the definition of a bubble function. The role played by stochasticity and environmental conditions is included as a driver for these phenotypic (and thus modelling) transitions. The proposed modelling environment is then enriched with the inclusion of further cell behaviour, such as migratory dynamics and duplication/apoptotic processes, as well as with chemical kinetics.
After having set this resulting multi-scale hybrid approach in a generic biological context, we pass to a direct application to the scenario of a heterogeneous tumour aggregate cultured *in vitro*. More in detail, we use this formulation to catch the reversible transition between epithelial and mesenchymal phenotype. Contents of this chapter are published in Ref. [110].

5.2 The modelling strategy

We propose a theoretical and computational approach to characterise cells both at the genotypic and phenotypic levels. A discrete trait variable structures the cell population based on individual genetic makeup, where each value corresponds to a specific gene sequence. A mathematical representation is employed to distinguish cells by their phenotype or effective behaviour, utilizing either a discrete or continuous approach, depending on the phenotype's nature. Cells with a specific phenotype are represented by a set of particles, while a continuous density function depicts those with an alternative phenotype.

The connection between a cell phenotype and its mathematical representation is established based on plausible biological reasoning. A pointwise description is

deemed more fitting for specialised, activated, highly metabolic cells or those with mesenchymal characteristics, displaying individual directional movement in response to environmental cues. Conversely, a density-based representation, offering lower individual detail, is better suited for non-specialised, quiescent, poorly metabolic cell ensembles or those with epithelial characteristics, engaging in collective dynamics primarily guided by intercellular communication. See that, even if it could seem counterintuitive, proliferative dynamics usually characterise epithelial cells, but these do not need individual precision, so a continuous modelling approach, in which divisions can be caught as a cell density increases, is suitable.

In our model, the “discrete vs. continuous" dichotomy is not referred to the spatial scale at which the system is modeled (i.e., “microscopic vs. macroscopic”) as in the classical approaches introduced in Chapter 2; rather it is employed to differentiate cell behavior.
As previously introduced, the transition between mathematical formulations is made possible by defining a bubble function that represents a plausible spatial distribution of the mass of a single individual. This strategy was firstly proposed in Ref. [122, 392] and can be considered as the mathematical mean to allow the representation of phenotypic plasticity, defined as the genotype-independent ability of cells to switch back and forth among multiple phenotypes [229]. Specifically, we posit that environmental signals, contingent on cell genetic traits and subject to randomness, instigate phenotypic conversions. The incorporation of this stochastic element constitutes a notable departure from prior works [122, 392]. While some models acknowledge the potential for cells to undergo phenotype evolution, as seen in individual-based/cellular automata models like the Cellular Potts Model [393], our approach introduces a distinctive feature: the discrete setting governs cell dynamics, and variations in mathematical representation accompany phenotypic changes.

Other methods employ a hybrid approach, utilizing discrete populations to describe distinct phenotypes Ref. [30]. However, in contrast to our modelling strategy, they employ a discrete setting for cell dynamics and a continuous description for microenvironmental dynamics, such as oxygen or the extracellular matrix; these models rely on a discrete setting for all cell dynamics.

Continuous cell description models, within the framework of the Theory of Mixtures, often associate each subpopulation with a distinct density function. Phenotypic conversions are implemented through mass-exchanging terms in the evolution equa-

tions for cell dynamics, as demonstrated in Ref. [199, 448]. For a comprehensive review of mathematical approaches addressing cell plasticity in tumour growth, we direct readers to [446].

Structured population models, where the trait variable pertains to behavioural determinants rather than cell genotype, often introduce random phenotypic transitions through a diffusion term on the trait domain, as exemplified in[175, 300, 301]. Nevertheless, these transitions do not entail variations in the mathematical representation of cells, a novel aspect introduced in the previously cited works [122, 392], and extended in our model to include genetic traits and probabilistic elements. Our model is further enhanced with cell migratory and growth dynamics, contingent on cell genotype and phenotype.

5.3 Applicative potential of the model

The presented modelling approach adeptly captures and depicts the genetic and phenotypic diversity within a given cell system, along with key mechanisms governing phenotypic adaptability. Its versatility allows for a broad range of applications, as the dynamics of cell aggregates, ranging from small clusters to large populations, are inherently shaped by cooperative interactions among individuals with variations both at the DNA and protein levels.

For instance, in collective cell movement scenarios, a minority of specialised individuals capable of sensing environmental chemical signals often act as guiding entities for the entire system. In contrast, the remaining components displace passively due to adhesion forces, as seen in processes like angiogenesis [232, 263]. In angiogenesis, a small subset of endothelial cells within pre-existing vessels adopts a leader/tip phenotype, serving as migratory cues for neighbouring cells exhibiting a follower/stalk behaviour [64]. We recall tha these mechanisms are initiated by diffusing growth factors (e.g., vascular endothelial growth factor - VEGF, hepatocyte growth factors - HGF) and are mediated through well-established Delta-Notch signalling pathways [291, 447].

Likewise, in the process of skin healing following an injury, the cells situated at the leading edge of the epidermal monolayers invading the wounded area exhibit actin-rich lamellipodia and pseudopodia, facilitating active movement. These cells

can synthesise a new basement membrane. In contrast, individuals located at the rear regions undergo passive displacement, primarily driven by cell-cell adhesive interactions.

Cell heterogeneity is evident in pathological conditions, such as tumour growth. Varied gene sequences and phenotypic determinants have been identified in individuals with various diseases, including breast cancer [9], colorectal cancer [343], brain cancer [406], and prostate cancer [120]. Intriguingly, even within the same tumour mass, malignant cells with identical genetic alterations exhibit diverse behaviours [313]. Cancer cells demonstrate the ability to transition between alternative phenotypic states either spontaneously or in response to environmental cues. For instance, under nutrient deprivation, malignant cells activate pathways leading to a shift toward more aggressive behaviour. During this epithelial-to-mesenchymal transition, cells lose epithelial traits, such as high adhesiveness and duplication capacity, and acquire mesenchymal features, including enhanced motility, enabling more effective tissue invasion. EMT is not limited to pathological scenarios; it is also involved in physiological processes such as morphogenesis and organogenesis. Conversely, tumour cells with mesenchymal characteristics can revert to an epithelial state, expressing junctional proteins, in response to sufficient environmental substrates [337]. Phenotypic differentiation and conversions among genetically identical tumour cells contribute to disease survival, adaptation to therapeutic regimes, and subsequent genetic evolution [382, 433, 73, 324].

5.4 Proposed approach and representative simulation

We are interested in modelling the evolution of an aggregate of cells in a time range $T = [0, t_F] \subset \mathbb{R}_0^+$ (we denote t the time variable). We consider a closed two-dimensional domain $D \subset \mathbb{R}^2$ that may reproduce a planar section of an *in vivo* tissue or the surface of a *Petri dish*. Characterisation of the space setting can be given when inserting the relative specific dynamics.

Fig. 5.1 (A) sketches the differentiation of the cells composing the system according to the two previously introduced determinants:

- their *genotype*, by the use of a *discrete trait variable u*;
- their *phenotype*, by the use of different *mathematical representations*.

Our approach operates under the assumption that there is not a deterministic or necessary connection between a cell's genetic traits and its phenotype. The phenotype is determined at the protein level, influenced by effective gene transcription and expression levels, which can be subject to stochasticity and external stimuli or conditions (referred to as the surrounding *ecology*).

The variable u is designed to take on a specified number of values, denoted as K, meaning $u \in U = u_k{}^K k = 1$. In this context, the particular state $u_{\hat{k}}$ represents the cell clone identified by the $\hat{k}$-th genetic composition, i.e., the $\hat{k}$-th gene sequence.

We then consider two distinct cell phenotypes, labelled as "A" and "B", and assign each of them to a unique mathematical representation, as proposed in Ref. [122, 392]. Specifically, for a given cell variant with genotypic trait $u_{\hat{k}} \in U$, individuals exhibiting phenotype A are characterised by a *discrete* representation: they are represented as dimensionless points with concentrated unitary mass and are identified by their specific spatial position (refer to panel (A) in Fig. 5.1). This subgroup of agents can be gathered in the following set:

$$\boldsymbol{X}^{\mathrm{A}}_{u_{\hat{k}}}(t) = \left\{ \boldsymbol{x}_{1,u_{\hat{k}}}(t), \ldots, \boldsymbol{x}_{N^{\mathrm{A}}_{u_{\hat{k}}}(t),u_{\hat{k}}}(t) \right\}, \tag{5.4.1}$$

with $\boldsymbol{x}i, u_{\hat{k}}(t) \in D$, where $i = 1, ..., N^{\mathrm{A}}u_{\hat{k}}(t)$, and $N^{\mathrm{A}}u_{\hat{k}}(t)$ represents the number of cells with phenotype A and genotype $u_{\hat{k}}$ at time t. The total count of individuals with phenotype A within the entire population can be calculated as

$$N^{\mathrm{A}}(t) = \sum_{k=1}^{K} N^{\mathrm{A}}_{u_k}(t). \tag{5.4.2}$$

The rest of the cell clone with the $\hat{k}$-th genetic trait is instead marked by phenotype B and is *collectively* represented by the number density function $a^{\mathrm{B}}(t, \boldsymbol{y}, u_{\hat{k}}) : T \times D \times U \mapsto \mathbb{R}^+_0$ (depicted in Fig. 5.1 (A)). The local count of individuals with phenotype B can then be determined as

$$\rho^{\mathrm{B}}(t, \boldsymbol{y}) = \sum_{k=1}^{K} a^{\mathrm{B}}(t, \boldsymbol{y}, u_k). \tag{5.4.3}$$

In this context, $a^{\mathrm{B}}(t, \boldsymbol{y}, \cdot)$ can be understood as the local distribution of cells with phenotype B in the genotype space U. The total number of agents with phenotype B

currently within the entire domain D can be approximated by integrating ρ^{B} across the spatial variable and rounding down the obtained value:

$$N^{\mathrm{B}}(t) = \left\lfloor \int_D \rho^{\mathrm{B}}(t,\boldsymbol{y})\,\mathrm{d}\boldsymbol{y} \right\rfloor. \tag{5.4.4}$$

The total number of cells composing the aggregate at any given time t is given by $N(t) = N^{\mathrm{A}}(t) + N^{\mathrm{B}}(t)$.

For the sake of completeness, some remarks must be provided on the above-proposed modelling framework:

- The correspondence between various cell genetic make-ups and the respective values of the variable u is arbitrary.
- The correlation between a cell phenotype and its corresponding mathematical representation is guided by biological considerations, as detailed before.
- In theory, our approach has the potential to incorporate more than two cell phenotypes. This extension would necessitate the use of hybrid mathematical representations capable of combining microscopic granularity within a macroscopic/continuous portrayal of the system. Such an incorporation could be achieved, for example, by employing tools from Measure Theory [123, 121].
- The proposed modelling framework is currently hybrid but not multi-scale. This indicates that different mathematical entities (e.g., material points and number densities) coexist but represent biological elements at the same spatial scale—distinct types of cells.

Modelling cell phenotypic plasticity. In a wide range of biological phenomena, cells are able to change phenotype while maintaining their genetic makeup, i.e., to vary the expression level of one or more of their genes. To reproduce this phenomenon in our modelling framework, we need to set up a procedure to switch between the two cell descriptive instances. It is indeed necessary to define a proper correspondence between the pointwise and the density-based representation of a single cell. In this respect, we use the approach of Ref. [122, 392] and we introduce a function $\varphi_{\boldsymbol{x}}(\boldsymbol{y}) : D \times D \mapsto \mathbb{R}_0^+$ such that:

$$\int_D \varphi_{\boldsymbol{x}}(\boldsymbol{y})\,\mathrm{d}\boldsymbol{y} = 1. \tag{5.4.5}$$

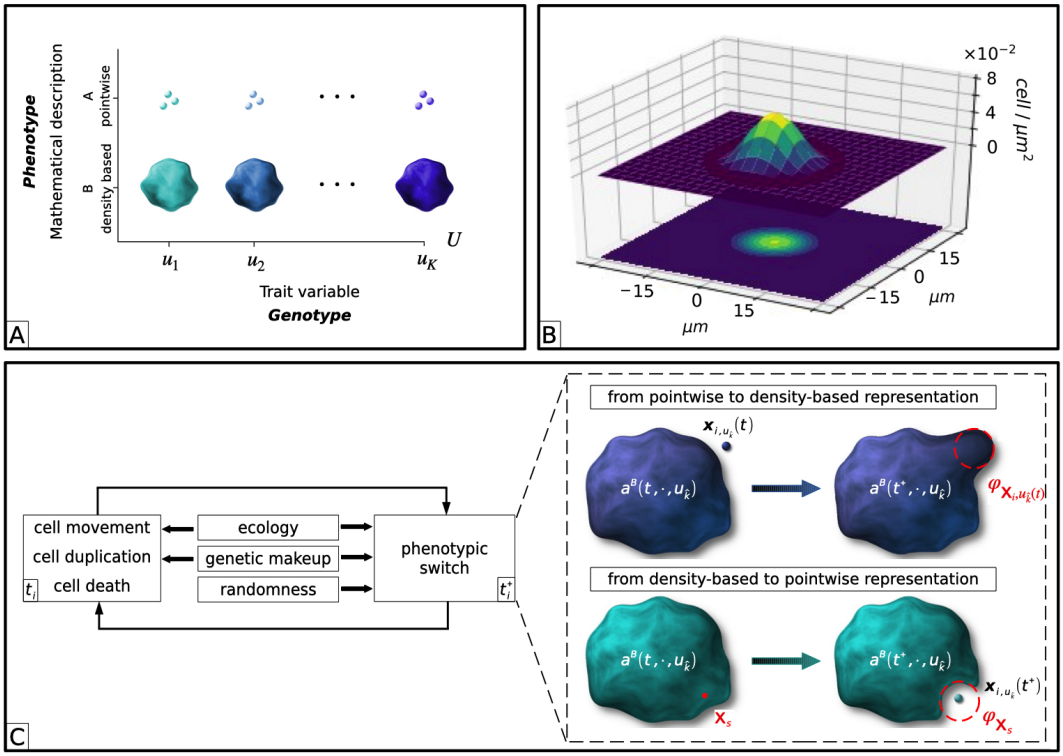

Fig. 5.1 (A) In our modelling environment, each cell is characterised by a discrete structuring variable $u \in U$, catching its genotype, and by a specific mathematical representation determined by its phenotype. In particular, we only consider two alternative individual phenotypes, which are set to correspond either to a pointwise or to a density-based descriptive instance. (B) For representative purposes, 2-dimensional and 3-dimensional plots of the bubble function centred in $\boldsymbol{x} = (0,0)$, i.e., $\varphi_{(0,0)}$ (cf. Equation ((5.4.6))). We recall that the radius r of the round support of φ is constantly taken equal to 15 μm. (C) We here set that cell dynamics such as growth, migration, and phenotypic switches are affected both by individual genetic trait and by variations in environmental (i.e., ecological) conditions. Stochasticity plays a role as well. In particular, A-to-B phenotypic transition of the generic cell i with genotype $u_{\hat{k}}$ is implemented by the removal of the material point located in $\boldsymbol{x}_{i,u_{\hat{k}}}$ and the simultaneous addition of the corresponding bubble function $\varphi_{\boldsymbol{x}_{i,u_{\hat{k}}}}$ to the mass distribution $a^{\mathrm{B}}(\cdot,\cdot,u_{\hat{k}})$. Conversely, a B-to-A phenotypic switch, stimulated in the domain point $\boldsymbol{x}_{\mathrm{s}}$ and involving the cell variant with genotype $u_{\hat{k}}$, amounts in the local creation of a new material point $\boldsymbol{x}_{N^{\mathrm{A}}_{u_{\hat{k}}}(t)+1,u_{\hat{k}}}$ and in the simultaneous removal of the bubble function $\varphi_{\boldsymbol{x}_{\mathrm{s}}}$ to the mass distribution $a^{\mathrm{B}}(\cdot,\cdot,u_{\hat{k}})$.

$\varphi_{\boldsymbol{x}}$ approximates the spatial distribution of a cell whose centre is located in $\boldsymbol{x} \in D$. In principle, there exist several possible options to explicit $\varphi_{\boldsymbol{x}}(\boldsymbol{y})$. However, in accordance with Ref. [122, 392], we hereafter use the following *bubble* function,

which assumes a greater amount of cell mass around $\boldsymbol{x}$, as shown in Fig. 5.1 (B):

$$\varphi_{\boldsymbol{x}}(\boldsymbol{y}) = \begin{cases} \dfrac{4}{\pi r^8}(r^2 - |\boldsymbol{y}-\boldsymbol{x}|^2)^3, & \text{if } |\boldsymbol{y}-\boldsymbol{x}| \leq r; \\ 0, & \text{otherwise.} \end{cases} \tag{5.4.6}$$

In Equation ((5.4.6)), $|\cdot|$ identifies the Euclidean norm while r is set to approximate a mean cell radius: hereafter, it will have a value of 15 μm.

Let us now assume that, at a certain time t, the i-th cell with phenotype A and genotype $u_{\hat{k}} \in U$ undergoes a transition to phenotype B. From a biological perspective, this may be the result of environmental stimuli (triggered by chemical signals or by intercellular communication) or of the fact that the individual i is able to maintain phenotype A only for a limited period of time (e.g., due to high metabolic costs). The proposed A-to-B phenotypic switch can be then implemented in our modelling framework by removing the material point located in $\boldsymbol{x}_{i,u_{\hat{k}}}(t)$ and by simultaneously adding the equivalent mass function $\varphi_{\boldsymbol{x}_{i,u_{\hat{k}}}(t)}$ to the density of the cell variant characterised by the same trait $u_{\hat{k}}$, as shown in Fig. 5.1 (C). In mathematical terms, we indeed get the following relations:

$$\begin{cases} \boldsymbol{X}^{\mathrm{A}}_{u_{\hat{k}}}(t^+) = \boldsymbol{X}^{\mathrm{A}}_{u_{\hat{k}}}(t) \setminus \{\boldsymbol{x}_{i,u_{\hat{k}}}(t)\}; \\ \boldsymbol{X}^{\mathrm{A}}_{u_k}(t^+) = \boldsymbol{X}^{\mathrm{A}}_{u_k}(t), \quad \text{for all } k \neq \hat{k}; \\ a^{\mathrm{B}}(t^+, \boldsymbol{y}, u_{\hat{k}}) = a^{\mathrm{B}}(t, \boldsymbol{y}, u_{\hat{k}}) + \varphi_{\boldsymbol{x}_{i,u_{\hat{k}}}(t)}(\boldsymbol{y}), \quad \text{for all } \boldsymbol{y} \in D; \\ a^{\mathrm{B}}(t^+, \boldsymbol{y}, u_k) = a^{\mathrm{B}}(t, \boldsymbol{y}, u_k), \quad \text{for all } k \neq \hat{k}; \ \text{ and } \ \boldsymbol{y} \in D. \end{cases} \tag{5.4.7}$$

Finally, the remaining particles with phenotype A and genotype $u_{\hat{k}}$ are renumbered according to the rule

$$\boldsymbol{x}_{j,u_{\hat{k}}}(t^+) = \begin{cases} \boldsymbol{x}_{j,u_{\hat{k}}}(t), & \text{if } j < i; \\ \boldsymbol{x}_{j-1,u_{\hat{k}}}(t), & \text{if } j > i. \end{cases} \tag{5.4.8}$$

In Equations ((5.4.7)) and ((5.4.8)), as well as in the following, the notation t^+ is used to specify that, from a *numerical point of view*, phenotypic transitions are not simultaneously implemented with the other processes, e.g., cell movement, duplication, death, that occur at the same time instant (see also Ref. [122, 392]). The generalisa-

tion of the above procedure to more cells that actually switch from phenotype A to phenotype B, possibly with different genotypic traits, is straightforward.

Let us then conversely assume that, at time t, an environmental stimulus that is in principle able to trigger a transition from phenotype B to phenotype A in individuals with the generic genotype $u_{\hat{k}} \in U$, is active in a given domain location, say $\boldsymbol{x}_{\mathrm{s}} \in D$. Such a switch can occur only if there is a sufficient density of the cell variant of interest to have a localised agent placed in $\boldsymbol{x}_{\mathrm{s}}$. In mathematical terms, this amounts to satisfy the following local constraint:

$$a^{\mathrm{B}}(t,\boldsymbol{y},u_{\hat{k}}) \geq \varphi_{\boldsymbol{x}_{\mathrm{s}}}(\boldsymbol{y}), \quad \text{for all } \boldsymbol{y} \in D. \tag{5.4.9}$$

In this case, the cell phenotypic transition from B to A (and the corresponding representation switch) results from the removal of $\varphi_{\boldsymbol{x}_{\mathrm{s}}}$ from the distribution $a^{\mathrm{B}}(t,\cdot,u_{\hat{k}})$, accompanied by the addition of the corresponding new element to the set $\mathbf{X}^{\mathrm{A}}_{u_{\hat{k}}}$ (see panel (C) in Fig. 5.1):

$$\begin{cases} \boldsymbol{X}^{\mathrm{A}}_{u_{\hat{k}}}(t^{+}) = \boldsymbol{X}^{\mathrm{A}}_{u_{\hat{k}}}(t) \cup \{\boldsymbol{x}_{N^{\mathrm{A}}_{u_{\hat{k}}}(t)+1,u_{\hat{k}}}(t) \equiv \boldsymbol{x}_{\mathrm{s}}\}; \\ \boldsymbol{X}^{\mathrm{A}}_{u_k}(t^{+}) = \boldsymbol{X}^{\mathrm{A}}_{u_k}(t), \quad \text{for all } k \neq \hat{k}; \\ a^{\mathrm{B}}(t^{+},\boldsymbol{y},u_{\hat{k}}) = a^{\mathrm{B}}(t,\boldsymbol{y},u_{\hat{k}}) - \varphi_{\boldsymbol{x}_{\mathrm{s}}(t)}(\boldsymbol{y}), \quad \text{for all } \boldsymbol{y} \in D; \\ a^{\mathrm{B}}(t^{+},\boldsymbol{y},u_k) = a^{\mathrm{B}}(t,\boldsymbol{y},u_k), \quad \text{for all } k \neq \hat{k} \text{ and } \boldsymbol{y} \in D. \end{cases} \tag{5.4.10}$$

Furthermore, the following rules are set:

- in the case of B-to-A phenotypic transitions involving the same cell clone, e.g., with genotype $u_{\hat{k}}$, and simultaneously stimulated in two distinct domain points $\boldsymbol{x}_{\mathrm{s}1}$ and $\boldsymbol{x}_{\mathrm{s}2}$ such that $\varphi_{\boldsymbol{x}_{\mathrm{s}1}}$ and $\varphi_{\boldsymbol{x}_{\mathrm{s}2}}$ overlap, two alternative options are accounted for: (i) if $a^{\mathrm{B}}(t,\boldsymbol{y},u_{\hat{k}}) \geq \varphi_{\boldsymbol{x}_{\mathrm{s}1}}(\boldsymbol{y}) + \varphi_{\boldsymbol{x}_{\mathrm{s}2}}(\boldsymbol{y})$ for any $\boldsymbol{y} \in D$, then both behavioral switches occur; (ii) if, otherwise, $a^{\mathrm{B}}(t,\boldsymbol{y},u_{\hat{k}}) \geq \varphi_{\boldsymbol{x}_{\mathrm{s}1}}(\boldsymbol{y}), \varphi_{\boldsymbol{x}_{\mathrm{s}2}}(\boldsymbol{y})$ but $a^{\mathrm{B}}(t,\boldsymbol{y},u_{\hat{k}}) < \varphi_{\boldsymbol{x}_{\mathrm{s}1}}(\boldsymbol{y}) + \varphi_{\boldsymbol{x}_{\mathrm{s}2}}(\boldsymbol{y})$ for at least one domain point, then only one transition takes place, which is randomly established. The same rule is extended in the case of more than two phenotypic transitions with analogous characteristics;
- B-to-A phenotypic transitions are not allowed in any domain point effectively occupied by a pointwise agent (regardless its genotype). Coherently, only

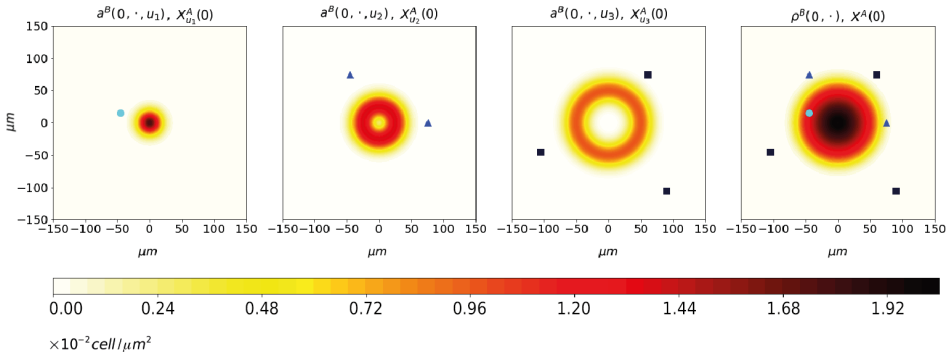

Fig. 5.2 Initial condition of the representative simulation, as specified by Equation ((5.4.11)). The subpopulation with phenotype B has a radial symmetry: in particular, the cell variant with genotype u_1 is mainly located at the bulk of the cluster, the cell variant with u_3 forms an external ring, whereas the cell variant with u_2 is distributed in the intermediate region. A group of individuals with phenotype A is then dispersed around and within the distribution of cells with phenotype B. In particular, we hereafter use light blue circles to indicate particles with phenotype A and genotype u_1, dark blue triangles to indicate particles with phenotype A and genotype u_2, and black squares to indicate particles with phenotype A and genotype u_3. Such an initial cell configuration is maintained in the case of the model application proposed in Section 5.5.

one B-to-A phenotypic switch is allowed (and arbitrarily established) at the same time in the same domain point. These constraints are consistent with the observation that, in a wide range of phenomena, a cell that activates inhibits the surrounding individuals to undergo the same process. It is the case, for instance, of the tip cell selection and lateral inhibition mechanism controlled by the Delta-Notch pathways during physio-pathological angiogenesis;

- simultaneous B-to-A phenotypic switches occurring at far enough spatial regions are instead always permitted.

It is useful to remark that the rules above are somewhat arbitrary and therefore can be in principle neglected and/or replaced by other assumptions.

Sample simulation. Before including in the proposed modelling framework more realistic biological mechanisms and dynamics, let us propose and comment a representative numerical realisation. It deals with a colony of cells which do not grow or move but only undergo arbitrarily selected phenotypic transitions. In more detail, in the spatial domain $D = [-150\ \mu\text{m}, 150\ \mu\text{m}]^2$, we place an aggregate whose component individuals can have three different genetic make-ups, i.e., $U = \{u_1, u_2, u_3\}$,

while showing the usual dycothomy in the phenotype, i.e., A and B. The initial system configuration is then given by the following distribution of cells:

$$\begin{cases} \boldsymbol{X}^{\mathrm{A}}_{u_1}(0) = \left\{ \boldsymbol{x}_{1,u_1} = (-45,15) \right\}; \\ \boldsymbol{X}^{\mathrm{A}}_{u_2}(0) = \left\{ \boldsymbol{x}_{1,u_2} = (75,0);\ \boldsymbol{x}_{2,u_2} = (-45,75) \right\}; \\ \boldsymbol{X}^{\mathrm{A}}_{u_3}(0) = \left\{ \boldsymbol{x}_{1,u_3} = (60,75);\ \boldsymbol{x}_{2,u_3} = (90,-105);\ \boldsymbol{x}_{3,u_3} = (-105,-45) \right\}; \\ a^{\mathrm{B}}(0,\boldsymbol{y},u_1) = 3.1\ m_\varphi \exp\Big(-\dfrac{|\boldsymbol{y}|^2}{325}\Big); \\ a^{\mathrm{B}}(0,\boldsymbol{y},u_2) = 2.4\ m_\varphi \exp\Big(-\dfrac{|\boldsymbol{y}-25|^2}{325}\Big); \\ a^{\mathrm{B}}(0,\boldsymbol{y},u_3) = 1.7\ m_\varphi \exp\Big(-\dfrac{|\boldsymbol{y}-50|^2}{325}\Big), \end{cases} \tag{5.4.11}$$

for all $\boldsymbol{y} \in D$, being $m_\varphi = 4/\pi r^8$ the maximum of the *bubble* function (cf. Equation ((5.4.6))), see Fig. 5.2. The overall number of cells at the onset of the simulation, which remains constant in time due to the absence of duplication/death mechanisms, amounts to:

$$\begin{aligned} N(0) &= N^{\mathrm{A}}(0) + N^{\mathrm{B}}(0) \\ &= [\boldsymbol{X}^{\mathrm{A}}_{u_1}(0)] + [\boldsymbol{X}^{\mathrm{A}}_{u_2}(0)] + [\boldsymbol{X}^{\mathrm{A}}_{u_3}(0)] + \left\lfloor \int_D \rho^{\mathrm{B}}(0,\boldsymbol{y})\,\mathrm{d}\boldsymbol{y} \right\rfloor \\ &= 6 + \left\lfloor \int_D [a^{\mathrm{B}}(0,\boldsymbol{y},u_1) + a^{\mathrm{B}}(0,\boldsymbol{y},u_2) + a^{\mathrm{B}}(0,\boldsymbol{y},u_3)]\,\mathrm{d}\boldsymbol{y} \right\rfloor = 6 + 188 = 194, \end{aligned} \tag{5.4.12}$$

where $[Q]$ indicates the cardinality of a generic set Q.

At a given time t_1, an external input able to stimulate a switch from phenotype B to phenotype A for all cell clones, regardless their genetic trait, activates in an arbitrary set of domain points, radially disposed along the main axies: $\boldsymbol{x}_{\mathrm{s}1} = (15,0)$, $\boldsymbol{x}_{\mathrm{s}2} = (50,0)$, $\boldsymbol{x}_{\mathrm{s}3} = (85,0)$, $\boldsymbol{x}_{\mathrm{s}4} = (0,15)$, $\boldsymbol{x}_{\mathrm{s}5} = (0,50)$, $\boldsymbol{x}_{\mathrm{s}6} = (0,85)$, $\boldsymbol{x}_{\mathrm{s}7} = (-15,0)$, $\boldsymbol{x}_{\mathrm{s}8} = (-50,0)$, $\boldsymbol{x}_{\mathrm{s}9} = (-85,0)$, $\boldsymbol{x}_{\mathrm{s}10} = (0,15)$, $\boldsymbol{x}_{\mathrm{s}11} = (0,-50)$, and $\boldsymbol{x}_{\mathrm{s}12} = (0,-85)$, see top panels in Fig. 5.3. In this respect:

- no transition takes place in $\boldsymbol{x}_{\mathrm{s}3}$, $\boldsymbol{x}_{\mathrm{s}6}$, $\boldsymbol{x}_{\mathrm{s}9}$, and $\boldsymbol{x}_{\mathrm{s}12}$ due to the lack of sufficient mass density of any cell genetic variant;
- in $\boldsymbol{x}_{\mathrm{s}2}$, $\boldsymbol{x}_{\mathrm{s}5}$, $\boldsymbol{x}_{\mathrm{s}8}$, $\boldsymbol{x}_{\mathrm{s}11}$, only the subpopulation with genetic trait u_3 is able to undergoes phenotypic switch, as $a^{\mathrm{B}}(0,\boldsymbol{y},u_3) \geq \varphi_{\boldsymbol{x}_{\mathrm{sj}}}(\boldsymbol{y})$ for all $\boldsymbol{y} \in D$ and

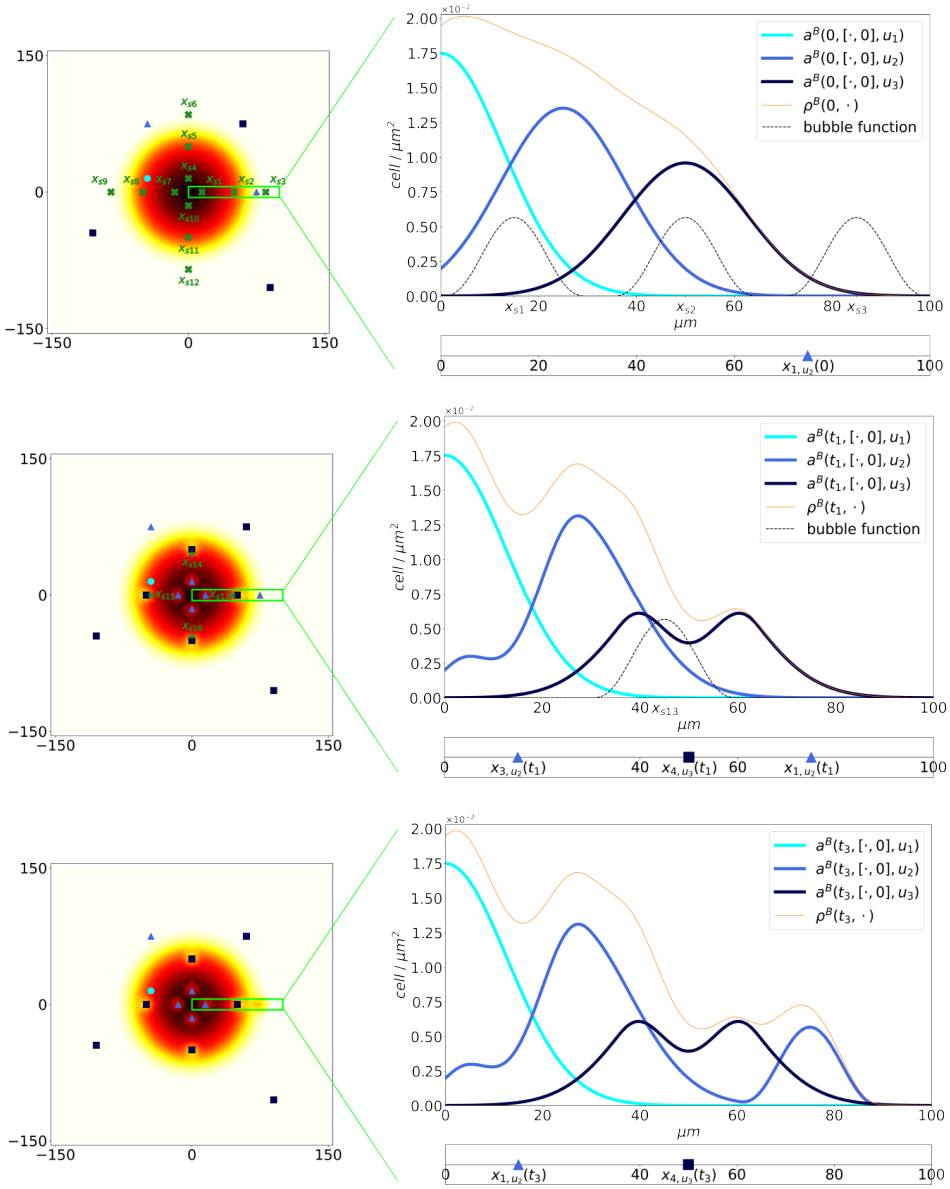

Fig. 5.3 Sample simulation showing how phenotypic switches are implemented in the proposed modelling environment. In the left panels, we represent the evolution of the entire aggregate of cells: in particular, we plot both the overall density of the subpopulation with phenotype B, i.e., ρ^B (cf. Equation ((5.4.3))), and the set of particles with phenotype A. Within this subgroup, the light blue circles identify cells with genotype u_1, the dark blue triangles identify cells with genotype u_2, and the black squares identify cells with genotype u_3. The right panels depict the dynamics of a representative section of the domain.

sj $\in$ s2, s5, s8, s11, a condition that instead is not satisfied by the distributions of the other cell genotypes;

- in $\boldsymbol{x}_{\mathrm{s}1}$, $\boldsymbol{x}_{\mathrm{s}4}$, $\boldsymbol{x}_{\mathrm{s}7}$, $\boldsymbol{x}_{\mathrm{s}10}$, both the cell clone with genotype u_1 and the cell clone with genotype u_2 have in principle enough mass to undergo a single-cell switch from phenotype B to phenotype A (i.e., $a^{\mathrm{B}}(0,\boldsymbol{y},u_1), a^{\mathrm{B}}(0,\boldsymbol{y},u_2) \geq \varphi_{\boldsymbol{x}_{\mathrm{sj}}}(\boldsymbol{y})$ for all $\boldsymbol{y} \in D$ and sj $\in$ s1, s4, s7, s10). However, as previously mentioned, only a single B-to-A phenotypic switch is allowed to occur at a given time in a given domain location: in this respect, we arbitrarily establish that in each of the four points only the genetic variant u_2 is subjected to phenotypic conversion.

The above-described dynamics are schematically visualised, in the case of a representative domain section, in the top-right graph of Fig. 5.3. The updated system configuration then reads as[1]

$$\begin{cases} \boldsymbol{X}^{\mathrm{A}}_{u_1}(t_1) = \boldsymbol{X}^{\mathrm{A}}_{u_1}(0); \\ \boldsymbol{X}^{\mathrm{A}}_{u_2}(t_1) = \boldsymbol{X}^{\mathrm{A}}_{u_2}(0) \cup \left\{ \boldsymbol{x}_{3,u_2} \equiv \boldsymbol{x}_{\mathrm{s}1}; \boldsymbol{x}_{4,u_2} \equiv \boldsymbol{x}_{\mathrm{s}4}; \boldsymbol{x}_{5,u_2} \equiv \boldsymbol{x}_{\mathrm{s}7}; \boldsymbol{x}_{6,u_2} \equiv \boldsymbol{x}_{\mathrm{s}10} \right\}; \\ \boldsymbol{X}^{\mathrm{A}}_{u_3}(t_1) = \boldsymbol{X}^{\mathrm{A}}_{u_3}(0) \cup \left\{ \boldsymbol{x}_{4,u_3} \equiv \boldsymbol{x}_{\mathrm{s}2}; \boldsymbol{x}_{5,u_3} \equiv \boldsymbol{x}_{\mathrm{s}5}; \boldsymbol{x}_{6,u_3} \equiv \boldsymbol{x}_{\mathrm{s}8}; \boldsymbol{x}_{7,u_3} \equiv \boldsymbol{x}_{\mathrm{s}11} \right\}; \\ a^{\mathrm{B}}(t_1,\boldsymbol{y},u_1) = a^{\mathrm{B}}(0,\boldsymbol{y},u_1); \\ a^{\mathrm{B}}(t_1,\boldsymbol{y},u_2) = a^{\mathrm{B}}(0,\boldsymbol{y},u_2) - \varphi_{\boldsymbol{x}_{\mathrm{s}1}}(\boldsymbol{y}) - \varphi_{\boldsymbol{x}_{\mathrm{s}4}}(\boldsymbol{y}) - \varphi_{\boldsymbol{x}_{\mathrm{s}7}}(\boldsymbol{y}) - \varphi_{\boldsymbol{x}_{\mathrm{s}10}}(\boldsymbol{y}); \\ a^{\mathrm{B}}(t_1,\boldsymbol{y},u_3) = a^{\mathrm{B}}(0,\boldsymbol{y},u_3) - \varphi_{\boldsymbol{x}_{\mathrm{s}2}}(\boldsymbol{y}) - \varphi_{\boldsymbol{x}_{\mathrm{s}5}}(\boldsymbol{y}) - \varphi_{\boldsymbol{x}_{\mathrm{s}8}}(\boldsymbol{y}) - \varphi_{\boldsymbol{x}_{\mathrm{s}11}}(\boldsymbol{y}), \end{cases} \tag{5.4.13}$$

for all $\boldsymbol{y} \in D$. We indeed have that $N(t_1) = N^{\mathrm{A}}(t_1) + N^{\mathrm{B}}(t_1) = 14 + 180 = 194 = N(0)$.

Successively, at t_2, an analogous local signal is present in the following set of points: $\boldsymbol{x}_{\mathrm{s}13} = (45,0)$, $\boldsymbol{x}_{\mathrm{s}14} = (0,45)$, $\boldsymbol{x}_{\mathrm{s}15} = (-45,0)$, and $\boldsymbol{x}_{\mathrm{s}16} = (0,-45)$, see the central panels in Fig. 5.3. In all cases, no phenotypic switch actually occurs. In fact, no cell genetic variant has a sufficient amount of mass over the support of $\varphi_{\boldsymbol{x}_{\mathrm{sj}}}$ (with j=13, 14, 15, 16) despite the overall mass of individuals with phenotype B, measured by ρ^{B} would be in principle high enough. In this respect, the system does not vary with respect to ((5.4.13)).

We finally set that at time t_3, the cell $\boldsymbol{x}_{1,u_2}$, located in (75, 0) from the beginning of the observation time, is triggered to turn back to phenotype B, as shown in the bottom panels of Fig. 5.3. The pointwise particle is indeed replaced by the corresponding

[1] *Notation remark:* since in this simulation setting cell dynamics only include phenotypic plasticity, the differentiation between t_i and t_i^+ (for $i = 1,2,3$) is not necessary and therefore avoided for the sake of simplicity.

bubble function, which is added to the mass of the proper cell genetic variant, as

$$\begin{cases} \boldsymbol{X}^{\mathrm{A}}_{u_1}(t_3) = \boldsymbol{X}^{\mathrm{A}}_{u_1}(t_2) = \boldsymbol{X}^{\mathrm{A}}_{u_1}(t_1) = \boldsymbol{X}^{\mathrm{A}}_{u_1}(0); \\ \boldsymbol{X}^{\mathrm{A}}_{u_2}(t_3) = \boldsymbol{X}^{\mathrm{A}}_{u_2}(t_2) \setminus \{\, \boldsymbol{x}_{1,u_2} \,\} = \boldsymbol{X}^{\mathrm{A}}_{u_2}(t_1) \setminus \{\, \boldsymbol{x}_{1,u_2} \,\}; \\ \boldsymbol{X}^{\mathrm{A}}_{u_3}(t_3) = \boldsymbol{X}^{\mathrm{A}}_{u_3}(t_2) = \boldsymbol{X}^{\mathrm{A}}_{u_3}(t_1); \\ a^{\mathrm{B}}(t_3, \boldsymbol{y}, u_1) = a^{\mathrm{B}}(t_2, \boldsymbol{y}, u_1) = a^{\mathrm{B}}(t_1, \boldsymbol{y}, u_1) = a^{\mathrm{B}}(0, \boldsymbol{y}, u_1); \\ a^{\mathrm{B}}(t_3, \boldsymbol{y}, u_2) = a^{\mathrm{B}}(t_2, \boldsymbol{y}, u_2) + \varphi_{\boldsymbol{x}_{1,u_2}}(\boldsymbol{y}) = a^{\mathrm{B}}(t_1, \boldsymbol{y}, u_2) + \varphi_{\boldsymbol{x}_{1,u_2}}(\boldsymbol{y}); \\ a^{\mathrm{B}}(t_3, \boldsymbol{y}, u_3) = a^{\mathrm{B}}(t_2, \boldsymbol{y}, u_3) = a^{\mathrm{B}}(t_1, \boldsymbol{y}, u_3), \end{cases} \tag{5.4.14}$$

for all $\boldsymbol{y} \in D$, so that $N(t_3) = N^{\mathrm{A}}(t_3) + N^{\mathrm{B}}(t_3) = 13 + 181 = 194 = N(0)$. For the sake of reader's convenience, we recall that the element belonging to the set $\boldsymbol{X}^{\mathrm{A}}_{u_2}$ have to be renumbered according to ((5.4.8)).

Remark. As already discussed and sketched in Fig. 5.1 (C), a cell is stimulated to undergo phenotyic plasticity by environmental signals, but the effective transition depends on its genetic makeup and on the intrinsic stochasticity of the mechanism. These aspects have not been accounted for so far, as all the proposed cell phenotypic switches have been set to actually take place (provided a sufficient cell mass in the case of B-to-A conversions). Such a model shortcoming is tackled in the next section, where more realistic rules underlying variations in cell phenotype will be given.

5.5 Model application: early dynamics of an *in vitro* tumour aggregate

We now apply the proposed model to one of the scenarios introduced in Section 5.2, i.e., the tumour growth. In particular, we hereafter show how our approach can be used to reproduce selected aspects of the early dynamics of a malignant aggregate cultured *in vitro*. In the context of our interest, the trait variable u is set to assume three values, i.e., $U = \{u_1 = 0; u_2 = 0.5; u_3 = 1\}$, each indicating a distinct sequence of genes. In this respect, the higher the value of u the more the corresponding genotype is associated to cells that in principle have high migratory potential and low proliferation capacity, see Fig. 5.4 (A).

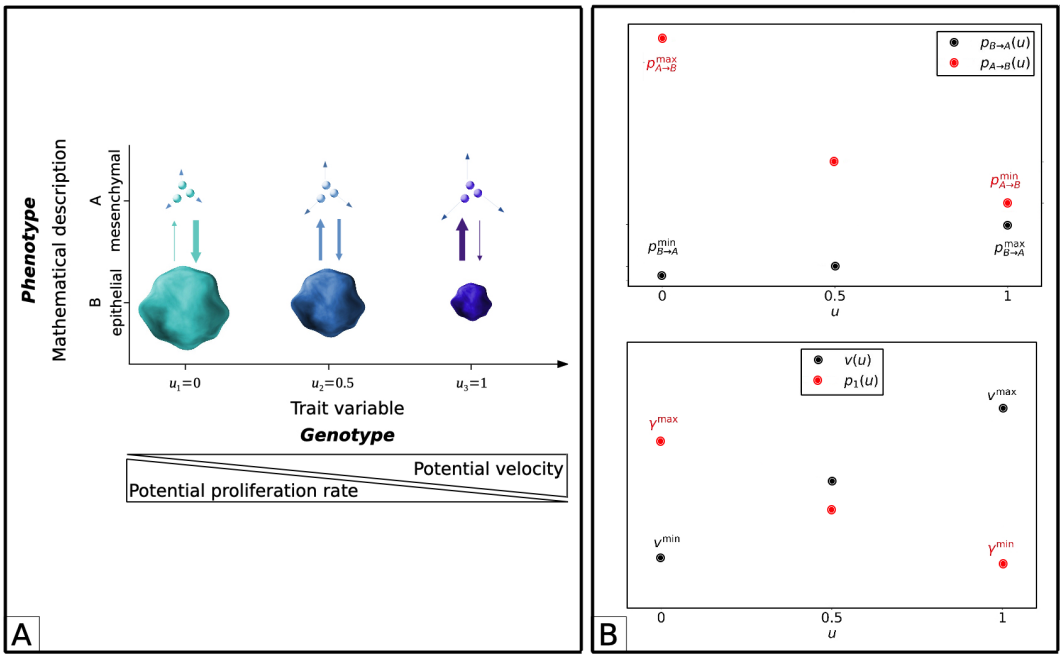

Fig. 5.4 (A) In the proposed application, the trait value u is set to qualitatively evaluate the cell motility/proliferation potential. In particular, the higher the value of u, the more a tumour individual is assigned a sequence of genes that, if expressed, enhances its migratory ability while dropping its duplication capacity. The phenotype A, and therefore the corresponding pointwise representation, is given to malignant cells with mesenchymal characteristics; the phenotype B, and the corresponding density-based representation, is instead assigned to tumour agents with epithelial hallmarks. The thickness of the vertical arrows gives a qualitative indication of the probability that a cell with a given genotype has to undergo one of the two phenotypic transitions. In particular, as also shown in the bottom graph of the panel (B), cells with genotype $u = u_1 = 0$ are more likely to acquire (or maintain) an epithelial behaviour. In contrast, cells with genotype $u = u_3 = 1$ are more likely to acquire (or maintain) mesenchymal hallmarks. (B) Top plot: influence of the genetic trait of a cell on the probability of phenotypic conversions (see Equations ((5.5.3)) and ((5.5.6))). Bottom plot: genotypic-dependent duplication rate of malignant epithelial cells (p_1, see Equation ((5.5.9))) and speed of mesenchymal individuals (v, see Equation ((5.5.13))).

The definition of the structuring variable u is indeed coherent with the "Go or Grow" (GoG) assumption, which finds support from both the experimental [197, 198] and the theoretical literature [215]. Phenotype A, and therefore an individual pointwise representation, is then assigned to describe tumour cells with *mesenchymal* determinants (i.e., that show an effectively high invasiveness and a poor mitotic activity). Phenotype B, as long as a collective density-based representation, is instead assigned to malignant individuals with *epithelial* hallmarks (i.e., low migratory

ability but high duplication rates). Such modelling assumptions are sketched in the already-cited panel (A) of Fig. 5.4.

In agreement with the scheme shown in Fig. 5.1 (C), we then assume that phenotypic transitions are:

- stimulated by variations in environmental conditions, in particular in the availability of oxygen, whose local concentration will be given by the field variable $O(t,\boldsymbol{y}) : T \times D \mapsto \mathbb{R}_0^+$. In this respect, hypoxia has been widely shown to boost phenotypic instability, acting as a fuel of selective pressure that stimulates tumour cells to shift towards more aggressive (mesenchymal) hallmarks [254]. For instance, tumour cells displaying high levels of hypoxia-inducible factors, such as HIF-1, have been demonstrated to overexpress genes relative to the migratory machinery and underexpress genes related to mitotic processes, see Ref. [44] and references therein. In the case of a sufficient amount of resources, malignant individuals have been instead shown to maintain or recover a less invasive (epithelial) behaviour. In this respect, cells with low levels of HIF-1 have been shown to transcript mainly genes implicated in duplication activities [44];

- affected by the cell genetic makeup: for instance, a variant characterised by a sequence of genes mainly relative to the migratory machinery more likely maintains or acquires a mesenchymal behaviour (and *vice versa*)[380];

- subjected to randomness, which is a critical aspect in most biological phenomena.

In principle, transition probabilities have to be given as random variables defined on spatio-temporal continuous domains. However, in the perspective of numerical realisations of the proposed model, we here account only for their discretised counterpart. According to these considerations, the probability of a cell $\boldsymbol{x}_{i,u_{\hat{k}}}(t)$ with phenotype A and genotype $u_{\hat{k}} \in U$ to undergo phenotypic transition in an interval of time $(t-\Delta t, t] \subset T$, being Δt the size of the time grid (see below), is equal to:

$$P_{\mathrm{A}\to\mathrm{B}}(O(t,\boldsymbol{x}_{i,u_{\hat{k}}}(t)),u_{\hat{k}}) = q_{\mathrm{A}\to\mathrm{B}}(O(t,\boldsymbol{x}_{i,u_{\hat{k}}}(t)))\; p_{\mathrm{A}\to\mathrm{B}}(u_{\hat{k}}). \tag{5.5.1}$$

In ((5.5.1)), the first factor evaluates the environmental conditions experienced by the i-th individual, i.e.,

$$q_{\mathrm{A}\to\mathrm{B}}(O(t,\boldsymbol{x}_{i,u_{\hat{k}}}(t))) = H(O(t,\boldsymbol{x}_{i,u_{\hat{k}}}(t)) - O_{\mathrm{M}}) \tag{5.5.2}$$

being

$$H(O(t,\boldsymbol{x}_{i,u_{\hat{k}}}(t)) - O_{\mathrm{M}}) = \left\{1\,,\text{ if } O(t,\boldsymbol{x}_{i,u_{\hat{k}}}(t)) \geq O_{\mathrm{M}};\, 0\,,\text{ if } O(t,\boldsymbol{x}_{i,u_{\hat{k}}}(t)) < O_{\mathrm{M}}\right\}$$

the Heaviside function and O_{M} the amount of molecular substance needed by tumour cells to remain in a normoxic condition., i.e., to avoid hypoxia. With Equation ((5.5.2)), we are assuming that mesenchymal cells experiencing oxygen deprivation do not undergo phenotypic transitions. The second factor in ((5.5.1)) instead reads as:

$$p_{\mathrm{A}\to\mathrm{B}}(u_{\hat{k}}) = (p^{\max}_{\mathrm{A}\to\mathrm{B}} - p^{\min}_{\mathrm{A}\to\mathrm{B}})(1-u_{\hat{k}})^2 + p^{\min}_{\mathrm{A}\to\mathrm{B}}. \tag{5.5.3}$$

It indeed sets a quadratic dependence between the genetic makeup of the cell and its possibility to switch phenotype. In this respect, in the case of normoxic conditions, mesenchymal individuals with genotype $u_1 = 0$ acquire epithelial hallmarks with a probability equal to $p^{\max}_{\mathrm{A}\to\mathrm{B}}$ whereas particles with genotype $u_3 = 1$ with a probability equal to $p^{\min}_{\mathrm{A}\to\mathrm{B}}$ where, according to the above-explained biological arguments, $p^{\min}_{\mathrm{A}\to\mathrm{B}} < p^{\max}_{\mathrm{A}\to\mathrm{B}}$, see Fig. 5.4 (B-top plot).

Conversely, considering the same time and space discretisation of the previous case, a cell clone with genotype $u_{\hat{k}}$ and phenotype B, i.e., whose distribution is given by the density $a^{\mathrm{B}}(t,\cdot,u_{\hat{k}})$, is set to acquire mesenchymal determinants at a certain point $\boldsymbol{x}_{\mathrm{s}} \in D$ of the discretised space and in an interval of time $(t-\Delta t, t] \subset T$ with a probability equal to

$$P_{\mathrm{B}\to\mathrm{A}}(O(t,\boldsymbol{x}_{\mathrm{s}}),u_{\hat{k}}) = q_{\mathrm{B}\to\mathrm{A}}(O(t,\boldsymbol{x}_{\mathrm{s}}))\; p_{\mathrm{B}\to\mathrm{A}}(u_{\hat{k}}), \tag{5.5.4}$$

where, recalling ((5.5.2)),

$$q_{\mathrm{B}\to\mathrm{A}}(O(t,\boldsymbol{x}_{\mathrm{s}})) = H(O_{\mathrm{M}} - O(t,\boldsymbol{x}_{\mathrm{s}})). \tag{5.5.5}$$

The above formula implies that only hypoxic conditions can trigger epithelial-to-mesenchymal transitions, whose probability to effectively occur also depends in this

case by the cell genotype:

$$p_{\mathrm{B}\to\mathrm{A}}(u_{\hat{k}}) = (p^{\max}_{\mathrm{B}\to\mathrm{A}} - p^{\min}_{\mathrm{B}\to\mathrm{A}})u^2_{\hat{k}} + p^{\min}_{\mathrm{B}\to\mathrm{A}}, \tag{5.5.6}$$

where $p^{\max}_{\mathrm{B}\to\mathrm{A}}$ characterises the cell clone with trait $u_3 = 1$ and $p^{\min}_{\mathrm{B}\to\mathrm{A}}$ the cell variant with $u_1 = 0$, being $p^{\max}_{\mathrm{B}\to\mathrm{A}} > p^{\min}_{\mathrm{B}\to\mathrm{A}}$, as plotted in the top graph of Fig. 5.4 (B). Obviously, the B-to-A phenotypic transition actually takes place if the $u_{\hat{k}}$-th cell variant has enough mass over the support of $\varphi_{\boldsymbol{x}_s}$.

Remarks. For the sake of completeness, we now give some comments on the above-proposed modelling framework:

- as we will see in details in the section devoted to the simulation details, the sizes of the time and space discretisation steps affect the estimate of the parameters $p^{\max}_{\mathrm{A}\to\mathrm{B}}, p^{\max}_{\mathrm{A}\to\mathrm{B}}, p^{\max}_{\mathrm{B}\to\mathrm{A}}$ and $p^{\min}_{\mathrm{B}\to\mathrm{A}}$;
- phenotypic transitions are actually employed according to the corresponding procedures explained in the previous section;
- in the case of simultaneously possible epithelial-to-mesenchymal switches occurring in the same domain point, it only takes place the one involving the cell variant with the highest value of u;
- in Equations ((5.5.3)) and ((5.5.6)), we have assumed a quadratic relationship between the value of the structuring variable u and the transition probabilities. Different laws may of course be chosen: however, they have to maintain the same qualitative trends of those proposed here;
- more sophisticated functions may be set also to describe the influence of oxygen on phenotypic variations. For instance, the probability of a cell to acquire mesenchymal determinants may increase upon decrements in the chemical concentration below the threshold O_{M}. One could also consider two different oxygen thresholds $O_{\mathrm{M1}} < O_{\mathrm{M2}}$ such that the phenotypic switch from A to B occurs for oxygen concentrations above O_{M1} and the phenotypic switch from B to A occurs for oxygen concentrations below O_{M2}.

Cell dynamics. Malignant cells with epithelial determinants are here assumed to proliferate and undergo random movement. The evolution of the density of the $u_{\hat{k}}$-th

variant with phenotype B can be indeed described by means of the following partial differential equation (PDE), whose boundary and initial conditions will be specified later on:

$$\frac{\partial a^{\mathrm{B}}}{\partial t}(t,\boldsymbol{y},u_{\hat{k}}) = \underbrace{D_{\mathrm{B}}\Delta a^{\mathrm{B}}(t,\boldsymbol{y},u_{\hat{k}})}_{\text{diffusive movement}} + \underbrace{p(u_{\hat{k}},\rho(t,\boldsymbol{y}))\, a^{\mathrm{B}}(t,\boldsymbol{y},u_{\hat{k}})}_{\text{proliferation}}, \tag{5.5.7}$$

where $\rho(t,\boldsymbol{y})$ account for the local tumour mass (see below Equations ((5.5.11)) and ((5.5.12))). The diffusion term at the r.h.s. of Equation (5.5.7), with constant coefficient $D_{\mathrm{B}} > 0$, models Brownian cell displacements. The reaction term instead expresses local variations in the mass of the $u_{\hat{k}}$-th epithelial cell variant. In particular, they are assumed to depend on (i) individual genetic traits and (ii) physical limitations determined by the available space. In this respect, p can be factorised as it follows:

$$p(u_{\hat{k}},\rho(t,\boldsymbol{y})) = p_1(u_{\hat{k}})\, p_2(\rho(t,\boldsymbol{y})). \tag{5.5.8}$$

The duplication law p_1 accounts for the fact that higher proliferation rates characterise cell variants with lower values of the trait variable u (that, as previously seen, are associated to sequence of genes mainly implicated in the mitotic machinery). In this respect, to avoid overcomplications, we assign to p_1 a linear trend, see Fig. 5.4 (B-bottom plot):

$$p_1(u_{\hat{k}}) = (\gamma^{\max} - \gamma^{\min})(1 - u_{\hat{k}}) + \gamma^{\min}, \tag{5.5.9}$$

being $\gamma^{\max}$ a maximal duplication rate, characteristic of cells with genotype $u = u_1 = 0$, and $\gamma^{\min}$ the corresponding minimal value, that is instead assigned to individuals with genotype $u = u_3 = 1$. The factor p_2 in Equation ((5.5.8)) instead models the fact that the mitotic cycle is typically disrupted in overcompressed cells, although abnormal proliferation is a relevant characteristic of malignant masses. This phenomenon can be replicated by setting the following logistic law:

$$p_2(\rho(t,\boldsymbol{y})) = 1 - \frac{\rho(t,\boldsymbol{y})}{c}, \tag{5.5.10}$$

where $c > 0$ is a carrying capacity while

$$\rho(t,\boldsymbol{y}) = \rho^{\mathrm{A}}(t,\boldsymbol{y}) + \rho^{\mathrm{B}}(t,\boldsymbol{y}), \tag{5.5.11}$$

being ρ^{B} defined as in Equation ((5.4.3)), and

$$\rho^{\mathrm{A}}(t,\boldsymbol{y}) = \sum_{k=1}^{3} \sum_{i=1}^{N_{u_k}^{\mathrm{A}}} \varphi_{\boldsymbol{x}_{i,u_k}(t)}(\boldsymbol{y}). \tag{5.5.12}$$

In Equation ((5.5.10)), we consider that the available space is reduced by the presence also of mesenchymal individuals, whose influence on the overall mass distribution can be accounted by the use of the corresponding set of bubble functions, as given in Equation ((5.5.12)). Equation (5.5.7) is then complemented by Neumann homogeneous boundary conditions on the spatial domain D, which are consistent with the fact that cells can not physically cross the border of an experimental *Petri dish*.

The dynamics of tumour cells with mesenchymal determinants only include a directional movement towards domain regions with higher oxygen concentrations. In this respect, for the i-th individual with phenotype A and generic genotype $u_{\hat{k}}$, we set:

$$\frac{d\boldsymbol{x}_{i,u_{\hat{k}}}}{dt}(t) = \frac{\nabla O(t,\boldsymbol{x}_{i,u_{\hat{k}}}(t))}{|\nabla O(t,\boldsymbol{x}_{i,u_{\hat{k}}}(t))|}\, v(u_{\hat{k}}), \tag{5.5.13}$$

with $v(u_{\hat{k}}) = (v^{\max} - v^{\min})u_{\hat{k}} + v^{\min}$, see the bottom graph in Fig. 5.4 (B). In Equation ((5.5.13)), cell speed and direction of movement are decoupled, given their distinct physical meaning. The former depends on the pattern of available resources, the latter, quantified by the scalar functions $v : U \mapsto [v^{\min}, v^{\max}]$, is instead affected by individual genetic makeup. In this respect, recalling that higher values of u imply higher motile potential, $v^{\max}$ is the speed of cells with genotype $u = u_3 = 1$, whereas $v^{\min}$ of cells with genotype $u = u_1 = 0$. It is finally useful to underline that Equation ((5.5.13)) is based on the *overdamped force-velocity assumption*: it establishes that, in extremely viscous regimes such as biological environments, the velocity of moving agents and not their acceleration is proportional to the sensed forces (see Ref. [393] and references therein for a detailed comment). When a mesenchymal cancer cells reaches a point of the border of D, the component of its velocity locally normal to the boundary itself is arbitrarily set equal to zero.

Summing up, it is possible to conclude that, in this sample model application, genetic traits and ecological/environmental conditions affect not only the phenotypic transitions of the cancer cells but also their effective growth and migratory dynamics, as sketched in panel (C) of Fig. 5.1.

Chemical dynamics. We assume that oxygen diffuses within the domain and is consumed equally by all tumour individuals, regardless of their genotype and phenotype. Its kinetics can be therefore described by the following reaction-diffusion (RD) equation:

$$\frac{\partial O}{\partial t}(t,\boldsymbol{y}) = \underbrace{D_{\mathrm{O}}\Delta O(t,\boldsymbol{y})}_{\text{diffusion}} - \underbrace{\lambda_{\mathrm{O}}\,\rho(t,\boldsymbol{y})\,O(t,\boldsymbol{y})}_{\substack{\text{consumption by}\\ \text{tumour cells}}} - \underbrace{\alpha_{\mathrm{O}}O(t,\boldsymbol{y})}_{\text{decay}}, \tag{5.5.14}$$

where D_{O}, λ_{O}, and α_{O} are constant coefficients, that quantify chemical diffusion, consumption by malignant cells and natural decay, respectively, being ρ defined as in Equation ((5.5.11)). Equation (5.5.14) is finally completed with Dirichlet conditions along the entire domain boundary ∂D, i.e., $O(t,\partial D) = \overline{O}$, for all $t \in T$: we are indeed assuming a continuous and constant chemical supply within our virtual *Petri dish*. The initial oxygen pattern will be specified below instead. It is useful to remark that the inclusion of chemical dynamics gives to our model a *multi-scale* aspect, as it now deals with elements characteristic of both the cellular and the subcellular levels.

Numerical details. For the spatial domain D, we have employed a triangular mesh with radial symmetry with respect to the centre point $(0,0)$. The characteristic diameter of each grid element has been taken equal to $\Delta x = 5\,\mu$m. For the time domain T, we have used an uniform discretisation with step equal to $\Delta t = 1$ h.

Equations (5.5.7) and ((5.5.14)), describing the dynamics of the continuous population and of the oxygen, have been solved employing a time-explicit Euler method coupled with a Galerkin finite-element technique. An explicit Euler method has been also employed for the system of ODEs describing movement of pointwise cells (cf. Equation ((5.5.13))). At any discrete time-step, phenotypic switches are implemented (as explained in Section 5.4) just *after* the numerical solution of the above-cited equation for cell dynamics.

Considering B-to-A switches, the following algorithmic rules are implemented for each numerical node of the domain:

1. the oxygen level is checked: if it is higher than O_{M}, then no phenotypic transition occurs and we pass to another domain point;
2. otherwise, we check the mass of the cell subpopulation with $u = u_3 = 1$: if it satisfies condition (5.4.9) then a random number from the uniform distribution

between 0 and 1 is drown. If this number is lower than the value of the probability given in (5.5.4) and evaluated in the case of our interest, then the phenotypic transition occurs, and we pass to another domain point (recall that a B-to-A phenotypic transition of a given subpopulation locally inhibits analogous processes involving other subpopulations);

3. otherwise, the same evaluations described at point (ii) are performed for the other subpopulations in descending order with respect to u (to be coherent with the fact that cells with higher genotypic traits u are more likely to switch phenotype).

We keep into account that, when a B-to-A transition takes place in one point, it affects the possibility of transition in neighboring points, as some of the continuous mass is removed. Thus, in order to avoid biases in spatial location of B-to-A phenotypic switches, at every iteration we randomise the order in which the points of the numerical lattice are visited.

We then turn on considering possible A-to-B transitions, which take place in areas with oxygen concentration above O_{M} with probability given by (5.5.1) (using the same drawing algorithm described above). We finally remark that the order in which cells with phenotype A are checked for possible transitions does not affect numerical outcomes since A-to-B transitions are independent of each other. Note that all numerical computations have been performed in Fenics, see Ref. [20, 294].

Parameter estimate. As previously commented, the probabilities of phenotypic transitions introduced in Equations ((5.5.1)) and ((5.5.4)) are the discretised approximations of the corresponding continuous-in-time (and in-space) laws. In more detail, the coefficient $p^{\max}_{\mathrm{A}\to\mathrm{B}}$ ($p^{\min}_{\mathrm{A}\to\mathrm{B}}$, rsp.) defines the probability that the i-th cell with genotype $u = u_1 = 0$ ($u = u_3 = 1$, rsp.) undergoes phenotypic transition at a given time step, i.e., in the case of normoxic conditions. The estimation of these values is based on the average time that a cell with mesenchymal characteristics takes to re-acquire epithelial hallmarks; in our model we assume that it ranges from $T^{\min}_{\mathrm{A}\to\mathrm{B}} = 50$ h to $T^{\max}_{\mathrm{A}\to\mathrm{B}} = 200$ h. Such quantities (poorly measured in the empirical literature, see [7] for one of the few contributions in this respect) have been fixed in order to have a reasonable number of phenotypic transitions in the period of observation. By recalling that our model is based on the assumption that cells with lower values of the trait variable are more likely undergo A-to-B transitions, we can

indeed set

$$p^{\max}_{\mathrm{A}\to\mathrm{B}} = \frac{\Delta t}{T^{\min}_{\mathrm{A}\to\mathrm{B}}} \qquad \text{and} \qquad p^{\min}_{\mathrm{A}\to\mathrm{B}} = \frac{\Delta t}{T^{\max}_{\mathrm{A}\to\mathrm{B}}},$$

so that $p^{\max}_{\mathrm{A}\to\mathrm{B}} = 2\times 10^{-2}$, $p^{\min}_{\mathrm{A}\to\mathrm{B}} = 5\times 10^{-3}$. The coefficients $p^{\max,\min}_{\mathrm{B}\to\mathrm{A}}$ instead give the probability that a single-cell-fraction of mass with phenotype B and centred in $\boldsymbol{x}_{\mathrm{s}}$ changes phenotype at a given time step when falls in hypoxic conditions. A proper estimate can be obtained by taking into account three aspects: (i) epithelial cells experiencing oxygen deprivation are here assumed to acquire mesenchymal determinants in a time lapse that ranges from $T^{\min}_{\mathrm{B}\to\mathrm{A}} = 8.8$ h to $T^{\max}_{\mathrm{B}\to\mathrm{A}} = 35.4$ h; (ii) in our modeling framework higher values of the genotypic variable implies more possibility to switch towards phenotype A; and (iii) a finer spatial grid requires a smaller transition probability for each node $\boldsymbol{x}_{\mathrm{s}}$, otherwise an higher amount of possible nodes of the domain in principle could allow a higher number of transitions. Taken together, the above considerations lead to

$$p^{\max}_{\mathrm{B}\to\mathrm{A}} \propto \Delta t, (T^{\min}_{\mathrm{B}\to\mathrm{A}})^{-1}, \Delta x^2 \qquad \text{and} \qquad p^{\min}_{\mathrm{B}\to\mathrm{A}} \propto \Delta t, (T^{\max}_{\mathrm{B}\to\mathrm{A}})^{-1}, \Delta x^2.$$

In particular, after preliminary simulations, we have fixed $p^{\max}_{\mathrm{B}\to\mathrm{A}} = 4\times 10^{-3}$, and $p^{\min}_{\mathrm{B}\to\mathrm{A}} = 10^{-3}$, which have allowed us to have a reasonable rate of B-to-A phenotypic conversions.

The diffusion coefficient of epithelial cell movement, i.e., D_{B}, has been taken equal to $1.29\times 10^3 \mu\mathrm{m}^2/\mathrm{h}$, as in Ref. [312]. The coefficients $\gamma^{\min}$ and $\gamma^{\max}$ quantify the minimal and maximal mitotic rate of cells with phenotype B, in the case of fully available space. The chosen values $\gamma^{\min} = \ln(2)/48\ \mathrm{h}^{-1}$ and $\gamma^{\max} = \ln(2)/24\ \mathrm{h}^{-1}$ fall within the range quantified for glioblastoma cell lines in either hypoxic or normoxic conditions, see again Ref. [312]. The carrying capacity c has been set equal to $1.69\ \mathrm{cell}/\mu\mathrm{m}^2$, in order to maintain a quasi-monolayered cell configuration, in agreement with the bi-dimensional nature of experimental cultures in a *Petri dish*.

Cells with phenotype A are allowed to freely move within the domain. In this respect, the maximal value of their speed $v^{\max}$, which characterise mesenchymal individuals with trait $u_3 = 1$ has been fixed to 10 μm/h, whereas the minimal threshold $v^{\min}$, which characterises mesenchymal individuals with trait $u_1 = 0$, is set to 2.5 μm/h. These parameters have been taken from Ref. [188] and assure that the modulus of the overall cell velocity substantially falls within the range of the corresponding experimental counterparts evaluated for different malignancies.

Parameter	Value [Units]	Reference(s)
r	15 [μm]	[11]
$p^{\min}_{A\to B}$	5×10^{-3}	model estimate
$p^{\max}_{A\to B}$	2×10^{-2}	model estimate
$p^{\min}_{B\to A}$	10^{-3}	model estimate
$p^{\max}_{B\to A}$	4×10^{-3}	model estimate
D_B	1.29×10^{3} [μm^2/h]	[312]
$\gamma_{\min}$	$\ln(2)/48$ [h^{-1}]	[312]
$\gamma_{\max}$	$\ln(2)/24$ [h^{-1}]	[312]
c	1.69 [cell/μm^2]	model estimate
$v^{\min}$	2.5 [μm/h]	[312]
$v^{\max}$	10 [μm/h]	[312]
D_O	3.60×10^{6} [μm^2/h]	[312]
λ_O	1.67×10^{-10} [μm^2/(cell$\cdot$h)]	model estimate
α_O	3.60×10^{-4} [h^{-1}]	[136]
O_M	2.56×10^{-15} [μmol/μm^2]	[312]

Table 5.1 Simulation parameter setting.

The chemical threshold that leads to hypoxia, i.e., O_M, has been set equal to $2.56\times10^{-15}\,\mu\text{mol}/\mu\text{m}^2$ and the diffusion coefficient of oxygen has been fixed to $D_O = 3.60\times10^{6}\ \mu\text{m}^2/\text{h}$, and taken again from Ref. [312]. The chemical consumption rate then amounts to $\lambda_O = 1.67\times10^{-10}\ \mu\text{m}^2/(\text{cell}\cdot\text{h})$: it has been empirically measured taking into account of the proposed computational setup, in order to have a realistic time-evolution of the molecular pattern. The oxygen decay coefficient has been fixed to $\alpha_O = 3.60\times10^{-4}\ \text{h}^{-1}$, according to Ref. [136]. The constant production of oxygen at the domain border, i.e., $\overline{O}$, has been set equal to $2.8\times10^{-15}\,\mu\text{mol}/\mu\text{m}^2$: for the reader's convenience, we remark that this value is $1.1\times O_M$. The final observation time t_F has been instead set equal to 35 h. The employed parameter setting is listed in Table 5.1.

Simulation results. The spatial domain D, as well as the initial configuration of the cell system, is the same employed in the representative simulation given in Section 5.4, specified by Equations ((5.4.11)) and ((5.4.12)), and shown in Fig 5.2. At the onset of the forthcoming numerical realisation, we indeed have a tumour aggregate with few mesenchymal cells (heterogeneous for genotype) dispersed within and around a cluster of malignant epithelial individuals.

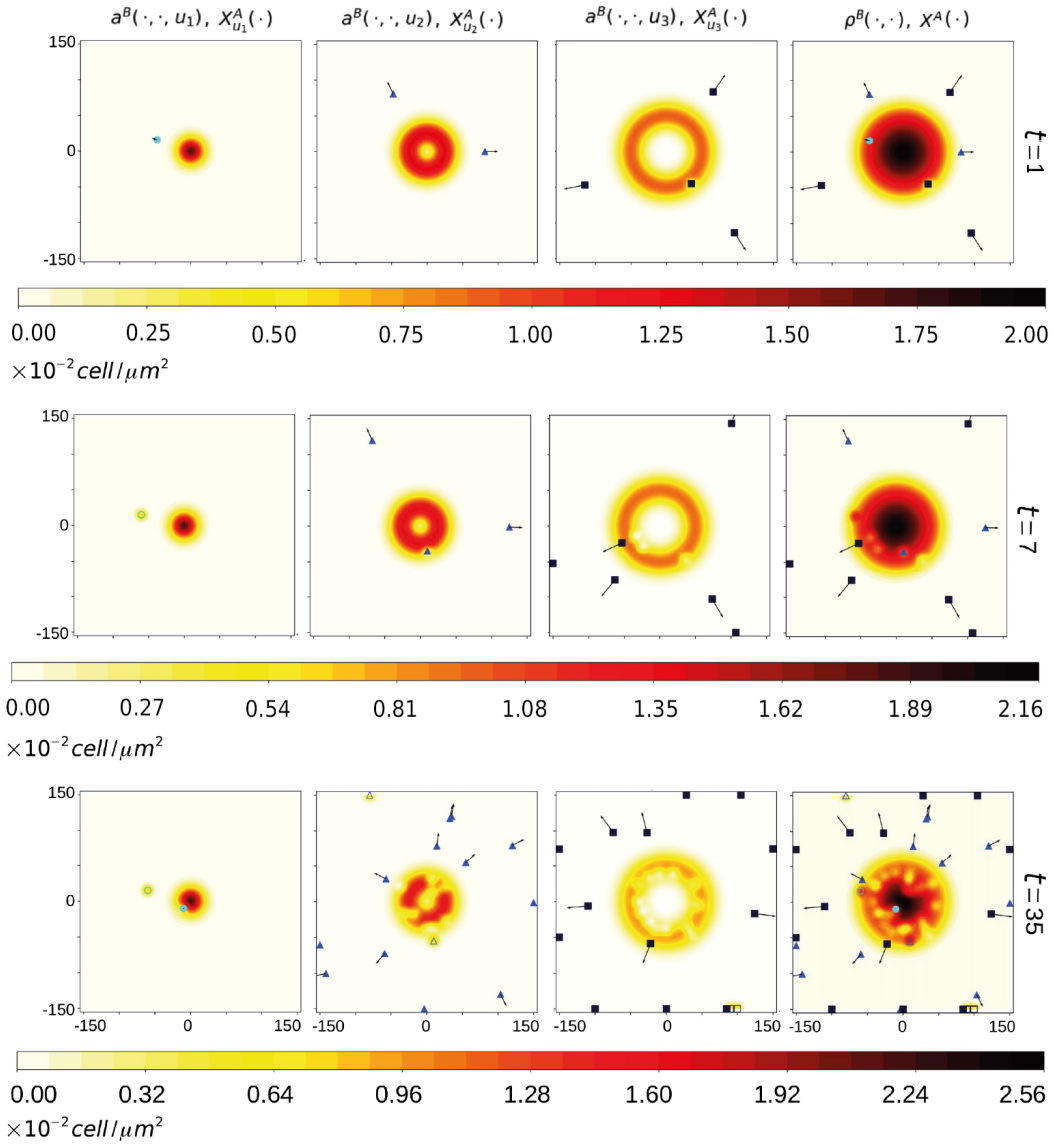

Fig. 5.5 Representative time instants of the evolution of our virtual tumour aggregate. The initial condition of the cell system is exactly the same as in Section 5.4; see Fig. 5.2. At the onset of the numerical realisation, the oxygen is quasi-homogenously present within the entire domain with a level that is higher than the hypoxic threshold O_{M}. Subsequent oxygen consumption results in harsh conditions for malignant epithelial cells: some of them are then able to acquire mesenchymal hallmarks (according to the genotype-dependent probabilistic rule given in ((5.5.4))) and move towards domain regions with more availability of resources (see top and middle panels, i.e., those relative to $t = 1$ and 7 h). Arrived close to the border of our virtual *Petri dish*, few of them experience normoxia and recover epithelial determinants (see the bottom panels, i.e., those relative to $t = t_{\mathrm{F}} = 35$ h). We remark that light blue circles identify mesenchymal cells with genotype u_1, dark blue triangles identify mesenchymal cells with genotype u_2, and black squares identify mesenchymal cells with genotype u_3. The same *empty* geometric labels instead identify mesenchymal cell variants that have undergone the inverse, i.e., A-to-B, phenotypic transition. The arrow attached to each mesenchymal individual identifies its velocity: its length is qualitatively proportional to the individual genotype-dependent speed.

In particular, the node of tumour cells with phenotype B has a radial distribution w.r.t. the centre of the domain, with the bulk mainly constituted by the cell variant with $u_1 = 0$ and the external region by the cell variant with $u_3 = 1$. The initial oxygen concentration is instead given by the stationary solution of Equation (5.5.14), evaluated in the absence of cancer cells (i.e., in the case only of chemical diffusion and decay): given the low value of the decay rate α_O (see above and Table 5.1), it consists of a spatially quasi-homogeneous pattern with a chemical level approximately equal to $2.8 \times 10^{-15}\,\mu\text{mol}/\mu\text{m}^2$. The initial oxygen level indeed exceeds the hypoxic threshold O_M in the entire domain.

Oxygen consumption then starts to occur at the domain area occupied by the tumour aggregate, with the extent of local decrements obviously determined by the density of malignant individuals. The level of chemicals at the inner part of the mass indeed drops to the critical value O_M, and an increasing number of epithelial tumour cells (characterised by negligible motility) experiences hypoxia. Some of them are then able to undergo phenotypic transition and acquire mesenchymal determinants, see Fig. 5.5. This group is mainly composed of individuals with a trait value $u_3 = 1$, which is associated with the sequence of genes that favours (from a probabilistic point of view) such a phenotypic switch.

The just-differentiated mesenchymal cells, as long as those already present at the onset of the simulation, crawl towards oxygenated domain regions: in particular, each of them moves with speed dictated by its genetic trait, as shown by the length of the arrows attached to the particles in Fig. 5.5. The remaining fraction of epithelial individuals is instead not able to escape harsh environmental conditions: in the case of long-term hypoxia (e.g., long-lasting oxygen deprivation), their fate would be an irreversible necrosis.

As the simulation proceeds, the domain region with a low chemical level enlarges: as a result, the above-described cell dynamics take place in more peripheral areas of the tumour aggregate and involve an increasing amount of epithelial mass. In particular, at the end of the observation time (i.e., at $t = t_F = 35$ hours), the cell configuration consists of a hypoxic cluster of epithelial tissue, mainly formed by individuals with a trait variable equal to $u_1 = 0$. It is surrounded by scattered mesenchymal cells, that have reached the external regions of the domain, i.e., those with higher oxygen availability. Interestingly, few of these agents have been able to undergo the inverse transition and reacquire epithelial hallmarks (see the bottom

panels of Fig. 5.5). During the entire observation time, the fraction of malignant epithelial mass goes on proliferating (cf. the variations in the values of the colorbar in Fig. 5.5).

Our numerical results qualitatively agree with a wide range of experimental evidence, which has shown that malignant cells with different phenotypic properties occupy tumour regions characterised by different oxygen levels. For instance, glioblastoma spheroids cultured *in vitro* have the core mainly populated by cells with a proliferative activity higher than those located at the invasive edges [3, 93, 262, 415]. Analogously, mesenchymal cancer stem cells have been found to be abundant near the tumour-stroma boundary (i.e., at the external region of the malignant mass) [291]. Similar phenotypic spatial heterogeneity has been observed in malignant spheroids of ovarian [77, 402] or breast [194] carcinomas grown in spinner cultures.

Similar growth of tumour masses, i.e., characterised by an inner region of poorly motile individuals unable to escape nutrient deprivation and by an external possibly scattered ring of aggressive cells, has also been predicted by a wide spectrum of theoretical models, as illustrated in the comprehensive books [134, 370] and the excellent reviews [34, 53, 80, 100, 373].

5.6 Conclusions and future perspectives

We have here proposed a modelling framework where cells are distinguished in terms of genotype by a discrete structuring variable and in terms of phenotype by the assigned mathematical representation (i.e., pointwise or density-based). A procedure to consistently switch between the two descriptive instances, which is based on the definition and the use of a bubble function, has then allowed for phenotypic plasticity to be accounted for.

We have then presented a representative simulation to show how phenotypic transitions actually take place within our theoretical environment, which has been finally applied to a more realistic scenario, i.e., the early evolution of a heterogeneous tumour aggregate hypothetically cultured *in vitro*. In particular, we have assumed that malignant cells can have one of three distinct genotypes and one of two alternatives, i.e., mesenchymal vs epithelial, behaviour. Phenotypic conversions have been set to depend on (i) oxygenation levels, (ii) intrinsic genotype, and (iii) randomness,

which is a novelty of this work respect to existing literature [122, 392]. The resulting numerical realisation has captured the realistic emergence of a hypoxic core within the tumour cluster with the consequent cell tendency to acquire a more aggressive and invasive (i.e., mesenchymal) phenotype.

Model improvements. The proposed mathematical environment may be improved at least in two directions.

From a strictly modelling perspective, it would be relevant to account for genetic alterations that may be induced by cell-cell communication and changes in environmental conditions but that are usually determined by random mutations. This last aspect can be included in the proposed modelling environment by stochastic variations of the value of the trait variable u assigned to one or more pointwise individuals and/or to one or more portions of the cell mass with the density-based representation. Furthermore, one could consider a continuous trait u that takes values in a given interval (e.g., $[0, 1]$). This would amount to using a structuring variable to represent not only genetic heterogeneity (as in our model) but also epigenetic heterogeneity: each value of u, in fact, would represent the (normalised) expression of a gene or a group of genes (or the level of one or more proteins). In this case, epigenetic variations in the cell population could be accounted for by including a diffusion term in the trait domain, as done in the already cited works [175, 300, 301].

From an application perspective, our model could be extended to reproduce the evolution of a malignant mass *in vivo*, i.e., to shed light on the effect of intratumoral heterogeneity and phenotypic plasticity on the invasiveness of the disease. In this respect, one may include the presence of both the preexisting and the tumour-induced vasculature in the picture. As a natural extension of our model assumptions, we would have to take into account that cancer cells in hypoxic conditions not only shift towards more aggressive phenotypes but also secrete proangiogenic factors that induce the formation of new blood vessels departing from existing ones [360]. In addition, our model could be developed to incorporate a more comprehensive description of the metabolism of the different cell variants. However, to provide consistent results of such an *in vivo* scenario, model parametrisation should be better calibrated, for instance, by focusing on a specific tumour type and using proper sets of existing data.

Chapter 6

Multiscale modelling for the impact of Snail-mediated response to hypoxia on tumour progression

As we have already underlined in Chapter 1, migration of tumour cells into the normal tissue under the influence of biochemical and biophysical components of the micro-environment is one of the hallmarks of cancer [214].

However, because of the highly complex biology at the cellular and molecular level and in the interactions with the surrounding environment, the exact dynamics driving cell migration are still not completely well understood. In this chapter, we keep our interest in the invasive and proliferative dynamics of tumour cells, deepening our biological investigation. In particular, we try to link microscopic dynamics, using a multiscale approach, in order to include their effect in a macroscopic model. The investigations here presented are part of joint work with Dr. Martina Conte (Politecnico di Torino, Beckman Research Institute City of Hope National Medical Center), whose results are collected in a paper titled "Multi-scale modelling of Snail-mediated response to hypoxia in tumour progression" (arXiv and as Ref. [109]), submitted in April 2024 to *Communications in Nonlinear Science and Numerical Simulation* journal.

6.1 Introduction

In the context of the interaction between tumour and its micro-environment, tissue oxygenation is one of the prominent traits. It has been suggested that oxygen concentration highly influences the switch between migrating and proliferating cell behaviour, the invasiveness and aggressiveness of the tumour cells, and that the deprivation of oxygen acts as an environmental stressor, promoting a long series of mutations that strongly impact the tumour dynamics. It has been clinically observed that, in solid tumours, the oxygen distribution is heterogeneous, with oxygen levels ranging from normal to hypoxic and severe hypoxic [312].

Hypoxia has long been recognised as a contributing factor to the tumour microenvironment (TME) [107]. Not only can these induce a pronounced migratory bias of the cells towards favourable areas, but they can even determine their phenotype and interaction strategies. Under hypoxic conditions, tumour cells undergo morphological and molecular changes to adjust their behaviours and acquire the abilities to adapt to hypoxia and escape apoptosis [386]. There are several adaptive responses of tumour cells to hypoxia [107], which may involve the secretion of specific transcription factors, like hypoxia-inducible factor 1 (HIF-1), the upregulation of hypoxia-inducible angiogenic factors, sustaining new vessels formation [458], or glycolysis activation [389]. Among others, HIF-1 activation controls the expression of Snail transcription.

The Snail superfamily of transcription factors includes Snail1, Slug, and Scratch proteins [258]. It is well documented that Snail protein directly represses E-cadherin, and thus, it is a key inducer of epithelial-mesenchymal transition, a biological process defining progression from a polarised epithelial cell phenotype to a mesenchymal phenotype [351, 226]. In addition to regulating epithelial-to-mesenchymal transition (EMT) and cell migration, overexpression of Snail induces resistance to apoptosis and tumour recurrence [247]. The Snail-mediated survival of epithelial cells may thus enhance the ability of tumour cells to invade and metastasize. Overexpression of Snail has been reported to be a sufficient inducer of EMT as well as a predictor for an aggressive tumour phenotype. It has recently been demonstrated that Snail expression is induced by hypoxic conditions and is regulated by HIF-1α expression at the transcriptional level [85, 305, 233]. Up-regulation of Snail-1 correlates with metastasis and poor prognosis, whereas silencing of Snail-1 is critical for reducing

tumour growth and invasiveness [45]. Since such complex processes and their mutual conditioning scenarios are difficult to assess experimentally, mathematical models can help understand the underlying biological mechanisms, test hypotheses, and even make predictions.

Cancer progression is a complex process involving several factors and taking place as both an individual and a collective process. Microscopic intracellular dynamics, occurring at the individual level, influence the mesoscopic cell behaviour of cells, which determines the macroscopic evolution of the cell population density. Previous models for tumour invasion have been proposed in discrete or continuous frameworks. The former is based on the description of individual cell dynamics moving on a lattice [200, 420] and can involve continuous equations for the evolution of external factors (e.g., chemoattractant concentration, the density of ECM fibres, low pH levels) - the so-called hybrid models [241, 23, 29]. Concerning the latter, different classes of fully continuous models for tumour cell migration have been developed. Many of them are versions or extensions of a classical reaction-diffusion model proposed by Murray [331], while more recent works take into account the advection bias of tumour cells describing motility adjustment to extracellular signals. Some of these are directly set on the macroscopic scale and rely on balance equations for mass, flux, or momentum [22, 99, 24], or on integro-differential equations accounting for the development of specific intra-tumour structure [36, 175, 418, 112] (see also the review in Ref. [270] for settings with multiple taxis in the larger context of cell migration). More recently, the use of kinetic transport equations (KTEs) in the kinetic theory of active particles (KTAP) framework has been largely applied to the study of cell migration, in general [96, 126, 221, 302, 102, 127, 260], and in the specific context of tumour evolution [125, 169, 75, 170, 270, 295, 464]. Kinetic models are intrinsically multi-scale models that characterize the dynamics of distribution functions of densities of tumour cells which may depend, besides time and position, on several kinetic variables, such as microscopic velocity or activity variables. These models use Boltzmann-type equations for the cell population density and scaling arguments to derive the macroscopic setting. Among those models [124, 128, 171, 129, 273] accounts for effects of hypoxia or hypoxia-driven acidity on the migration and invasion process of tumour cells. Concerning the taxis terms obtained in this class of models [124, 171, 169, 155] they are derived from the modelling of subcellular dynamics for receptor binding, which leads in the mesoscopic KTE to transport terms w.r.t. the activity variables. In Ref. [128, 273, 302], instead,

the use of turning rates depending on the pathwise gradient of some chemotactic signal leads to various types of taxis at the macroscopic level. Moreover, in Ref. [102, 129, 155], forces and stress, acting on the cells and depending on the chemical and physical composition of the environment, translates into transport terms w.r.t. the velocity variable in the corresponding KTE. In particular, in Ref. [155], the authors consider the flux-limited description of the transport terms. Flux limitations have been introduced in the modelling of cell motility to reduce the infinite speed of propagation triggered by linear diffusion and the excessive influence of the latter on the spread of cells. Their derivation from KTEs has been provided formally in Ref. [52] and rigorously in Ref. [356]. In both cases, the derivation is based on an appropriate choice of the signal response function involved in the turning operator and depending on the directional derivative of the signal. In Ref. [155], instead, an alternative approach based on characterizing velocity dynamics at the single-cell level is proposed. Lastly, concerning the mathematical modelling of Snail dynamics, several works have been proposed for theoretically studying Snail's role in the epithelial-to-mesenchymal transition process, especially looking at the interactions among microRNAs and transcription factors - miR-34, miR-200, Zeb, and Snail - at the single cell level [242, 303, 425], while its connection to cellular motility has been largely investigated.

In the KTAP framework, in the present work, we propose a multi-scale mathematical modelling approach for describing tumour invasion in response to tissue hypoxia, investigating the interplay between molecular signalling pathways and cell dynamics. The model connects single-cell behaviour driven by Snail expression with macroscopic scale dynamics describing tumour migration in the tissue. Starting from the approach proposed in Ref. [155], we introduce a novel description of the internal variable dynamics for Snail expression, and we account for flux-limited operators in the single-cell velocity dynamics. At the mesoscopic level, cell evolution is described in terms of a classical kinetic transport equation with different formulations for the proliferative operator. From this description, using proper up-scaling arguments, we derive the macroscopic setting. Moreover, we numerically investigate the model's capability of capturing different biologically relevant scenarios concerning hypoxia and Snail effects on cell migration and proliferation. We show how the model is reliable in replicating different experimental results and offers new perspectives for interpreting experimental findings.

The paper is organised as follows. Section 6.2 provides the set-up of micro-

scopic and mesoscopic equations for the dynamics of tumour cells. Section 6.3 contains the derivation of the macroscopic equation for tumour cell density evolution, which features flux-limited chemotaxis towards increasing oxygen concentrations and self-diffusion, as well as a proliferation term modelling the inverse correlation between moving and proliferating cell capability in two possible manners. In Section 6.4, four numerical tests are proposed to show both the qualitative behaviour of the proposed model in different scenarios and its capability to qualitatively replicate experimental data concerning the Snail impact of tumour cell migration in different oxygen conditions. Finally, Section 6.5 provides a discussion of the main outcome of our model, along with some perspectives.

6.2 Modelling

In this note, we propose a multi-scale model for describing tumour progression in response to tissue hypoxia, whose influence on the cancer cells is mediated by Snail dynamics. Following well-established literature regarding the multi-scale models for tumour invasion [260, 169, 171, 129, 125], the model setting proposed here is built using the classical tools and methods of kinetic theory. Our main aim is to obtain a detailed description of the tumour cell dynamics, taking into account the effect of microscopic signalling pathways in the mechanisms of tumour response to hypoxia.

Starting from the microscopic level of interaction between cells and oxygen, we consider the dynamics of the Snail signalling pathway, which is involved in the cell response to hypoxic microenvironmental conditions. Moreover, following [155], we provide a microscopic description of velocity dynamics that depend on oxygen and macroscopic cell density tactic gradient, and the Snail expression influences the cell motility. Then, we set up the corresponding kinetic transport equations (KTEs) describing the evolution of the cell distribution in relation to the prescribed microscopic dynamics. Performing a proper model upscaling, we obtain the equations for the statistical moments of the cell distribution. These describe the dynamics of tumour cells, which are driven by limited diffusion and oxygen-mediated drift, and the evolution of the average Snail expression of the tumour population.

6.2.1 Microscopic scale

At this level, we model the dynamics of the microscopic variable $y \in \mathbf{Y}$, describing the expression of the Snail protein and the microscopic cell velocity $\mathbf{v} \in \mathbf{V}$, both influenced by the oxygen levels. We assume oxygen to be time-independent, i.e., $O_2 = O_2(\mathbf{x})$ has a fixed distribution which does not evolve in time. Possible extensions of this approach are discussed in Section 6.4.

Dynamics of Snail protein expression

Concerning Snail protein expression, we model the process of protein synthesis from gene transcription and its regulation depending on the oxygen dynamics. Snail proteins are transcription factors involved in the regulation of hypoxia-driven cell migration and invasion [233, 465]. It has been shown in several different types of human cancer that overexpression of Snail induces invasion and metastasis [62, 385, 367, 465]. The expression of Snail protein is controlled by the oxygen levels, decreasing when the tumour mass is properly oxygenated. Relying on the description of the temporal evolution of the total level of Snail proposed in Ref. [425], here we model its dynamics with the following equation:

$$\frac{dy}{dt} = g_s H(y) H(O_2) - \gamma_s y, \tag{6.2.1}$$

where g_s and γ_s represent the basal transcription and degradation rates, respectively, while the functions $H(\cdot)$ model the transcription activation/inhibition mechanisms. We recall here that $O_2 = O_2(\mathbf{x})$. Generally, the functions $H(G)$ can be described as

$$H(G) = \frac{1 + \lambda_G \frac{G}{G_0}}{1 + \frac{G}{G_0}},$$

where G is a generic agent influencing the transcription and G_0 is its reference value. In particular, $\lambda_G > 1$ models an activation mechanism supported by the agent G, while $\lambda_G < 1$ refers to an inhibition mechanism driven by G. In the case of Snail, it has been shown that it has a self-regulatory (inhibition) mechanism [143, 304], which we describe as

$$H(y) = \frac{1}{1 + \frac{y}{y_0}},$$

with y_0 maximum Snail expression.

Observation 1. *The assumption $\lambda_G = 0$ is made to avoid overloading the model with further parameters. However, other choices of this function can be included in the model.*

Concerning O_2, it exerts an inhibitory mechanism on the transcription of Snail. However, for the definition of the microscopic dynamics and the derivation of the macroscopic model, we keep a general expression for the function $H(O_2)$. We specify the value of the parameter λ_{O_2} in Table 6.1. Rescaling $y/y_0 \rightsquigarrow y$ and $g_s/y_0 \rightsquigarrow g_s$, we simplify the notation as

$$\frac{dy}{dt} = g_s \frac{1}{1+y} H(O_2) - \gamma_s y := G(y, O_2). \tag{6.2.2}$$

with $y \in \mathbf{Y} = (0,1)$. Looking at its quasi-steady state solutions y^*, we observe that

$$\begin{aligned}
\frac{dy}{dt} = 0 &\iff g_s \frac{1}{1+y} H(O_2) - \gamma_s y = 0 \\
&\iff [g_s H(O_2) - \gamma_s y(1+y)] \frac{1}{1+y} = 0 \\
&\iff y(1+y) = \frac{g_s}{\gamma_s} H(O_2) \\
&\iff y^2 + y - \frac{g_s}{\gamma_s} H(O_2) = 0 \\
&\iff y = -\frac{1}{2}\left(1 \pm \sqrt{1 + 4\frac{g_s}{\gamma_s} H(O_2)}\right).
\end{aligned}$$

As y represents a biological quantity accounting for the expression of Snail, no negative values are admitted. Thus, the only acceptable steady-state solution for our system is given by

$$y^* = \frac{1}{2}\left(\sqrt{1 + 4\frac{g_s}{\gamma_s} H(O_2)} - 1\right).$$

Observation 2. *To ensure that the equilibrium distribution y^* belongs to $\mathbf{Y}$, we have to require that*

$$\frac{g_s}{\gamma_s} \max_{\mathbf{x} \in \mathbb{R}^n} \{H(O_2(\mathbf{x}))\} < 2. \tag{6.2.3}$$

If we consider an inhibitory function $H(O_2)$ such that $\lambda_{O_2} = 0$, than the condition reads $g_s < 2\gamma_s$.

Dynamics of cell velocity

Concerning the microscopic velocity $\mathbf{v}$, we model the mechanism by which cells tend to migrate by aligning to two different gradients. Precisely, increasing gradients of oxygen attract tumour cells towards better-oxygenated areas, while tumour cells tend to avoid crowded regions of high cell densities. In both cases, the smaller the amount of Snail expression, the lower the cell's tendency to move along the directions of these gradients. Under these assumptions, the preferred direction of a cell can be modelled by a weighted sum of the two gradients. Thus, velocity dynamics are modelled with the following equation.

$$\frac{d\mathbf{v}}{dt} = g(y, O_2, M) - a_2\mathbf{v}\,, \tag{6.2.4}$$

where the function $g(y, O_2, M)$ describes cell acceleration, while the second term models cell deceleration, with a_2 a positive constant scaling cell deceleration. In fact, cells tend to slow down or randomly move in the absence of external signals. Concerning cell acceleration, we set

$$g(y, O_2, M) = a_1\mathbf{b}(y, O_2, M)\,. \tag{6.2.5}$$

Here, $\mathbf{b}(y, O_2, M)$ is the vector gradient modelling cell alignment along the directions given by the gradient of oxygen O_2 and the gradient of macroscopic tumour cell density M, while a_1 is a positive constant scaling cell acceleration. As introduced above, we assume that the cell's tendency to follow oxygen gradient is enhanced by high Snail expression, which is one of the mechanisms of cell response to hypoxia. At the same time, since low levels of Snail promote high levels of E-cadherin expression [443, 258], which is responsible for cell-cell adhesion, we assume that cell tendency to avoid high cell density region is also positively regulated by y. In fact, high levels of Snail would promote less adhesion between cells and, thus, a more enhanced tendency to escape from the tumour core. Thus, we choose

$$\mathbf{b}(y, O_2, M) = y\left(\beta\frac{\nabla_{\mathbf{x}}O_2}{\sqrt{\left(\frac{O_{2,0}}{X}\right)^2 + |\nabla_{\mathbf{x}}O_2|^2}} - (1-\beta)\frac{\nabla_{\mathbf{x}}M}{\sqrt{\left(\frac{K_M}{X}\right)^2 + |\nabla_{\mathbf{x}}M|^2}}\right). \tag{6.2.6}$$

Here, K_M and $O_{2,0}$ are reference values for tumour cells and oxygen, $X > 0$ is a constant to be selected in correspondence to appropriate time and length scales, while the parameter $\beta \in (0,1)$ weights the contributions of the two tactic terms, depending on the main microenvironmental cues. Thus, (6.2.4) can be written as

$$\begin{aligned}\frac{d\mathbf{v}}{dt} &= a_1 y \left(\beta \frac{\nabla_{\mathbf{x}} O_2}{\sqrt{\left(\frac{O_{2,0}}{X}\right)^2 + |\nabla_{\mathbf{x}} O_2|^2}} - (1-\beta) \frac{\nabla_{\mathbf{x}} M}{\sqrt{\left(\frac{K_M}{X}\right)^2 + |\nabla_{\mathbf{x}} M|^2}} \right) - a_2 \mathbf{v} \\ &=: S(\mathbf{v}, y, O_2, M)\,.\end{aligned} \tag{6.2.7}$$

We observe that $g(y, O_2, M)$ is bounded

$$|g(y, O_2, M)| = |a_1 \mathbf{b}| < a_1$$

and, thus, the speed $s = |\mathbf{v}| < \dfrac{a_1}{a_2} := s_{ub}$, with s_{ub} an upper bound for cell speed. Finally, we complete the microscopic level system by modelling the changes in the cell position $\mathbf{x} \in \mathbb{R}^n$ as

$$\frac{d\mathbf{x}}{dt} = \mathbf{v}\,. \tag{6.2.8}$$

Thus, collecting Equations (6.2.2), (6.2.7), and (6.2.8), the complete system for the microscopic level dynamics reads

$$\begin{cases} \dfrac{d\mathbf{x}}{dt} = \mathbf{v}\,, \\ \dfrac{d\mathbf{v}}{dt} = a_1 y \left(\beta \dfrac{\nabla_{\mathbf{x}} O_2}{\sqrt{\left(\frac{O_{2,0}}{X}\right)^2 + |\nabla_{\mathbf{x}} O_2|^2}} - (1-\beta) \dfrac{\nabla_{\mathbf{x}} M}{\sqrt{\left(\frac{K_M}{X}\right)^2 + |\nabla_{\mathbf{x}} M|^2}} \right) - a_2 \mathbf{v}\,, \\ \dfrac{dy}{dt} = g_s \dfrac{1}{1+y} H(O_2) - \gamma_s y\,. \end{cases} \tag{6.2.9}$$

6.2.2 Mesoscopic scale

At this level, we consider the cell density distribution $p(t,\mathbf{x},\mathbf{v},y) : [0,T]\times\mathbb{R}^n\times\mathbf{V}\times\mathbf{Y}\to\mathbb{R}$, depending on time t, position $\mathbf{x}\in\mathbb{R}^n$, microscopic velocity $\mathbf{v}\in\mathbf{V}$, and internal variable for Snail protein expression $y\in\mathbf{Y}$. In particular, the microscopic velocity vector $\mathbf{v}$ can be written as $\mathbf{v}=s\theta$ with cell speed $s\in(0,s_{ub})$ and cell direction $\theta\in\mathbb{S}^{n-1}$. For describing the mesoscopic dynamics of tumour cells, we consider the following kinetic transport equation:

$$\frac{\partial p}{\partial t}+\nabla_{\mathbf{x}}\cdot(\mathbf{v}p)+\frac{\partial}{\partial y}(G(y,O_2)p)+\nabla_{\mathbf{v}}\cdot(S(\mathbf{v},y,O_2,M)p)=\mathscr{P}[p]\,. \tag{6.2.10}$$

Here, the functions $G(y,O_2)$ and $S(\mathbf{v},y,O_2,M)$ are given by (6.2.2) and (6.2.7), respectively, while the operator $\mathscr{P}[p]$ describes the proliferation process. We generally describe it as

$$\mathscr{P}[p]=\mu_1(M,O_2,s)\int_{\mathbf{Y}}\mu_2(y')\chi(t,\mathbf{x},y,y')p(t,\mathbf{x},\mathbf{v},y')dy'\,.$$

Here, the coefficient function $\mu_1(M,O_2,s)$ accounts for the possible effect of cell speed and oxygen level changes, as well as the crowdedness of the environment, on cell proliferation. Instead, the integral operator, involving the coefficient function $\mu_2(y)$ and the kernel $\chi(t,\mathbf{x},y,y')$, describes the role of Snail expression in the proliferation process. In particular, $\chi(t,\mathbf{x},y,y')$ is the probability kernel representing the likelihood of cells to receive a Snail expression regime y after the division of a cell with expression y'. We propose two possible choices for the proliferation term expression, both based on the assumption that cells' capabilities of moving and proliferating are inversely correlated (go-or-grow dichotomy)[463].

- In the first case, we assume that

$$\mu_1(M,O_2,s):=\mu\frac{s_{ub}-s^*}{s_{ub}}\left(1-\frac{M}{K_M}\right)\frac{O_2}{O_{2,0}+O_2}\quad\text{and}\quad\mu_2(y):=1\,\forall y\in\mathbf{Y}.$$

  Moreover, we assume that the level of Snail expression in a daughter cell is equal to the one of its mother, i.e., the kernel $\chi(t,\mathbf{x},y,y')=\delta(y-y')$. With

these assumptions, the proliferative operator reads

$$\mathscr{P}_1[p] = \mu \frac{s_{ub} - s^*}{s_{ub}} \left(1 - \frac{M}{K_M}\right) \frac{O_2}{O_{2,0} + O_2} p(t, \mathbf{x}, \mathbf{v}, y) \tag{6.2.11}$$

With this choice, the mentioned dichotomous behaviour is taken into account by relating $\mu_1(M, O_2, s)$ to cell speed in a decreasing manner, thus accounting for the impact of y only in an indirect manner, namely through the variation of s. Moreover, as the adaptation of speed to the surrounding environment is faster than the proliferation time, the velocity is approximated by its steady state $\mathbf{v}^*$ and the corresponding speed is denoted by $s^* = |\mathbf{v}^*|$.

- As a second case, we assume that

$$\mu_1(M, O_2, s) := \mu \left(1 - \frac{M}{K_M}\right) \frac{O_2}{O_{2,0} + O_2} \qquad \text{and} \qquad \mu_2(y) := 1 - y \; \forall y \in \mathbf{Y}.$$

With this choice, the mentioned dichotomous behaviour is taken into account in the integral term, which models a reduced proliferation for a high level of Snail expression. In particular, we assume that the kernel does not depend on the level of Snail expression of the mother cell, i.e., $\chi = \chi(t, \mathbf{x}, y)$ and distribution of the level of Snail expression in a daughter cell is symmetrical around the quasi-steady state y^*, i.e.,

$$\int_{\mathbf{Y}} (y - y^*) \chi(t, \mathbf{x}, y) dy = 0$$

and with these assumptions, the proliferative operator reads

$$\mathscr{P}_2[p] := \mu \left(1 - \frac{M}{K_M}\right) \frac{O_2}{O_{2,0} + O_2} \int_{\mathbf{Y}} (1 - y') \chi(t, \mathbf{x}, y) p(t, \mathbf{x}, \mathbf{v}, y') dy' \tag{6.2.12}$$

In both cases, the macroscopic cell density M is given by

$$M := \int_{\mathbf{V}} \int_{\mathbf{Y}} p(t, \mathbf{x}, \mathbf{v}, y) dy d\mathbf{v}. \tag{6.2.13}$$

In both cases, the introduced descriptions of the proliferation process are such that proliferation is reduced for highly motile cells, with a direct or indirect effect of

Snail expression. We will compare, then, the macroscopic models derived in the cases in Section 6.4.

6.3 Derivation of macroscopic system

Due to the high dimensionality of (6.2.10), solving directly this kinetic equation has to face several challenges, especially related to its complexity and a high computational cost. Therefore, in this section, we aim at deducing a macroscopic counterpart of (6.2.10).

6.3.1 Assumptions

In order to obtain a closed system of macroscopic equations from the integration of (6.2.10) w.r.t y and $\mathbf{v}$, we need to make the following assumptions on the moments of the distribution function:

$$\begin{aligned}
&\nabla_{\mathbf{x}} \cdot \int_{\mathbf{V}} (\mathbf{v}-\mathbf{v}^*)(v_i - v_i^*) p d\mathbf{v} \approx 0 \\
&\int_{\mathbf{V}} \int_{\mathbf{Y}} (v_i - v_i^*)(y-y^*) p dy d\mathbf{v} \approx 0 \\
&\int_{\mathbf{V}} \int_{\mathbf{Y}} (y-y^*)^2 p dy d\mathbf{v} \approx 0 \,.
\end{aligned}$$

Precisely, with v_i, we indicate the i-th component of the velocity vector $\mathbf{v}$, while y^* and $\mathbf{v}^*$ are the steady-state solutions of microscopic equations (6.2.2) and (6.2.7), respectively. With these assumptions, we state that some of the second-order moments for the tumour cell distribution w.r.t. deviations of $\mathbf{v}$ and y from their steady-states are negligible, as well as the second-order moment w.r.t y. These are reasonable choices since the microscopic dynamics of protein expression and velocity changes happen faster in comparison to the kinetic behaviour of tumour cells.

Considering the rescaling described in the above Sections, the domains $\mathbf{Y}$ and $\mathbf{V}$ are given by $\mathbf{Y} = (0,1)$ and $\mathbf{V} = B^n_{s_{ub}}(0) = (0, s_{ub}) \times \mathbb{S}^{n-1}$. Following the approach proposed in various references [155, 125, 128, 169], we assume the distribution p to

be compactly supported in the $\mathbf{V} \times \mathbf{Y}$ space. Precisely, for equation (6.2.10), boundary conditions w.r.t. these variables need to be prescribed at the inflow boundary of $\mathbf{Y}$ and $\mathbf{V}$. Considering the dynamics in Ref. (6.2.2), a protein expression state $y \in \partial\mathbf{Y}$ is part of the inflow boundary if $G(y, O_2) \cdot \mathbf{n} \leq 0$ for $\mathbf{n}$ outward normal on the boundary. Given $\partial\mathbf{Y} = \{0, 1\}$, it holds

$$\begin{aligned} &G(0, O_2) \cdot n = g_s H(O_2) \cdot (-1) < 0 \\ &G(1, O_2) \cdot n = (2\, g_s H(O_2) - \gamma_s) \cdot (1) \leq 0 \text{ if condition (6.2.3) holds.} \end{aligned} \tag{6.3.1}$$

Thus, the inflow boundary of $\mathbf{Y}$ coincides with $\partial\mathbf{Y}$ and boundary conditions can be prescribed on the whole $\partial\mathbf{Y}$. Instead, considering the dynamics in (6.2.7) and a velocity vector $\mathbf{v} \in \partial\mathbf{V}$, we have that $|\mathbf{v}| = s_{ub}$ and the outward normal $\mathbf{n} = \mathbf{v}/s_{ub}$. The velocity vector $\mathbf{v}$ is part of the inflow boundary if $S(\mathbf{v}, y, O_2, M) \cdot \mathbf{n} \leq 0$, i.e.,

$$\begin{aligned} S(\mathbf{v}, y, O_2, M) \cdot \mathbf{n} &= \frac{a_1}{s_{ub}} \left(\mathbf{b}(y, O_2, M) \cdot \mathbf{v}\right) - \frac{a_2}{s_{ub}} \left(\mathbf{v} \cdot \mathbf{v}\right) \\ &\leq \frac{a_1}{s_{ub}} |\mathbf{b}(y, O_2, M)|\, |\mathbf{v}| - \frac{a_2}{s_{ub}} |\mathbf{v}|^2 \\ &\leq a_1 - a_2 s_{ub} = 0\,. \end{aligned} \tag{6.3.2}$$

Thus, the inflow boundary of $\mathbf{V}$ coincides with $\partial\mathbf{V}$ and boundary conditions can be prescribed on the whole $\partial\mathbf{V}$. Precisely, (6.3.1) and (6.3.2) allow us to conclude that the characteristics of the transport part of equation (6.2.10) that start in $\mathbb{R}^n \times \mathbf{V} \times \mathbf{Y}$ do not leave this set.

6.3.2 Equation for the moments

Here, we upscale (6.2.10) to obtain the equation for the macroscopic cell density $M(t, \mathbf{x})$. Firstly, we rescale the quantities introduced above as

$$p/K_M \rightsquigarrow p, \quad M/K_M \rightsquigarrow M, \quad O_2/O_{2,0} \rightsquigarrow O_2, \quad \text{and } s^*/s_{ub} \rightsquigarrow s^*.$$

Then, we introduce a small parameter $\varepsilon \ll 1$ to rescale time and space as

$$\hat{t} = \varepsilon^{\kappa} t, \quad \hat{\mathbf{x}} = \varepsilon \mathbf{x},$$

$$\hat{g}_s = \varepsilon^{-\nu} g_s, \quad \hat{\gamma}_s = \varepsilon^{-\nu} \gamma_s,$$

with $\kappa, \nu > 0$. The rescaling of reaction g_s and γ_s means rescaling of dy/dt, while the negative epsilon power is chosen to reflect the fact that these dynamics are the fastest among all included processes. Moreover, assuming that $1/X$ is of order ε, we observe that $\hat{\mathbf{v}}^* = \mathbf{v}^*$. For simplicity of writing, we drop the hat symbol from all variables and, thus, equation (6.2.10) reads

$$\varepsilon^{\kappa} \frac{\partial p}{\partial t} + \varepsilon \nabla_{\mathbf{x}} \cdot (\mathbf{v} p) + \varepsilon^{-\nu} \frac{\partial}{\partial y}(G(y, O_2) p) + \nabla_{\mathbf{v}} \cdot (S(\mathbf{v}, y, O_2, M) p) = \varepsilon^{\kappa} \mathscr{P}_k[p] \tag{6.3.3}$$

where

$$G(y, O_2) = g_s \frac{1}{1+y} H(O_2) - \gamma_s y,$$

$$S(\mathbf{v}, y, O_2, M) = a_1 y \left(\beta \frac{\nabla_{\mathbf{x}} O_2}{\sqrt{1 + |\nabla_{\mathbf{x}} O_2|^2}} - (1-\beta) \frac{\nabla_{\mathbf{x}} M}{\sqrt{1 + |\nabla_{\mathbf{x}} M|^2}} \right) - a_2 \mathbf{v},$$

and $\mathscr{P}_k[p]$ would be given by either

$$\mathscr{P}_1[p] = \mu (1 - s^*) (1 - M) \frac{O_2}{1 + O_2} p(t, \mathbf{x}, \mathbf{v}, y) \tag{6.3.4}$$

or

$$\mathscr{P}_2[p] := \mu (1 - M) \frac{O_2}{1 + O_2} \int_{\mathbf{Y}} (1 - y') \chi(t, \mathbf{x}, y) p(t, \mathbf{x}, \mathbf{v}, y') dy', \tag{6.3.5}$$

which corresponds to the rescaled versions of (6.2.11) or (6.2.12), respectively. Together with the introduced macroscopic tumour density (6.2.13), let us consider the following notations for the moment of the distribution function p:

$$m(t,\mathbf{x},y) := \int_{\mathbf{V}} p(t,\mathbf{x},\mathbf{v},y)d\mathbf{v}, \qquad m^{\mathbf{v}}(t,\mathbf{x},y) := \int_{\mathbf{V}} \mathbf{v}p(t,\mathbf{x},\mathbf{v},y)d\mathbf{v},$$

$$m_i^{\mathbf{v}}(t,\mathbf{x},y) := \int_{\mathbf{V}} v_i p(t,\mathbf{x},\mathbf{v},y)d\mathbf{v}, \qquad M_i^{\mathbf{v}}(t,\mathbf{x}) = \int_{\mathbf{Y}}\int_{\mathbf{V}} v_i p(t,\mathbf{x},\mathbf{v},y)d\mathbf{v}dy,$$

$$M^{\mathbf{v}}(t,\mathbf{x}) = \int_{\mathbf{Y}}\int_{\mathbf{V}} \mathbf{v}p(t,\mathbf{x},\mathbf{v},y)d\mathbf{v}dy, \qquad M^{y}(t,\mathbf{x}) = \int_{\mathbf{Y}}\int_{\mathbf{V}} yp(t,\mathbf{x},\mathbf{v},y)d\mathbf{v}dy.$$

Considering (6.3.3) and integrating w.r.t $\mathbf{v}$ we derive the equation for $m(t,\mathbf{x},y)$, i.e.,

$$\varepsilon^{\kappa}\frac{\partial m}{\partial t} + \varepsilon\nabla_{\mathbf{x}}\cdot m^{\mathbf{v}} + \varepsilon^{-\nu}\frac{\partial}{\partial y}(G(y,O_2)m) + \int_{\mathbf{V}} \nabla_{\mathbf{v}}\cdot S(\mathbf{v},y,O_2,M)pd\mathbf{v} = \varepsilon^{\kappa}\int_{\mathbf{V}} \mathscr{P}_k[p]d\mathbf{v}. \tag{6.3.6}$$

Here

$$\int_{\mathbf{V}} \nabla_{\mathbf{v}}\cdot S(\mathbf{v},y,O_2,M)p\,d\mathbf{v} = 0$$

for the boundary conditions imposed on $\mathbf{v}$, while for the proliferative operator we have either

$$\begin{aligned}\int_{\mathbf{V}} \mathscr{P}_1[p]d\mathbf{v} &= \int_{\mathbf{V}} \mu(1-s^*)(1-M)\frac{O_2}{1+O_2}p(t,\mathbf{x},\mathbf{v},y)d\mathbf{v}\\ &= \mu(1-s^*)(1-M)\frac{O_2}{1+O_2}m(t,\mathbf{x},y)\\ &= \mathscr{P}_1[m]\end{aligned}$$

or

$$\begin{aligned}\int_{\mathbf{V}} \mathscr{P}_2[p]d\mathbf{v} &= \int_{\mathbf{V}} \mu\,(1-M)\frac{O_2}{1+O_2}\int_{\mathbf{Y}}(1-y')\chi(t,\mathbf{x},y)p(t,\mathbf{x},\mathbf{v},y')dy'd\mathbf{v}\\ &= \mu\,(1-M)\frac{O_2}{1+O_2}\int_{\mathbf{Y}}(1-y')\chi(t,\mathbf{x},y)m(t,\mathbf{x},y')dy'\\ &= \mathscr{P}_2[m]\,.\end{aligned}$$

Thus, the equation for $m(t,\mathbf{x},y)$ reads

$$\varepsilon^{\kappa}\frac{\partial m}{\partial t}+\varepsilon\nabla_{\mathbf{x}}\cdot m^{\mathbf{v}}+\varepsilon^{-\nu}\frac{\partial}{\partial y}(G(y,O_2)m)=\varepsilon^{\kappa}\mathscr{P}_k[m]\,. \tag{6.3.7}$$

Considering again (6.3.3), multiplying it by v_i and integrating w.r.t $\mathbf{v}$ we derive the equation for $m_i^{\mathbf{v}}(t,\mathbf{x},y)$, which is the i-th component of the vector $m^{\mathbf{v}}$, i.e.,

$$m^{\mathbf{v}}:=\begin{pmatrix} m_1^{\mathbf{v}} \\ m_2^{\mathbf{v}} \\ \dots \\ m_n^{\mathbf{v}} \end{pmatrix}.$$

The equation for $m_i^{\mathbf{v}}$ reads

$$\begin{aligned}\varepsilon^{\kappa}\frac{\partial m_i^{\mathbf{v}}}{\partial t}+\varepsilon\int_{\mathbf{V}} v_i\nabla_{\mathbf{x}}\cdot(\mathbf{v}p)d\mathbf{v}+\varepsilon^{-\nu}\int_{\mathbf{V}} v_i\frac{\partial}{\partial y}(G(y,O_2)p)d\mathbf{v}\\ +\int_{\mathbf{V}} v_i\nabla_{\mathbf{v}}\cdot(S(\mathbf{v},y,O_2,M)p)d\mathbf{v}=\varepsilon^{\kappa}\int_{\mathbf{V}} v_i\mathscr{P}_k[p]d\mathbf{v}\,.\end{aligned}$$

Here,

$$\begin{aligned}\int_{\mathbf{V}} v_i\nabla_{\mathbf{x}}\cdot(\mathbf{v}p)d\mathbf{v}&=\nabla_{\mathbf{x}}\cdot\int_{\mathbf{V}} v_i(\mathbf{v}p)d\mathbf{v}\\ &=\nabla_{\mathbf{x}}\cdot\int_{\mathbf{V}}(v_i-v_i^*)(\mathbf{v}-\mathbf{v}^*)pd\mathbf{v}+\nabla_{\mathbf{x}}\cdot\int_{\mathbf{V}}(v_i\mathbf{v}^*+v_i^*\mathbf{v}-v_i^*\mathbf{v}^*)pd\mathbf{v}\\ &=\nabla_{\mathbf{x}}\cdot(\mathbf{v}^*m_i^{\mathbf{v}}+v_i^*m^{\mathbf{v}}-v_i^*\mathbf{v}^*m)\end{aligned}$$

for the assumption done on Section 6.3.1, while

$$\int_{\mathbf{V}} v_i \nabla_{\mathbf{v}} \cdot (S(\mathbf{v}, y, O_2, M) p) d\mathbf{v} = \int_{\mathbf{V}} v_i \partial_{v_i}(S_i p) d\mathbf{v} + \sum_{\substack{j=1 \\ j \neq i}}^{N} \int_{\mathbf{V}} v_i \partial_{v_j}(S_j p) d\mathbf{v}$$

$$= \int_{\mathbf{V}_i^c} \int_{\mathbf{V}_i} v_i \partial_{v_i}(S_i p)\, dv_i\, d\tilde{\mathbf{v}} + \sum_{\substack{j=1 \\ j \neq i}}^{N} \int_{\mathbf{V}_j^C} v_i \int_{\mathbf{V}_j} \partial_{v_j}(S_j p)\, dv_j\, d\tilde{\mathbf{v}}$$

where $\mathbf{V}_i^C = \bigcup_{\substack{j=1 \\ j \neq i}}^{N} \mathbf{V}_j$ and $d\tilde{\mathbf{v}}$ is *(n-1)*-th components vector such that

$$\mathbf{v} = (v_i, \tilde{\mathbf{v}}) \in \mathbf{V}_i \times \bigcup_{\substack{j=1 \\ j \neq i}} \mathbf{V}_j .$$

Under the boundary conditions in Section 6.3.1, the second term on the right-hand-side is equal to 0, while using the chain rule, the first term reduces to

$$\int_{\bigcup_{\substack{j=1 \\ j \neq i}}^{N} \mathbf{V}_j} \int_{\mathbf{V}_i} v_i \partial_{v_i}(S_i p)\, dv_i\, d\tilde{\mathbf{v}} = \int_{\bigcup_{\substack{j=1 \\ j \neq i}}^{N} \mathbf{V}_j} \Big[v_i (S_i p)_{|\partial \mathbf{V}_i} - \int_{\mathbf{V}_i} S_i p dv_i \Big] d\tilde{\mathbf{v}} = -\int_{\mathbf{V}} S_i p d\mathbf{v}$$

$$= -a_1 y \left(\beta \frac{(\nabla_{\mathbf{x}} O_2)_i}{\sqrt{1 + |\nabla_{\mathbf{x}} O_2|^2}} - (1-\beta) \frac{(\nabla_{\mathbf{x}} M)_i}{\sqrt{1 + |\nabla_{\mathbf{x}} M|^2}} \right) m + a_2 m_i^{\mathbf{v}}$$

$$= -g_i(y, O_2, M) m + a_2 m_i^{\mathbf{v}} ,$$

where $g_i(y, O_2, M)$ represents the i-th component of the vector function $g(y, M, O_2)$ defined in (6.2.5). Concerning the proliferative operator, we have either

$$\int_{\mathbf{V}} v_i \mathscr{P}_1[p] d\mathbf{v} = \int_{\mathbf{V}} v_i \mu (1 - s^*)(1 - M) \frac{O_2}{1 + O_2} p(t, \mathbf{x}, \mathbf{v}, y) d\mathbf{v}$$

$$= \mu (1 - s^*)(1 - M) \frac{O_2}{1 + O_2} m_i^{\mathbf{v}}(t, \mathbf{x}, y) = \mathscr{P}_1[m_i^{\mathbf{v}}]$$

or

$$\int_{\mathbf{V}} v_i \mathscr{P}_2[p] d\mathbf{v} = \int_{\mathbf{V}} v_i \mu\,(1-M)\,\frac{O_2}{1+O_2} \int_{\mathbf{Y}} (1-y')\chi(t,\mathbf{x},y) p(t,\mathbf{x},\mathbf{v},y') dy' d\mathbf{v}$$

$$= \mu\,(1-M)\,\frac{O_2}{1+O_2} \int_{\mathbf{Y}} (1-y')\chi(t,\mathbf{x},y) m_i^{\mathbf{v}}(t,\mathbf{x},y') dy' = \mathscr{P}_2[m_i^{\mathbf{v}}]\,.$$

Thus, the equation for $m_i^{\mathbf{v}}$ reads

$$\begin{aligned} \varepsilon^{\kappa}\frac{\partial m_i^{\mathbf{v}}}{\partial t} + \varepsilon \nabla_{\mathbf{x}} \cdot (\mathbf{v}^* m_i^{\mathbf{v}} + v_i^* m^{\mathbf{v}} - \varepsilon v_i^* \mathbf{v}^* m) + \varepsilon^{-\nu}\frac{\partial}{\partial y}(G(y,O_2) m_i^{\mathbf{v}}) + \\ - (g_i(y,O_2,M) m - a_2 m_i^{\mathbf{v}}) = \varepsilon^{\kappa} \mathscr{P}_k[m_i^{\mathbf{v}}]\,. \end{aligned} \tag{6.3.8}$$

Therefore, the system for the n+1 variables $(m, m_1^{\mathbf{v}}, m_2^{\mathbf{v}}, .., m_n^{\mathbf{v}})$ is given by

$$\begin{cases} \varepsilon^{\kappa+\nu}\dfrac{\partial m}{\partial t}(t,\mathbf{x},y) + \varepsilon^{1+\nu}\nabla_{\mathbf{x}} \cdot m^{\mathbf{v}}(t,\mathbf{x},y) + \dfrac{\partial}{\partial y}\Big(G(y,O_2) m(t,\mathbf{x},y)\Big) \\ \qquad\qquad = \varepsilon^{\kappa+\nu}\mathscr{P}_k[m](t,\mathbf{x},y)\,, \\ \varepsilon^{\kappa+\nu}\dfrac{\partial m_i^{\mathbf{v}}}{\partial t}(t,\mathbf{x},y) + \varepsilon^{1+\nu}\nabla_{\mathbf{x}} \cdot \big[\mathbf{v}^* m_i^{\mathbf{v}} + v_i^* m^{\mathbf{v}} - v_i^* \mathbf{v}^* m\big](t,\mathbf{x},y) \\ \quad + \dfrac{\partial}{\partial y}\big[G(y,O_2) m_i^{\mathbf{v}}(t,\mathbf{x},y)\big] = \varepsilon^{\nu}\big[g_i(y,O_2,M) m(t,\mathbf{x},y) - a_2 m_i^{\mathbf{v}}(t,\mathbf{x},y)\big] + \\ \quad + \varepsilon^{\kappa+\nu}\mathscr{P}_k[m_i^{\mathbf{v}}](t,\mathbf{x},y) \qquad\qquad \forall i = 1...n\,. \end{cases} \tag{6.3.9}$$

We remark that $\nabla_{\mathbf{x}} \cdot m^{\mathbf{v}} = \sum_{j=1}^{n} \partial_{x_j} m_j^{\mathbf{v}}$. Then, integrating (6.3.7) w.r.t y, for the assumptions in Section 6.3.1 we immediately get

$$\varepsilon^{\kappa}\frac{\partial M}{\partial t}(t,\mathbf{x}) + \varepsilon \nabla_{\mathbf{x}} \cdot M^{\mathbf{v}}(t,\mathbf{x}) = \varepsilon^{\kappa} \int_{\mathbf{Y}} \mathscr{P}_k[m] \tag{6.3.10}$$

where for the proliferative operator, we have either

$$\int_{\mathbf{Y}} \mathscr{P}_1[m]dy = \int_{\mathbf{Y}} \mu(1-s^*)\,(1-M)\,\frac{O_2}{1+O_2} m(t,\mathbf{x},y)dy$$

$$= \mu(1-s^*)\,(1-M(t,\mathbf{x}))\,\frac{O_2}{1+O_2} M(t,\mathbf{x})$$

or

$$\int_{\mathbf{Y}} \mathscr{P}_2[m]dy = \int_{\mathbf{Y}} \mu\,(1-M(t,\mathbf{x}))\,\frac{O_2}{1+O_2} \int_{\mathbf{Y}} (1-y')\chi(t,\mathbf{x},y)m(t,\mathbf{x},y')dy'dy$$

$$= \mu\,(1-M)\,\frac{O_2}{1+O_2} \iint_{\mathbf{Y}} (1-y')\chi(t,\mathbf{x},y)m(t,\mathbf{x},y')dy'dy$$

$$= \mu\,(1-M(t,\mathbf{x}))\,\frac{O_2}{1+O_2}\,(M(t,\mathbf{x})-M^y(t,\mathbf{x}))\,.$$

Instead integrating (6.3.8) w.r.t. y, we obtain

$$\varepsilon^\kappa \frac{\partial M_i^{\mathbf{v}}}{\partial t} + \varepsilon \nabla_{\mathbf{x}} \cdot (\mathbf{v}^* M_i^{\mathbf{v}} + v_i^* M^{\mathbf{v}} - v_i^* \mathbf{v}^* M) + \varepsilon^{-\nu} \int_{\mathbf{Y}} \frac{\partial}{\partial y}(G(y,O_2)m_i^{\mathbf{v}})dy +$$

$$- \int_{\mathbf{Y}} (g_i(y,O_2,M)m - a_2 m_i^{\mathbf{v}})dy = \varepsilon^\kappa \int_{\mathbf{Y}} \mathscr{P}_k[m_i^{\mathbf{v}}]dy\,,$$

where the first integral vanishes for the boundary conditions in Section 6.3.1. Concerning the second integral on the left-hand-side, we have

$$\int_{\mathbf{Y}} (g_i(y,O_2,M)m - a_2 m_i^{\mathbf{v}})dy = \tilde{g}_i(O_2,M)M^y - a_2 M_i^{\mathbf{v}}\,,$$

where

$$\tilde{g}_i(O_2,M) = a_1 \left(\beta \frac{(\nabla_{\mathbf{x}} O_2)_i}{\sqrt{1+|\nabla_{\mathbf{x}} O_2|^2}} - (1-\beta)\frac{(\nabla_{\mathbf{x}} M)_i}{\sqrt{1+|\nabla_{\mathbf{x}} M|^2}} \right). \tag{6.3.11}$$

Instead, the proliferative operator reads either

$$\int_{\mathbf{Y}} \mathscr{P}_1[m_i^{\mathbf{v}}]dy = \int_{\mathbf{Y}} \mu(1-s^*)\,(1-M)\,\frac{O_2}{1+O_2} m_i^{\mathbf{v}}(t,\mathbf{x},y)dy$$

$$= \mu(1-s^*)\,(1-M)\,\frac{O_2}{1+O_2} M_i^{\mathbf{v}}(t,\mathbf{x}) = \mathscr{P}_1[M_i^{\mathbf{v}}]$$

or

$$\int_{\mathbf{Y}} \mathscr{P}_2[m_i^{\mathbf{v}}]dy = \int_{\mathbf{Y}} \mu\,(1-M)\,\frac{O_2}{1+O_2} \int_{\mathbf{Y}} (1-y')\chi(t,\mathbf{x},y) m_i^{\mathbf{v}}(t,\mathbf{x},y')dy'dy$$

$$= \mu\,(1-M)\,\frac{O_2}{1+O_2}\left(M_i^{\mathbf{v}} - \iint_{\mathbf{Y}} y'\chi(t,\mathbf{x},y) m_i^{\mathbf{v}}(t,\mathbf{x},y')dy'dy \right)$$

$$= \mu\,(1-M)\,\frac{O_2}{1+O_2}\cdot$$

$$\left(M_i^{\mathbf{v}} - \int_{\mathbf{Y}}\int_{\mathbf{V}} (v_i - v_i^*) y\, p(t,\mathbf{x},\mathbf{v},y)dyd\mathbf{v} - v_i^* \int_{\mathbf{Y}}\int_{\mathbf{V}} y\, p(t,\mathbf{x},\mathbf{v},y)dyd\mathbf{v} \right)$$

$$= \mu\,(1-M)\,\frac{O_2}{1+O_2}\left(M_i^{\mathbf{v}} - \int_{\mathbf{Y}}\int_{\mathbf{V}} (v_i - v_i^*)(y-y^*)\, p(t,\mathbf{x},\mathbf{v},y)dyd\mathbf{v} \right.$$

$$\left. - y^* \int_{\mathbf{Y}}\int_{\mathbf{V}} (v_i - v_i^*) p(t,\mathbf{x},\mathbf{v},y)dyd\mathbf{v} - v_i^* \int_{\mathbf{Y}}\int_{\mathbf{V}} y\, p(t,\mathbf{x},\mathbf{v},y)dyd\mathbf{v} \right)$$

$$= \mu\,(1-M(t,\mathbf{x}))\,\frac{O_2}{1+O_2}\left(M_i^{\mathbf{v}}(t,\mathbf{x}) - y^* M_i^{\mathbf{v}}(t,\mathbf{x}) - v_i^* M^y(t,\mathbf{x}) + y^* v_i^* M(t,\mathbf{x})\right).$$

Therefore, we obtain

$$\begin{aligned} \varepsilon^\kappa \frac{\partial M_i^{\mathbf{v}}}{\partial t}(t,\mathbf{x}) + \varepsilon \nabla_{\mathbf{x}} \cdot \left[\mathbf{v}^* M_i^{\mathbf{v}} + v_i^* M^{\mathbf{v}} - v_i^* \mathbf{v}^* M\right](t,\mathbf{x}) + \\ - \left[\tilde{g}_i(O_2,M) M^y(t,\mathbf{x}) - a_2 M_i^{\mathbf{v}}(t,\mathbf{x})\right] = \varepsilon^\kappa \int_{\mathbf{Y}} \mathscr{P}_k[m_i^{\mathbf{v}}]dy\,. \end{aligned} \tag{6.3.12}$$

Finally, multiplying (6.3.7) by y and integrating w.r.t. y we obtain

$$\varepsilon^{\kappa}\frac{\partial M^{y}}{\partial t}+\varepsilon\nabla_{\mathbf{x}}\cdot\int\limits_{\mathbf{Y}}yM^{\mathbf{v}}dy+\varepsilon^{-\nu}\int\limits_{\mathbf{Y}}y\frac{\partial}{\partial y}\Big(G(y,O_2)m\Big)dy=\varepsilon^{\kappa}\int\limits_{\mathbf{Y}}y\,\mathscr{P}_k[m](t,\mathbf{x},y)dy\,.$$

Here,

$$\begin{aligned}\nabla_{\mathbf{x}}\cdot\int\limits_{\mathbf{Y}}yM^{\mathbf{v}}dy&=\nabla_{\mathbf{x}}\cdot\int\limits_{\mathbf{Y}}\int\limits_{\mathbf{V}}y(\mathbf{v}p)d\mathbf{v}dy\\&=\nabla_{\mathbf{x}}\cdot\left(\int\limits_{\mathbf{Y}}\int\limits_{\mathbf{V}}(\mathbf{v}-\mathbf{v}^{*})(y-y^{*})pd\mathbf{v}dy+\int\limits_{\mathbf{Y}}\int\limits_{\mathbf{V}}(\mathbf{v}^{*}y+\mathbf{v}y^{*}-\mathbf{v}^{*}y^{*})pd\mathbf{v}dy\right)\\&=\nabla_{\mathbf{x}}\cdot(\mathbf{v}^{*}M^{y}+y^{*}M^{\mathbf{v}}-\mathbf{v}^{*}y^{*}M)\end{aligned}$$

thanks to the assumption in Section 6.3.1, while

$$\begin{aligned}\int\limits_{\mathbf{Y}}y\frac{\partial}{\partial y}\Big(G(y,O_2)m\Big)dy&=\left(y(Gm)_{|\partial\mathbf{Y}}-\int\limits_{\mathbf{Y}}G(y,O_2)mdy\right)\\&=-\int\limits_{\mathbf{Y}}G(y,O_2)mdy\\&=-\int\limits_{\mathbf{Y}}\left(g_s\frac{1}{1+y}H(O_2)-\gamma_s y\right)mdy\\&=\gamma_s M^{y}-g_sH(O_2)\int\limits_{\mathbf{Y}}\frac{1}{1+y}mdy\,.\end{aligned}$$

Considering the Taylor expansion of $\dfrac{1}{1+y}$ around y^{*} we get

$$\begin{aligned}\frac{1}{1+y}&=\frac{1}{1+y^{*}+y-y^{*}}\\&\approx(1+y^{*})^{-1}-(1+y^{*})^{-2}(y-y^{*})+(1+y^{*})^{-3}(y-y^{*})^{2}+O((y-y^{*})^{2})\,.\end{aligned}$$

Thus, ignoring the higher-order terms of this expansion, we obtain

$$\int_{\mathbf{Y}} \frac{1}{1+y} m dy = \int_{\mathbf{Y}} \left((1+y^*)^{-1} - (1+y^*)^{-2}(y-y^*) + (1+y^*)^{-3}(y-y^*)^2\right) m\, dy$$

$$= (1+y^*)^{-1} M - (1+y^*)^{-2} M^y + y^*(1+y^*)^{-2} M\,,$$

i.e.,

$$\int_{\mathbf{Y}} y \frac{\partial}{\partial y}\Big(G(y,O_2)p\Big) dy = \gamma_s M^y - g_s \frac{H(O_2)}{1+y^*}\left(M - \frac{1}{1+y^*}(M^y - y^* M)\right)$$

$$= -g_s \frac{H(O_2)}{(1+y^*)^2}(1+2y^*)M + \left(\gamma_s + g_s \frac{H(O_2)}{(1+y^*)^2}\right) M^y\,.$$

The proliferative operator, instead, reads either

$$\int_{\mathbf{Y}} y \mathscr{P}_1[m] dy = \int_{\mathbf{Y}} \mu(1-s^*)(1-M)\frac{O_2}{1+O_2} y m(t,\mathbf{x},y) dy$$

$$= \mu(1-s^*)(1-M)\frac{O_2}{1+O_2} M^y(t,\mathbf{x})$$

or

$$\int_{\mathbf{Y}} y \mathscr{P}_2[m] dy = \int_{\mathbf{Y}} \mu\,(1-M)\frac{O_2}{1+O_2} \int_{\mathbf{Y}} y(1-y')\chi(t,\mathbf{x},y) m(t,\mathbf{x},y') dy' dy$$

$$= \mu\,(1-M)\frac{O_2}{1+O_2}\left(\int_{\mathbf{Y}} y\chi(t,\mathbf{x},y) dy \int_{\mathbf{Y}} (1-y') m(t,\mathbf{x},y') dy'\right)$$

$$= \mu\,(1-M)\frac{O_2}{1+O_2}(M-M^y)\left(\int_{\mathbf{Y}} (y-y^*)\chi(t,\mathbf{x},y) dy + y^* \int_{\mathbf{Y}} \chi(t,\mathbf{x},y) dy\right)$$

$$= \mu\,(1-M(t,\mathbf{x}))\frac{O_2}{1+O_2} y^* \left[M(t,\mathbf{x}) - M^y(t,\mathbf{x})\right]\,.$$

Thus, the equation for M^y reads

$$\begin{aligned}
&\varepsilon^{\kappa}\frac{\partial M^y}{\partial t}(t,\mathbf{x})+\varepsilon\nabla_{\mathbf{x}}\cdot\left[\mathbf{v}^*M^y+y^*M^{\mathbf{v}}-\mathbf{v}^*y^*M\right](t,\mathbf{x})+\\
&\qquad-\varepsilon^{-\nu}g_s\frac{H(O_2)}{(1+y^*)^2}(1+2y^*)M(t,\mathbf{x})+\varepsilon^{-\nu}\left(\gamma_s+g_s\frac{H(O_2)}{(1+y^*)^2}\right)M^y(t,\mathbf{x})\\
&\qquad=\varepsilon^{\kappa}\int_{\mathbf{Y}}y\mathscr{P}_k[m](t,\mathbf{x},y)dy\,.
\end{aligned}\tag{6.3.13}$$

Thus, the system for $M(t,\mathbf{x})$, $M^{\mathbf{v}}(t,\mathbf{x})$, and $M^y(t,\mathbf{x})$ reads

$$\left\{\begin{aligned}
&\varepsilon^{\kappa-1}\frac{\partial M}{\partial t}(t,\mathbf{x})+\nabla_{\mathbf{x}}\cdot M^{\mathbf{v}}(t,\mathbf{x})=\varepsilon^{\kappa-1}\int_{\mathbf{Y}}\mathscr{P}_k[m](t,\mathbf{x},y)dy,\\
&\varepsilon^{\kappa}\frac{\partial M_i^{\mathbf{v}}}{\partial t}(t,\mathbf{x})+\varepsilon\nabla_{\mathbf{x}}\cdot\left[\mathbf{v}^*M_i^{\mathbf{v}}+v_i^*M^{\mathbf{v}}-v_i^*\mathbf{v}^*M\right](t,\mathbf{x})+\\
&\qquad-\left(\tilde{g}_i(O_2,M)M^y(t,\mathbf{x})-a_2M_i^{\mathbf{v}}(t,\mathbf{x})\right)=\varepsilon^{\kappa}\int_{\mathbf{Y}}\mathscr{P}_k[m_i^{\mathbf{v}}](t,\mathbf{x},y)dy,\quad\forall i=1...n,\\
&\varepsilon^{\kappa+\nu}\frac{\partial M^y}{\partial t}(t,\mathbf{x})+\varepsilon^{1+\nu}\nabla_{\mathbf{x}}\cdot\left[\mathbf{v}^*M^y+y^*M^{\mathbf{v}}-\mathbf{v}^*y^*M\right](t,\mathbf{x})+\\
&\qquad-g_s\frac{H(O_2)}{(1+y^*)^2}(1+2y^*)M(t,\mathbf{x})+\left(\gamma_s+g_s\frac{H(O_2)}{(1+y^*)^2}\right)M^y(t,\mathbf{x})\\
&\qquad=\varepsilon^{\kappa+\nu}\int_{\mathbf{Y}}y\mathscr{P}_k[m](t,\mathbf{x},y)dy\,.
\end{aligned}\right.\tag{6.3.14}$$

Now, we consider the expansion of the previously introduced model in the form.

$$\begin{aligned}
M&=M_0+\varepsilon M_1+O(\varepsilon^2),\\
M^{\mathbf{v}}&=M_0^{\mathbf{v}}+\varepsilon M_1^{\mathbf{v}}+O(\varepsilon^2),\\
M^y&=M_0^y+\varepsilon M_1^y+O(\varepsilon^2),
\end{aligned}$$

such that $M_0 = \lim_{\varepsilon\to 0} M$. As the focus of this study is on the tumour response to hypoxia and, thus, the influence of the environmental chemotactic cue given by the oxygen levels, cell movement has a very clear directional component. Therefore, following the well-established literature [223, 51, 50, 177, 126], we consider here a hyperbolic limit of the moment system (6.3.14), i.e., we choose $\kappa = 1$. Passing formally to the limit $\varepsilon \to 0$ in (6.3.14), from the first equation we get

$$\frac{\partial M_0}{\partial t}(t,\mathbf{x}) + \nabla_{\mathbf{x}} \cdot M_0^{\mathbf{v}}(t,\mathbf{x}) = \int_{\mathbf{Y}} \mathscr{P}_k[m_0](t,\mathbf{x},y)dy\,, \tag{6.3.15}$$

where m_0 is the zero-order term in the expansion of the moment $m(t,\mathbf{x},y)$. Then, from the equation for $M_i^{\mathbf{v}}$ in (6.3.14), we get

$$\tilde{g}_i(O_2,M_0)M_0^y - a_2 M_{i,0}^{\mathbf{v}} = 0 \iff M_{i,0}^{\mathbf{v}} = \frac{\tilde{g}_i(O_2,M_0)}{a_2} M_0^y \tag{6.3.16}$$

that, considering the vector $M_0^{\mathbf{v}}$ with i-th component $M_{i,0}^{\mathbf{v}}$, means

$$M_0^{\mathbf{v}} = \frac{\tilde{\mathbf{g}}(O_2,M_0)}{a_2} M_0^y \tag{6.3.17}$$

with

$$\tilde{\mathbf{g}}(O_2,M_0) = a_1 \left(\beta \frac{\nabla_{\mathbf{x}} O_2}{\sqrt{1+|\nabla_{\mathbf{x}} O_2|^2}} - (1-\beta)\frac{\nabla_{\mathbf{x}} M_0}{\sqrt{1+|\nabla_{\mathbf{x}} M_0|^2}} \right).$$

Finally, from the last equation in (6.3.14), we obtain

$$-g_s \frac{H(O_2)}{(1+y^*)^2}(1+2y^*)M_0 + \left(\gamma_s + g_s \frac{H(O_2)}{(1+y^*)^2}\right) M_0^y = 0$$

$$\Updownarrow$$

$$M_0^y = \frac{g_s H(O_2)(1+2y^*)}{\gamma_s (1+y^*)^2 + g_s H(O_2)} M_0\,. \tag{6.3.18}$$

Thus, substituting (6.3.18) into (6.3.17), and the latter in (6.3.15), we obtain the following equation for the evolution of the macroscopic cell density M_0

$$\frac{\partial M_0}{\partial t}(t,\mathbf{x}) + \nabla_{\mathbf{x}} \cdot [F(y^*, O_2(\mathbf{x}))M_0(t,\mathbf{x})\tilde{\tilde{g}}(O_2,M_0)] = \mathbb{P}_k[M_0](t,\mathbf{x}) \tag{6.3.19}$$

where

$$\tilde{\mathbf{g}}(O_2, M_0) = a_1 \left(\beta \frac{\nabla_{\mathbf{x}} O_2}{\sqrt{1+|\nabla_{\mathbf{x}} O_2|^2}} - (1-\beta) \frac{\nabla_{\mathbf{x}} M}{\sqrt{1+|\nabla_{\mathbf{x}} M|^2}} \right).$$

We set the velocity field (or chemotactic sensitivity) as

$$F(y^*, O_2(\mathbf{x})) := \frac{a_1}{a_2} \frac{g_s H(O_2(\mathbf{x}))(1+2y^*)}{\gamma_s (1+y^*)^2 + g_s H(O_2(\mathbf{x}))}, \tag{6.3.20}$$

while the proliferative operator is given by either

$$\mathbb{P}_1[M_0](t,\mathbf{x}) = \int_{\mathbf{Y}} \mathscr{P}_1[m_0](t,\mathbf{x},y)dy = \mu(1-s^*)(1-M_0(t,\mathbf{x})) \frac{O_2(\mathbf{x})}{1+O_2(\mathbf{x})} M_0(t,\mathbf{x}) \tag{6.3.21}$$

or

$$\begin{aligned} \mathbb{P}_2[M_0](t,\mathbf{x}) &= \int_{\mathbf{Y}} \mathscr{P}_2[m_0](t,\mathbf{x},y)dy \\ &= \mu\,(1-M_0(t,\mathbf{x}))\, \frac{O_2(\mathbf{x})}{1+O_2(\mathbf{x})} \left(1 - \frac{a_2}{a_1} F(y^*, O_2(\mathbf{x}))\right) M_0(t,\mathbf{x}). \end{aligned} \tag{6.3.22}$$

Since we are interested in the impact of the microscopic protein expression of the cell on the overall macroscopic evolution of the population, for the simulation described in Section 6.4, we also analyse the evolution of M_0^y that is linked to the average expression of the Snail protein in the cell population. Thus, discarding the zero subscripts, the resulting macroscopic system reads

$$\begin{cases} \dfrac{\partial M}{\partial t}(t,\mathbf{x}) + \nabla_{\mathbf{x}} \cdot [F(y^*, O_2(\mathbf{x})) M(t,\mathbf{x}) \tilde{g}(O_2, M)] = \mathbb{P}_k[M](t,\mathbf{x}), \\ \\ M^y(t,\mathbf{x}) = \dfrac{a_2}{a_1} F(y^*, O_2(\mathbf{x})) M(t,\mathbf{x}). \end{cases} \tag{6.3.23}$$

6.4 Numerical experiments

We perform 2D numerical simulations of the resulting macroscopic system (6.3.23) to analyse *in-silico* scenarios of tumour progression under varied oxygen conditions and Snail expressions. Numerical simulations are conducted using a self-developed code in Python 3.10.12, whose details are provided in Section 6.4.1. The parameter values used for the simulations are reported in Table 6.1. Sections 6.4.2, 6.4.3, 6.4.4, and 6.4.5 present the results of the four main numerical experiments we performed.

Experiment 1 - In Section 6.4.2, we analyse the differences in cell migration and Snail distribution over time between a chemotactic-dominated scenario and an anti-crowding-dominated scenario by varying the value of the weighting parameter β and, thus, its impact on cell motion.

Experiment 2 - In Section 6.4.3, we investigate the impact of Snail expression on cell proliferation, and we compare the model's evolution using two different choices of the proliferative operator given in (6.2.11) and (6.2.12).

Experiment 3 - In Section 6.4.4, we show our model capabilities to quantitatively replicate experimental results from two different studies on human cancer cells. Firstly, we consider the findings of [305] regarding the effect of Snail over-expression or knockdown on the migration capability of human breast cancer cells. Secondly, we refer to the comparison presented in Ref. [459], where the effects of hypoxia and a combination of hypoxia and Snail knockdown on the motility of human hepatocarcinoma cells are studied.

Experiment 4 - In Section 6.4.5, we analyse the hypoxia-driven spatial distribution of Snail expression within a tumour, and we show its consistency with the results shown in Ref. [305].

6.4.1 Numerical method

To perform numerical simulations of the model, we adapt the numerical method presented in Ref. [88] to our problem structure. In detail, we rewrite the first equation of (6.3.23) as

$$\frac{\partial M}{\partial t}(t,\mathbf{x}) = -T(y^*,O_2,M)(t,\mathbf{x}) + \mathbb{P}_k[M](t,\mathbf{x}) \tag{6.4.1}$$

Parameter	Description	Value (unit)	Source
g_s	basal Snail transcription rate	1.5 (molecules $\cdot$ min^{-1})	[304]
γ_s	basal Snail degradation rate	0.0021 (min^{-1})	[303]
a_1/a_2	scaling velocity parameter	0.1 (mm $\cdot$ min^{-1})	This work
β	weighting parameter for tactic contribution	varying in [0-1]	This work
μ	tumour proliferation rate	[6-9]$\cdot$ 10^{-4} (min^{-1})	[445, 128]

Table 6.1 **Model parameters.** The table provides the dimensional values for the parameters involved in setting (6.3.23) that are used in the numerical experiments.

where

$$\mathrm{T}(y^*, O_2, M))(t,\mathbf{x}) = \nabla_{\mathbf{x}} \cdot \left[F(y^*, O_2(\mathbf{x}))M(t,\mathbf{x}) \left(\beta \frac{\nabla_{\mathbf{x}} O_2(\mathbf{x})}{\sqrt{1+|\nabla_{\mathbf{x}} O_2(\mathbf{x})|^2}} - (1-\beta) \frac{\nabla_{\mathbf{x}} M(t,\mathbf{x})}{\sqrt{1+|\nabla_{\mathbf{x}} M(t,\mathbf{x})|^2}} \right) \right] \tag{6.4.2}$$

rules the movement of cells while $\mathbb{P}_k[M](t,\mathbf{x})$ is the proliferation term defined in (6.3.21) ($k=1$) and (6.3.22) ($k=2$). Setting $\mathbf{x}=(x_1,x_2)$, we consider the geometric domain $\Omega = [x_{1,min}, x_{1,max}] \times [x_{2,min}, x_{2,max}] \subseteq \mathbb{R}^2$, where we introduce a uniform Cartesian mesh consisting of the cells $C_{j,k} := [x_{1,j-\frac{1}{2}}, x_{1,j+\frac{1}{2}}] \times [x_{2,k-\frac{1}{2}}, x_{2,k+\frac{1}{2}}]$, for $j = 0,\dots,N_{x_1}$ and for $k = 0,\dots,N_{x_2}$, of size $\Delta x_1 \times \Delta x_2$. We adopt a splitting method, accounting first for the conservative part $\mathrm{T}(y^*, O_2, M)$ and, then, for the reaction term $\mathbb{P}_k[M]$. Precisely, defining

$$M_{j,k}(t) \approx \frac{1}{\Delta x_1 \Delta x_2} \int_{C_{j,k}} M(x_1,x_2) d\mathbf{x},$$

for the conservative part we adopt the general semi-discrete finite-volume scheme given by

$$T_{j+\frac{1}{2},k} = u^+_{j+\frac{1}{2},k} M^E_{j,k} + u^-_{j+\frac{1}{2},k} M^W_{j+1,k}$$

$$T_{j,k+\frac{1}{2}} = v^{+}_{j+\frac{1}{2},k} M^{N}_{j,k} + v^{-}_{j+\frac{1}{2},k} M^{S}_{j+1,k}\,.$$

Here:

- $(\cdot)^{+}$ and $(\cdot)^{-}$ indicate the positive and negative parts of their arguments, respectively, i.e., $(\cdot)^{+} = \max\{0,\cdot\}$ and $(\cdot)^{-} = \min\{0,\cdot\}$;
- the apices E, W, N, S indicate East, West, North and South and correspond to the evaluation of the piecewise linear reconstruction using the following first-order truncation of Taylor expansion

  $$\tilde{M}(x_1,x_2) = M_{j,k} + (\partial_{x_1} M)_{j,k}(x_1 - x_{1,j}) + (\partial_{x_2} M)_{j,k}(x_2 - x_{2,k}), \quad (x_1,x_2) \in C_{j,k}$$

  at the cell interfaces $(x_{1,j+\frac{1}{2}}, x_{2,k})$, $(x_{1,j-\frac{1}{2}}, x_{2,k})$, $(x_{1,j}, x_{2,k+\frac{1}{2}})$, $(x_{1,j}, x_{2,k-\frac{1}{2}})$, respectively;
- defined

  $$\begin{aligned} U_{j,k} =& F(y^{*}(x_{1,j},x_{2,k}), O_2(x_{1,j},x_{2,k}))\cdot \\ & \left(\beta \frac{\nabla_{\mathbf{x}} O_2(x_{1,j},x_{2,k})}{\sqrt{1+|\nabla_{\mathbf{x}} O_2(x_{1,j},x_{2,k})|^2}} - (1-\beta) \frac{\nabla_{\mathbf{x}} M(t,x_{1,j},x_{2,k})}{\sqrt{1+|\nabla_{\mathbf{x}} M(t,x_{1,j},x_{2,k})|^2}} \right), \end{aligned}$$

  then $u := U_{x_1}$ and $v := U_{x_2}$ are the components of U along the horizontal and vertical axis respectively.

Note that the derivatives in the middle points are evaluated as

$$(\partial_{x_1} M)_{j+\frac{1}{2},k} = \frac{M_{j+1,k} - M_{j,k}}{\Delta x_1}, \qquad (\partial_{x_2} M)_{j,k+\frac{1}{2}} = \frac{M_{j,k+1} - M_{j,k}}{\Delta x_2}$$

while the derivatives in the nodes are initially evaluated as

$$(\partial_{x_1} M)_{j,k} = \frac{M_{j+1,k} - M_{j-1,k}}{2\Delta x_1}, \qquad (\partial_{x_2} M)_{j,k} = \frac{M_{j,k+1} - M_{j,k-1}}{2\Delta x_2}$$

and then corrected using a generalised minmod limiter in order to preserve the positivity of the linear reconstruction $\tilde{M}$ (for further details, see [88]). For the time discretisation, we use the forward Euler method. We denote the discretised time step with apex l, i.e.,

$$t^{l} = t_0 + \sum_{i=1}^{l-1} \Delta t_i\,.$$

In order to optimize the performances, we use adaptive time steps obtained by imposing the positivity-preserving CFL.

$$\Delta t_l \leq \Delta \mathscr{T}_l := \min\left\{\frac{\Delta x_1}{4a}, \frac{\Delta x_2}{4b}\right\}$$

where $a = \max_{j,k}\left(|u^l_{j+\frac{1}{2},k}|\right)$ and $b = \max_{j,k}\left(|v^l_{j,k+\frac{1}{2}}|\right)$. Therefore, starting from a discretised initial condition $M^0_{j,k}$ provided for each $j = 0,\dots,N_{x_1}$ and for $k = 0,\dots,N_{x_2}$, the numerical scheme reads

$$\begin{cases} M^{l+\frac{1}{2}}_{j,k} = M^l_{j,k} - \dfrac{\Delta t_l}{\Delta x_1}\left(T^l_{j+\frac{1}{2},k} - T^l_{j-\frac{1}{2},k}\right) - \dfrac{\Delta t_l}{\Delta x_2}\left(T^l_{j,k+\frac{1}{2}} - T^l_{j,k-\frac{1}{2}}\right) \\ M^{l+1}_{j,k} = M^{l+\frac{1}{2}}_{j,k} + \Delta t_l P^{l+\frac{1}{2}}_{j,k} \end{cases} \tag{6.4.3}$$

for $l = 1,\dots,N_l$. In the proposed experiments, we set the spatial domain $\Omega = [0,50]\times[0,50]\,\text{mm}^2$ and we consider the time $t \in [0,T]$, with $T > 0$. Dealing with a limited domain, we set no entry flux boundary conditions.

6.4.2 Experiment 1: chemotactic or anti-crowding dominated motion

In this first experiment, we simulate our model with the aim of comparing cell behaviours in two different scenarios. We consider a first scenario in which cell movement is dominated by a chemotactic attraction toward increasing oxygen concentrations, strongly reducing the impact of the natural cell anti-crowding mechanisms. Instead, in a second scenario, we emphasize the role of anti-crowding dynamics, which helps cells to avoid highly dense regions.

Considering the macroscopic system (6.3.23), we note that the parameter $\beta \in (0,1)$ impacts the motility behaviour of cells, weighting the influence of oxygen and cell density gradients on the direction of tumour cell migration. Higher values of β imply a stronger impact of chemotaxis compared to anti-crowding dynamics. Thus, to capture the two described scenarios, we choose $\beta = 0.98$ to emphasize the role of chemotactic movement toward increasing oxygen concentrations, while $\beta = 0.8$ to account for a stronger effect of the anti-crowding mechanism. In our experiment,

we consider a fixed oxygen source located in the top-right corner of the domain Ω and whose expression is given by

$$O(\mathbf{x}) = A_O\, e^{-\frac{(\mathbf{x}-\mathbf{x}_O)^2}{\theta_O^2}} \tag{6.4.4}$$

with $A_O = 0.8$, $\mathbf{x}_O = [45,45]\,\text{mm}$, and $\theta_O = 34\,\text{mm}$. For the tumour cell, we assume that the initial tumour mass $M(t=0,\mathbf{x}) := M_0(\mathbf{x})$ is located in the opposite (bottom-left) corner of the domain Ω and it is defined as

$$M_0(\mathbf{x}) = A_M\, e^{-\frac{(\mathbf{x}-\mathbf{x}_M)^2}{\theta_M^2}} \tag{6.4.5}$$

with $A_M = 0.9$, $\mathbf{x}_M = [9,9]\,\text{mm}$, and $\theta_M = 3\,\text{mm}$. The initial configuration of this setting is shown in Fig. 6.1.

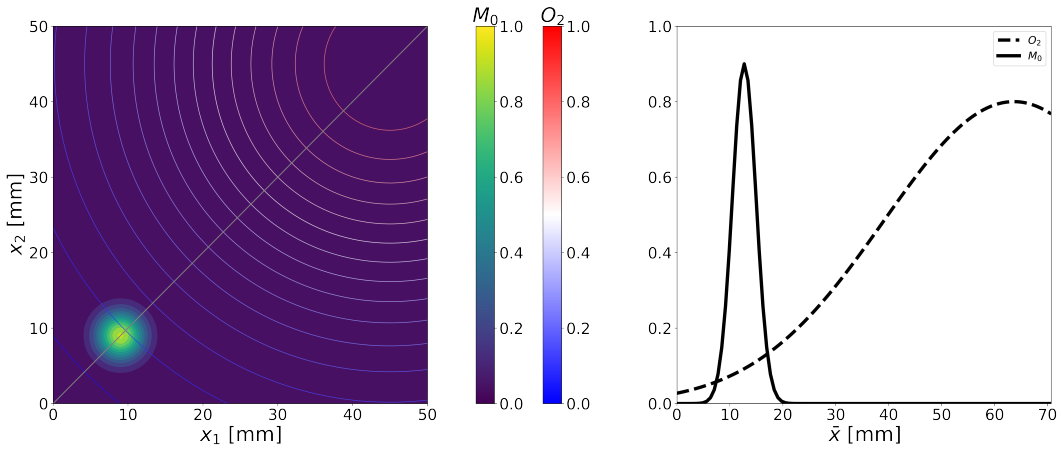

Fig. 6.1 **Experiment 1: initial conditions and setting.** Left: initial Gaussian distribution of the tumour cells M_0, centred in $\mathbf{x}_M = [9,9]\,\text{mm}$ in the domain $\Omega = [0,50]\times[0,50]\,\text{mm}^2$, together with the level plot for the fixed Gaussian distribution of oxygen $O_2(\mathbf{x})$, centred in $\mathbf{x}_O = [45,45]\,\text{mm}$. Right: 1D profiles of tumour (continuous line) and oxygen (dashed line) distributions along the bisecting line (light grey line in the 2D plot) of the domain Ω. $\bar{x}$ indicates the spatial position along this bisecting line.

To better characterised the dynamics we divide the domain in 4 different zones depending on the relative oxygen conditions, which trigger cell motility and proliferation. Fig. 6.2 and the related Table 6.2 summarize the combination of the environmental conditions in each of these areas in the 1D section the domain.

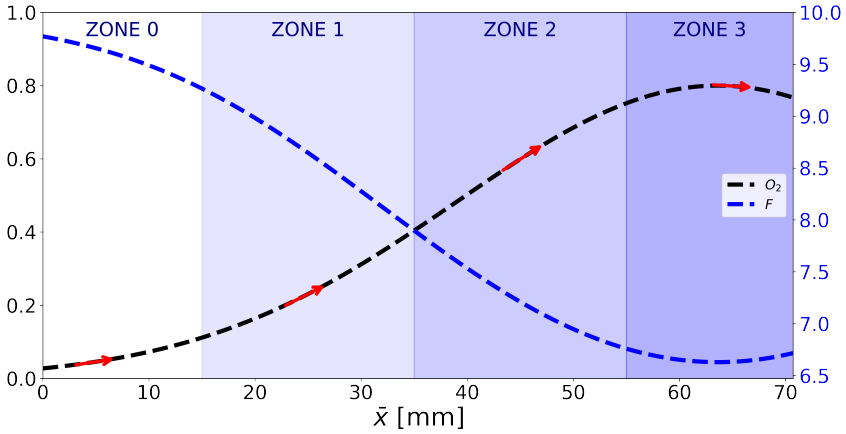

Fig. 6.2 **Experiment 1: spatial distribution of the environmental conditions triggering cell motility.** Graphical representation of the 1D section defined by the bisecting line of the domain Ω and its subdivision into four different areas depending on the combination between high/low motility, random/directed motion, and low/high proliferation capability of the tumour cells. Profiles of the oxygen distribution (black dashed line) and tactic sensitivity $F(y^*, O_2(\bar{x}))$ (blue dashed line) are shown, together with the oxygen gradient direction (red arrow). $\bar{x}$ indicates the spatial position along this bisecting line.

Zone	O_2	∇O_2	F	motility	direction	proliferation
0	low	low	high	high	random	low
1	low	high	high	high	directed	low
2	high	high	low	low	directed	high
3	high	low	low	low	random	high

Table 6.2 **Summary of the environmental conditions.** The table reports and summarizes the information received by the cells in the four identified areas shown in Fig. 6.2.

The results of this first experiment are illustrated in Fig. 6.3. Precisely, the left column refers to the simulations obtained for $\beta = 0.98$ (chemotactic dominated scenario), while the right column to $\beta = 0.8$ (anti-crowding dominated scenario).

The simulations track the evolution of the tumour mass over a time range of approximately $T = 21$ days. In the first row of Fig. 6.3, we illustrate the progression of the tumour mass in the domain Ω at four different temporal steps. The contour plot illustrates the density map, while the contour lines represent the tumour's edge (defined by a density threshold corresponding to 10% of the carrying capacity).

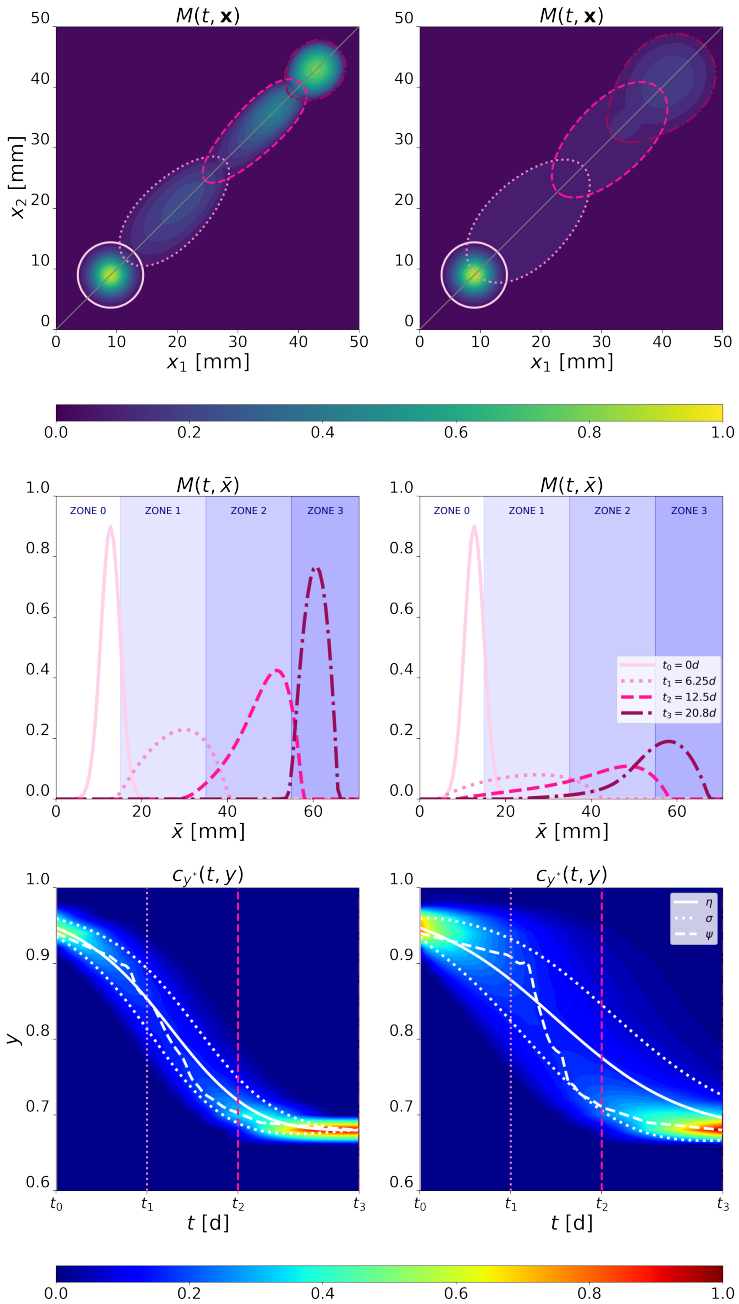

Fig. 6.3 **Experiment 1: chemotactic or anti-crowding dominated motion.** Evolution of model (6.3.23) in a chemotactic dominated ($\beta = 0.98$, left column) or anti-crowding dominated ($\beta = 0.8$, right column) scenario. Top row: evolution of the tumour mass in the domain $\Omega = [0,50] \times [0,50]\,\text{mm}^2$ at four different time steps, i.e., initial time $t = 0$ d (continuous light pink line), and progression at $t = 6.25$ d (dot pink line), $t = 12.5$ d (dashed dark pink line), and $t = 20.8$ d (dot-dashed purple line). Middle row: 1D profiles of the tumour mass evolution along the bisecting line (light grey line in the 2D plot) of the domain Ω at the same time steps used in the top row. $\bar{x}$ indicates the spatial position along this bisecting line. Bottom row: evolution in the (t,y)-space of the distribution $c_{y^*}(t,y)$, together with its mean $\eta(t)$, standard deviation $\sigma(t)$, and mode $\psi(t)$. References to the four selected time steps are repeated in each graph using consistent color and line styles. Parameter values are set as reported in Table 6.1.

To better visualize the differences in the tumour evolution in the two scenarios we consider a 1D section of the domain Ω illustrating the tumour profile along the bisecting line. Moreover, in order to account for the epigenetic trait information, for every value $y \in \mathbf{Y}$ and every time t, we evaluate the fraction of tumour mass having an equilibrium Snail expression y^* lower than y, i.e.,

$$C_{y^*}(t,y) = \int_{D_y} \bar{M}(t,\mathbf{x})d\mathbf{x}$$

where $D_y = \{\mathbf{x} \in \Omega : y^*(\mathbf{x}) \in (-\infty, y)\}$ and $\bar{M}(t,\mathbf{x})$ is the normalised tumour density distribution, and we introduce the quantity

$$c_{y^*}(t,y) = \partial_y C_{y^*}(t,y)\,,$$

which provides an indication of the fraction of mass that, at a given time t, has a certain Snail expression $y \in \mathbf{Y}$. For this quantity, we evaluate mean $\eta(t)$, mode $\psi(t)$, and standard deviation $\sigma(t)$ as

$$\eta(t) = \int_{\mathbf{Y}} y c_{y^*}(t,y)dy\,,$$

$$\psi(t) = \arg\max_{y\in\mathbf{Y}} \left(c_{y^*}(t,y)\right)\,,$$

$$\sigma(t) = \sqrt{\int_{\mathbf{Y}} y^2 c_{y^*}(t,y)dy - \eta(t)^2}\,.$$

Integrating the information about the environmental conditions (Fig. 6.2) with the data concerning the expression of Snail (third row of Fig. 6.3), we can better grasp the features characterizing the two depicted scenarios. Depending on β, cell behaviours towards more oxygenated regions show evident differences. Initially, low oxygen concentration corresponds to high Snail expression and they collectively contribute both to a high tactic sensitivity $F(y^*,O)$, driving cell drift, and a low proliferation rate. Thus, as the mass is situated in an area characterised by low oxygenation, this oxygen deprivation triggers cell motility. As the mass progresses towards the upper right corner (temporal step t_1), the low oxygen levels still induce a more motile than proliferative cell phenotype, enforced by a high mean $\eta(tt)$ of $c_{y^*}(y,t)$ (depicted

in the third row of Fig. 6.3). By time t_1, the mass has spread enough to develop a smoother profile, resulting in a reduced density gradient in favour of stronger chemotactic motion due to the oxygen gradient. This is particularly evident for $\beta = 0.98$. Cells are, thus, accelerated and move more compactly towards the oxygen source, and this is evidenced in both columns of Fig. 6.3 by the reduction in mass width orthogonal to the chemotactic gradient between times t_1 and t_2, confirming cell convergence towards the oxygen Gaussian distribution. As the cells reach areas closer to the source (temporal step t_2), a still strong oxygen gradient is countered by increased oxygenation levels, and, thus, inhibition of motility in favor of an enhanced proliferation rate. This results also in lower level of $\eta(t)$ (third row of Fig. 6.3). This combination results in masses developing a distinct tail to the left, with some cells remaining outside the region of orderly motility due to lower oxygen levels. Many motile cells originating from less oxygenated areas "push" against a slowing front where cells are less motile, but contributes to the increase of the density due to their proliferative capability. At final time t_3, the mass has reached a region characterised by high oxygenation levels with an almost negligible oxygen gradient. At this stage, ordered motile dynamics become nearly absent and the mean $\eta(t)$ has stabilize its value. This is particularly evident in the scenario with $\beta = 0.98$, where the mass tends to regain a more radial symmetry around its centroid and slightly expands under the influence of density pressure driven by proliferative dynamics and anti-crowding.

From a qualitatively viewpoint, in both scenarios the dynamics are initially characterised by a diffusing mass that expands orthogonally to the direction of chemotactic motion (more evident for $\beta = 0.8$) and then by a direct movement towards the oxygen source. Moreover, in both case, the presence of flux-limited operator in the drift term determines steep and well-defined invasion fronts, reducing the typical artificial tails characterizing linear diffusion and, thus, its excessive influence on cell spread. However, comparing the experiments conducted for the two scenarios makes it evident how conditions favoring anti-crowding dynamics can lead to significant changes in tumour shape even for small variations in β. In fact, when anti-crowding is the dominant mechanisms, cells tend to move toward the location of the oxygen source with an evident large spread in the domain, with respect to the chemotactic dominated scenario, which shows cells compactly migrating towards more oxygenated regions. Looking at the tumour profiles at time t_1 and t_2 (second row in Fig. 6.3), the differences in height and the size of the mass support are evident.

This is reflected also in the evolution of mean, mode, and standard deviation of $c_{y^*}(y,t)$. In fact, for higher value of β, mean η and mode ψ show a similar trends over time. However, the lower β, the greater the differences in their evolution. This is because the larger spread of the tumour mass and the slower cell movement in the domain keeps the value of the mean higher for longer time. Moreover, this determines the wider variety of values covered by the distribution and, thus, a larger standard deviation.

6.4.3 Experiment 2: impact of Snail expression on cell proliferation

In the second experiment, we focus on the proliferative dynamics characterizing tumour cells. Here, we concentrate on the scenario where chemotaxis drives cell motility and compare two proliferative models: $\mathbb{P}_1$, introduced in (6.3.21), and $\mathbb{P}_2$, introduced in (6.3.22). It is worth to recall that the shared elements in these two modelling choices are: (i) a proliferative rate inversely proportional to cell density; (ii) an increase in proliferative activity correlating with higher levels of available oxygen; (iii) the assumption that cells capabilities of moving and proliferating are inversely correlated. What distinguishes these approaches is the epigenetic or phenotypic characterisation of the duality between cells' motility and proliferative dynamics. In the case of $\mathbb{P}_1$, the factor $(1-s^*)$ ensures a direct correlation between higher Snail expression and lower proliferative activity. Instead, the environmental factor has a indirect impact on the trade-off characterisation, as oxygen density influences proliferative activity only indirectly by determining Snail expression. In contrast, for $\mathbb{P}_2$, the factor $1-\frac{a_2}{a_1}F\big(y,O_2(\mathbf{x})\big)$ ensures that the proliferative activity decreases as $F(y^*,O_2(\mathbf{x}))$ increases, which is directly proportional to Snail expression and inversely proportional to oxygen density.

To compare these two proliferative choices, we conduct two simulations under identical environmental and initial conditions for tumour and oxygen, as well as model parameters. The only difference between the simulations lies in the formulation of the proliferative term. To quantify the results, we consider the 1D section of the domain Ω along the bisector (similar to the previous example) and we shown the difference between the tumour densities resulting from (6.3.23) with $\mathbb{P}_1$ ($M_{\mathbb{P}_1}(t,\mathbf{x})$) or $\mathbb{P}_2$ ($M_{\mathbb{P}_2}(t,\mathbf{x})$).

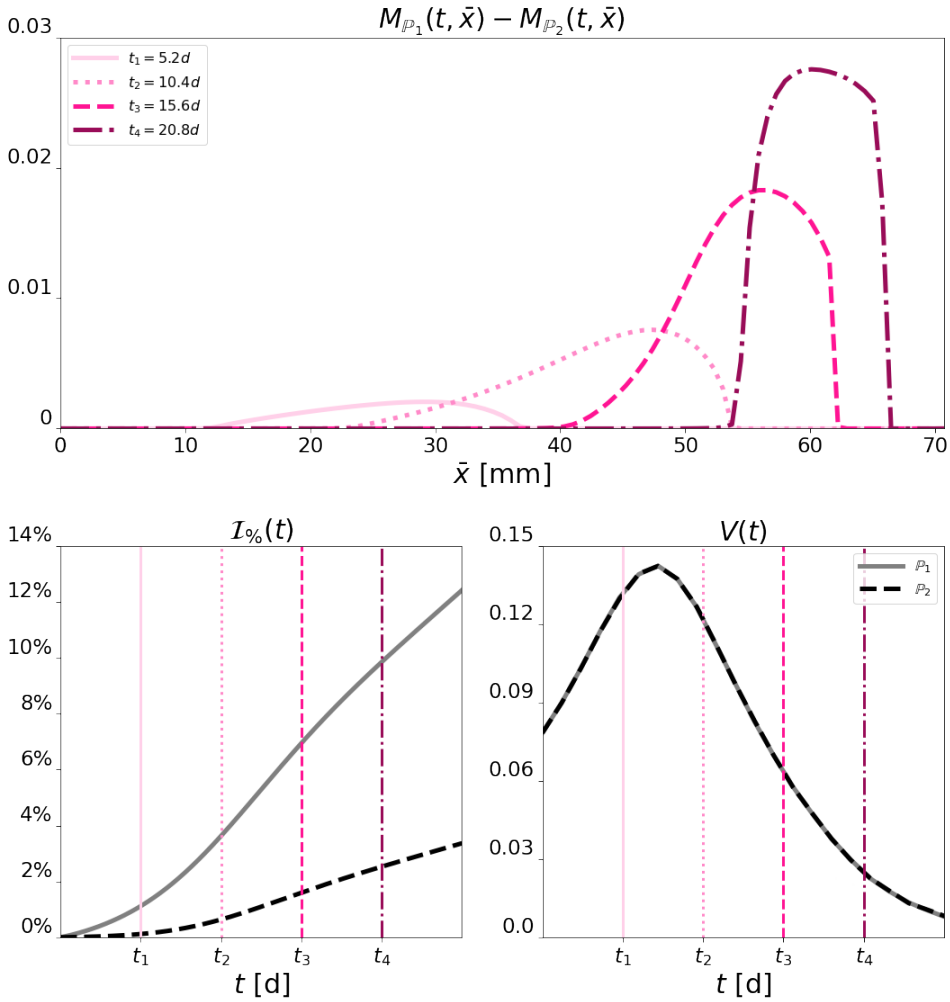

Fig. 6.4 **Experiment 2: impact of Snail expression on cell proliferation.** Top: 1D profiles representing the evolution along the bisecting line of Ω of the difference between the solution of the tumour equation in (6.3.23) with the proliferation term given in (6.3.21) ($M_{\mathbb{P}_1}(t,\bar{x})$) and the solution of tumour equation (6.3.23) with the proliferation term given in (6.3.22) ($M_{\mathbb{P}_2}(t,\bar{x})$) at four different time steps, i.e., $t = 5.2$ d, $t = 10.4$ d, $t = 15.6$ d, and $t = 20.8$ d. $\bar{x}$ indicates the spatial position along this bisecting line. Bottom: quantification of percentage tumour mass increment (left plot) and velocity of the centre of mass (right plot) over time with the two choices of the proliferative operator. Continuous grey line refers to the choice (6.3.21), while dashed black line to (6.3.22). The four time steps represented in the plot in the top rows are reported here with four different vertical bars. Vertical lines in the bottom-row plots mark the selected times depicted in the first row. References to the four selected time steps are repeated in each graph using consistent color and line styles. Parameter values are set as reported in Table 6.1.

We consider four equally spaced time points: $t_1 = 5.2$d, $t_2 = 10.4$d, $t_3 = 15.6$d, and $t_4 = 20.8$d. Moreover, defined

$$Q(t) = \int_{\Omega} M(t,\mathbf{x})d\mathbf{x} \tag{6.4.6}$$

as the *total amount of tumour cells* in the spatial domain, we introduce the *percentage mass increment* of tumour mass from the initial configuration as

$$\mathscr{I}_{\%}(t) = 100 \cdot \left(\frac{Q(t) - Q(0)}{Q(0)} \right), \tag{6.4.7}$$

and we compute the *centre of mass* of the tumour

$$\boldsymbol{\Upsilon}(t) = \int_{\Omega} \mathbf{x}\bar{M}_0(t,\mathbf{x})d\mathbf{x}$$

with $\bar{M}(t,\mathbf{x}) = M(t,\mathbf{x})/Q(t)$, and the *velocity of the centre of mass*

$$\mathbf{V}(t) = \partial_t \boldsymbol{\Upsilon}(t)\,. \tag{6.4.8}$$

Results of this experiment are shown in Fig. 6.4. Precisely, the top row illustrates the evolution of the difference between $M_{\mathbb{P}_1}(t,\mathbf{x})$ and $M_{\mathbb{P}_2}(t,\mathbf{x})$ along the 1D section In the bottom row, we depict the temporal evolution of the mass increase $\mathscr{I}_{\%}$ defined in (6.4.7) (left plot) and the velocity of the centre of mass along the bisector defined in (6.4.8) (right plot).

Analysis of the plot in the top row reveals that the difference is consistently positive, supporting the intuitive notion of a stronger trade-off is determined in the case of $\mathbb{P}_2$, where both the epigenetic trait and environmental factor directly contribute to module proliferation. This observation is further corroborated by the bottom-row plots of Fig. 6.4. In fact, we notice that the final percentage increment is six times higher for the epigenetic-driven duality ($\mathbb{P}_1$) with respect to the case in which there is a direct contribution of both epigenetic trait and environmental factor ($\mathbb{P}_2$). Considering, instead, the evolution for the centre of mass, from the bottom-right plot of Fig. 6.4 we observe a perfect overlap of its velocity dynamics throughout the experiment. This confirm the fact that any observed differences can

be solely attributed to the proliferative dynamics resulting from the distinct trade-offs under analysis, while the spatial dynamics are not affected.

6.4.4 Experiment 3: impact of Snail expression and hypoxia on cancer cell migration

In this third experiment, we aim to assess the impact of Snail expression and exposure to hypoxia on cancer cell migration. Our goal is to validate our model by replicating experimental results which investigate the role of hypoxia in cell migration and determine whether motility can be triggered by various factors, including inhibition of Snail expression. To achieve this, we specify the parameter values and the environmental conditions such that they replicate different experimental scenarios, and we compare the resulting outcomes with the empirical observations.

We consider the parameter g_s, accounting for Snail transcription and, from the reference value of $g_s = 1.5\,(\text{molecules} \cdot \text{min}^{-1})$, used for the experiments in Section 6.4.2 and 6.4.3, we define up-regulation and down-regulation of Snail expression by setting as $g_s = 2.1\,(\text{molecules} \cdot \text{min}^{-1})$ and $g_s = 0.9\,(\text{molecules} \cdot \text{min}^{-1})$ respectively. This corresponds to variations of 0.6 above and below the reference value. To ensure that the condition (2) holds true, we consider a slightly higher value for Snail degradation rate, i.e., $\gamma_s = 0.03\,(\text{min}^{-1})$. For the environmental conditions, by referring to [320] we considering levels of oxygenation compatible with physoxia (7%) and pathological hypoxia (1%) and we set the scaling factor $O_{2,0}$ such that, in our model, these conditions are represented by $O_2 = 0.7$ and $O_2 = 0.1$.

We aim at qualitatively replicate the experimental findings proposed in Ref. [305] and [459]. Specifically, in Ref. [305] the authors investigate human breast cancer cells (cell lineage MCF-7). In their experiment, they analyse fold change in tumour cell migration by migration assays using Transwell migration chambers. Precisely, cells were suspended in upper Transwell chambers in serum-free media and allowed to migrate towards a serum gradient (10%) in the lower chamber for 6 hours. The experiment was repeated in normoxic conditions by transiently overexpressed and silenced the protein expression. Instead, in Ref. [459], the authors employed a similar methodology with the human hepatocellular carcinoma (cell lines HepG2). They assessed cell motility with the same migration assays comparing experiments conducted in normoxic and hypoxic conditions.

We replicate the chamber setup by considering our square domain Ω intersected by a vertical membrane aligned parallel to the x_2 axis and positioned at $x_1 = 25\,\text{mm}$. A 1D section of the chamber setup is illustrated in Fig. 6.5.

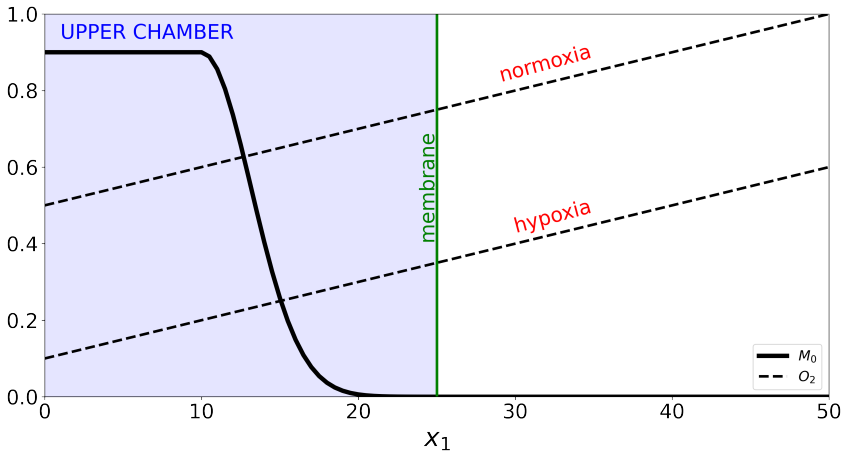

Fig. 6.5 **Experiment 3: initial conditions and setting.** 1D graphical illustration of the setting implemented for studying the impact of Snail expression and hypoxia on cancer migration. The domain Ω is divided in two chambers. Tumour cells are distributed in the upper chamber, i.e., in $\Omega_U = [0,25] \times [0,50]\,\text{mm}^2$, accordingly to Equation (6.4.9), while no cells are initially located in the bottom chamber, i.e., in $\Omega_B = [25,50] \times [0,50]\,\text{mm}^2$. Two different linear oxygen distributions (for normoxia and hypoxia scenarios) are represented as dashed black lines. The central membrane dividing the two chamber is shown in green.

Here, the left part of the domain (for $x_1 < 25$ mm) represents the upper chamber, where all cell are initially distribute following

$$M_0(\mathbf{x}) = \begin{cases} A & x_1 < x_s \\ Ae^{-\dfrac{(x_1 - x_s)^2}{\theta_M^2}} & x_1 \geq x_s \end{cases} \tag{6.4.9}$$

where $A = 0.9$, $x_s = 10\,\text{mm}$ and $\theta_M = 3\,\text{mm}$. We consider the following linear expression for the oxygen distribution

$$O(\mathbf{x}) = O_{min} + \frac{(O_{max} - O_{min})}{50} x_1$$

with $O_{min} = 0.7$ and $O_{max} = 1.0$ in normoxic conditions, while $O_{min} = 0.1$ and $O_{max} = 0.4$ in hypoxic conditions. This choice establish a fixed oxygen gradient

along the chamber, which is consistent with the biological setting. We conduct five experiments, which are summarised in Table 6.3.

Name	Oxygenation	Snail expression
A	normoxia	control
B	normoxia	up-regulated
C	normoxia	down-regulated
D	hypoxia	control
E	hypoxia	down-regulated

Table 6.3 **Summary of the conducted experiments.** The table show the information regarding tissue oxygenation and Snail expression in the five scenarios analysed in Section 6.4.4.

Under the aforementioned conditions, we allow cells to move in response to the environmental stimuli for a duration of $T = 6$ hours. Subsequently, we measure the quantity of tumour mass that has pass through the membrane as

$$\tilde{Q}(t) = \int_{\Omega_B} M(t,\mathbf{x})d\mathbf{x},$$

where $\Omega_B = [25,50] \times [0,50]\,\text{mm}^2$ represents the bottom chamber.

We designate the results obtained in scenario (A) as the control case and we use them to normalize the outcomes of other experiments. Fig. 6.6 collects all the results of the five tests. In the top row, we show the results related to the scenarios (A), (B), and (C) and we compare them with the data taken from [305], while in the bottom row, we refer to scenarios (A), (D), and (E) and we compare the results with the data taken from [459]. Each column comprises two column. The left column provides a map of the values taken by $F(y^*, O_2)$ against various levels of oxygenation and Snail transcription, while the right column provides histograms comparing the results of *in-vitro* (black) and *in-silico* (black) experiments. As clearly shown in Fig. 6.6, for both the breast cancer and the hepatocarcinoma cases the model is able to effectively replicate the experimental data.

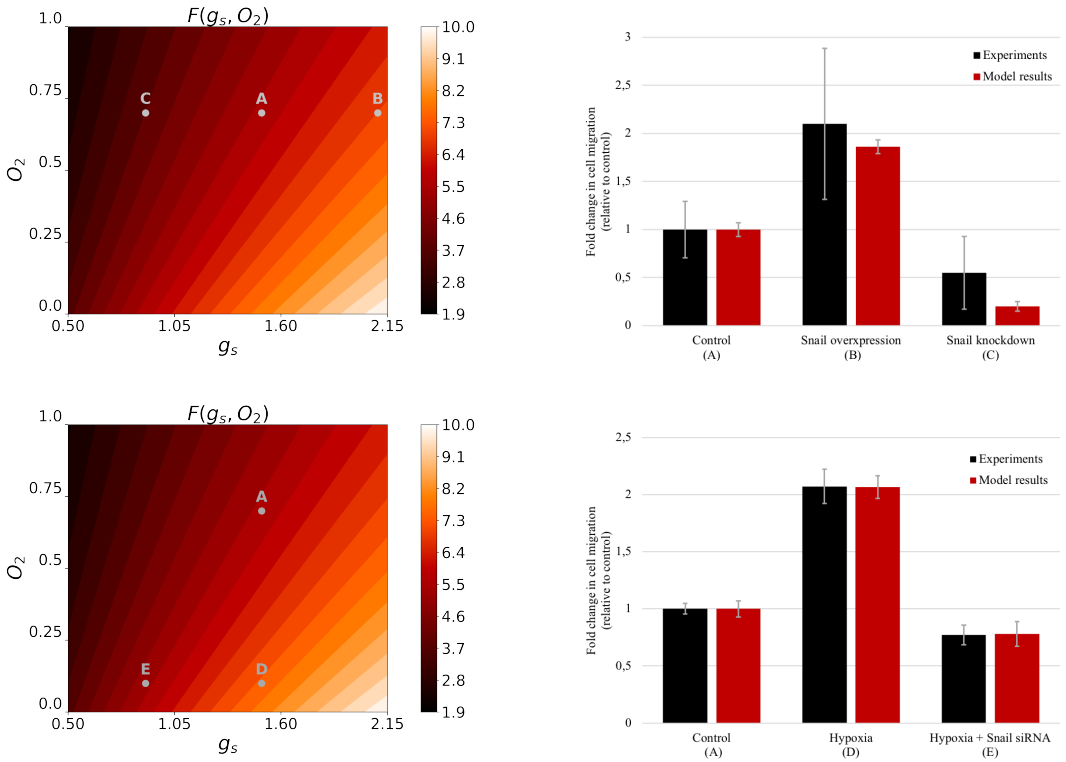

Fig. 6.6 **Experiment 3: impact of Snail expression and hypoxia on cancer cell migration.** Left: representation of the level curve of the tactic sensitivity $F(g_s, O_2)$ with respect to the Snail transcription rate g_s and the oxygen concentration O_2. The parameter combination referring to the five analysed scenario are indicated with grey bullets. Right: comparison between *in-vitro* (black) and *in-silico* (red) results concerning the fold change in cell migration (relative to control) in the five different scenarios. Precisely, in the top-right panel MCF-7 cells are considered in normal condition (control, scenario A), with Snail overexpression (B), or with Snail knockdown (C). *In-vitro* data were obtained from Figure 3B and 3D in Ref. [305]. In the bottom-right panel, HepG2 cells are considered in normoxic condition (control, A), hypoxic conditions (D), or hypoxic condition with Snail silencing (E). *In-vitro* data were obtained from Figure 1A and 1E in Ref. [459]. In both cases, *In-silico* results were obtained by simulating equation (6.3.23) under normoxic and hypoxic conditions and for different values of the parameter g_s. Means $\pm$ std in the simulations are obtained by varying the the parameter g_s within a range of ± 0.05.

Specifically, in the case of breast cancer, the *in-silico* results closely resemble those obtained in the *in-vitro* experiments for the scenario (B). In scenario (C), any discrepancy appears to be merely apparent, as the *in-silico* results fall within the error band of the *in-vitro* experiment, which notably exhibits a wider range of data. For hepatocarcinoma, there is a remarkably high correspondence between the *in-vitro* and *in-silico* data, experiments (D) and (E) showing a notable match. Furthermore, it

is worth to note how the level curves of $F(g_s, O_2)$ (left column of Fig. 6.6) provides insight into the experimental observations. Specifically, previous experimental work have noticed that the knockdown of Snail nullifies the motility advantage gained under hypoxic conditions (D) compared to normoxia (A), bringing the motility to a level comparable with the control case (as observable by comparing scenarios (E) and (A)). In our case, this can be observed by looking at the location of the corresponding bullets on the level plot of $F(g_s, O_2)$: (A) and (E) are located, in fact, almost on the same level curve. This implies that, given equal cell density (ensured at least initially with identical initial conditions) and a consistent oxygen gradient (maintained at the same value across the domain and for all oxygenation conditions in this experiment), the term governing cell speed assumes comparable values in both experiments (slightly lower for (E)). Consequently, the discrepancy in the number of cells passing through the membrane between the two cases differs slightly.

6.4.5 Experiment 4: hypoxia-driven ring structure in tumour and Snail distributions

As last experiment, we refer to additional results shown in Ref. [305], where the authors investigate the expression of Snail in non-invasive ductal carcinoma in situ (DCIS), an early breast cancer, considering a model system of hypoxia *in-vivo*. Considering a central necrotic area, their analysis of several DCIS samples revealed a typical pattern of HIF-1α expression, with increasing staining intensity approaching the areas necrosis, and similar spatial distribution for the nuclear expression of Snail, gradually increased approaching the necrosis (see Figure 6 in Ref. [305]). In particular, the authors show that hypoxia induces Snail expression independently of other EMT markers.

To qualitatively reproduce these observations, we simulate an initial tumour mass located in the centre of the domain. We assume an oxygen distribution that decreases towards the centre of the domain, leading to highly hypoxic (or necrotic) areas due to higher consumption in regions with higher cell density. The initial condition for cancer cells is given in (6.4.5) setting $A_M = 1$, $\mathbf{x}_M = [25, 25]\,\text{mm}$, and $\theta_M = 5\,\text{mm}$ while for oxygen the fixed distribution is given by $1 - O(\mathbf{x})$, with $O(\mathbf{x})$ defined in (6.4.4) and $A_O = 0.8$, $\mathbf{x}_O = [25, 25]\,\text{mm}$, and $\theta_O = 13\,\text{mm}$. The initial condition for tumour and oxygen are illustrate in Fig. 6.7.

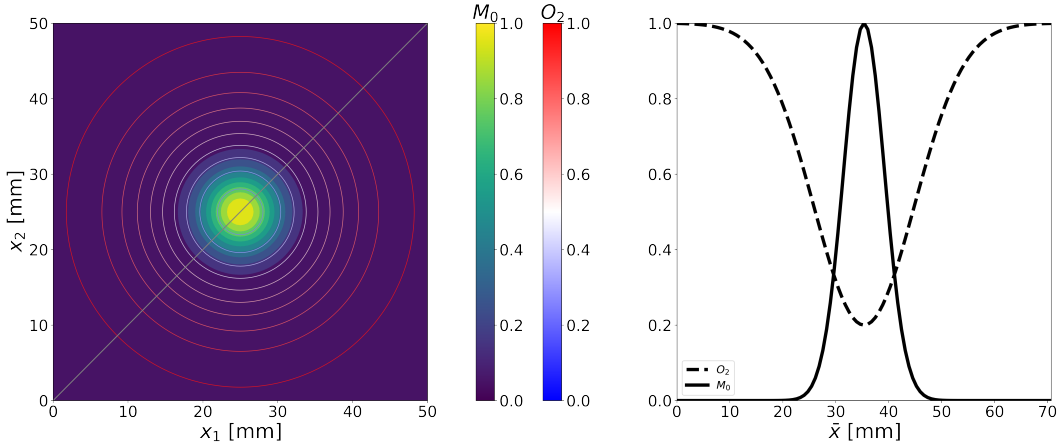

Fig. 6.7 **Experiment 4: initial conditions and setting.** Left: initial Gaussian distribution of the tumour cells M_0, located at position $\mathbf{x}_M = [25,25]$ mm in the domain $\Omega = [0,50] \times [0,50]\,\text{mm}^2$, together with the level plot for the fixed Gaussian distribution of oxygen O_2, located at the same position. Right: 1D profiles of tumour (continuous line) and oxygen (dashed line) distribution along the bisecting line (light grey line in the 2D plot) of the domain Ω. $\bar{x}$ indicates the spatial position along this bisecting line.

Fig. 6.8 collects the results of this experiment at four time steps: $t_0 = 0$, $t_1 = 5$, $t_2 = 20$, and $t_3 = 35$ hours. The first row depict a 2D representation of the tumour mass, including density map and contour lines highlighting the tumour's edge (defined by a density threshold corresponding to 10% of the carrying capacity). From system (6.3.23), defined the average expression of the Snail protein in the cell population as

$$\bar{M}^y(t,\mathbf{x}) = \frac{M^y(t,\mathbf{x})}{M(t,\mathbf{x})} = \frac{a_2}{a_1} F(y^*, O_2) \quad \text{for } \mathbf{x} \in \text{supp}(M)\,, \tag{6.4.10}$$

we illustrate its evolution in the second row of Fig. 6.8. Finally, in the third row, the 1D section of the tumour mass density along the bisector at the four specified times is shown.

We observe that, initially, both anti-crowding and chemotactic stimuli point in the same direction, which tend to move the cells away from the central hypoxic region, where cell density is high and oxygen concentration is low. Consequently, in this initial phase, cell migration is rapid, leading to a fast transformation of the peaked initial Gaussian cell distribution into a smoother bubble profile (as shown at time t_1).

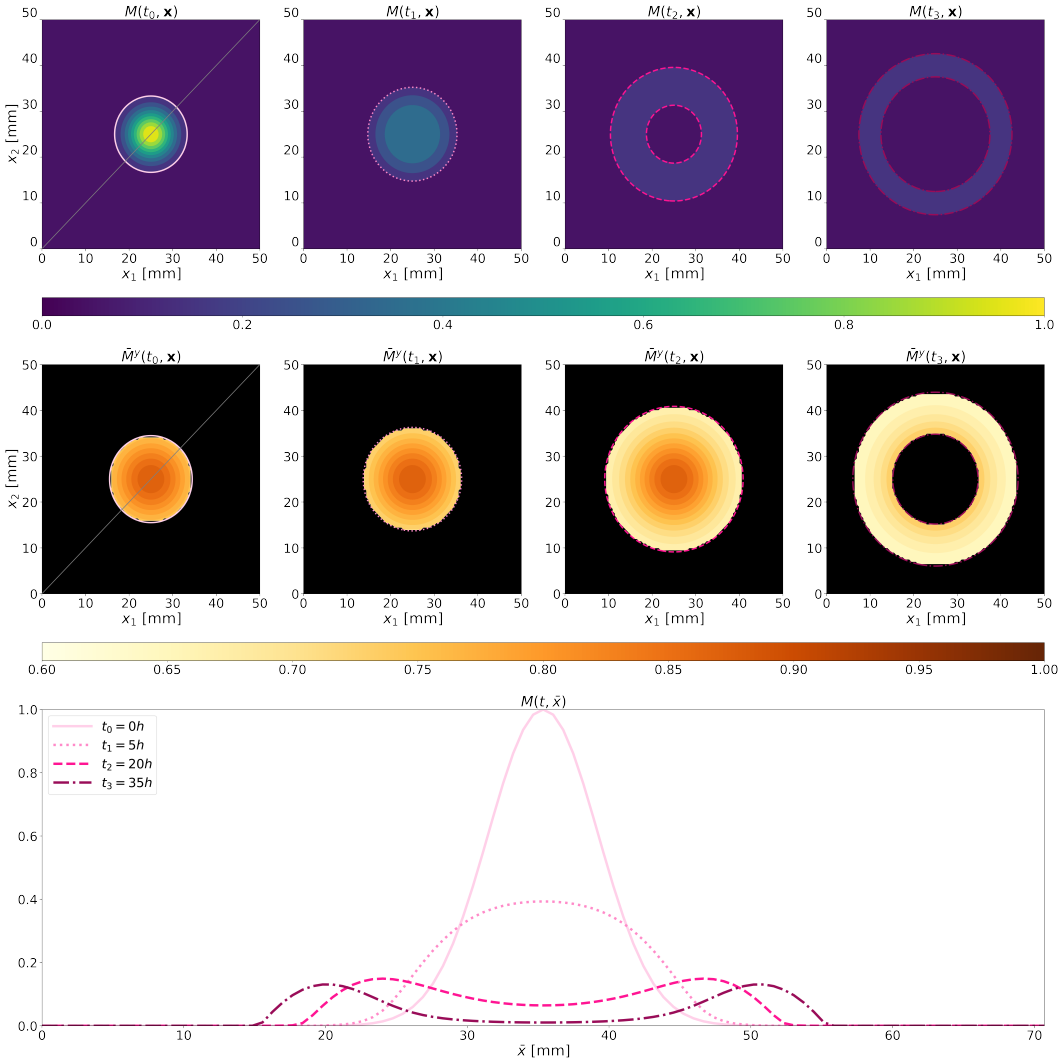

Fig. 6.8 **Experiment 4: hypoxia-driven ring structure in tumour and Snail distribution.** Evolution of model (6.3.23) with the initial conditions shown in Fig. 6.7. Top row: evolution of the tumour mass $M(t,\mathbf{x})$ in the domain $\Omega = [0,50]\times[0,50]\,\text{mm}^2$ at four different time step, i.e., initial time $t_0 = 0$ h (continuous light pink line), progression at $t_1 = 5$ h (dot pink line), $t_2 = 20$ h (dashed dark pink line), and $t_3 = 35$ h (dot-dashed purple line). Middle row: evolution of the average $M^y(t,\mathbf{x})$ defined in (6.4.10) at the same time steps. Bottom row: 1D profiles of the tumour mass evolution along the bisecting line (light grey line in the first 2D plot) of the domain Ω at the same time steps. $\bar{x}$ indicates the spatial position along this bisecting line. References to the four selected time steps are repeated in each graph using consistent color and line styles. Parameter values are set as reported in Table 6.1.

As time progresses, the prevalence of chemotactic motion results in a depletion of cells from the central mass, gradually giving rise to a ring-like structure (times t_2 and t_3). During this phase, movement starts to slow down due to two main

factors. Firstly, comparing the position of the ring with respect to the oxygen profile (shown in Fig. 6.7), we observe a decrease in motility caused by both high levels of oxygenation (reducing the tactic sensitivity $F(y^*, O_2)$) and low oxygen gradients (reducing the chemotactic stimulus). Secondly, the slowdown is due to the anti-crowding mechanism, which, once the void forms at the centre of the mass, would induce cells from the inner part of the ring to move towards the centre, conflicting with the chemoattractant-driven movement. These observations are also consistent with the plots in the second row of Fig. 6.8, where $\bar{M}^y(t, \mathbf{x})$ is shown. They illustrate how, initially the average expression of Snail is high, inducing rapid cell migration, and it increases approaching the central hypoxic region. Then, while the tumour mass moves outward, this expression decreases as cells reach more oxygenated areas, still maintaining higher values around the inner border of the ring. It is interesting how the model is able to qualitatively capture the two main dynamics shown in the data from [305]. In fact, the model reproduces both the experimentally observed ring shape of the tumour mass and the spatial distribution of the average Snail expression, mirroring the findings of the experimental study.

6.5 Conclusion and future perspectives

The migration of tumour cells in response to oxygen concentration gradients remains a critical area of investigation in cancer biology. While the role of hypoxia in promoting tumour aggressiveness and metastasis is well recognised, the exact mechanisms driving cell migration in response to oxygen levels are still an area of investigation and understanding these mechanisms may be crucial for developing effective therapeutic strategies.

In this study, we developed a novel mathematical model to investigate the interplay between hypoxia, molecular signaling pathways, and tumour cell migration. Specifically, we proposed a multi-scale model that naturally integrates single-cell behaviour driven by Snail expression with macroscopic scale dynamics describing tumour migration in the tissue. Our approach employs tools and methods from the kinetic theory of active particles to construct a kinetic transport equations that describe the evolution of the tumour cell distribution based on detailed microscopic dynamics. By employing proper scaling arguments, we formally derived the equations for the statistical moments of the cell distribution. These capture cells density

dynamics, influenced by limited non-linear diffusion and oxygen-mediated drift, and the evolution of the average Snail expression within the tumour population, which directly relates to tumour migratory capability. Overall, our model offers a detailed description of macroscopic tumour cell dynamics, considering the effect of microscopic Snail signalling pathways in the mechanisms of tumour response to hypoxia. This modelling approach represents a promising way to integrate molecular signaling pathways with cell migration dynamics.

We validated the model in different scenarios with biological relevance, focusing on the role of chemotactic-dominated motion and anti-crowding effects, and analyzing the effect of Snail expression on cell migration and proliferation. We also tested the reliability of our approach by testing its ability to quantitative replicate experimental experimental results from two different studies published in the literature. We investigated the effect of hypoxia and Snail knockdown on the motility of cancer cells, comparing our results with those presented by [459] on human hepatocarcinomas. Moreover, we considered the findings of [305] and we replicate *in-silico* the results regarding the effect of Snail over-expression and Snail knockdown on the migration capability of human breast cancer cells. We also analysed the spatial distribution of Snail expression within the tumour mass in response to hypoxia, showing how the model is able to reproduce the ring patterns observed experimentally in Ref. [305]. These results support the idea that our mathematical framework offers new perspectives for interpreting experimental data and understanding the underlying biological mechanisms driving tumour migration.

Moving forward, it will be important to explore the implications of our findings in the context of clinical outcomes and therapeutic interventions. Particularly, our results highlight the importance of considering the dynamic regulation of Snail expression in response to hypoxia. This finding underscores the potential significance of developing strategies to target Snail as a therapeutic approach to control tumour cell migration and metastasis. Furthermore, incorporating heterogeneous and dynamic environmental factors, such as a non-stationary oxygen distribution with its consumption by tumour cells, could improve the predictive power of our model and enhance the quantitative fitting of the experimental data, ultimately leading to a better understanding of tumour invasion.

In summary, the proposed mathematical modelling approach is a novel and valuable tool to integrate the detail microscopic cell dynamics with cell migration

dynamics at a macroscopic (tissue) level. In particular, the multi-scale modelling approach allows to properly derive the macroscopic terms driving cell evolution from a detailed description of the single-cells dynamics, instead of phenomenological stating them directly at macroscopic level. Our findings offer interesting interpretations of the complex dynamics underlying tumour progression and motility, providing new perspectives for interpreting experimental data and understanding the biological mechanisms driving tumour development. This paves the way for personalised medicine approaches tailored to individual tumour characteristics.

Part III

Future perspectives

Chapter 7

Continuous modelling for go or/and grow: mathematical hints for tumour edge analysis

7.1 Introduction

Motility and proliferation are two essential aspects to be considered when analysing tumour mass development. As already stated, the "go or grow" hypothesis [215], arising from the observation of glioblastoma multiforme, states that glioma cells either favour proliferation or migration at the expense of the other. Multiple factors, such as ECM components, microRNAs and transcription factors, could regulate this migration/proliferation dichotomy.

In previous chapters, we have highlighted the role of the environment in determining both the intake and the localisation of different phenotypic traits. In this chapter, however, we focus on the fundamental dynamics of tumour cell movement and try to understand how a simple mathematical model can capture different structures deriving from them. In this way, temporarily suspending the role of the environment on phenotypic determination and localisation, we try to find an explanation both for the possible existence of an effective trade-off between proliferation and motility and for the generation of niche spaces for each phenotype.

In Ref. [278], recent research has unveiled the role of glucose metabolism in driving these distinct phenotypes. Specifically, the authors identified an oxygen-dependent metabolic switch between the pentose phosphate pathway (PPP) and the preparatory phase of glycolysis in glioma stem-like cells and tissues, each associated with unique cellular behaviours. Under hypoxic conditions, there is an upregulation of glycolysis enzymes and an increase in glycolytic flux, which correlates with enhanced cell migration. Conversely, the PPP is favoured when oxygen is available, promoting cell proliferation [256]. The dichotomous hypothesis of go or grow, however, seems to be too strong: recent investigations have concluded that if, on the one hand, the interaction with the environment and transcription factors can favour one phenotype over the other, it is not granted an a priori exclusion of the other. In Ref. [191], authors showed that highly invasive cells exhibited exclusive biological activities, including invasion, migration, urokinase-type plasminogen activation, and branching morphogenesis. In contrast, the highly proliferative subcloned cells demonstrated distinct traits such as anchorage-independent growth in soft agar and robust tumourigenicity when transplanted as xenografts in immune-compromised mice. Upon exposure to HGF/SF, the highly invasive cells activated the MAPK pathway, whereas the highly proliferative cells favoured signalling through Myc. Interestingly, subcloned cells displaying both invasive and proliferative characteristics exhibited concurrent activation of both signalling pathways in response to HGF/SF stimulation. These findings underscore the collaborative role of the mitogen-activated protein kinase and Myc pathways in conferring invasive and proliferative phenotypes to tumour cells. Moreover, the authors establish a model for investigating how the interplay between invasion and proliferation transitions contributes to malignancy progression. The role of hypoxia, considered in Ref. [215] as the primary environmental stressor for the phenotypic switch, is controversial. In most cell types, exposure to hypoxia typically results in decreased cell proliferation, as the increased cellular density, accompanied by higher oxygen demand, would further intensify hypoxic conditions. However, specific cell populations exhibit sustained cell proliferation despite hypoxic environments. This phenomenon is frequently observed in cancer pathology, where malignant cells continue to proliferate vigorously even under low oxygen conditions. Interestingly, this ability to maintain proliferation in hypoxia is not exclusive to cancer cells but also serves a physiological role, particularly in preserving stem cell populations residing within hypoxic niches. In such cases, the capacity for sustained proliferation enables stem cells to perpetuate their pool and

contribute to tissue homeostasis and regeneration despite the limited oxygen availability in their microenvironment [227]. Moreover, in Ref. [289], authors show that HIF-1α exerts an influence on mouse embryonic fibroblast cell migration unrelated to hypoxia-induced effects. In Ref. [438], authors test the validity of the go-or-grow hypothesis using two-dimensional in vitro assays involving melanoma cells tagged with fluorescent cell-cycle indicators and treated with cell-cycle-inhibiting drugs. They present evidence indicating that cell motility remains unaffected by the cell-cycle phase, and non-proliferative arrested cells exhibit comparable motility to actively cycling cells. This does not counter the observations of inhibition of one phenotype over the other but makes the hypothesis that the trade-off is due to energy optimisation (i.e., the cell must decide whether to invest in movement or proliferation) less plausible. More likely, this leads us to believe that the activation pathways, triggered by environmental factors, which lead to the two different phenotypes, are often mutually inhibitory but, in some cases, can coexist. Both in the proliferation/motility dichotomy and in considering the EMT, it therefore makes more sense to talk about plasticity and transition rather than switches.

What is certain is that heterogeneity of proliferation and motility coexists within the same tumour mass and that these different traits lead to a geometric characterisation of the acquired phenotypes. Understanding the localisation of the different phenotypes is particularly important for understanding the leading dynamics of tumour evolution and from the perspective of a targeted therapeutic or surgical intervention. As an example, in Ref. [322], it is noticed how the molecular and phenotypic characteristics of cells at the invasive tumour periphery in unresectable glioblastoma (GBM) are not yet fully understood. Their findings indicate that within the invasive edge and central core of the tumour, there exist two distinct varieties of glioma stem-like cells (GSCs), resembling the proneural (PN) and mesenchymal (MES) subtypes, respectively. In Ref. [398], authors propose a stratification model in which an external proliferation rim is separated by an inner necrotic core by an intermediate rim of quiescent cells. How these two structures intersect (proliferative and migratory rims) is still unknown.

From a biological point of view, different rims can be detected by analysing medical images. We refer to Magnetic Resonance Imaging (MRI) and Positron Emission Tomography (PET) techniques. In particular, MRIs differentiate between T1 and T2. T1 MRI emphasises anatomy, delivering clear images and depicting fluids as dark. In contrast, T2 MRI is tailored to highlight pathology, rendering fluids

bright, which proves advantageous in visualising inflammation, oedema, and specific lesions. The differentiation between T1 and T2 sequences is pivotal for precise medical diagnoses. Essentially, while T1 delineates structures, T2 detects anomalies. Moreover, PET provides physiological data instead of morphological information, such as MRI. The procedure begins with the injection of a radiopharmaceutical composed of a radioisotope chemically bound to a metabolically active molecule (carrier). When the active molecule reaches a specific concentration within the organic tissues to be analysed, the atoms of the isotope decay, each emitting a positron, which annihilates after a few millimetres with an electron, producing a pair of gamma photons emitted in opposite directions. These photons are detected when they reach a scintillator and only if they are in pairs. The hypothetical position of the body from which they were emitted can be reconstructed by measuring the position where the photons hit the detector. In oncology, the most common tracer is based on a modified molecule of glucose, which is taken up to a greater extent by metabolically hyperactive neoplastic cells having anaerobic glycolysis as their primary metabolic pathway for energy supply.

In this chapter, our modelling procedure pays attention to building a mathematical structure that allows for descriptors comparable to the medical images introduced so far.

Some works have already moved in the direction of this characterisation in mathematical terms. In Ref. [118], the pivotal role of mechanical alterations in the progression of solid tumours is studied. It is shown how changes in stromal-epithelial interactions can lead to a sustained elevation in cytoskeletal tension, thereby promoting the expression of malignant traits. Authors model the avascular tumour as an expanding elastic spheroid, with growth occurring through both volume expansion and mass production within a cellular rim, integrating growth rate, solid stress, and the diffusion of biomolecules within a heterogeneous mass. In Ref. [246], authors validate with PET images diverse in silico modelling techniques to capture tumour heterogeneity, hypothesising that regions exhibiting heightened metabolic activity would relocate towards the periphery as tumours progress towards a more aggressive state. Moreover, in Ref. [188], authors hypothesise different reasons for selective processes for various phenotypes such as tumour's specific niche, cell turnover rates, the nature of the trade-off between different traits, and the causes of cell deaths (demographic or environmental). They use a spatially explicit ABM in order to investigate the evolution of proliferative and motile traits, noticing a geometric

characterisation of niches, having migration favoured at the tumour's edge and proliferation favoured in the interior. Higher cell turnover rates marginally decelerate tumour growth but expedite the evolutionary process for both proliferation and migration. Without a trade-off, proliferation and migration values tend to increase continuously, while a convex trade-off typically promotes proliferation, fostering the coexistence of generalist and specialist phenotypes. Conversely, a concave trade-off favours migration at lower death rates but switches to proliferation at higher rates. Demographic stochasticity-induced mortality favours proliferation, whereas environmental stochasticity favours migration. Other relevant works in this direction also exist in Ref. [330, 397, 195, 309, 413, 455, 401, 383].

In the next section, we introduce and analyse two continuous mathematical modelling approaches that are able to describe cell movement, proliferation, and epigenetic characterisation of both motile and proliferative traits. The results obtained so far are part of a joint project with the Mathematical Oncology Laboratory (MOLAB) of Ciudad Real (Spain), in particular under the supervision of Professor Victor M. Pérez García and in collaboration with Professor Gabriel Fernández Calvo, Dr. Julián Pérez Beteta, Dr. Carmen Ortega Sabater, and Dr. Juan Jiménez Sánchez. The chapter is organised in the following sections. In Section 7.2, we give an overview of the adopted modelling framework, explaining the derivation procedure (in Section 7.2.1) and presenting the derived models (in Section 7.2.2) organised in two macro-settings. In Section 7.3, we conduct a theoretical analysis of the models, investigating the specific characteristics of two settings and comparing them. In Section 7.4, we present the results obtained so far via numerical simulations of the models, and we compare the two settings considering mathematical aspects and biological coherence. Finally, Section 7.5 summarises the findings so far and shows this work's next steps and future perspectives.

7.2 The modelling framework

7.2.1 Model derivation

In this section, we want to highlight how different continuous formulations, with respect to spatial dynamics, arise from a discrete-continuous limit when considering different dynamics at the cell level. Firstly, let us consider a one-dimensional domain

for space. Note that we consider two traits, referring to them with U and W, which are responsible for epigenetically characterising tumour cells. In particular, trait U defines the proliferative potential of cells while trait W define their motility potential. Thus, considering N_U and N_W possible states for, respectively, U and W traits and labelling them with $u = 1,\dots,N_U$ and $w = 1,\dots,N_W$, we consider a number $N_U \cdot N_W$ of cell populations including all possible combinations. We adopt a voxel structure, discretising the space with a step h, and we use the following notation: $a_{k,j}^{u,w}$ is the density of population having traits u and w, at time step k in voxel j where $t_k = k\tau$ and voxel j is centered at $x_j = jh$ and of size h. Let us define $\rho_{k,j} = \rho(t_k, x_j) := \sum_{u=1}^{N_U}\sum_{w=1}^{N_W} a_{k,j}^{u,w}$ as the total cell density at time step k in voxel j (summing up all cell populations). Let $P_{k,j}^{u,w} = P_1(u)P_2(\rho_{k,j})$ be the net growth rate of population u,w at time t_k in voxel x_j. P is such that $\frac{dP_2}{d\rho} < 0$, $P_2(K) = 0$ where K is the carrying capacity, and $P_1(u) > P_1(u-1)\ \forall u = 2,\dots,N_U$ and $P_1(1) > 0$. This means that cells, regardless of their characterisation, proliferate proportionally to the available space and that populations are ordered, with respect to U trait, so that a higher trait corresponds to a higher proliferation rate. Defining $(\cdot)_+$ and $(\cdot)_-$ as the positive and negative part, for the net growth rate, we say that cells of population u,w which are in voxel j at the time t_k will divide with probability $\tau(P_{k,j}^{u,w})_+$, die with probability $\tau(P_{k,j}^{u,w})_-$ and stay quiescent with probability $1-\tau(P_{k,j}^{u,w})_+ - \tau(P_{k,j}^{u,w})_- = 1-\tau|P_{k,j}^{u,w}|$.

The anti-crowding case

Now, let us consider, for the first case, a density-dependent probability of movement. We refer to this scenario as the *anti-crowding* modelling strategy, as cells tend to move away from high-density (crowded) zones. In particular, we let cells move toward a less dense zone with a probability proportional to the strength of the negative gradient in that direction. $LF_{k,j}^{u,w} = \nu(w)\frac{(\rho_{k,j}-\rho_{k,j-1})_+}{2K}$ is the probability that cells of the population u,w in voxel j at time k move to the voxel at their left and $RG_{k,j}^{u,w} = \nu(w)\frac{(\rho_{k,j}-\rho_{k,j+1})_+}{2K}$ the probability they move to the right. Here $\nu(w)$ is such that $\nu(w) > \nu(w-1)\ \forall w = 2,\dots,N_W$ and $\nu(1) > 0$. Considering the principle of

mass balance, we obtain:

$$\begin{aligned} a_{k+1,j}^{u,w} = {} & RG_{k,j-1}^{u,w}\left[2\tau(P_{k,j-1}^{u,w})_+ + 1 - \tau|P_{k,j-1}^{u,w}|)\right] a_{k,j-1}^{u,w} \\ & + LF_{k,j+1}^{u,w}\left[2\tau(P_{k,j+1}^{u,w})_+ + 1 - \tau|P_{k,j+1}^{u,w}|)\right] a_{k,j+1}^{u,w} \\ & + \left(1 - LF_{k,j}^{u,w} - RG_{k,j}^{u,w}\right)\left[2\tau(P_{k,j}^{u,w})_+ + 1 - \tau|P_{k,j}^{u,w}|\right] a_{k,j}^{u,w}. \end{aligned}$$

Considering the mathematical definition of $|.|$ and the possible sign of P we obtain:

$$\begin{aligned} a_{k+1,j}^{u,w} = {} & \nu(w)\frac{(\rho_{k,j-1} - \rho_{k,j})_+}{2K}\left(1 + \tau P_{k,j-1}^{u,w}\right) a_{k,j-1}^{u,w} \\ & + \nu(w)\frac{(\rho_{k,j+1} - \rho_{k,j})_+}{2K}\left(1 + \tau P_{k,j+1}^{u,w}\right) a_{k,j+1}^{u,w} \\ & + \left(1 - \nu(w)\frac{(\rho_{k,j} - \rho_{k,j-1})_+}{2K} - \nu(w)\frac{(\rho_{k,j} - \rho_{k,j+1})_+}{2K}\right)\left(1 + \tau P_{k,j}^{u,w}\right) a_{k,j}^{u,w}. \end{aligned}$$

We rewrite the equation as follows:

$$\begin{aligned} a_{k+1,j}^{u,w} = {} & a_{k,j}^{u,w} + \tau P_{k,j}^{u,w} a_{k,j}^{u,w} \\ & + \frac{\nu(w)}{2K}\left[(\rho_{k,j-1} - \rho_{k,j})_+ a_{k,j-1}^{u,w} + (\rho_{k,j+1} - \rho_{k,j})_+ a_{k,j+1}^{u,w}\right] \\ & - \frac{\nu(w)}{2K}\left[(\rho_{k,j} - \rho_{k,j-1})_+ a_{k,j}^{u,w} + (\rho_{k,j} - \rho_{k,j+1})_+ a_{k,j}^{u,w}\right] \\ & + \frac{\nu(w)\tau}{2K}\left[(\rho_{k,j-1} - \rho_{k,j})_+ P_{k,j-1}^{u,w} a_{k,j-1}^{u,w} + (\rho_{k,j+1} - \rho_{k,j})_+ P_{k,j+1}^{u,w} a_{k,j+1}^{u,w}\right] \\ & - \frac{\nu(w)\tau}{2K}\left[(\rho_{k,j} - \rho_{k,j-1})_+ P_{k,j}^{u,w} a_{k,j}^{u,w} + (\rho_{k,j} - \rho_{k,j+1})_+ P_{k,j}^{u,w} a_{k,j}^{u,w}\right]. \end{aligned}$$

We can consider the continuous formulation of indices in time and space, assuming $a_{k,j} = a(t,x)$, $a_{k\pm1,j} = a(t \pm \tau, x)$ and $a_{k,j\pm1} = a(t, x \pm h)$

$$
\begin{aligned}
a^{u,w}(t+\tau,x) = \; & a^{u,w}(t,x) + \tau P_1(u) P_2(\rho(t,x)) a^{u,w}(t,x) \\
& + \frac{\nu(w)}{2K} \left[(\rho(t,x-h) - \rho(t,x))_+ a^{u,w}(t,x-h) \right] \\
& + \frac{\nu(w)}{2K} \left[(\rho(t,x+h) - \rho(t,x))_+ a^{u,w}(t,x+h) \right] \\
& - \frac{\nu(w)}{2K} \left[(\rho(t,x) - \rho(t,x-h))_+ a^{u,w}(t,x) \right] \\
& - \frac{\nu(w)}{2K} \left[(\rho(t,x) - \rho(t,x+h))_+ a^{u,w}(t,x) \right] \\
& + \frac{\nu(w)\tau}{2K} \left[(\rho(t,x-h) - \rho(t,x))_+ P_1(u) P_2(\rho(t,x-h)) a^{u,w}(t,x-h) \right] \\
& + \frac{\nu(w)\tau}{2K} \left[(\rho(t,x+h) - \rho(t,x))_+ P_1(u) P_2(\rho(t,x+h)) a^{u,w}(t,x+h) \right] \\
& - \frac{\nu(w)\tau}{2K} \left[(\rho(t,x) - \rho(t,x-h))_+ P_1(u) P_2(\rho(t,x)) a^{u,w}(t,x) \right] \\
& - \frac{\nu(w)\tau}{2K} \left[(\rho(t,x) - \rho(t,x+h))_+ P_1(u) P_2(\rho(t,x)) a^{u,w}(t,x) \right].
\end{aligned}
$$

With all the necessary regularity hypothesis, moving $a^{u,w}(t,x)$ term to the left, we use Taylor expansion considering infinitesimal time step τ and space step h to obtain:

$$\begin{aligned}\tau\partial_t a^{u,w}(t,x)+\frac{\tau^2}{2}\partial_{tt}^2 a^{u,w}(t,x)\approx\ & \tau\, P_1(u)P_2(\rho(t,x))\, a^{u,w}(t,x)\\ &+\frac{\nu(w)h^2}{2K}\, a^{u,w}(t,x)\,\partial_{xx}^2\rho(t,x)\\ &+\frac{\nu(w)h^2}{2K}\left[\big(\partial_x\rho(t,x)\big)_+ - \big(-\partial_x\rho(t,x)\big)_+\right]\partial_x a^{u,w}(t,x)\\ &+\frac{\nu(w)\tau}{2K}\, a^{u,w}(t,x)\, P_1(u)P_2(\rho(t,x-h))\,\big(-h\partial_x\rho(t,x)\big)_+\\ &+\frac{\nu(w)\tau}{2K}\, a^{u,w}(t,x)\, P_1(u)P_2(\rho(t,x+h))\,\big(h\partial_x\rho(t,x)\big)_+\\ &-\frac{\nu(w)\tau}{2K}\, a^{u,w}(t,x)\, P_1(u)P_2(\rho(t,x))\,\big(h\partial_x\rho(t,x)\big)_+\\ &-\frac{\nu(w)\tau}{2K}\, a^{u,w}(t,x)\, P_1(u)P_2(\rho(t,x))\,\big(-h\partial_x\rho(t,x)\big)_+\end{aligned}$$

Calculating:

$$\begin{aligned}\tau\partial_t a^{u,w}(t,x)+\frac{\tau^2}{2}\partial_{tt}^2 a^{u,w}(t,x)\approx\ & \tau\, P_1(u)P_2(\rho(t,x))\, a^{u,w}(t,x)\\ &+\frac{\nu(w)h^2}{2K}\left(a^{u,w}(t,x)\,\partial_{xx}^2\rho(t,x)\ +\ \partial_x a^{u,w}\partial_x\rho(t,x)\right)\\ &+\frac{\nu(w)\tau h}{2K}\, F(t,x)\end{aligned}$$

with

$$\begin{aligned}F(t,x)=&\Big[P_1(u)P_2(\rho(t,x-h))(-\partial_x\rho(t,x))_+ +\\ &+P_1(u)P_2(\rho(t,x-h))\big(\partial_x\rho(t,x)\big)_+\Big]\, a^{u,w}(t,x)\\ &-\left[\big(\partial_x\rho(t,x)\big)_+ +\ \big(-\partial_x\rho(t,x)\big)_+\right]P_1(u)P_2(\rho(t,x))\, a^{u,w}(t,x)\end{aligned}$$

We divide by τ:

$$\partial_t a^{u,w}(t,x) + \frac{\tau}{2}\partial_{tt}^2 a^{u,w}(t,x) \approx P_1(u)P_2(\rho(t,x))a^{u,w}(t,x) + \frac{\nu(w)h^2}{2K\tau}\left[a^{u,w}(t,x)\ \partial_{xx}^2\rho(t,x)\ +\ \partial_x a^{u,w}\ \partial_x\rho(t,x)\right] + \frac{\nu(w)h}{2K}F(t,x)$$

And then compute the limit for $\tau \to 0$, $h \to 0$ such that $\forall w\ \frac{\nu(w)h^2}{2\tau} \to D(w)$:

$$\begin{aligned}\partial_t a^{u,w}(t,x) &= P_1(u)P_2(\rho(t,x))\ a^{u,w}(t,x) + \\ &+\ \frac{D(w)}{K}\left[a^{u,w}(t,x)\partial_{xx}^2\rho(t,x)\ +\ \partial_x a^{u,w}\partial_x\rho(t,x)\right] \\ &= P_1(u)P_2(\rho(t,x))\ a^{u,w}(t,x)\ +\ \frac{D(w)}{K}\ \partial_x\left(a^{u,w}(t,x)\partial_x\rho(t,x)\right)\end{aligned}$$

The Fisher-like case

For the second case we assume that cells move because of random motion, meaning that $LF_{k,j}^{u,w} = RG_{k,j}^{u,w} = \frac{\nu(w)}{2}$ is the probability that cells of the population u,w in voxel j at time k move to the voxel at their left or right. We refer to this as *Fisher* modelling approach since (as we show below) this translates into a Fisher-like diffusive model when we infer the continuous model. Considering the principle of mass balance and inviting the reader to reproduce the previously considered steps for the current case, we arrive at the following:

$$\begin{aligned}a_{k+1,j}^{u,w} = &\frac{\nu(w)}{2}(1+\tau P_{k,j-1}^{u,w})\ a_{k,j-1}^{u,w} + \frac{\nu(w)}{2}(1+\tau P_{k,j+1}^{u,w})\ a_{k,j+1}^{u,w} \\ &+(1-\nu(w))(1+\tau P_{k,j}^{u,w})\ a_{k,j}^{u,w}\end{aligned}$$

We rewrite the equation as follows:

$$\begin{aligned} a_{k+1,j}^{u,w} = a_{k,j}^{u,w} &+ \tau P_{k,j}^{u,w} a_{k,j}^{u,w} \\ &+ \frac{\nu(w)}{2}\left(a_{k,j-1}^{u,w} + a_{k,j+1}^{u,w} - 2a_{k,j}^{u,w}\right) \\ &+ \frac{\nu(w)}{2}\tau\left(P_{k,j-1}^{u,w} a_{k,j-1}^{u,w} + P_{k,j+1}^{u,w} a_{k,j+1}^{u,w} - 2P_{k,j}^{u,w} a_{k,j}^{u,w}\right) \end{aligned}$$

As previously, we pass to the continuous counterpart and use Taylor expansions to get:

$$\begin{aligned} \tau\partial_t a^{u,w}(t,x) + \frac{\tau^2}{2}\partial_{tt}^2 a^{u,w}(t,x) \approx \tau\, P_1(u)P_2(\rho(t,x))\, a^{u,w}(t,x) \\ + \frac{\nu(w)}{2}h^2\partial_{xx}^2 a^{u,w}(t,x) \\ + \frac{\nu(w)}{2}h^2\tau\left(\partial_{xx}^2 a^{u,w}(t,x)\rho(t,x)\right) \\ + \frac{\nu(w)}{2}h^2\tau\left(\partial_{xx}^2 \rho(t,x) a^{u,w}(t,x)\right) \end{aligned}$$

We can divide by τ to get:

$$\begin{aligned} \tau\partial_t a^{u,w}(t,x) + \frac{\tau^2}{2}\partial_{tt}^2 a^{u,w}(t,x) \approx P_1(u)P_2(\rho(t,x))\, a^{u,w}(t,x) \\ + \frac{\nu(w)h^2}{2\tau}\partial_{xx}^2 a^{u,w}(t,x) \\ + \frac{\nu(w)}{2}h^2\, F(t,x) \end{aligned}$$

with

$$F(t,x) = \partial_{xx}^2 a^{u,w}(t,x)\rho(t,x) + \partial_{xx}^2 \rho(t,x) a^{u,w}(t,x)$$

And then compute the limit for $\tau \to 0$, $h \to 0$ such that $\forall w\ \frac{\nu(w)h^2}{2\tau} \to D(w)$:

$$\partial_t a^{u,w}(t,x) = P_1(u)P_2(\rho(t,x))\, a^{u,w}(t,x) \;+\; D(w)\partial_{xx}^2 a^{u,w}(t,x)$$

In both cases, we can also consider the continuous counterpart of the epigenetic trait. Thus we can consider a domain $\Omega_u \times \Omega_w$, discretize with steps h_U and h_W and put $a^{u,w}(t,x) = a(t,x,u,w)$. We can also admit a random mutation dynamics, analogous to the one occurring in the space domain in the second case presented (and thus resulting in a diffusive continuous element) with speed diffusive term η_u and η_w. Thus, the final equations for the two systems are:

$$\partial_t a = P_1(u)P_2(\rho)\, a \,+\, D(w)\, \partial^2_{xx} a \,+\, \eta_u \partial^2_{uu} a \,+\, \eta_w \partial^2_{ww} a \tag{7.2.1}$$

$$\partial_t a = P_1(u)P_2(\rho)\, a + \frac{D(w)}{K}\, \partial_x\big(a \partial_x \rho\big) \,+\, \eta_u \partial^2_{uu} a \,+\, \eta_w \partial^2_{ww} a \tag{7.2.2}$$

Note that the procedure considering higher dimensions for the space domain does not change, providing the following equations:

$$\partial_t a = P_1(u)P_2(\rho)\, a \,+\, D(w)\, \Delta_{\mathbf{x}} a \,+\, \eta_u \partial^2_{uu} a \,+\, \eta_w \partial^2_{ww} a \tag{7.2.3}$$

$$\partial_t a = P_1(u)P_2(\rho)\, a + \frac{D(w)}{K}\, \nabla_{\mathbf{x}} \cdot \big(a \nabla_{\mathbf{x}} \rho\big) \,+\, \eta_u \partial^2_{uu} a \,+\, \eta_w \partial^2_{ww} a \tag{7.2.4}$$

7.2.2 The models

We are interested in considering both models in the three cases: (i) without epigenetic structure, (ii) only with the epigenetic characterisation of proliferation (as in Ref. [246]), and (iii) with both the motility and proliferation epigenetic traits. Moreover, we consider three-dimensional tumours with the constraint of radial symmetry.
We set $u \in \Omega_u = [0,1]$ and $w \in \Omega_w = [0,1]$. Variables u and v can be interpreted as measures of the expression (epigenetic state) of two (sets of) genes independent of and responsible for proliferation and motility. The higher the expression, the higher the proliferative or motility rate. Note that u and w are normalised between a minimum and a maximum level of expression here. We move from Cartesian

(x_1, x_2, x_3) to spherical coordinates (r, θ, φ), where

$$\begin{aligned} r &= \sqrt{x_1^2 + x_2^2 + x_3^2} \\ \theta &= \arccos \frac{x_3}{\sqrt{x_1^2 + x_2^2 + x_3^2}} \\ \varphi &= \text{sign}(y) \arccos \frac{x_1}{\sqrt{x_1^2 + x_2^2}} \end{aligned}$$

and exploit radial symmetry to write $a(t, r, \theta, \varphi, u, w) = a(t, r, u, w)$.
We consider a domain $\Omega_t = [0, t_{fin}]$ for time t and $\Omega_r = [0, r_{max}]$ for radius r. Let us remember that, under radial symmetry conditions, we have:

$$\nabla_{\mathbf{x}} a = \partial_{x_1} a \hat{\mathbf{x}}_1 + \partial_{x_2} a \hat{\mathbf{x}}_2 + \partial_{x_3} a \hat{\mathbf{x}}_3 = \partial_r a \hat{\mathbf{r}}$$

$$\Delta_{\mathbf{x}} a = \partial^2_{x_1 x_1} a + \partial^2_{x_2 x_2} a + \partial^2_{x_3 x_3} a = \frac{1}{r} \partial_r \big(r \partial_r a \big)$$

$$\nabla_{\mathbf{x}} \cdot a = \partial_{x_1} a + \partial_{x_2} a + \partial_{x_3} a = \frac{1}{r} \partial_r \big(r \partial_r a \big)$$

This way, formulating derivatives in the new coordinate system, we obtain the six following models:

$$\partial_t a = \tilde{P}_1 P_2(\rho)\, a \,+\, \tilde{D}\, \frac{1}{r} \partial_r \big(r \partial_r a \big) \qquad (\mathscr{F})$$

$$\partial_t a = P_1(u) P_2(\rho)\, a \,+\, \tilde{D}\, \frac{1}{r} \partial_r \big(r \partial_r a \big) \,+\, \eta_u \partial^2_{uu} a \qquad (\mathscr{F}_u)$$

$$\partial_t a = P_1(u) P_2(\rho)\, a \,+\, D(w)\, \frac{1}{r} \partial_r \big(r \partial_r a \big) \,+\, \eta_u \partial^2_{uu} a \,+\, \eta_w \partial^2_{ww} a \qquad (\mathscr{F}_{u,w})$$

$$\partial_t a = \tilde{P}_1 P_2(\rho)\, a \,+\, \frac{\tilde{D}}{K}\, \frac{1}{r} \partial_r \big(r\, a\, \partial_r \rho \big) \qquad (\mathscr{A})$$

$$\partial_t a = P_1(u) P_2(\rho)\, a \,+\, \frac{\tilde{D}}{K}\, \frac{1}{r} \partial_r \big(r\, a\, \partial_r \rho \big) \,+\, \eta_u \partial^2_{uu} a \qquad (\mathscr{A}_u)$$

$$\partial_t a = P_1(u) P_2(\rho)\, a \,+\, \frac{D(w)}{K}\, \frac{1}{r} \partial_r \big(r\, a\, \partial_r \rho \big) \,+\, \eta_u \partial^2_{uu} a \,+\, \eta_w \partial^2_{ww} a \qquad (\mathscr{A}_{u,w})$$

where $a : (\Omega_t \times \Omega_r) \to \mathbb{R}$ for $\mathscr{A}$ and $(\mathscr{F})$, $a : (\Omega_t \times \Omega_r \times \Omega_u) \to \mathbb{R}$ for $\mathscr{A}_u$ and $\mathscr{F}_u$, and $a : (\Omega_t \times \Omega_r \times \Omega_u \times \Omega_w) \to \mathbb{R}$ for $\mathscr{A}_{u,w}$ and $\mathscr{F}_{u,w}$.

Here, $\rho(t,r)$ is the cell density, considering all cells regardless of the epigenetic trait they show, and is defined as follows:

$$\rho(t,r) = \begin{cases} a(t,r), & \text{for } \mathscr{F}, \mathscr{A} \\ \displaystyle\int_{\Omega_u} a(t,r,u)du, & \text{for } \mathscr{F}_u, \mathscr{A}_u \\ \displaystyle\int_{\Omega_w}\int_{\Omega_u} a(t,r,u)dudw, & \text{for } \mathscr{F}_{u,w}, \mathscr{A}_{u,w} \end{cases}$$

Moreover, we set:

$$D(w) = \nu_{min} + (\nu_{max} - \nu_{min})w \tag{7.2.5}$$

$$P_1(u) = \gamma_{min} + (\gamma_{max} - \gamma_{min})w, \quad P_2(\rho) = 1 - \frac{\rho}{K} \tag{7.2.6}$$

and we consider $\tilde{P}_1 = \gamma_{min}$ and $\tilde{D} = \nu_{min}$.

For the boundary conditions concerning the epigenetic variables, we have the following:

$$\begin{cases} \partial_u a(t,r,0,w) = \partial_u a(t,r,1,w) = 0 \\ \partial_w a(t,r,u,0) = \partial_w a(t,r,u,1) = 0 \end{cases} \tag{7.2.7}$$

Considering the boundary condition for the domain Ω_r, we also set:

$$\partial_r a|_{r=0} = \partial_r a|_{r=r_{max}} = 0 \tag{7.2.8}$$

.

Notation statement and interpretation: to give a more immediate reading throughout the chapter, we point out here that we will not refer to the models with the usual numbering of equations (so as to avoid a continuous reference to the reading of the same) but we denote with $\mathscr{F}$ and $\mathscr{A}$ respectively the Fisher-like and anti-crowding modelling approaches in their radially symmetric 3d versions. We then use the subscripts to characterise, in order, unstructured models (absence of subscript), structured with respect to the proliferative trait alone (subscript u) and with respect to both the proliferative and motile traits (subscripts u,w). In this sense, we say that a model

has an *"higher degree of structure"* (or is "more structured") the higher the number of structuring variables it has(referring to models as *non-structured*, *mono-structured* and *bi-structured*). In biological terms, this corresponds to a more precise population characterisation from an epigenetic point of view.

7.3 Theoretical analysis

We now want to study some theoretical aspects of the models we introduce. In order to do that, we set a simple case of the model and for the sake of simplicity, we carry out the analysis adopting the one-dimensional models in Equations (7.2.1) and (7.2.2). We define two quantities to indicate the average proliferation and motility rate at a given space point and at a fixed time, introducing:

- the *average proliferation rate*:

$$\begin{aligned}\bar{P}(t,x) &= \frac{1}{\rho(t,x)} \int_{\Omega_u}\int_{\Omega_w} [\gamma_{\min} + (\gamma_{\max} - \gamma_{\min})\, u]\, a(t,x,u,w)\, du dw \\ &= \gamma_{\min} + \frac{(\gamma_{\max} - \gamma_{\min})}{\rho(t,x)} \int_{\Omega_u}\int_{\Omega_w} u\, a(t,x,u,w)\, du dw; \end{aligned} \tag{7.3.1}$$

- the *average motility rate*:

$$\begin{aligned}\bar{D}(t,x) &= \frac{1}{\rho(t,x)} \int_{\Omega_u}\int_{\Omega_w} [\nu_{\min} + (\nu_{\max} - \nu_{\min})\, w]\, a(t,x,u,w)\, du dw \\ &= \nu_{\min} + \frac{(\nu_{\max} - \nu_{\min})}{\rho(t,x)} \int_{\Omega_u}\int_{\Omega_w} w\, a(t,x,u,w)\, du dw \end{aligned} \tag{7.3.2}$$

Integrating both Equations (7.2.1) and (7.2.2) with respect to variables u and w, and using the boundary conditions in Equations (7.2.7), we obtain:

$$\partial_t \rho = \bar{P} P_2(\rho)\, \rho \; + \; \partial^2_{xx}\big(\bar{D}\rho\big) \tag{7.3.3}$$

$$\partial_t a = \bar{P} P_2(\rho)\, \rho \; + \; \partial_x\left(\frac{\bar{D}}{K}\rho\, \partial_x \rho\right) \tag{7.3.4}$$

In order to facilitate the calculation, we now consider the following simplification:

$$\gamma_{\max} = \gamma_{\min} = \gamma, \quad \nu_{\max} = \nu_{\min} = \nu.$$

From a biological point of view, this is the same as considering non-structured populations with respect to the two traits under analysis, i.e., having all populations displaying the same proliferation and motility rates.
This results in:

$$\bar{P}(t,x) = \gamma, \quad \bar{D}(t,x) = \nu$$

and leads to

$$\partial_t \rho = \gamma P_2(\rho)\, \rho \; + \; \nu \partial^2_{xx} \rho \tag{7.3.5}$$

$$\partial_t \rho = \gamma P_2(\rho)\, \rho \; + \; \frac{\nu}{K} \partial_x \Big(\rho \partial_x \rho \Big) \tag{7.3.6}$$

Equations of the form of the ones introduced in Equation (7.3.3) and Equation (7.3.4) were studied respectively in Ref. [331] and [336], showing to admit travelling wave solutions. Due to the centrality of the theoretical investigation in the interpretation of the experimentation conducted in this chapter, we reproduce those calculations presented in[331] and [336], adapting them to our models, which are only slightly different in formulation.

Both for Equation (7.3.3) and Equation (7.3.4), we look for travelling wave solutions of the form $\rho(t,x) = \rho(x-ct)$, where c is the propagation velocity of the wavefront. Formally, let $\zeta = x - ct$ and set $\phi(\zeta) = \frac{\rho(\zeta)}{K}$, together with $\psi(\zeta) = \phi'(\zeta)$.

The Fisher-like case

When considering Equation (7.3.3) this translates into:

$$\begin{cases} \phi' &= \psi \\ \psi' &= -\frac{c}{\nu}\psi - \frac{\gamma}{\nu}(1-\phi)\phi \end{cases} \tag{13}$$

We can then analyse the phase plane trajectories on the portrait (ϕ, ψ), having:

$$\frac{d\psi}{d\phi} = -\frac{c\psi\gamma(1-\phi)\phi}{\nu\psi} \tag{7.3.7}$$

Two steady states are possible: $(1,0)$ and $(0,0)$. Evaluating eigenvalues λ_1 and λ_2 of the referred jacobian matrix we get:

$$\lambda_1 = \frac{1}{2}\big(-c-\sqrt{c^2-4\gamma\nu}\big), \quad \lambda_2 = \frac{1}{2}\big(-c+\sqrt{c^2-4\gamma\nu}\big) \qquad \text{for } (0,0)$$
$$\lambda_1 = \frac{1}{2}\big(-c-\sqrt{c^2+4\gamma\nu}\big), \quad \lambda_2 = \frac{1}{2}\big(-c+\sqrt{c^2+4\gamma\nu}\big) \qquad \text{for } (1,0)$$

resulting in an unstable equilibrium for $(1,0)$ (that is, a saddle point) and a stable equilibrium for $(0,0)$. In particular, denoting $c_{min} = 2\sqrt{\gamma\nu}$, we obtain a spiral for $|c| < c_{min}$ and a node for $|c| \geq c_{min}$.

Note that if $|c| < c_{min}$, having a spiral around point $(0,0)$ implies negative values for ϕ, which is not admissible in our case. Thus, we do not consider this case of travelling waves. By continuity arguments, there is a trajectory from $(1,0)$ to $(0,0)$ lying entirely in the fourth quadrant in the case of $|c| \geq c_{min}$.

Now, we want to find a shape for the solution. In order to do that, we linearise Equation (7.3.5) considering that in the proliferative term, we have

$$\gamma\rho\left(1-\frac{\rho}{K}\right) = \gamma\left(\rho-\frac{\rho^2}{K}\right) = \gamma K\left(\frac{\rho}{K}-\left(\frac{\rho}{K}\right)^2\right) \approx \gamma K\left(\frac{\rho}{K}\right) = \gamma\rho$$

since $\frac{\rho}{K} < 1$ and then we can consider only the linear term $\frac{\rho}{K}$ as the quadratic one is negligible in comparison to that. Thus we obtain:

$$\partial_t\rho = \gamma\rho + \partial^2_{xx}(\nu\rho) \tag{7.3.8}$$

Considering arbitrary $\alpha > 0$ and $A > 0$, one can impose an initial condition with a behaviour like $\rho(0,x) \sim Ae^{-\alpha x}$ for $x \to \infty$ and look for solutions of the form $\rho(t,x) = Ae^{-\alpha(x-ct)}$. Inserting it in Equation (7.3.8), we obtain the following relation:

$$c = \frac{\gamma}{\alpha} + \nu\alpha.$$

Note that this is a convex function, with a minimum in $\alpha = \sqrt{\frac{\gamma}{\nu}}$ where $c = c_{min} = 2\sqrt{\gamma\nu}$. Considering that if $\alpha \geq \frac{\gamma}{\nu}$ then $e^{-\alpha x}$ is bounded by $e^{-\frac{\gamma}{\nu}x}$ and the front with wave speed $c = c_{min} = 2\sqrt{\gamma\nu}$, we can state that, with such initial conditions, the asymptotic wave speed of the travelling wave solution of (7.3.8) is

$$c = \frac{\gamma}{\alpha} + \nu\alpha \quad \text{for } 0 < \alpha < \frac{\gamma}{\nu}, \qquad c = c_{min} = 2\sqrt{\gamma\nu} \quad \text{for } \alpha \geq \frac{\gamma}{\nu}.$$

From a biological point of view, the most relevant waves are the ones that propagate with minimum speed. It is biologically coherent to adopt compact support functions as initial conditions that do not show a sufficiently slow decay to allow for faster wavefronts.

The anti-crowding case

Now let us take into account Equation (7.3.4). In this case, defining ϕ and ψ as before, the equation translates into:

$$\begin{cases} \phi' & = \psi \\ \phi\psi' & = -\frac{c}{\nu}\psi - \psi^2 - \frac{\gamma}{\nu}(1-\phi)\phi \end{cases} \tag{7.3.9}$$

Let us observe that the same linearisation procedure as above does not provide a minimum propagation speed, and a different procedure is needed. Upon analysing the phase plane trajectories on the portrait (ϕ, ψ), corresponding to the solutions of the following autonomous ordinary differential equation

$$\frac{d\psi}{d\phi} = -\frac{c\psi + \nu\psi^2 + \gamma_0(1-\phi)\phi}{\nu\phi\psi},$$

there is a straight line, having slope $\sigma > 0$, that connects the critical point $(1,0)$ with point $(0,-\sigma)$. Qualitatively, this is because in the half-plane $\phi < 0$ the trajectories tend to the left and considering values of ϕ between 0 and 1, the ψ' is positive in an interval of ψ between two negative values $\psi_1 < \psi_2$, meaning that there is a rectangle $[0,1] \times [\psi_2, 0]$ in which all the trajectories go down left and among them there is one with constant $\frac{d\psi}{d\phi}$. Hence, $\psi = -\sigma(1-\phi)$. When inserting this expression into Equation (7.3.9) we find that $c \geq 4\gamma\nu\phi(1-2\phi)$ providing a minimum propagation velocity of

$$c_{\min} = \sqrt{\frac{\gamma\nu}{2}}$$

Moreover, $\sigma = \frac{c}{\nu}$. Putting them together, we obtain

$$\phi' = \psi = -\sigma(1-\phi) = -\frac{c}{\nu}(1-\phi) = \sqrt{\frac{\gamma}{2\nu}}(1-\phi).$$

As done previously, we now impose initial condition $\phi(\zeta_0) = \phi_0 \geq 0$. Since $\phi(\zeta) \geq 0$ for all $\zeta \in \mathbb{R}$, we must require that $\phi(\zeta) = \phi_0$ for $\zeta \geq \zeta_0$. Recalling that $\phi(\zeta) = \frac{\rho(\zeta)}{K}$ and $\zeta = x - ct$, we obtain the exact solution that reads

$$\rho(t,x) = \begin{cases} K\left(1-(1-\phi_0)\,e^{\sqrt{\frac{\gamma}{2\nu}}(x-c_{\min}t-\zeta_0)}\right), & \text{for } x - c_{\min}t < \zeta_0 \\ K\phi_0, & \text{for } x - c_{\min}t \geq \zeta_0 \end{cases} \tag{7.3.10}$$

corresponding to the minimum propagation velocity $c_{\min}$.
Let us notice that choosing $\phi_0 = 0$ is the same as taking into account a compact support function as an initial condition. Thus, solution (7.3.10) ensures that the compactness of the initial data is preserved.

Comparison of the modelling approaches

Now, comparing the two models, one can notice two important differences:

1. the minimum propagation velocity for (7.3.4) is smaller (by a factor $2\sqrt{2}$) than the minimum propagation velocity associated with (7.3.3);

2. Taking into account solutions at a fixed time t, the derivative of the solution of (7.3.4) with respect to x has a discontinuity at $x = \zeta_0 + c_{\min}t$ (see Equation (7.3.10)), which is responsible for the jump from the concave profile of the solution $x < c_{\min}t + \zeta_0$ to its constant behaviour for $x \geq c_{\min}t + \zeta_0$. This is a feature not encountered in the solution of (7.3.3), which, as shown in the paragraph relating to the Fisher-like case, displays a progressive and decaying infiltrative front instead. In the case of compact support initial condition, this leads to a solution preserving the compactness in the anti-crowding approach, contrary to the Fisher-like approach.

A common consideration, valid for both the modelling approaches, is that it is possible to exploit the finding, both in Ref. [331] and in Ref. [336], that the results obtained so far are proved to be asymptotically valid also for the radial symmetry 3d counterpart of the models.

7.4 Results

7.4.1 Descriptors

To analyse and quantify our results, some useful descriptors are introduced. First of all, we define the quantity

$$N(t) = \int_{\Omega_r} \rho(t,r)dr \tag{7.4.1}$$

as the *total number of cells*.

Moreover, to provide indications regarding the geometry of the tumour, we consider:

$$R_Q(t) = \max_r \{r \quad s.t.\ \rho(t,r) > QK/100\} \tag{7.4.2}$$

$$R_{MET}(t) = \frac{\int_{\Omega_r} P_1(u)P_2(\rho)r^3}{\int_{\Omega_r} P_1(u)P_2(\rho)r^2} \tag{7.4.3}$$

Considering the aim of comparing our results with the ones obtained from medical images described in Section 7.1 we consider R_{80} as the reference radius for T1 ($R_{T1} = R_{80}$) and R_{10} for T2 ($R_{T2} = R_{10}$) so that R_{T1} limits high-density areas, recognisable as the main structure. In contrast, R_{T2} defines the edge of the infiltrating part of the mass. Moreover, we use R_{MET} as a comparison radius for the one provided by PET imaging. Furthermore, we define:

$$V_I = \frac{4}{3}\pi R_I^3 \quad \text{for } I = 10, 80, MET \tag{7.4.4}$$

To end with the descriptors relating to the temporal evolution of the geometric characterisation of the tumour mass, we define the radial velocity as follows:

$$v_{R_I} = \frac{dR_I}{dt} \quad \text{for } I = 10, 80, MET. \tag{7.4.5}$$

With respect to the epigenetic characterisation of the mass, we introduce the following quantities:

- *local average proliferation and motility traits*:

$$\bar{u}(t,r) = \frac{\int_{\Omega_w}\int_{\Omega_u} u\,a(t,r,u,w)\,dudw}{\rho(t,r)} \qquad \bar{w}(t,r) = \frac{\int_{\Omega_w}\int_{\Omega_u} w\,a(t,r,u,w)\,dudw}{\rho(t,r)}$$

- *global average proliferation and motility traits*:

$$\bar{\bar{u}}(t) = \frac{\int_{\Omega_r} \bar{u}(t,r)\rho(t,r)\,dr}{N(t)} \qquad \bar{\bar{w}}(t) = \frac{\int_{\Omega_r} \bar{w}(t,r)\rho(t,r)\,dr}{N(t)} \quad .$$

Moreover we denote

$$\bar{u}_{T1}(t) = \bar{u}(t,R_{80}(t)), \quad \bar{u}_{T2}(t) = \bar{u}(t,R_{10}(t)), \quad \bar{u}_{MET}(t) = \bar{u}(t,R_{MET}(t)),$$

and respectively the same for $\bar{w}$.

7.4.2 Comparison of invasiveness and speed

In the following section, we perform numerical simulations of our model. We adopt a finite difference scheme applying an explicit Euler discretisation for the time domain.

We consider a closed spatial domain $\Omega_r = [0, r_{max}] = [0,10]cm$. As initial conditions, we set:

$$a(0,r) = A\mathbb{I}_{\{r\leq 0.1\}} e^{-\frac{r^2}{2\theta_r^2}} \quad \text{for } \mathscr{F}, \mathscr{A}$$

$$a(0,r,u) = A_u\mathbb{I}_{\{r\leq 0.1\}} e^{-\frac{u^2}{2\theta_u^2}} \quad \text{for } (\mathscr{F}_u), \mathscr{A}_u$$

$$a(0,r,u,w) = A_{u,w}\mathbb{I}_{\{r\leq 0.1\}} e^{-\frac{u^2}{2\theta_u^2}-\frac{v^2}{2\theta_w^2}} \quad \text{for } (\mathscr{F}_{u,w}), \mathscr{A}_{u,w}$$

where $\theta_r = 3 \cdot 10^{-1}$ cm, $\theta_u = \theta_w = 3 \cdot 10^{-3}$, and $A = 5 \cdot 10^{-7}$ cell/cm^3 while A_u and $A_{u,w}$ are evaluated so that $\rho(0,r)$ for $\mathscr{F}_u$, $\mathscr{A}_u$, $\mathscr{F}_{u,w}$, $\mathscr{A}_{u,w}$ are equal to $a(0,r)$ for $(\mathscr{F})$, $\mathscr{A}$.

Moreover, with interest in validating the biological reliability of our work, we keep coherent parameter values with the ones used by previous authors in Ref. [246], which had already proved to be able to reproduce medical data. Thus, we set a diffusive coefficient on the epigenetic variable equal to $\eta_u = \eta_w = 3.6 \cdot 10^{-6}$ 1/day, and we adopt a carrying capacity of $8 \cdot 10^7$ cell/cm^3. Moreover, we fix a basal proliferation rate of $\bar{P}_1 = \gamma_{\min} = 1.7 \cdot 10^{-2}$ and a basal motility rate of $\bar{D} = \nu_{\min} = 3.5 \cdot 10^{-4}$ cm/day and we let random mutation on the epigenetic variables (when present) increase $P_1(u)$ up to $\gamma_{\max} = 1.4 \cdot 10^{-1}$ 1/day and $D(w)$ up to $\nu_{\max} = 3.5 \cdot 10^{-2}$ cm/day.

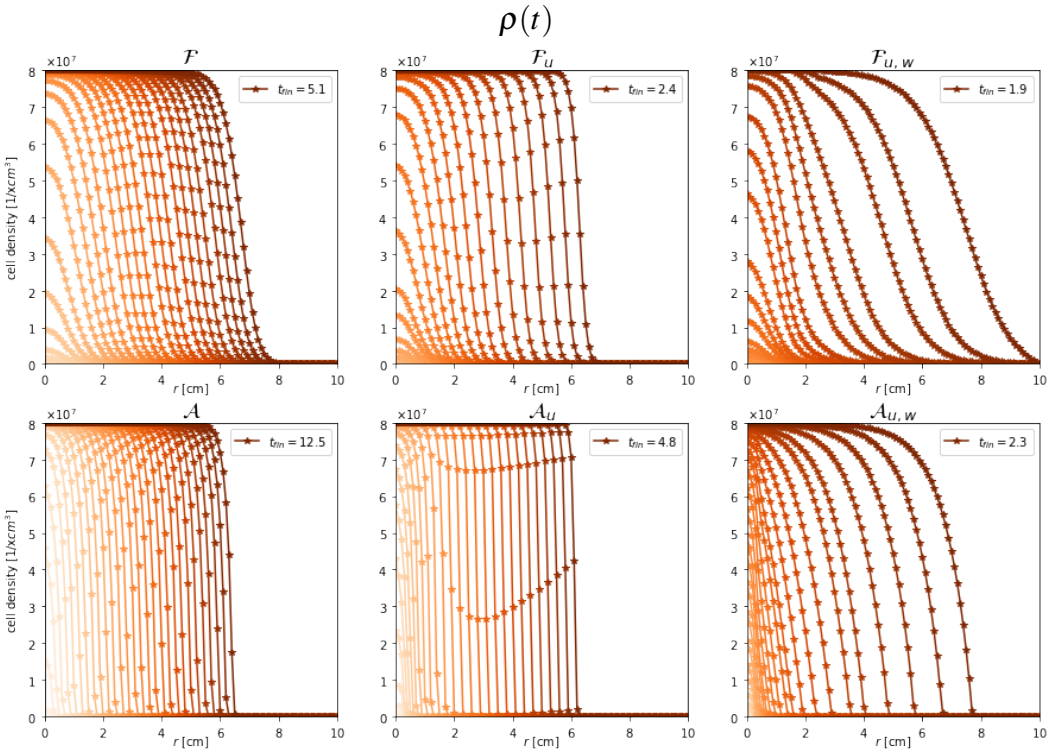

Fig. 7.1 From lighter to darker colors, time evolution of $\rho(t,r)$ for the six models introduced. Rows differentiate modelling strategies (first row: Fisher-like, second row: anti-crowding). Columns differentiated degree of structure (first column: no structure, second column: proliferation structure, third column: proliferation and motility structure). Reported time (in years, in the legend) refers to the time at which $\dfrac{K - \rho(t,6)}{K} > 0.1$.

Analysis of the edge shapes and speeds

Fig. 7.1 collects the evolution in time of $\rho(t,r)$, considering all six models in their radially symmetric version (($\mathscr{F}$),($\mathscr{F}_u$),($\mathscr{F}_{u,w}$), $\mathscr{A}$,$\mathscr{A}_u$,$\mathscr{A}_{u,w}$). Every plot shows the final time in the legend, expressed in years, corresponding to the instant at which the tumour density at a radius of 6 cm is bigger than 90% of the carrying capacity.

A qualitative analysis of the plots shows a more delineated edge of the tumour in the case of the anti-crowding modelling strategy: this is coherent with the preservation of compactness of the initial data support observed in Section 7.3 (we are here referring to compactness in the spatial domain).

Observing the final times of the simulation, it appears evident that Fisher-like models are faster than the anti-crowding ones. In our models, structuring is responsible for admitting a wider range of proliferation and motility rates, higher than the ones set in non-structured models. Thus, it is not surprising that the higher the degree of structure, the higher the speed of tumour progression. Nevertheless, the speed-up is more consistent with the anti-crowding modelling. Let us also observe that, even if keeping a concave profile (theoretically coherent with the solution in Equation (7.3.10)), the inclusion of both the epigenetic variables causes the appearance of a wider invasive rim in the anti-crowding model. This is easily noticeable if we observe, in the plot for $\mathscr{A}_{u,w}$, the portion of tumour at carrying capacity, and we compare the position of its external edge with the foot of the profile of $\rho(t,r)$. This is an important feature. In fact, when switching from a Fisher-like to an anti-crowding modelling approach, one of the costs of the advantage of compact support is given by the loss of the ability to reproduce tails. On the contrary, this observation ensures that the inclusion of epigenetic structures, particularly those relating to the motility potential of cells, allows us to reproduce invasive lower-density rims even by adopting an anti-crowding approach, thus maintaining consistency with biological observations. In fact, if, on the one hand, in practice, an instantaneous dispersion of cells throughout the domain is not reasonable (as happens when adopting diffusion models), on the other hand, the hypothesis of a tumour with precise edges, characterised by a spatially homogeneous high density within and the total absence of cells in the immediate surroundings, is also unrealistic.

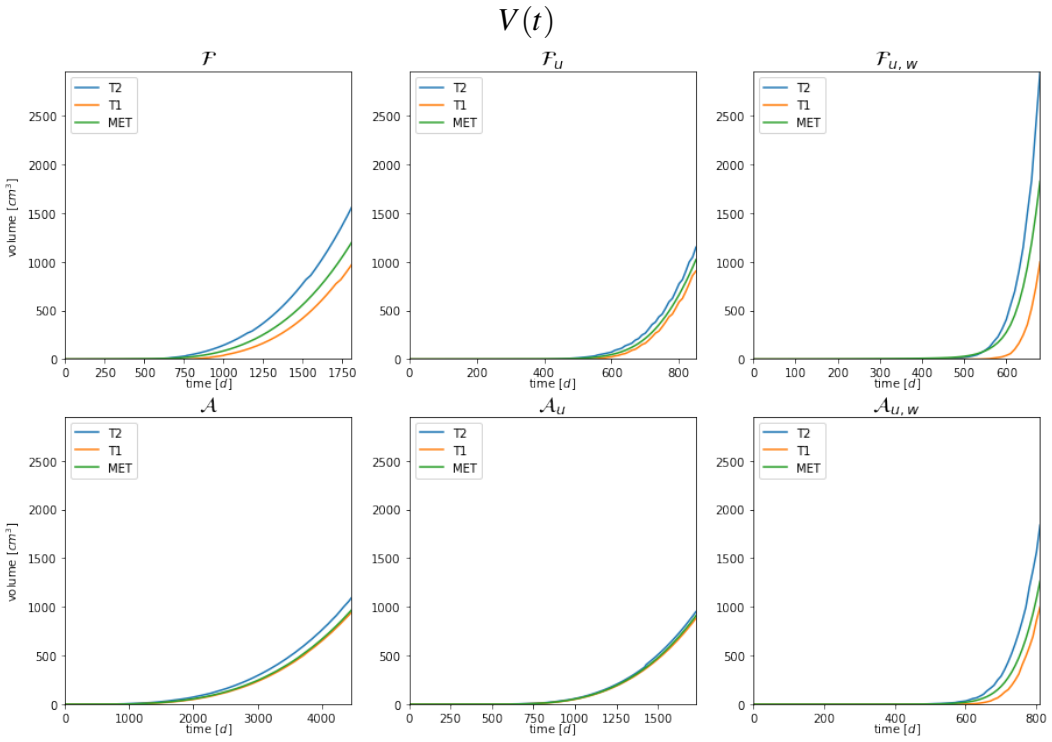

Fig. 7.2 Evolution in time of V_{T1} (orange), V_{T2} (blue) and V_{MET} (green) volumes, defined as in Equation (7.4.4). Plot organisations and end time are considered as in Fig. 7.1.

Radii, volumes and radial speeds

To analyse more quantitatively the observations made so far, in Fig. 7.2, 7.3 and 7.4, we analyse respectively the time evolutions of volumes, radius and radius speed for the six models. To define these quantities, let us recall Section 7.4.1. First of all, let us notice that when considering $\mathscr{F}_u$, Fig. 7.1 shows that the wavefront is the steepest among the Fisher models. This is reflected by the comparison between times and volumes in Equation ($\mathscr{F}$) and Equation ($\mathscr{F}_u$) shown in Fig. 7.2. The final time, taken with the same condition as before, is smaller for ($\mathscr{F}_u$) than for ($\mathscr{F}$), which is coherent with the higher speed of the front wave. Nevertheless, the volume of T2 is more extended in Equation ($\mathscr{F}$), meaning that in Equation ($\mathscr{F}_u$), the invasive rim is nearer the high-density one (thus, we have a smaller invasive finger). The same consideration stands for the corresponding anti-crowding models. In Fig. 7.4, in the plot referring to ($\mathscr{F}$) and ($\mathscr{A}$), a horizontal black dotted line indicated the theoretical minimum speed of propagation evaluated in Section 7.3. First of all,

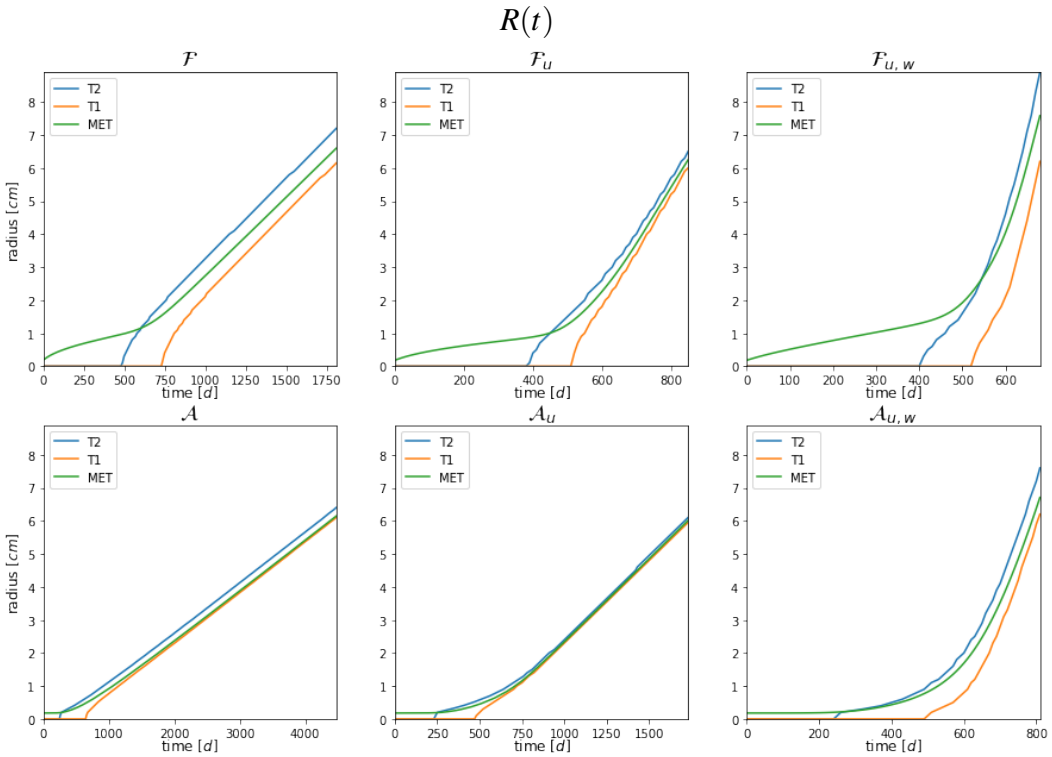

Fig. 7.3 Evolution in time of R_{T1} (orange), R_{T2} (blue) and R_{MET} (green) volumes, defined as in Equations (7.4.2) and (7.4.3) . Plot organisations and end time are considered as in Fig. 7.1.

let us remark that considering the dynamics of $\rho(t,r)$ for ($\mathscr{F}$) and $\mathscr{A}$ is the same as considering the radial symmetry 3D version of the model analysed in Section 7.3. Thus, the convergence of the computational speed to this value confirms the asymptotic prediction made elsewhere [331, 336]. Considering Fig. 7.3, it seems relevant that, as expected, the insertion of the epigenetic variables causes the loss of linear behaviour in the radius growth in both modelling strategies. The change in this behaviour opens up the question for the next section.

Comparison with universal growth law

Even though with different gradients and speeds, the volume behaviours in Fig. 7.2 are similar to an exponential function. In Ref. [371], authors propose universal scaling laws to describe the explosive growth in human cancers. In this direction,

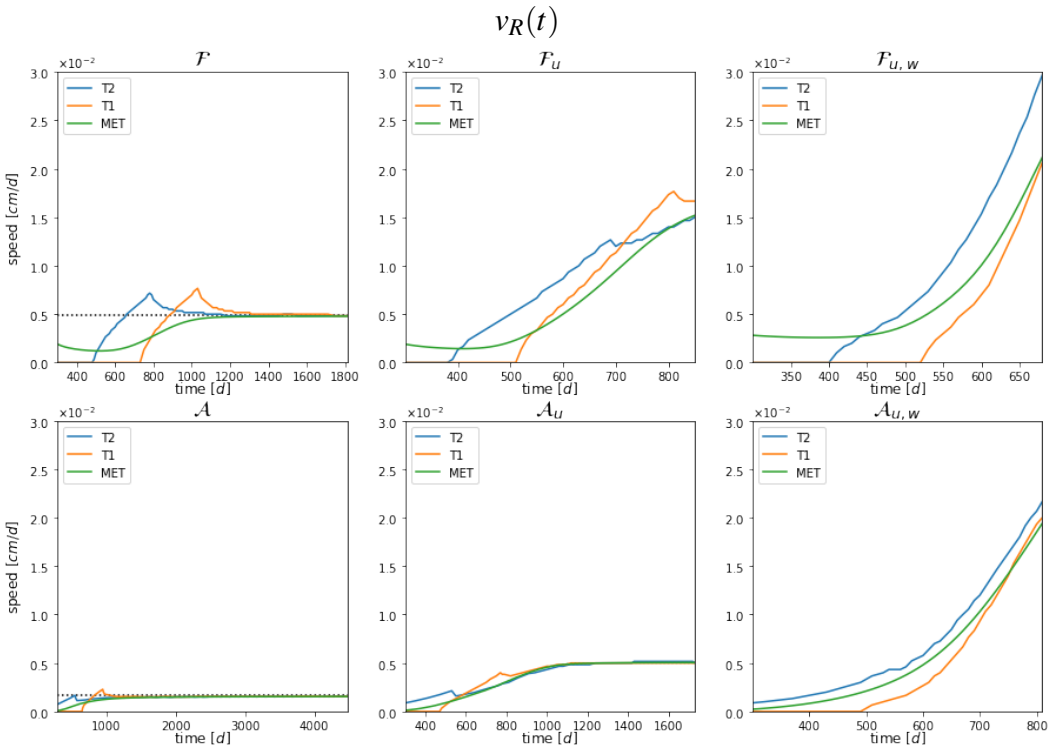

Fig. 7.4 Evolution in time of $v_{R_{T_1}}$ (orange), $v_{R_{T_2}}$ (blue) and $v_{R_{MET}}$ (green) radial velocities, defined as in Equations (7.4.5). Plot organisations and end time are considered as in Fig. 7.1.

one of the models introduced is the following:

$$\begin{cases} \frac{dV}{dt} = \alpha V^{\beta} \\ V(0) = V_0 \end{cases} \tag{7.4.6}$$

with $V(t)$ being the tumour volume. Here, β is biologically interpreted as the growth parameter, providing the speed of reproduction and invasion of the tumour. At the same time, α is an indicator of the speed with which the tumour begins its actual growth curve after what can be approximated as an initial plateau. The solution of this system is

$$V(t) = \begin{cases} \left[V_0^{1-\beta} - \alpha(\beta-1)(t)\right]^{\frac{1}{1-\beta}} & \text{for } \beta \neq 1 \\ V_0 e^{\alpha t} & \text{for } \beta = 1 \end{cases} \tag{7.4.7}$$

and if $\beta > 1$ it blows up in a finite time given by

$$t_{crit} = \frac{V_0^{1-\beta}}{(\beta-1)\alpha}.$$

Note that it is impossible to reproduce such a behaviour with our model. In fact, either if we consider ($\mathscr{F}$) and ($\mathscr{A}$) with boundary conditions $\partial_x a(t,r)\big|_{\partial\Omega_r} = 0$ (see Equation (7.2.8)), or ($\mathscr{F}_u$), ($\mathscr{A}_u$) , ($\mathscr{F}_{u,w}$), and ($\mathscr{A}_{u,w}$) with relative boundary conditions of Equation (7.2.7), we obtain:

$$\frac{dN}{dt} = \int_{\Omega_r} \bar{P}(t,r)\left(1 - \frac{\rho(t,r)}{K}\right)\rho(t,r)dr \leq \gamma_{max} N(t,r)$$

from which we deduce that $N(t)$ is bounded from above by a standard exponential growth $N_{sup}(t) = N_0\, e^{\gamma_{max} t}$, where N_0 is the number of tumour cells at $t = 0$ and that is the solution of Eq. (7.4.6) with $\beta = 1$.

We use a non-linear least squares error minimisation strategy to fit the data in Fig. 7.2 with a solution of the form (7.4.7). In Fig. 7.5, we plot with a continuous line the volume evolutions in time introduced in Fig. 7.2, and we overlap the plot of the solution (7.4.7) evaluated with optimised parameters (starred scatter). In Table 7.1, we collect the parameter values obtained with the fitting procedure, considering V_{T1}, V_{T2}, V_{MET} for all six models. First, let us consider that the model in Equation (7.4.6) differs consistently from the six proposed models since it is formulated using an ODE that directly uses the volume as the dependent variable. Instead, our models are based on PDE formulation; the volumes are obtained via geometric considerations and dimension reduction through integration. This observation enhances the already visible quality of the fit presented in Fig. 7.5. Moreover, analysing the results from a quantitative point of view, we observe that a general trend is the increment of parameter value considering models with a higher degree of structure. Given the biological interpretation of parameters α and β introduced before, this reflects the speed up in the tumour growth when considering epigenetic characterisation already observed in the previous section. Concentrating on the different volumes considered, in all the models, T1 is the one having the lower β and the higher α. In comparison (with the only exception of $\mathscr{A}_u$), the metabolic radius has the lower α and the higher β and T2 the intermediate values for both.

$(\mathscr{F})$		
Radius	α	β
T2	$3.296 \cdot 10^{-2}$	$6.151 \cdot 10^{-1}$
T1	$3.723 \cdot 10^{-2}$	$5.925 \cdot 10^{-1}$
MET	$1.863 \cdot 10^{-2}$	$7.009 \cdot 10^{-1}$

$\mathscr{A}$		
Radius	α	β
T2	$6.804 \cdot 10^{-3}$	$6.814 \cdot 10^{-1}$
T1	$7.914 \cdot 10^{-3}$	$6.569 \cdot 10^{-1}$
MET	$6.231 \cdot 10^{-3}$	$6.958 \cdot 10^{-1}$

$\mathscr{F}_u$		
Radius	α	β
T2	$5.163 \cdot 10^{-2}$	$7.325 \cdot 10^{-1}$
T1	$8.099 \cdot 10^{-2}$	$6.708 \cdot 10^{-1}$
MET	$3.080 \cdot 10^{-2}$	$8.236 \cdot 10^{-1}$

$\mathscr{A}_u$		
Radius	α	β
T2	$1.353 \cdot 10^{-2}$	$7.663 \cdot 10^{-1}$
T1	$2.007 \cdot 10^{-2}$	$6.979 \cdot 10^{-1}$
MET	$1.434 \cdot 10^{-2}$	$7.554 \cdot 10^{-1}$

$\mathscr{F}_{u,w}$		
Radius	α	β
T2	$5.587 \cdot 10^{-2}$	$8.839 \cdot 10^{-1}$
T1	$8.861 \cdot 10^{-2}$	$8.510 \cdot 10^{-1}$
MET	$2.274 \cdot 10^{-2}$	$9.999 \cdot 10^{-1}$

$\mathscr{A}_{u,w}$		
Radius	α	β
T2	$2.575 \cdot 10^{-2}$	$9.316 \cdot 10^{-1}$
T1	$5.182 \cdot 10^{-2}$	$8.460 \cdot 10^{-1}$
MET	$2.337 \cdot 10^{-2}$	$9.508 \cdot 10^{-1}$

Table 7.1 Values for parameters α and β obtained via the fitting of V_{10},V_{80},V_{MET} (defined in Equation (7.4.4)) resulting from numerical simulation of our models with a solution in Equation (7.4.7).

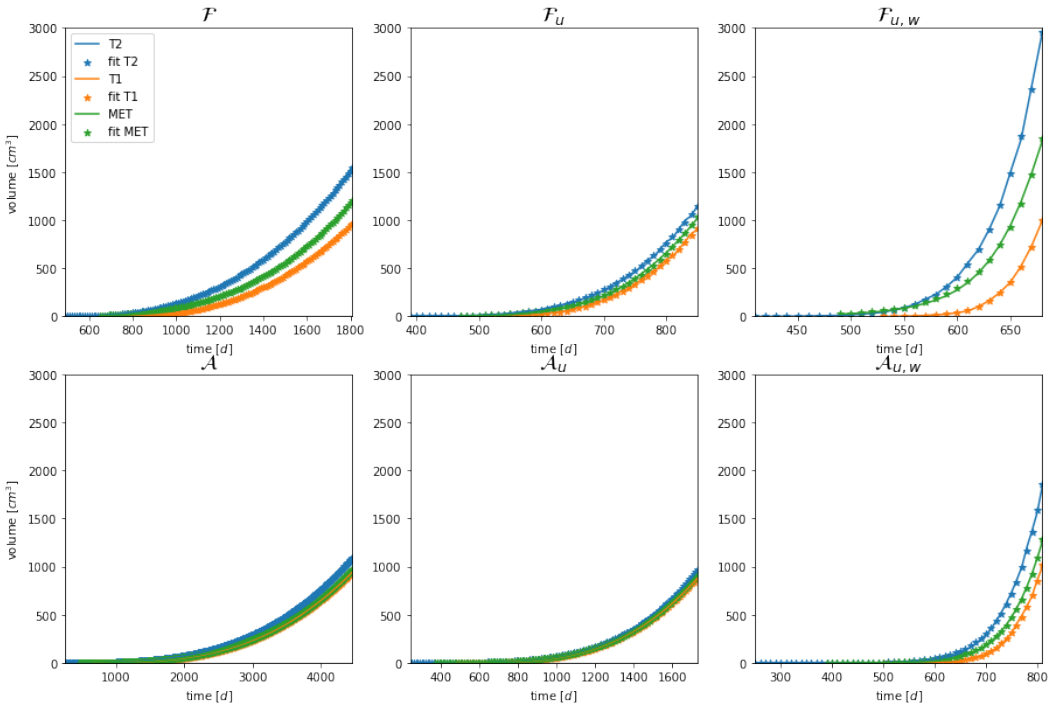

Fig. 7.5 V_{10},V_{80},V_{MET} plots (continuous lines) and fit (starred scatter) with parameter estimation of α and β parameters in Equation (7.4.7). Colours, plot organisations and end time are considered as in Fig. 7.1.

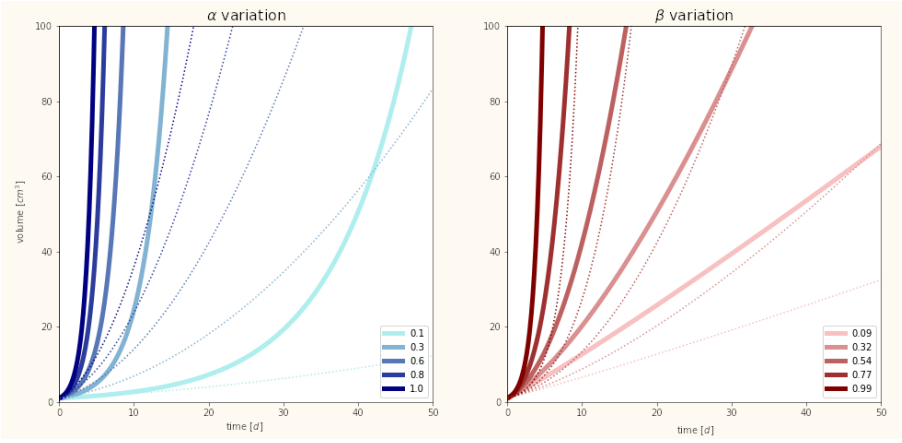

Fig. 7.6 Equation (7.4.7) computed adopting same V_O and α, β resulting from the fit of V_{T_2} (first row), V_{T_1} (first row), and V_{MET} (first row) of the six models. Blue shades refer to the Fisher-like approach and red shades to anti-crowding. Dotted, dashed and solid lines correspond to non-structured, mono-structured, and bi-structured modelling strategies.

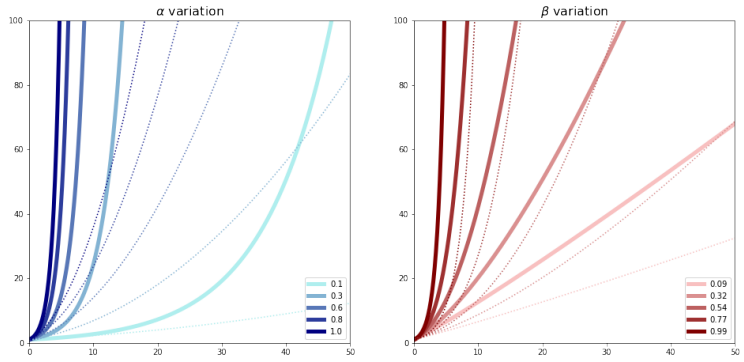

Fig. 7.7 Study of Equation (7.4.7). First plot varies α as indicated in the legend with two fixed β values ($\beta = 0.99$ solid thick line, $\beta = 0.5$ dotted thin line) Second plot varies β as indicated in the legend with two fixed α values ($\alpha = 1$ solid thick line, $\alpha = 0.5$ dotted thin line)

.

To compare the behaviour of different models, in Fig. 7.6, we overlap the initial times of the temporal evolutions of the various models and group them by type of volume considered (T1, T2, metabolic). With an analogue study of the one in Ref. [344], in Fig. 7.7, we separately analyse the impact of the variation of α and β parameters. In the latter, it is clear that the α parameter influences the starting time of the blow-up, in the sense that the higher α, the shorter the initial latency behaviour. On the other side, β influences the slope of the curve, increasing its steepness as it assumes higher values. What appears evident from 7.6 is again that the more we structure the models, the more the anti-crowding modelling strategy tends to be able to catch all the dynamics observed using Fisher models, which are well established in the literature. We can then finalise this initial study by saying that, in the case of double-structured modelling strategies, considering the analytical aspects (and so the parameter values to be used) makes it possible to equalise the speed of the processes. In the context of proliferative and motile tumours, anti-crowding modelling keeps the advantages of Fisher modelling (invasive rim and analytical prediction) unaltered, adding the benefit of preserving compactness. One could ask if adding two dimensions to the problem (extending the spatial domain with the 2D epigenetic domain) is worth gaining this only additional feature. In the next section, we observe that double epigenetic structure is not only a means to allow anti-crowding modelling to have the same beneficial features as Fisher modelling, but it is moreover true that anti-crowding modelling itself guarantees some additional

advantages in the consideration of tumour mass geometric characterisation of these two biologically relevant aspects.

7.4.3 Spatial epigenetic distribution

In this section, we want to investigate the geometry of the tumour with respect to its epigenetic composition. Thus, we concentrate on bi-structured models. In a first analysis, we consider the time evolution of $(\bar{u}_I(t), \bar{w}_I(t))$ for $I = T1, T2, MET$ (introduced in Equation (7.4.1)), collecting the results in Fig. 7.8.

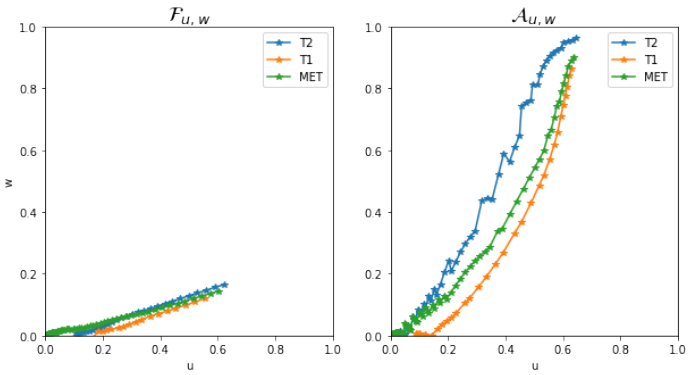

Fig. 7.8 Time evolution of $(\bar{u}_I(t), \bar{w}_I(t))$ for $I = T1, T2, MET$ as defined in Section 7.4.1 for bi-structured models.

Already from this first plot, we notice two aspects. The first one is that in Fisher's modelling, the epigenetic condition is quite homogeneous in space, having a similar behaviour for the three evolving radii considered. The second one is that, although the diffusive dynamics on the two epigenetic traits (i.e. the epimutation speed) have the same coefficient $\eta_u = \eta_w$, the evolutionary dynamics favour the evolution on the proliferative trait way more than on the motile one. Conversely, the anti-crowding model characterises the tumour population at different locations with respect to its epigenetic traits. In fact, cells belonging to the invasive rim (T2) tend to evolve faster in their motility trait, while cells belonging to the edge of the high-density zone (T1) tend to evolve faster in their proliferative trait. The metabolic radius in the first phase shares its epigenetic characterisation with T2 and, in a later phase, becomes more similar to T1 cells. This could be explained by the fact that space availability has a bigger impact on proliferation in the first phase. In contrast, in the second moment, the increase in the proliferation rate provided by the accumulation

of epigenetic mutation weighs more. This is also recognizable in Fig. 7.3, where R_{MET} starts nearer to R_{T2} and then approaches R_{T1}. Anti-crowding modelling has a more equilibrated evolution comparing the two traits, slightly favouring the motile one.

Now let us take into account three reference times $\bar{t}_0, \bar{t}_1, \bar{t}_2$, which are different for the two models and correspond to the instants in which the detectable tumour radius is respectively 2cm, 4cm, and 6cm. Fig. 7.9, 7.10, and 7.11 refer respectively to these times.

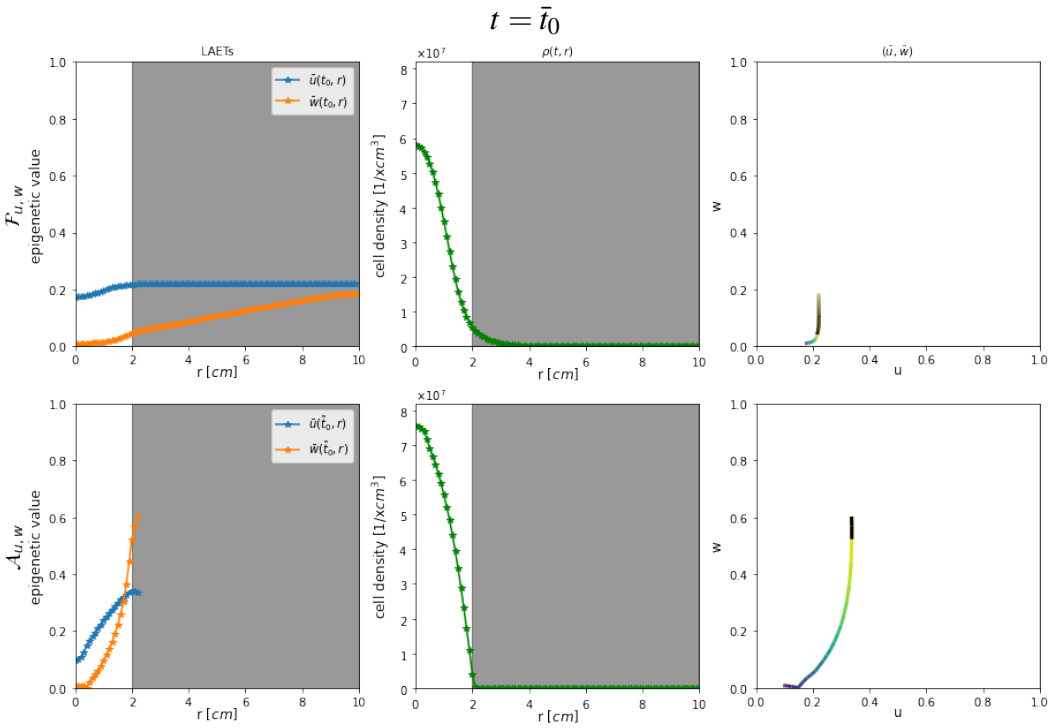

Fig. 7.9 Graphic analysis of the spatial characterisation of epigenetic traits according to tumour evolution phases. Plot refers to $t = \bar{t}_0$ corresponding, for every simulation, at the time at which tumour detectable radius is about 2 cm. The first column presents the profile of $\bar{u}(t,r)$, $\bar{w}(t,r)$, column two shows $\rho(t,r)$ state at the chosen time, and third column $(\bar{u}(t,r),\bar{w}(t,r))$ where darker colours define small distance from the centre of the tumour and lighter regions near the outer edge. In all the plots, the region of the tumour (and relative data) with a density lower than the detectable threshold is obscured.

For both the models, the three figures present the profile of $\bar{u}(t,r)$ and $\bar{w}(t,r)$ as a function of the radius (first column), $\rho(t,r)$ as a function of the radius (second column), and $(\bar{u}(t,r),\bar{w}(t,r))$ in the phase plane (u,w) (third column). In all the

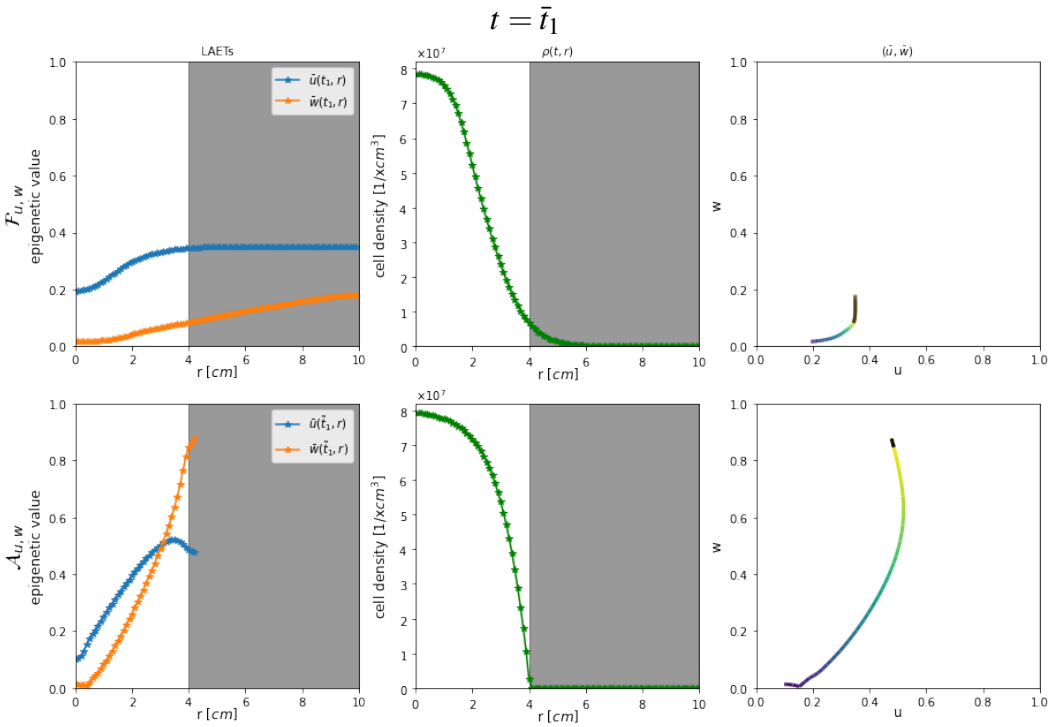

Fig. 7.10 Graphic analysis of spatial characterisation of epigenetic traits according to tumour evolution phases. Plot refers to $t = \bar{t}_1$ corresponding, for every simulation, at the time at which tumour detectable radius is about 4 cm. Fig. details as in Fig. 7.9

plots, the region of the tumour (and relative data) with a density lower than the detectable threshold is obscured. Let us observe that the diffusive dynamics in Fisher-like models make $\rho(t,r)$ occupies all the domains (even at very low density) coherently with the lack of compactness preservation exposed in the previous sections. Comparing the first columns, we see that in the detectable domain, Fisher-like modelling presents the proliferative trait more expressed than the motile one. Oppositely, in the anti-crowding model, there is always a switch radius at which the predominant trait changes. As time advances, the size of the domain where the motile trait is higher than the proliferative trait increases, showing that the tumour becomes more infiltrating as time passes. This configuration is confirmed by the third column, where the coloured part (dark colours correspond to areas near the centre of the tumour while light colours to the ones near the edge) of the Fisher-like model has a behaviour similar to a straight line with a low slope. This only proves the accumulation of mutation at the edge of the tumour, which was already observed in Ref. [246] without the need to insert a structure with respect to the motility trait.

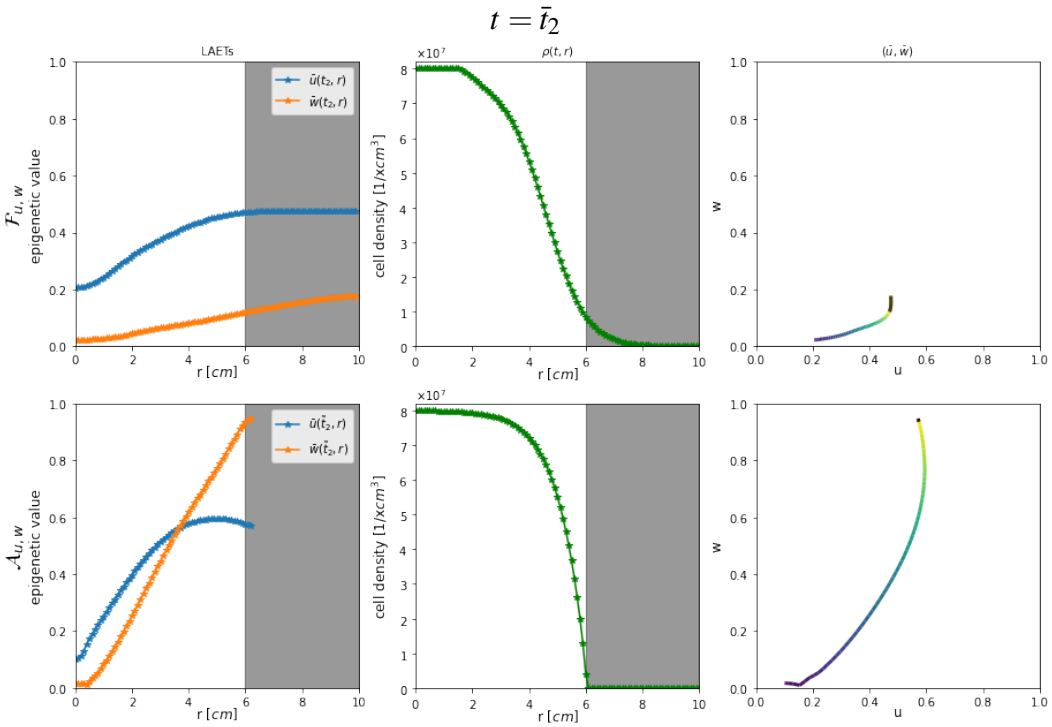

Fig. 7.11 Graphic analysis of spatial characterisation of epigenetic traits according to tumour evolution phases. Plot refers to $t = \bar{t}_2$ corresponding, for every simulation, at the time at which tumour detectable radius is about 6 cm. Fig. details as in Fig. 7.9

Conversely, the anti-crowding model is shaped as a "comma", initially growing up in both traits and then losing in proliferation to gain in motility while approaching the edge.

This is an essential feature of the anti-crowding model since it is more coherent with the biological observation presented in Section 7.1, where the tumour spheroid was presented as a stratified mass with an internal necrotic (or at least quiescent) core, a proliferative rim near the edge and a motile rim invading nearby tissues.

7.5 Conclusion and future perspectives

In the investigation that has been carried out so far, we have developed and compared Fisher-like and anti-crowding models with different degrees of epigenetic structure. We found that adopting bi-structured anti-crowding models allows compactness preservation of compact support initial data, the emergence of invasive lower-density

rims, and geometric characterisation of epigenetic and phenotypic traits expressed by cells.

Given the derivation of the model from the discrete case, we are currently working on developing the correspondent hybrid stochastic mesoscale model based on the same setting adopted in Ref. [246] to compare results with the continuous counterpart.

Moreover, we have introduced clinical-comparable mathematical descriptors to test the models' reliability in medical practice. In order to move in this direction, based on a database of tumour images held by MOLAB, we began to sequence the data coming from T1 and T2 MRI and PET. In particular, we applied segmentation and 3D reconstruction techniques of tumour masses to obtain information on the shape, regularity and phenotype disposition from images. Future perspectives go in the direction of testing the capability of the models to reproduce geometrical patterns observed qualitatively. Later, our interest is in applying this procedure to time-series data for parameter estimation. Furthermore, focusing on an edge recognition problem that emerged during the experience in applying sequencing techniques, an inverse approach appears to be of particular interest. In fact, especially in the case of the segmentation of glioblastomas (which constitute the database on which we have worked so far), it is significant to note how, despite the rapid and constant advances in artificial intelligence in the image recognition sector, human visual inspection and analysis are still necessary for the delineation of tumour edges and in the distinction of various tissues, which however leaves room for errors in sensitivity of the operator and individuality in the data interpretation. In this sense, it would be interesting to be able to develop the model, avoiding radial symmetry and including environmental factors, in the direction of better catching tumour evolution, but also offering a supporting tool in image analysis.

One other open question stands in the observation of medical data that, once fitted with Equation (7.4.7), present $\beta > 1$. In Ref. [371], authors present an alternative non-local model, where proliferative activity increases with the size of the mass, that is able to reproduce this behaviour. An exciting challenge stands in exploiting the bi-structure of the model to reproduce similar results.

Chapter 8

Continuous modelling for oncolytic virotherapy: a study of the influence of hypoxia

8.1 Introduction

As introduced in Section 1.4.2, the chance of oncolytic virotherapy to circumvent problems relating to immunoevasion and hypoxia-related resistance makes them a valid therapy combined with treatments that are in general more effective, but also sensitive to the problems mentioned above. In this chapter, we analyse the possible effects of different oxygenations on the outcome of treatment with oncolytic viruses alone, keeping an eye on the next step of integrating the therapy with more standard treatments (such as, for example, the radiotherapy analysed in Chapter 4).

More precisely, in this chapter, we aim to investigate this aspect, keeping into account two characterisations of the tumour mass: (i) its geometry and (ii) its epigenetic composition. With respect to the second, in detail, we address the trade-off between proliferation rate and resistance to hypoxia.

Considering oncolytic virotherapy, previous models have been developed without considering spatial and epigenetic characterisation, adopting ODE systems. A simple model strategy is to include two populations: one for uninfected tumour cells

(susceptibles) and one for the infected cells. This strategy does not include abiotic factors or the virus itself as a player in the model.

In Ref. [271], they identify the dependence of predicted dynamics on particular mathematical terms as the main limitation of mathematical modelling of oncolytic virus therapy. In order to solve this dependence, they propose different modelling strategies both for tumour growth (exponential, linear, logistic) and virus spread, revealing two categories: fast spread models, in which sufficiently high viral replication rates can lead to tumour eradication, and slow spread models, in which the suboptimal diffusion of the virus is the cause of treatment failure even in the case of high replicative potential. From a mathematical point of view, the virus is not directly inserted in the model, while they use an infective term that reads as $\beta I f(U,I)$ where we call U the uninfected cells and I the infected and the fast or slow spread is given by the behaviour of function f when $U \to \infty$ (respectively tending to a positive value or zero).

Also, in the context of Lotka-Volterra models with two populations considered, in Ref. [342], they suggested a parametric analysis of dynamic regimes, considering cytotoxicity and transmission rate of the virus and proliferation rate of tumour cells in both the state (infected and susceptible) as main parameters. Here, the spread of the virus is expressed as a function of the ratio of susceptible to infected tumour cells, defining the system with non-trivial equilibrium points. Also, under specific parameter values, complete eradication is possible (i.e., asymptotically stable equilibrium in (0,0)).

Moving to models that incorporate virus as a dependent variable separated from tumour population, in Ref. [239] authors use a Gompertz growth law for tumour growth and a frequency-dependent function to reproduce the dependence of the likelihood of a virus infecting a tumour cell based on the number of susceptible tumour cells. Exploiting local stability analysis and bifurcation plots, they highlight the singular equilibrium of the system and find long-period oscillations and bistable states so that they can obtain different outcomes depending on the initial conditions. From a mathematical point of view, the model introduced here is a follow-up of Ref. [240], in which they highlight the central role of viral infectivity and, for some particular values of that of the application profile, as a key parameter in engineering new treatments.

When moving to consider geometric space, a different approach is proposed in Ref. [449] where an agent-based, stochastic model is used to reproduce experimentally observed patterns and long-term outcomes under different conditions. In the paper, a parameter investigation determines the key parameters that determine the emergence of particular patterns of virus growth. Remaining in the context of discrete models, in Ref. [238], the authors put their interest on therapeutical strategies in terms of timing and location of virus injection. They adopt a 2d Voronoi Cell-Based model (VCBM) to investigate the sensitivity of the treatment efficacy applied to differently shaped tumours to the configuration of the treatment injections.

An interest in the geometry of the dynamics can be achieved with continuous modelling only with the use of partial derivative equations (PDEs). The same investigation on optimal therapeutical choices leads to the development of a radially-symmetric epidemic model embedded in a Stefan problem presented in Ref. [452]. The authors express the effectiveness of the therapy with a binary outcome (control or not control of the virus on the tumour) and delineate conditions that predict it in three different therapeutical approaches: homogeneous, centred or rim injections (here not of the virus itself, but of infected cells as the virus itself is not considered as a dependent variable). In a later work they also incorporate the immune response [453].

In Ref. [21], authors adopt a moving boundary model for virus-tumour interaction. They follow a multi-scale approach, including, at a micro-scale level, essential dynamics of the urokinase plasminogen activator (uPA) system. This leads to a macroscopic model that includes uninfected and infected tumour cells, the oncolytic viruses and (as a novelty with respect to the previously cited works) extracellular matrix (ECM), whose degradation as a result of microscopic dynamics directly influences cancer invasion potential.

Importance of ECM is remarked also in Ref. [266] where a promoted degradation of extracellular matrix in gliomas obtained with OV-expressing bacterial Chase-ABC is proven to cause an enhancement of OV spread and an increase of antitumour efficacy. A free boundary problem is introduced in Ref. [184]. Here, ECM is substituted by necrotic cell population, and the effects of the therapy are measured in terms of volume reduction of the tumour, whose surface is considered as the free boundary.

Moreover, in a more recent work [366], authors adopt a radial diffusion model and concentrate on the infective parameter, connecting it with the environment characteristics. Adopting bifurcation analysis, they devalue the strategy of creating longer-lasting virus particles or using strategies for reducing infected cell lifespan.

The last category includes models that keep into account some kind of heterogeneity, related either to cancer cells, viral particles or both at the same time. We remark that the most basic kind of heterogeneity is the spatial one, which has already been extensively mentioned in the previous sections: the ways to deal with it are PDEs and spatial agent-based model. We now focus on other heterogeneities, keeping in mind that the addition of the spatial structure is always possible.

In the epidemiological settings, the infectivity of an individual depends strongly on how much time has elapsed from infection. The inclusion of the time from the infection as a structuring variable for the infected individuals dates back to the first modern SI model [261]; an extension of the model taking into account spatial heterogeneity was later studied in Ref. [153].

Analogous considerations hold true in the case of oncolytic virotherapy, since it takes some time for a newly infected cell to start the viral production at the most efficient rate. Indeed, the age-structured approach was adopted in Ref. [156]. An alternative approach to model the phenomenon, which is more widely used, is through delay differential equations [135, 145, 333, 374, 442, 444], in which there is a sharp transition between newly infected cells and "mature" infected cells; this approximation is justified by the fact that the period of transition is relatively short with respect to other processes, hence the exact dynamics of the transition may be neglected. These second kind of models differ significantly from the mathematical formulations of the thesis, therefore we do not provide further details.

Moving our attention on the heterogeneity of traits, the easiest way to model heterogeneous populations is to structure them in discrete compartments, using an approach that is common in general epidemic models. For example, the model developed in Ref. [135] takes into account the fact that vesicular stomatitis viruses (VSV) is unable to replicate in T-lymphocites in the resting phase. As a consequence, uninfected cells are divided in a quiescent population, which cannot be infected, and a susceptible population: as time passes, cells move between the two states. An analogous approach may be used also to model heterogeneity involving the virus, either genetically [237] or as a coating level that prevents immune recognition [282].

Another possible approach is to consider a continuous trait variable and describe the evolution of the system via PDEs, similarly to the case of age-structured infections. Several examples can be found in the epidemiological settings [18, 41, 55, 299, 298, 341, 435], as well as in the ecological settings [33, 149]; in the context of oncolytic virotherapy, this approach was used in Ref. [255] to model several kinds of heterogeneity (susceptibility to infections, death rates, virulence).

A common characteristic of continuous structured models is the presence of a *trade-off* between different features, in the sense that the increase of a specific ability corresponds to the decrease of a different trait. Under this assumption, the fittest population depends on the specific situation that is modelled. In the context of infections, one may consider a trade-off involving the susceptible compartment between proliferation rate and resistance to the infection [299]; in the context of oncolytic viral infections, this is a way to model the fact that less proliferative cells have a slower metabolic activity, resulting in a slower infection. In absence of infection, the fittest trait is clearly the more proliferative one; on the other hand, the infection modifies the fitness landscape and the situation becomes less clear.

To our knowledge, there is no extension of the model presented in Ref. [299] that takes into account spatial heterogeneity in addition to phenotypic heterogeneity. This motivates the model developed in this work.

Few mathematical models are dedicated to the relationship between oxygen concentration and virotherapy effectiveness. [66] presents a mathematical model that simulates the infiltration of macrophages, engineered to release an oncolytic adenovirus under low-oxygen conditions, into an in vitro tumour spheroid. The model is employed to forecast the effectiveness of treatment protocols combined with radiotherapy. The model introduced in Ref. [377] examines the influence of hypoxia on disease dynamics, accounting for its effects on tumour growth and spread, as well as its impact on the effectiveness of oncolytic virotherapy as a treatment method.

In this chapter, we introduce a novel model for oncolytic virotherapy (Section 8.2). The model take into account hypoxia effects and includes an epigenetic structure for cancer population which addresses the trade-off between proliferation rate and resistance to hypoxia, involving, as a novelty, the effectiveness of virus in killing cancer cells. We present preliminary results (Section 8.3), including a draft of theoretical analysis of the model (Section 8.3.1), an explanation of the

numerical scheme developed to approximate solutions (Section 8.3.2), the derivation of the adopted parameter values (Section 8.3.3) and a presentation of the dynamics resulting from numerical simulations in a simplified scenario (Section 8.3.4). Finally, in Section 8.4 we summarize the state of the work and we present next steps and future perspectives.

8.2 Model description

We are interested in studying the influence of hypoxia on the infection of tumour cells by oncolytic viruses. Let us denote by $t \in [0,+\infty)$ the time, by $\boldsymbol{x} \in \Omega$ the space variable and by $y \in Y$ the epigenetic variable.

Our model describes the time evolution of four dependent variables: uninfected (or susceptible) cancer cells $u\colon [0,+\infty)\times\Omega\times Y \to [0,+\infty)$, infected cancer cells $I\colon [0,+\infty)\times\Omega \to [0,+\infty)$, virus $v\colon [0,+\infty)\times\Omega \to [0,+\infty)$ and oxygen $O\colon [0,+\infty)\times\Omega \to [0,+\infty)$.

Uninfected cancer cells $u(t,\boldsymbol{x},y)$ are the only elements to be characterised by the epigenetic structure. We assume a trade-off between proliferation on one side and resistance to hypoxia and virus infection on the other side. In this sense, we can assume y as the level of expression of a set of gene responsible for this trade-off and normalise it so that $Y=[0,1]$, where $y=0$ and $y=1$ are respectively the lowest and highest possible expressions. $y=0$ corresponds to the highest intrinsic proliferative rate, lowest resistance to hypoxia and highest infectivity rate. Also, $y=1$ corresponds to the lowest intrinsic proliferative rate, highest resistance to hypoxia and lowest infectivity rate. The regulating equation reads:

$$\begin{aligned}\partial_t u(t,\boldsymbol{x},y) =& D_y \overbrace{\partial^2_{yy} u(t,\boldsymbol{x},y)}^{\text{random mutation}} + \overbrace{D_{\boldsymbol{x}}\nabla\cdot(u(t,\boldsymbol{x},y)\nabla\rho(t,\boldsymbol{x}))}^{\text{anti-crowding movement}} + \\ &\big(\underbrace{P(y,\rho(t,\boldsymbol{x}))}_{\text{proliferation}} - \underbrace{S(y,O(t,\boldsymbol{x}))}_{\text{selection}}\big)\,u(t,\boldsymbol{x},y) - \underbrace{\beta(y)\,u(t,\boldsymbol{x},y)\,v(t,\boldsymbol{x})}_{\text{infection}}\end{aligned} \tag{8.2.1}$$

Uninfected cancer cells undergo random mutation, described as a diffusive term along the epigenetic domain with coefficient D_y. Moreover, cancer cells move with coefficient $D_{\boldsymbol{x}}$ in the spatial domain against the gradient of the local cancer cell

density

$$\rho(t,\boldsymbol{x}) = I(t,\boldsymbol{x}) + \int_Y u(t,\boldsymbol{x},y)\,\mathrm{d}y \tag{8.2.2}$$

that takes into account all infected and uninfected cells, despite their epigenetic trait (i.e. uninfected cells move away from the crowded zone, so we refer to this as an *anti-crowding* movement). Furthermore, cancer cells proliferate at a rate determined by the intrinsic proliferation rate $p(y)$ and the local cancer cell density $\rho(t,\boldsymbol{x})$, according to a logistic term where

$$P(y,\rho(t,\boldsymbol{x})) = p(y)\left(1-\frac{\rho(t,\boldsymbol{x})}{K}\right). \tag{8.2.3}$$

The equation for $u(t,\boldsymbol{x})$ includes a death factor caused by environmental selection driven by oxygen concentration. The fittest trait according to the oxygen availability is determined by function

$$\varphi(O) := \begin{cases} 1 & \text{if } O \le O_m \\ \dfrac{O_M - O}{O_M - O_m} & \text{if } O_m < O < O_M \\ 0 & \text{if } O \ge O_M. \end{cases} \tag{8.2.4}$$

Thus, the selective terms are expressed through a quadratic function of the distance of trait y from the fittest one

$$S(y,O(t,\boldsymbol{x})) = \eta(y-\varphi(O))^2. \tag{8.2.5}$$

Lastly, susceptible cancer cells are infected by the virus according to the density of virions and the infection rate $\beta(y)$. Note that y trait is directly involved in the selection term and both in the proliferation and infection term through the determination of coefficients $p(y)$ and $\beta(y)$. In order to catch the above-described trade-off, we define:

$$p(y) = p_M - (p_M - p_m)y, \qquad \beta(y) = \beta_m + (\beta_M - \beta_m)y. \tag{8.2.6}$$

Infected cancer cell $I(t,\boldsymbol{x})$ dynamics are described by equation:

$$\partial_t I(t,\boldsymbol{x}) = \underbrace{D_{\boldsymbol{x}}\nabla\cdot(I(t,\boldsymbol{x})\nabla\rho(t,\boldsymbol{x}))}_{\text{anti-crowding movement}} + \underbrace{v(t,\boldsymbol{x})\int_Y \beta(y)u(t,\boldsymbol{x},y)\,\mathrm{d}y}_{\text{infection}} - \underbrace{q_I I(t,\boldsymbol{x})}_{\text{death}}. \quad (8.2.7)$$

Infected cancer cells move according to the same law that regulates uninfected cancer cells. All susceptible cells undergoing infection are collected in the infected cancer cell population. Finally, infected cells die at rate q_I. Note that infected cells do not undergo proliferation, selection or infection, motivating the absence of structure in the population (since, in this model, these are dynamics influenced by the epigenetic trait).

Virus $v(t,\boldsymbol{x})$ is expressed in term of virions concentration and governed the following equation:

$$\partial_t v(t,\boldsymbol{x}) = \underbrace{D_v\Delta v(t,\boldsymbol{x})}_{\text{diffusion}} + \underbrace{\alpha q_I I(t,\boldsymbol{x})}_{\text{release}} - \underbrace{q_v v(t,\boldsymbol{x})}_{\text{natural decay}} + \underbrace{v_{\text{inj}}(\boldsymbol{x})\delta_{T_{\text{inj}}}(t)}_{\text{injection}} \quad (8.2.8)$$

The virus diffuses in the space domain with coefficient D_v, is released at rate α by dying infected cells and decays with rate q_v.

Oxygen $O(t,\boldsymbol{x})$ behavior is determined by:

$$\partial_t O(t,\boldsymbol{x}) = \underbrace{D_O\Delta O(t,\boldsymbol{x})}_{\text{diffusion}} - \underbrace{q_O O(t,\boldsymbol{x})}_{\text{natural decay}} - \underbrace{\lambda\rho(t,\boldsymbol{x})O(t,\boldsymbol{x})}_{\text{cancer cell consumption}} + \underbrace{Q(\boldsymbol{x})}_{\text{source}} \quad (8.2.9)$$

Oxygen diffuses in the space domain with diffusion coefficient D_O, is delivered by tissue vascularisation with a space-dependent intensity $Q(\boldsymbol{x})$ and is then consumed both by healthy tissue and cancer cells. Healthy cell consumption is captured avoiding a direct insertion of the cells in the model, using a decay term at rate q_O that assumes that the carrying capacity of the tissue is filled up by healthy cells. Moreover, when the tumour begins to populate, the $\lambda\rho(t,\boldsymbol{x})O(t,\boldsymbol{x})$term is responsible for increasing, from the average rate of healthy cells to that of tumour cells, the oxygen consumption of the proportion of healthy cells that have been replaced by tumour cells. Both infected and uninfected cells are responsible for oxygen consumption.

Putting all equations together, the evolution of the system reads:

$$\begin{cases} \partial_t u(t,\boldsymbol{x},y) = D_y \partial^2_{yy} u(t,\boldsymbol{x},y) + D_{\boldsymbol{x}} \operatorname{div}_{\boldsymbol{x}}(u(t,\boldsymbol{x},y)\nabla\rho(t,\boldsymbol{x})) + P(y,\rho(t,\boldsymbol{x}))\, u(t,\boldsymbol{x},y) - \\ \qquad\qquad - S(y,O(t,\boldsymbol{x}))\, u(t,\boldsymbol{x},y) - \beta(y)\, u(t,\boldsymbol{x},y)\, v(t,\boldsymbol{x}) \\ \partial_t I(t,\boldsymbol{x}) = D_{\boldsymbol{x}} \operatorname{div}(I(t,\boldsymbol{x})\nabla\rho(t,\boldsymbol{x})) + v(t,\boldsymbol{x}) \int_Y \beta(y) u(t,\boldsymbol{x},y)\,\mathrm{d}y - q_I I(t,\boldsymbol{x}) \\ \partial_t v(t,\boldsymbol{x}) = D_v \Delta v(t,\boldsymbol{x}) + \alpha q_I I(t,\boldsymbol{x}) - q_v v(t,\boldsymbol{x}) + v_{\text{inj}}(\boldsymbol{x})\delta_{T_{\text{inj}}}(t) \\ \partial_t O(t,\boldsymbol{x}) = D_O \Delta O(t,\boldsymbol{x}) - q_O O(t,\boldsymbol{x}) - \lambda\rho(t,\boldsymbol{x}) O(t,\boldsymbol{x}) + Q(\boldsymbol{x}) \\ \rho(t,\boldsymbol{x}) \coloneqq \int_Y u(t,\boldsymbol{x},y)\,\mathrm{d}y + I(t,\boldsymbol{x}) \end{cases} \tag{8.2.10}$$

with the already defined $\rho(t,\boldsymbol{x})$ in Eq. (8.2.2), $P(y,\rho(t,\boldsymbol{x}))$ in Eq. (8.2.3), $S(y,O(t,\boldsymbol{x}))$ in Eq.(8.2.5) based on $\varphi(O(t,\boldsymbol{x}))$ in Eq. (8.2.4), and $p(y)$ and $\beta(y)$ chosen as in Eq. (8.2.6). We keep $V(x)$ in general form as it will change according to the biological setting we reproduce. We define the Cauchy problem imposing:

$$\begin{cases} u(0,\boldsymbol{x},y) = u_0(\boldsymbol{x},y) \\ I(0,\boldsymbol{x}) = I_0(\boldsymbol{x}) \\ v(0,\boldsymbol{x}) = v_0(\boldsymbol{x}) \\ O(0,\boldsymbol{x}) = O_0(\boldsymbol{x}) \end{cases} \tag{8.2.11}$$

where $u_0(\boldsymbol{x},y)$, $I_0(\boldsymbol{x})$, $v_0(\boldsymbol{x})$ and $O_0(\boldsymbol{x})$ will be defined in the context of the various scenarios in Section 8.3. Moreover, we put no flux boundary conditions on ∂Y that reads

$$\partial_y u(t,\boldsymbol{x},0) = \partial_y u(t,\boldsymbol{x},1) = 0.$$

Finally, when considering $\Omega \subset \mathbb{R}^2$, we put no flux boundary condition for all $u(t,\boldsymbol{x},y)$, $I(t,\boldsymbol{x})$, $v(t,\boldsymbol{x})$ and $O(t,\boldsymbol{x})$ at $\partial\Omega$.

8.3 Results

In this Section we describe the results of numerical simulations and compare them with the theoretical analysis performed in Section 8.3.1. For the sake of simplicity, we first consider a stationary oxygen distribution independent of time, corresponding to a situation in which the tumour has no influence on the oxygen distribution: while this is clearly an oversimplification, it allows us to focus our attention on the tumour's

evolutionary and infectious dynamics. We then analyse the full model that includes oxygen dynamics, taking into account different configurations of oxygen sources. Finally, we briefly mention the case of a virus that specifically infects hypoxic cells, looking towards the combination of oncolytic virotherapy with other treatments.

In all the simulation we start with an uninfected tumour of the form

$$u(0,\boldsymbol{x},y) = \begin{cases} A_u\, e^{-\frac{|\boldsymbol{x}-\boldsymbol{x}_0|^2}{\theta_{\boldsymbol{x}}}-\frac{(y-y_0)^2}{\theta_y}} & \text{if } A_u\, e^{-\frac{|\boldsymbol{x}-\boldsymbol{x}_0|^2}{\theta_{\boldsymbol{x}}}-\frac{(y-y_0)^2}{\theta_y}} > 1 \\ 0 & \text{otherwise} \end{cases} \tag{8.3.1}$$

The truncation is performed in order to have an initial condition with compact support; the form of the equations is such that the solution will still be compactly supported at all times. In all the simulations we set $A_u = \frac{K}{10}$, $\boldsymbol{x}_0 = (0,0)$, $y_0 = \varphi(O(0,\boldsymbol{x}_0))$, $\theta_{\boldsymbol{x}} = 0.5$, $\theta_y = 0.5$. We then assume that viral injection is performed after some time, so that the tumour can adapt to the environment. In most of the case, we perform a central viral injection as soon as the tumour reaches a given size: in mathematical terms, we set

$$T_{\text{inj}} := \inf\left\{ t \in [0,+\infty) \,\middle|\, d(t) \geq d_{\text{inj}} \right\} \tag{8.3.2}$$

where d_{inj} is the tumour size at which we choose to inject the virus and

$$d(t) := diam\left\{ \boldsymbol{x} \in \Omega \,\middle|\, \rho(\boldsymbol{x},t) \geq \frac{K}{10} \right\}$$

We recall that the diameter of a general set E is defined as

$$diam\, E := \sup\{\, |\boldsymbol{x}_1 - \boldsymbol{x}_2| \mid \boldsymbol{x}_1, \boldsymbol{x}_2 \in E \,\}$$

In the particular situation of a circle, this definition clearly coincides with the standard diameter; in the general case, the diameter is the longest length that can be found inside the set. This choice is based on the assumptions that small tumours cannot be clinically detected, hence the therapy may only start when cancer cells reach a density of at least one tenth of the carrying capacity in a big region. We set $d_{\text{inj}} = 5.2$ mm, as in Ref. [264]. The central viral injection takes the form

$$v_{\text{inj}}(\boldsymbol{x}) = A_v\, e^{-\frac{|\boldsymbol{x}-\boldsymbol{x}_0|^2}{\theta_v}}, \tag{8.3.3}$$

with $A_v = 10^9$, $\theta_v = 0.5$. This allows to equalise the total number of viral particles in the experiments performed in Ref. [264].

8.3.1 Draft of asymptotic analysis

Let us assume that the tumour dynamics do not significantly affect the oxygen density so that $O(t,\boldsymbol{x}) \equiv O$ is stationary and homogeneous. Eq. (8.2.10) then becomes

$$\begin{cases} \partial_t u(t,\boldsymbol{x},y) = D_y \partial^2_{yy} u(t,\boldsymbol{x},y) + D_{\boldsymbol{x}} \operatorname{div}_{\boldsymbol{x}}(u(t,\boldsymbol{x},y)\nabla\rho(t,\boldsymbol{x})) \\ \qquad\qquad + R(y,\rho(t,\boldsymbol{x}),O,v(t,\boldsymbol{x}))\, u(t,\boldsymbol{x},y) \\ \partial_t I(t,\boldsymbol{x}) = D_{\boldsymbol{x}} \operatorname{div}(I(t,\boldsymbol{x})\nabla\rho(t,\boldsymbol{x})) + v(t,\boldsymbol{x}) \int_Y \beta(y) u(t,\boldsymbol{x},y)\,\mathrm{d}y - q_I I(t,\boldsymbol{x}) \\ \partial_t v(t,\boldsymbol{x}) = D_v \Delta v(t,\boldsymbol{x}) + \alpha q_I I(t,\boldsymbol{x}) - q_v v(t,\boldsymbol{x}) \\ \rho(t,\boldsymbol{x}) \coloneqq \int_Y u(t,\boldsymbol{x},y)\,\mathrm{d}y + I(t,\boldsymbol{x}) \end{cases} \tag{8.3.4}$$

with

$$R(y,\rho,O,v) \coloneqq [p_M + (p_m - p_M)y]\left(1 - \frac{\rho}{K}\right) - \eta(y - \varphi(O))^2 - [\beta_M + (\beta_m - \beta_M)y]v$$

Building upon previous models [43, 154], we introduce a small parameter ε and assume that

$$D_{\boldsymbol{x}} = \varepsilon, \qquad D_y = D_v = \varepsilon^2$$

Furthermore, we use the time scaling $t \mapsto \frac{t}{\varepsilon}$ (which allows us to study the long-time behaviour of the system) and define.

$$u_\varepsilon(t,\boldsymbol{x},y) \coloneqq u\left(\frac{t}{\varepsilon},\boldsymbol{x},y\right), \qquad I_\varepsilon(t,\boldsymbol{x}) \coloneqq I\left(\frac{t}{\varepsilon},\boldsymbol{x}\right), \qquad v_\varepsilon(t,\boldsymbol{x}) \coloneqq v\left(\frac{t}{\varepsilon},\boldsymbol{x}\right)$$

The previous system becomes

$$\begin{cases} \varepsilon\partial_t u_\varepsilon(t,\boldsymbol{x},y) = \varepsilon^2 \partial^2_{yy} u_\varepsilon(t,\boldsymbol{x},y) + \varepsilon \operatorname{div}_{\boldsymbol{x}}(u_\varepsilon(t,\boldsymbol{x},y)\nabla\rho_\varepsilon(t,\boldsymbol{x})) \\ \qquad\qquad + R(y,\rho_\varepsilon(t,\boldsymbol{x}),O,v_\varepsilon(t,\boldsymbol{x}))\, u_\varepsilon(t,\boldsymbol{x},y) \\ \varepsilon\partial_t I_\varepsilon(t,\boldsymbol{x}) = \varepsilon \operatorname{div}(I_\varepsilon(t,\boldsymbol{x})\nabla\rho_\varepsilon(t,\boldsymbol{x})) + v_\varepsilon(t,\boldsymbol{x}) \int_Y \beta(y) u(t,\boldsymbol{x},y)\,\mathrm{d}y - q_I I(t,\boldsymbol{x}) \\ \varepsilon\partial_t v_\varepsilon(t,\boldsymbol{x}) = \varepsilon^2 \Delta v_\varepsilon(t,\boldsymbol{x}) + \alpha q_I I_\varepsilon(t,\boldsymbol{x}) - q_v v_\varepsilon(t,\boldsymbol{x}) \\ \rho_\varepsilon(t,\boldsymbol{x}) \coloneqq \int_Y u_\varepsilon(t,\boldsymbol{x},y)\,\mathrm{d}y + I_\varepsilon(t,\boldsymbol{x}) \end{cases} \tag{8.3.5}$$

Let us observe that, letting $\varepsilon \to 0$ and assuming that all the functions converge, we immediately get from the third equation

$$v(t,\boldsymbol{x}) = \frac{\alpha q_I}{q_v} I(t,\boldsymbol{x}) \tag{8.3.6}$$

and from the second equation

$$I(t,\boldsymbol{x}) = 0 \quad \vee \quad \int_Y \beta(y) u(t,\boldsymbol{x},y)\,\mathrm{d}y = \frac{q_I I(t,\boldsymbol{x})}{v(t,\boldsymbol{x})} = \frac{q_v}{\alpha} \tag{8.3.7}$$

However, it is important to note that the system may not converge to an equilibrium: indeed, central oscillations, which persist for very long times, can be observable when choosing parameter values in specific ranges. This is not surprising, as it resembles the behaviour of similar models of infections mediated by a virus [366].

We then make for uninfected cells the real phase WKB ansatz [42]

$$u_\varepsilon(t,\boldsymbol{x},y) = e^{\frac{n_\varepsilon(t,\boldsymbol{x},y)}{\varepsilon}}$$

which implies

$$\partial_t u_\varepsilon = \frac{\partial_t n_\varepsilon}{\varepsilon} u_\varepsilon, \quad \nabla_{\boldsymbol{x}} u_\varepsilon = \frac{\nabla_{\boldsymbol{x}} n_\varepsilon}{\varepsilon} u_\varepsilon \quad \partial^2_{yy} u_\varepsilon = \Big(\frac{(\partial_y n_\varepsilon)^2}{\varepsilon^2} + \frac{\partial^2_{yy} n_\varepsilon}{\varepsilon} \Big) u_\varepsilon$$

The first equation of Eq. (8.3.5) yields

$$\begin{aligned} \varepsilon \frac{\partial_t n_\varepsilon}{\varepsilon} u_\varepsilon =& \varepsilon^2 \Big(\frac{(\partial_y n_\varepsilon)^2}{\varepsilon^2} + \frac{\partial^2_{yy} n_\varepsilon}{\varepsilon} \Big) u_\varepsilon + \varepsilon \Big(\frac{\nabla_{\boldsymbol{x}} n_\varepsilon}{\varepsilon} \cdot \nabla \rho(t,\boldsymbol{x}) + \Delta \rho(t,\boldsymbol{x}) \Big) u_\varepsilon \\ &+ R(y, \rho_\varepsilon(t,\boldsymbol{x}), O, v_\varepsilon(t,\boldsymbol{x})) u_\varepsilon \end{aligned}$$

and this simplifies to

$$\partial_t n_\varepsilon = (\partial_y n_\varepsilon)^2 + \varepsilon \partial^2_{yy} n_\varepsilon + \nabla_{\boldsymbol{x}} n_\varepsilon \cdot \nabla \rho(t,\boldsymbol{x}) + \varepsilon \Delta \rho(t,\boldsymbol{x}) + R(y, \rho_\varepsilon(t,\boldsymbol{x}), O, v_\varepsilon(t,\boldsymbol{x}))$$

Letting $\varepsilon \to 0$ and assuming convergence, we obtain

$$\partial_t n = (\partial_y n)^2 + \nabla_{\boldsymbol{x}} n \cdot \nabla \rho(t,\boldsymbol{x}) + R(y, \rho(t,\boldsymbol{x}), O, v(t,\boldsymbol{x})) \tag{8.3.8}$$

All the functions without the subscript ε are the leading order terms of the asymptotic expansion. Under appropriate concavity hypotheses, we expect n to be a strictly

concave function of y and we define

$$\bar{y}(t,\boldsymbol{x}) \coloneqq \arg\max_{y\in Y} n(t,\boldsymbol{x},y)$$

Let us fix $\boldsymbol{x} \in \mathrm{supp}(\rho)$. The fact that $\rho_\varepsilon(t,\boldsymbol{x}) < +\infty$ for all ε implies that

$$n(t,\boldsymbol{x},\bar{y}(t,\boldsymbol{x})) = \max_{y\in Y} n(t,\boldsymbol{x},y) = 0$$

and therefore trivially

$$\partial_y n(t,\boldsymbol{x},\bar{y}(t,\boldsymbol{x})) = 0$$

We also observe that

$$0 = \frac{\partial}{\partial t} n(t,\boldsymbol{x},\bar{y}(t,\boldsymbol{x})) = \partial_t n(t,\boldsymbol{x},y)|_{y=\bar{y}(t,\boldsymbol{x})} + \partial_y n(t,\boldsymbol{x},y)|_{y=\bar{y}(t,\boldsymbol{x})} \partial_t \bar{y}(t,\boldsymbol{x})$$

implying that $\partial_t n(t,\boldsymbol{x},\bar{y}(t,\boldsymbol{x})) = 0$; similarly, $\nabla_{\boldsymbol{x}} n(t,\boldsymbol{x},\bar{y}(t,\boldsymbol{x})) = 0$.

We evaluate Eq. (8.3.8) in $y = \bar{y}(t,\boldsymbol{x})$ to get

$$\begin{aligned} &[p_M + (p_m - p_M)y]\left(1 - \frac{\rho}{K}\right) - \eta(y - \varphi(O))^2 - [\beta_M + (\beta_m - \beta_M)y]v = \\ &\quad = R(\bar{y}(t,\boldsymbol{x}),\rho(t,\boldsymbol{x}),O,v(t,\boldsymbol{x})) = \partial_t n - (\partial_y n)^2 - \nabla_{\boldsymbol{x}} n \cdot \nabla\rho(t,\boldsymbol{x}) = 0 \end{aligned} \tag{8.3.9}$$

We can also derive Eq. (8.3.8) with respect to y to get

$$\partial^2_{ty} n = 2\partial_y n\, \partial^2_{yy} n + \partial_y \nabla_{\boldsymbol{x}} n \cdot \nabla\rho(t,\boldsymbol{x}) + \nabla_{\boldsymbol{x}} n \cdot \partial_y \nabla\rho(t,\boldsymbol{x}) + \partial_y R(y,\rho(t,\boldsymbol{x}),O,v(t,\boldsymbol{x}))$$

which computed at $y = \bar{y}(t,\boldsymbol{x})$ yields

$$\partial^2_{ty} n(t,\boldsymbol{x},\bar{y}(t,\boldsymbol{x})) = \partial_y \nabla_{\boldsymbol{x}} n(t,\boldsymbol{x},\bar{y}(t,\boldsymbol{x})) \cdot \nabla\rho(t,\boldsymbol{x}) + \partial_y R(\bar{y}(t,\boldsymbol{x}),\rho(t,\boldsymbol{x}),O,v(t,\boldsymbol{x}))$$

If we look for a homogeneous steady state, then the previous equation implies

$$\begin{aligned} \partial_y R(\bar{y},\rho,O,v) &= (p_m - p_M)\left(1 - \frac{\rho}{K}\right) - 2\eta(y - \varphi(O)) - (\beta_m - \beta_M)v \\ &= 0 \end{aligned} \tag{8.3.10}$$

It is reasonable to consider $u_\varepsilon \overset{*}{\rightharpoonup} U\,\delta_{\bar{y}}$ and so

$$\int_Y \beta(y) u_\varepsilon(t,\boldsymbol{x},y)\,\mathrm{d}y \to \beta(\bar{y})U$$

With this observation, Eqs. (8.3.6), (8.3.7), (8.3.9) and (8.3.10) constitute a system of four equations in the four variables $U, I, v, \bar{y}$, which in principle can be solved. The case $I = 0$ clearly implies $v = 0$ and there exist two solutions: the first one is $\rho = K, \bar{y} = \varphi(O)$; the second one is

$$\bar{y} = \frac{2p_M}{p_M - p_m} - \varphi(O) > \frac{2p_M}{p_M - p_m} - 1 = \frac{p_M + p_m}{p_M - p_m} > 1$$
$$U = K + \frac{4p(\varphi(O))}{(p_m - p_M)^2} > K$$

and it clearly has no biological meaning. Let us now assume $I \neq 0$, which according to Eq. (8.3.7) implies

$$U = \frac{q_v}{\alpha\beta(\bar{y})}$$

We need to solve the system

$$\begin{cases} U = \dfrac{q_v}{\alpha[\beta_M + (\beta_m - \beta_M)\bar{y}]} \\ v = \dfrac{\alpha q_I}{q_v} I \\ R(\bar{y}, U+I, O, v) = [p_M + (p_m - p_M)\bar{y}]\left(1 - \dfrac{U+I}{K}\right) - \eta(\bar{y} - \varphi(O))^2 \\ \qquad\qquad - [\beta_M + (\beta_m - \beta_M)\bar{y}]v = 0 \\ \partial_y R(\bar{y}, U+I, O, v) = (p_m - p_M)\left(1 - \dfrac{U+I}{K}\right) - 2\eta(\bar{y} - \varphi(O)) \\ \qquad\qquad - (\beta_m - \beta_M)v = 0 \end{cases}$$

We can easily include the expressions of U and v in the last two equations, obtaining

$$\begin{cases} [p_M + (p_m - p_M)\bar{y}]\left(1 - \dfrac{\frac{q_v}{\alpha[\beta_M + (\beta_m - \beta_M)\bar{y}]} + I}{K}\right) - \eta(\bar{y} - \varphi(O))^2 \\ \qquad - [\beta_M + (\beta_m - \beta_M)\bar{y}]\dfrac{\alpha q_I}{q_v} I = 0 \\ (p_m - p_M)\left(1 - \dfrac{\frac{q_v}{\alpha[\beta_M + (\beta_m - \beta_M)\bar{y}]} + I}{K}\right) - 2\eta(\bar{y} - \varphi(O)) - (\beta_m - \beta_M)\dfrac{\alpha q_I}{q_v} I = 0 \end{cases}$$

We then computed I as a function of $\bar{y}$ from the second equation

$$I = \frac{p_M - p_m - \frac{q_v(p_M-p_m)}{K\alpha(\bar{y}[\beta_m-\beta_M]+\beta_M)} + 2\eta(\bar{y}-\varphi(O))}{\frac{p_M-p_m}{K}+\beta_M-\beta_m}$$

and $\bar{y}$ is the solution of the equation

$$\begin{aligned}
&\frac{(\bar{y}p_m-(\bar{y}-1)p_M)\cdot\left(\beta_m\left(\alpha(K-2K\bar{y})\beta_M-q_v+2\alpha\eta\bar{y}(\bar{y}-\varphi(O))\right)+\alpha K\bar{y}\beta_m^2\right)}{\alpha\left(\bar{y}\beta_m-(\bar{y}-1)\beta_M\right)\left(K\left(\beta_m-\beta_M\right)+p_m-p_M\right)}\cdot\\
&+\frac{(\bar{y}p_m-(\bar{y}-1)p_M)\left(+\beta_M\left(q_v-\alpha(\bar{y}-1)\left(-2\eta\varphi(O)-K\beta_M+2\eta\bar{y}\right)\right)\right)}{\alpha\left(\bar{y}\beta_m-(\bar{y}-1)\beta_M\right)\left(K\left(\beta_m-\beta_M\right)+p_m-p_M\right)}\\
&-\frac{\alpha K q_I\left(\bar{y}\beta_m-(\bar{y}-1)\beta_M\right)\left(\frac{q_v(p_m-p_M)}{\alpha K(\bar{y}\beta_m-(\bar{y}-1)\beta_M)}-p_m+p_M+2\eta(\bar{y}-\varphi(O))\right)}{q_v\left(K\left(\beta_M-\beta_m\right)-p_m+p_M\right)}\\
&-\eta(\bar{y}-\varphi(O))^2=0
\end{aligned} \tag{8.3.11}$$

Let us also observe that we may obtain $\bar{y}$ from the equation $\partial_y R = 0$:

$$\bar{y} = \varphi(O) + \frac{1}{2\eta}\left[-(p_M-p_m)\left(1-\frac{\rho}{K}\right)+(\beta_m-\beta_M)v\right] \tag{8.3.12}$$

This formula has a clear interpretation: $\varphi(O)$ is the epigenetic trait selected by the oxygen concentration; the fittest trait tends to grow when the total cell population ρ is low due to the different proliferation rates of cell lines in a situation of low competition, while it grows in the presence of viral infection.

8.3.2 Numerical method

To perform numerical simulations of the model, we use the finite volume method, adapting the procedure presented in Ref. [88] to our problem. We firstly consider equations of the form:

$$\frac{\partial f}{\partial t}(t,\mathbf{x}) = \mathscr{M}(t,\mathbf{x}) + \mathscr{R}(t,\mathbf{x}) \tag{8.3.13}$$

where

$$\mathscr{M}(t,\mathbf{x}) = \nabla_{\boldsymbol{x}}\cdot(\Phi(t,\boldsymbol{x})f) \tag{8.3.14}$$

regulates the movement and $\mathscr{R}(t,\boldsymbol{x})$ the reactions.
Concerning the space, we consider a proper closed subset of $\mathbb{R}^2$ $\tilde{\Omega} = [x_{1,min}, x_{1,max}] \times [x_{2,min}, x_{2,max}] \subseteq \mathbb{R}^2$. We introduce a uniform mesh consisting of the cells $C_{j,k} := [x_{1,j-\frac{1}{2}}, x_{1,j+\frac{1}{2}}] \times [x_{2,k-\frac{1}{2}}, x_{2,k+\frac{1}{2}}]$, for $j = 0,\dots,N_{x_1}$ and for $k = 0,\dots,N_{x_2}$, of size $\Delta x_1 \times \Delta x_2$ where $\Delta x_i = \frac{x_{i,max}-x_{i,min}}{N_{x_i}+1}$ for $i = 1,2$.

We adopt a splitting method, considering separately the movement and reaction terms. We begin with the conservative part $\mathscr{M}(t,x)$. We define:

$$f_{j,k}(t) = \frac{1}{\Delta x_1 \Delta x_2} \int_{C_{j,k}} f(t,\boldsymbol{x}) d\boldsymbol{x}.$$

Then, we adopt a general semi-discrete finite-volume scheme, which is defined as:

$$M_{j+\frac{1}{2},k} = (\Phi^1_{j+\frac{1}{2},k})^+ f^E_{j,k} + (\Phi^1_{j+\frac{1}{2},k})^- f^W_{j+1,k}$$
$$M_{j,k+\frac{1}{2}} = (\Phi^2_{j,k+\frac{1}{2}})^+ f^N_{j,k} + (\Phi^2_{j,k+\frac{1}{2}})^- f^S_{j,k+1}\,.$$

Here:

- $(\cdot)^+$ and $(\cdot)^-$ indicate the positive and negative part of their arguments, respectively, i.e., $(\cdot)^+ = \max\{0,\cdot\}$ and $(\cdot)^- = \min\{0,\cdot\}$;
- the apices E, W, N, S indicate East, West, North, and South and correspond to the evaluation of the piecewise reconstruction using the following d-order truncation of Taylor expansion. In this case we consider $d = 0$, so we adopt piecewise constant reconstruction assuming $f^E_{j,k} = f^W_{j,k} = f^N_{j,k} = f^S_{j,k} = f_{j,k}$.
- $\Phi^1 := \Phi_{x_1}$ and $\Phi^2 := \Phi_{x_2}$ are the components of Φ^1 along the x_1 and x_2 axis respectively.

Note that the derivatives in the middle points are evaluated as

$$(\partial_{x_1} f)_{j+\frac{1}{2},k} = \frac{f_{j+1,k} - f_{j,k}}{\Delta x_1}, \qquad (\partial_{x_2} f)_{j,k+\frac{1}{2}} = \frac{f_{j,k+1} - f_{j,k}}{\Delta x_2},$$

while the derivatives in the nodes are evaluated as

$$(\partial_{x_1} f)_{j,k} = \frac{f_{j+1,k} - f_{j-1,k}}{2\Delta x_1}, \qquad (\partial_{x_2} f)_{j,k} = \frac{f_{j,k+1} - f_{j,k-1}}{2\Delta x_2}.$$

For the time discretisation, we use the forward Euler method. We denote the discretised time step with apex l, i.e.,

$$t^l = t_0 + \sum_{i=1}^{l-1} \Delta t_i \,.$$

To optimise the performances, we use adaptive time steps obtained by imposing the positivity-preserving CFL

$$\Delta t_l \leq \Delta \mathscr{T}_l := \min \left\{ \frac{\Delta x_1}{4\Phi_M^1}, \frac{\Delta x_2}{4\Phi_M^2} \right\}$$

where $\Phi_M^1 = \max\limits_{j,k} \left(|\Phi^{1\,l}_{j+\frac{1}{2},k}| \right)$ and $\Phi_M^2 = \max\limits_{j,k} \left(|\Phi^{2\,l}_{j,k+\frac{1}{2}}| \right)$.

For the reaction term $\mathscr{R}(t,\boldsymbol{x})$, we adopt a simple forward Euler method for the time derivative. We set the discretized initial condition $f^0_{j,k}$ provided for each $j = 0,\ldots,N_{x_1}$ and for $k = 0,\ldots,N_{x_2}$, being $f^l_{j,k}$ the numerical approximation of $f_{j,k}(t^l)$. The complete split numerical scheme reads

$$\begin{cases} f^{l+\frac{1}{2}}_{j,k} = f^l_{j,k} - \dfrac{\Delta t_l}{\Delta x_1} \left(M^l_{j+\frac{1}{2},k} - M^l_{j-\frac{1}{2},k} \right) - \dfrac{\Delta t_l}{\Delta x_2} \left(M^l_{j,k+\frac{1}{2}} - M^l_{j,k-\frac{1}{2}} \right) \\ f^{l+1}_{j,k} = f^{l+\frac{1}{2}}_{j,k} + \Delta t_l R^{l+\frac{1}{2}}_{j,k} \end{cases} \tag{8.3.15}$$

for $l = 1,\ldots,N_l$. In the proposed experiments, we set the spatial domain $\Omega = [-10,10] \times [-10,10]\,\mathrm{mm}^2$ and we consider the time $t \in [0,T]$, with $T > 0$. Dealing with a limited domain, we set no flux boundary conditions.

Moreover, we have equations of the form:

$$\frac{\partial f}{\partial t}(t,\mathbf{x}) = \mathscr{M}(t,\mathbf{x}) + \mathscr{R}(t,\mathbf{x}) \tag{8.3.16}$$

with

$$\mathscr{M}(t,\mathbf{x}) = D\Delta_{\boldsymbol{x}} f = D\nabla_{\boldsymbol{x}} \cdot (\nabla_{\boldsymbol{x}} f) \tag{8.3.17}$$

so that M expression in Equation 8.3.15 reads

$$M_{j+\frac{1}{2},k} = -D\partial_{x_1} f_{j+\frac{1}{2},k}$$

$$M_{j,k+\frac{1}{2}} = -D\partial_{x_2} f_{j,k+\frac{1}{2}},$$

where derivatives are computed as introduced above.

Lastly, we consider functions of the type

$$\frac{\partial f}{\partial t}(t,\mathbf{x},y) = \mathscr{M}(t,\mathbf{x},y) + \mathscr{R}(t,\mathbf{x},y) \tag{8.3.18}$$

where

$$\mathscr{M}(t,\mathbf{x},y) = \nabla_{\boldsymbol{x}} \cdot (\Phi(t,\boldsymbol{x}) f) + D\Delta_y f \tag{8.3.19}$$

We discretize the space $\tilde{\Omega} \times Y$ with a uniform mesh consisting of the cells $C_{j,k,m} := [x_{1,j-\frac{1}{2}}, x_{1,j+\frac{1}{2}}] \times [x_{2,k-\frac{1}{2}}, x_{2,k+\frac{1}{2}}] \times [y_{m-\frac{1}{2}}, y_{m+\frac{1}{2}}]$, for $j = 0,\dots,N_{x_1}$, $k = 0,\dots,N_{x_2}$, and $m = 0,\dots,N_y$ of size $\Delta x_1 \times \Delta x_2 \times \Delta y$ where $\Delta x_i = \frac{x_{i,max} - x_{i,min}}{N_{x_i}+1}$ for $i = 1,2$ and $\Delta y = \frac{1}{N_y+1}$.
We define:

$$M_{j+\frac{1}{2},k,m} = (\Phi^1_{j+\frac{1}{2},k,m})^+ f^E_{j,k,m} + (\Phi^1_{j+\frac{1}{2},k,m})^- f^W_{j+1,k,m}$$
$$M_{j,k+\frac{1}{2},m} = (\Phi^2_{j,k+\frac{1}{2},m})^+ f^N_{j,k,m} + (\Phi^2_{j,k+\frac{1}{2},m})^- f^S_{j,k+1,m}$$
$$M_{j,k,m+\frac{1}{2}} = -D\partial_y f_{j,k,m+\frac{1}{2}}$$

and we consider the following split numerical scheme:

$$\begin{cases} f^{l+\frac{1}{3}}_{j,k,m} = f^l_{j,k,m} - \dfrac{\Delta t_l}{\Delta x_1}\left(M^l_{j+\frac{1}{2},k,m} - M^l_{j-\frac{1}{2},k,m}\right) - \dfrac{\Delta t_l}{\Delta x_2}\left(M^l_{j,k+\frac{1}{2},m} - M^l_{j,k-\frac{1}{2},m}\right) \\ f^{l+\frac{2}{3}}_{j,k,m} = f^{l+\frac{1}{3}}_{j,k,m} + \Delta t_l R^{l+\frac{1}{3}}_{j,k,m} \\ f^{l+1}_{j,k,m} = f^{l+\frac{2}{3}}_{j,k,m} - \dfrac{\Delta t_l}{\Delta y}\left(M^{l+\frac{2}{3}}_{j,k,m+\frac{1}{2}} - M^{l+\frac{2}{3}}_{j,k,m-\frac{1}{2}}\right) \end{cases} \tag{8.3.20}$$

Parameter	Description	Value [Units]	Reference
p_M	maximal duplication rate	2.88×10^{-2} [h^{-1}]	[259]
p_m	minimal duplication rate	1.44×10^{-2} [h^{-1}]	[312]
K	tissue carrying capacity	10^6 [cells/mm^3]	[293]
$D_{\boldsymbol{x}}$	cell spatial diffusion coefficient	9.74×10^{-10} [(mm×cells×h)]	estimate based on [264]
η	selection rate by oxygen	4.16×10^{-2} [h^{-1}]	[112]
D_y	cell epigenetic diffusion coefficient	5.00×10^{-6} [h^{-1}]]	[95]
β_M	maximal infection rate	7.00×10^{-10} [mm^3/(viruses×h)]	[185]
β_m	minimal infection rate	1.75×10^{-10} [mm^3/(viruses×h)]	model estimate
q_I	death rate of infected cells	4.17×10^{-2} [h^{-1}]	[190]
α	viral burst size	1000 [viruses/cells]	model estimate
D_v	virus diffusion coefficient	3.6×10^{-2} [mm^2/h]	[264]
$O_{\max}$	maximal oxygen concentration	2.16×10^{-3} [$mm^3_{O_2}/mm^3_{\text{plasma}}$]	[320, 359]
O_M	oxygen normoxic threshold	1.71×10^{-3} [$mm^3_{O_2}/mm^3_{\text{plasma}}$]	[320, 359]
O_m	oxygen hypoxic threshold	2.28×10^{-4} [$mm^3_{O_2}/mm^3_{\text{plasma}}$]	[320, 359]
q_O	oxygen physiological decay	5.60×10^{-1} [h^{-1}]	estimate based on [440]
λ	oxygen consumption rate	6.55×10^{-4} [mm^3/(cell×h)]	estimate based on [205]
D_O	oxygen diffusion coefficient	3.60 [mm^2/h]	[328]

Table 8.1 Reference parameter set.

8.3.3 Parameter values

In Table 8.1, we list the parameters we adopt as a reference in the numerical simulations. The majority of the parameters have been estimated from the empirical literature, while a few others are specific to our formulation of the model and have been set to reasonable values in order to reproduce plausible dynamics. We recall that our two-dimensional simulations represent the section of a tumour that is approximately homogeneous along the third spatial dimension (which can, therefore, be neglected). Hence, the parameters are estimated in the three-dimensional settings.

The maximal duplication rate of uninfected cells p_M, corresponding to the normoxic situation, has been taken equal to $\log(2)/24\,\text{h}^{-1} \approx 2.88 \times 10^{-2}\,\text{h}^{-1}$; the duplication time of 24 hours is among the fastest values reported in Ref. [259] for glioblastoma. On the other hand, we assume that severely hypoxic cells duplicate in 48 hours, as done in Ref. [312]: this leads to a minimal proliferation rate $p_m = 1.44 \times 10^{-2}\,\text{h}^{-1}$. The carrying capacity K has been estimated assuming that a cell has diameter 10 μm$= 10^{-2}$ mm [293]: this implies that the carrying capacity is 10^6 cells/mm^3.

The spatial diffusion coefficient of tumour cells $D_{\boldsymbol{x}}$ has been estimated from the experimental data of the U343 control group in Ref. [264], as already applied elsewhere in Ref. [366, 326]. In their experiments, the tumour volume passes in 40 days from 70 mm^3 to 1000 mm^3, which corresponds to a change in the tumour radius

from approximately 2.6 mm to approximately 6.2 mm. We assume that hypoxia plays no central role in that process, so the dynamics of uninfected cells in the absence of viral infection follow the equation:

$$\partial_t u(t,\boldsymbol{x}) = D_{\boldsymbol{x}} \operatorname{div}_{\boldsymbol{x}}(u(t,\boldsymbol{x})\nabla u(t,\boldsymbol{x})) + p\Big(1 - \frac{u(t,\boldsymbol{x})}{K}\Big)u(t,\boldsymbol{x})$$

with $p = p_M$. It is well-known that there exist travelling waves solutions of this equation with speed at least $\sqrt{D_{\boldsymbol{x}} K p/2}$ and an initial condition with compact support evolves into a wave that travels with the minimal speed [37, 336]; this yields the estimate

$$\begin{aligned} D_{\boldsymbol{x}} = \frac{2c^2}{Kp} &= \Big(\frac{6.2 - 2.6\ \text{mm}}{40 \times 24\ \text{h}}\Big)^2 \times \frac{2}{10^6 \times \text{cells/mm}^3 \times 2.88 \times 10^{-2}\,\text{h}^{-1}} \\ &\approx \frac{9.74 \times 10^{-4}\ \text{mm}^2/\text{h}}{10^6 \times \text{cells/mm}^3} \approx 9.74 \times 10^{-10}\ (\text{mm} \times \text{cells} \times \text{h})^{-1}. \end{aligned}$$

We assume that this coefficient is the same also for infected cells, as we have no reason to believe that the infection affects cellular movement.

The death rate of uninfected tumour cells due to oxygen-driven selection η and the epigenetic diffusion coefficient of tumour cells D_y are not easily accessible in the empirical literature, hence they have been taken from previous mathematical papers about epigenetically structured populations: their values have been set respectively to $1/24\ \text{h}^{-1} \approx 4.16 \times 10^{-2}\ \text{h}^{-1}$, as in Ref. [112], and $5.00 \times 10^{-6}\ \text{h}^{-1}$, as in [95] .

The maximal infection rate of the oncolytic virus β_M has been set to $7.00 \times 10^{-10}\ \text{mm}^3/(\text{viruses} \times \text{h})$, as in Ref. [185]; their model does not explicitly take into account hypoxia, we are assuming that they are considering normoxic conditions. Since we are not aware of any experimental estimate of infection rate under hypoxic conditions, we set β_m to one-fourth of the value of β_m. The death rate of infected cells q_I has been taken equal to $1/24\ \text{h}^{-1} = 4.17 \times 10^{-2}\ \text{h}^{-1}$, following [190]. The viral load released by the death of infected cells depends highly on the type of virus and ranges from the value 157 viruses/cells estimated in Ref. [451] to the value 3500 viruses/cells [106]; we chose an intermediate value of $\alpha = 1000$ viruses/cells. It is important to remark that all these values are highly dependent on the exact type of oncolytic virus employed. The outcome of the therapy is mostly determined by the aggregate value $\beta\alpha q_I/q_v$, and our choices allow us to model significant differences in the effectiveness of oncolytic virotherapy as the oxygen level varies. The spatial

diffusion coefficient of tumour cells D_v has been set to 3.6×10^{-2} mm^2/h, as in Ref. [185].

We consider the oxygen thresholds defined in Ref. [320]: the oxygen partial pressure (pO_2) in arterial blood is 70 mmHg and we consider this as the maximal oxygen concentration $O_{\max}$); the physiological pO_2 ranges approximately between 57 mmHg and 30.4 mmHg, so we consider the higher value as the normoxic threshold O_M, keeping in mind that we may observe lower oxygen values also in healthy tissue; the pathological hypoxic pO_2 value is 7.6 mmHg, which we consider as O_m. All these pressure values are converted in volume ratios by multiplying them by the solubility constant $3 \cdot 10^{-5}\,\mathrm{mm}^3_{O_2}/(\mathrm{mm}^3{}_{\mathrm{plasma}} \times \mathrm{mmHg})$ [359].

We assume that the oxygen decay is due to the consumption of the healthy cells present in the region. According to existing work [440], cells have an average rate of oxygen utilisation of 9.00×10^{-15} mol/(cell$\times$h), corresponding approximately to $2.02 \times 10^{-7}\,\mathrm{mm}_{\mathrm{O}_2}/(\mathrm{cells} \times \mathrm{h})$, but this value may vary several orders of magnitude among different cell types. We, therefore, assume that a single healthy cell consumes six times this amount of oxygen when the available oxygen level is at $O_{\max}$ and the consumption scales linearly with the oxygen concentration, meaning that the consumption in the case of unitary cell density is given by $O(t,\boldsymbol{x})$ multiplied by

$$\frac{1.21 \times 10^{-6}\,\mathrm{mm}^3_{\mathrm{O}_2}}{\mathrm{cell} \times \mathrm{h}} \, \frac{1}{O_{\max}} = 5.60 \times 10^{-4}\ \mathrm{mm}^3/(\mathrm{cell} \times \mathrm{h}).$$

Considering K as the healthy cell density in absence of tumour, we obtain a decay rate $q_O = 5.60 \times 10^2\ \mathrm{h}^{-1}$. We adopt a similar way of reasoning for the consumption by cancer cells, starting from the fact that the consumption of a single cell is estimated to be $2.62 \times 10^{-6}\,\mathrm{mm}_{\mathrm{O}_2}/(\mathrm{cells} \times \mathrm{h})$ [205] and assuming again that this is only possible when the oxygen level is $O_{\max}$. We then assume that cancer cells take the place of healthy cells, meaning that they cause an additional consumption of

$$\lambda = \frac{2.62 \times 10^{-6}\mathrm{mm}_{\mathrm{O}_2}/(\mathrm{cells} \times \mathrm{h})}{O_{\max}} - \frac{q_O}{K} = 6.55 \times 10^{-4}\ \mathrm{mm}^3/(\mathrm{cell} \times \mathrm{h}).$$

The oxygen diffusion coefficient D_O has been set to 3.60 mm^2/h, as in Ref. [328].

For the spatial domain, $[-L,L]^2$, we set $L = 10$ mm. Numerical simulations are run until the tumour mass reaches the spatial boundaries.

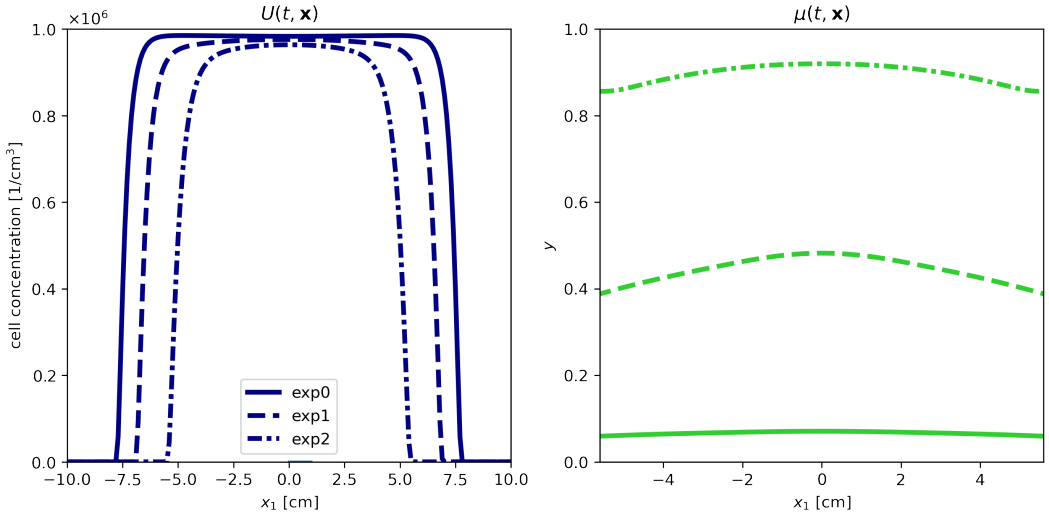

Fig. 8.1 Overlapped results of the numerical simulation adopting stationary oxygen, for three spatially homogeneous oxygen condition: $O = O_M$ (solid lines), $O = \frac{O_M+O_m}{2}$ (dashed lines), and $O = O_m$ (dot-dashed lines). In the representation, we plot data at time $t = 1500$ h, before virus injection. Blue lines represent the profile of uninfected cancer cells $U(t,\boldsymbol{x})$, green lines show the average epigenetic trait $\mu(t,\boldsymbol{x})$).

8.3.4 Stationary oxygen

Homogeneous distribution The most elementary situation is obtained by considering that the oxygen concentration is constant in space and time. We focus on three oxygen values, namely O_M (normoxia), O_m (sever hypoxia) and their average $\frac{O_m+O_M}{2}$ (physiological hypoxia), whose corresponding selected traits are respectively 1, 0 and 0.5; other values clearly produce intermediate situations.

As a starting point, it is helpful to observe how a tumour evolves in these environmental conditions without treatment, as shown in Fig. 8.1 (for the sake of clarity, the figure represents the central section of the domain, i.e. the set $[-L,L] \times \{0\}$). In this experiments we represent time $t = 1500$ hours, which in this case precedes virus injection. Left panel shows total uninfected cancer cell $U(t,\boldsymbol{x})$ profiles. We naturally define

$$U(t,\boldsymbol{x}) = \int_Y u(t,\boldsymbol{x},y)dy$$

and consider that, since uninfected population $I(t,\boldsymbol{x})$ is still not present because of the absence of the virus, in this case $U(t,\boldsymbol{x}) = \rho(t,\boldsymbol{x})$. Overall, we observe the behaviour predicted by the theoretical asymptotic analysis in all the cases. The three

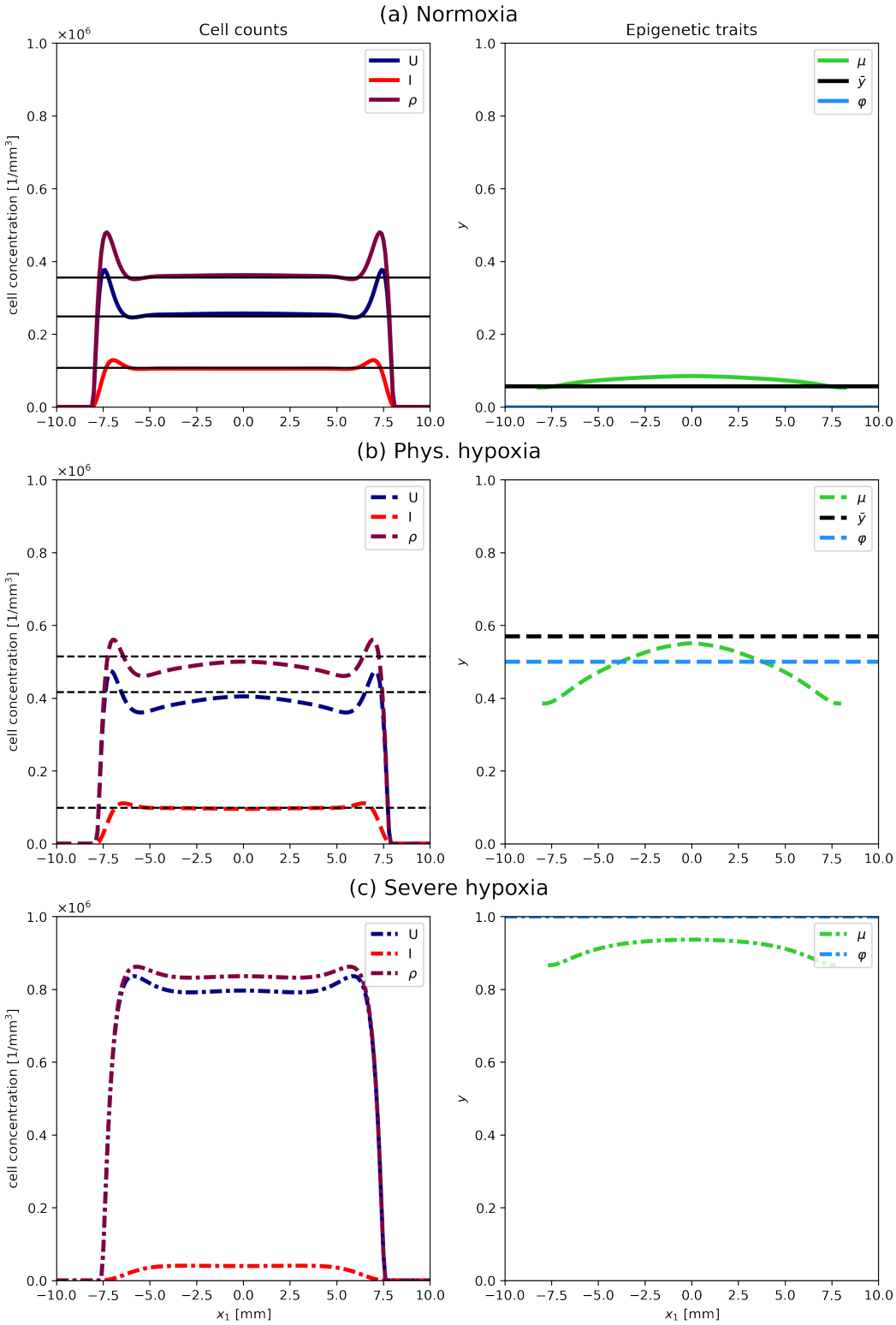

Fig. 8.2 Comparison of the results obtained from numerical simulation of stationary oxygen model, for three spatially homogeneous oxygen condition: $O = O_M$ (solid lines, plots (a)), $O = \frac{O_M+O_m}{2}$ (dashed lines, plots (b)), and $O = O_m$ (dot-dashed lines, plots (c)). First column shows $U(t,\boldsymbol{x})$ in blue, $I(t,\boldsymbol{x})$ in red, and $\rho(t,\boldsymbol{x})$ in purple. Second column provide the average epigenetic trait $\mu(t,\boldsymbol{x})$ in green and $\varphi(O(t,\boldsymbol{x}))$ in light-blue. Black lines show theoretical approximation of asymptotic equilibria (when they are evaluable).

initial conditions are given by Eq. (8.3.1) with $y_0 = \varphi(O)$. However, the density ρ is much lower than K; hence, unless we are in a normoxic situation, the fittest epigenetic trait is lower than $\varphi(O)$, as predicted by Eq. (8.3.12); on the other hand, in the normoxic situation $\varphi(O) = 0$ is already the lowest attainable value. As time passes, the cell density grows up to close to carrying capacity and the cancer starts to invade the surrounding area at a speed approximately proportional to the square root of the proliferation rate. In the hypoxic scenarios the fittest epigenetic trait grows with ρ until reaching the value $\varphi(O)$; however, that trait is never completely selected due to epigenetic diffusion. An important consequence of the presence of different epigenetic characteristics is the fact that ρ is always slightly below K, as the oxygen selection never completely stops: this effect is especially evident in the hypoxic situation, in which the slow proliferation contrasts the selective pressure less effectively. In order to make the comparison between the epigenetic composition and spatial characterisation clearer, we introduce the quantity:

$$\mu(t,\boldsymbol{x}) = \frac{\int_Y y\,u(t,\boldsymbol{x},y)dy}{\int_Y u(t,\boldsymbol{x},y)dy}$$

referring to that as the *average epigenetic trait*. Right panel of Figure 8.1 shows $\mu(t,\boldsymbol{x})$ for the three experiments. It is important to observe that in all cases the average epigenetic traits are lower at the invasion front, due to the lower total densities, and increase as we get close to the tumour centre. Overall, high oxygen levels are associated with more proliferative tumours, which reach carrying capacity earlier and invade the surrounding tissues faster.

From the previous discussion, it could appear that hypoxic tumours do not constitute a significant threat; however, this situation overturns in the presence of treatment, as the adaptation to hypoxia makes the tumour less susceptible to therapies. Indeed, Fig. 8.2 shows the effect of oncolytic virotherapy on the tumours described above. The different growth rates imply that the viral injection is performed at different times in the three situations: this happens respectively around $t = 434$ h for normoxia, 482 h for physiological hypoxia and 663 h for severe hypoxia. In order to facilitate the comparison between the different scenarios, Fig. 8.2 shows the section of the simulation approximately 1500 h after the viral injection. In all the three cases, the central region of the tumour is quickly infected and viral particles are able to reach the tumour front in a relatively short time due to their fast diffusion. In the severely hypoxic case, this initial successful infection might appear surprising, but it

can be easily explained that at T_{inj} the tumour has not reached the carrying capacity and the epigenetic characteristics are still not fully adapted to the environment (the lack of complete adaptation is also true in the other cases, but less evident).

The following dynamics appear quite different in the three cases. In the normoxic case (Figure 8.2a), cell densities at the centre of the tumour converge with damped oscillations to the equilibrium predicted by the theoretical analysis. The average of the epigenetic traits in the central area sensibly increases right after the viral injection, then oscillates towards the equilibrium. It is interesting to observe that epigenetic traits at the invasion front are lower, since in this area both ρ and I are lower. In the physiologically hypoxic case (Figure 8.2b), the situation is qualitatively similar, but the equilibrium value for ρ is higher. The spatial difference of the average epigenetic trait is much more evident than in the previous case: the convergence to the equilibrium value is slower than before and takes place mostly from the lower side. We remark that, unlike the other two situations, here the dynamics take place for values of the epigenetic trait in the inner of the interval $(0,1)$, hence we observe a better agreement with theoretical results (which do not take into account the constraints on y). While these two situations can be described as partial successes of the therapy, the severely hypoxic case (Fig. 8.2c) is clearly a complete failure: the tumour density decreases only for a short time, after which it starts to regrow up to around 80% of carrying capacity, with just a small fraction of infected cells. The infection causes a further increase of the epigenetic trait, making the tumour even less sensitive to therapies than before.

8.4 Conclusion and future perspectives

In this chapter, we have introduced a novel approach to oncolytic virotherapy modelling. The major novelty stands in the combination of epigenetically structured cancer cell population with hypoxia's effect and spatial characterization. Even if numerical simulations are preliminary and still reduced to simplified scenarios, results show biologically coherent patterns, with environmental selection and abiotic conditions influencing the capability of the virus to control tumour mass expansions. From a mathematical point of view, numerical observations show coherence with the theoretical results obtained.

Future steps include examining stationary oxygen scenario with spatially heterogeneous profiles and then move to consider oxygen evolution, keeping into account cell consumption and inflow.

Moreover, given the interest on hypoxia influence and considered the radiotherapy models already developed in the same setting, coherently with the clinical interest in the use of oncolytic virotherapy in combination with radiation, we aim to develop a model to study the interaction of the two treatments. Mathematical modelling could help in designing the optimal combination, considering contemporary, subsequent or alternating treatments and investigating doses, orders and timing according to the environmental conditions.

Chapter 9

Continuous modelling for immune system-cancer interaction: geometric and epigenetic characterisation to explain hot and cold tumours

This chapter presents the foundations of a work that has just started in collaboration with Professor José A. Carrillo (Oxford University). This project takes its idea from the analysis of [91], in which authors present a macroscopic cell-cell adhesion continuum model, derived from underlying microscopic dynamics. The model is designed to catch sharp fronts and mixture invasion fronts between different cell-type populations. The work investigates different mechanisms and intensities of attraction and repulsion between cell populations. The experiments leading to this model, presented in Ref. [257], were analysing the rise of mosaic pattern in the olfactory epithelium, considering cellular rearrangement dynamics driven by the different expressions of nectins and cadherins. The similarity of these dynamics with the interaction occurring between the immune system and cancer cells led to the idea of adapting the original model in Ref. [91] to describe it.

9.1 Introduction

An ODE setting is one of the simplest approaches to dealing with tumour-immune system interaction. The majority of this category of models is based on the prey-predator model [276] (then generalised [166]), in which authors use two equations to define the behaviour of tumour cells and cytotoxic T lymphocytes. In Ref. [141], authors adopt a system of ODEs, omitting tumour escape intrinsic mechanisms, to concentrate on the anti-tumour immune response generated by the interaction between macrophage and T cells. In general, non-spatial models often directly include dynamics of antigen-mediated tumour recognition by T cells [269, 56, 182] sometime modeled using integro-differential equations [150, 147, 297]. Also, when moving to immunotherapy, most of the works are based on systems of ODEs and are mainly interested in the death of tumour cells and inactivation of CTLs [268, 347, 399].

Although this type of modelling is interesting for analysing the effectiveness of the immune response (in terms of cell number) and the antigenic dynamics in its activation, it prevents the analysis of the important mechanism of immune invasion, which requires spatial modelling of the mass. A passage to PDEs can be seen in Ref. [314], where a Fisher-Kolmogorov-like model is used to describe the logistic growth of the tumour with T cells being attracted via chemotaxis.

With particular attention on the geometrical characterisation of tumour infiltration by the immune system, in Ref. [314] they present a model based on a four PDE system describing tumour cells, immune cells, chemokines and complexes that focuses upon the attack of tumour cells by tumour-infiltrating cytotoxic lymphocytes (TICLs). This work is of particular relevance both for its interest in spatial dynamics and for the biological framework since it considers tumours in the same phase as the one we take into account (small size, without necrosis, prior to angiogenesis dynamics). Unlike what is done there, we choose not to model abiotic factors directly, such as inserting antigens and chemokines as agents with their equations, but we rather insert their effect as a function of the cells that secrete them. Other PDE's approaches to the problem can be found in Ref. [39, 315, 10].

In Ref. [349], they propose a tumour classification with respect to the interaction with the immune system based on two features: mutational burden and inflammatory gene signatures. This leads to the description of four tumour types, represented in

Figure 9.1. We aim to propose a mathematical model able to fill the gap between the initial conditions of the primary tumor mass and the outcome, classified in one of these four categories.

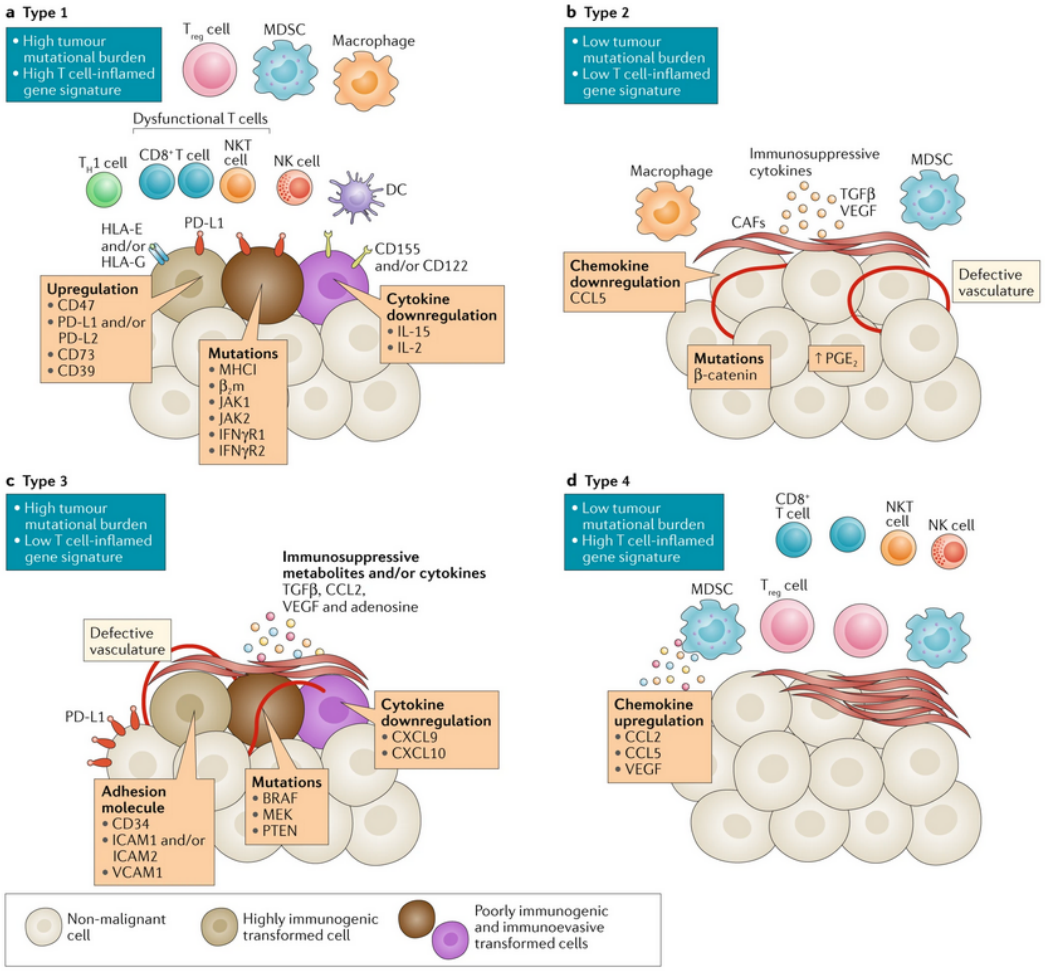

Fig. 9.1 tumour classification according to mutational burden and inflammatory gene signatures. Figure taken from [349].

In the following sections, we present a starting model and some possible variations (Section 9.2) with few very early results (Section 9.3). In addition, we present future perspectives for this work (Section 9.4).

9.2 The model

9.2.1 Single population model

In the first version of the model, we consider the tumour mass to be composed of a single cell population. Therefore, the model includes two main contributors: the cancer cells $\rho(t,\mathbf{x})$ and the T cells $\ell(t,\mathbf{x})$. We consider a time domain $t \in \Omega_T = [0,t_{fin}] \subset \mathbb{R}$ and a 2D space domain $\mathbf{x} \in \Omega_{\mathbf{x}} = [x_{min},x_{max}] \times [y_{min},y_{max}] \subset \mathbb{R}^2$.

Cancer cell population $\rho(t,\mathbf{x})$ equation reads:

$$\frac{\partial \rho}{\partial t} = \overbrace{\gamma_\rho\ \psi(\rho,\ell)\ \rho}^{\text{proliferation}} + \overbrace{\nabla\cdot\Big(\psi(\rho,\ell)\ \rho\ \nabla\big(H'(\rho)+W*\rho\big)\Big)}^{\text{movement}} - \overbrace{\lambda_\rho \frac{\ell}{\rho+\varepsilon}\rho}^{\text{immune effect}}. \quad (9.2.1)$$

The population is characterised by a proliferation rate γ_ρ, and cell proliferation replicates a logistic behaviour, where the filling saturation

$$\psi(\rho,\ell) = 1-\rho-\ell$$

is determined both by cancer and T cells. Moreover, cancer cells move driven by two different dynamics. The first one is an anti-crowding dynamic defined via the following factor:

$$H(\rho) = \frac{\nu_\rho}{2}\rho^2,$$

with cancer cells moving away from high cancer cell density zones characterised with speed influenced by parameter ν_ρ. The second one is an adhesive motion, keeping cancer cells stuck together, defined by function

$$W(\mathbf{x}) = W(|\mathbf{x}|) = A_\rho \mathbb{1}_{\{|\mathbf{x}|<r_\rho\}}.$$

Note that $W*\rho$ indicates the convolution product and parameter A_ρ characterises the strength of the attraction between cells. Note that the same term $\psi(\rho,\ell)$ that regulates the proliferation is also responsible for the slow down of the migratory dynamics, reproducing the fact that overcrowding hinders cellular movement. Finally, cancer cells undergo death caused by the suppressive action operated by T cells, with a rate λ_ρ that characterises the cancer cell population.

T cell population $\ell(t,\mathbf{x})$ equation reads:

$$\frac{\partial \ell}{\partial t} = \underbrace{S\,\psi(\rho,\ell)}_{\text{source}} + \underbrace{\nabla\cdot\Big(\psi(\rho,\ell)\,\ell\,\nabla\big(\tilde{H}'(\ell)+\tilde{W}*\rho\big)\Big)}_{\text{movement}} - \underbrace{\lambda_T\ell}_{\text{exhaustion}} \tag{9.2.2}$$

T cells are generated at a maximum S rate, which is slowed down by high cell density (considering both cancer and T cells). Moreover, T cells move both with a volume-filling dynamic, moving away from high T cell density zones with speed coefficient ν_ℓ, and attracted by cancer cells. Equation (9.2.4) shows that functions $\tilde{H}$ and $\tilde{W}$ have the same mathematical formulation of $\tilde{H}$ and $\tilde{W}$ and are just characterized by different parameters ν_ℓ and A_ℓ. In particular, A_ℓ is an important parameter, since it defines the intensity of the attraction on T cells by cancer cell and when addressing heterogeneity in the cancer population it ise seen as a characterizing parameters for the subpopulation features, as well as λ_ρ and γ_ρ. Finally, we collect T cells exhausting and dying in the same linear decaying process, with a rate λ_ℓ.

The final system reads:

$$\begin{cases} \dfrac{\partial \rho}{\partial t} = \gamma_\rho\,\psi(\rho,\ell)\,\rho + \nabla\cdot\Big(\psi(\rho,\ell)\,\rho\,\nabla\big(H'(\rho)+W*\rho\big)\Big) - \lambda_\rho\dfrac{\ell}{\rho+\varepsilon}\rho \\[2ex] \dfrac{\partial \ell}{\partial t} = S\,\psi(\rho,\ell) + \nabla\cdot\Big(\psi(\rho,\ell)\,\ell\,\nabla\big(\tilde{H}'(\ell)+\tilde{W}*\rho\big)\Big) - \lambda_\ell\ell \end{cases} \tag{9.2.3}$$

where we have also defined:

$$\begin{cases} \psi(\rho,\ell) = 1-\rho-\ell \\ H(\rho) = \frac{\nu_\rho}{2}\rho^2 \\ \tilde{H}(\ell) = \frac{\nu_\ell}{2}\ell^2 \\ W(\mathbf{x}) = W(|\mathbf{x}|) = A_\rho \mathbb{1}_{\{|\mathbf{x}|<r_\rho\}} \\ \tilde{W}(\mathbf{x}) = \tilde{W}(|\mathbf{x}|) = A_\ell \mathbb{1}_{\{|\mathbf{x}|<r_\ell\}} \end{cases} \tag{9.2.4}$$

Furthermore, we impose no flux boundary conditions at $\partial\Omega_\mathbf{x}$ and we define the Cauchy problem associating initial conditions:

$$\begin{cases} \rho(0,\mathbf{x}) = \rho_0(\mathbf{x}) \\ \ell(0,\mathbf{x}) = \ell_0(\mathbf{x}) \end{cases} \tag{9.2.5}$$

We provide an explicit formulation for $\rho_0(\mathbf{x})$ and $\ell_0(\mathbf{x})$ when presenting the simulation settings adopted.

9.2.2 Two population model

Extending the model presented in Section 9.2.1, we now allow for a primitive heterogeneous composition of the tumour mass. In particular we consider cancer cell population $\rho(t,\boldsymbol{x})$ as composed of two subpopulations $a_1(t,\boldsymbol{x})$ and $a_2(t,\boldsymbol{x})$ (so that $\rho(t,\boldsymbol{x}) = a_1(t,\boldsymbol{x}) + a_2(t,\boldsymbol{x})$). We consider such a differentiation for a cancer cell population with a non-homogeneous proliferation rate and immune effectiveness. Here, with immune effectiveness, we refer jointly to the killing rate of the immune system in a population and the strength of its attractive potential on T cells.

The model, with this modification, becomes:

$$\begin{cases} \dfrac{\partial a_1}{\partial t} = \gamma_{a_1}\, \psi(\rho,\ell)\, a_1 + \nabla\cdot\Big(\ \psi(\rho,\ell)\, a_1\, \nabla\big(H'(\rho)+W\rho\big)\Big) - \lambda_{a_1}\dfrac{\ell}{a_1+\varepsilon}a_1 \\ \dfrac{\partial a_2}{\partial t} = \gamma_{a_2}\, \psi(\rho,\ell)\, a_2 + \nabla\cdot\Big(\ \psi(\rho,\ell)\, a_2\, \nabla\big(H'(\rho)+W\rho\big)\Big) - \lambda_{a_2}\dfrac{\ell}{a_2+\varepsilon}a_2 \\ \dfrac{\partial \ell}{\partial t} = S\, \psi(\rho,\ell) + \nabla\cdot\Big(\ \psi(\rho,\ell)\, \ell\, \nabla\big(\tilde{H}'(\ell)+\tilde{W}_1 * a_1 + \tilde{W}_2 * a_2\big)\Big) - \lambda_T \ell \end{cases} \tag{9.2.6}$$

with:

$$\begin{cases} \psi(\rho,\ell) = 1-\rho-\ell \\ H(\rho) = \frac{\nu_\rho}{2}\rho^2 \\ \tilde{H}(\ell) = \frac{\nu_\ell}{2}\ell^2 \\ W(\mathbf{x}) = W(|\mathbf{x}|) = A_\rho \mathbb{1}_{\{|\mathbf{x}|<r_\rho\}} \\ \tilde{W}_1(\mathbf{x}) = \tilde{W}(|\mathbf{x}|) = A_{\ell_1}\mathbb{1}_{\{|\mathbf{x}|<r_\ell\}} \\ \tilde{W}_2(\mathbf{x}) = \tilde{W}(|\mathbf{x}|) = A_{\ell_2}\mathbb{1}_{\{|\mathbf{x}|<r_\ell\}} \end{cases} \tag{9.2.7}$$

See that the mathematical characterisation of the populations is observable in:

- the proliferation being determined by different coefficients γ_{a_1}, γ_{a_2},
- the attractive potential being influenced by different coefficients A_{ℓ_1}, A_{ℓ_2} (but same radius of detectability r_ℓ),

- the effectiveness of the immune action depending on different coefficients λ_{ℓ_1}, λ_{ℓ_2}.

On the other hand, let us observe that the movement dynamics of the two cancer cell populations are not modified with respect to the model presented in Section 9.2.1 since anti-crowding shift continues to depend on total cancer cell density despite their characterisation and all cell subpopulations adhere equally to cells belonging to the same or the other subpopulation.

9.2.3 Structured population model

In this final version, we structure the cancer population $a(t,\boldsymbol{x},u)$ with a variable $u \in \Omega_u = [0,1]$. Total cancer cell population is thus defined as $\rho(t,\boldsymbol{x}) = \int_{\Omega_u} a(t,\boldsymbol{x},u)\,du$. Independent variable u has to be interpreted as a normalised quantification of the gene expression of a set of genes, selected to be responsible for the trade-off between proliferation and immune effectiveness (defined as in Section 9.2.2). Mathematically, we catch this aspect defining $u = 0$ the level of expression that leads to a maximum proliferation rate γ_{max}, losing in evasion capability and resistance to immune action (i.e. having maximal killing rate λ_{max} and maximum attractive strength A_{max}). Oppositely, cells with $u = 1$ gene expression present minimum proliferative rate γ_{min}, but gain in evasion potential (A_{min}) and resistance to death (λ_{min}). We model intermediate states with a linear trade-off. Thus, the complete system reads:

$$\begin{cases} \dfrac{\partial a}{\partial t} = \gamma_a(u)\ \psi(\rho,\ell)\ a + \nabla\cdot\left(\ \psi(\rho,\ell)\ a\ \nabla\big(H'(\rho) + W*\rho\big)\right) - \lambda_a(u)\dfrac{\ell}{a+\varepsilon}a \\ \dfrac{\partial \ell}{\partial t} = S\ \psi(\rho,\ell) + \nabla\cdot\left(\ \psi(\rho,\ell)\ \ell\ \nabla\left(\tilde{H}'(\ell) + \int\limits_{\Omega_u}\tilde{W}*a\,du\right)\right) - \lambda_T\ell \end{cases} \tag{9.2.8}$$

with:

$$\begin{cases} \gamma_a(u) = \gamma_{min} + (\gamma_{max} - \gamma_{min})u \\ \lambda_a(u) = \lambda_{min} + (\lambda_{max} - \lambda_{min})u \\ A_\ell(u) = A_{min} + (A_{max} - A_{min})u \\ \psi(\rho,\ell) = 1 - \rho - \ell \\ H(\rho) = \frac{\nu_\rho}{2}\rho^2 \\ \tilde{H}(\ell) = \frac{\nu_\ell}{2}\ell^2 \\ W(\mathbf{x}) = W(|\mathbf{x}|) = A_\rho \mathbb{1}_{\{|\mathbf{x}|<r_\rho\}} \\ \tilde{W}(\mathbf{x},u) = \tilde{W}(|\mathbf{x}|,u) = A_\ell(u)\mathbb{1}_{\{|\mathbf{x}|<r_\ell\}}. \end{cases} \tag{9.2.9}$$

9.3 Results

An exhaustive investigation of the model has not yet been conducted and the results obtained so far are reduced to the outcomes of the first computed numerical simulation.Further, a parametric calibration has not been performed yet; therefore, we present the results in terms of relative values of the parameters, without focusing on their quantification. Nonetheless, some valuable insights can be drawn from initial findings.

9.3.1 Investigation strategy

We developed a model whose mathematical structures can be easily reconnected to the two features that define the classification presented in Figure 9.1 of [349]. In fact, the mutational burden can be quantified in mathematical terms with any indication of tumour heterogeneity with respect to the chosen epigenetic structure. Moreover, inflammatory gene signatures represent both the killing action of immune cells and the geometrical effective invasion of T cells in the tumour mass. Our model allows for a mathematical representation of these: term $\lambda_a(u)\frac{\ell}{a+\varepsilon}a$ in Equation (9.2.8) is quantifiable, locally or integrated on the spatial domain, representing a descriptor for the inflammatory activity. The model also provides a spatial characterisation of the interaction between the tumour and T cells, which can result in a quantification of the infiltration.

At first, considering an epigenetically homogeneous tumour population (see model in Section 9.2.1), our objective is to determine which range of parameters that

characterise proliferation and immune effectiveness of the tumour population lead to each of the four outcomes presented in Figure 9.1. We also insert the data of the initial condition as a determining factor: in fact, depending on whether the immune system detects the tumour mass at a primitive or advanced stage, the tumour's infiltrability conditions will be different.

Next, once the parameters range is selected, we consider the model with two different subpopulations (see Section 9.2.2) in order to analyse the impact of (i) different combinations of values for the two subpopulations, (ii) different proportion of the two subpopulations in the initial tumour mass, and (iii) different geometrical layouts in the tumour initial mass.

In the last step, using an epigenetically structured tumour mass (with continuous structure, as proposed in (9.2.8)), we aim to recognise an index of initial epigenetic variability and different distribution models along the epigenetic domain that leads to the four different outcomes.

All these investigations involve an initial qualitative analysis and subsequent quantification through a numerical bifurcation study.

Numerical methods

Concerning the numerical method, we adopt the same finite elements approach adopted in the work presented in Chapter 6, with exhaustive explanations provided in Section 6.4.1. Note that the only difference here is the presence of a convolution product, which is numerically approximated, according to the discretisation of the domains, as a discrete convolution [369].

9.3.2 Single population model

Referring to the model of Section 9.2.1, we consider reference values $\bar{\gamma}_\rho$, $\bar{\lambda}_\rho$, $\bar{A}_\rho$ and consider the following initial conditions:

$$\rho_0(\boldsymbol{x}) = Q_\rho \mathbb{I}_{\{|\boldsymbol{x}| \leq r_\rho\}}$$

$$\ell_0(\boldsymbol{x}) = Q_\ell \mathbb{I}_{\{|\boldsymbol{x}| > r_\rho\}}$$

setting $\bar{Q}_\rho$, $\bar{Q}_\ell$, and $\bar{r}_\rho$ as reference values. We consider two different settings for the initial values:

- early detection, with $Q_\rho = \frac{1}{2}\bar{Q}_\rho$, $Q_\ell = \bar{Q}_\ell$;
- late detection, with $Q_\rho = 2\bar{Q}_\rho$, $Q_\ell = \bar{Q}_\ell$, and $r_\rho = 2\bar{r}_\rho$.

Furthermore, we take into account two possible population characterisations, coherent with the trade-off used in Section 9.2.3:

- proliferative population, with $\gamma_\rho = 2\bar{\gamma}_\rho$, $\lambda_\rho = 2\bar{\lambda}_\rho$, and $A_\rho = 2\bar{A}_\rho$;
- resistant population, with $\gamma_\rho = \bar{\gamma}_\rho$, $\lambda_\rho = \bar{\lambda}_\rho$, and $A_\rho = \bar{A}_\rho$.

Fig. 9.2 collates results at final simulation time. It appears evident that, in panel (a), due to an early detected proliferative population, the cancer mass is fully eradicated by the immune system. The same asymptotic behaviour is shown in panel (b), considering an early detected resistant population. In this case, the dynamics are slower since, at the same time, it is clear that the immune population is predominant, fully infiltrated and manages to control and eradicate the tumour mass, while the last is still visible. When it comes to considering late detection, the proliferative population (panel (c)) presents a reduced external rim of infiltration and a high-density central core that cannot be penetrated by tumour cells crowded outside the edges of the tumour. It is clear that in this case, the immune system fails both in infiltrating and in opposing the advance of the tumour front, which is only slowed down in its dynamics. The resistant population, on the other hand, is characterised by complete infiltration but with a low percentage of T cells compared to the tumour density. So, the mass is half-formed, and the final outcome could both go in the direction of eradication, control or spread of the tumour. The interesting aspect is that both features adopted to characterise the tumour mass affect the outcome, resulting in different configurations. Moreover, combining different characteristics can change the fate of the tumour mass. for example, given the first row, one could think that resistant populations are harder to contrast, while when moving to the second row, the scenario is the opposite.

This confirms the relevance of the line of experimentation proposed above and the presence of open questions that can be investigated with this model.

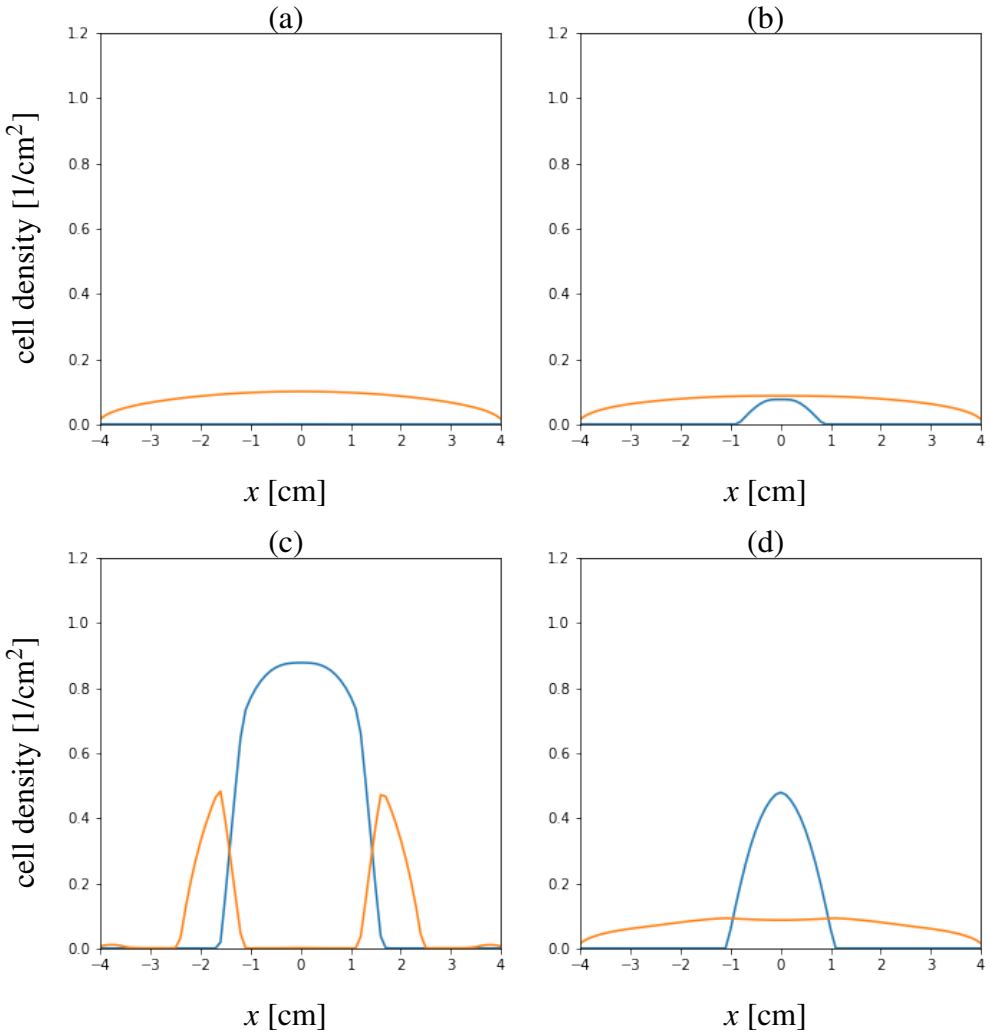

Fig. 9.2 Final time of numerical simulation of one population system introduced in Equation (9.2.3). Cancer cells $a(t,\boldsymbol{x})$ are represented with a blue line, and T cells $\ell(t,\boldsymbol{x})$ with an orange line. We consider different cancer population characterisations (proliferative/resistant) and detection times (early/late). (a) Proliferative population, early detection. (b) Resistant population, early detection. (c) Proliferative population, late detection. (d) Resistant population, late detection.

9.3.3 Two population model

In this next experiment, according to the guidelines presented in Section 9.2.2, we move to consider a heterogeneous cancer population. In particular, we take population types (proliferative and resistant) respectively as subpopulation a_1 and a_2

that compose the total tumour mass ρ. Let us define the ratio

$$R = \frac{\int_{\Omega_x} a_1 \, d\mathbf{x}}{\int_{\Omega_x} \rho \, d\mathbf{x}}$$

as the ratio of population ρ belonging to the first subpopulation. Thus, recalling the definition of ρ, we have:

$$1 - R = \frac{\int_{\Omega_x} a_2 \, d\mathbf{x}}{\int_{\Omega_x} \rho \, d\mathbf{x}}.$$

We now move to characterise the initial data from a geometrical point of view. Keeping the initial condition:

$$\rho_0(\boldsymbol{x}) = Q_\rho \mathbb{I}_{\{|\boldsymbol{x}| \le r_\rho\}}$$

$$\ell_0(\boldsymbol{x}) = Q_\ell \mathbb{I}_{\{|\boldsymbol{x}| > r_\rho\}}$$

and we set $Q_\rho = \bar{Q}_\rho$, $Q_\ell = \bar{Q}_\ell$, and $r_\rho = \bar{r}_\rho$. We consider two geometrical layouts:

- mixed, with $a_{1,0}(\boldsymbol{x}) = RQ_\rho \mathbb{I}_{\{|\boldsymbol{x}| \le r_\rho\}}$ and $a_{2,0}(\boldsymbol{x}) = (1-R)Q_\rho \mathbb{I}_{\{|\boldsymbol{x}| \le r_\rho\}}$
- in&out, with $a_{1,0}(\boldsymbol{x}) = Q_\rho \mathbb{I}_{\{|\boldsymbol{x}| \le \sqrt{R} r_\rho\}}$ and $a_{2,0}(\boldsymbol{x}) = Q_\rho \mathbb{I}_{\{\sqrt{R} r_\rho < |\boldsymbol{x}| \le r_\rho\}}$

were mixed is a homogeneous mixture of the two subpopulations, and in&out corresponds to a concentric figuration.

For this experiment, we consider $R = 0.5$, i.e. a population with balanced composition between the two subpopulations, and refer to experiment "(c)" when adopting mixed initial condition and "(d)" when using in&out configuration. In Fig. 9.3 we collect results at three times (initial, intermediate, and final, disposed in three rows). The first row provides a graphical representation of the identic initial conditions for ρ and ℓ in the two experiments, with (c) (column one) showing overlapped subpopulations and (d) (column two) presenting concentric layouts. Moving to intermediate time, in experiment (c), T cells infiltrate the mass slightly better, and cancer subpopulations continue to cohabit, with some changes in the spatial disposition, with the proliferative subpopulation more present inside and the resistant subpopulation pushed in the outer part of the tumour. Experiment (d) is characterised by steeper edges, with the core of the tumour being populated only by a proliferative population (denser than in the previous experiment), the external rim composed of resistant cells, and T cells that struggle to invade the densest area. T

cells infiltrate the mass slightly better, and cancer subpopulations continue to coexist, with some changes in the spatial disposition, as the proliferative subpopulation are more present inside and the resistant subpopulations are pushed in the outer part of the tumour. Plots at the final time (row three) clarify the two experiments' different asymptotic outcomes. In the first, the tumour mass is reduced in total size, highly invaded by immune cells and presents a smooth edge carved out by the action of the T cells. On the contrary, in the second case, a more significant number of T cells accumulate outside the edge of the tumour, which grows in size and can counteract both the infiltration and the killing activity of the immune system.

Even in lack of a proper model calibration and parameter estimation, these early results underline that the sole spatial characterisation of tumour epigenetic heterogeneity is able to change the fate of a tumour with fixed composition and size.

9.4 Conclusion and future perspectives

Although preliminary, the adaptability of the model introduced in Ref. [91] to our problem and the results obtained so far confirm the interest of the line of research.

It is evident, even from the early results we obtained, that the parameters inserted in the model and considered for the investigation (proliferation rate, killing rate, attraction strength and characterisation of composition and geometrical layout of the initial data) are strictly correlated with the resulting pattern. Moreover, the layouts obtained as final results are highly comparable with the characterisation adopted for tumour classification in Ref. [349].

Future steps expect an analytical and numerical investigation of this correlation, including model calibration, parameter quantification and bifurcation analysis. Moreover, so far, we have only presented the modelling setting relating to the structured population, which deserves a complete analytical and numerical investigation.

Finally, the parameters taken into account in the investigation are eligible for the inclusion of ICI therapies in the model. Immunotherapy could be modelled as the insertion of targeted T cells, i.e. a variation both of the source term S and of the immune effectiveness on different subpopulations (terms A and λ).

This paves the way for investigation of immunotherapy alone or as combined therapy, merging, for example, models presented in Chapter 4 and Chapter 8.

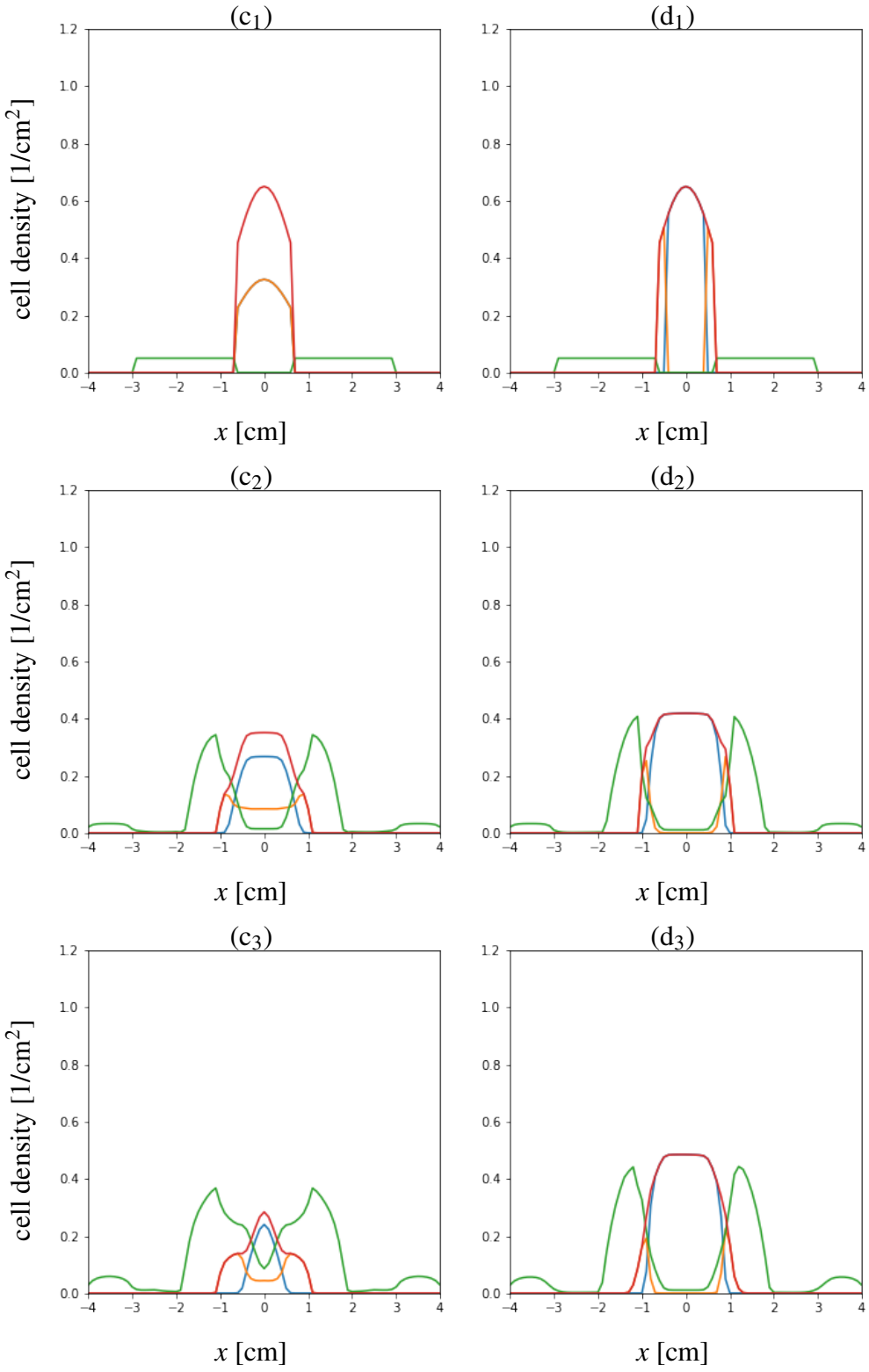

Fig. 9.3 Initial (first row), intermediate (second row), and final (third row) times of numerical simulation of two population systems introduced in Equation (9.2.6). Subpopulations involved are proliferative and resistant populations introduced in Section 9.3.2. Ratio R is set at 0.5. Experiment (c) (column one) has mixed population as initial data, experiment (d) (column two) adopts in&out configuration. Cancer subpopulations $a_1(t,\boldsymbol{x})$ and $a_2(t,\boldsymbol{x})$ are represented with blue and orange lines, total cancer cell population $\rho(t,\boldsymbol{x})$ with red line, T cells $\ell(t,\boldsymbol{x})$ with green line.

Conclusions

The word *"conclusion"* seems paradoxical in the field of mathematical oncology, which is still characterised by a large number of unanswered questions, both from the theoretical and the clinical point of view.

The complex and varied processes involved in tumour dynamics, and by consequence in this thesis, make a global treatment of the problem difficult. For this reason, we have preferred to dedicate a separate chapter to each dynamic analysed and accompany it with a discussion of each work's specific conclusions and future prospects. Here, we limit ourselves to collecting and summarizing the results obtained from the previous studies and presenting a common guideline for the next steps.

After dedicating **Part I** to the introduction of the biological (Chapter 1) and mathematical (Chapter 2) framework in which the works are set, **Part II** collects all the research results obtained so far.

In Chapter 3, we propose a mathematical model able to catch eco-evolutionary spatial dynamics of tumour cells, considering the impact of hypoxia on the trade-off between *maximizing cell survival* and *maximizing cell growth* affecting cancer cells [8]. Our findings reproduce experimental observations, allowing us to mathematically investigate the proven impact of the oxygen map. This influences both the delineation of niche spaces and the determination of tumour growth speed and epigenetic composition of the population [386]. The model proves to be a powerful tool in analyzing the multiplicity of evolutionary pathways that can lead to the development of hypoxia resistance. Moreover, it reproduces the shift of epigenetic dominance toward resistant phenotypes, allowing cells to survive both hostile environments and treatments.

In Chapter 4, based on the previous model, we enclose a novel mathematical continuous formulation for radiotherapy, in which the killing potential of the treatments depends on both the oxygenation of the area and the epigenetic trait assumed by the cells. Our model is presented as a valuable tool in analyzing the dependence on tumour oxygenation of repopulation, reoxygenation, and radiosensitivity dynamics and its effect on tumour-host interaction [376]. In this work, we introduce possible personalised indicators, complementary to the nominal tumour size, since that proves insufficient to predict tumour growth and therapy response. The model provides essential predictive information that could be useful for clinical practice, guiding the delineation of optimal protocols in terms of doses and timing.

In Chapter 5, we propose a plasticity-oriented modelling framework where discrete structuring variables distinguish cells in terms of genotype and assigned mathematical representation to differentiate them in terms of phenotype. The model proves to be capable of representing the early evolution of an in vitro heterogeneous tumour aggregate. From a biological point of view, numerical realisation captures the emergence of a hypoxic core within the tumour cluster with the consequent trigger of epithelial-mesenchymal transition, resulting in invasive dynamics. In the future, the model opens the perspective for investigating the influence of oxygenation levels, intrinsic genotype, and randomness on phenotypic conversions that characterise metastasis genesis and movement.

In Chapter 6, we develop an innovative mathematical multi-scale model to examine the interactions between hypoxia, molecular signalling pathways, and tumour cell migration. This model provides a comprehensive description of macroscopic tumour cell dynamics, incorporating the influence of microscopic Snail signalling pathways on the mechanisms of tumour response to hypoxic conditions. We prove the validity of the proposed mathematical framework as a tool for interpreting experimental data and understanding the underlying biological mechanisms driving tumour migration. We successfully replicate experimental results on human hepatocarcinoma [459] and breast cancer [305], underlining the effect of hypoxia and Snail knockdown or over-expression on the motility of cancer cells. Our model proves to be decisive in delineating the spatial distribution of Snail expression with promising clinical perspectives.

Moving to **Part III**, which includes not fully completed works, in Chapter 7, we propose mathematical models able to catch the stratified epigenetic and pheno-

typic spatial structure of tumour spheroids. Comparison between Fisher-like and anti-crowding frameworks with different degrees distinguishes bi-structured anti-crowding models as a successful model for compactness preservation of compact support initial data, emerging of invasive lower density rims, and geometric characterization of traits expressed by cells. The applicability of the model to clinical practice is enhanced by the introduction of clinical-comparable mathematical descriptors.

In Chapter 8, we have introduced a novel approach to oncolytic virotherapy modelling, considering epigenetically structured cancer cell population and the effect of hypoxia on effectiveness. First numerical simulations of the model in simple scenarios under stationary tissue oxygenation show biologically coherent patterns, with environmental selection and abiotic conditions that influence the capability of the virus to control tumour mass expansions.

Finally, in Chapter 9, we introduce a novel mathematical formulation in the context of tumour-immune system interaction. Although preliminary, the results already highlight the model's capabilities to provide a set of parameters whose values can determine different outcomes in terms of the tumour classification introduced in Ref. [349]. As presented in the paper, this classification strongly correlates with the effectiveness of different immunotherapy strategies, making our model a potentially helpful tool in delineating them and discriminate between "hot" and "cold" scenarios.

The models presented include central dynamics to understanding the evolution of tumour masses, the impact of interaction with the environment on them, and the effect of both on the effectiveness of treatments. By exploiting information obtained with such investigations, the mathematical model is a tool for clinical support in the optimization of therapeutic protocols. The results obtained so far are promising. On the one hand, they answer some biological questions that are not directly observable and introduce novel mathematical approaches developed to catch specific dynamics. On the other hand, from the point of view of future perspectives, the models have been developed in such a way as to have natural extensions and characterizations, opening the field both to an improvement in modelling terms and to an attempt to exhaust clinical questions that are still open.

From a purely mathematical point of view, the thesis's theoretical aspects concentrate predominantly on the modelling procedure. The need for capturing complex phenomena motivates the level of mathematical difficulty embedded in the models. This leads the theoretical studies included in this work to focus on the use of theoret-

ical analyses to control and forecast behaviours of the examined quantities. Among them, we consider numerousness and geometry for tumour growth, estimation of mass advancement speeds and characterization of optimal epigenetic/phenotypic trait. Addressing the future perspective, next steps include detailed studies of trajectories and equilibrium points, considering corresponding ODEs of our spatial models or local analysis. The construction of discrete stochastic models corresponding to the continuous models presented will also allow a theoretical parametric calibration (with limit techniques) with the advantage of traceability to measurable quantities. Again, from a mathematical point of view, investigating bifurcation analysis and optimal therapy control would allow a quantitative characterization capable of correlating the values of the parameters included and the possible initial conditions with the outcomes. In these terms, another aspect to consider is that of the stability of the results, which can be investigated in theoretical terms and by conducting further sensitivity analyses.

When considering the biologically-driven open questions concerning cancer cell dynamics, one relevant point is to account for better-described genetic alterations that may be induced by cell-cell communication and changes in environmental conditions but are usually determined by random mutations. We actually take into account them in a few models and with a generic diffusive dynamics modelling that we aim to improve.

From the epigenetic point of view, medicine and biology practice is moving toward novel, discovered, and more precisely investigated trade-off dynamics. Thus including more realistic trade-offs affecting tumour evolution would be of interest, either by characterizing the strength and shape of the trade-off or considering different phenotypical features that define it.

We could move in the direction of a specific characterization of cell state with respect to their metabolic activity (differentiating, for example, viable, quiescent, and necrotic cells). Specifically, considering quiescence dynamics would highlight problems of resistance to therapies based on targeting cells during their replicative cycle. Considering the formation of a necrotic population due to increased oxygen consumption as the tumour mass grows would be attractive for its effect on the morphology and invasion ability of the mass, being it responsible for the secretion of motility-promoting cytokines [281]. In this context, one can consider fingering invasive formation and dispersal metastatic mechanisms [380] and their correlation with necrosis and environmental conditions.

Moving to consider interaction with the environment and other factors, even though we consider healthy cell compartments via their effect on tumour cell and abiotic dynamics, a novel perspective would be to include tissue cells as a direct agent of the systems describing cell interactions.
Among all possible extension and future perspectives, an interesting aspect is also the insertion of more mechanical aspects, determinants in the interaction with intracellular fluid or extracellular matrix. This kind of characterization is strictly related to the spatial analysis of cancer masses and could sensitively improve the work in the study of tumours in tissues characterized by singular morphologies, such as the brain. When applying the presented model to reproduce the evolution of in vivo malignant masses toward invasive and metastatic dynamics, one may also include the presence of both the preexisting and the tumour-induced vasculature in the picture. In fact, blood vessels play a central role in tumour dynamics not only as carriers of oxygen but also as an escape route, through extravasation, for cellular agglomerates, which will form metastases in other areas of the body.

Let us finally recall that, although they are also interesting from an independent investigative point of view, this thesis focuses on therapies. This is evident in the choice to include biological elements and microscopic dynamics strictly related to their effectiveness and, sometimes, in the inclusion of the therapies themselves in the model. This focus has currently only been investigated partially and in qualitative terms and in this sense the works of this thesis are to be considered a first step in the direction of (hopefully) effective patient-specific modelling that supports clinical practice. Many works presented here show a clear correlation between epigenetic characteristics and the consequent phenotype expressed by the various cell subpopulations on therapeutic efficacy. This offers a starting point, from the perspective of target therapy, to select the most significant ones to target among many cellular pathways. The parameters inserted into the models, often taken from the medical literature to ensure the representative quality of the models, are the key to the patient-specific characterization. The initial data taken here as a generic representation of a tumour mass can be obtained from medical imaging and clinical analyses, being able to adapt the general model to specific situations of individual patients and use it with predictive intent. Furthermore, data relating to the speed of proliferation, movement and reaction of cells under external stimuli can be quantified in the case of the individual patient thanks to clinical tests, which over the years improve in the variability and precision of the obtainable information. In this sense,

it is interesting not only for the mathematician to be open to the use of medical data for the validation of their results, but also for a dialogue with the clinical world so that the mathematical model is recognized in its support for therapeutic practice and data collection operated in the field by medical personnel takes into account their needs in order to have a statistically significant predictive value. In the specific case of the future perspective for these works, my aim is to characterize my research, also understood in terms of establishing new collaborations and investigative realities, intensifying this dialogue and moving toward better medical reliability. This includes improving the calibration of all model parametrisation, for instance, by focusing on a specific tumour type and using proper sets of existing data. Once the model is used to determine the pros and cons of different therapeutical approaches, enlightening the environmental and tumour characteristics for which a strategy results in the optimal one, a natural step is to exploit the mathematical modelling to overlap different therapies (as it happens in combined therapies) and analyse the resulting outcome. In this direction, a complete sensitivity analysis on the models (already included in the future developments of the work due to its mathematical relevance) would be beneficial also in therapeutical terms: evaluating the impact of individual parameters and initial data on the final outcome would provide an important suggestion in clinical practice on the relevance of the various patient values.

All these pave the way for personalised medicine approaches tailored to individual tumour characteristics.

To finish, let me end with the same lack of formality that I used to open my introduction (and that characterises me more than the style of these hundreds of pages).
I started studying mathematics when I realized I didn't have the coldness and emotional detachment to become a doctor. I had never thought about the possibility of using analytical thinking to expand the possibilities of clinical practice.
The vastness of the unexplored territories and the steps still to be taken to make this possible is both sad and inspiring.
The conclusion is that I simply can not wait to see what more can be done, and I really hope to be part of it!

Acknowledgements

Academic acknowledgement

Non posso che iniziare questi ringraziamenti con un gigantesco grazie a Marcello, meglio noto come Professor M. E. Delitala (o "capo"). Per un percorso che si è tenuto saldamente alla larga dalla perfezione, ma rifarei da capo e con te; per essere stato un confronto accogliente e sfidante; per i brain storming sprementi, le email notturne, la correzione di testi incomprensibili; per aver condiviso con me la tua conoscenza e passione, per essere stato un distaccato osservatore e un entusiasta compagno di idee; per la tua guida accademica, spesso efficace e funzionale e talvolta rinfrancante nella sua umana difficoltà; per lo sbattimento infinito al fine di darmi la possibilità di vivermi contesti ed esperienze; per la tua timidezza che mi ha costretto a un anno di perifrasi per appellarti e per le tue spiazzanti aperture che mi hanno regalato un confortevole calore umano. Per un rapporto che difficilmente troverà un'onesta (e concisa!) descrizione in questa sede, e che sarebbe probabilmente causa di un imbarazzo che non voglio arrecare. Ma dal profondo del cuore spero tu sappia quanto ti sia grata di tutto.

Un altro caloroso grazie va a Federico, aka Professor Federico Frascoli, per avermi dato una calorosa accoglienza in Australia; per avermi aiutato accademicamente e umanamente con un'intensità che eccedeva il dovuto; per essere stato un prezioso insegnante e motivatore; per aver ampliato la mia rete di conoscenze e avermi aperto le porte di un nuovo mondo; per avermi fatto sentire a mio agio in un periodo e contesto poco facili; per aver creduto in me e nelle mie idee, per aver gestito la nostra collaborazione nel pieno rispetto e interesse della mia carriera accademica, per essere stato un prezioso ascoltatore e consigliere. Spero che questo sia solo il primo step e che il futuro ci offra modo e tempo per proseguire insieme: sarei onorata di poter lavorare ancora con te.

I would like to extend my kind thanks to Professors Thomas Stiehl and Haralampos Hatzikirou who agreed, in the midst of the summer heat, to devote themselves to the refereeing of this difficult tome and who gave me precious indications for its improvement.

Mi más sincero agradecimiento al profesor Víctor M. Pérez García, por la confianza que depositó en mí cuando era novata (no ha cambiado mucho ahora), por darme la bienvenida a su maravilloso grupo de investigación y brindarme herramientas y orientación de incomparable valor, por haberme arrepentido de mi pésimo español el cual decido darle un último intento con estos agradecimientos. Incluyo en el agradecimiento a todos los miembros del MOLAB de Ciudad Real, con especial atención al Profesor Gabriel Fernández Calvo, Dr. Julián Pérez Beteta,Dr. Carmen Ortega Sabater, y al Dr. Juan Jiménez Sánchez, por el ambiente heterogéneo y estimulante que crean en el laboratorio y por haberme acogido con una rara sinceridad.

Another heartful thank you goes to Professor Carrillo (it was difficult to choose a language), who has allowed me to come into contact with his infinite competence and has given me the means to continue this journey in the world of the academy. Our collaboration is still young, but I hope to deserve the trust given to me. As far as I have already felt, I thank you infinitely for the academic and human occasions in which you welcomed me and for giving me the opportunity to interact with a vital and engaging academic and human world. I am truly honoured to join your team and I hope to live up to it.

Uno (stranamente formale) ringrazimento va alla dottoressa Martina Conte, per avermi avvicinato al suo brillante lavoro ed essere stata un prezioso esempio e confronto, insegnandomi il valore costruttivo di un atteggiamento critico: la mia ammirazione per il tuo lavoro e la tua determinazione hanno poco a che fare con il sentimento di profonda amicizia che mi lega a te (e troverà posto nelle successive pagine), e ti sono sinceramente grata per averli condivisi con me.

Ci tengo a ringraziare anche i bimbi di Marcello, aka la dottoressa Giada Fiandaca e il dottor David Morselli, per essere stati compagni di viaggio in questi anni di dottorato, fieri membri del Delitala's Lab; per aver condiviso gioie e dolori nello sviluppo e stesura di paper inverosimilmente amati e odiati. E per aver chiuso i momenti più felici e difficili della collaborazione con un (oddio, un...) bicchiere di vino e una pacca sulla spalla.

Un ringraziamento va al professor Marco Scianna, per avermi accompagnato nei primi passi del primo articolo e per aver condiviso con me tempo e competenze.

Another grateful thought, a little further in time but close in memory, is dedicated to to Professor Anna Marciniak-Czochra and (again, but in another role) to Professor Thomas Stiehl, first guides in my journey into the academic world, for showing me an effective and passionate approach to the research that convinced me to take this path (in these terms, I don't know whether to thank or curse) and with whom I hope to have the opportunity to continue a joint research path in the future.

I finally thank all the members of the biomathematics sector I met in these years, to nourish an effervescent community full of brilliant minds, for the thousand projects sketched together and which I hope to have the opportunity to actually carry out, to be faces to be found with a smile in the corners of the world where this wonderful and exhausting work takes us.

References

[1] Abbas, Z., Rehman, S., Abbas, Z., and Rehman, S. (2018). An overview of cancer treatment modalities. In *Neoplasm*. IntechOpen.

[2] Abouheif, E., Favé, M. J., Ibarrarán Viniegra, A. S., Lesoway, M. P., Rafiqi, A. M., and Rajakumar, R. (2014). Eco-evo-devo: the time has come. *Advances in Experimental Medicine and Biology*, 781.

[3] Abramovitch, R., Meir, G., and Neeman, M. (1995). Neovascularization induced growth of implanted c6 glioma multicellular spheroids: magnetic resonance microimaging. *Cancer Research*, 55(9).

[4] Adam, J. A. (1986). A simplified mathematical model of tumor growth. *Mathematical Biosciences*, 81(2).

[5] Adam, J. A. (1988). A mathematical model of tumor growth by diffusion. *Mathematical and Computer Modelling*, 11.

[6] Aghi, M. K., Liu, T. C., Rabkin, S., and Martuza, R. L. (2009). Hypoxia enhances the replication of oncolytic herpes simplex virus. *Molecular Therapy*, 17(1).

[7] Aiello, N. M., Maddipati, R., Norgard, R. J., Balli, D., Li, J., Yuan, S., Yamazoe, T., Black, T., Sahmoud, A., Furth, E. E., Bar Sagi, D., and Stanger, B. Z. (2018). EMT subtype influences epithelial plasticity and mode of cell migration. *Developmental Cell*, 45(6).

[8] Aktipis, C. A., Boddy, A. M., Gatenby, R. A., Brown, J. S., and Maley, C. C. (2013). Life history trade-offs in cancer evolution. *Nature Reviews Cancer*, 13(12).

[9] Al Hajj, M., Wicha, M. S., Benito Hernandez, A., Morrison, S. J., and Clarke, M. F. (2003). Prospective identification of tumorigenic breast cancer cells. *Proceedings of the National Academy of Sciences*, 100(7).

[10] Al Tameemi, M., Chaplain, M., and d'Onofrio, A. (2012). Evasion of tumours from the control of the immune system: consequences of brief encounters. *Biology Direct*, 7.

[11] Alberts, B., Johnson, A., Lewis, J., Raff, M., Roberts, K., and Walter, P. (2002). *Molecular biology of the cell*. Garland Science, 4th edition.

[12] Albini, S., Zakharova, V., and Ait Si Ali, S. (2019). Histone modifications. In Palacios, D., editor, *Epigenetics and regeneration*, Translational Epigenetics. Academic Press.

[13] Alfaro, M., Berestycki, H., and Raoul, G. (2015). The effect of climate shift on a species submitted to dispersion, evolution, growth and nonlocal competition. 49(1).

[14] Alfaro, M., Coville, J., and Raoul, G. (2013). Travelling waves in a nonlocal reaction-diffusion equation as a model for a population structured by a space variable and a phenotypic trait. *Communications in Partial Differential Equations*, 38(12).

[15] Alfarouk, K. O., Ibrahim, M. E., Gatenby, R. A., and Brown, J. S. (2013). Riparian ecosystems in human cancers. *Evolutionary Applications*, 6(1).

[16] Allen, L. J. S. (2010). *An introduction to stochastic processes with applications to biology - second edition*. Taylor and Francis Inc.

[17] Almeida, L., Audebert, C., Leschiera, E., and Lorenzi, T. (2022). A hybrid discrete–continuum modelling approach to explore the impact of t-cell infiltration on anti-tumour immune response. *Bulletin of Mathematical Biology*, 84(12).

[18] Almeida, L., Bliman, P. A., Nadin, G., Perthame, B., and Vauchelet, N. (2021). Final size and convergence rate for an epidemic in heterogeneous populations. *Mathematical Models and Methods in Applied Sciences*, 31(5).

[19] Almeida, L., Chisholm, R. H., Clairambault, J., Lorenzi, T., Lorz, A., Pouchol, C., and Trélat, E. (2018). Why is evolution important in cancer and what mathematics should be used to treat cancer? Focus on drug resistance. In Mondaini, R. P., editor, *Trends in biomathematics: modeling, optimization and computational problems*. Springer International Publishing.

[20] Alnæs, M., Blechta, J., Hake, J., Johansson, A., Kehlet, B., Logg, A., Richardson, C., Ring, J., Rognes, M. E., and Wells, G. N. (2015). The FEniCS project version 1.5. *Archive of Numerical Software*, 3(100).

[21] Alzahrani, T., Eftimie, R., and Trucu, D. (2019). Multiscale modelling of cancer response to oncolytic viral therapy. *Mathematical Biosciences*, 310.

[22] Ambrosi, D. and Preziosi, L. (2002). On the closure of mass balance models for tumor growth. *Mathematical Models and Methods in Applied Sciences*, 12(05).

[23] Anderson, A. R. (2007). A hybrid multiscale model of solid tumour growth and invasion: evolution and the microenvironment. In *Single-cell-based models in biology and medicine*. Springer.

[24] Anderson, A. R., Chaplain, M. A., Newman, E. L., Steele, R. J., and Thompson, A. M. (2000). Mathematical modelling of tumour invasion and metastasis. *Computational and mathematical methods in medicine*, 2(2).

[25] Anderson, A. R. A. (2005). A hybrid mathematical model of solid tumour invasion: the importance of cell adhesion. *Mathematical Medicine and Biology: A Journal of the IMA*, 22(2).

[26] Anderson, A. R. A. and Chaplain, M. A. J. (1998). Continuous and discrete mathematical models of tumor-induced angiogenesis. *Bulletin of Mathematical Biology*, 60(5).

[27] Anderson, A. R. A., Chaplain, M. a. J., Newman, E. L., Steele, R. J. C., and Thompson, A. M. (1999). Mathematical modelling of tumour invasion and metastasis. *Computational and Mathematical Methods in Medicine*, 2.

[28] Anderson, A. R. A. and Quaranta, V. (2008). Integrative mathematical oncology. *Nature Reviews Cancer*, 8(3).

[29] Anderson, A. R. A., Rejniak, K. A., Gerlee, P., and Quaranta, V. (2009). Microenvironment driven invasion: a multiscale multimodel investigation. *Journal of Mathematical Biology*, 58(4).

[30] Anderson, A. R. A., Weaver, A. M., Cummings, P. T., and Quaranta, V. (2006). Tumor morphology and phenotypic evolution driven by selective pressure from the microenvironment. *Cell*, 127(5).

[31] Ansari, D., Friess, H., Bauden, M., Samnegård, J., and Andersson, R. (2018). Pancreatic cancer: disease dynamics, tumor biology and the role of the microenvironment. *Oncotarget*, 9(5).

[32] Aplin, A. E., Howe, A., Alahari, S. K., and Juliano, R. L. (1998). Signal transduction and signal modulation by cell adhesion receptors: the role of integrins, cadherins, immunoglobulin-cell adhesion molecules, and selectins. *Pharmacological Reviews*, 50(2).

[33] Araujo, A. L. A. d., Fassoni, A. C., Madalena, K. F. L., and Salvino, L. F. (2024). Analysis and simulation of an integro-differential Lotka–Volterra model with variable reproduction rates and optimal control. *Communications in Nonlinear Science and Numerical Simulation*, 134.

[34] Araujo, R. P. and McElwain, D. L. S. (2004). A history of the study of solid tumour growth: the contribution of mathematical modelling. *Bulletin of Mathematical Biology*, 66(5).

[35] Ardaševa, A., Gatenby, R. A., Anderson, A. R. A., Byrne, H. M., Maini, P. K., and Lorenzi, T. (2020a). Evolutionary dynamics of competing phenotype-structured populations in periodically fluctuating environments. *Journal of Mathematical Biology*, 80(3).

[36] Ardaševa, A., Gatenby, R. A., Anderson, A. R. A., Byrne, H. M., Maini, P. K., and Lorenzi, T. (2020b). A mathematical dissection of the adaptation of cell populations to fluctuating oxygen levels. *Bulletin of Mathematical Biology*, 82(6).

[37] Aronson, D. G. (1980). Density-dependent interaction–diffusion systems. In Stewart, W. E., Ray, W. H., and Conley, C. C., editors, *Dynamics and modelling of reactive systems*. Academic Press.

[38] Astanin, S. and Preziosi, L. (2009). Mathematical modelling of the Warburg effect in tumour cords. *Journal of Theoretical Biology*, 258(4).

[39] Atsou, K., Anjuère, F., Braud, V. M., and Goudon, T. (2020). A size and space structured model describing interactions of tumor cells with immune cells reveals cancer persistent equilibrium states in tumorigenesis. *Journal of Theoretical Biology*, 490.

[40] Baker, S. G. (2015). A cancer theory kerfuffle can lead to new lines of research. *Journal of the National Cancer Institute*, 107(2).

[41] Barbarossa, M. V. and Röst, G. (2015). Immuno-epidemiology of a population structured by immune status: a mathematical study of waning immunity and immune system boosting. *Journal of Mathematical Biology*, 71(6–7).

[42] Barles, G., Evans, L., and Souganidis, P. (1990). Wavefront propagation for reaction-diffusion systems of PDE. *Duke Mathematical Journal*, 61.

[43] Barles, G., Mirrahimi, S., and Perthame, B. (2009). Concentration in Lotka-Volterra parabolic or integral equations: a general convergence result. *Methods and Applications of Analysis*, 16.

[44] Barrak, N. H., Khajah, M. A., and Luqmani, Y. A. (2020). Hypoxic environment may enhance migration/penetration of endocrine resistant MCF7- derived breast cancer cells through monolayers of other non-invasive cancer cells in vitro. *Scientific Reports*, 10(1).

[45] Barrallo Gimeno, A. and Nieto, M. A. (2005). The snail genes as inducers of cell movement and survival: implications in development and cancer. *Development (Cambridge, England)*, 132(14).

[46] Barton, M. B., Jacob, S., Shafiq, J., Wong, K., Thompson, S. R., Hanna, T. P., and Delaney, G. P. (2014). Estimating the demand for radiotherapy from the evidence: a review of changes from 2003 to 2012. *Radiotherapy and Oncology: Journal of the European Society for Therapeutic Radiology and Oncology*, 112(1).

[47] Baskar, R., Lee, K. A., Yeo, R., and Yeoh, K. W. (2012a). Cancer and radiation therapy: current advances and future directions. *International Journal of Medical Sciences*, 9(3).

[48] Baskar, R., Yap, S. P., Chua, K. L. M., and Itahana, K. (2012b). The diverse and complex roles of radiation on cancer treatment: therapeutic target and genome maintenance. *American Journal of Cancer Research*, 2(4).

[49] Baumann, M., Krause, M., Overgaard, J., Debus, J., Bentzen, S. M., Daartz, J., Richter, C., Zips, D., and Bortfeld, T. (2016). Radiation oncology in the era of precision medicine. *Nature Reviews Cancer*, 16(4).

[50] Bellomo, N., Bellouquid, A., Nieto, J., and Soler, J. (2007). Multicellular biological growing systems: hyperbolic limits towards macroscopic description. *Mathematical Models and Methods in Applied Sciences*, 17(supp01).

[51] Bellomo, N., Bellouquid, A., Nieto, J., and Soler, J. (2010a). Complexity and mathematical tools toward the modelling of multicellular growing systems. *Mathematical and Computer Modelling*, 51(5-6).

[52] Bellomo, N., Bellouquid, A., Nieto, J., and Soler, J. (2010b). Multiscale biological tissue models and flux-limited chemotaxis for multicellular growing systems. *Mathematical Models and Methods in Applied Sciences*, 20(07).

[53] Bellomo, N., Li, N. K., and Maini, P. K. (2008). On the foundations of cancer modelling: selected topics, speculations, and perspectives. *Mathematical Models and Methods in Applied Sciences*, 18(04).

[54] Benzekry, S., Lamont, C., Beheshti, A., Tracz, A., Ebos, J. M. L., Hlatky, L., and Hahnfeldt, P. (2014). Classical mathematical models for description and prediction of experimental tumor growth. *PLoS computational biology*, 10(8).

[55] Bernardi, E., Pareschi, L., Toscani, G., and Zanella, M. (2022). Effects of vaccination efficacy on wealth distribution in kinetic epidemic models. *Entropy*, 24(2).

[56] Besse, A., Clapp, G. D., Bernard, S., Nicolini, F. E., Levy, D., and Lepoutre, T. (2017). Stability analysis of a model of interaction between the immune system and cancer cells in chronic myelogenous leukemia. *Bulletin of Mathematical Biology*.

[57] Bethge, A., Schumacher, U., and Wedemann, G. (2015). Simulation of metastatic progression using a computer model including chemotherapy and radiation therapy. *Journal of Biomedical Informatics*, 57.

[58] Bhatia, S., Wang, P., Toh, A., and Thompson, E. W. (2020). New insights into the role of phenotypic plasticity and EMT in driving cancer progression. *Frontiers in Molecular Biosciences*, 7.

[59] Biava, P. M., Basevi, M., Biggiero, L., Borgonovo, A., Borgonovo, E., and Burigana, F. (2011). Cancer cell reprogramming: stem cell differentiation stage factors and an agent based model to optimize cancer treatment. *Current Pharmaceutical Biotechnology*, 12(2).

[60] Biddle, A., Liang, X., Gammon, L., Fazil, B., Harper, L. J., Emich, H., Costea, D. E., and Mackenzie, I. C. (2011). Cancer stem cells in squamous cell carcinoma switch between two distinct phenotypes that are preferentially migratory or proliferative. *Cancer Research*, 71(15).

[61] Bitsouni, V., Chaplain, M. A. J., and Eftimie, R. (2017). Mathematical modelling of cancer invasion: the multiple roles of TGF-β pathway on tumour proliferation and cell adhesion. *Mathematical Models and Methods in Applied Sciences*, 27(10).

[62] Blanco, M. J., Moreno Bueno, G., Sarrio, D., Locascio, A., Cano, A., Palacios, J., and Nieto, M. A. (2002). Correlation of snail expression with histological grade and lymph node status in breast carcinomas. *Oncogene*, 21(20).

[63] Blank, C. U., Haining, W. N., Held, W., Hogan, P. G., Kallies, A., Lugli, E., Lynn, R. C., Philip, M., Rao, A., Restifo, N. P., Schietinger, A., Schumacher, T. N., Schwartzberg, P. L., Sharpe, A. H., Speiser, D. E., Wherry, E. J., Youngblood, B. A., and Zehn, D. (2019). Defining 'T cell exhaustion'. *Nature Reviews Immunology*, 19(11).

[64] Boareto, M., Jolly, M. K., Goldman, A., Pietilä, M., Mani, S. A., Sengupta, S., Ben Jacob, E., Levine, H., and Onuchic, J. N. (2016). Notch-jagged signalling can give rise to clusters of cells exhibiting a hybrid epithelial/mesenchymal phenotype. *Journal of the Royal Society, Interface*, 13(118).

[65] Boddy, A. M., Huang, W., and Aktipis, A. (2018). Life history trade-offs in tumors. *Current Pathobiology Reports*, 6(4).

[66] Boemo, M. A. and Byrne, H. M. (2019). Mathematical modelling of a hypoxia-regulated oncolytic virus delivered by tumour-associated macrophages. *Journal of Theoretical Biology*, 461.

[67] Bomford, C. K. and Kunkler, I. H. (2002). *Walter and miller's textbook of radiotherapy: radiation physics, therapy and oncology*. Churchill Livingstone, Edinburgh, 6th edition edition.

[68] Bonilla, L. L. and Soler, J. S. (2001). High-field limit of the Vlasov–Poisson–Fokker–Planck system: a comparison of different perturbation methods. *Mathematical Models and Methods in Applied Sciences*, 11(08).

[69] Bouin, E. and Calvez, V. (2014). Travelling waves for the cane toads equation with bounded traits. *Nonlinearity*, 27(9).

[70] Bouin, E., Calvez, V., Meunier, N., Mirrahimi, S., Perthame, B., Raoul, G., and Voituriez, R. (2012). Invasion fronts with variable motility: phenotype selection, spatial sorting and wave acceleration. *Comptes Rendus. Mathématique*, 350(15-16).

[71] Bouin, E. and Mirrahimi, S. (2015). A hamilton–jacobi approach for a model of population structured by space and trait. *Communications in Mathematical Sciences*, 13(6).

[72] Brady Nicholls, R., Zhang, J., Zhang, T., Wang, A. Z., Butler, R., Gatenby, R. A., and Enderling, H. (2021). Predicting patient-specific response to adaptive therapy in metastatic castration-resistant prostate cancer using prostate-specific antigen dynamics. *Neoplasia (New York, N.Y.)*, 23(9).

[73] Brooks, M. D., Burness, M. L., and Wicha, M. S. (2015). Therapeutic implications of cellular heterogeneity and plasticity in breast cancer. *Cell Stem Cell*, 17(3).

[74] Brown, J. M. and Wilson, W. R. (2004). Exploiting tumour hypoxia in cancer treatment. *Nature Reviews Cancer*, 4(6).

[75] Buckwar, E., Conte, M., and Meddah, A. (2023). A stochastic hierarchical model for low grade glioma evolution. *Journal of Mathematical Biology*, 86(6).

[76] Burger, M., Francesco, M. D., Fagioli, S., and Stevens, A. (2018). Sorting phenomena in a mathematical model for two mutually attracting/repelling species. *SIAM Journal on Mathematical Analysis*, 50(3).

[77] Burleson, K. M., Boente, M. P., Pambuccian, S. E., and Skubitz, A. P. N. (2006). Disaggregation and invasion of ovarian carcinoma ascites spheroids. *Journal of Translational Medicine*, 4.

[78] Burrell, R. A. and Swanton, C. (2014). Tumour heterogeneity and the evolution of polyclonal drug resistance. *Molecular Oncology*, 8(6).

[79] Byrne, H. and Preziosi, L. (2003). Modelling solid tumour growth using the theory of mixtures. *Mathematical Medicine and Biology: A Journal of the IMA*, 20(4).

[80] Byrne, H. M., Alarcon, T., Owen, M. R., Webb, S. D., and Maini, P. K. (2006). Modelling aspects of cancer dynamics: a review. *Philosophical Transactions. Series A, Mathematical, Physical, and Engineering Sciences*, 364(1843).

[81] Byrne, H. M., King, J. R., McElwain, D. L. S., and Preziosi, L. (2003). A two-phase model of solid tumour growth. *Applied Mathematics Letters*, 16(4).

[82] Böttger, K., Hatzikirou, H., Chauviere, A., and Deutsch, A. (2012). Investigation of the migration/proliferation dichotomy and its impact on avascular glioma invasion. *Mathematical Modelling of Natural Phenomena*, 7(1).

[83] Böttger, K., Hatzikirou, H., Voss Böhme, A., Cavalcanti Adam, E. A., Herrero, M. A., and Deutsch, A. (2015). An emerging allee effect is critical for tumor initiation and persistence. *PLoS computational biology*, 11(9).

[84] Calvez, V., Henderson, C., Mirrahimi, S., Turanova, O., and Dumont, T. (2018). Non-local competition slows down front acceleration during dispersal evolution. *Annales Henri Lebesgue*, 5.

[85] Cano, A., Pérez Moreno, M. A., Rodrigo, I., Locascio, A., Blanco, M. J., del Barrio, M. G., Portillo, F., and Nieto, M. A. (2000). The transcription factor Snail controls epithelial–mesenchymal transitions by repressing e-cadherin expression. *Nature cell biology*, 2(2).

[86] Capasso, V. and Morale, D. (2009). Asymptotic behavior of a system of stochastic particles subject to nonlocal interactions. *Stochastic Analysis and Applications*, 27(3).

[87] Capp, J. P., DeGregori, J., Nedelcu, A. M., Dujon, A. M., Boutry, J., Pujol, P., Alix Panabières, C., Hamede, R., Roche, B., Ujvari, B., Marusyk, A., Gatenby, R., and Thomas, F. (2021). Group phenotypic composition in cancer. *eLife*, 10.

[88] Carrillo, J. A., Chertock, A., and Huang, Y. (2015). A finite-volume method for nonlinear nonlocal equations with a gradient flow structure. *Communications in computational physics*, 17(1).

[89] Carrillo, J. A., Colombi, A., and Scianna, M. (2018). Adhesion and volume constraints via nonlocal interactions determine cell organisation and migration profiles. *Journal of Theoretical Biology*, 445.

[90] Carrillo, J. A., Fornasier, M., Toscani, G., and Vecil, F. (2010). Particle, kinetic, and hydrodynamic models of swarming. In Naldi, G., Pareschi, L., and Toscani, G., editors, *Mathematical modeling of collective behavior in socio-economic and life sciences*. Birkhäuser Boston, Boston.

[91] Carrillo, J. A., Murakawa, H., Sato, M., Togashi, H., and Trush, O. (2019). A population dynamics model of cell-cell adhesion incorporating population pressure and density saturation. *Journal of Theoretical Biology*, 474.

[92] Carvalho, M. C. and Rodrigues, J. F. (2004). *Recent advances in the theory and applications of mass transport*. American Mathematical Society.

[93] Castro, M. a. A., Klamt, F., Grieneisen, V. A., Grivicich, I., and Moreira, J. C. F. (2003). Gompertzian growth pattern correlated with phenotypic organization of colon carcinoma, malignant glioma and non-small cell lung carcinoma cell lines. *Cell Proliferation*, 36(2).

[94] Celora, G. L., Byrne, H. M., and Kevrekidis, P. G. (2023). Spatio-temporal modelling of phenotypic heterogeneity in tumour tissues and its impact on radiotherapy treatment. *Journal of Theoretical Biology*, 556.

[95] Celora, G. L., Byrne, H. M., Zois, C. E., and Kevrekidis, P. G. (2021). Phenotypic variation modulates the growth dynamics and response to radiotherapy of solid tumours under normoxia and hypoxia. *Journal of Theoretical Biology*, 527.

[96] Chalub, F. A., Markowich, P. A., Perthame, B., and Schmeiser, C. (2004). *Kinetic models for chemotaxis and their drift-diffusion limits*. Springer.

[97] Chaplain, M. A. (1995). The mathematical modelling of tumour angiogenesis and invasion. *Acta Biotheoretica*, 43(4).

[98] Chaplain, M. A. and Britton, N. F. (1993). On the concentration profile of a growth inhibitory factor in multicell spheroids. *Mathematical Biosciences*, 115(2).

[99] Chaplain, M. A., Giverso, C., Lorenzi, T., and Preziosi, L. (2019). Derivation and application of effective interface conditions for continuum mechanical models of cell invasion through thin membranes. *SIAM Journal on Applied Mathematics*, 79(5).

[100] Chaplain, M. A. J. (1996). Avascular growth, angiogenesis and vascular growth in solid tumours: the mathematical modelling of the stages of tumour development. *Mathematical and Computer Modelling*, 23(6).

[101] Chaplain, M. A. J., Lorenzi, T., and MacFarlane, F. R. (2020). Bridging the gap between individual-based and continuum models of growing cell populations. *Journal of Mathematical Biology*, 80(1-2).

[102] Chauviere, A., Preziosi, L., and Hillen, T. (2007). Modeling the motion of a cell population in the extracellular matrix. In *Conference publications*, volume 2007. Conference Publications.

[103] Chen, W., Dong, J., Haiech, J., Kilhoffer, M. C., and Zeniou, M. (2016). Cancer stem cell quiescence and plasticity as major challenges in cancer therapy. *Stem Cells International*, 2016.

[104] Chen, X., Cui, S., and Friedman, A. (2005). A hyperbolic free boundary problem modeling tumor growth: asymptotic behavior. *Transactions of the American Mathematical Society*, 357(12).

[105] Chen, X. and Friedman, A. (2003). A free boundary problem for an elliptic-hyperbolic system: an application to tumor growth. *SIAM Journal on Mathematical Analysis*, 35(4).

[106] Chen, Y., DeWeese, T., Dilley, J., Zhang, Y., Li, Y., Ramesh, N., Lee, J., Pennathur Das, R., Radzyminski, J., and Wypych, J. (2001). CV706, a prostate cancer-specific adenovirus variant, in combination with radiotherapy produces synergistic antitumor efficacy without increasing toxicity. *Cancer Research*, 61(14).

[107] Chen, Z., Han, F., Du, Y., Shi, H., and Zhou, W. (2023). Hypoxic microenvironment in cancer: molecular mechanisms and therapeutic interventions. *Signal Transduction and Targeted Therapy*, 8(1).

[108] Chesson, P. (2000). General theory of competitive coexistence in spatially-varying environments. *Theoretical Population Biology*, 58(3).

[109] Chiari, G., Conte, M., and Delitala, M. (2024). Multi-scale modeling of snail-mediated response to hypoxia in tumor progression. *arXiv*, 2404.16769.

[110] Chiari, G., Delitala, M. E., Morselli, D., and Scianna, M. (2022). A hybrid modeling environment to describe aggregates of cells heterogeneous for genotype and behavior with possible phenotypic transitions. *International Journal of Non-Linear Mechanics*, 144.

[111] Chiari, G., Fiandaca, G., and Delitala, M. E. (2023a). Hypoxia-related radiotherapy resistance in tumors: treatment efficacy investigation in an eco-evolutionary perspective. *Frontiers in Applied Mathematics and Statistics*, 9.

[112] Chiari, G., Fiandaca, G., and Delitala, M. E. (2023b). Hypoxia-resistance heterogeneity in tumours: the impact of geometrical characterization of environmental niches and evolutionary trade-offs. a mathematical approach. *Mathematical Modelling of Natural Phenomena*, 18.

[113] Chisholm, R. H., Lorenzi, T., Desvillettes, L., and Hughes, B. D. (2016). Evolutionary dynamics of phenotype-structured populations: from individual-level mechanisms to population-level consequences. *Zeitschrift für angewandte Mathematik und Physik*, 67(4).

[114] Cho, H., Lewis, A. L., Storey, K. M., and Byrne, H. M. (2023). Designing experimental conditions to use the Lotka–Volterra model to infer tumor cell line interaction types. *Journal of Theoretical Biology*, 559.

[115] Chopard, B., Ouared, R., Deutsch, A., Hatzikirou, H., and Wolf Gladrow, D. (2010). Lattice-gas cellular automaton models for biology: from fluids to cells. *Acta Biotheoretica*, 58(4).

[116] Chow, B., Warkentin, B., and Menon, G. M. (2019). Radiobiological dose calculation parameters for cervix cancer brachytherapy: A systematic review. *Brachytherapy*, 18(4).

[117] Chun, Y. S., Adusumilli, P. S., and Fong, Y. (2005). Employing tumor hypoxia for oncolytic therapy in breast cancer. *Journal of Mammary Gland Biology and Neoplasia*, 10(4).

[118] Ciarletta, P., Ambrosi, D., Maugin, G. A., and Preziosi, L. (2013). Mechano-transduction in tumour growth modelling. *The European Physical Journal E*, 36(3).

[119] Clairambault, J. and Fercoq, O. (2016). Physiologically structured cell population dynamic models with applications to combined drug delivery optimisation in oncology. *Mathematical Modelling of Natural Phenomena*, 11(6).

[120] Collins, A. T., Berry, P. A., Hyde, C., Stower, M. J., and Maitland, N. J. (2005). Prospective identification of tumorigenic prostate cancer stem cells. *Cancer Research*, 65(23).

[121] Colombi, A., Scianna, M., and Preziosi, L. (2015a). A measure-theoretic model for collective cell migration and aggregation. *Mathematical Modelling of Natural Phenomena*, 10(1).

[122] Colombi, A., Scianna, M., and Preziosi, L. (2017). Coherent modelling switch between pointwise and distributed representations of cell aggregates. *Journal of Mathematical Biology*, 74(4).

[123] Colombi, A., Scianna, M., and Tosin, A. (2015b). Differentiated cell behavior: a multiscale approach using measure theory. *Journal of Mathematical Biology*, 71(5).

[124] Conte, M., Dzierma, Y., Knobe, S., and Surulescu, C. (2023). Mathematical modeling of glioma invasion and therapy approaches via kinetic theory of active particles. *Mathematical Models and Methods in Applied Sciences*, 33(05).

[125] Conte, M., Gerardo Giorda, L., and Groppi, M. (2020). Glioma invasion and its interplay with nervous tissue and therapy: a multiscale model. *Journal of theoretical biology*, 486.

[126] Conte, M. and Loy, N. (2022). Multi-cue kinetic model with non-local sensing for cell migration on a fiber network with chemotaxis. *Bulletin of Mathematical Biology*, 84(3).

[127] Conte, M. and Loy, N. (2023). A non-local kinetic model for cell migration: a study of the interplay between contact guidance and steric hindrance. *SIAM Journal on Applied Mathematics*.

[128] Conte, M. and Surulescu, C. (2021). Mathematical modeling of glioma invasion: acid-and vasculature mediated go-or-grow dichotomy and the influence of tissue anisotropy. *Applied Mathematics and Computation*, 407.

[129] Corbin, G., Klar, A., Surulescu, C., Engwer, C., Wenske, M., Nieto, J., and Soler, J. (2021). Modeling glioma invasion with anisotropy-and hypoxia-triggered motility enhancement: from subcellular dynamics to macroscopic PDEs with multiple taxis. *Mathematical Models and Methods in Applied Sciences*, 31(01).

[130] Cordon Cardo, C. and Prives, C. (1999). At the crossroads of inflammation and tumorigenesis. *The Journal of Experimental Medicine*, 190(10).

[131] Corwin, D., Holdsworth, C., Rockne, R. C., Trister, A. D., Mrugala, M. M., Rockhill, J. K., Stewart, R. D., Phillips, M., and Swanson, K. R. (2013). Toward patient-specific, biologically optimized radiation therapy plans for the treatment of glioblastoma. *PloS One*, 8(11).

[132] Counter, C. M., Hahn, W. C., Wei, W., Caddle, S. D., Beijersbergen, R. L., Lansdorp, P. M., Sedivy, J. M., and Weinberg, R. A. (1998). Dissociation among in vitro telomerase activity, telomere maintenance, and cellular immortalization. *Proceedings of the National Academy of Sciences of the United States of America*, 95(25).

[133] Coussens, L. M., Raymond, W. W., Bergers, G., Laig Webster, M., Behrendtsen, O., Werb, Z., Caughey, G. H., and Hanahan, D. (1999). Inflammatory mast cells up-regulate angiogenesis during squamous epithelial carcinogenesis. *Genes and Development*, 13(11).

[134] Cristini, V. and Lowengrub, J. (2010). *Multiscale modeling of cancer*. Cambridge University Press.

[135] Crivelli, J. J., Földes, J., Kim, P. S., and Wares, J. R. (2012). A mathematical model for cell cycle-specific cancer virotherapy. *Journal of Biological Dynamics*, 6(SUPPL. 1).

[136] Cumsille, P., Coronel, A., Conca, C., Quiñinao, C., and Escudero, C. (2015). Proposal of a hybrid approach for tumor progression and tumor-induced angiogenesis. *Theoretical Biology and Medical Modelling*, 12.

[137] Cushing, J. M. (1980). Two species competition in a periodic environment. *Journal of Mathematical Biology*, 10.

[138] Cushing, J. M. (1998). *An introduction to structured population dynamics*. Society for Industrial and Applied Mathematics.

[139] Damaghi, M., West, J., Robertson Tessi, M., Xu, L., Ferrall Fairbanks, M. C., Stewart, P. A., Persi, E., Fridley, B. L., Altrock, P. M., Gatenby, R. A., Sims, P. A., Anderson, A. R. A., and Gillies, R. J. (2021). The harsh microenvironment in early breast cancer selects for a Warburg phenotype. *Proceedings of the National Academy of Sciences of the United States of America*, 118(3).

[140] Daşu, A., Toma Daşu, I., and Karlsson, M. (2003). Theoretical simulation of tumour oxygenation and results from acute and chronic hypoxia. *Physics in Medicine and Biology*, 48(17).

[141] De Boer, R. J., Hogeweg, P., Dullens, H. F., De Weger, R. A., and Den Otter, W. (1985). Macrophage T lymphocyte interactions in the anti-tumor immune response: a mathematical model. *Journal of Immunology*, 134(4).

[142] de Gruijl, T. D., Janssen, A. B., and van Beusechem, V. W. (2015). Arming oncolytic viruses to leverage antitumor immunity. *Expert Opinion on Biological Therapy*, 15(7).

[143] De Herreros, A. G., Peiró, S., Nassour, M., and Savagner, P. (2010). Snail family regulation and epithelial mesenchymal transitions in breast cancer progression. *Journal of mammary gland biology and neoplasia*, 15.

[144] de Oliveira, V. M., Amado, A., and Campos, P. R. A. (2018). The interplay of tradeoffs within the framework of a resource-based modelling. *Ecological Modelling*, 384.

[145] de Rioja, V. L., Isern, N., and Fort, J. (2016). A mathematical approach to virus therapy of glioblastomas. *Biology Direct*, 11(1).

[146] de Thé, H. (2018). Differentiation therapy revisited. *Nature Reviews. Cancer*, 18(2).

[147] Delitala, M., Dianzani, U., Lorenzi, T., and Melensi, M. (2013). A mathematical model for immune and autoimmune response mediated by T-cells. *Computers and Mathematics with Applications*, 6(66).

[148] Delitala, M. and Lorenzi, T. (2012). Asymptotic dynamics in continuous structured populations with mutations, competition and mutualism. *Journal of Mathematical Analysis and Applications*, 389(1).

[149] Delitala, M. and Lorenzi, T. (2013a). Evolutionary branching patterns in predator-prey structured populations. *Discrete and Continuous Dynamical Systems - Series B*, 18(9).

[150] Delitala, M. and Lorenzi, T. (2013b). Recognition and learning in a mathematical model for immune response against cancer. *Discrete and Continuous Dynamical Systems - B*, 18(4).

[151] Demaria, S. and Formenti, S. C. (2012). Radiation as an immunological adjuvant: current evidence on dose and fractionation. *Frontiers in Oncology*, 2.

[152] Deutsch, A. (2007). Lattice-gas cellular automaton modeling of developing cell systems. In Anderson, A. R. A., Chaplain, M. A. J., and Rejniak, K. A., editors, *Single-cell-based models in biology and medicine*. Birkhäuser, Basel.

[153] Diekmann, O. (1978). Thresholds and travelling waves for the geographical spread of infection. *Journal of Mathematical Biology*, 6(2).

[154] Diekmann, O., Jabin, P. E., Mischler, S., and Perthame, B. (2005). The dynamics of adaptation: an illuminating example and a Hamilton-Jacobi approach. *Theoretical population biology*, 67.

[155] Dietrich, A., Kolbe, N., Sfakianakis, N., and Surulescu, C. (2022). Multiscale modeling of glioma invasion: from receptor binding to flux-limited macroscopic PDEs. *Multiscale Modeling and Simulation*, 20(2).

[156] Ding, C., Wang, Z., and Zhang, Q. (2022). Age-structure model for oncolytic virotherapy. *International Journal of Biomathematics*, 15(01).

[157] Dingle, H. and Drake, V. A. (2007). What is migration? *BioScience*, 57(2).

[158] Doerfler, W. and Böhm, P., editors (2006). *DNA methylation: development, genetic disease and cancer*. Springer, Berlin Heidelberg, 2006th edition edition.

[159] Domschke, P., Trucu, D., Gerisch, A., and A. J. Chaplain, M. (2014). Mathematical modelling of cancer invasion: implications of cell adhesion variability for tumour infiltrative growth patterns. *Journal of Theoretical Biology*, 361.

[160] Domschke, P., Trucu, D., Gerisch, A., and Chaplain, M. A. J. (2017). Structured models of cell migration incorporating molecular binding processes. *Journal of Mathematical Biology*, 75(6-7).

[161] Drasdo, D. (2005). Coarse graining in simulated cell populations. *Advances in Complex Systems*, 08(02n03).

[162] Drasdo, D., Buttenschön, A., and Van Liedekerke, P. (2018). Agent-based lattice models of multicellular systems: numerical methods, implementation, and applications. In Cerrolaza, M., Shefelbine, S. J., and Garzón-Alvarado, D., editors, *Numerical methods and advanced simulation in biomechanics and biological processes*. Academic Press.

[163] Drasdo, D., Hoehme, S., and Block, M. (2007). On the role of physics in the growth and pattern formation of multi-cellular systems: what can we learn from individual-cell based models? *Journal of Statistical Physics*, 128(1).

[164] Drasdo, D. and Höhme, S. (2005). A single-cell-based model of tumor growth in vitro: monolayers and spheroids. *Physical Biology*, 2(3).

[165] Dujon, A. M., Aktipis, A., Alix-Panabières, C., Amend, S. R., Boddy, A. M., Brown, J. S., Capp, J., DeGregori, J., Ewald, P., Gatenby, R., Gerlinger, M., Giraudeau, M., Hamede, R. K., Hansen, E., Kareva, I., Maley, C. C., Marusyk, A., McGranahan, N., Metzger, M. J., Nedelcu, A. M., Noble, R., Nunney, L., Pienta, K. J., Polyak, K., Pujol, P., Read, A. F., Roche, B., Sebens, S., Solary, E., Staňková, K., Swain Ewald, H., Thomas, F., and Ujvari, B. (2021). Identifying key questions in the ecology and evolution of cancer. *Evolutionary Applications*, 14(4).

[166] d'Onofrio, A. (2005). A general framework for modeling tumor-immune system competition and immunotherapy: mathematical analysis and biomedical inferences. *Physica D: Nonlinear Phenomena*, 208(3).

[167] Ehrlich, E., Becks, L., and Gaedke, U. (2017). Trait–fitness relationships determine how trade-off shapes affect species coexistence. *Ecology*, 98(12).

[168] Elmore, S. (2007). Apoptosis: a review of programmed cell death. *Toxicologic pathology*, 35(4).

[169] Engwer, C., Hillen, T., Knappitsch, M., and Surulescu, C. (2015). Glioma follow white matter tracts: a multiscale DTI-based model. *Journal of mathematical biology*, 71.

[170] Engwer, C., Hunt, A., and Surulescu, C. (2016). Effective equations for anisotropic glioma spread with proliferation: a multiscale approach and comparisons with previous settings. *Mathematical medicine and biology: a journal of the IMA*, 33(4).

[171] Engwer, C., Stinner, C., and Surulescu, C. (2017). On a structured multiscale model for acid-mediated tumor invasion: the effects of adhesion and proliferation. *Mathematical Models and Methods in Applied Sciences*, 27(07).

[172] Fasullo, M., Burch, A., and Britton, A. (2009). Hypoxia enhances the replication of oncolytic herpes simplex virus in p53- breast cancer cells. *Cell Cycle*, 8(14).

[173] Ferguson, M. S., Lemoine, N. R., and Wang, Y. (2012). Systemic delivery of oncolytic viruses: hopes and hurdles. *Advances in Virology*, 2012.

[174] Ferreira, S. C., Martins, M. L., and Vilela, M. J. (1999). A growth model for primary cancer (ii). new rules, progress curves and morphology transitions. *Physica A: Statistical Mechanics and its Applications*, 272(1).

[175] Fiandaca, G., Delitala, M., and Lorenzi, T. (2021). A mathematical study of the influence of hypoxia and acidity on the evolutionary dynamics of cancer. *Bulletin of Mathematical Biology*, 83(7).

[176] Figueroa Iglesias, S. and Mirrahimi, S. (2018). Long time evolutionary dynamics of phenotypically structured populations in time-periodic environments. *SIAM Journal on Mathematical Analysis*, 50(5).

[177] Filbet, F., Laurençot, P., and Perthame, B. (2005). Derivation of hyperbolic models for chemosensitive movement. *Journal of Mathematical Biology*, 50(2).

[178] Fisher, R., Pusztai, L., and Swanton, C. (2013). Cancer heterogeneity: implications for targeted therapeutics. *British Journal of Cancer*, 108(3).

[179] Flashner Abramson, E., Vasudevan, S., Adejumobi, I. A., Sonnenblick, A., and Kravchenko Balasha, N. (2019). Decoding cancer heterogeneity: studying patient-specific signaling signatures towards personalized cancer therapy. *Theranostics*, 9(18).

[180] Fletcher, A. G., Breward, C. J. W., and Jonathan Chapman, S. (2012). Mathematical modeling of monoclonal conversion in the colonic crypt. *Journal of Theoretical Biology*, 300.

[181] Folkman, J. and Hochberg, M. (1973). Self-regulation of growth in three dimensions. *The Journal of Experimental Medicine*, 138(4).

[182] Frascoli, F., Kim, P. S., Hughes, B. D., and Landman, K. A. (2014). A dynamical model of tumour immunotherapy. *Mathematical Biosciences*, 253.

[183] Friedman, A. (2009). Free boundary problems associated with multiscale tumor models. *Mathematical Modelling of Natural Phenomena*, 4(3).

[184] Friedman, A. and Tao, Y. (2003). Analysis of a model of a virus that replicates selectively in tumor cells. *Journal of Mathematical Biology*, 47(5).

[185] Friedman, A., Tian, J. P., Fulci, G., Chiocca, E. A., and Wang, J. (2006). Glioma virotherapy: effects of innate immune suppression and increased viral replication capacity. *Cancer Research*, 66(4).

[186] Fry, T. J., Shah, N. N., Orentas, R. J., Stetler Stevenson, M., Yuan, C. M., Ramakrishna, S., Wolters, P., Martin, S., Delbrook, C., Yates, B., Shalabi, H., Fountaine, T. J., Shern, J. F., Majzner, R. G., Stroncek, D. F., Sabatino, M., Feng, Y., Dimitrov, D. S., Zhang, L., Nguyen, S., Qin, H., Dropulic, B., Lee, D. W., and

Mackall, C. L. (2018). CD22-targeted CAR T cells induce remission in B-all that is naive or resistant to CD19-targeted car immunotherapy. *Nature Medicine*, 24(1).

[187] Fukumura, D. and Jain, R. K. (2007). Tumor microvasculature and microenvironment: targets for anti-angiogenesis and normalization. *Microvascular Research*, 74(2-3).

[188] Gallaher, J. A., Brown, J. S., and Anderson, A. R. A. (2019). The impact of proliferation-migration tradeoffs on phenotypic evolution in cancer. *Scientific Reports*, 9(1).

[189] Gameiro, P. A. and Struhl, K. (2018). Nutrient deprivation elicits a transcriptional and translational inflammatory response coupled to decreased protein synthesis. *Cell Reports*, 24(6).

[190] Ganly, I., Mautner, V., and Balmain, A. (2000). Productive replication of human adenoviruses in mouse epidermal cells. *Journal of virology*, 74(6).

[191] Gao, C. F., Xie, Q., Su, Y. L., Koeman, J., Khoo, S. K., Gustafson, M., Knudsen, B. S., Hay, R., Shinomiya, N., and Vande Woude, G. F. (2005). Proliferation and invasion: plasticity in tumor cells. *Proceedings of the National Academy of Sciences of the United States of America*, 102(30).

[192] Gao, X., McDonald, J. T., Hlatky, L., and Enderling, H. (2013). Acute and fractionated irradiation differentially modulate glioma stem cell division kinetics. *Cancer Research*, 73(5).

[193] Gatenby, R. A., Avdieiev, S., Tsai, K. Y., and Brown, J. S. (2020). Integrating genetic and nongenetic drivers of somatic evolution during carcinogenesis: the biplane model. *Evolutionary Applications*, 13(7).

[194] Gatenby, R. A., Smallbone, K., Maini, P. K., Rose, F., Averill, J., Nagle, R. B., Worrall, L., and Gillies, R. J. (2007). Cellular adaptations to hypoxia and acidosis during somatic evolution of breast cancer. *British Journal of Cancer*, 97(5).

[195] Gentry, S. N. and Jackson, T. L. (2013). A mathematical model of cancer stem cell driven tumor initiation: implications of niche size and loss of homeostatic regulatory mechanisms. *PLOS ONE*, 8(8).

[196] Gerisch, A. and Chaplain, M. A. J. (2008). Mathematical modelling of cancer cell invasion of tissue: local and non-local models and the effect of adhesion. *Journal of Theoretical Biology*, 250(4).

[197] Giese, A., Kluwe, L., Laube, B., Meissner, H., Berens, M. E., and Westphal, M. (1996a). Migration of human glioma cells on myelin. *Neurosurgery*, 38(4).

[198] Giese, A., Loo, M. A., Tran, N., Haskett, D., Coons, S. W., and Berens, M. E. (1996b). Dichotomy of astrocytoma migration and proliferation. *International Journal of Cancer*, 67(2).

[199] Giverso, C., Lorenzi, T., and Preziosi, L. (2022). Effective interface conditions for continuum mechanical models describing the invasion of multiple cell populations through thin membranes. *Applied Mathematics Letters*, 125.

[200] Giverso, C., Scianna, M., Preziosi, L., Buono, N. L., and Funaro, A. (2010). Individual cell-based model for in-vitro mesothelial invasion of ovarian cancer. *Mathematical Modelling of Natural Phenomena*, 5(1).

[201] Glazier, J. A., Balter, A., and Poplawski, N. J. (2007). Magnetization to morphogenesis: a brief history of the Glazier–Graner–Hogeweg model. *Mathematics and Biosciences in Interaction*.

[202] Gomes, A. P. and Blenis, J. (2015). A nexus for cellular homeostasis: the interplay between metabolic and signal transduction pathways. *Current opinion in biotechnology*, 34.

[203] Graner, F. and Glazier, J. A. (1992). Simulation of biological cell sorting using a two-dimensional extended Potts model. *Physical Review Letters*, 69(13).

[204] Gray, L. H., Conger, A. D., Ebert, M., Hornsey, S., and Scott, O. C. (1953). The concentration of oxygen dissolved in tissues at the time of irradiation as a factor in radiotherapy. *The British Journal of Radiology*, 26(312).

[205] Grimes, D. R., Fletcher, A. G., and Partridge, M. (2014). Oxygen consumption dynamics in steady-state tumour models. *Royal Society Open Science*, 1(1).

[206] Grimes, D. R., Warren, D. R., and Warren, S. (2017). Hypoxia imaging and radiotherapy: bridging the resolution gap. *The British Journal of Radiology*, 90(1076).

[207] Guo, Z. S. (2011). The impact of hypoxia on oncolytic virotherapy. *Virus Adaptation and Treatment*, 3.

[208] Gupta, M. K. and Qin, R. Y. (2003). Mechanism and its regulation of tumor-induced angiogenesis. *World Journal of Gastroenterology*, 9(6).

[209] Hadjicharalambous, M., Wijeratne, P. A., and Vavourakis, V. (2021). From tumour perfusion to drug delivery and clinical translation of in silico cancer models. *Methods*, 185.

[210] Hamis, S., Powathil, G. G., and Chaplain, M. A. J. (2019). Blackboard to bedside: a mathematical modeling bottom-up approach toward personalized cancer treatments. *JCO clinical cancer informatics*, 3.

[211] Hanahan, D. (2022). Hallmarks of cancer: new dimensions. *Cancer Discovery*, 12(1).

[212] Hanahan, D. and Coussens, L. M. (2012). Accessories to the crime: functions of cells recruited to the tumor microenvironment. *Cancer Cell*, 21(3).

[213] Hanahan, D. and Weinberg, R. A. (2000). The hallmarks of cancer. *Cell*, 100(1).

[214] Hanahan, D. and Weinberg, R. A. (2011). Hallmarks of cancer: the next generation. *Cell*, 144(5).

[215] Hatzikirou, H., Basanta, D., Simon, M., Schaller, K., and Deutsch, A. (2012). 'go or grow': the key to the emergence of invasion in tumour progression? *Mathematical Medicine and Biology: A Journal of the IMA*, 29(1).

[216] Hatzikirou, H., Brusch, L., Schaller, C., Simon, M., and Deutsch, A. (2010). Prediction of traveling front behavior in a lattice-gas cellular automaton model for tumor invasion. *Computers and Mathematics with Applications*, 59(7).

[217] Hatzikirou, H. and Deutsch, A. (2008). Cellular automata as microscopic models of cell migration in heterogeneous environments. *Current Topics in Developmental Biology*, 81.

[218] Hatzikirou, H. and Deutsch, A. (2010). Lattice-gas cellular automaton modeling of emergent behavior in interacting cell populations. In *Simulating complex systems by cellular automata*. Springer Verlag.

[219] Hausser, J., Szekely, P., Bar, N., Zimmer, A., Sheftel, H., Caldas, C., and Alon, U. (2019). Tumor diversity and the trade-off between universal cancer tasks. *Nature Communications*, 10(1).

[220] Hayflick, L. (1997). Mortality and immortality at the cellular level. a review. *Biochemistry. Biokhimiia*, 62(11).

[221] Hillen, T. (2006). M5 mesoscopic and macroscopic models for mesenchymal motion. *Journal of mathematical biology*, 53(4).

[222] Hillen, T. and Painter, K. J. (2009). A user's guide to PDE models for chemotaxis. *Journal of Mathematical Biology*, 58(1-2).

[223] Hillen, T. and Painter, K. J. (2013). Transport and anisotropic diffusion models for movement in oriented habitats. In *Dispersal, individual movement and spatial ecology: a mathematical perspective*. Springer.

[224] Hong, B. J., Kim, J., Jeong, H., Bok, S., Kim, Y. E., and Ahn, G. O. (2016). Tumor hypoxia and reoxygenation: the yin and yang for radiotherapy. *Radiation Oncology Journal*, 34(4).

[225] Horsman, M. R., Mortensen, L. S., Petersen, J. B., Busk, M., and Overgaard, J. (2012). Imaging hypoxia to improve radiotherapy outcome. *Nature Reviews. Clinical Oncology*, 9(12).

[226] Hotz, B., Arndt, M., Dullat, S., Bhargava, S., Buhr, H. J., and Hotz, H. G. (2007). Epithelial to mesenchymal transition: expression of the regulators snail, slug, and twist in pancreatic cancer. *Clinical cancer research*, 13(16).

[227] Hubbi, M. E. and Semenza, G. L. (2015). Regulation of cell proliferation by hypoxia-inducible factors. *American Journal of Physiology - Cell Physiology*, 309(12).

[228] Hudson, J. D., Shoaibi, M. A., Maestro, R., Carnero, A., Hannon, G. J., and Beach, D. H. (1999). A proinflammatory cytokine inhibits p53 tumor suppressor activity. *The Journal of Experimental Medicine*, 190(10).

[229] Hölzel, M., Bovier, A., and Tüting, T. (2013). Plasticity of tumour and immune cells: a source of heterogeneity and a cause for therapy resistance? *Nature Reviews. Cancer*, 13(5).

[230] Iannelli, M. (1995). *Mathematical theory of age-structured population dynamics*. Giardini editori e stampatori.

[231] Ibrahim Hashim, A., J. Gillies, R., S. Brown, J., and A. Gatenby, R. (2017). Coevolution of tumor cells and their microenvironment: "Niche construction in cancer". In Ujvari, B., Roche, B., and Thomas, F., editors, *Ecology and Evolution of Cancer*. Academic Press.

[232] Ilina, O. and Friedl, P. (2009). Mechanisms of collective cell migration at a glance. *Journal of Cell Science*, 122(18).

[233] Imai, T., Horiuchi, A., Wang, C., Oka, K., Ohira, S., Nikaido, T., and Konishi, I. (2003). Hypoxia attenuates the expression of e-cadherin via up-regulation of snail in ovarian carcinoma cells. *The American Journal of Pathology*, 163(4).

[234] Irtan, S., Van Tinteren, H., Graf, N., van den Heuvel Eibrink, M. M., Heij, H., Bergeron, C., de Camargo, B., Acha, T., Spreafico, F., Vujanic, G., Powis, M., Okoye, B., Wilde, J., Godzinski, J., and Pritchard Jones, K. (2019). Evaluation of needle biopsy as a potential risk factor for local recurrence of Wilms tumour in the SIOP WT 2001 trial. *European Journal of Cancer*, 116.

[235] Jabin, P. E. and Schram, R. S. (2016). Selection-mutation dynamics with spatial dependence. *Journal de Mathématiques Pures et Appliquées*, 176.

[236] Jacqueline, C., Biro, P. A., Beckmann, C., Moller, A. P., Renaud, F., Sorci, G., Tasiemski, A., Ujvari, B., and Thomas, F. (2016). Cancer: a disease at the crossroads of trade-offs. *Evolutionary Applications*, 10(3).

[237] Jenner, A., Yun, C. O., Yoon, A., Kim, P. S., and Coster, A. C. F. (2018a). Modelling heterogeneity in viral-tumour dynamics: the effects of gene-attenuation on viral characteristics. *Journal of Theoretical Biology*, 454.

[238] Jenner, A. L., Frascoli, F., Coster, A. C. F., and Kim, P. S. (2020). Enhancing oncolytic virotherapy: observations from a voronoi cell-based model. *Journal of Theoretical Biology*, 485.

[239] Jenner, A. L., Kim, P. S., and Frascoli, F. (2019). Oncolytic virotherapy for tumours following a Gompertz growth law. *Journal of Theoretical Biology*, 480.

[240] Jenner, A. L., Yun, C. O., Kim, P. S., and Coster, A. C. F. (2018b). Mathematical modelling of the interaction between cancer cells and an oncolytic virus: insights into the effects of treatment protocols. *Bulletin of Mathematical Biology*, 80(6).

[241] Jeon, J., Quaranta, V., and Cummings, P. T. (2010). An off-lattice hybrid discrete-continuum model of tumor growth and invasion. *Biophysical journal*, 98(1).

[242] Jia, D., Jolly, M. K., Tripathi, S. C., Den Hollander, P., Huang, B., Lu, M., Celiktas, M., Ramirez Peña, E., Ben Jacob, E., and Onuchic, J. N. (2017). Distinguishing mechanisms underlying EMT tristability. *Cancer convergence*, 1.

[243] Jiang, Y., Pjesivac Grbovic, J., Cantrell, C., and Freyer, J. P. (2005). A multiscale model for avascular tumor growth. *Biophysical Journal*, 89(6).

[244] Jiao, Y. and Torquato, S. (2011). Emergent behaviors from a cellular automaton model for invasive tumor growth in heterogeneous microenvironments. *PLoS Computational Biology*, 7(12).

[245] Jiao, Y. and Torquato, S. (2013). Evolution and morphology of microenvironment-enhanced malignancy of three-dimensional invasive solid tumors. *Physical Review. E, Statistical, Nonlinear, and Soft Matter Physics*, 87(5).

[246] Jiménez Sánchez, J., Bosque, J. J., Jiménez Londoño, G. A., Molina García, D., Martínez, A., Pérez Beteta, J., Ortega Sabater, C., Honguero Martínez, A. F., García Vicente, A. M., Calvo, G. F., and Pérez García, V. M. (2021). Evolutionary dynamics at the tumor edge reveal metabolic imaging biomarkers. *Proceedings of the National Academy of Sciences*, 118(6).

[247] Jin, H., Yu, Y., Zhang, T., Zhou, X., Zhou, J., Jia, L., Wu, Y., Zhou, B. P., and Feng, Y. (2010). Snail is critical for tumor growth and metastasis of ovarian carcinoma. *International Journal of Cancer*, 126(9).

[248] Joiner, M. C. and Kogel, A. J. v. d., editors (2018). *Basic clinical radiobiology*. CRC Press, Boca Raton, FL, 5th edition edition.

[249] Jones, L., Hoban, P., and Metcalfe, P. (2001). The use of the linear quadratic model in radiotherapy: a review. *Australasian Physical and Engineering Sciences in Medicine*, 24(3).

[250] Kalluri, R. (2016). The biology and function of fibroblasts in cancer. *Nature Reviews. Cancer*, 16(9).

[251] Kalluri, R. and Neilson, E. G. (2003). Epithelial-mesenchymal transition and its implications for fibrosis. *The Journal of Clinical Investigation*, 112(12).

[252] Kalluri, R. and Weinberg, R. A. (2009). The basics of epithelial-mesenchymal transition. *The Journal of Clinical Investigation*, 119(6).

[253] Kansal, A. R., Torquato, S., Harsh GR, I. V., Chiocca, E. A., and Deisboeck, T. S. (2000). Simulated brain tumor growth dynamics using a three-dimensional cellular automaton. *Journal of Theoretical Biology*, 203(4).

[254] Kao, S. H., Wu, K. J., and Lee, W. H. (2016). Hypoxia, epithelial-mesenchymal transition, and TET-mediated epigenetic changes. *Journal of Clinical Medicine*, 5(2).

[255] Karev, G. P., Novozhilov, A. S., and Koonin, E. V. (2006). Mathematical modeling of tumor therapy with oncolytic viruses: effects of parametric heterogeneity on cell dynamics. *Biology Direct*, 1.

[256] Kathagen, A., Holz, M., Schulte, A., Weller, J., Westphal, M., and Lamszus, K. (2015). METB-05 glycolysis and the pentose phosphate pathway are differentially associated with the dichotomous regulation of glioblastoma cell migration versus proliferation. *Neuro-Oncology*, 17(Suppl 5).

[257] Katsunuma, S., Honda, H., Shinoda, T., Ishimoto, Y., Miyata, T., Kiyonari, H., Abe, T., Nibu, K. i., Takai, Y., and Togashi, H. (2016). Synergistic action of nectins and cadherins generates the mosaic cellular pattern of the olfactory epithelium. *The Journal of Cell Biology*, 212(5).

[258] Kaufhold, S. and Bonavida, B. (2014). Central role of snail1 in the regulation of EMT and resistance in cancer: a target for therapeutic intervention. *Journal of Experimental and Clinical Cancer Research*, 33.

[259] Ke, L. D., Shi, Y. X., Im, S. A., Chen, X., and Yung, W. A. (2000). The relevance of cell proliferation, vascular endothelial growth factor, and basic fibroblast growth factor production to angiogenesis and tumorigenicity in human glioma cell lines. *Clinical Cancer Research*, 6(6).

[260] Kelkel, J. and Surulescu, C. (2012). A multiscale approach to cell migration in tissue networks. *Mathematical Models and Methods in Applied Sciences*, 22(03).

[261] Kermack, W. O. and McKendrick, A. G. (1927). A contribution to the mathematical theory of epidemics. *Proceedings of the royal society of london. Series A, Containing papers of a mathematical and physical character*, 115(772).

[262] Khaitan, D., Chandna, S., Arya, M., and Dwarakanath, B. (2006). Establishment and characterization of multicellular spheroids from a human glioma cell line; implications for tumor therapy. *Journal of Translational Medicine*, 4(1).

[263] Khalil, A. A. and Friedl, P. (2010). Determinants of leader cells in collective cell migration. *Integrative Biology: Quantitative Biosciences from Nano to Macro*, 2(11-12).

[264] Kim, J. H., Lee, Y. S., Kim, H., Huang, J. H., Yoon, A. R., and Yun, C. O. (2006). Relaxin expression from tumor-targeting adenoviruses and its intratumoral spread, apoptosis induction, and efficacy. *Journal of the National Cancer Institute*, 98(20).

[265] Kim, W., Lee, S., Seo, D., Kim, D., Kim, K., Kim, E., Kang, J., Seong, K. M., Youn, H., and Youn, B. (2019). Cellular stress responses in radiotherapy. *Cells*, 8(9).

[266] Kim, Y., Kang, H., and Lawler, S. (2014). The role of the MIR-451-AMPK signaling pathway in regulation of cell migration and proliferation in glioblastoma. In Eladdadi, A., Kim, P., and Mallet, D., editors, *Mathematical models of tumor-immune system dynamics*, Springer Proceedings in Mathematics and Statistics, New York, NY. Springer.

[267] Kim, Y. and Othmer, H. G. (2013). A hybrid model of tumor-stromal interactions in breast cancer. *Bulletin of Mathematical Biology*, 75(8).

[268] Kirschner, D. and Panetta, J. C. (1998). Modeling immunotherapy of the tumor-immune interaction. *Journal of Mathematical Biology*, 37(3).

[269] Kirschner, D. E., Jackson, T. L., and Arciero, J. C. (2003). A mathematical model of tumor-immune evasion and sirna treatment. *Discrete and Continuous Dynamical Systems - Series B*, 4(1).

[270] Kolbe, N., Sfakianakis, N., Stinner, C., Surulescu, C., and Lenz, J. (2020). Modeling multiple taxis: tumor invasion with phenotypic heterogeneity, haptotaxis, and unilateral interspecies repellence. *Discrete and Continuous Dynamical Systems - B*, 26(1).

[271] Komarova, N. L. and Wodarz, D. (2010). ODE models for oncolytic virus dynamics. *Journal of theoretical biology*, 263(4).

[272] Korolev, K. S., Xavier, J. B., and Gore, J. (2014). Turning ecology and evolution against cancer. *Nature Reviews Cancer*, 14(5).

[273] Kumar, P., Li, J., and Surulescu, C. (2021). Multiscale modeling of glioma pseudopalisades: contributions from the tumor microenvironment. *Journal of Mathematical Biology*, 82.

[274] Kumari, R. and Jat, P. (2021). Mechanisms of cellular senescence: cell cycle arrest and senescence associated secretory phenotype. *Frontiers in Cell and Developmental Biology*, 9.

[275] Kuznetsov, M. and Kolobov, A. (2020). Optimization of dose fractionation for radiotherapy of a solid tumor with account of oxygen effect and proliferative heterogeneity. *Mathematics*, 8(8).

[276] Kuznetsov, V. A., Makalkin, I. A., Taylor, M. A., and Perelson, A. S. (1994). Nonlinear dynamics of immunogenic tumors: parameter estimation and global bifurcation analysis. *Bulletin of Mathematical Biology*, 56(2).

[277] Kåver, G., Lind, B. K., Löf, J., Liander, A., and Brahme, A. (1999). Stochastic optimization of intensity modulated radiotherapy to account for uncertainties in patient sensitivity. *Physics in Medicine and Biology*, 44(12).

[278] Lamszus, K., Kathagen, A., Holz, M., Schulte, A., and Westphal, M. (2014). "go or grow" - links between cellular function, glucose metabolism and glioma microenvironment. *Neuro-Oncology*, 16(3).

[279] Langtangen, H. P. and Logg, A. (2017). *Solving pdes in python: the FEniCS tutorial I*. Springer, 1st ed. 2016 edizione edition.

[280] Lee, H. O., Silva, A. S., Concilio, S., Li, Y. S., Slifker, M., Gatenby, R. A., and Cheng, J. D. (2011). Evolution of tumor invasiveness: the adaptive tumor microenvironment landscape model. *Cancer Research*, 71(20).

[281] Lee, S. Y., Ju, M. K., Jeon, H. M., Jeong, E. K., Lee, Y. J., Kim, C. H., Park, H. G., Han, S. I., and Kang, H. S. (2018). Regulation of tumor progression by programmed necrosis. *Oxidative Medicine and Cellular Longevity*, 2018.

[282] Lee, T., Jenner, A. L., Kim, P. S., and Lee, J. (2020). Application of control theory in a delayed-infection and immune-evading oncolytic virotherapy. *Mathematical Biosciences and Engineering*, 17(3).

[283] Leszczyński, M., Ledzewicz, U., and Schättler, H. (2020). Optimal control for a mathematical model for chemotherapy with pharmacometrics. *Mathematical Modelling of Natural Phenomena*, 15.

[284] Letort, G., Montagud, A., Stoll, G., Heiland, R., Barillot, E., Macklin, P., Zinovyev, A., and Calzone, L. (2019). Physiboss: a multi-scale agent-based modelling framework integrating physical dimension and cell signalling. *Bioinformatics (Oxford, England)*, 35(7).

[285] Lewin, T. D., Maini, P. K., Moros, E. G., Enderling, H., and Byrne, H. M. (2018). The evolution of tumour composition during fractionated radiotherapy: implications for outcome. *Bulletin of Mathematical Biology*, 80(5).

[286] León Triana, O., Sabir, S., Calvo, G. F., Belmonte Beitia, J., Chulián, S., Martínez Rubio, A., Rosa, M., Pérez Martínez, A., Ramirez Orellana, M., and Pérez García, V. M. (2021). CAR T cell therapy in B-cell acute lymphoblastic leukaemia: insights from mathematical models. *Communications in Nonlinear Science and Numerical Simulation*, 94.

[287] Li, J. and Lowengrub, J. (2011). Effects of motility and contact inhibition on tumor viability: a discrete simulation using the cellular Potts model. In *Biomat 2010*. World Scientific.

[288] Li, J. F. and Lowengrub, J. (2014). The effects of cell compressibility, motility and contact inhibition on the growth of tumor cell clusters using the cellular Potts model. *Journal of Theoretical Biology*, 343.

[289] Li, L., Madu, C. O., Lu, A., and Lu, Y. (2010). HIF-1α promotes a hypoxia-independent cell migration. *The open biology journal*, 3.

[290] Ling, C. C., Humm, J., Larson, S., Amols, H., Fuks, Z., Leibel, S., and Koutcher, J. A. (2000). Towards multidimensional radiotherapy (md-crt): biological imaging and biological conformality. *International Journal of Radiation Oncology, Biology, Physics*, 47(3).

[291] Liu, S., Cong, Y., Wang, D., Sun, Y., Deng, L., Liu, Y., Martin Trevino, R., Shang, L., McDermott, S. P., Landis, M. D., Hong, S., Adams, A., D'Angelo, R., Ginestier, C., Charafe Jauffret, E., Clouthier, S. G., Birnbaum, D., Wong, S. T., Zhan, M., Chang, J. C., and Wicha, M. S. (2014). Breast cancer stem cells transition between epithelial and mesenchymal states reflective of their normal counterparts. *Stem Cell Reports*, 2(1).

[292] Lo, S. S., Fakiris, A. J., Chang, E. L., Mayr, N. A., Wang, J. Z., Papiez, L., Teh, B. S., McGarry, R. C., Cardenes, H. R., and Timmerman, R. D. (2010). Stereotactic body radiation therapy: a novel treatment modality. *Nature Reviews Clinical Oncology*, 7(1).

[293] Lodish, H., Berk, A., Kaiser, C. A., Kaiser, C., Krieger, M., Scott, M. P., Bretscher, A., Ploegh, H., Matsudaira, P., and others (2008). *Molecular cell biology*. Macmillan.

[294] Logg, A., Mardal, K.-A., and Wells, G., editors (2012). *Automated solution of differential equations by the finite element method: the fenics book*, volume 84 of *Lecture Notes in Computational Science and Engineering*. Springer Berlin Heidelberg, Berlin, Heidelberg.

[295] Lorenz, T. and Surulescu, C. (2014). On a class of multiscale cancer cell migration models: well-posedness in less regular function spaces. *Mathematical Models and Methods in Applied Sciences*, 24(12).

[296] Lorenzi, T., Chisholm, R. H., and Clairambault, J. (2016). Tracking the evolution of cancer cell populations through the mathematical lens of phenotype-structured equations. *Biology Direct*, 11(1).

[297] Lorenzi, T., Chisholm, R. H., Melensi, M., Lorz, A., and Delitala, M. (2015). Mathematical model reveals how regulating the three phases of T-cell response could counteract immune evasion. *Immunology*, 146(2).

[298] Lorenzi, T., Paparelli, E., and Tosin, A. (2023). Modelling coevolutionary dynamics in heterogeneous SI epidemiological systems across scales.

[299] Lorenzi, T., Pugliese, A., Sensi, M., and Zardini, A. (2021). Evolutionary dynamics in an SI epidemic model with phenotype-structured susceptible compartment. *Journal of Mathematical Biology*, 83(6-7).

[300] Lorenzi, T., Venkataraman, C., Lorz, A., and Chaplain, M. A. J. (2018). The role of spatial variations of abiotic factors in mediating intratumour phenotypic heterogeneity. *Journal of Theoretical Biology*, 451.

[301] Lorz, A., Lorenzi, T., Clairambault, J., Escargueil, A., and Perthame, B. (2015). Modeling the effects of space structure and combination therapies on phenotypic heterogeneity and drug resistance in solid tumors. *Bulletin of Mathematical Biology*, 77(1).

[302] Loy, N. and Preziosi, L. (2020). Kinetic models with non-local sensing determining cell polarization and speed according to independent cues. *Journal of Mathematical Biology*, 80(1).

[303] Lu, M., Jolly, M. K., Gomoto, R., Huang, B., Onuchic, J., and Ben Jacob, E. (2013a). Tristability in cancer-associated microrna-TF chimera toggle switch. *The Journal of Physical Chemistry B*, 117(42).

[304] Lu, M., Jolly, M. K., Levine, H., Onuchic, J. N., and Ben Jacob, E. (2013b). Microrna-based regulation of epithelial–hybrid–mesenchymal fate determination. *Proceedings of the National Academy of Sciences*, 110(45).

[305] Lundgren, K., Nordenskjöld, B., and Landberg, G. (2009). Hypoxia, Snail and incomplete epithelial–mesenchymal transition in breast cancer. *British journal of cancer*, 101(10).

[306] Lv, X., Li, J., Zhang, C., Hu, T., Li, S., He, S., Yan, H., Tan, Y., Lei, M., Wen, M., and Zuo, J. (2016). The role of hypoxia-inducible factors in tumor angiogenesis and cell metabolism. *Genes and Diseases*, 4(1).

[307] Macklin, P. and Lowengrub, J. (2007). Nonlinear simulation of the effect of microenvironment on tumor growth. *Journal of Theoretical Biology*, 245(4).

[308] Maley, C. C., Aktipis, A., Graham, T. A., Sottoriva, A., Boddy, A. M., Janiszewska, M., Silva, A. S., Gerlinger, M., Yuan, Y., Pienta, K. J., Anderson, K. S., Gatenby, R., Swanton, C., Posada, D., Wu, C. I., Schiffman, J. D., Hwang, E. S., Polyak, K., Anderson, A. R. A., Brown, J. S., Greaves, M., and Shibata, D. (2017). Classifying the evolutionary and ecological features of neoplasms. *Nature Reviews. Cancer*, 17(10).

[309] Manzo, G. (2020). Defined mathematical relationships among cancer cells suggest modular growth in tumor progression and highlight developmental features consistent with a para-embryonic nature of cancer. *Frontiers in Cell and Developmental Biology*, 8.

[310] Marciniak Czochra, A., Stiehl, T., Ho, A. D., Jäger, W., and Wagner, W. (2009). Modeling of asymmetric cell division in hematopoietic stem cells—regulation of self-renewal is essential for efficient repopulation. *Stem Cells and Development*, 18(3).

[311] Marshall, J. S., Warrington, R., Watson, W., and Kim, H. L. (2018). An introduction to immunology and immunopathology. *Allergy, Asthma and Clinical Immunology*, 14(2).

[312] Martínez González, A., Calvo, G. F., Pérez Romasanta, L. A., and Pérez García, V. M. (2012). Hypoxic cell waves around necrotic cores in glioblastoma: a biomathematical model and its therapeutic implications. *Bulletin of Mathematical Biology*, 74(12).

[313] Marusyk, A., Almendro, V., and Polyak, K. (2012). Intra-tumour heterogeneity: a looking glass for cancer? *Nature Reviews Cancer*, 12(5).

[314] Matzavinos, A. (2004). Mathematical modelling of the spatio-temporal response of cytotoxic T-lymphocytes to a solid tumour. *Mathematical Medicine and Biology*, 21(1).

[315] Matzavinos, A. and Chaplain, M. A. J. (2004). Travelling-wave analysis of a model of the immune response to cancer. *Comptes Rendus Biologies*, 327(11).

[316] McDougall, S. R., Anderson, A. R. A., and Chaplain, M. A. J. (2006). Mathematical modelling of dynamic adaptive tumour-induced angiogenesis: clinical implications and therapeutic targeting strategies. *Journal of Theoretical Biology*, 241(3).

[317] McDougall, S. R., Anderson, A. R. A., Chaplain, M. a. J., and Sherratt, J. A. (2002). Mathematical modelling of flow through vascular networks: implications for tumour-induced angiogenesis and chemotherapy strategies. *Bulletin of Mathematical Biology*, 64(4).

[318] McElwain, D. L. S. and Morris, L. E. (1978). Apoptosis as a volume loss mechanism in mathematical models of solid tumor growth. *Mathematical Biosciences*, 39(1).

[319] McElwain, D. L. S. and Ponzo, P. J. (1977). A model for the growth of a solid tumor with non-uniform oxygen consumption. *Mathematical Biosciences*, 35(3).

[320] McKeown, S. R. (2014). Defining normoxia, physoxia and hypoxia in tumours-implications for treatment response. *The British Journal of Radiology*, 87(1035).

[321] Metzcar, J., Wang, Y., Heiland, R., and Macklin, P. (2019). A review of cell-based computational modeling in cancer biology. *JCO Clinical Cancer Informatics*, 3.

[322] Minata, M., Audia, A., Shi, J., Lu, S., Bernstock, J., Pavlyukov, M. S., Das, A., Kim, S. H., Shin, Y. J., Lee, Y., Koo, H., Snigdha, K., Waghmare, I., Guo, X., Mohyeldin, A., Gallego Perez, D., Wang, J., Chen, D., Cheng, P., Mukheef, F., Contreras, M., Reyes, J. F., Vaillant, B., Sulman, E. P., Cheng, S. Y., Markert, J. M., Tannous, B. A., Lu, X., Kango Singh, M., Lee, L. J., Nam, D. H., Nakano, I., and Bhat, K. P. (2019). Phenotypic plasticity of invasive edge glioma stem-like cells in response to ionizing radiation. *Cell reports*, 26(7).

[323] Mirrahimi, S. and Perthame, B. (2015). Asymptotic analysis of a selection model with space. *Journal de Mathématiques Pures et Appliquées*, 104(6).

[324] Mooney, S. M., Jolly, M. K., Levine, H., and Kulkarni, P. (2016). Phenotypic plasticity in prostate cancer: role of intrinsically disordered proteins. *Asian Journal of Andrology*, 18(5).

[325] Moreira, J. and Deutsch, A. (2002). Cellular automaton models of tumor development: a critical review. *Advances in Complex Systems*, 05(02n03).

[326] Morselli, D., Delitala, M. E., and Frascoli, F. (2023). Agent-based and continuum models for spatial dynamics of infection by oncolytic viruses. *Bulletin of Mathematical Biology*, 85(10).

[327] Mpekris, F., Baish, J. W., Stylianopoulos, T., and Jain, R. K. (2017). Role of vascular normalization in benefit from metronomic chemotherapy. *Proceedings of the National Academy of Science*, 114.

[328] Mueller Klieser, W. F. and Sutherland, R. M. (1984). Oxygen consumption and oxygen diffusion properties of multicellular spheroids from two different cell lines. *Advances in experimental medicine and biology*, 180.

[329] Mullen, J. T. and Tanabe, K. K. (2002). Viral oncolysis. *The Oncologist*, 7(2).

[330] Munoz, A. I. and Tello, J. I. (2017). On a mathematical model of bone marrow metastatic niche. *Mathematical Biosciences and Engineering*, 14(1).

[331] Murray, J. D. . L. (1989). *Mathematical biology*. Springer, Berlin, first edition edition.

[332] Murray, P. J., Edwards, C. M., Tindall, M. J., and Maini, P. K. (2009). From a discrete to a continuum model of cell dynamics in one dimension. *Physical Review. E, Statistical, Nonlinear, and Soft Matter Physics*, 80(3 Pt 1).

[333] Najm, F., Ahmed, M., Yafia, R., Aziz Alaoui, M. A., and Boukrim, L. (2023). Hopf bifurcation and normal form in a delayed oncolytic model. *International Journal of Biomathematics*.

[334] Nanda, S., Moore, H., and Lenhart, S. (2007). Optimal control of treatment in a mathematical model of chronic myelogenous leukemia. *Mathematical Biosciences*, 210(1).

[335] Nawaz, S., Trahearn, N. A., Heindl, A., Banerjee, S., Maley, C. C., Sottoriva, A., and Yuan, Y. (2019). Analysis of tumour ecological balance reveals resource-dependent adaptive strategies of ovarian cancer. *EBioMedicine*, 48.

[336] Newman, W. I. (1980). Some exact solutions to a non-linear diffusion problem in population genetics and combustion. *Journal of Theoretical Biology*, 85(2).

[337] Nieto, M. A., Huang, R. Y. J., Jackson, R. A., and Thiery, J. P. (2016). EMT: 2016. *Cell*, 166(1).

[338] Nordmann, S. and Perthame, B. (2021). Dynamics of concentration in a population structured by age and a phenotypic trait with mutations. convergence of the corrector. *Journal of Differential Equations*, 290.

[339] Norton, K. A., Jin, K., and Popel, A. S. (2018). Modeling triple-negative breast cancer heterogeneity: effects of stromal macrophages, fibroblasts and tumor vasculature. *Journal of Theoretical Biology*, 452.

[340] Norton, K. A., Wallace, T., Pandey, N. B., and Popel, A. S. (2017). An agent-based model of triple-negative breast cancer: the interplay between chemokine receptor CCR5 expression, cancer stem cells, and hypoxia. *BMC Systems Biology*, 11(1).

[341] Novozhilov, A. S. (2008). On the spread of epidemics in a closed heterogeneous population. *Mathematical biosciences*, 215(2).

[342] Novozhilov, A. S., Berezovskaya, F. S., Koonin, E. V., and Karev, G. P. (2006). Mathematical modeling of tumor therapy with oncolytic viruses: regimes with complete tumor elimination within the framework of deterministic models. *Biology Direct*, 1(1).

[343] O'Brien, C. A., Pollett, A., Gallinger, S., and Dick, J. E. (2007). A human colon cancer cell capable of initiating tumour growth in immunodeficient mice. *Nature*, 445(7123).

[344] Ocaña Tienda, B., León Triana, O., Pérez Beteta, J., Jiménez Sánchez, J., and Pérez García, V. M. (2024). Radiation necrosis after radiation therapy treatment of brain metastases: a computational approach. *PLOS Computational Biology*, 20(1).

[345] Ocaña Tienda, B., Pérez Beteta, J., Jiménez Sánchez, J., Molina García, D., Ortiz de Mendivil, A., Asenjo, B., Albillo, D., Pérez Romasanta, L. A., Valiente, M., Zhu, L., García Gómez, P., González Del Portillo, E., Llorente, M., Carballo, N., Arana, E., and Pérez García, V. M. (2023). Growth exponents reflect evolutionary processes and treatment response in brain metastases. *npj Systems Biology and Applications*, 9(1).

[346] Oraiopoulou, M. E., Tzamali, E., Tzedakis, G., Vakis, A., Papamatheakis, J., and Sakkalis, V. (2017). In vitro/in silico study on the role of doubling time heterogeneity among primary glioblastoma cell lines. *BioMed Research International*, 2017.

[347] Osojnik, A., Gaffney, E. A., Davies, M., Yates, J. W. T., and Byrne, H. M. (2020). Identifying and characterising the impact of excitability in a mathematical model of tumour-immune interactions. *Journal of Theoretical Biology*, 501.

[348] Otto, A. M. (2016). Warburg effect(s) — a biographical sketch of Otto Warburg and his impacts on tumor metabolism. *Cancer and Metabolism*, 4(1).

[349] O'Donnell, J. S., Teng, M. W. L., and Smyth, M. J. (2019). Cancer immunoediting and resistance to T cell-based immunotherapy. *Nature Reviews Clinical Oncology*, 16(3).

[350] Page, L. T. (2024). Cell cycle. https://theory.labster.com/cell-cycle-hs/.

[351] Peinado, H., Ballestar, E., Esteller, M., and Cano, A. (2004). Snail mediates E-cadherin repression by the recruitment of the Sin3A/histone deacetylase 1 (HDAC1)/HDAC2 complex. *Molecular and cellular biology*.

[352] Penington, C. J., Hughes, B. D., and Landman, K. A. (2011). Building macroscale models from microscale probabilistic models: a general probabilistic approach for nonlinear diffusion and multispecies phenomena. *Physical Review E*, 84(4).

[353] Perthame, B. (2004). Mathematical tools for kinetic equations. *Bulletin of the American Mathematical Society*, 41(2).

[354] Perthame, B. (2006). *Transport equations in biology*. Springer Science and Business Media.

[355] Perthame, B. (2015). *Parabolic equations in biology*. Springer.

[356] Perthame, B., Vauchelet, N., and Wang, Z. (2019). The flux limited Keller–Segel system; properties and derivation from kinetic equations. *Revista matemática iberoamericana*, 36(2).

[357] Philippi, T. and Seger, J. (1989). Hedging one's evolutionary bets, revisited. *Trends in Ecology and Evolution*, 4(2).

[358] Pin, R. H., Reinblatt, M., and Fong, Y. (2004). Employing tumor hypoxia to enhance oncolytic viral therapy in breast cancer. *Surgery*, 136(2).

[359] Pittman, R. N. (2011). Regulation of tissue oxygenation. *Colloquium Series on Integrated Systems Physiology: From Molecule to Function*, 3(3).

[360] Plate, K. H., Breier, G., Weich, H. A., and Risau, W. (1992). Vascular endothelial growth factor is a potential tumour angiogenesis factor in human gliomas in vivo. *Nature*, 359(6398).

[361] Poleszczuk, J., Hahnfeldt, P., and Enderling, H. (2015). Evolution and phenotypic selection of cancer stem cells. *PLoS computational biology*, 11(3).

[362] Poleszczuk, J., Macklin, P., and Enderling, H. (2016). Agent-based modeling of cancer stem cell driven solid tumor growth. *Methods in molecular biology (Clifton, N.J.)*, 1516.

[363] Poleszczuk, J., Walker, R., Moros, E. G., Latifi, K., Caudell, J. J., and Enderling, H. (2018). Predicting patient-specific radiotherapy protocols based on mathematical model choice for proliferation saturation index. *Bulletin of Mathematical Biology*, 80(5).

[364] Polireddy, K. and Chen, Q. (2016). Cancer of the pancreas: molecular pathways and current advancement in treatment. *Journal of Cancer*, 7.

[365] Pollheimer, M. J., Kornprat, P., Lindtner, R. A., Harbaum, L., Schlemmer, A., Rehak, P., and Langner, C. (2010). Tumor necrosis is a new promising prognostic factor in colorectal cancer. *Human Pathology*, 41(12).

[366] Pooladvand, P., Yun, C. O., Yoon, A. R., Kim, P. S., and Frascoli, F. (2021). The role of viral infectivity in oncolytic virotherapy outcomes: a mathematical study. *Mathematical Biosciences*, 334.

[367] Poser, I., Domınguez, D., de Herreros, A. G., Varnai, A., Buettner, R., and Bosserhoff, A. K. (2001). Loss of e-cadherin expression in melanoma cells involves up-regulation of the transcriptional repressor snail. *Journal of Biological Chemistry*, 276(27).

[368] Pouchol, C., Clairambault, J., Lorz, A., and Trélat, E. (2018). Asymptotic analysis and optimal control of an integro-differential system modelling healthy and cancer cells exposed to chemotherapy. *Journal de Mathématiques Pures et Appliquées*, 116.

[369] Press, W. H., Flannery, B. P., Teukolsky, S. A., and Vetterling, W. T. (1989). *Numerical recipes in Pascal: the art of scientific computing*. Cambridge University Press, 1 edition.

[370] Preziosi, L. (2003). *Cancer modelling and simulation*. CRC Press.

[371] Pérez García, V. M., Calvo, G. F., Bosque, J. J., León Triana, O., Jiménez, J., Perez Beteta, J., Belmonte Beitia, J., Valiente, M., Zhu, L., García Gómez, P., Sánchez Gómez, P., Hernández San Miguel, E., Hortigüela, R., Azimzade, Y., Molina García, D., Martinez, \., Rojas, \. A., de Mendivil, A. O., Vallette, F., Schucht, P., Murek, M., Pérez Cano, M., Albillo, D., Honguero Martínez, A. F., Jiménez Londoño, G. A., Arana, E., and García Vicente, A. M. (2020). Universal scaling laws rule explosive growth in human cancers. *Nature physics*, 16(12).

[372] Qu, X., Tang, Y., and Hua, S. (2018). Immunological approaches towards cancer and inflammation: a cross talk. *Frontiers in Immunology*, 9.

[373] Quaranta, V., Weaver, A. M., Cummings, P. T., and Anderson, A. R. A. (2005). Mathematical modeling of cancer: the future of prognosis and treatment. *Clinica Chimica Acta*, 357(2).

[374] Rajalakshmi, M. and Ghosh, M. (2022). Hopf-bifurcation analysis of a delayed model for the treatment of cancer using virotherapy. *Kyungpook Mathematical Journal*, 62(1).

[375] Rajman, L., Chwalek, K., and Sinclair, D. A. (2018). Therapeutic potential of NAD-boosting molecules: the in vivo evidence. *Cell Metabolism*, 27(3).

[376] Rakotomalala, A., Escande, A., Furlan, A., Meignan, S., and Lartigau, E. (2021). Hypoxia in solid tumors: how low oxygenation impacts the "six Rs" of radiotherapy. *Frontiers in Endocrinology*, 12.

[377] Ramaj, T. and Zou, X. (2023). On the treatment of melanoma: a mathematical model of oncolytic virotherapy. *Mathematical Biosciences*, 365.

[378] Rentzeperis, F. and Wallace, D. (2022). Local and global sensitivity analysis of spheroid and xenograft models of the acid-mediated development of tumor malignancy. *Applied Mathematical Modelling*, 109.

[379] Ribatti, D., Tamma, R., and Annese, T. (2020). Epithelial-mesenchymal transition in cancer: a historical overview. *Translational Oncology*, 13(6).

[380] Rocha, H. L., Godet, I., Kurtoglu, F., Metzcar, J., Konstantinopoulos, K., Bhoyar, S., Gilkes, D. M., and Macklin, P. (2021). A persistent invasive phenotype in post-hypoxic tumor cells is revealed by fate mapping and computational modeling. *iScience*, 24(9).

[381] Rockwell, S., Dobrucki, I. T., Kim, E. Y., Marrison, S. T., and Vu, V. T. (2009). Hypoxia and radiation therapy: past history, ongoing research, and future promise. *Current Molecular Medicine*, 9(4).

[382] Roesch, A. (2015). Tumor heterogeneity and plasticity as elusive drivers for resistance to MAPK pathway inhibition in melanoma. *Oncogene*, 34(23).

[383] Roose, T., Chapman, S. J., and Maini, P. K. (2007). Mathematical models of avascular tumor growth. *SIAM Review*, 49(2).

[384] Rosenberg, S. A., Yang, J. C., Sherry, R. M., Kammula, U. S., Hughes, M. S., Phan, G. Q., Citrin, D. E., Restifo, N. P., Robbins, P. F., Wunderlich, J. R., Morton, K. E., Laurencot, C. M., Steinberg, S. M., White, D. E., and Dudley, M. E. (2011). Durable complete responses in heavily pretreated patients with metastatic melanoma using t-cell transfer immunotherapy. *Clinical Cancer Research: An Official Journal of the American Association for Cancer Research*, 17(13).

[385] Roy, H. K., Smyrk, T. C., Koetsier, J., Victor, T. A., and Wali, R. K. (2005). The transcriptional repressor snail is overexpressed in human colon cancer. *Digestive diseases and sciences*, 50.

[386] Ruan, K., Song, G., and Ouyang, G. (2009). Role of hypoxia in the hallmarks of human cancer. *Journal of Cellular Biochemistry*, 107(6).

[387] Russell, L., Peng, K. W., Russell, S. J., and Diaz, R. M. (2019). Oncolytic viruses: priming time for cancer immunotherapy. *BioDrugs: Clinical Immunotherapeutics, Biopharmaceuticals and Gene Therapy*, 33(5).

[388] Russell, S. J., Peng, K. W., and Bell, J. C. (2012). Oncolytic virotherapy. *Nature Biotechnology*, 30(7).

[389] Samanta, D. and Semenza, G. L. (2018). Metabolic adaptation of cancer and immune cells mediated by hypoxia-inducible factors. *Biochimica et Biophysica Acta (BBA)-Reviews on Cancer*, 1870(1).

[390] Santos Apolonio, J., Lima de Souza Gonçalves, V., Cordeiro Santos, M. L., Silva Luz, M., Silva Souza, J. V., Rocha Pinheiro, S. L., de Souza, W. R., Sande Loureiro, M., and de Melo, F. F. (2021). Oncolytic virus therapy in cancer: a current review. *World Journal of Virology*, 10(5).

[391] Schmitz, J. E., Kansal, A. R., and Torquato, S. (2002). A cellular automaton model of brain tumor treatment and resistance. *Journal of Theoretical Medicine*, 4(4).

[392] Scianna, M. and Colombi, A. (2017). A coherent modeling procedure to describe cell activation in biological systems. *Communications in Applied and Industrial Mathematics*, 8(1).

[393] Scianna, M. and Preziosi, L. (2012). Multiscale developments of the cellular Potts model. *Multiscale Modeling and Simulation*, 10(2).

[394] Scianna, M. and Preziosi, L. (2014). A cellular Potts model for the MMP-dependent and -independent cancer cell migration in matrix microtracks of different dimensions. *Computational Mechanics*, 53(3).

[395] Scianna, M., Preziosi, L., and Wolf, K. (2013). A cellular Potts model simulating cell migration on and in matrix environments. *Mathematical Biosciences and Engineering*, 10(1).

[396] Seevinck, M. P. (2004). Holism, physical theories and quantum mechanics. *Studies in History and Philosophy of Science Part B: Studies in History and Philosophy of Modern Physics*, 35(4).

[397] Sehl, M. E. and Wicha, M. S. (2018). Modeling of interactions between cancer stem cells and their microenvironment: predicting clinical response. *Methods in molecular biology (Clifton, N.J.)*, 1711.

[398] Seidi, K., Jahanban Esfahlan, R., and Zarghami, N. (2017). Tumor rim cells: from resistance to vascular targeting agents to complete tumor ablation. *Tumor Biology*, 39(3).

[399] Shariatpanahi, S. P., Shariatpanahi, S. P., Madjidzadeh, K., Hassan, M., and Abedi Valugerdi, M. (2018). Mathematical modeling of tumor-induced immunosuppression by myeloid-derived suppressor cells: implications for therapeutic targeting strategies. *Journal of Theoretical Biology*, 442.

[400] Shashni, B., Ariyasu, S., Takeda, R., Suzuki, T., Shiina, S., Akimoto, K., Maeda, T., Aikawa, N., Abe, R., Osaki, T., Itoh, N., and Aoki, S. (2018). Size-based differentiation of cancer and normal cells by a particle size analyzer assisted by a cell-recognition pc software. *Biological and Pharmaceutical Bulletin*, 41(4).

[401] Sherratt, J. and Chaplain, M. (2001). A new mathematical model for avascular tumour growth. *Journal of mathematical biology*, 43.

[402] Shield, K., Ackland, M. L., Ahmed, N., and Rice, G. E. (2009). Multicellular spheroids in ovarian cancer metastases: biology and pathology. *Gynecologic Oncology*, 113(1).

[403] Shirinifard, A., Gens, J. S., Zaitlen, B. L., Popławski, N. J., Swat, M., and Glazier, J. A. (2009). 3d multi-cell simulation of tumor growth and angiogenesis. *PloS One*, 4(10).

[404] Shymko, R. M. and Glass, L. (1976). Cellular and geometric control of tissue growth and mitotic instability. *Journal of Theoretical Biology*, 63(2).

[405] Simonič, A. (1996). A construction of Lomonosov functions and applications to the invariant subspace problem. *Pacific Journal of Mathematics*, 175(1).

[406] Singh, S. K., Hawkins, C., Clarke, I. D., Squire, J. A., Bayani, J., Hide, T., Henkelman, R. M., Cusimano, M. D., and Dirks, P. B. (2004). Identification of human brain tumour initiating cells. *Nature*, 432(7015).

[407] Skobe, M. and Fusenig, N. E. (1998). Tumorigenic conversion of immortal human keratinocytes through stromal cell activation. *Proceedings of the National Academy of Sciences of the United States of America*, 95(3).

[408] Slack, J. M. W. and Dale, L. (2021). *Essential developmental biology*. Wiley, 4th edition edition.

[409] Smallbone, K., Gatenby, R. A., Gillies, R. J., Maini, P. K., and Gavaghan, D. J. (2007). Metabolic changes during carcinogenesis: potential impact on invasiveness. *Journal of Theoretical Biology*, 244(4).

[410] Smolle, J. and Stettner, H. (1993). Computer simulation of tumour cell invasion by a stochastic growth model. *Journal of Theoretical Biology*, 160(1).

[411] Sonnenschein, C., Soto, A. M., Rangarajan, A., and Kulkarni, P. (2014). Competing views on cancer. *Journal of biosciences*, 39(2).

[412] Soto, A. M. and Sonnenschein, C. (2011). The tissue organization field theory of cancer: a testable replacement for the somatic mutation theory. *BioEssays : news and reviews in molecular, cellular and developmental biology*, 33(5).

[413] Sottoriva, A., Sloot, P., Medema, J. P., and Vermeulen, L. (2010). Exploring cancer stem cell niche directed tumor growth. *Cell Cycle*, 9.

[414] Sporn, M. B. (1996). The war on cancer. *Lancet (London, England)*, 347(9012).

[415] Stein, A. M., Demuth, T., Mobley, D., Berens, M., and Sander, L. M. (2007). A mathematical model of glioblastoma tumor spheroid invasion in a three-dimensional in vitro experiment. *Biophysical Journal*, 92(1).

[416] Stiehl, T., Baran, N., Ho, A. D., and Marciniak Czochra, A. (2014). Clonal selection and therapy resistance in acute leukaemias: mathematical modelling explains different proliferation patterns at diagnosis and relapse. *Journal of The Royal Society Interface*, 11(94).

[417] Stiehl, T., Baran, N., Ho, A. D., and Marciniak Czochra, A. (2015). Cell division patterns in acute myeloid leukemia stem-like cells determine clinical course: a model to predict patient survival. *Cancer Research*, 75(6).

[418] Strobl, M. A. R., Krause, A. L., Damaghi, M., Gillies, R., Anderson, A. R. A., and Maini, P. K. (2020). Mix and match: phenotypic coexistence as a key facilitator of cancer invasion. *Bulletin of Mathematical Biology*, 82(1).

[419] Stylianopoulos, T. and Jain, R. K. (2013). Combining two strategies to improve perfusion and drug delivery in solid tumors. *Proceedings of the National Academy of Sciences of the United States of America*, 110(46).

[420] Szabó, A. and Merks, R. M. H. (2013). Cellular Potts modeling of tumor growth, tumor invasion, and tumor evolution - pubmed.

[421] Szymańska, Z., Cytowski, M., Mitchell, E., Macnamara, C. K., and Chaplain, M. A. J. (2018). Computational modelling of cancer development and growth: modelling at multiple scales and multiscale modelling. *Bulletin of Mathematical Biology*, 80(5).

[422] Thieme, H. R. (1991). Analysis of age-structured population models with an additional structure. In *Mathematical population dynamics*. CRC Press.

[423] Thieme, H. R. (2003). *Mathematics in population biology*. Princeton University Press.

[424] Torres, C. M., Biran, A., Burney, M. J., Patel, H., Henser Brownhill, T., Cohen, A. H. S., Li, Y., Ben Hamo, R., Nye, E., Spencer Dene, B., Chakravarty, P., Efroni, S., Matthews, N., Misteli, T., Meshorer, E., and Scaffidi, P. (2016). The linker histone H1.0 generates epigenetic and functional intratumor heterogeneity. *Science (New York, N.Y.)*, 353(6307).

[425] Tripathi, S., Xing, J., Levine, H., and Jolly, M. K. (2021). Mathematical modeling of plasticity and heterogeneity in EMT. In *The epithelial-to mesenchymal transition*. Springer.

[426] Trucu, D., Domschke, P., Gerisch, A., and Chaplain, M. (2016). Multiscale computational modelling and analysis of cancer invasion. In Preziosi, L., Ciarletta, P., Hillen, T., Chaplain, M., Pugliese, A., Othmer, H., and Truccu, D., editors, *Mathematical models and methods for living systems*, C.I.M.E. Foundation Subseries. Springer International Publishing.

[427] Tucker, S. L. and Thames, H. D. (1989). The effect of patient-to-patient variability on the accuracy of predictive assays of tumor response to radiotherapy: a theoretical evaluation. *International Journal of Radiation Oncology, Biology, Physics*, 17(1).

[428] Turner, S. and Sherratt, J. A. (2002). Intercellular adhesion and cancer invasion: a discrete simulation using the extended Potts model. *Journal of Theoretical Biology*, 216(1).

[429] Tähtinen, S., Grönberg Vähä Koskela, S., Lumen, D., Merisalo Soikkeli, M., Siurala, M., Airaksinen, A. J., Vähä Koskela, M., and Hemminki, A. (2015). Adenovirus improves the efficacy of adoptive t-cell therapy by recruiting immune cells to and promoting their activity at the tumor. *Cancer Immunology Research*, 3(8).

[430] Van Leeuwen, C., Oei, A., Crezee, J., Bel, A., Franken, N., Stalpers, L., and Kok, H. (2018). The alfa and beta of tumours: a review of parameters of the linear-quadratic model, derived from clinical radiotherapy studies. *Radiation Oncology*, 13(96).

[431] van Leeuwen, C. M., Oei, A. L., Crezee, J., Bel, A., Franken, N. a. P., Stalpers, L. J. A., and Kok, H. P. (2018). The alfa and beta of tumours: a review of parameters of the linear-quadratic model, derived from clinical radiotherapy studies. *Radiation Oncology*, 13(1).

[432] Vander Heiden, M. G., Cantley, L. C., and Thompson, C. B. (2009). Understanding the Warburg effect: the metabolic requirements of cell proliferation. *Science*, 324(5930).

[433] Varga, J., De Oliveira, T., and Greten, F. R. (2014). The architect who never sleeps: tumor-induced plasticity. *FEBS letters*, 588(15).

[434] Vaupel, P., Thews, O., and Hoeckel, M. (2001). Treatment resistance of solid tumors: role of hypoxia and anemia. *Medical Oncology*, 18(4).

[435] Veliov, V. M. and Widder, A. (2016). Aggregation and asymptotic analysis of an SI-epidemic model for heterogeneous populations. *Mathematical Medicine and Biology: a journal of the IMA*, 33(3).

[436] Villa, C., Chaplain, M. A., and Lorenzi, T. (2021a). Modeling the emergence of phenotypic heterogeneity in vascularized tumors. *SIAM Journal on Applied Mathematics*, 81(2).

[437] Villa, C., Chaplain, M. A. J., and Lorenzi, T. (2021b). Evolutionary dynamics in vascularised tumours under chemotherapy: mathematical modelling, asymptotic analysis and numerical simulations. *Vietnam Journal of Mathematics*, 49(1).

[438] Vittadello, S. T., McCue, S. W., Gunasingh, G., Haass, N. K., and Simpson, M. J. (2020). Examining go-or-grow using fluorescent cell-cycle indicators and cell-cycle-inhibiting drugs. *Biophysical Journal*, 118(6).

[439] Voutouri, C., Kirkpatrick, N. D., Chung, E., Mpekris, F., Baish, J. W., Munn, L. L., Fukumura, D., Stylianopoulos, T., and Jain, R. K. (2019). Experimental and computational analyses reveal dynamics of tumor vessel cooption and optimal treatment strategies. *Proceedings of the National Academy of Sciences*, 116(7).

[440] Wagner, B. A., Venkataraman, S., and Buettner, G. R. (2011). The rate of oxygen utilization by cells. *Free Radical Biology and Medicine*, 51(3).

[441] Wang, L., Geng, H., Liu, Y., Liu, L., Chen, Y., Wu, F., Liu, Z., Ling, S., Wang, Y., and Zhou, L. (2023). Hot and cold tumors: immunological features and the therapeutic strategies. *MedComm*, 4(5).

[442] Wang, Y., Tian, J. P., and Wei, J. (2013). Lytic cycle: a defining process in oncolytic virotherapy. *Applied Mathematical Modelling*, 37(8).

[443] Wang, Y. L., Zhao, X. M., Shuai, Z. F., Li, C. Y., Bai, Q. Y., Yu, X. W., and Wen, Q. T. (2015). Snail promotes epithelial-mesenchymal transition and invasiveness in human ovarian cancer cells. *International journal of clinical and experimental medicine*, 8(5).

[444] Wang, Z., Guo, Z., and Smith, H. (2019). A mathematical model of oncolytic virotherapy with time delay. *Mathematical Biosciences and Engineering*, 16(4).

[445] Weber, T. S., Jaehnert, I., Schichor, C., Or Guil, M., and Carneiro, J. (2014). Quantifying the length and variance of the eukaryotic cell cycle phases by a stochastic model and dual nucleoside pulse labelling. *PLoS computational biology*, 10(7).

[446] Weerasinghe, H. N., Burrage, P. M., Burrage, K., and Nicolau, D. V. (2019). Mathematical models of cancer cell plasticity. *Journal of Oncology*, 2019.

[447] Williams, C. K., Li, J. L., Murga, M., Harris, A. L., and Tosato, G. (2006). Up-regulation of the Notch ligand Delta-like 4 inhibits VEGF-induced endothelial cell function. *Blood*, 107(3).

[448] Wise, S. M., Lowengrub, J. S., Frieboes, H. B., and Cristini, V. (2008). Three-dimensional multispecies nonlinear tumor growth–I model and numerical method. *Journal of Theoretical Biology*, 253(3).

[449] Wodarz, D., Hofacre, A., Lau, J. W., Sun, Z., Fan, H., and Komarova, N. L. (2012). Complex spatial dynamics of oncolytic viruses in vitro: mathematical and experimental approaches. *PLoS Computational Biology*, 8(6).

[450] Woller, N., Gürlevik, E., Fleischmann Mundt, B., Schumacher, A., Knocke, S., Kloos, A. M., Saborowski, M., Geffers, R., Manns, M. P., Wirth, T. C., Kubicka, S., and Kühnel, F. (2015). Viral infection of tumors overcomes resistance to pd-1-immunotherapy by broadening neoantigenome-directed T-cell responses. *Molecular Therapy: The Journal of the American Society of Gene Therapy*, 23(10).

[451] Workenhe, S. T., Simmons, G., Pol, J. G., Lichty, B. D., Halford, W. P., and Mossman, K. L. (2014). Immunogenic HSV-mediated oncolysis shapes the antitumor immune response and contributes to therapeutic efficacy. *Molecular Therapy*, 22(1).

[452] Wu, J. T., Byrne, H. M., Kirn, D. H., and Wein, L. M. (2001). Modeling and analysis of a virus that replicates selectively in tumor cells. *Bulletin of Mathematical Biology*, 63(4).

[453] Wu, J. T., Kirn, D. H., and Wein, L. M. (2004). Analysis of a three-way race between tumor growth, a replication-competent virus and an immune response. *Bulletin of Mathematical Biology*, 66(4).

[454] Wyllie, A. H., Kerr, J. F., and Currie, A. R. (1980). Cell death: the significance of apoptosis. *International Review of Cytology*, 68.

[455] Xin, Y., Li, K., Huang, M., Liang, C., Siemann, D., Wu, L., Tan, Y., and Tang, X. (2023). Biophysics in tumor growth and progression: from single mechano-sensitive molecules to mechanomedicine. *Oncogene*, 42(47).

[456] Xu, S. (2020). Analysis of a free boundary problem for tumor growth with angiogenesis and time delays in proliferation. *Nonlinear Analysis: Real World Applications*, 51.

[457] Xu, S. H. and Wu, J. d. (2019). Qualitative analysis of a time-delayed free boundary problem for tumor growth with angiogenesis and Gibbs-Thomson relation. *Mathematical Biosciences and Engineering*, 16(6).

[458] Yehya, A. H. S., Asif, M., Petersen, S. H., Subramaniam, A. V., Kono, K., Majid, A. M. S. A., and Oon, C. E. (2018). Angiogenesis: managing the culprits behind tumorigenesis and metastasis. *Medicina*, 54(1).

[459] Yu, L. X., Zhou, L., Li, M., Li, Z. W., Wang, D. S., and Zhang, S. G. (2013). The Notch1/cyclooxygenase-2/Snail/E-cadherin pathway is associated with hypoxia-induced hepatocellular carcinoma cell invasion and migration. *Oncology Reports*, 29(1).

[460] Yuan, S., Norgard, R. J., and Stanger, B. Z. (2019). Cellular plasticity in cancer. *Cancer Discovery*, 9(7).

[461] Zayed, A. I. (2019). A new perspective on the role of mathematics in medicine. *Journal of Advanced Research*, 17.

[462] Zhang, D., Tang, D. G., and Rycaj, K. (2018). Cancer stem cells: regulation programs, immunological properties and immunotherapy. *Seminars in Cancer Biology*, 52.

[463] Zheng, P. P., Severijnen, L. A., van der Weiden, M., Willemsen, R., and Kros, J. M. (2009). Cell proliferation and migration are mutually exclusive cellular phenomena in vivo: implications for cancer therapeutic strategies. *Cell Cycle*, 8(6).

[464] Zhigun, A. and Surulescu, C. (2022). A novel derivation of rigorous macroscopic limits from a micro-meso description of signal-triggered cell migration in fibrous environments. *SIAM Journal on Applied Mathematics*, 82(1).

[465] Zhu, G. H., Huang, C., Feng, Z. Z., Lv, X. H., and Qiu, Z. J. (2013). Hypoxia-induced snail expression through transcriptional regulation by HIF-1α in pancreatic cancer cells. *Digestive diseases and sciences*, 58.